THE NEOTECTONICS OF THE SAN BERNARDINO MOUNTAINS AND ADJACENT SAN ANDREAS FAULT: A CASE STUDY OF UPLIFT ASSOCIATED WITH STRIKE-SLIP FAULT SYSTEMS

Thesis by

James A. Spotila

In Partial Fulfillment of the Requirements

for the Degree of

Doctor of Philosophy

California Institute of Technology

Pasadena, California

1999

(Submitted August 27, 1998)

Dedicated to Janet Sinclair, Ralph Dittrich,

Mary Nyiri, and John Spotila.

ACKNOWLEDGMENTS

I thank Kerry Sieh for advising me as a graduate student. Kerry gave me the latitude to pursue my own research interests and did not give up on me during the unproductive first few years of San Bernardino Mountains work. What I have learned from his scientific savvy and observational skills, his defense of my presence at Caltech, and the financial support he helped acquire have been critical to this thesis. I thank Ken Farley for working with me on the helium dating project, which arguably was the most exciting part of my thesis research. Ken has also taught me a great deal about analytical geochemistry and scientific thought. I also extend my appreciation to my academic advisor, Brian Wernicke, who I have learned a tremendous amount from regarding tectonics and science in general. Similarly, I thank Lee Silver, whose ideas and help have been critical, as well as Rob Clayton, a member of my thesis committee.

I am particularly grateful to various individuals who have both helped me directly in my research and coursework, as well as helped to make me into a scientist through many conversations and other interactions. These include my mother and father (James R. and Loretta Spotila), Doug Yule, Slawek Tulaczyk, Mark Peters, Mihai Ducea, Des Patterson, Martha House, Andrew Meigs, Judy Zachariesen, Rob Brady, Jean Hsieh, Nathan Niemi, Elizabeth Nagy, Bob Sharp, as well as other members of the structure-tectonics research group at Caltech. Direct help in my research has also been provided by Rich Wolf (helium), Shawn Biehler (gravity), Egill Hauksson (seismicity), Peter Sadler (SBMs geology), and Tony Soeller (GIS).

I thank the Southern California Earthquake Center and National Science Foundation for funding my research for four years, despite limited resources available for geological studies that bear on regional seismic hazard and the physics of earthquake processes. I also acknowledge Caltech for providing an efficient environment conducive to the execution of hard work (*labor bonus et multus*). The Caltech experience includes interaction with top-notch graduate students, post-docs, and faculty, as well as exposure to great geological

minds of other institutions. This experience has been as important to my scientific development as course-work or research. Other aspects of Caltech, such as the outstanding academic and administrative staff (Donna Sackett, Jim O'Donnel, and others) and the *laissez faire* attitude towards research have also been very helpful.

It is also my pleasure to thank additional individuals, without whose guidance along the road of life, a dead-end surely would have obstructed this journey. These include my family (my four grandparents, Jeni and David, Loretta, Jack, Lois, Alex, Tom and Marybeth), officemates and lunch pals (Liz, Julia, John, and others), the "Sierra" Club (the Irish, TCK, Pz, Boo, Les Fructoses, Pete R.), the first-years of 1992 (Abby, Laura, Dave, and others), the Boston College geology department (especially Juliet McKenna, John Ebel, Jim Skehan, and Jamie Walker), Sean Faherty, JB, NB, SB, and VPI.

ABSTRACT

The San Bernardino Mountains have uplifted over the last few million years at the hub of structural systems along the southern San Andreas fault zone and represent an excellent opportunity to study the interplay between orogeny and transpressive strike-slip faulting. To attain a better understanding of the complex architecture of deformation in this range, I have constrained several basic kinematic aspects of its development. First, the timing and magnitude of rock uplift and exhumation of fault blocks have been constrained using the thermochronometry of radiogenic helium in apatite (Chapter 2). This has shown that small crustal slivers within the San Andreas fault zone were exhumed several kilometers over the last few million years, due to slip-partitioning along geometrically-complex, high-angle faults. Second, a detailed constraint on the vertical deformation field of the largest fault block in the range has been determined using a deeply weathered granite surface as a structural datum (Chapter 3). A structural analysis of this deformation pattern has provided the total displacements, slip rates, and subsurface geometries of the major thrust faults within the range (Chapter 4). As a whole, the San Bernardino Mountains appear to have uplifted within a complex system of both high and low-angle faults. The total horizontal plate motion accommodated by this uplift is on the order of 6 km and is focused tightly about a restraining bend in the San Andreas fault zone at San Gorgonio Pass. This suggests the entire range has been built due to convergence associated with a small geometric perturbation of a major strike-slip system.

To acquire a different perspective on the relationship of strike-slip faulting and uplift, I have also studied the deformation pattern around a restraining bend resulting from a single fault rupture. Structural analysis of surficial breaks at a slip gap during the 1992 Landers earthquake has revealed how complex, secondary thrust and normal faulting were induced to accommodate simple strike-slip motion where a through-going connection between two dextral fault segments has yet to develop (Chapter 5). This illustrates a single episode in the incremental evolution of a transpressive orogenic system.

TABLE OF CONTENTS

end = 5- 51

Total = 378 pages

Plates 1-6.....(enclosed in envelope on backside cover)

Chapter One

Introduction

Spotila, James A.

California Institute of Technology

August, 1999

One of the key building blocks for understanding continental tectonics is detailed analysis of the architecture of deformation systems. The architecture of a tectonic complex consists of the three-dimensional geometry of structural arrays and the kinematics of crustal motions within these arrays, which together explain how far-field plate motions are accommodated locally by continental deformation. Analyses of such architecture are critical for elucidating the rheologic structure of continental crust and the driving conditions of its deformation, and offer insights that help assess theories of continental dynamics (cf. Thatcher, 1995). When the focus of such analyses are actively deforming systems, this class of investigation is also useful for understanding the interaction of tectonics and surficial processes and evaluating regional seismic hazard.

Ideally, these types of study should address crustal-scale (10^1-10^3 km) structural systems at the timescales at which they function (10^1-10^9 s) and evolve (10^{13} s [Myr]). Although seismologic and geodetic studies document the kinematics and character of active deformation over short timescales, they neglect their long-term evolution. This is particularly true for strike-slip plate margins, whose long-term behavior is not generally not known. There are several basic concepts for how transcurrent systems should develop, such as the control cumulative slip has on the weakening of strike-slip faults (Wesnousky, 1988) or that strike-slip plate boundaries should widen as strain accumulates due to the viscoelastic stratification of the crust (Roy, 1998), but little direct constraint exists and uncertainty remains as to how transcurrent systems evolve. This is partly due to the poor preservation of strike-slip fault zones in the geologic record and in three-dimensions. This is also due to the complexity of active transcurrent plate boundaries, which typically consist of various interacting components and often experience significant convergence or divergence (and related vertical deformation) regardless of maturity.

Although it is a challenge to interpret the kinematic development of complex strike-slip margins, they offer the greatest potential to understand strike-slip faults in general. Plate margins that consist of many interacting components are in many ways unstable, and

thus complex strike-slip systems are constantly evolving at a rapid rate and offer a good opportunity to observe the development of such systems in action. In addition, vertical deformation is often a part of divergent and convergent transcurrent systems, which can add aspects to our understanding that are not obtainable from purely strike-slip plate boundaries. For example, studying vertical deformations incorporates the depth dimension into understanding of strike-slip systems. Vertical deformation also produces a better imprint in the geologic record. For instance, the development of a transtensional fault systems may be recorded in pull-apart basins, while that of transpressional systems may be represented by uplift of sedimentary beds or the exhumation of isotherms in crystalline rock. Transpressive systems that involve uplift are particularly useful, given that their perturbation of surficial systems is recorded in the geomorphology of the resulting orogen. The study of orogeny associated with strike-slip fault systems thus holds the potential to be very useful in continental tectonics.

The San Bernardino Mountains (SBMs) of southern California are an excellent specimen of uplift along a transpressive plate margin (the Pacific-North America margin and San Andreas fault system [Figure 1]). The size of this range (~100 km long, ~40 km wide, ~3 km relief) indicates that it has been produced by crustal-scale structures, while its age indicates that it may record several million years of transcurrent fault history (May and Repenning, 1982; Meisling and Weldon, 1989). In addition, the SBMs lie at a hub of major structural elements that comprise the complex strike-slip margin (Figure 1). The range is adjacent to the San Bernardino segment of the San Andreas fault (~25 mm/yr right-slip; Weldon and Sieh, 1985) and abuts the San Andreas' confluence with the Eastern California shear zone (~8 mm/yr right-slip; Savage et al., 1990), San Jacinto fault (~10 mm/yr right-slip; Sharp, 1981), western Transverse Ranges (~10 mm/yr shortening on thrust faults and ~6°/Myr clockwise rotation; Donnellan et al., 1993; Molnar and Gipson, 1994), and eastern Transverse Ranges (sinistral faulting and ~4°/Myr counterclockwise rotation; Carter et al., 1987). In addition, this southern stretch of the San Andreas fault is

transpressive due to its "Big Bend" and the 15-km-wide left-step in San Gorgonio Pass (Figure 1). These structural systems have been evolving and interacting over the past 4-5 million years (cf. Weldon et al., 1993) and represent the primary kinematic players in the "non-ideal transform" motion (Humphreys and Weldon, 1994) of the Pacific relative to North America at this latitude (~5 cm/yr, N38°W; DeMets, 1995).

Because the SBMs occur at the focus of this tectonic complex and are linked to the San Andreas fault system, their uplift history is a part of the poorly understood kinematic development of this strike-slip plate boundary. By constraining the kinematics and deformational architecture of a fragment of the plate margin, a greater understanding of the entire system may be attained. The SBMs offer a valuable opportunity to study how uplift and exhumation relate to convergence across strike-slip faults and the role of such transpression in the long-term (Myr) evolution of major transform systems. The purpose of this study is thus to explore the relationship of strike-slip faulting and uplift in the SBMs.

Previous studies of the neotectonics and uplift kinematics of the SBMs have delineated the major structures of the range and shown that these define a series of tectonic blocks of distinct geomorphic character (cf. Vaughan, 1922; Dibblee, 1975; Sadler, 1982; Meisling and Weldon, 1989 [Figure 2]). The SBMs consist of a broad plateau on the north (Big Bear block) that is bound by two east-west trending, gently-dipping, opposing thrusts (North Frontal thrust system [NFTS] and Santa Ana thrust [SAT]), a narrow, higher block (San Gorgonio block) to the south that may have been formed by localized warping, and a series of rugged crystalline slices that may have been mobilized within the San Andreas fault zone on the south (Yucaipa Ridge, Wilson Creek, and Morongo blocks). The relationship between this orogenic system and the strike-slip system it lies adjacent to is not well understood, however. The mechanisms by which convergence across the San Andreas fault is translated to uplift are not known, largely because the subsurface geometry of structures and kinematics of crustal blocks have not been well constrained. The

conditions driving this convergence have also not been determined, although the "Big Bend" in the San Andreas (cf. Dickinson, 1996), local geometric complexities along the strike-slip faults (cf. Dibblee, 1975), and downwelling in the mantle (cf. Hadley and Kanamori, 1977; Humphreys et al., 1984) have been proposed as causes.

To secure a better understanding of the association of uplift and strike-slip faulting in the SBMs, several basic kinematic constraints must be determined. First, the timing and magnitude of rock uplift and exhumation needs to be established for different blocks within the range. Given the lack of sedimentary deposits or other marker beds across these blocks, the pattern of rock uplift has not yet been discriminated from topographic uplift alone. Better constraints on the pattern of vertical deformation are required to learn about the subsurface geometry of block-bounding faults and their relative roles and timing in uplifting the range, which itself is required to develop an interpretive architecture that can explain how transpression has translated to convergent deformation. Absolute age constraints on deformation, as well as interpretations of the geomorphic development of the range, are also necessary to understand the long-term evolution of structures in the SBMs. In addition, 5total horizontal shortening (i.e., plate motion) accommodated by convergent structures in the SBMs, as well as its variation across the range, must be constrained to test hypotheses for the origin of convergence and uplift. Until such a kinematic understanding of the SBMs is secured, the relationship of strike-slip and orogeny will remain obscured and our ability to characterize seismogenic sources in the region will be hindered. This is unacceptable given the likelihood that the next great (M8) earthquake on the San Andreas fault will occur along the flank of the SBMs (Stein et al., 1992; Sykes and Seeber, 1985).

This investigation consists of three individual studies concerned with constraining aspects of orogeny and strike-slip faulting in the SBMs. Each of these was conceived by isolating the most glaring kinematic unknowns and applying methods previously unused in the SBMs that offered the best chance to acquire new, useful neotectonic constraints. The first study was designed to determine the timing and magnitude of rock uplift and

exhumation in the southern SBMs, where no previous constraint existed, with the hopes of learning more about the direct role the San Andreas fault zone has played in orogeny. This study utilized the recently-developed method of radiogenic helium thermochronometry and revealed exciting new constraints on the uplift kinematics of the range. The second component was driven by the need for a structural datum across the range that could constrain the pattern of vertical deformation, which in turn could be used to learn about the structures responsible for uplift and to calculate the horizontal plate motions accommodated. This study consists of a detailed geomorphic analysis of a low-relief, deeply weathered granitic surface (Oberlander, 1972; Meisling, 1984) that investigates its potential as a marker horizon and results in an understanding of its origins that enables detailed reconstruction of the pattern of rock uplift associated with construction of the SBMs. Equipped with this structural datum, the final segment of this investigation of the SBMs pursues an understanding of the kinematics of low-angle structures responsible for uplift. Detailed analysis of fault activity, analysis of subsurface fault geometry in cross sections, and calculation of horizontal shortening accommodated across the SBMs all advance understanding of the architecture of deformation and the causes of convergence in the SBMs.

In addition to these studies of uplift of the SBMs, the final chapter of this thesis consists of an investigation of uplift and deformation in a restraining bend during a single strike-slip fault rupture. The 1992 Landers, California, earthquake (M7.3) provided an unprecedented opportunity to study how strike-slip faulting translates to secondary contraction when fault stepovers are encountered by propagating ruptures. This study provides a case example of the architecture of secondary deformation and uplift induced by gaps in strike-slip rupture, in addition to providing a snap-shot in the development of a new, through-going connecting between fault segments of the Eastern California shear zone. Although this study does not fit directly into the broad study of uplift of the SBMs,

it does address the theme of the relationship of orogeny and strike-slip faulting and was completed as a portion of my graduate research at Caltech, and has thus been included.

Because this thesis consists of four separate studies, I have written each chapter as an independent component that can be digested individually. Each chapter is thus furnished with its own abstract, introduction, conclusions, and references, and some duplication of information may occur. Two of these chapters (2 and 5) have been published as manuscripts in referee-reviewed journals and are reprinted here in their original form. The other two entities have not yet been published and are thus more explorative, detailed, and prolix, but will be polished and submitted for publication in the near future. For convenience, figures are ordered at the end of Chapters 2, 4, and 5, but the size of Chapter 3 demanded that figures be incorporated into the text.

References cited

Carter, J.N., Luyendyk, B.P., and Terres, R.R., Neogene clockwise rotation of the eastern Transverse Ranges, California, suggested by paleomagnetic vectors, Geol. Soc. Amer. Bull., 98, 199-206, 1987.

DeMets, C., Reappraisal of seafloor spreading lineations in the Gulf of California: Implications for the transfer of Baja California to the Pacific Plate and estimates of Pacific-North America motion, Geophys. Res. Lett., 22, 3545-3548, 1995.

Dibblee, T.W., Late Quaternary uplift of the San Bernardino Mountains on the San Andreas and related faults, *in* Crowell, J.C., ed., San Andreas fault in southern California, CA Division of Mines and Geology Special Report, 118, 127-135, 1975.

Dickinson, W.R., Kinematics of transrotational tectonism in the California Transverse Ranges and its contribution to cumulative slip along the San Andreas transform fault system, Geol. Soc. Amer. Spec. Paper, 305, 46 p., 1996.

Donnellan, A., Hager, B.H., King, R.W., and Herring, T.A., Geodetic measurement of

deformation in the Ventura-Basin-region, southern California, J. Geophys. Res., 98, 21727-21739, 1993.

Hadley, D.M., and Kanamori, H., Seismic structure of the Transverse Ranges, California, Geol. Soc. Amer. Bull., 88, 1469-1478, 1977.

Humphreys, E., Clayton, R., and Hager, B.H., A tomographic image of mantle structure beneath southern California, Geophys. Res. Lett., 11, 625-627, 1984.

Humphreys, E.D., and Weldon, R.J., Deformation across the western United States: A local estimate of Pacific-North America transform deformation, J. Geophys. Res., 99, 19975-20010, 1994.

May, S.R., and Repenning, C.A., New evidence for the age of the Old Woman sandstone, Mojave Desert, California, *in* Sadler, P.M., and Kooser, M.A., eds., Late Cenozoic stratigraphy and structure of the San Bernardino Mountains, Geol. Soc. Amer. Cordilleran Section Meeting Guidebook, 6, 93-96, 1982.

Meisling, K.E., Neotectonics of the north frontal fault system of the San Bernardino Mountains: Cajon Pass to Lucerne Valley, California (Ph.D. thesis), Pasadena, CA, California Institute of Technology, 394 pp., 1984.

Meisling, K.E., and Weldon, R.J., Late Cenozoic tectonics of the northwestern San Bernardino Mountains, southern California, Geol. Soc. Amer. Bull., 101, 106-128, 1989.

Molnar, P., and Gipson, J.M., Very long baseline interferometry and active rotations of crustal blocks in the western Transverse Ranges, California, Geol. Soc. Amer. Bull., 106, 594-606, 1994.

Oberlander, T.M., Morphogenesis of granitic boulder slopes in the Mojave Desert, California, Journal of Geology, 80, 1-20, 1972.

Roy, M., Evolution of fault systems at a strike-slip plate boundary, submitted to Geophys. Res. Lett., 1998.

Sadler, P.M., An introduction to the San Bernardino Mountains as the product of young

orogenesis, *in* Cooper, J.D., ed., Geologic excursions in the Transverse Ranges, Geol. Soc. Amer. Annual Meeting Guidebook, Fullerton, California, California State University, 57-65, 1982.

Savage, J.C., Lisowski, M., and Prescott, W.H., An apparent shear zone trending north-northwest across the Mojave Desert into Owens Valley, eastern California, Geophys. Res. Lett., 17, 2113-2116, 1990.

Sharp, R.V., Variable rates of late Quaternary strike slip on the San Jacinto fault zone, southern California, J. Geophys. Res., 86, 1754-1762, 1981.

Stein, R.S., King, G., Lin, J., Change in failure stress on the southern San Andreas fault system caused by the 1992 magnitude = 7.4 Landers earthquake, Science, 258, 1328-1332, 1992.

Sykes, L.R., and Seeber, L., Great earthquakes and great asperities, San Andreas fault, southern California, Geology, 13, 835-838, 1985.

Thatcher, W., Microplate versus continuum descriptions of active tectonic deformation, J. Geophys. Res., 100, 3885-3894, 1995.

Vaughan, F.E., Geology of the San Bernardino Mountains north of San Gorgonio Pass, Univ. Cal., Dept. Geol. Sci. Bull., 13, 319-411, 1922.

Weldon, R.J., Meisling, K.E., and Alexander, J., A speculative history of the San Andreas fault in the central Transverse Ranges, California, *in* Powell, R.E., Weldon, R.J., and Matti, J.C., eds., The San Andreas fault system: Displacement, palinspastic reconstruction, and geologic evolution, Geol. Soc. Amer. Memoir, 178, 161-198, 1993.

Weldon, R.J., and Sieh, K.E., Holocene rate of slip and tentative recurrence interval for large earthquakes on the San Andreas fault in Cajon Pass, southern California, Geol. Soc. Amer. Bull., 96, 793-812.

Wesnousky, S.G., Seismological and structural evolution of strike-slip faults, Nature, 335, 340-343, 1988.

Figure 1: Summary of the major tectonic elements surrounding the San Bernardino Mountains (SBMs, shown as box delineating Figure 2). Inset shows location of southern California with respect to California and the San Andreas fault. The "big bend" of the San Andreas fault occurs south of the Garlock fault, and the circle indicates the location of the "little bend," or the restraining bend of San Gorgonio Pass. The relative motion of the Pacific plate relative to North America is shown as an arrow (N38°W trend; DeMets, 1995). BCF = Blue Cut fault, BWF = Blackwater fault, CF = Calico fault, CHF = Chiriaco fault, CRF = Camp Rock fault, DVFZ = Death Valley fault zone, ECsz = Eastern California shear zone (gray shade), eTR = eastern Transverse Ranges (ruled), GF = Garlock fault, GHF = Gravel Hills fault, HF = Helendale fault, LeF = Lenwood fault, LoF = Lockhart fault, LuF = Ludlow fault, N-IF = Newport-Inglewood fault, OV-SNFZ = Owens-Valley-Sierra-Nevada fault zone, PVF = Panamint Valley fault, Pen. Ranges = Peninsular Ranges, PiF = Pisgah fault, PMF = Pinto Mountain fault, PTF = Pleito thrust fault, SAF = San Andreas fault (m = Mojave segment, sb = San Bernardino segment, cv = Coachella Valley segment), SCF = Salton Creek fault, SGMs = San Gabriel Mountains, SJF = San Jacinto fault, SJMs = San Jacinto Mountains, SM-CF = Sierra Madre-Cucamonga fault, W-EF = Whittier-Elsinore fault, WWF = White Wolf fault, wTR = western Transverse Ranges (ruled).

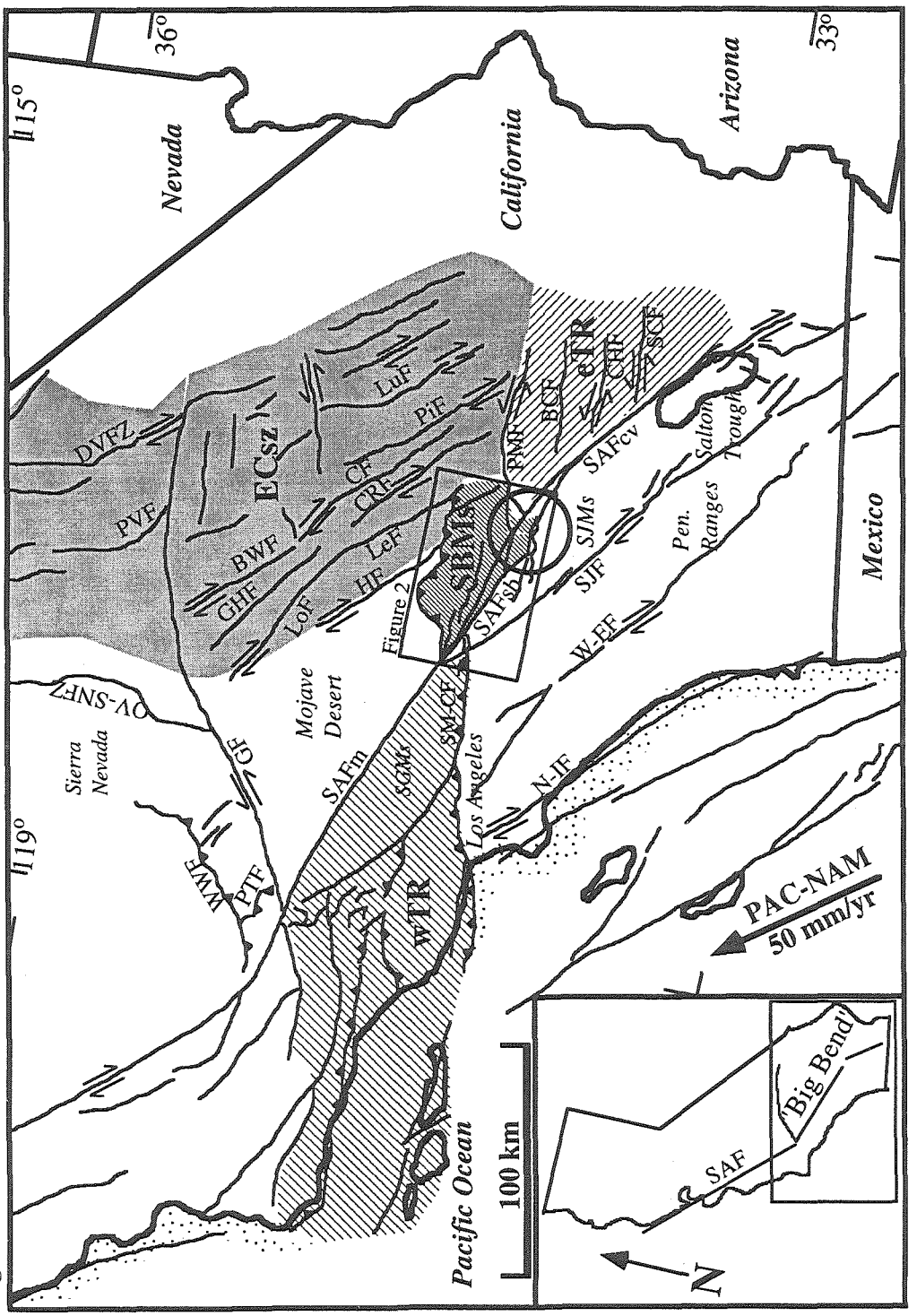
Nevada
California
Arizona
Mexico
Pacific Ocean
Sierra Nevada
Mojave Desert
Los Angeles
Pen. Ranges
Salton Trough
ECSZ
eTR
wTR
SJMs
SGMs
SAFm
SAFsb
SAFcv
DVFZ
PVF
BWF
GHF
LoF
HF
LeF
CF
CRF
LuF
PiF
PMF
BCF
CHF
SCF
SJF
W-EF
N-JF
SM-CF
OV-SNFZ
WWF
GF
PTF
Figure 2
PAC-NAM
50 mm/yr
100 km
N
SAF
"Big Bend"
115°
119°
36°
33°

Figure 1:

Figure 2: Simplified geologic and tectonic map of the San Bernardino Mountains (see Figure 1 for location). This shows the major blocks of the range and the fault systems that bound them. In addition, Tertiary sediments and the basic distribution of the weathered surface are shown. Letters refer to locations of Tertiary sediments as A = Old Woman Sandstone, B = eastern Santa Ana Sandstone overlying weathered surface and buried by basalt, C = central Santa Ana Sandstone, D = eastern Crowder Formation, E = Potato Sandstone, F = Mill Creek formation, G = Crowder Formation overlying weathered surface, H = general location of Cajon, Crowder, and Phelan Peak formations. BBB = Big Bear block, CHFZ = Crafton Hills fault zone, MB = Morongo block, Old WS = Old Woman Springs, SAV = Santa Ana Valley, SGB = San Gorgonio block, SGP-FZ = San Gorgonio Pass fault zone, YRB = Yucaipa Ridge block, WCB = Wilson Creek block, WCF = Wilson Creek fault.

Figure 2:

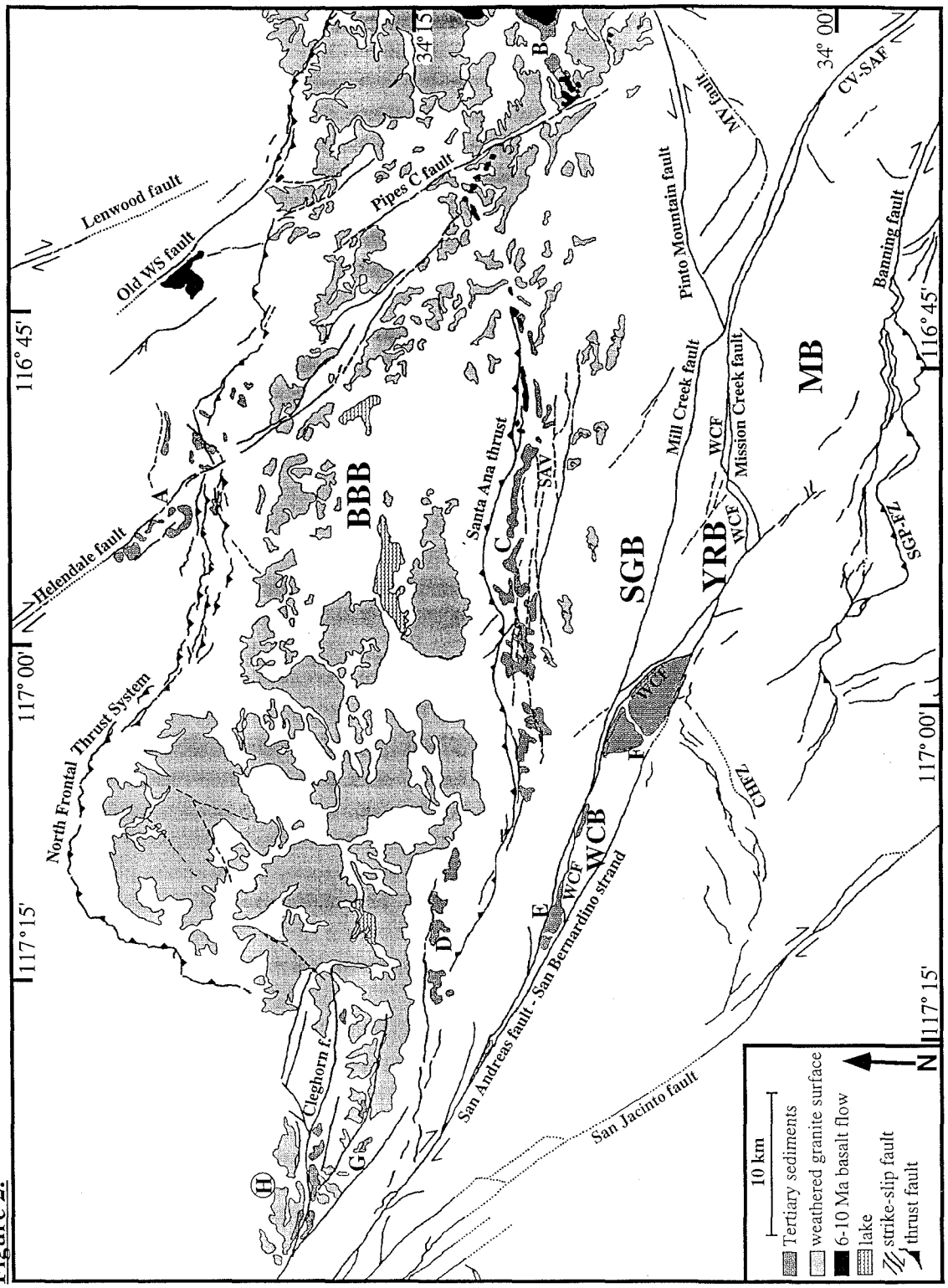
Lenwood fault
Old WS fault
Pipes C fault
Helendale fault
North Frontal Thrust System
Cleghorn f.
San Andreas fault - San Bernardino strand
San Jacinto fault
Santa Ana thrust
Mill Creek fault
Pinto Mountain fault
MV fault
Mission Creek fault
Banning fault
CV-SAF
SGP-FZ
CHZ
WCF
BBB
SGB
YRB
MB
WCB
SAV
A
B
C
D
E
F
G
H
117° 15'
117° 00'
116° 45'
34° 15'
34° 00'
10 km
Tertiary sediments
weathered granite surface
6-10 Ma basalt flow
lake
strike-slip fault
thrust fault
N

Chapter Two

Uplift and erosion of the San Bernardino Mountains associated with transpression along the San Andreas Fault, California, as constrained by radiogenic helium thermochronometry

Spotila, James A.

Farley, Kenneth A.

Sieh, Kerry

California Institute of Technology

Reprinted from *Tectonics*

Volume 17, No. 3, Pages 360-378, June, 1998

2.1. Abstract

Apatite helium thermochronometry provides new constraints on the tectonic history of a recently uplifted crystalline mass adjacent to the San Andreas fault. By documenting aspects of the low-temperature (40°-100°C) thermal history of the tectonic blocks of the San Bernardino Mountains in southern California, we have placed new constraints on the magnitude and timing of uplift. Old helium ages (64-21 Ma) from the large Big Bear plateau predate the recent uplift of the range and show that only several kilometers of exhumation has taken place since the Late Cretaceous period. These ages imply that the surface of the plateau may have been exposed in the late Miocene and was uplifted only ~1 km above the Mojave Desert in the last few Myr by thrusting on the north and south. A similar range in helium ages (56-14 Ma) from the higher San Gorgonio block to the south suggests that its crest was once contiguous with that of the Big Bear block and that its greater elevation represents a localized uplift that the Big Bear plateau did not experience. The structure of the San Gorgonio block appears to be a gentle antiform, based on the geometry of helium isochrons and geologic constraints. Young ages (0.7-1.6 Ma) from crustal slices within the San Andreas fault zone indicate uplift of a greater magnitude than blocks to the north. These smaller blocks probably experienced $\geq$3-4 km of uplift at rates $\geq$1.5 mm/yr in the past few Myr and would stand $\geq$2.5 km higher than the Big Bear plateau if erosion had not occurred. The greater uplift of tectonic blocks adjacent to and within the San Andreas fault zone is more likely the result of oblique displacement along high-angle faults than motion along the thrust fault that bounds the north side of the range. We speculate that this uplift is the result of convergence and slip partitioning associated with local geometric complexities along this strike-slip system. Transpression thus appears to have been accommodated by both vertical displacement within the San Andreas fault zone and thrusting on adjacent structures.

2.2. Introduction

The San Bernardino Mountains (SBMs) have risen during the past few Myr in association with transpression along the San Andreas fault zone in southern California (cf. Dibblee, 1975; Sadler, 1982a; Meisling and Weldon, 1989). The complex evolution of this convergent stretch of the San Andreas system and the relationship between transpression and orogeny along it are not fully understood (Matti and Morton, 1993; Weldon et al., 1993; Dibblee, 1982). At first glance, the SBMs appear to be a single structural entity, because of their discrete geographic form (Figure 1). However, the range actually consists of several distinct, fault-bounded blocks that diminish in size and become more structurally complex toward the San Andreas fault zone that bounds them on the south (Figure 2). Although the uplift of the largest of these blocks has been explained by motion along the low-angle thrust fault that bounds the range on the north (cf. Dibblee, 1975; Meisling, 1984), it is unknown whether the blocks to the south were raised by the same mechanism. This is because the magnitude, form, and chronology of uplift are less well constrained in the southern part of the range.

The poor understanding of the uplift kinematics of the southern SBMs exemplifies the more general problem of determining the role that strike-slip faults play in accommodating transpression through uplift. Because it bounds the range on the south, it is possible that significant vertical motion has taken place along the high-angle faults of the San Andreas system, perhaps in concert with uplift along the thrust fault that bounds the range on the north. Alternatively, it is conceivable that the topography of the southern SBMs formed adjacent to and in conjunction with the uplift of the San Gabriel Mountains, which now lie 50 km to the northwest. Strike-slip offset of these ranges along a purely strike-slip San Andreas fault system may thus have occurred subsequent to uplift along the thrusts that bound each mountain block (Weldon, 1986). These hypotheses represent very different concepts for the kinematics of the San Andreas fault. A better understanding of the timing and evolution of uplift of the range would facilitate our understanding of

transpression along the San Andreas fault and is important for assessing the degree of current activity on all of the bounding structures.

To learn more about the evolution of uplift and how it has accommodated transpression in the SBMs, the history and magnitude of uplift of the major blocks must be constrained. Existing data on the timing of bedrock uplift from strata adjacent to the range do not allow us to discriminate different histories for different blocks. There are also no recognized structural or stratigraphic datums that constrain the degree of exhumation and rock uplift (cf. England and Molnar, 1990) of the southern blocks relative to the north (Dibblee, 1975). To better understand these aspects of the uplift history, we utilized the recently developed low-temperature thermochronometer of radiogenic helium ([U-Th]/He) in apatite on granitic samples from the range (Zeitler et al., 1987; Lippolt et al., 1994; Wolf et al., 1996a, 1997). We compare these results to geologic and geomorphic observations and present new structural interpretations for the uplift of the major tectonic blocks. Thus we provide new constraints on the evolution of transpression over the last few Myr and on the role the San Andreas fault has played during uplift of elements of the SBMs.

2.3. Geological background

The San Bernardino Mountains (SBMs) are an isolated, high range within the central Transverse Ranges province (Figure 1). They are distinct from neighboring lowlands and are separated from adjacent mountain blocks by the San Andreas and Pinto Mountain faults (Figure 2). The northern two thirds of the range consists of the broad plateau of the Big Bear (BB) block, which is characterized by gentle highland topography surrounded by steep northern and southern escarpments and moderately sloping eastern and western flanks (Figures 1 and 2). The steep northern and southern escarpments of the plateau are bounded by the North Frontal thrust system and Santa Ana thrust, respectively. To the south, the range is narrower and significantly higher and consists of rugged, east-

west trending ridges and intervening canyons. This topography is similar to the basic form predicted for continental plateaus, in which high peaks form along windward margins due to isostatic compensation of deep incision (Masek et al., 1994; Molnar and England, 1990). The high, elongate ridges of the SBMs are separated by major faults within intermontane valleys, however, suggesting the SBMs consist of a series of distinct tectonic blocks.

The San Gorgonio (SG) block is the largest of these southern fault-bounded tectonic blocks and has steep northern and southern margins, moderate eastern and western flanks, and a rugged crest that includes the highest peak in southern California (San Gorgonio Peak, 3506 m). This block is separated from the low Santa Ana Valley on the north by unnamed high-angle faults (Sadler, 1993) and is bound on the south by the Mill Creek strand of the San Andreas fault zone, across which lie the smaller Wilson Creek (WC) and Yucaipa Ridge (YR) blocks (Figure 2). These are not as high as the SG block but are slightly steeper (Figure 1). To the south of these lie the Mission Creek and San Bernardino strands of the San Andreas fault zone, across which sits the rugged Morongo block. The southern third of the SBMs thus consists of higher and steeper topography, which could indicate more rapid erosion due to more recent or greater tectonic or isostatic uplift than the BB block may have experienced.

Uplift of the modern SBMs initiated sometime after the Miocene epoch. Pre-Pliocene strata, particularly in the northwestern part of the range, do not record evidence of the SBMs as a major topographic high (Figure 2) (cf. Meisling and Weldon, 1989; Weldon, 1986; Meisling, 1984; Sadler, 1993; Sadler et al., 1993; Allen, 1957; Woodburne, 1975). Late Miocene basalt flows in several isolated places atop the BB block also suggest that uplift is younger than ~6-10 Myr ago, because they were probably associated with crustal extension prior to the most recent transpression (Neville and Chambers, 1982). Further stratigraphic evidence shows uplift of the range began between 2 and 3 Myr ago. These data include facies and provenance changes in clastic deposits of the Old Woman sandstone on the north, the Phelan Peak Formation on the northwest, and

the San Timoteo Formation on the south (Meisling and Weldon, 1989; May and Repenning, 1982; Reynolds and Reeder, 1986). Excepting the northwesternmost part of the range, however, the stratigraphic record lacks the resolution to constrain the uplift history of the SBMs subsequent to its initiation. Thus it is not known whether the mountain rose en masse or the different blocks rose independently and whether the uplift proceeded at uniform rates or had more complicated histories. Geodetic evidence argues that the entire region has uplifted substantially in most recent time (Castle and Gilmore, 1992).

In several localities in the SBMs and Mojave Desert, basalts and Miocene sediments overlie a horizon of deeply weathered granite that may have begun forming during the more humid climate of the late Miocene (Oberlander, 1972). Both the covered and the uncovered weathered granite surfaces are nearly contiguous across the BB block and extend over large regions of gentle topography separated by incised stream canyons (Figures 1 and 2). This suggests that the basic form of the plateau and its deep weathering predate uplift (Dibblee, 1975; Sadler and Reeder, 1983; Meisling, 1984). The extensive distribution of this surface could further suggest there has been limited erosion of the BB block subsequent to initiation of uplift. If so, then its gross shape may reflect the uplift of the portions of the range that it covers (Dibblee, 1975). The vertical displacement of the plateau relative to the surrounding lowlands may thus be loosely constrained by its topography. The entire length of the plateau (east to west) is confined by the North Frontal thrust system that dips beneath it (Figure 2), indicating that the thrust was at least partly responsible for the uplift of the BB block (Meisling, 1984). The Santa Ana thrust also dips beneath the plateau and bounds part of its length on the south (Figure 2), suggesting it may have also contributed to recent uplift of the BB block (Sadler, 1993). These opposing thrusts may steepen and converge into a high-angle transpressive zone at depth (Sadler, 1982b), or the North Frontal thrust may flatten into a decollement that undercuts the Santa Ana thrust and

continues to the south (Corbett, 1984; Webb and Kanamori, 1985; Meisling and Weldon, 1989; Li et al., 1992; Seeber and Armbruster, 1995).

The SG block has minor patches of weathered granite that are similar to those atop the BB block but are not directly correlative, because of the intervening low Santa Ana Valley and the faults therein (Figure 2). The preservation of the Mio-Pliocene Santa Ana sandstone in the valley shows that it is a structural low rather than an erosional canyon. The sandstone overlies a deeply weathered granite in the valley as well, but this cannot be uniquely correlated with that atop either the BB or SG blocks because of intervening faults. Thus the relative vertical displacement between the blocks is uncertain (Dibblee, 1975; Sadler and Reeder, 1983). The crest of the SG block is about 1 km higher than the southern crest of the BB block, despite the fact that the intervening Santa Ana thrust has moved the BB block upward relative to the SG block (Sadler, 1993) (Figures 1 and 2). The lack of correlative, deeply weathered surfaces atop the YR, WC, and Morongo blocks, within the San Andreas fault zone, and the likelihood of large lateral offsets along the San Andreas obscure the relative vertical motion between these blocks and the SG and BB blocks. The lack of such relict surfaces atop these southern blocks is also consistent with the more rugged topography that suggests greater erosion than on the SG and BB blocks.

Because the magnitude of uplift is not constrained for the southern blocks, the degree to which they have been uplifted by a southward continuation of the North Frontal thrust system or the more proximal high-angle strands of the San Andreas fault zone is unknown. In the northwesternmost part of the range, where the stratigraphic record is more detailed, it has been argued that the San Andreas fault produced the substantial uplift and tilting of the western San Bernardino arch (Meisling and Weldon, 1989). Lack of suitable marker horizons and datable, syntectonic strata in the southern SBMs have thus far obscured similar study of the role the San Andreas fault has played in uplift there.

2.4. Methods

We have attempted to document the low-temperature cooling history of the SBMs to constrain the history and magnitude of rock uplift and exhumation associated with the construction of the modern range. Given that the SBMs consist of several tectonic blocks defined on the basis of geomorphology and the distribution of major faults, we compared the cooling histories of each to learn about their relative surface uplift and exhumation. In each block, we collected multiple samples of granitic rock that maximized relief and minimized lateral separations in order to document the age-elevation relationship through a near-vertical crustal section.

Thermochronometry of radiogenic helium in apatite ($Ca_5[PO_4]_3[F, Cl, OH]$) is a recently developed method that constrains the low-temperature cooling history of rocks (Zeitler et al., 1987; Lippolt et al., 1994; Wolf et al., 1996a, 1997; House et al., 1998). This method is based on the thermally activated diffusion and retention of ^4He, which is produced by the radioactive decay of uranium and thorium series nuclides. A "helium age" is calculated from the measured quantities of the parent and daughter isotopes and represents the amount of time required to radiogenically produce a given amount of ^4He assuming no initial helium and secular equilibrium in the decay series. Because helium is nearly completely lost by diffusion from apatite over geological timescales at temperatures >100°C and is only partially retained (because of slow, partial diffusion) at temperatures of 40°-100°C, this method is sensitive to the cooling rocks experience as they rise through the "helium partial retention zone" of the uppermost crust (a few kilometers depth for typical geothermal gradients). This technique is sensitive to lower temperatures than other thermochronometers. For example, with a constant cooling rate of 10°C/Ma, the helium closure temperature (Dodson, 1973) is 75°C, significantly lower than for apatite fission track annealing (~105°C) (Wolf et al., 1996a).

Helium ages are thus useful for learning about recent exhumation, even though they are a function of cooling history and do not necessarily represent ages of specific geologic

events or cooling through a specific temperature. A single helium age does not uniquely determine the time-temperature path of a rock, but suites of helium ages can significantly narrow the range of plausible thermal histories, particularly when combined with other geologic and thermochronometric data. In addition, isochronous surfaces constructed from helium ages can serve as marker horizons that constrain postcooling deformation or relative vertical displacements, which is particularly useful in crystalline rocks (Wolf et al., 1997). This is true only when exhumation during cooling was laterally uniform and isotherms in the upper crust were approximately horizontal. Techniques for interpreting apatite helium ages are presented in detail elsewhere (Wolf, 1997; Wolf et al., 1997; House et al., 1998).

We have dated replicate aliquots of apatite from granitic rocks in the SBMs. Samples of apatite consisted of ~10-20 crystals (~0.1-0.3 mg) of roughly 0.1- to 0.4-mm dimension. Apatites were selected on the basis of morphology, size, and the absence of visible defects. Crystals were also carefully screened for U- and Th-bearing silicate inclusions, which can produce anomalously old helium ages (House et al., 1998). Two of the samples analyzed in this study (15 and 16) had high concentrations of zircon inclusions and were difficult to date accurately. Helium was outgassed in a high-vacuum furnace and measured by quadrupole mass spectrometry in the Noble Gas Laboratory of the California Institute of Technology following the procedures of Wolf (1997). Analytical precision of helium measurements (typically ~0.1-1.0 pmol ^{4}He) is estimated to be ~3-4% (1σ), based on reproducibility of standards (Wolf, 1997). Helium contents of samples were corrected for alpha ejection, a phenomenon in which helium that is produced near a crystal surface is expelled because of the long stopping distance of alpha particles during radioactive decay (independent of cooling history or diffusion). Following the procedures of Farley et al. (1996), we corrected for this using a coefficient (F_T, typically 0.65-0.85) derived from the average size and shape of individual crystals in each sample. We estimate the uncertainty of measuring F_T to be ~2-3% (1σ), based on repeated measurements on single samples. Following helium outgassing, samples were retrieved from the furnace, dissolved in

HNO_3, and their U and Th contents were measured by isotope dilution (inductively coupled plasmas mass spectrometer (ICP-MS) analyses at the California Institute of Technology with ~2% analytical precision. The 1σ uncertainties of these different measurements (He, F_T, U, and Th) propagate to yield an uncertainty of about ±5% (1σ) for individual helium ages. Because we replicated analyses, our precision on average helium ages should be about ±7% (2σ). This is consistent with our observed external reproducibility of helium ages (2σ = 8% for samples with >0.1-pmol helium). We conservatively use 8% (2σ) errors in this study.

2.5. Results

We have measured replicate helium ages on 14 samples of Mesozoic granitoid rocks whose crystallization ages range from the ~90-Myr-old Cactus quartz monzonite, which makes up the majority of the SBMs basement (Dibblee, 1982) to a 215-Myr-old megaporphyritic monzogranite (Frizzel et al., 1986). The samples span elevations ranging between 652 m and 3506 m within the principal structural blocks of the range (Figure 2). Four samples from the steep southern flank of the BB block and two samples from the YR block comprise nearly vertical series, whereas other samples are spread laterally over the BB block, SG block, and YR and WC blocks. Our measured helium ages and related data are listed in Table 1 and are plotted against elevation in Figure 3.

Helium ages from the five samples in the BB block are early Miocene and older. The highest sample (17, 2113 m) is from atop the weathered plateau and gave the oldest age of 64.3 ± 5.1 Ma. A second sample (10, 1329 m) from atop the plateau about 20 km to the northwest gave a similar average age of 51.2 ± 4.1 Ma, suggesting isochronous surfaces tilt very slightly to the northwest (Figure 4). The helium ages beneath sample 17 (samples 15, 16, and 7) from the steep transect along the side of Bear Creek Canyon decrease roughly linearly with elevation to 20.6 ± 1.6 Ma (sample 7, 1233 m). Together

these make a very steep age-elevation gradient of ~50 ± 8 Myr/km. If the isochrons between these samples are slightly tilted as they are to the northwest, the elevation difference that defines this gradient may be slightly different than the paleodepth difference (i.e., during cooling) between samples. In addition, the gradient defined by the upper three samples (17, 15, and 16) alone is lower (~30 Myr/km) (Figure 3), showing that the young age of sample 7 affects the gradient strongly. Given that this sample was located only several hundred meters from the Santa Ana thrust (Figure 2), it may be anomalously young as a consequence of hot fluids circulating near the fault zone. There is no way of determining whether this is the case, however, and thus we interpret the measured ages at face value.

Six helium ages from the SG block are older than middle Miocene, comparable to the old ages from the BB block. As in the BB block, the cooling history recorded by these ages predates the recent uplift of the SBMs. Helium ages from the high ridge line of the SG block (55.7 ± 4.5 atop San Gorgonio Peak, sample 27) are very similar to the ages from the weathered plateau surface atop the BB block. The ages decrease roughly with elevation to 18.2 ± 1.5 Ma at the Santa Ana River (sample 20, 756 m). The age-elevation gradient of the SG block is best constrained by the sample pairs that have the greatest vertical separation and the smallest lateral separation, given that the samples are laterally spaced over more than 20 km distance. Two such sample pairs (27 and 26, 24 and 26) give gradients of ~26 Myr/km, roughly comparable to the BB block.

The samples from blocks within the strands of the San Andreas fault zone yielded helium ages that are far younger than those from the SG and BB blocks to the north. Two samples (21 and 23) from the YR block yielded average ages of 1.6 ± 0.5 Ma, and one sample (19) from the WC block yielded an average age of only 0.7 ± 0.2 Ma. These young ages suggest very rapid cooling that is contemporaneous with the recent construction of the SBMs. The YR block samples came from a continuous body of granodiorite (Dibblee, 1974) but were separated vertically by nearly 1 km (2323- to 1387-m elevation).

The WC block is separated from the YR block by the Wilson Creek fault (Matti and Morton, 1993), and the elevation of the sample was the lowest in this study (652 m). The apatite helium contents associated with these young ages were low enough to approach the detection limit on the quadrupole mass spectrometer (0.01-0.1 pmol ^{4}He). Because line blanks were typically 10-30% of these helium measurements, the uncertainty in these young ages is much higher than for the other samples. The reproducibility of these ages averaged ~15% (Table 1), and we have thus assigned a 2σ error limit of $\pm$30% (about $\pm$0.5 Ma) for the young samples from the southern blocks.

2.6. Interpretations

2.6.1 Big Bear Block

The old helium ages from the BB block do not record the post-Miocene cooling history associated with recent uplift of the SBMs, but they do limit the magnitude of exhumation that could have taken place during the uplift of the modern range. The preservation of the weathered granite, basalts, and sediments atop the surface of the plateau led previous workers to suggest that postuplift erosion has been confined to incision of minor stream courses and that the shape of the plateau reflects structural relief (Dibblee, 1975; Sadler and Reeder, 1983). The helium ages are a useful test of this suggestion, because they should reflect a lack of significant exhumation associated with uplift of the modern range.

The oldest helium age from the BB block (64.3 $\pm$ 5.1 Ma, sample 17, 2113 m) is located near granitic samples from the plateau surface that yield ~70 Ma K/Ar (biotite) ages (Miller and Morton, 1980). Biotite K/Ar ages represent the time at which samples cooled through a closure temperature of about 300°C, so that cooling of more than 200°C had to have occurred over just a few Myr for granitic rocks atop the plateau. This rapid cooling episode (>50°C/Myr) may represent either a major Late Cretaceous exhumation event

associated with the Laramide orogeny (cf. George and Dokka, 1994; Foster et al., 1991) or cooling of a shallowly emplaced granitic pluton (cf. House et al., 1998; Wolf et al., 1997). Following this rapid cooling, sample 17 had to have been cooler than the temperature range of helium partial retention (<40°C or <2 km depth for a typical geothermal gradient) to have achieved such an old age. This suggests that there has been very little erosion from the top of the BB block since the Late Cretaceous. It is also consistent with the idea that granitic weathering atop the plateau has been preserved because of very limited erosion since the Miocene (Oberlander, 1972).

The suite of younger helium ages beneath sample 17 along the side of Bear Creek Canyon (samples 16, 15, and 7) (Figures 1 and 2) further constrains the thermal history of the BB block. The steep age-elevation profile of these samples (~50 Myr/km) is indicative of very slow cooling but is not easy to interpret. Because the profile consists of only one uniform segment without a break in slope, there is no segue into the more recent thermal history of the block. The difficulty in interpreting such age profiles has been discussed in fission track studies (cf. Gleadow and Fitzgerald, 1987). However, there are two end-member thermal histories involving slow cooling that are consistent with geologic constraints, which we explore below. First, the steep age-elevation gradient could have been produced by very slow, uniform uplift through the helium partial retention zone, in which case different ages would correspond to the same closure temperature, and the age gradient could be inverted for the approximate uplift rate (~0.02 mm/yr). The second possibility is that the ages represent temporary stagnation (zero uplift) in the zone, in which case the age gradient would have steepened with time (deeper samples retaining less helium than higher, cooler ones) and represent an exhumed helium partial retention zone when subsequently uplifted to the surface (Wolf et al., 1997; Wolf, 1997).

Numerical solutions to the helium production/diffusion equation determine the helium age that would be produced for a hypothetical thermal history of a given rock (based on calibration of Durango apatite [Wolf, 1997; Wolf et al., 1996b]). Such numerical

modeling can thus be used to test the viability of these end-member thermal histories for the BB block. To be viable, a thermal history must produce the observed set of helium ages at different elevations and meet the thermal constraints of other data, which in this case include the K/Ar ages from atop the plateau and the likelihood that the plateau was exposed to deep weathering and deposition of basalt flows in the late Miocene (Oberlander, 1972). Implicit assumptions to this test are that exhumation and cooling were uniform over the horizontal distance between samples and that the present-day elevation difference between samples approximates the difference in paleodepth during exhumation and cooling.

In each case, the numerical model is run with the above constraints for different geothermal gradients on hypothetical samples separated by depths corresponding to present elevation differences. In the first thermal history, slow, constant cooling/uplift follows rapid unroofing in the Late Cretaceous. For example, the helium age from the uppermost sample (64.3 $\pm$ 5.1 Ma, sample 17) could have been produced if it cooled from 300°C to 60°C between 70 and 67 Ma, then cooled slowly (<1°C/Myr) to 15°C by 10 Ma, and remained at ambient surface temperature until the present. This thermal history could have produced the observed helium ages beneath sample 17 only if the geothermal gradient was ~50°C/km throughout the Tertiary, which is geologically unlikely (Lachenbruch et al., 1985). In the second example, a prolonged period of crustal stasis follows the rapid unroofing of the Late Cretaceous, which, in turn, is followed by a short period of exhumation. For example, the helium age from the upper sample could have been produced if it cooled from 300°C to 40°C between 70 and 67 Ma, remained at 40°C until 20 Ma, and cooled to ambient surface temperature (15°C) by 10 Ma. This thermal history could have produced the helium ages of the lower samples with a more reasonable geothermal gradient of ~25°C/km. This suggests that the case of temporary crustal stasis gives a thermal history that is more consistent with helium ages for the BB block.

Although these numerical models are nonunique, the thermal history that best reproduces the available data argues that the BB block was stable at shallow crustal depths

throughout the Tertiary. Following rapid cooling in the Late Cretaceous, the uppermost sample would have sat at ~1 km depth until exhumed to the surface during the Miocene. The implied Miocene rock uplift rate of ~0.1 mm/yr would contrast with the lack of crustal motion throughout the earlier part of the Tertiary and could correlate with uplift along the Squaw Peak thrust system (Meisling and Weldon, 1989). Both of the above cases show that the helium ages are consistent with Oberlander's (1972) proposed subaerial exposure of the top of the BB block in the late Miocene. Once exposed, the lower samples within the block (less than 1 km elevation below sample 17) would still be buried but would be cooler than the temperature range of helium partial retention, given a reasonable geothermal gradient. The subsequent uplift of the BB block along bounding thrust faults in the last few Myr (Meisling and Weldon, 1989; May and Repenning, 1982) would have displaced the surface of the plateau from the surrounding Mojave Desert, but it would have resulted in cooling that did not affect the helium ages of lower samples. The exposure of lower samples would have resulted from erosion along the margins of the block during uplift, as opposed to lowering of the entire plateau surface, and thus significant exhumation did not accompany post-3-Ma rock uplift across most of the BB block.

The geometries of isochronous surfaces in the BB block are also important. The similarity of the two helium ages from atop the plateau (samples 17 and 10, ~20 km apart) suggests that the weathered surface exposes similar structural levels on the northwest and southeast, with respect to the helium system. The weathered surface dips roughly 2°-3° northwestward from the southcentral part of the plateau (Meisling and Weldon, 1989), whereas the 50-Ma helium isochron dips ~1°-2° (Figure 4). While not perfectly parallel, these two horizons have roughly the same orientation, which is remarkable considering they have such different origins. The weathering may thus have developed while helium isochrons were still relatively flat, and their geometric relationship may be similar across the entire plateau. The weathered surface mimics the table-like topography of the BB block and defines an uplifted region that fits the spatial distribution of the bounding North Frontal

thrust system and Santa Ana thrust (Figure 2). By analogy, the isochronous surfaces may also have a smooth shape across the plateau, indicating that they are consistent with uniform uplift of the block along the bounding thrust faults.

2.6.2 San Gorgonio Block

The similar range in helium ages from the SG and BB blocks suggests that the two blocks shared similar cooling histories throughout the Tertiary. Although the younger ages from the SG block (samples 20, 12, and 26) are at similar elevations as the youngest in the BB block (sample 7), the old ages (samples 27 and 24) from the top of the SG block occur more than a kilometer higher than similarly old ages in the BB block (samples 17 and 16) (Figures 2 and 3). The helium isochrons in the SG block thus span a greater range of elevation than similar isochrons in the BB block. Ages of the SG block also fail to show as simple a relationship with elevation as in the BB block (Figure 3) but have a lower age-elevation gradient. This suggests that localized uplift occurred in the SG block following the closure (cooling) of the helium system for these samples. The greater elevation span of isochronous surfaces in the SG block may thus be analogous to the greater apparent thickness of tilted sedimentary strata when not measured orthogonal to bedding.

Several lines of geologic evidence suggest that the magnitude of uplift varies systematically across the SG block and that the block was locally deformed. Patches of weathered granite along its northern crest may have once been aligned with the weathered surface atop the BB block but now sit higher and dip 10^{o}-20^{o} to the north (Sadler and Reeder, 1983) (Figure 4). The eastern and western exposures of the Santa Ana sandstone show similar orientation (10^{o}-40^{o} north dip [Sadler, 1993; Jacobs, 1982; Dibblee, 1964]), although there are faults of uncertain displacement that separate the SG block from the Santa Ana Valley (Figure 2). The very presence of the Mio-Pliocene Santa Ana sandstone in the Santa Ana Valley also argues for a gradient of increasing uplift from north to south in the vicinity of the SG block. The topography of the SG block can be described as an east-

west elongate dome (Sadler, 1993; Dibblee, 1982), which is highest in the middle and tapers gently to either side. If this topography is not the result of differential erosion from east to west, then the central portion of the block has experienced the greatest uplift. This is consistent with the central exposures of the Santa Ana sandstone, which show the most intense deformation below the highest portion of the SG block (Sadler, 1993). Although other geologic features, such as foliations in crystalline bedrock, do not exhibit a coherent pattern that would support or refute this structural geometry, it seems plausible that the SG block is a broad structural dome.

Helium ages should reflect a similar variation in uplift magnitude across the SG block, if the above structural interpretation is correct. If the ages are consistent with the basic structural framework presented by the geologic observations, the hypothesis that the SG block has been warped into a dome is supported.

The helium ages lack a uniform relationship with elevation, which could be the result of differential rock uplift along the 20-km-long sample transect (Figures 1 and 2). If the SG block experienced very slow cooling throughout the Tertiary in a geothermal gradient that did not vary sharply over short distances, as suggested by the similarity of ages in the BB block, then helium isochrons should have been roughly horizontal when they formed. The ages of five samples (20, 12, 24, 26, and 27) that fall roughly on an east-west axis along the SG block (Figure 2), however, form curved helium isochrons that mimic the geological evidence mentioned above (Figure 5a). Although these isochrons are only loosely defined by the data, they do show upward warping toward the center of the block (sample 27, San Gorgonio Peak) (Figure 5a). The one helium age that does not fit these isochrons is from sample 25, which coincidentally lies 4.5 km to the north of the east-west line of the others (Figure 2). When projected onto this line, sample 25 is too old for its present elevation (or too low for its age) relative to these helium isochrons, suggesting uplift of the SG block increases to the south.

The helium ages of the SG block thus seem to reflect a similar variation in uplift magnitude as implied by geologic data. This can be further evaluated by restoring the deformation suggested by geologic features and observing the resulting relationship between helium age and elevation. The patches of weathered granite atop the block suggest northward tilting of ~10°, which is the basis for adjusting the elevation of sample 25 relative to the other samples that fall along an approximate east-west line. Once the northward tilt is restored, the age of sample 25 fits the isochronous surfaces constructed from other ages (Figure 5a). The topography and weathered surface also suggest westward tilting of the block, but these do not offer tight constraints on the magnitude of tilting because of possible erosion and limited preservation of the surface. The helium isochrons have a convex shape that can be approximated by a ~2° down-to-the-west tilt from the center of the block (sample 27) to sample 25 and a ~5.5° westward tilt from samples 25 to 20 (Figure 5a). This geometry is consistent with the geomorphic indicators and is thus used as the basis for correcting sample elevations. These westward tilts are restored by holding the elevation of sample 20 fixed and lowering samples successively greater amounts to the east.

Once this deformation has been restored, the relationship between helium age and corrected elevation in the SG block is much more uniform (Figure 5b). The resulting age-elevation gradient is about 26 Myr/km, the same as calculated from two sample pairs that are separated by substantial relief and minimal lateral distance within the block. This gradient is also comparable to that in the BB block. The elevation adjustments reduce the SG block samples to similar elevations as the BB block samples of similar age (Figure 5c) and compress the relief of the SG block to be more similar to that of the BB block. This supports the hypothesis that the two blocks expose similar structural levels that were aligned during Tertiary cooling and argues that their weathered surfaces are correlative, despite their separation by the structurally low Santa Ana Valley.

Helium ages are thus consistent with the structural hypothesis of local warping of the western SG block that is suggested by other geologic and geomorphic data. The topography of the eastern half of the block suggests a similar warp down to the east. This pattern of differential uplift is reminiscent of a gentle, north-south trending antiform that plunges moderately to the north. Because samples south of the crest of the block do not appear tilted downward to the south, the structure does not appear to have a south plunging limb. Helium ages would have to be determined from the eastern half of the block to confirm whether an eastern limb exists as well. The maximum elevation adjustment in the restoration of this deformation (~1.5 km, sample 27) is slightly greater than the difference in elevation of the crests of both blocks (~1.3 km). This suggests minor erosion has occurred atop the south central portion of the SG block, consistent with the preservation of only tiny patches of weathered granite on the northwestern part of the block (Figure 2). The westward tilt indicated by isochronous surfaces in the SG block is also less steep than the topographic surface (Figure 5a). This suggests that the relief of the block is a function of both uplift (greater in the center) and erosion (greater on the west).

2.6.3 Yucaipa Ridge and Wilson Creek Blocks

The very young helium ages determined on samples from the southern blocks indicate that they only recently cooled below the temperature range of helium partial retention in apatite. The ages are probably related in some way to activity of the San Andreas fault system because of their locations between its strands.

The corresponding closure temperatures and depths for these ages depend on the cooling histories and the local geothermal gradient. Owing to the proximity to the San Andreas fault, there is the possibility that fault friction produced heat that resulted in a locally high geothermal gradient, so that the young helium ages might reflect exhumation from only the shallowest crustal levels. In this case, elevated lateral heat flow from the fault would be observed in elevated vertical geothermal gradients on either side of the fault.

However, the San Andreas lacks the heat flow anomaly expected if fault friction were high. Average heat flow measurements of ~70 mW/m^2 in the vicinity of the southern San Andreas fault correspond to geothermal gradients of ~30°C/km and are inconsistent with a near-fault heat anomaly (Turcotte and Schubert, 1982, p. 136; Lachenbruch et al., 1985; Lachenbruch and Sass, 1988). A slightly higher geothermal gradient was measured along the San Andreas fault to the northwest in the scientific well at Cajon Pass, but this has been explained as a transient phenomenon due to very recent erosion of overburden rather than fault friction (Sass et al., 1992). These gradients indicate that the partial retention zone of helium is several kilometers beneath the surface, and thus the young ages represent significant recent exhumation, not local heating. A possible exception to this could be that hot fluids migrated upward along fractures to heat samples at very shallow crustal levels. However, it seems unlikely that all three young samples would have been so similarly affected by such a nonuniform process, whereas old samples in the SG block that are equally close to the San Andreas fault fail to exhibit any such effect (Figure 2).

We thus propose that the young ages of the YR and WC blocks reflect cooling due to recent exhumation from significant depth. To interpret the magnitude and rate of this exhumation, it is necessary to make several assumptions. First, we assume that the present-day geothermal gradient of ~30°C/km (and ambient surface temperature of ~15°C) has been constant for the past few Myr. This assumption requires that perturbations of the thermal gradient due to uneven surface topography have been small. Given the narrow width (<5 km) of the present-day YR and WC blocks, it is likely that the gradient is not strongly disrupted by their ≤1-km relief (Mancktelow and Grasemann, 1997). However, we do not know how their topography has varied in the past, nor to what degree the high San Gabriel Mountains insulated the southern SBMs as they passed alongside over the past few Myr because of displacement along the San Andreas fault zone. In addition, it is not certain to what degree isotherms were advected upward during the rapid (see below) exhumation of the YR and WC blocks (Mancktelow and Grasemann, 1997). Given the

lack of control on these important factors, however, we have chosen to assume the simplest case of a constant geothermal gradient, in order to infer physical meaning from these young helium ages.

On the basis of these assumptions and assuming monotonic cooling, the samples from the YR block had to have been within the depth range of helium partial retention (~1-3 km, or hotter than 40°C and colder than 100°C) at 1.6 Ma. If hotter than 100°C after 1.6 Ma, they would not have accumulated enough helium to be this old. If cooler than 40°C prior to 1.6 Ma, they would have accumulated too much helium and would be too old. Although the same is true for the 0.7 Ma sample from the WC block, the cooling history of this block is more difficult to interpret. Suites of helium ages more tightly constrain a thermal history than does a single sample age, and the exhumation histories of the YR and WC blocks cannot be interpreted jointly because of the poor constraint on the slip history of the intervening Wilson Creek fault (Figure 2). In addition, the presence of the Mill Creek Formation (10-13 Ma) in the WC block (Figure 2) requires that both subsidence (i.e., transtension) and uplift (i.e., transpression) have occurred since the mid-Miocene (Sadler et al., 1993). For these reasons, we focus our interpretation on the magnitude and rate of exhumation of the YR block.

Given that the ages from the YR block are so young (1.6 Ma), their large errors ($\pm$0.5 Ma) significantly affect interpretations of cooling/uplift history. If the average ages are accepted at face value, their similarity suggests that the two samples shared cooling histories and exhumed from the helium partial retention zone at roughly the same time. Because these samples were separated by ~1-km elevation (Table 1), this scenario implies extremely rapid exhumation over a short period. For example, 4 km of exhumation at 10 mm/yr between 1.7 and 1.3 Ma would have resulted in nearly identical upper and lower ages (1.6 and 1.5 Ma), based on numerical solutions to the helium production/diffusion equation and the above geothermal gradient. Although even more rapid exhumation rates are permitted by these data, much slower YR block cooling is also possible given the large

error bars. For example, exhumation of the block at a constant rate of 1.5 mm/yr over the past few Myr would have produced upper and lower ages of 2.1 Ma (within error limits of sample 21) and 1.6 Ma (sample 23). In another possible case, exhumation at 2.25 mm/yr could have produced an upper age of 1.6 Ma (sample 21) and a lower age of 1.1 Ma (within error limits of sample 23). Both of these cases of uniform uplift predict ~3-4 km total exhumation occurred in the past 2 Myr.

More complex thermal histories are also permitted by the data, but more helium ages would have to be determined to further constrain the exhumation history of the YR block. We hope to pursue a more rigorous collection and analysis of samples from this block to improve our understanding of its thermal history. Regardless of cooling history, however, the young ages require roughly 3-4 km of exhumation in the past 2 Myr, given the above assumptions. Because there are no older helium ages from the YR block, there is also no constraint on how much exhumation occurred prior to 2 Ma.

If the YR block has risen at least ~3-4 km in the past 2 Myr, the present topography (just over 1-km relief above base level) requires at least 2-3 km of crust to have been removed by erosion. This suggests that the top of the YR block would stand at least 1 km higher than the present crest of the SG block if no erosion had occurred over the past few Myr (Figure 6). Even more exhumation and erosion may have occurred prior to this. In addition, the minimum uplift rate required for post-2-Ma exhumation is ~1.5 mm/yr. This rate could be much higher, as shown above, and could rival those observed in other orogenic environments such as the Himalayas (Burbank and Beck, 1991).

2.7. Implications for the role of the San Andreas fault in uplift

Helium ages from the SBMs provide new constraints on the timing and amount of exhumation and uplift beyond what has been determined by other geologic observations. The amount of recent uplift within each fault-bounded block is, as suggested by the greater

elevation and ruggedness of topography, greater in the south than in the north (Figure 6). This greater uplift of the southern SBMs coincides with the most rapid uplift suggested by geodetic data in southern California (Castle and Gilmore, 1992). Leveling data suggest that uplift over the past few decades may have proceeded at rates greater than ~1 cm/yr in the southern SBMs, which could suggest that the rapid uplift of the southern blocks is continuing. Although short-term (<100 yr) geodetic data may not reflect the long-term (> 1 Myr) uplift history of a region and the geodetic evidence of this uplift is controversial (cf. Stein et al., 1986), the comparison with rates from helium ages is intriguing.

Helium ages offer uplift constraints that can be used as arguments in structural interpretation of the SBMs. Old helium ages from the BB block are consistent with the hypothesis that its central portion has risen uniformly, presumably as the hanging wall block of the North Frontal thrust system and perhaps along the Santa Ana thrust, and that its plateau has had minimal erosion and internal deformation over the last few Myr. These ages neither confirm nor refute geological observations that suggest the block began rising between 2 and 3 Ma (Meisling and Weldon, 1989; May and Repenning, 1982). They also fail to record whether uplift has been uniform since then, although the sizes and ages of scarps along the bounding thrust faults argue that uplift rate has been decreasing throughout the Pleistocene (Meisling and Weldon, 1989; Sadler, 1993).

South of the BB block, the magnitude of vertical displacement is much more irregular. The Santa Ana Valley to the south sits 1 km below the BB block and is a structural low rather than a recent incision (Sadler, 1993) (Figure 2). Helium ages from farther south indicate the SG block has been uplifted by as much as 1.5 km above the BB block and even more relative to the valley. Ages from the YR and WC blocks suggest uplift on the south exceeds that of the SG block by more than 1 km. The greater irregularity and magnitude of uplift on the south is difficult to explain simply with displacement on the North Frontal thrust system (Figure 6). The thrust dips southward and may flatten to extend beneath these blocks as a decollement, but significant variations in

slip or geometry along the thrust would be required to produce this pattern of uplift. A simpler explanation would thus be favored.

The greater uplift on the south also significantly exceeds that expected for local isostatic compensation of valley incision. The magnitude of uplift due to local compensation depends on the volume of eroded material in a given area and the ratio of crustal and mantle densities (Montgomery, 1994). The degree of local compensation is also limited by the flexural rigidity and lateral dimension of a mountain block. On the basis of a probable range of flexural rigidities of 10^{21}-10^{23} N m (south and north plates [Li et al., 1992; Sheffels and McNutt, 1986]), a length scale of 10^{1}-10^{2} km, a 0.8-crust/mantle density ratio, and a ratio of eroded volume per area (akin to depth of incision) of ~1 km, the magnitude of uplift due to local compensation expected for the southern SBMs is only 0-200 m (Montgomery, 1994). This is consistent with the idea that block uplift was tectonic and that the faults between them control their basic topographic form more significantly than erosion. It is also consistent with the observation that many of the low regions between the blocks, such as the Santa Ana Valley, preserve preuplift sediments and thus appear to be structurally controlled and not due to recent incision.

The greater and more localized deformation experienced by the southern blocks coincides with increased structural complexity represented by high angle faults associated with the San Andreas fault zone. We thus propose that these faults are responsible for the observed vertical motions of crustal blocks and that the San Andreas fault played a significant role in uplift of the southern SBMs. In Section 6.1, we examine the possible causes and implications of this deformation of the YR-WC and the SG blocks.

2.7.1 Uplift of the Yucaipa Ridge and Wilson Creek Blocks

The young helium ages from the YR and WC blocks document young cooling due to recent uplift that exceeds the magnitude of uplift experienced by blocks to the north. We propose that these blocks were squeezed up as pressure ridges along the subparallel strike-

slip faults that bound them. This supports the contention of Dibblee (1982) that the greatest uplift in the SBMs has occurred along crustal slices within the San Andreas fault system. The mechanism by which these strike-slip faults produced uplift depends on the configuration of active strike-slip faulting at the time.

Below we discuss plausible mechanisms of uplift for the YR block. Although the WC block uplift may have been produced by the same mechanism, these blocks are separated by the Wilson Creek fault, a major strand of the San Andreas fault system. Although this fault is likely to have been extinct by the time these blocks began to uplift, lateral motion during or after uplift are not precluded by existing evidence (Matti et al., 1985). We thus discuss the uplift of the YR block, for which we have two dated samples, and only acknowledge that the WC block may have been uplifted by a similar mechanism.

Greater uplift of the YR block relative to the SG block to the north seems to require vertical motion on the intervening Mill Creek fault (Figures 1 and 5). This is consistent with south-side-up scarps in Pleistocene alluvium (Farley, 1979) and slickensides along the fault (Allen, 1957) between Mill and Whitewater Creeks. Vertical motion may have also accumulated on the Mission Creek and San Bernardino fault strands that bound the block on the south (Figure 2). However, the lack of helium ages from the Morongo block prevents us from knowing whether it has experienced a similar magnitude of rock uplift. The greater relief of the YR block relative to the Morongo block suggests uplift may have been localized to north of the Mission Creek fault. If the YR block did rise relative to the Morongo block, the sense and magnitude of motion would mimic the north-side-up separation of the base in seismicity (~15-20 km depth) below the surface trace of the Mission Creek fault (Corbett, 1984; Webb and Kanamori, 1985; Magistrale and Sanders, 1996). The exhumation suggested by the helium ages thus appears consistent with the surrounding geologic relations.

Vertical motion along a strike-slip system can result from a number of different configurations of active faulting. For example, reverse slip can accommodate horizontal

displacement if a strike-slip fault is nonvertical and there is convergence across the fault zone (Figure 7a). Such slip partitioning can occur on oblique-slip faults that are parallel to and decoupled from the main strand of a strike-slip system when the maximum horizontal stress is nearly perpendicular to the fault zone (Mount and Suppe, 1987). Ruptures during the 1989 Loma Prieta and 1986 Palm Springs earthquakes are recent examples of this, in which substantial components of horizontal plate motion were accommodated by vertical slip (Jones and Wesnousky, 1992). Depending on the dip of the fault, slip partitioning can result in large vertical displacements. For example, the ratio of horizontal to vertical slip on the 45° dipping rupture that produced the Palm Springs earthquake was nearly 3 to 1 (Pacheco and Nabelek, 1988). The Mill Creek and Mission Creek faults dip moderately (~60°) southward and northward, respectively, under the YR block in present exposures (Figure 6) (Allen, 1957). If these faults were active and had such dips at around 1.6 Ma, their geometry could have led to slip partitioning and the exhumation of the YR block. For example, a 60° dip on the Mill Creek fault, a 30° angle between it and the regional direction of strike-slip motion, and ~3-4 km of YR block vertical motion translate to about 3.5-4.6 km of dextral slip accommodated on the Mill Creek fault in the last 1.6 Myr (about 10% of the total San Andreas slip in 1.6 Myr [Weldon and Sieh, 1985]). More strike-slip motion may have been accommodated by uplift prior to this.

A second configuration of active strike-slip faulting that can result in vertical motion is that of a contractional fault stepover or restraining bend (Figure 7b). The YR block is situated just northwest of the 15-km-wide stepover between the San Bernardino and Coachella Valley strands of the San Andreas fault zone in San Gorgonio Pass (Figure 2). Given that a minimum of 8-10 km of right slip has taken place across the Mill Creek fault in the Pleistocene (Matti et al., 1985), the YR block could have been located in this stepover region during its exhumation. Convergence in this stepover could have produced uplift by north-south thrusting on a major ramp structure, such as the modern San Gorgonio Pass fault zone (Allen, 1957; Matti et al., 1985), or more diffuse internal deformation

(Nicholson et al., 1986) (Figure 7b). Such north-south convergence is evident in recent seismicity in the present-day San Gorgonio Pass block (Seeber and Armbruster, 1995). The restoration of the volume (i.e., mass balance, as if the block were fluid) of the uplifted YR block (minimum of ~3 km exhumed times ~15 km length times ~4.5 km width equals ~200 km^3) back into the 15-km-wide by 15-km-deep stepover requires ~1 km of fault-parallel convergence. This is only about 5% of the total convergence that would have occurred in 1.6 Myr if all of the San Andreas fault motion was accommodated (25 mm/yr times 1.6 Ma equals 40 km [Weldon and Sieh, 1985]). Hence the uplift of the block could easily have resulted from this mechanism. The present-day Morongo block may be a nascent expression of this mechanism (Figure 6).

These two possible explanations seem equally likely, and although we cannot determine which plays a greater role, both are favored over other possible explanations. In order to test these hypotheses, exact knowledge of the relative position of the block through the past few Myr due to strike-slip faulting would be needed. Several other possible causes of the recent uplift of the YR block include the following. One possibility is that the YR block was deformed by a subsurface bulge propagating along one of the strands of the San Andreas fault (Figure 7c). This has been proposed to explain local tilting of sediments that has migrated to the northwest at approximately the rate of slip on the San Andreas fault in the northwesternmost SBMs (the western San Bernardino arch [Meisling and Weldon, 1989]). However, this specific subsurface geometric perturbation was beneath Lake Arrowhead (25 km northwest of the YR block) at ~1.5 Ma (Meisling and Weldon, 1989), making it an unlikely cause for YR block uplift. A similar subsurface geometric perturbation could have existed to the south during the time of YR block uplift. A second possibility is that local convergence and uplift along the San Andreas fault has resulted from its intersection with other strike-slip faults, such as the Pinto Mountain or San Jacinto faults (Figures 1 and 6d) (Dibblee, 1975). This could be similar to the convergence that

produced uplift at the intersection of the San Andreas and Garlock faults to the northwest (Bohannon and Howell, 1982).

A final possibility is that the uplift was produced by a structure that has subsequently been offset laterally along the San Andreas fault. The young helium ages from the YR block could be related to young fission track ages determined for rocks of the San Gabriel Mountains to the west (Blythe et al., 1996), if the Cucamonga thrust system had uplifted them together prior to large lateral displacement (Figure 7e). In this case, the Banning fault (or San Gorgonio Pass fault zone) could be a stranded section of the Cucamonga thrust and may have uplifted the entire region between it and the Mill Creek strand. Determining helium ages within the Morongo block to the south of the YR block would help to test this hypothesis. The proposal seems unlikely, however, because of the timing of uplift and strike slip. Given the present slip rates on the San Andreas and San Jacinto faults (Weldon and Sieh, 1985), the 50-km separation between the San Gabriel Mountains and YR block would have accrued in ~1.5 Myr or more (depending on what fraction of the slip occurred on the Mill Creek fault, Figure 2). The San Gabriel Mountains may have been uplifting continuously since then, however, based on the similarity between modern (faulted alluvium) and long-term (fission track on bedrock) rates of uplift (Dolan et al., 1996; Ann Blythe, personal communication, 1997). In addition, helium ages argue that significant exhumation had to proceed the time when the San Gabriel Mountains were adjacent to the YR and WC blocks, when samples were likely still within the helium partial retention zone (several kilometers deep). The hypothesis thus seems unlikely, although it cannot presently be ruled out.

2.7.2 Deformation of the San Gorgonio Block

Like the YR block, the helium ages from the SG block imply that it has been deformed and uplifted more than the BB block (Figure 6). The deformation that produced this structure may have been localized by the faults that bound it, such as the Mill Creek

strand of the San Andreas fault zone on the south and the unnamed high-angle, oblique (south-side-up and dextral) structures that break sediments and juxtapose sediments and SG block basement to the north in Santa Ana Valley (Dibblee, 1964; Jacobs, 1982; Sadler, 1993) (Figure 2). Displacement on the northern faults is required, given that the down to the north tilting is not sufficient to explain the total relief between the weathered granite surfaces atop the SG block and the structural low of Santa Ana Valley (Figure 4). It is likely that the local warping of the SG block resulted from a geometric complexity along a strike-slip fault system, similar to the one of the mechanisms illustrated in Figure 7.

Unlike the YR block, the helium ages from the SG block do not constrain when this local deformation occurred. The youngest feature that shows the northward block tilting is the Mio-Pliocene Santa Ana sandstone. This unit contains clasts from the San Gabriel Mountains that would have been transported northward prior to uplift of the SG block and thus constrains uplift of the block to after 4 Ma (unless substantial lateral offset has occurred along the structures between the SG block and Santa Ana Valley [Sadler, 1993]). There is no upper constraint to the uplift of the SG block, and it could be actively rising today. Without knowing exactly when this deformation occurred, however, we can only speculate on what produced it.

The geometry of SG block deformation offers some hints as to how it was produced. The apparent northward and westward tilt of isochronous surfaces and geologic features, as well as the east and west slope of the SG ridge line, suggest that the block is an elongate, northward plunging, north-south trending antiform. The shape of the antiform indicates east-west shortening and localized uplift on the south, with the maximum amplitude centered at San Gorgonio Peak (sample 27, Figure 2). Because the folding postdates helium ages (i.e., cooler than 40°C), it is unlikely that it could have been due to ductile deformation of crystalline rock. It is also unlikely that the fold was created by pure elastic bending, given that the magnitude of uplift varies 1.5 km over ~22 km distance (~7% strain) (Figures 1 and 4). The warping of the block may thus have been produced by

internal brittle deformation. Folding could have been produced by displacement on the Mill Creek fault if it had a significant component of reverse slip along the center of the SG block that gradually gave way to pure strike slip in either direction (Figure 2). Such a reverse component of slip could have resulted from convergence in San Gorgonio Pass or simply the orientation of the fault relative to the regional direction of right shear. The convergence accommodated by the SG block uplift is of the same order as that accommodated by the YR block (~1 km), based on the volume restoration and given the SG block's greater lateral extent and smaller magnitude of uplift (Figures 1 and 5).

2.8. Conclusions

Radiogenic helium thermochronometry offers new constraints on the tectonic development of the San Bernardino Mountains. Paleocene to Miocene helium ages from the Big Bear block show that very little exhumation has taken place there since the Late Cretaceous. The geometry of the isochronous surfaces are consistent with the hypotheses that the block's surface has been only slightly eroded since exposed to deep weathering in the late Miocene and that the block was uplifted as an intact massif, presumably as the hanging wall block the North Frontal thrust system and Santa Ana thrust.

Helium ages from the San Gorgonio block are similar to those from the Big Bear block (~56-14 Ma) and predate the recent uplift of the San Bernardino Mountains. The geometry of isochronous surfaces constructed from these ages suggests that the weathered granitic surface atop the block was originally continuous with that atop the Big Bear plateau. This implies that the San Gorgonio block has experienced roughly 1.5 km more uplift than the Big Bear block and that this uplift is mimicked by the topographic form of the block. The structure of the block appears to be a gentle antiform, based on the orientations of geologic datums and warped isochronous surfaces. Such a structure is better explained by uplift due to local complexities associated with the high-angle faults that

bound it than slip along the North Frontal thrust system that has produced more uniform uplift of the Big Bear plateau. We speculate that convergence associated with geometric complexities along the San Andreas fault zone produced this structure, but lack of constraint on the exact timing of this deformation prevents knowing what configuration of faulting was active at the time.

The helium ages from the Wilson Creek and Yucaipa Ridge blocks within the San Andreas fault zone are very young (0.7-1.6 Ma) and indicate recent, rapid cooling. These ages suggest thermal histories that require $\geq$3-4 km of uplift in the past few Myr. This magnitude of uplift indicates that the Yucaipa Ridge block would have stood at least 1 km above the present topography of the San Gorgonio block, if no erosion had occurred. Such uplift would have proceeded at a rate of $\geq$1.5 mm/yr but may have been shorter lived at a rate $\geq$10 mm/yr. This high rate and magnitude of uplift is confined to crustal slices within the San Andreas fault zone and implies local uplift associated with strike-slip faulting as opposed to displacement on the North Frontal thrust system. The uplift rate may have been a significant component of the total slip rate across the strike-slip system. As in the case of the San Gorgonio block, this uplift may have resulted from geometrical complexities along the San Andreas fault.

These results imply that the San Bernardino Mountains consist of several tectonic blocks that have risen because of both thrusting and oblique slip associated with complexities along the San Andreas fault zone on the south. Transpression thus appears to have occurred in several modes, which include significant magnitudes of vertical motion along the San Andreas fault itself. Likewise, a significant component of San Andreas fault motion was probably accommodated by uplift that resulted from convergence.

2.9. Acknowledgments

We thank Martha House and Rich Wolf for significant help with lab work, Doug Yule for help with sample collection, and Martha, Rich, Doug, Andrew Meigs, and Leon Silver for valuable help with interpretations and regional geology. We also thank Robert Castle and Peter Sadler for helpful reviews of this manuscript. This project was funded by the National Science Foundation and U.S. Geological Survey through the Southern California Earthquake Center (contribution 379). This is Seismological Laboratory of California Institute of Technology contribution 6205.

2.10. References

Allen, C.R., San Andreas fault zone in San Gorgonio Pass, southern California, Geol. Soc. Am. Bull., 68, 315-350, 1957.

Blythe, A.E., E.J. Fielding, and D.W. Burbank, Morphology as a function of bedrock uplift and climate: A case study of the Transverse Ranges, southern California, from apatite fission track and DEM analysis (abstract), EOS Trans., AGU, 77 (46), Fall Meet. Suppl., F644, 1996.

Bohannon, R.G., and D.G. Howell, Kinematic evolution of the junction of the San Andreas, Garlock, and Big Pine faults, California, Geology, 10, 358-363, 1982.

Bortugno, E.J., and T.E. Spittler, Geologic map of the San Bernardino Quadrangle, California, 1:250,000 scale, Reg. Geologic Map Ser., Map 3A, Calif. Div. Mines Geol., 1986.

Burbank, D.W., and R.A. Beck, Rapid, long-term rates of denudation, Geology, 19, 1169-1172, 1991.

Castle, R.O., and T.D. Gilmore, A revised configuration of the southern California uplift, Geol. Soc. Am. Bull., 104, 1577-1591, 1992.

Corbett, E.J., Seismicity and crustal structure of southern California: Tectonic implications from improved earthquake locations, Ph.D. thesis, 231 pp., Calif. Inst. of Technol.,

Pasadena, Calif., 1984.

DeMets, C., Reappraisal of seafloor spreading lineations in the Gulf of California: Implications for the transfer of Baja California to the Pacific Plate and estimates of Pacific-North America motion, Geophys. Res. Lett., 22, 3545-3548, 1995.

Dibblee, T.W., Geologic map of the San Gorgonio Mountain 15' Quadrangle, 1:62,500 scale, U.S. Geol. Surv. Misc. Geologic Invest. Map, I-431, 1964.

Dibblee, T.W., Geologic map of the Redlands 15' Quadrangle, 1:62,500 scale, U.S. Geol. Surv. Open File Map, 74-1022, 1974.

Dibblee, T.W., Late Quaternary uplift of the San Bernardino Mountains on the San Andreas and related faults, in San Andreas Fault in Southern California, edited by J.C. Crowell, Spec. Rep. Calif. Div. Mines Geol., 118, 127-135, 1975.

Dibblee, T.W., Geology of the San Bernardino Mountains, southern California, in Geology and Mineral Wealth of the California Transverse Ranges, edited by D.L. Fife and J.A. Minch, pp.148-169, South Coast Geol. Soc., Santa Ana, Calif., 1982.

Dodson, M.H., Closure temperature in cooling geochronological and petrological systems, Contrib. Mineral. Petrol., 40, 259-274, 1973.

Dolan, J.F., F. Jordon, G. Rasmussen, D. Stevens, W. Reeder, and L.M. McFadden, Evidence for probable moderate-sized (Mw 6.5-7.0) paleoearthquake on the Cucamonga Fault, northwestern Los Angeles metropolitan region, California (abstract), EOS Trans., AGU, 77 (46), Fall Meet. Suppl., F461, 1996.

England, P., and P. Molnar, Surface uplift, uplift of rocks, and exhumation of rocks, Geology, 18, 1173-1177, 1990.

Farley, K.A., R.A. Wolf, and L.T. Silver, The effects of long alpha-stopping distances on (U-Th)/He dates, Geochim. Cosmochim. Acta, 60, 4223-4229, 1996.

Farley, T., Geology of a part of northern San Gorgonio Pass, California, M.S. thesis, 159 pp., Calif. State Univ., Los Angeles, 1979.

Foster, D.A., D.S. Miller, and C.F. Miller, Tertiary extension in the Old Woman

Mountains area, California: Evidence from apatite fission track analysis, Tectonics, 10, 875-886, 1991.

Frizzel, V.A., J.M. Mattinson, and J.C. Matti, Distinctive Triassic megaporphyritic monzogranite: Evidence for only 160 km offset along the San Andreas fault, southern California, J. Geophys. Res., 91, 14080-14088, 1986.

George, R.G., and R.K. Dokka, Major Late Cretaceous cooling events in the eastern Peninsular Ranges, California, and their implications for Cordilleran tectonics, Geol. Soc. Am. Bull., 106, 903-914, 1994.

Gleadow, A.J.W., and P.G. Fitzgerald, Uplift history and structure of the Transantarctic Mountains - New evidence from fission-track dating of basement apatites in the Dry Valley area, southern Victoria Land, Earth Planet. Sci. Lett., 82, 1-14, 1987.

House, M.A., B.P. Wernicke, K.A. Farley, and T.A. Dumitru, Cenozoic thermal evolution of the central Sierra Nevada from (U-Th)/He thermochronometry, Earth Planet. Sci. Lett., 151, 167-179, 1997.

Jacobs, S.E., Geology of a part of the upper Santa Ana River Valley, San Bernardino Mountains, San Bernardino County, California, M.S. thesis, 107 pp., Calif. State Univ., Los Angeles, 1982.

Jones, C.H., and S.G. Wesnousky, Variations in strength and slip rate along the San Andreas fault system, Science, 256, 83-86, 1992.

Jones, L.M., E. Hauksson, and H. Qian, Where is the San Andreas Fault in the San Bernardino Mountains of southern California, Seismol. Res. Lett., 64, 22, 1993.

Lachenbruch, A.H., and J.H. Sass, The stress heat-flow paradox and thermal results from Cajon Pass, Geophys. Res. Lett., 15, 981-984, 1988.

Lachenbruch, A.H., J.H. Sass, and S.P. Galanis, Jr., Heat flow in southern California and the origin of the Salton Trough, J. Geophys. Res., 90, 6709-6736, 1985.

Li, Y.-G., T.L. Henyey, and P.C. Leary, Seismic reflection constraints on the structure of the crust beneath the San Bernardino Mountains, Transverse Ranges, southern

California, J. Geophys. Res., 97, 8817-8830, 1992.

Lippolt, H.J., M. Leitz, R.S. Wernicke, and B. Hagedorn, (Uranium + thorium) / helium dating of apatite: Experience with samples from different geochemical environments, Chem. Geol. Isot. Geosci., 112, 179-191, 1994.

Magistrale, H., and C. Sanders, Evidence from precise earthquake hypocenters for segmentation of the San Andreas fault in San Gorgonio Pass, J. Geophys. Res., 101, 3031-3044. 1996.

Mancktelow, N.S. and B. Grasemann, Time dependent effects of heat advection and topography on cooling histories during erosion, Tectonophysics, 270, 167-195, 1997.

Masek, J.G., B.L. Isacks, T.L. Gubbels, and E.J. Fielding, Erosion and tectonics at the margins of continental plateaus, J. Geophys. Res., 99, 13941-13956, 1994.

Matti, J.C., and D.M. Morton, Paleogeographic evolution of the San Andreas fault in southern California: A reconstruction based on a new cross-fault correlation, in The San Andreas Fault System: Displacement, Palinspastic Reconstruction, and Geologic Evolution, edited by R.E. Powell, R.J. Weldon, and J.C. Matti, Mem. Geol. Soc. Am., 178, 107-160, 1993.

Matti, J.C., D.M. Morton, and B.F. Cox, Distribution and geologic relations of fault systems in the vicinity of the central Transverse Ranges, southern California, U.S. Geol. Surv. Open File Rep., 85-365, 27 pp., 1985.

May, S.R., and Repenning, C.A., New evidence for the age of the Old Woman sandstone, Mojave Desert, California, in Late Cenozoic Stratigraphy and Structure of the San Bernardino Mountains, Field Trip 6, edited by P.M. Sadler and M.A. Kooser, in Geologic Excursions in the Transverse Ranges, Geol. Soc. Am. Cordilleran Sect. Meet. Guideb., 78, edited by J.D. Cooper, pp. 93-96, 1982.

Meisling, K.E., Neotectonics of the north frontal fault system of the San Bernardino Mountains: Cajon Pass to Lucerne Valley, California, Ph.D. thesis, 394 pp., Calif. Inst. of Technol., Pasadena, Calif., 1984.

Meisling, K.E., and R.J. Weldon, Late Cenozoic tectonics of the northwestern San Bernardino Mountains, southern California, Geol. Soc. Am. Bull., 101, 106-128, 1989.

Miller, F.K., and D.M. Morton, Potassium-argon geochronology of the eastern Transverse Ranges and southern Mojave Desert, southern California, U.S. Geol. Surv. Prof. Pap., 1152, 30 pp., 1980.

Molnar, P., and P. England, Late Cenozoic uplift of mountain ranges and global climate change: Chicken or egg, Nature, 346, 29-34, 1990.

Montgomery, D.R., Valley incision and the uplift of mountain peaks, J. Geophys. Res., 99, 13913-13921, 1994.

Mount, V.S., and J. Suppe, State of stress near the San Andreas fault: Implications for wrench tectonics, Geology, 15, 1143-1146, 1987.

Neville, S.L., and J.M. Chambers, Late Miocene alkaline volcanism, northeastern San Bernardino Mountains and adjacent Mojave Desert, in Late Cenozoic Stratigraphy and Structure of the San Bernardino Mountains, Field Trip 6, edited by P.M. Sadler and M.A. Kooser, in Geologic Excursions in the Transverse Ranges, Geol. Soc. Am. Cordilleran Sect. Meet. Guideb., 78, edited by J.D. Cooper, pp. 103-106, 1982.

Nicholson, C., L. Seeber, P. Williams, and L.R. Sykes, Seismicity and fault kinematics through the eastern Transverse Ranges, California: Block rotation, strike-slip faulting, and low-angle thrusts, J. Geophys. Res., 91, 4891-4908, 1986.

Oberlander, T.M., Morphogenesis of granitic boulder slopes in the Mojave Desert, California, J. Geol., 80, 1-20, 1972.

Pacheco, J., and J. Nabelek, Source mechanisms of three moderate California earthquakes of July, 1986, Bull. Seismol. Soc. Am., 78, 1907-1929, 1988.

Proctor, R.J., Geology of the upper Coachella Valley area, California, Spec. Rep. Calif. Div. Mines Geol., 94, 8-43, 1968.

Reynolds, R.E., and W.A. Reeder, Age and fossil assemblages of the San Timoteo

Formation, Riverside County, California, in Geology Around the Margins of the Eastern San Bernardino Mountains, Pub. Inland Geol. Soc., 1, edited by M.A. Kooser and R.E. Reynolds, pp. 51-56, Inland Geol. Soc., Redlands, Calif., 1986.

Sadler, P.M., An introduction to the San Bernardino Mountains as the product of young orogenesis, in Late Cenozoic Stratigraphy and Structure of the San Bernardino Mountains, Field Trip 6, edited by P.M. Sadler and M.A. Kooser, in Geologic Excursions in the Transverse Ranges, Geol. Soc. Am. Cordilleran Sect. Meet. Guideb., 78, edited by J.D. Cooper, pp. 57-65, 1982a.

Sadler, P.M., Provenance and structure of late Cenozoic sediments in the northeast San Bernardino Mountains, in Late Cenozoic Stratigraphy and Structure of the San Bernardino Mountains, Field Trip 6, edited by P.M. Sadler and M.A. Kooser, in Geologic Excursions in the Transverse Ranges, Geol. Soc. Am. Cordilleran Sect. Meet. Guideb., 78, edited by J.D. Cooper, pp. 83-91, 1982b.

Sadler, P.M., and Reeder, W.A., Upper Cenozoic, quartzite-bearing gravels of the San Bernardino Mountains, southern California; recycling and mixing as a result of transpressional uplift, in Tectonics and Sedimentation Along Faults of the San Andreas System, edited by D.W. Anderson and M.J. Rymer, pp. 45-57, Pacific Section, SEPM, Los Angeles, Calif., 1983.

Sadler, P.M., The Santa Ana basin of the central San Bernardino Mountains: Evidence of the timing and uplift and strike-slip relative to the San Gabriel Mountains, in The San Andreas Fault System: Displacement, Palinspastic Reconstruction, and Geologic Evolution, edited by R.E. Powell, R.J. Weldon, and J.C. Matti, Mem. Geol. Soc. Am., 178, 307-322, 1993.

Sadler, P.M., A. Demirer, D. West, and J.M. Hillenbrand, The Mill Creek basin, the Potato sandstone, and fault strands in the San Andreas fault south of the San Bernardino Mountains, in The San Andreas Fault System: Displacement, Palinspastic Reconstruction, and Geologic Evolution, edited by R.E. Powell, R.J. Weldon, and J.C.

Matti, Mem. Geol. Soc. Am., 178, 289-306, 1993.

Sass, J.H., A.H. Lachenbruch, and T.H. Moses, Jr., Heat flow from a scientific research well at Cajon Pass, California, J. Geophys. Res., 97, 5017-5030, 1992.

Seeber, L., and J.G. Armbruster, The San Andreas fault system through the Transverse Ranges as illuminated by earthquakes, J. Geophys. Res., 100, 8285-8310, 1995.

Sheffels, B., and M. McNutt, Role of subsurface loads and regional compensation in the isostatic balance of the Transverse Ranges, California: Evidence for intracontinental subduction, J. Geophys. Res., 91, 6419-6431, 1986.

Stein, R.S., C.T. Whalen, S.R. Holdahl, W.E. Strange, and W.R. Thatcher, Saugus-Palmdale, California, field test for refraction error in historical leveling surveys, J. Geophys. Res., 91, 9031-9044, 1986.

Turcotte, D.L., and G. Schubert, Geodynamics: Applications of Continuum Physics to Geological Problems, 450 pp., John Wiley, New York, 1982.

Webb, T.H., and H. Kanamori, Earthquake focal mechanisms in the eastern Transverse Ranges and San Emigdio Mountains, southern California, and evidence for a regional decollement, Bull. Seismol. Soc. Am., 75, 735-757, 1985.

Weldon, R.J., The late Cenozoic geology of Cajon Pass: Implications for tectonics and sedimentation along the San Andreas fault, Ph.D. thesis, 400 pp., Calif. Inst. of Technol., Pasadena, Calif., 1986.

Weldon, R.J., and K. Sieh, Holocene rate of slip and tentative recurrence interval for large earthquakes on the San Andreas fault in Cajon Pass, southern California, Geol. Soc. Am. Bull., 96, 793-812, 1985.

Weldon, R.J., K.E. Meisling, and J. Alexander, A speculative history of the San Andreas fault in the central Transverse Ranges, California, in The San Andreas Fault System: Displacement, Palinspastic Reconstruction, and Geologic Evolution, edited by R.E. Powell, R.J. Weldon, and J.C. Matti, Mem. Geol. Soc. Am., 178, 161-198, 1993.

Wolf, R.A., The development of the (U-Th)/He thermochronometer, Ph.D. thesis, 211 pp., Calif. Inst. of Technol., Pasadena, Calif., 1997.

Wolf, R.A., K.A. Farley, and L.T. Silver, Assessment of (U-Th)/He thermochronometry: The low-temperature history of the San Jacinto mountains, California, Geology, 25, 65-68, 1997.

Wolf, R.A., K.A. Farley, and L.T. Silver, Helium diffusion and low temperature thermochronometry of apatite, Geochim. Cosmochim. Acta, 60, 4231-4240, 1996a.

Wolf, R.A., D. Kass, and K. Farley, Sensitivity of apatite (U-Th)/He ages to thermal history (abstract), EOS Trans., AGU, 77 (46), Fall Meet. Suppl., F644, 1996b.

Woodburne, M.O., Cenozoic stratigraphy of the Transverse Ranges and adjacent areas, southern California, Spec. Pap. Geol. Soc. Am., 162, 91 pp., 1975.

Zeitler, P.K., A.L. Herczeg, I. McDougall, and M. Honda, U-Th-He dating of apatite: A potential thermochronometer, Geochim. Cosmochim. Acta, 51, 2865-2868, 1987.

Table 1. Helium Ages and Associated Data

Sample	Longitude x Latitude	Elev., m	Rock Type	He, pmol	Th, ppm	U, ppm	Mass, mg	F_T	Corrected Age, Ma	Average Age*, Ma
				Big Bear Block						
7(1)	117.0073x34.1872	1233	qtz. monz.	0.108	16.4	11.7	0.083	0.78	20.2	20.6±1.6
(2)				0.135	11.8	12.3	0.099	0.82	21.0	
10(1)	117.1993x34.3221	1329	qtz. monz.	0.976	10.9	9.43	0.349	0.86	51.2	51.2±4.1
(2)				0.994	10.9	8.40	0.388	0.87	51.1	
15(12)	117.0186x34.2137	1614	qtz. monz.	0.066	26.6	15.3	0.017	0.71	49.4†	49.4±3.9
16(2)	117.0161x34.2173	1812	qtz. monz.	0.496	8.12	5.69	0.269	0.87	52.8	52.4±4.2
(4)				0.279	20.3	14.4	0.065	0.81	51.9†	
17(1)	117.0235x34.2247	2113	qtz. monz.	1.213	16.8	7.09	0.360	0.87	66.5	64.3±5.1
(3)				0.449	12.0	5.26	0.201	0.85	62.0	
				San Gorgonio Block						
12(3)	116.9783x34.1162	1526	qtz. monz.	0.144	8.17	9.68	0.191	0.83	14.9	14.3±1.1
(3b)				0.147	12.1	9.70	0.176	0.86	14.9	
(4)				0.090	9.06	9.00	0.142	0.83	13.1	
20(1)	117.0703x34.1362	756	qtz. monz.	0.483	20.0	17.8	0.280	0.85	17.2	18.2±1.5
(2)				0.489	21.6	18.7	0.239	0.86	19.1	
24(1)	116.8934x34.1247	3311	qtz. monz.	0.450	9.58	5.35	0.265	0.87	48.8	52.6±4.2
(2)				0.479	12.5	5.83	0.219	0.84	56.4	
25(1)	116.9290x34.1588	1861	qtz. monz.	0.777	21.8	18.1	0.166	0.83	46.3	40.8±3.3
(2)				1.162	15.7	19.4	0.307	0.86	36.1	
(3)				1.363	16.7	27.1	0.239	0.87	40.1	
26(2)	116.8894x34.0833	1899	qtz. monz.	0.376	17.0	17.8	0.258	0.86	14.7	14.5±1.2
(3)				0.151	2.61	15.6	0.150	0.83	14.3	
27(1)	116.828x34.101	3506	qtz. monz.	1.724	29.8	24.2	0.222	0.83	56.9	55.7±4.5
(3)				1.025	34.7	25.8	0.134	0.79	54.5	
				Wilson Creek Block						
19(3)	117.0955x34.1102	652	granodiorite	0.0033	27.7	16.0	0.051	0.73	0.76	0.7±0.2††
(4)				0.0084	29.5	16.4	0.160	0.78	0.55†	
				Yucaipa Ridge Block						
21(1)	116.9453x34.0078	2323	granodiorite	0.032	58.6	22.9	0.147	0.81	1.38	1.6±0.5††
(2)				0.089	48.4	23.3	0.361	0.86	1.57	
(3)				0.114	61.7	26.7	0.366	0.86	1.67†	
23(1)	116.9676x34.0897	1387	granodiorite	0.058	7.75	24.0	0.299	0.85	1.68	1.6±0.5††
(2)				0.038	6.18	15.1	0.373	0.87	1.35	
(3)				0.081	6.49	20.8	0.451	0.85	1.80†	

Numbers in parentheses are replicates from the same rock. Abbreviation elev. is elevation and qtz. monz. is quartz monzonite.

* With 2σ error equal to 8%.

† Samples on which helium was measured with greater precision on a different mass spectrometer (MAP) at Caltech.

†† The 2σ error limits on samples with small amounts of helium are ±30%, see text.

Figure 1: Digital elevation model of the San Bernardino Mountains (SBMs), color coded for elevation. Elevation divisions are 100 m, as shown by the scale on the right, and increase from dark green (low elevation) to white (high elevation). Note that the elevation model is shaded for relief (lit from the north), so that colors may be darker on the map than on the legend. Inset shows location of the SBMs and the digital elevation model (boxed) relative to the San Andreas fault zone, San Gabriel Mountains (SGMs), and velocity of the Pacific Plate relative to the North American Plate (NUVEL-1A CFR [DeMets, 1995]) in southern California. Circles show the approximate locations of helium samples (refer to Figure 2 for numbers). The Big Bear block makes up the broad northern plateau, and the tectonic blocks in the southern part of the range are outlined. The average elevation and slope of the SBMs and SGMs, as well as that of the major tectonic blocks, are listed in the lower right. These parameters are based on the 90-m resolution digital elevation model, from which this map was generated. Abbreviations are as follows: BBB, Big Bear block; SGB, San Gorgonio block; YR-WC, Yucaipa Ridge-Wilson Creek blocks; and MB, Morongo block.

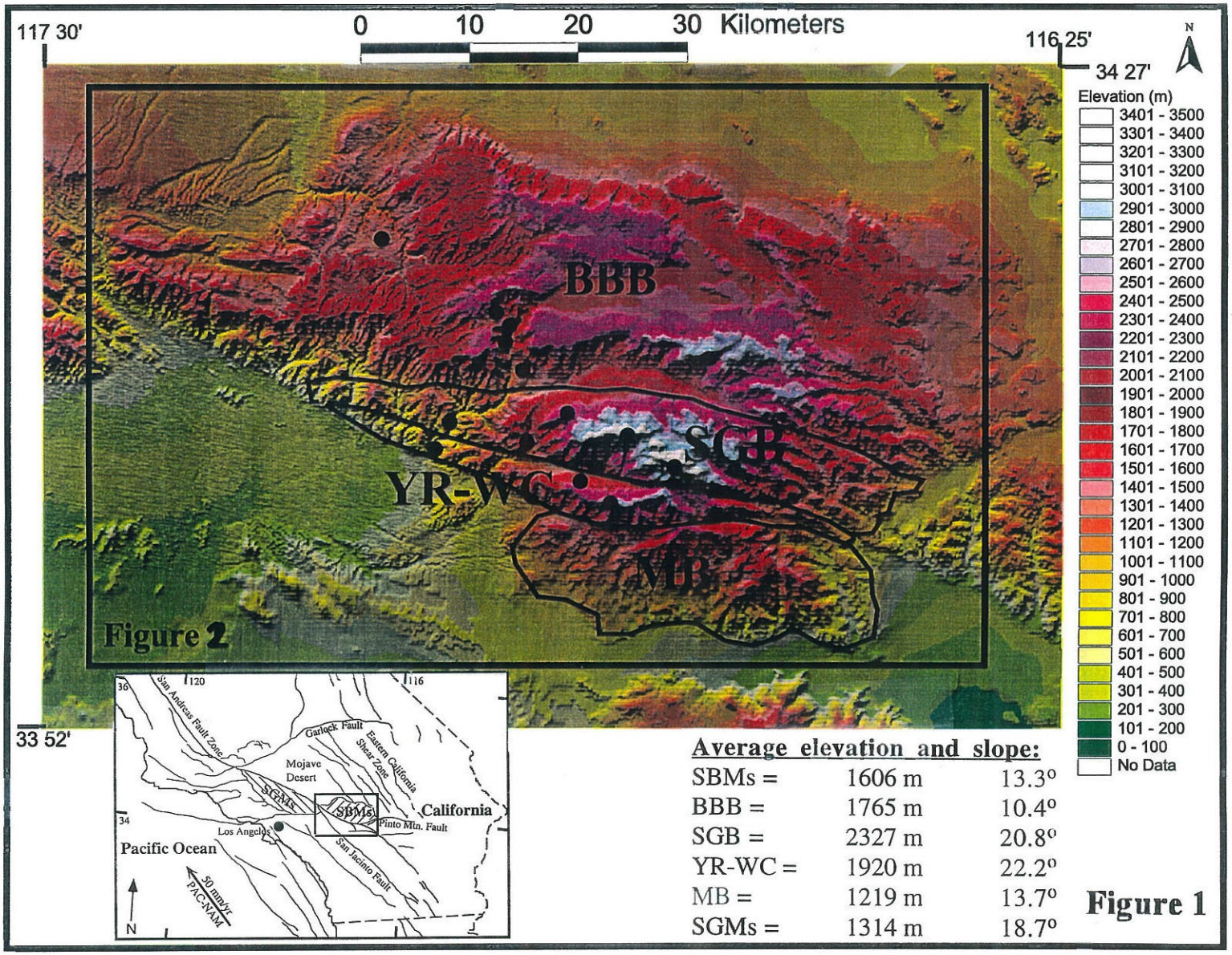

Average elevation and slope:

SBMs =	1606 m	13.3°
BBB =	1765 m	10.4°
SGB =	2327 m	20.8°
YR-WC =	1920 m	22.2°
MB =	1219 m	13.7°
SGMs =	1314 m	18.7°

Figure 1

Figure 2: Tectonic and simplified geologic map of the San Bernardino Mountains (location shown on Figure 1), showing sample locations and average ages (in Myr), as in Table 1. The major tectonic blocks, Quaternary faults (adapted from Matti and Morton, 1993), Tertiary sediments, Miocene basalts (6-10 Ma [Neville and Chambers, 1982]), and the preuplift, weathered granitic surface (Oberlander, 1972) are also indicated. The distributions of the weathered surface, faults of the North Frontal thrust system, and the faults between the Santa Ana thrust and the San Gorgonio block are based on airphoto mapping and field investigations by the first author. Letters refer to Tertiary deposits (from Dibblee, 1964, 1974; Bortugno and Spittler, 1986) as follows: A, Old Woman sandstone (2-3 Ma, records initiation of uplift [May and Repenning, 1982]); B, eastern Santa Ana sandstone (Sadler, 1993); C, Santa Ana sandstone (4-15 Ma, preuplift facies and source [Sadler, 1993]); D, Crowder Formation (Sadler, 1993); E, Potato sandstone (~13 Ma, preuplift strike-slip basin [Sadler et al., 1993]); F, Mill Creek Formation (10-13 Ma, preuplift strike-slip basin [Sadler et al., 1993]); G, Crowder Formation deposited atop the weathered surface (Meisling and Weldon, 1989); H, general location of the San Francisquito, Vaqueros, and Cajon Formations (Paleocene to Miocene, preuplift), Crowder Formation (17-9.5 Ma, preuplift facies and source), and Phelan Peak Formation (4-1.5 Ma, facies and source record uplift) (Woodburne, 1975; Meisling and Weldon, 1989); I, general location of Mount Eden Formation (Pliocene) and San Timoteo Formation (Plio-Pleistocene, syntectonic) (Reynolds and Reeder, 1986); and J, general location of Coachella Fanglomerate (Miocene), Imperial Formation (Mio-Pliocene, marine), Painted Hill Formation (Pliocene, nonmarine), and Cabezon Fanglomerate (Pleistocene, synuplift) (Allen, 1957; Proctor, 1968). Straight lines show locations of elevation profiles in Figures 3, 4, and 5. Abbreviations are as follows: BCC, Bear Creek Canyon; CHFZ, Crafton Hills fault zone; CV-SAF, Coachella Valley-San Andreas fault; MV fault, Morongo Valley fault; Old WS fault, Old Woman Springs fault; Pipes C fault, Pipes Canyon fault; SAV, Santa Ana Valley; SGP-FZ, San Gorgonio Pass fault zone; WCF, Wilson Creek fault.

Figure 2:

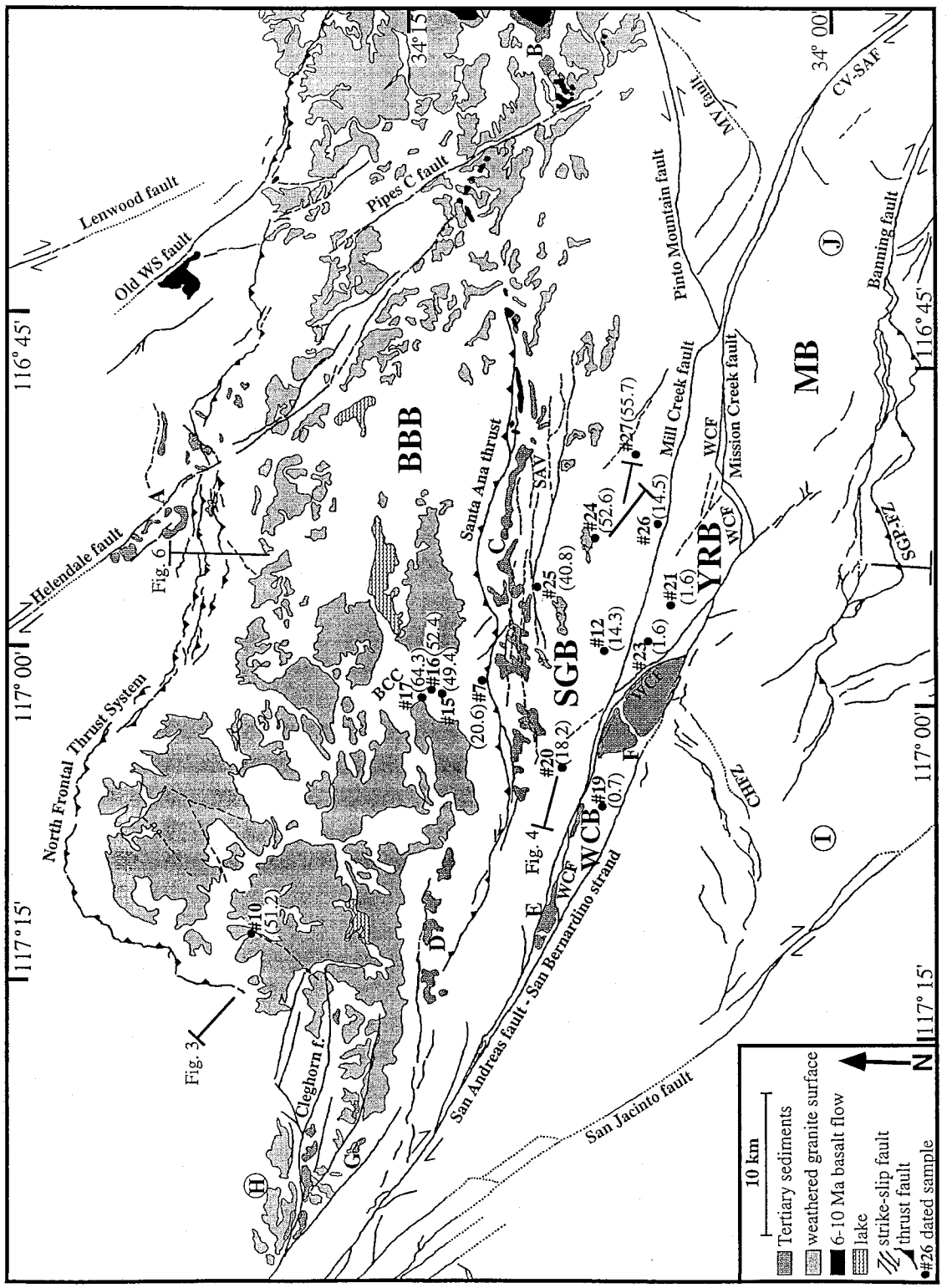
117° 15'
117° 00'
116° 45'
34° 15'
34° 00'
Lenwood fault
Old WS fault
Helendale fault
North Frontal Thrust System
Pipes C fault
MV fault
Pinto Mountain fault
Mill Creek fault
Mission Creek fault
Banning fault
CV-SAF
Santa Ana thrust
San Andreas fault - San Bernardino strand
San Jacinto fault
Cleghorn f.
CHF
SGP-FZ
WCF
SAV
BCC
WCB
BBB
SGB
YRB
MB
Fig. 3
Fig. 4
Fig. 6
A
B
C
D
E
F
G
H
I
J
#10 (51.2)
#15 (49.4)
#16 (52.4)
#17 (64.3)
#7 (20.6)
#20 (18.2)
#19 (0.7)
#25 (40.8)
#12 (14.3)
#23 (1.6)
#21 (1.6)
#24 (52.6)
#26 (14.5)
#27 (55.7)
10 km
Tertiary sediments
weathered granite surface
6-10 Ma basalt flow
lake
strike-slip fault
thrust fault
#26 dated sample
N

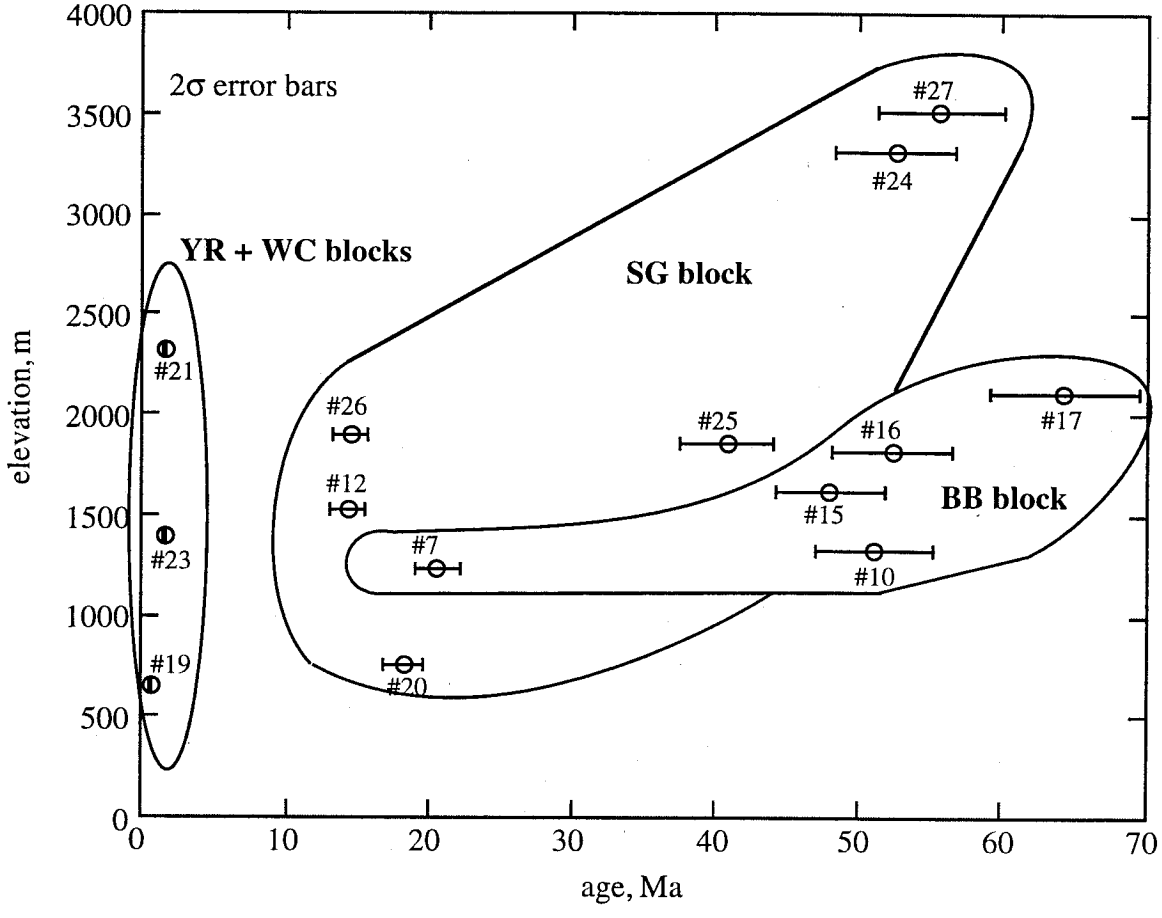

Figure 3: Elevation-age plot for individual helium ages of samples dated in this study. Numbers refer to samples in Table 1 and Figure 2. The ages are grouped within the main blocks as shown (YR+WC, Yucaipa Ridge and Wilson Creek; SG, San Gorgonio; and BB, Big Bear blocks). The tectonic blocks are defined by the location of faults and geomorphology, as discussed in text. Error bars (8%, 2σ) are shown for averaged ages, which appear as circles.

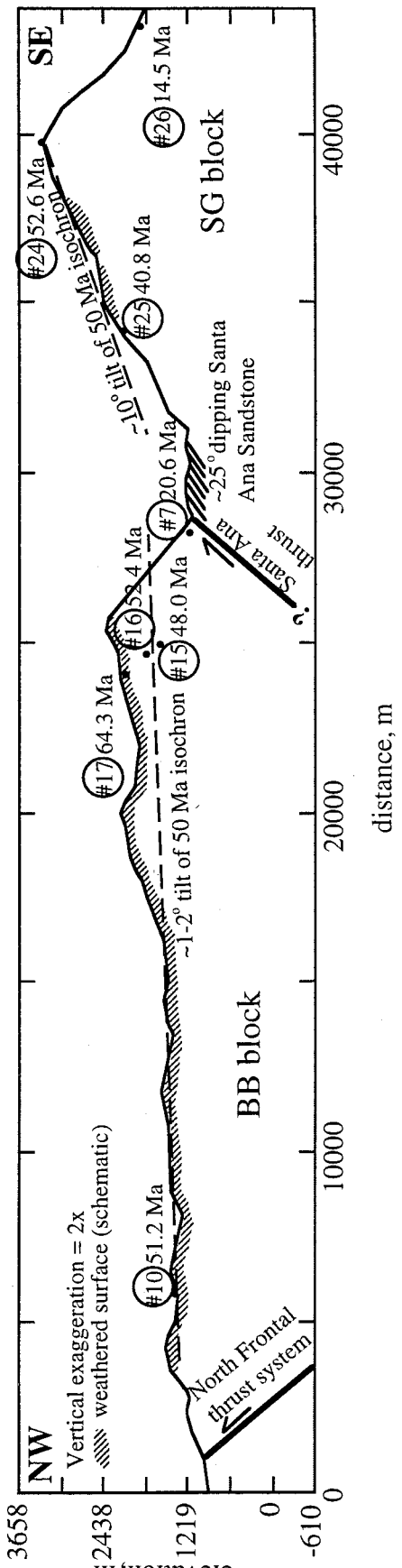

Figure 4: Elevation profile from northwest to southeast along the Big Bear and San Gorgonio blocks. The weathered surface, shown schematically by hachures, tilts more steeply northwestward than the 50-Ma helium isochron. Helium ages from Bear Creek Canyon are projected onto this section. Line of section shown in Figure 2.

Figure 5: (a) West to east elevation profile along the ridge line of the San Gorgonio block (line of section shown in Figure 2). Profile runs from Santa Ana River on the west to San Gorgonio Peak on the east. Sample locations have been projected on to this line and are shown with their ages. Approximate isochrons (50 and 20 Ma) for helium ages are shown, both sloping 5.5° on the west and 2° in the east. Sample 25 fits these isochrons only when corrected for a 10° dip to the north, based on the slope of the patches of weathered granite. (b) Age-elevation plot of helium ages from the SG block after being corrected for the warping of the block, indicated by geologic data and the dip of isochrons shown in Figure 5a. These define a tight monotonic relationship once corrected. Samples received the following corrections: sample 12 lowered 830 m (5.5°W tilt over 8.6 km from hinge at sample 20), sample 25 lowered 1131 m (5.5°W over 11.8 km) and raised 793 m (10°N over 4.5 km from other samples), sample 24 lowered 1131 m (same as sample 25) plus 135 m (2°W over 3.9 km from sample 25), sample 26 lowered 1131 m plus 223 m (2°W over 6.4 km), and sample 27 lowered 1131 m plus 362 m (2°W over 10.4 km). (c) Corrected age-elevation plot for the SG block (as in Figure 5b) along with the measured age-elevations of upper samples from the BB block (from Bear Creek Canyon, samples 15, 16, and 17). The two sets of age-elevations align more closely when the localized warp of the SG block has been removed.

Figure 5:

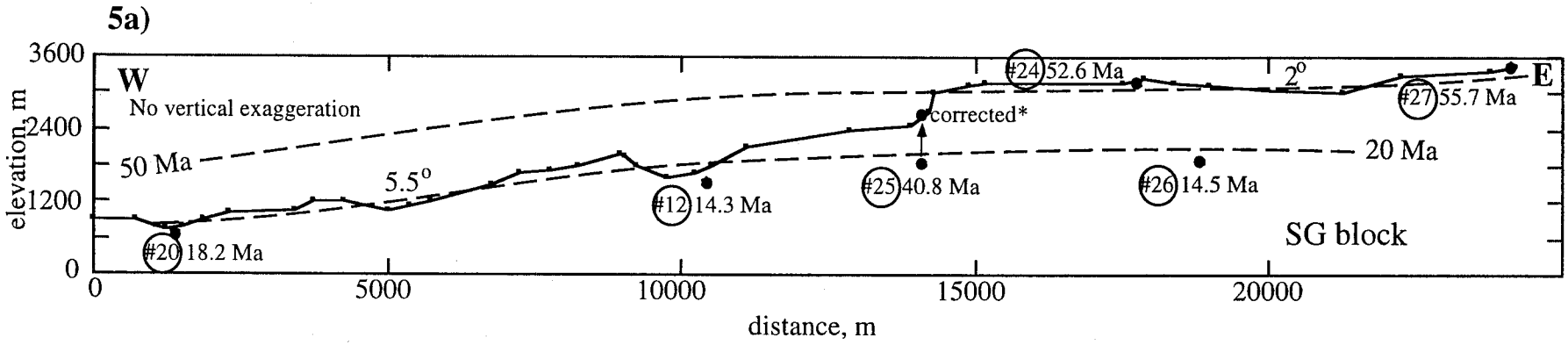
5a)
3600
2400
1200
0
elevation, m
W
No vertical exaggeration
50 Ma
5.5°
#20 18.2 Ma
#12 14.3 Ma
#25 40.8 Ma
corrected*
#24 52.6 Ma
2°
#27 55.7 Ma
E
20 Ma
#26 14.5 Ma
SG block
0
5000
10000
15000
20000
distance, m

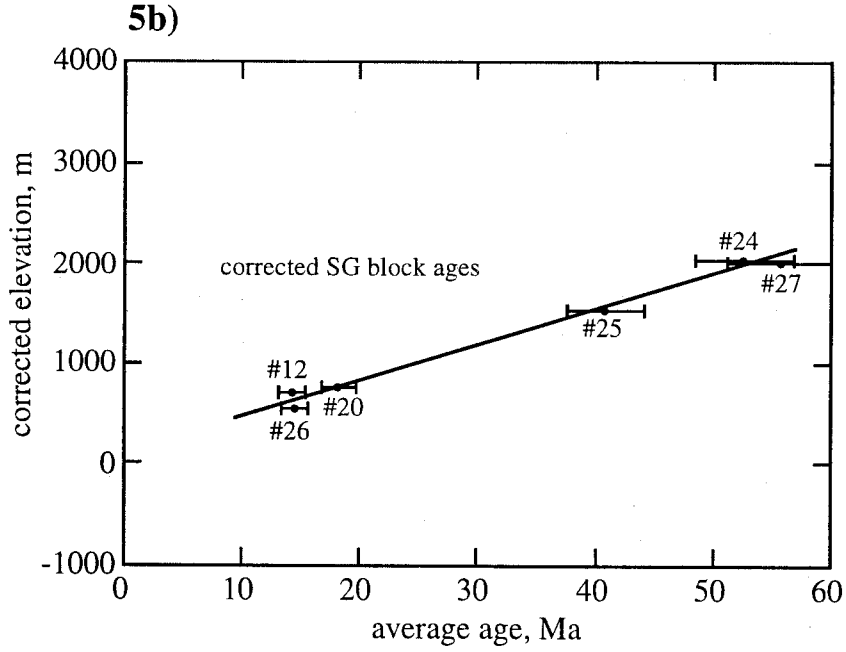
5b)
4000
3000
2000
1000
0
-1000
corrected elevation, m
corrected SG block ages
#24
#27
#25
#12
#20
#26
0
10
20
30
40
50
60
average age, Ma

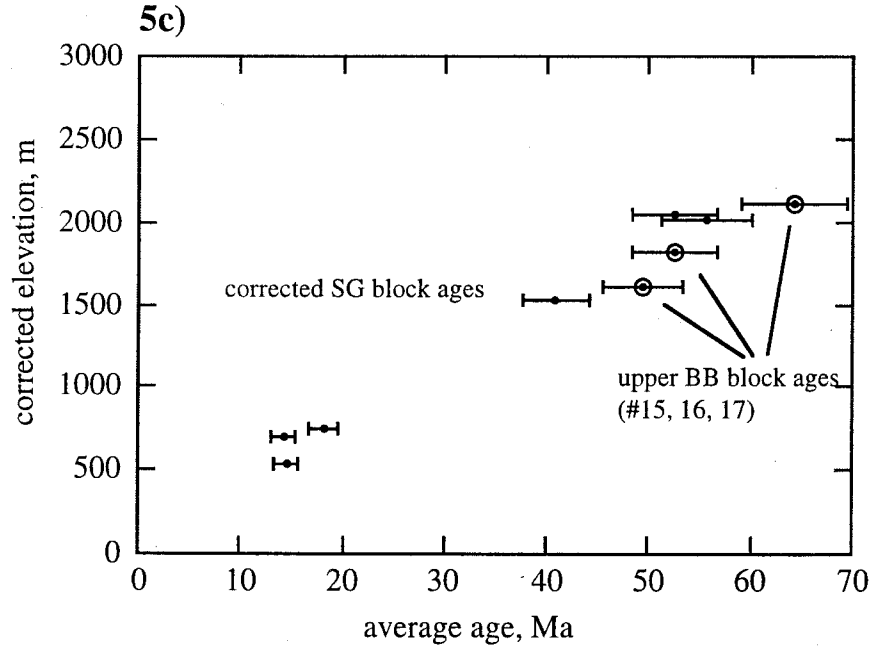
5c)
3000
2500
2000
1500
1000
500
0
corrected elevation, m
corrected SG block ages
upper BB block ages
(#15, 16, 17)
0
10
20
30
40
50
60
70
average age, Ma

Figure 6: Schematic block diagram of the San Bernardino Mountains along a north-south transect, showing our interpretation of the relief of major blocks if no erosion had occurred in the last few Myr. The solid line shows the present-day topography along a north-south transect (line of section shown in Figure 2, vertical exaggeration is 2.5 times). The dashed lines represent the relief of the blocks when erosion is restored. Major faults are shown with approximate dips (Allen, 1957; Meisling, 1984; Sadler, 1993). The Yucaipa Ridge block may have stood at an elevation of ~4.5 km, one kilometer higher than the present-day crest of the San Gorgonio block and 2 km higher than the Big Bear block. The San Gorgonio block is shown tilting upward to the south, and the Big Bear block is shown with only minor erosion restored from the top of the plateau and weathered granite surface. Abbreviations are as follows: MB, Morongo block; YRB, Yucaipa Ridge block; SGB, San Gorgonio block; BBB, Big Bear block; and SB-SAF, San Bernardino strand of the San Andreas fault zone.

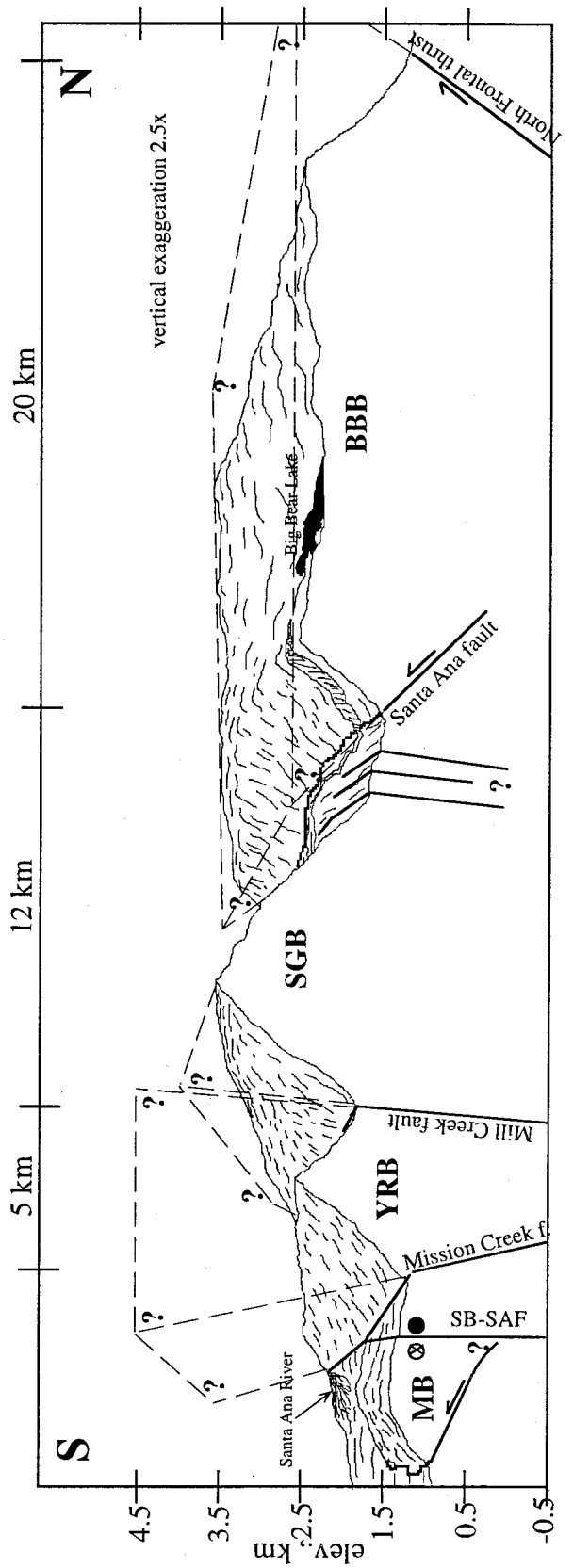
S
N
5 km
12 km
20 km
vertical exaggeration 2.5x
elev. km
4.5
3.5
2.5
1.5
0.5
-0.5
Santa Ana River
MB
SB-SAF
Mission Creek f.
YRB
Mill Creek fault
SGB
Santa Ana fault
Big Bear Lake
BBB
North Frontal thrust
?

Figure 6:

Figure 7: Generalized block diagrams that show examples of how vertical motion may occur in association with strike-slip faulting. (a) Uplift of block due to vertical motion associated with slip partitioning on a dipping fault strand in a strike-slip zone. (b) Uplift of block due to convergence within a fault stepover or restraining bend, either as a single thrust ramp or as diffuse internal shortening (concentric circles are elevation contours symbolizing uplift and small planes represent minor reverse faults at depth). (c) Uplift due to a subsurface bend or other geometric perturbation propagating along a strike-slip fault (the western San Bernardino arch [Meisling and Weldon, 1989]). (d) Uplift due to convergence associated with intersecting subparallel or conjugate strike-slip faults. (e) Apparent uplift along a strike-slip fault due to pure strike-slip offset of a topographic high.

Figure 7:

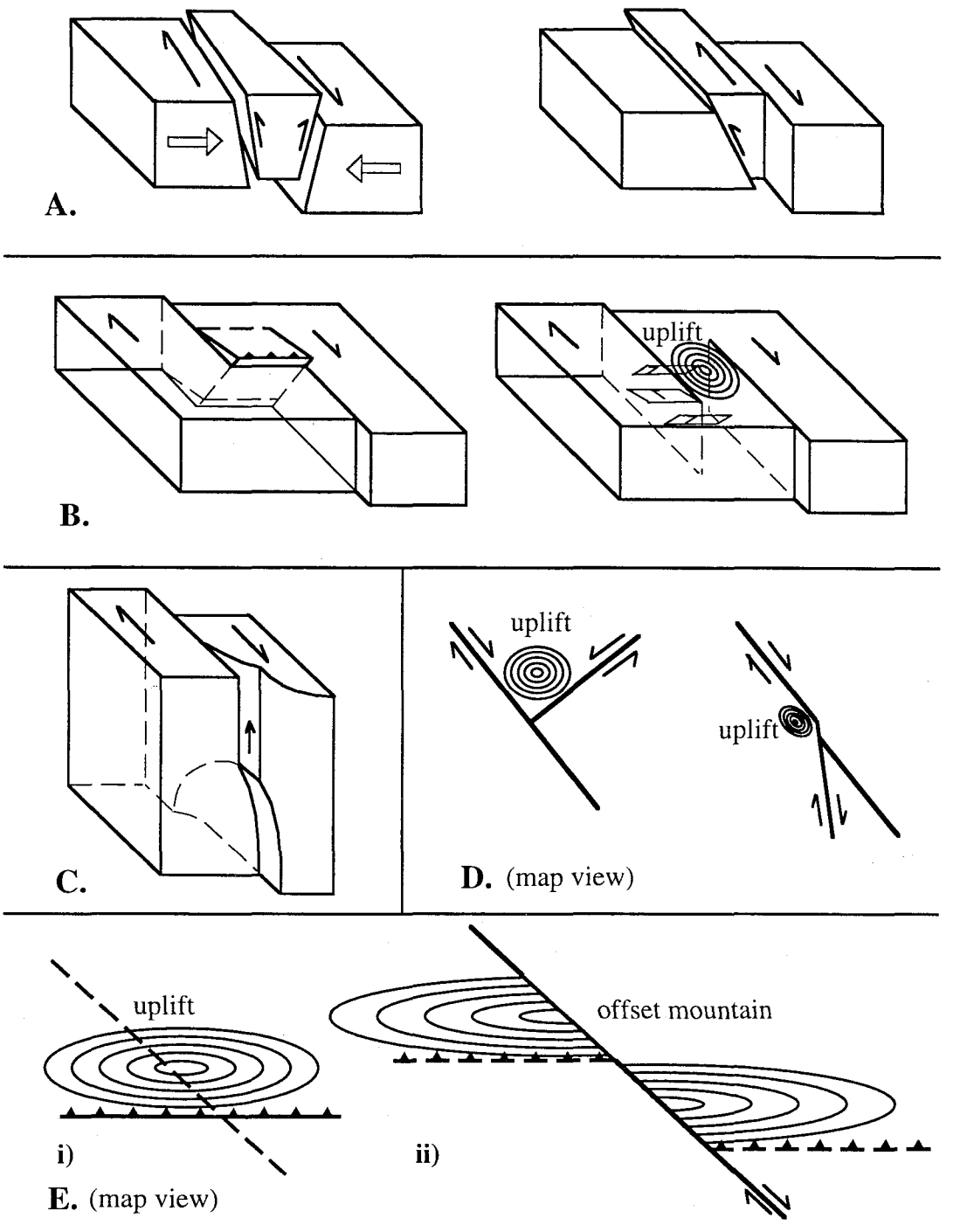
A.
B.
uplift
C.
uplift
uplift
D. (map view)
uplift
offset mountain
i)
ii)
E. (map view)

Chapter Three

Geomorphic constraints on the uplift of the Big Bear plateau: Use of a deeply weathered granitic surface as a structural datum

Spotila, James A.

California Institute of Technology

August, 1998

3.1. Abstract

To better understand the architecture of deformation in the San Bernardino Mountains, the kinematics of the major thrust faults must be constrained. A structural datum must be found that constrains the vertical displacement field of the main thrust-fault block, the Big Bear plateau, and a previously-recognized, low-relief, deeply weathered granite surface represents the best potential. This horizon is locally buried and dated as relict (pre-uplift), but has not been shown everywhere to be a correlative, synchronous, pre-uplift feature. This detailed geomorphic study investigates the origins of this surface and provides the information necessary to use it to constrain vertical displacement.

The weathered surface consists of a thick profile of regolith and corestones that fits the idealized character of deeply weathered granite. Based on field characterization and airphoto mapping, the surface has an extensive distribution across the range. Comparison of the field and laboratory character of soils and saprolites with other weathered granite surfaces reveals that the weathered horizon is not necessarily relict of a previous climatic regime, but that weathering rates probably have not exceeded 0.01 mm/yr. This implies the surface of the plateau has not been lowered substantially by weathering and removal of saprolite since uplift. Similarly, the thick saprolites atop the plateau may have required several million years to form and thus, where preserved, indicate that erosion has been limited since uplift initiated. Erosion has been greatest on the eastern flank of the plateau, based on geomorphic indications, but has only proceeded at <0.02 mm/yr (constrained by dated basalts). This suggests that the weathered surface represents a horizon that has not been modified significantly (±50 m) by forces other than tectonic dislocation since uplift. Lastly, the present geomorphology of the surface and paleogeographic indicators suggest that the original geometry of the surface was nearly level, although a pre-uplift dome may have existed where the central plateau now sits. The difficulty posed by this possible non-horizontal geometry can be assuaged by using the weathered surfaces atop both the hanging- and footwall-blocks to constrain tectonic dislocations along the thrust faults.

3.2. Introduction

The San Bernardino Mountains (SBMs) consist of several tectonic blocks that are distinct in topographic form and separated by major faults (cf. Dibblee, 1975; Sadler, 1982a; Spotila et al., 1998) (Figure 1). These blocks of crystalline basement have risen over the past few million years in association with transpression along the San Andreas fault system (Meisling and Weldon, 1989; May and Repenning, 1982). Although the pattern and timing of uplift and exhumation have been demonstrated with radiogenic helium thermochronometry for the southern blocks that are bounded by high-angle structures (Spotila et al., 1998), the vertical deformation associated with the Big Bear plateau on the north is largely unconstrained. The plateau makes up the bulk of the SBMs and is bounded by the North Frontal thrust system (NFTS) on the north and the Santa Ana thrust (SAT) on the south. Both of these major faults have high escarpments along their hanging walls and seem to have been the main structures responsible for the uplift of the plateau, but their kinematics are poorly understood because of the lack of constraint on the vertical deformation they have produced.

Although both thrust faults have steep bedrock escarpments at the margins of the Big Bear plateau, their roles in uplifting the plateau are not certain. Both faults juxtapose crystalline basement over Tertiary sediment (NFTS overthrusts Pliocene Old Woman Sandstone [Sadler, 1982b; May and Repenning, 1982]; SAT overthrusts late Miocene Santa Ana Sandstone [Jacobs, 1982; Sadler, 1993]), suggesting they are opposed components of a symmetric thrust system responsible for uplift of the plateau. However, the NFTS has well-developed scarps in late Pleistocene alluvium, whilst the SAT has few scarps in Quaternary sediments (Bryant, 1986a/b; Jacobs, 1982). It has thus been proposed that the SAT was a part of the late Miocene (pre-4 Ma) Squaw Peak thrust system and did not play a role in uplift of the modern range (Meisling and Weldon, 1989). The relative degrees to which the thrusts have uplifted the plateau are thus poorly resolved.

Figure 1a: Tectonic and simplified geologic map of the San Bernardino Mountains of southern California (location shown on Figure 1b). The major tectonic blocks, Quaternary faults (adapted from Matti and Morton, 1993), Tertiary sediments, and Miocene basalts (6-10 Ma; Neville and Chambers, 1982) are indicated. The basic distribution of weathered granite atop the Big Bear plateau and San Gorgonio block is shown, based on airphoto mapping discussed in the text (see Section 3.6). Faults of the North Frontal thrust system and those between the San Gorgonio and Big Bear blocks are also based on airphoto mapping done in this study. Uppercase letters refer to Tertiary deposits (from Dibblee, 1964a, 1964b, 1967b; Bortugno and Spittler, 1986) as follows: A =Old Woman sandstone (May and Repenning, 1982); B and C = Santa Ana sandstone (Sadler, 1993); D = Crowder Formation (Sadler, 1993); E = Potato sandstone (Sadler et al., 1993); F = Mill Creek Formation (Sadler et al., 1993); G = Crowder Formation deposited atop the weathered surface (Meisling and Weldon, 1989); H = general location of the San Francisquito, Vaqueros, and Cajon Formations, Crowder Formation, and Phelan Peak Formation (Woodburne, 1975; Meisling and Weldon, 1989); I = general location of Mt. Eden Formation and San Timoteo Formation (Reynolds and Reeder, 1986); J = general location of Coachella Fanglomerate, Imperial Formation, Painted Hill Formation, and Cabezon Fanglomerate (Allen, 1957; Proctor, 1968). Refer to Chapter 2 for more information on these deposits. Lowercase letters show locations where field observations of weathering were made, as follows: a = White Mtn., b = Butler Peak, c = Coxey Road, d = Big Bear Lake, e = Holcomb Valley, f = The Pinnacles, g = John Bull Flat, h = Running Springs, i = Sugarloaf Mtn., j = Manzanita Springs, k = Yucaipa Ridge, l = Onyx Mtn., n = Rattlesnake Mtn., o = Ord Mtn., p = Crestline, q = Black Lava Butte, r = Keller Peak, s = Rt. 38, t = Santa Ana River. Numbers refer to soil profile locations (#1-7). Lines show sections for elevation profiles in later figures (AB, DC, EG, EF). Abbreviations as follows: BBB = Big Bear block, BCC = Bear Creek Canyon, CHFZ = Crafton Hills fault zone, CV-SAF = Coachella Valley-San Andreas fault, MB = Morongo block, MV =

Morongo Valley (fault), PC = Pipes Canyon (fault), SAV = Santa Ana Valley, SGB = San Gorgonio block, SGP-FZ = San Gorgonio Pass fault zone, WCB = Wilson Creek block, WCF = Wilson Creek fault, WS = (Old) Woman Springs (fault), YRB = Yucaipa Ridge block. Dashed box on the right shows location of Figure 37.

Figure 1

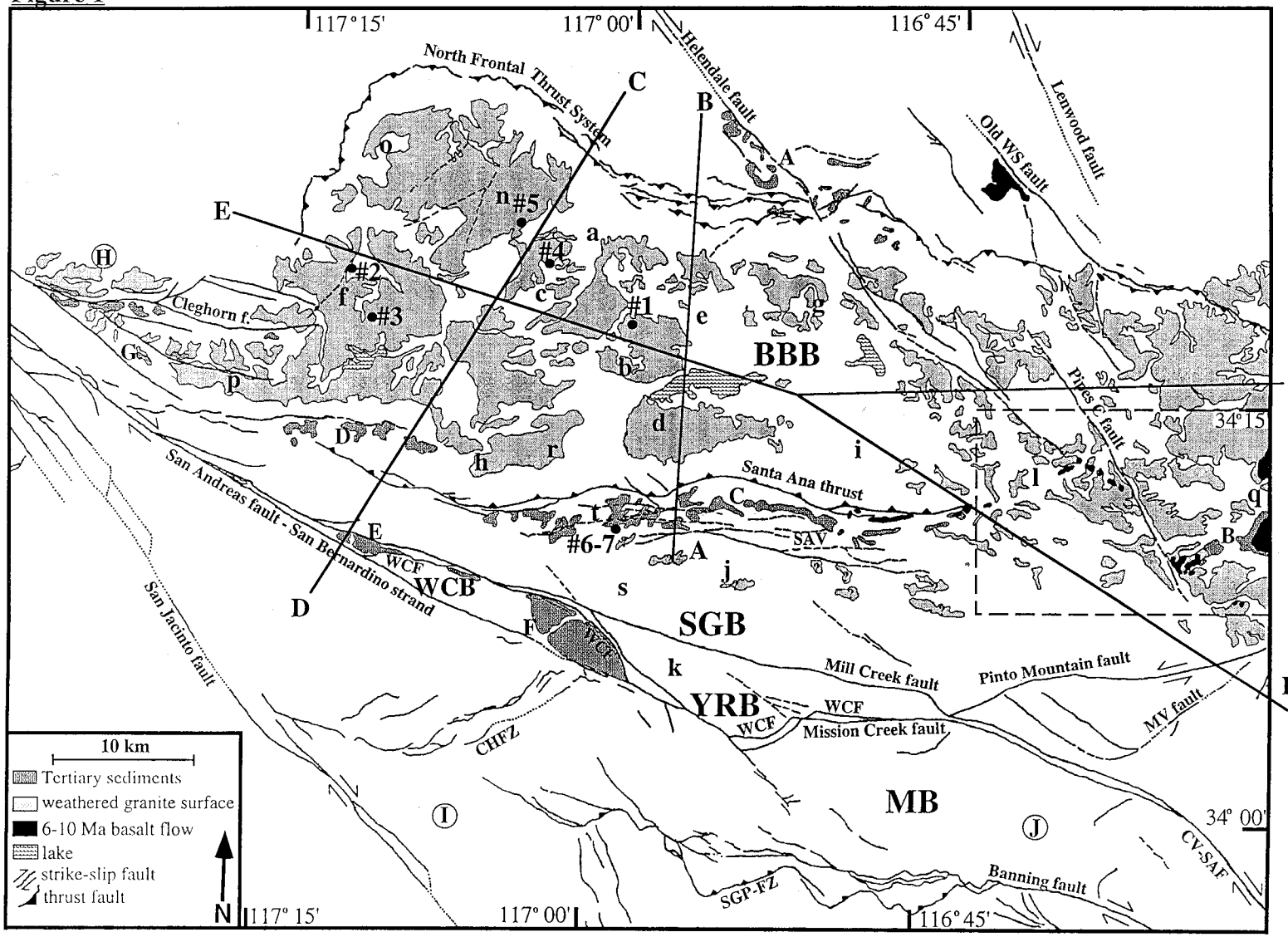
117°15'
117° 00'
116° 45'
34° 15
34° 00'
North Frontal Thrust System
Helendale fault
Lenwood fault
Old WS fault
Cleghorn f.
Pipes Canyon fault
San Andreas fault - San Bernardino strand
Santa Ana thrust
SAV
WCF
San Jacinto fault
CHFZ
Mill Creek fault
Pinto Mountain fault
MV fault
Mission Creek fault
SGP-FZ
Banning fault
CV-SAF
BBB
WCB
SGB
YRB
MB
#1
#2
#3
#4
#5
#6-7
A
B
C
D
E
F
G
H
I
J
10 km
Tertiary sediments
weathered granite surface
6-10 Ma basalt flow
lake
strike-slip fault
thrust fault
N

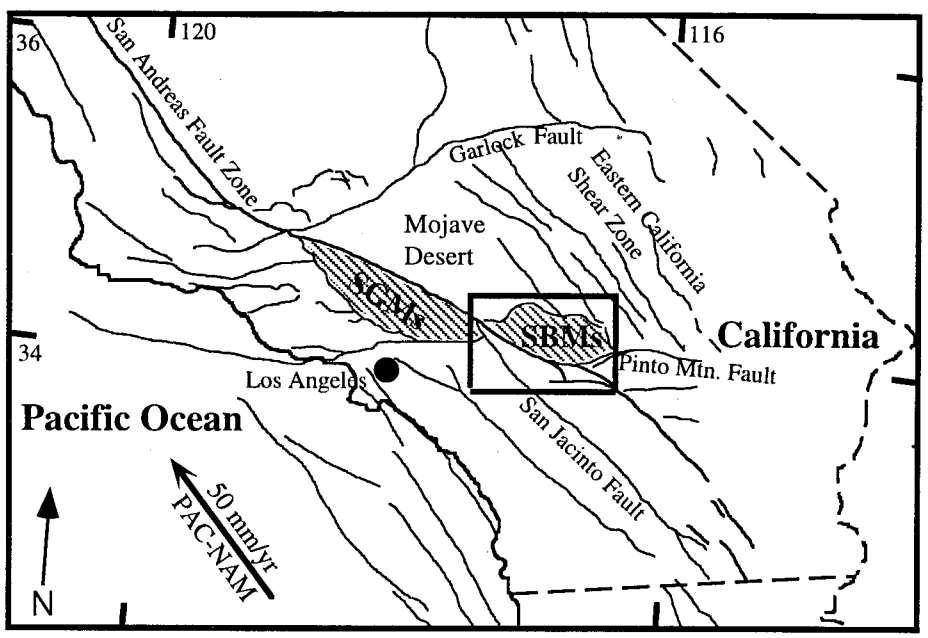

Figure 1b: Location of the San Bernardino Mountains (SBMs) in southern California. Box shows the location of Figure 1a. SGMs = San Gabriel Mountains.

A second major problem with the structures presumably responsible for uplift of the Big Bear plateau is that their subsurface geometries are uncertain. Both thrust faults have low-angle dips near the surface (~30°; Meisling, 1984; Li et al., 1992; Sadler, 1993; Jacobs, 1982), but may either flatten or steepen at depth. Some previous workers have speculated that the northern thrust flattens beneath the plateau into a mid-crustal decollement (Corbett, 1984; Meisling and Weldon, 1989; Li et al., 1992), thus undercutting the SAT. An alternative hypothesis is that the antithetic NFTS and SAT have symmetrical convex shapes below the Big Bear plateau, steepening with depth to join in a near-vertical zone of distributed transpression (Sadler, 1982b).

Existing data is thus not sufficient to show the relative relationships and subsurface geometries of the major faults responsible for uplift of the SBMs. This represents not only a substantial gap in our kinematic understanding of the tectonics of the range, but also makes it difficult to assess the potential seismic hazard of the structures. One potentially enlightening aspect of the plateau uplift that has not been tightly constrained is the distribution of vertical displacement associated with these structures. Constraints on the displacement field would enhance our understanding of the interaction and subsurface geometry of these structures, much as geodetic records of vertical displacement are useful in constraining the subsurface ruptures of thrusts faults.

Unfortunately, a regional marker bed of appropriate age does not exist to constrain the orogenic elevation change with certainty. Pre-uplift Miocene-Pliocene basalts and sediments are preserved on the far eastern and western flanks of the range, but only locally provide constraint on the relief and position of the ground surface prior to Plio-Pleistocene uplift (Meisling and Weldon, 1989; Neville, 1983) (Figure 1a). Across the high plateau, the only possible pre-uplift deposits are scattered remnants of quartzite gravels that may have been derived from a central source, but these are of uncertain age and uncertain original distribution (Sadler and Reeder, 1983). As described below, however, the Big Bear plateau does have a distinctive geomorphic form, which may yield clues about the

vertical displacement on the bounding thrusts faults. The goals of this study are to gain an understanding of how the geomorphology of the plateau has evolved and to determine whether it can be used to learn about the uplift kinematics of the range.

In the first part of this study, a characterization of the basic geomorphology of the Big Bear plateau introduces a low-relief, deeply weathered granite surface as a candidate datum to constrain structural displacement. Its potential use as a marker horizon is explored in the next section, in which it is shown that the surface must meet several criteria if it is to be used to extract tectonic information. This requires an understanding of the evolution of the surface, which can be attained by detailed study of its character. Insights on the evolution of the surface from previous work are presented next, but these fail to fully explain how and when the surface formed and do not define its original and present-day distributions. Results of a detailed geomorphologic study of the weathered surface follow, which offer a better understanding of its nature. The resulting understanding supports use of the weathered surface as a structural datum (with some limitations). The vertical displacement field of the plateau is reconstructed and implications for uplift kinematics are explored in Chapter 4.

3.3. The geomorphology of the Big Bear plateau

The Big Bear plateau has a distinctive topographic form, consisting of a relatively flat, high elevation surface bounded by steep margins. This is evident on maps of elevation and slope and contour maps generated from digital elevation models (Figure 2a/b/c). The upper surface of the plateau makes up nearly half (~40%) of the total area of the SBMs (~3100 km^2) and has an average elevation of 1691 m, nearly the same as that of the whole range (1606 m). Elevation in the SBMs is bimodally distributed as a result of the plateau, with a secondary peak at ~2 km, which corresponds to the upland surface and lakes that partially cover it (Figure 1a, 3a). At its highest, the plateau reaches ~2.5 km elevation, and

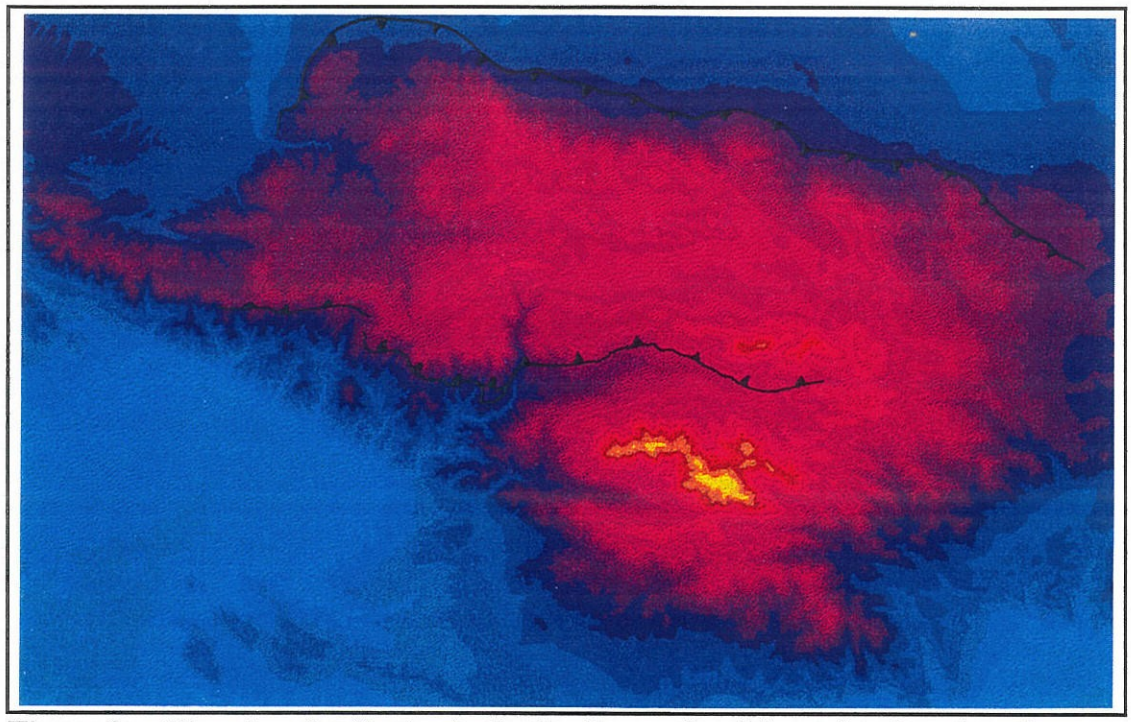

Figure 2a: Elevation distribution in the San Bernardino Mountains, based on the USGS 90-m-resolution digital elevation model. Elevations are color-coded in 100 m bins, with light blue as the lowest elevation (<1000 m), dark blue to purple intermediate (1000-2000 m), and red to yellow high elevation (2000-3500 m).

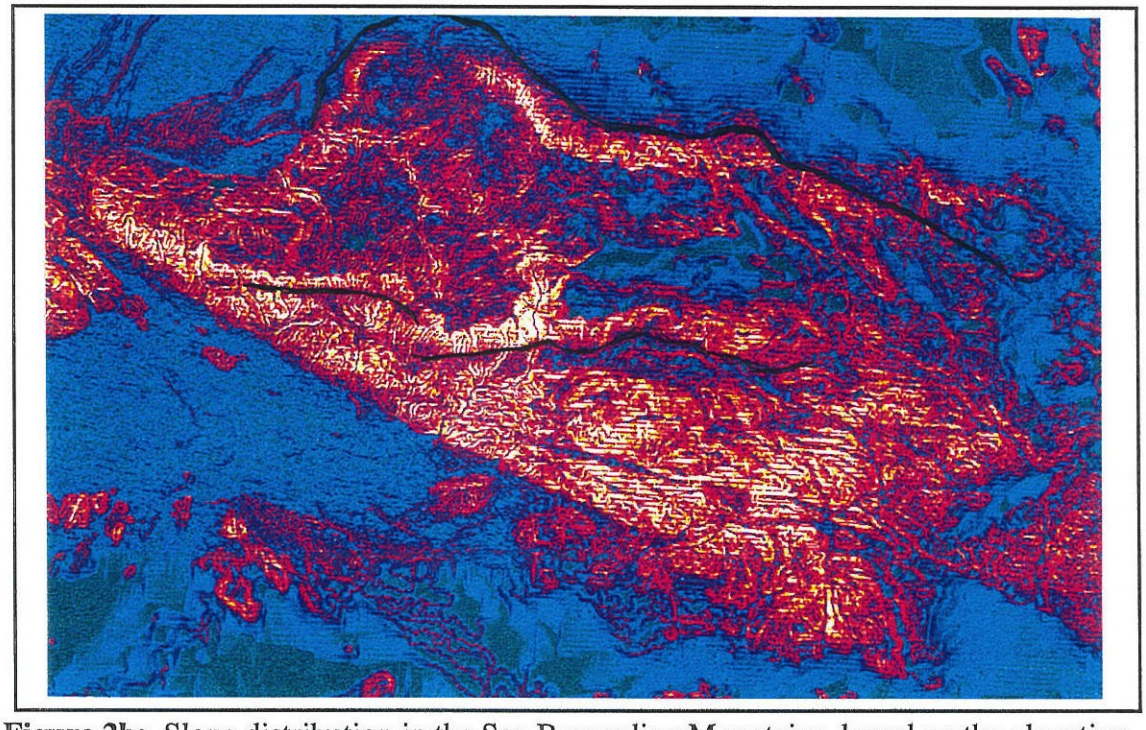

Figure 2b: Slope distribution in the San Bernardino Mountains, based on the elevation data shown in Figure 2a. Slopes increase from green to light blue (0-6°), to purples (7-12°), to reds (13-24°), to yellows (25-30°), to white (>30°).

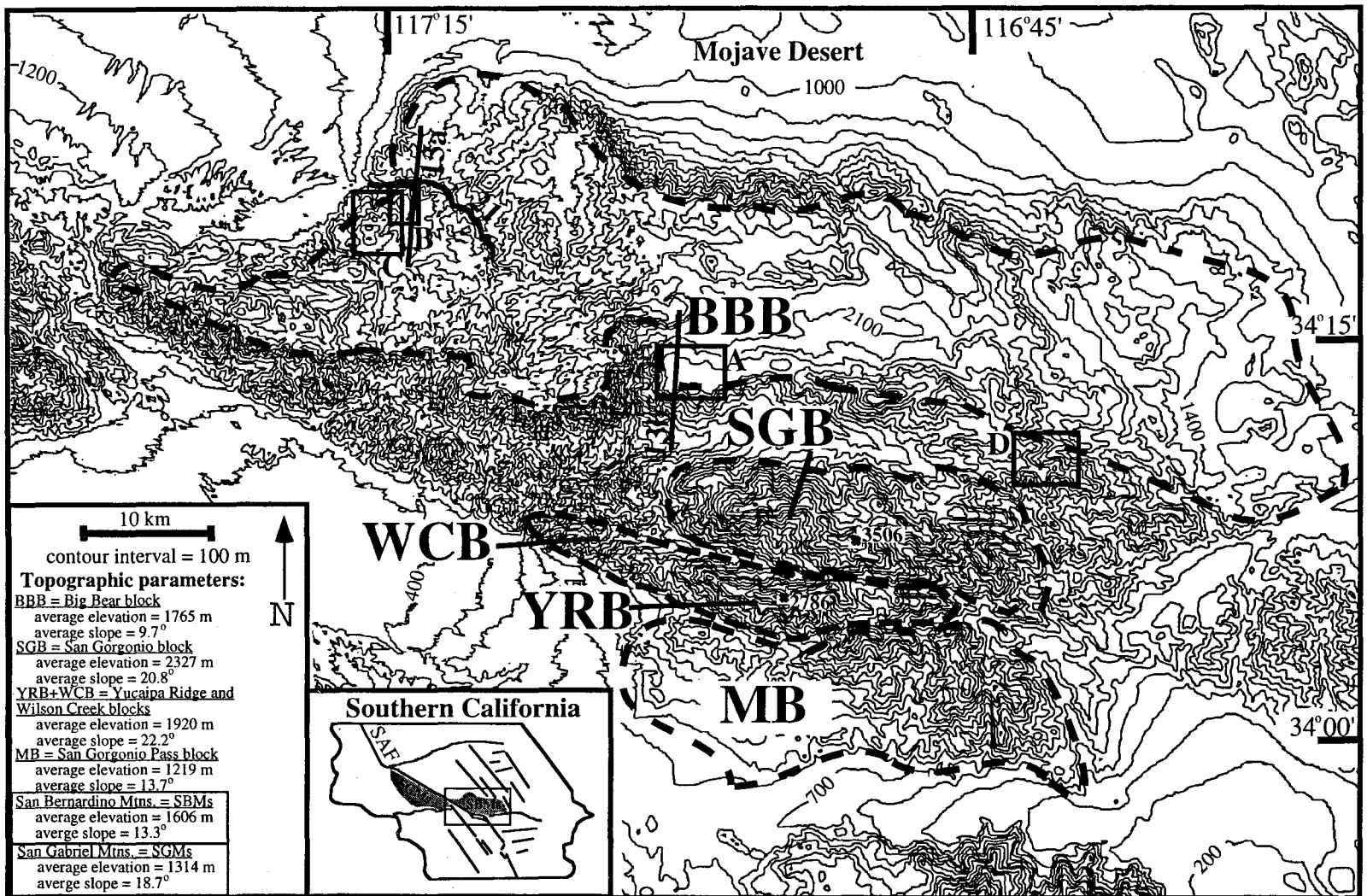

Figure 2c: Topographic map of the San Bernardino Mountains. Inset shows location of the range in southern California. The major tectonic blocks of the range are drawn, and their topographic parameters (average slope and elevation) are listed in the lower left corner. The topographic parameters of the entire San Bernardino Mountains are also given, as are those for the San Gabriel Mountains (for comparison). The boxes show the locations of Figures 16a-d, lines are profiles of Figures 13a-b and 21.

its relief above the surrounding Mojave Desert and San Bernardino Valley lowlands varies from ~0.5 to 1.5 km. The average slope (calculated from 90-m-resolution digital elevation models using a least squares algorithm) of the upper surface is 9.7°, somewhat lower than that of the whole range (13.3°). The distribution of slope along the plateau is dominated by peaks at 3-4° and 0°, due to both the low relief surface and its lakes (Figure 3b). The SBMs thus contrast with other mountains in the Transverse Ranges that are generally steep throughout their entirety. The San Gabriel Mountains, for example, have an average slope of 18.7° and have no comparable upland surface.

The gentle topography of the upland surface is distinct from the plateau's steep margins and is indicative of stable, slowly eroding conditions. The surface has a rolling topography and is only dissected by young, steep canyons near its perimeter. Its overall form is convex, rising in the middle ånd tapering gently downwards to unfaulted eastern and western margins (Figure 1a, 4a). Such convex slopes are typical of surfaces on which material moves downslope by slow creep, rather than rapid mass wasting (cf. Bloom, 1991; p. 201). The fault-bounded northern and southern escarpments, however, are much steeper, often approaching the angle of repose (average slope ~17°). They have concave forms that are typical of rapid erosion by rainwash or mass sliding and have sharp transitions to the convex plateau surface (Figure 4b). Based on this geomorphology, early workers proposed that the escarpments had recently formed by uplift along the bounding faults and continue to erode rapidly, whereas the plateau retains a mature, relict topography that erodes slowly (Mendenhall, 1907; Vaughan, 1922; Noble, 1932; Dibblee, 1975).

The lack of rapid erosion atop the plateau is also evident geomorphically. The erosive power of streams, a function of several factors (including slope), can be represented by average stream gradients in different areas. The streams atop the plateau are much more gentle than those on its northern and southern margins. These typically average ~1-3° gradient, in comparison to the 15-20° streams that plummet to the surrounding lowlands. Erosion that is driven purely by gravity without the aid of water flow or other

Figure 3a: Frequency of elevation in the San Bernardino Mountains, based on the 90 m resolution digital elevation model. The mountains were defined by the topographic boundary between high and low topography. Each pixel is 76.956 m on a side, so that the number of pixels can be translated to surface area. The total number of pixels is 522,424 and total area is 3093.9 km^2.

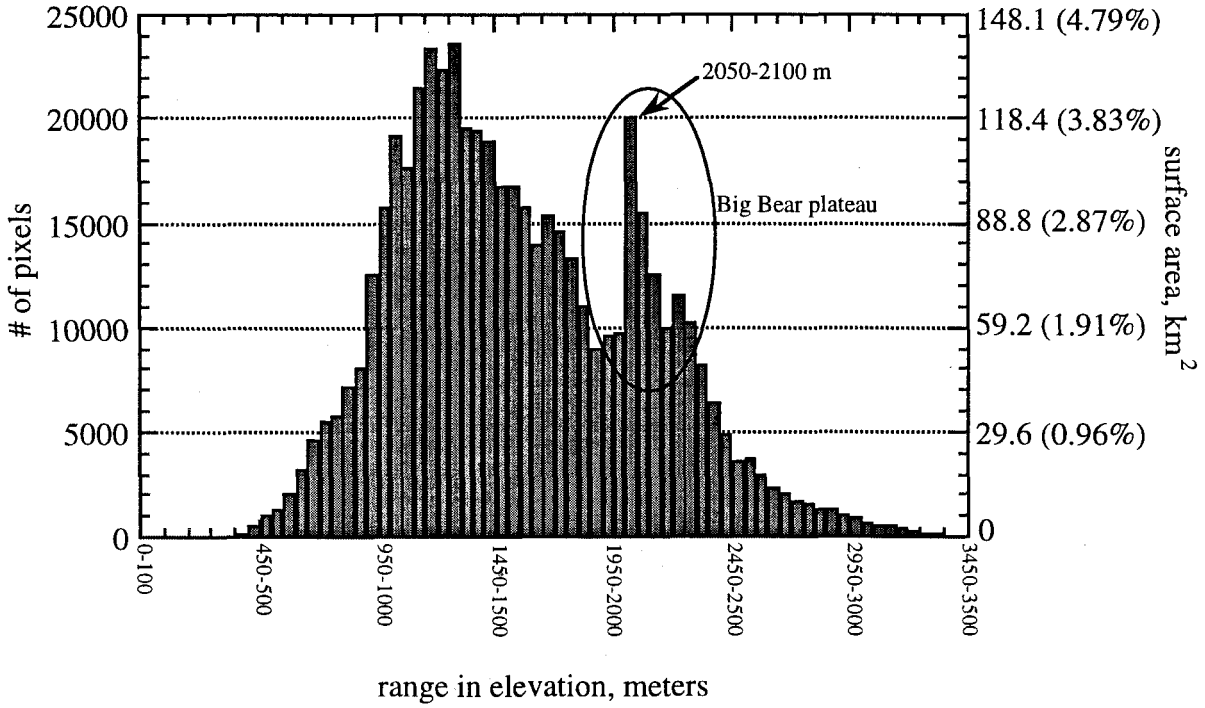

Figure 3b: Frequency of slope in the San Bernardino Mountains based on the same digital elevation model as used in Figure 3a. The number of pixels were translated directly into the percentage of surface area. The size and number of pixels are the same as in Figure 3a.

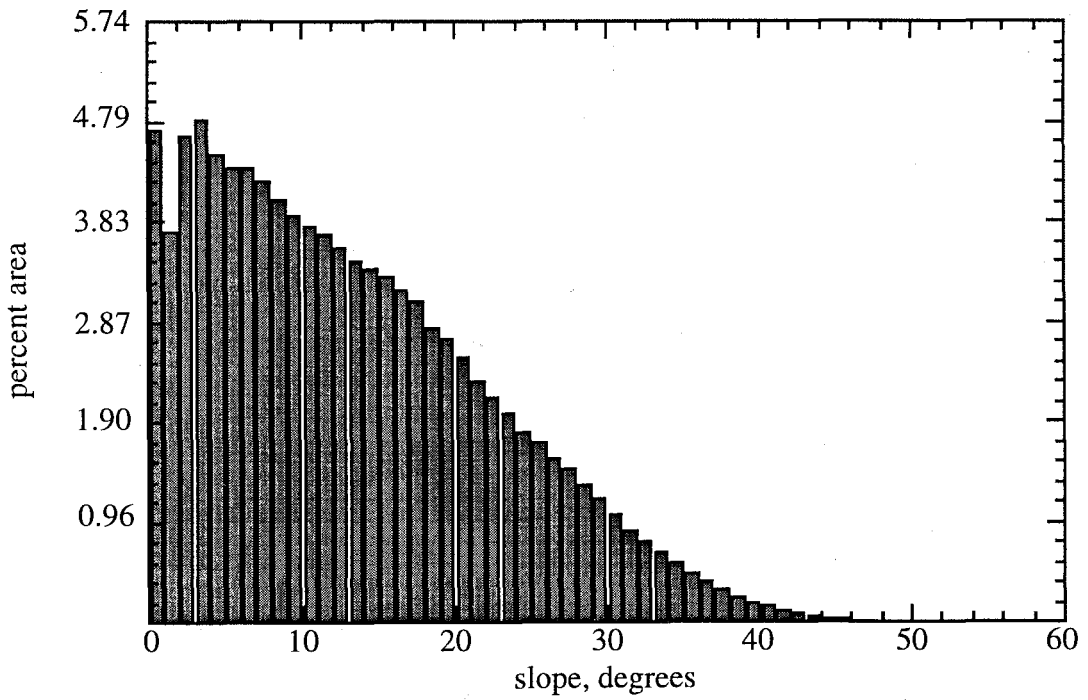

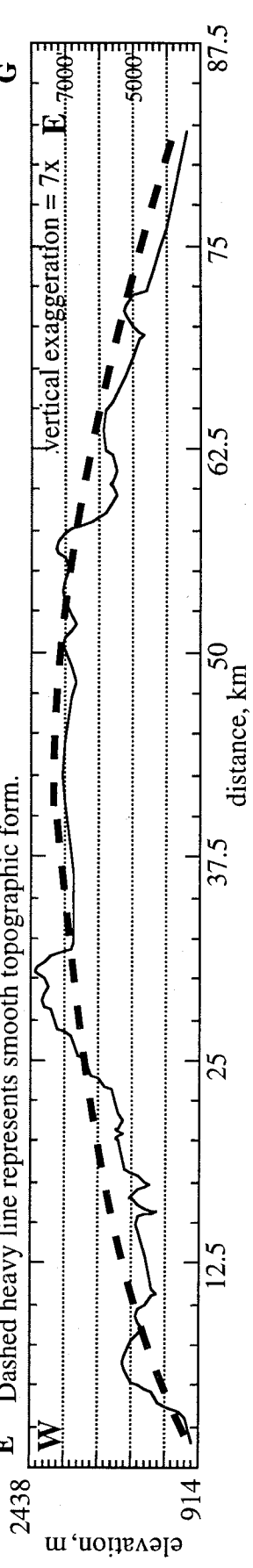

Figure 4a: West to east elevation profile across the Big Bear plateau (location shown in Figure 1). Dashed heavy line represents smooth topographic form.

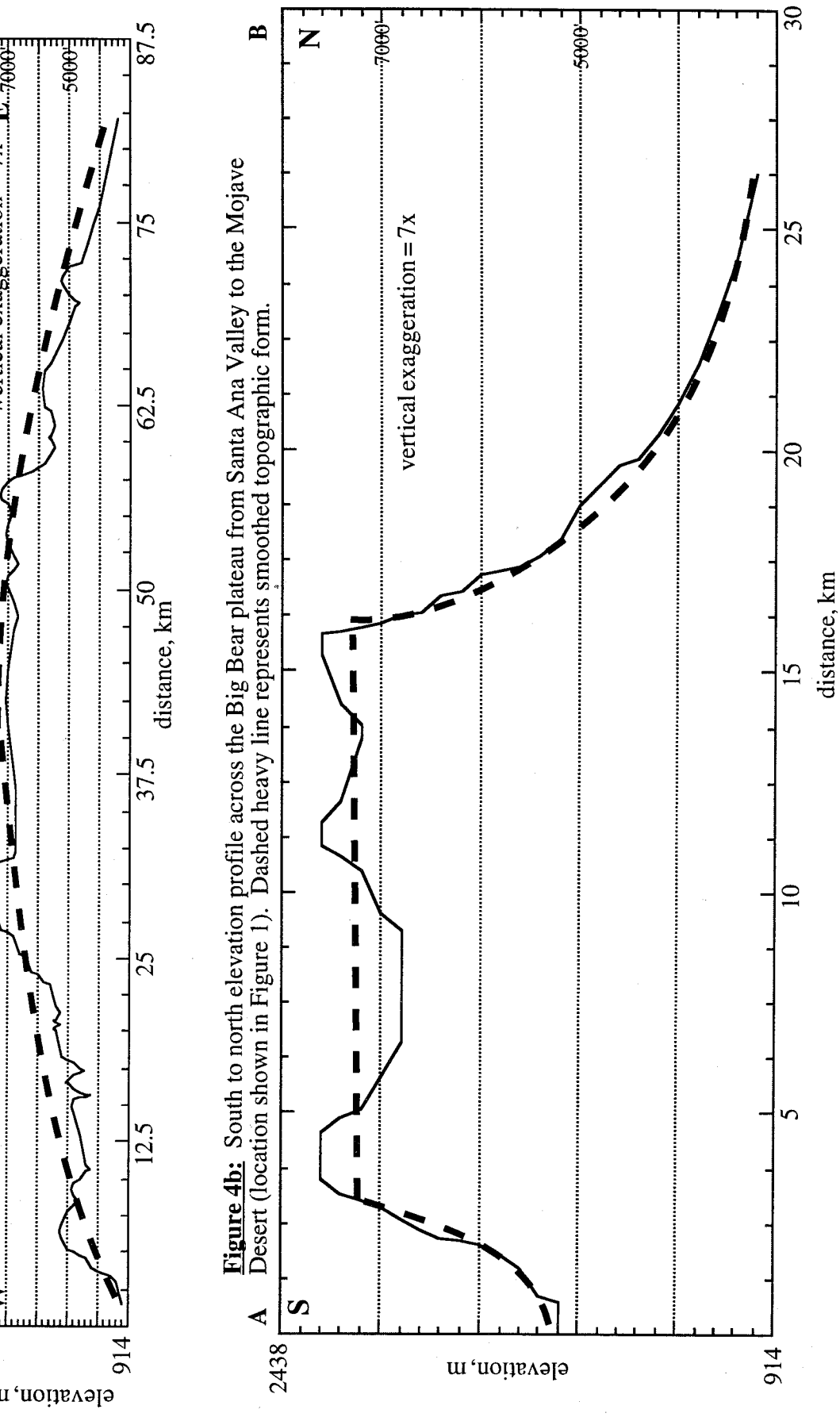

Figure 4b: South to north elevation profile across the Big Bear plateau from Santa Ana Valley to the Mojave Desert (location shown in Figure 1). Dashed heavy line represents smoothed topographic form.

transporting media (i.e., mass wasting) also occurs more rapidly at steep slopes, at which sliding dominates, than gentle slopes, at which soil creep is the primary mode of downslope movement. The relative rate of erosion in different areas can thus be represented qualitatively by the distribution of surfaces that are eroding by sliding (i.e., talus landforms). Figure 5 shows this for the SBMs, based on mapping talus slopes by their distinct morphology (paucity of vegetation, down-slope lineations, sliderock accumulations below) with 1:50,000 airphotos. On the plateau, mass wasting occurs only in canyons cut inwards from the margins (such as Deep Creek) or along fault scarps produced by northwest secondary faults on the eastern flank (locs. A and B respectively, Figure 5). In contrast, dense areas of mass wasting define the northern and southern escarpments of the plateau and the thin crustal slices of the southern SBMs. These two observations show that the plateau surface undergoes much less active erosion than the other parts of the range.

The distributions of rapidly eroding slopes on the northern and southern escarpments of the plateau are coincident with the extent of the bounding thrust faults (Figure 1a, 5). This is consistent with the hypothesis that uplift along the faults has recently created the escarpments, which erode much faster than the interior plateau. There is also symmetry between the along-strike width of the thrust faults and escarpment size and plateau shape. Along the NFTS, for example, the escarpment rises gently from the eastern and western limits of its surficial trace (where it is several hundred meters high) to crest along the middle of the fault (where it is >1 km above the fault trace) (Figure 1, 6). This correlation argues that the plateau topography is largely the result of tectonic uplift, rather than erosion or pre-thrusting topography. The upper topography of the plateau could thus reflect the vertical displacement field associated with the thrusts.

Topography alone, however, cannot uniquely constrain uplift magnitude or history. A topographic surface is a transitory feature and tectonic conclusions cannot be drawn from it without understanding its evolution. Although the present topography may record fault

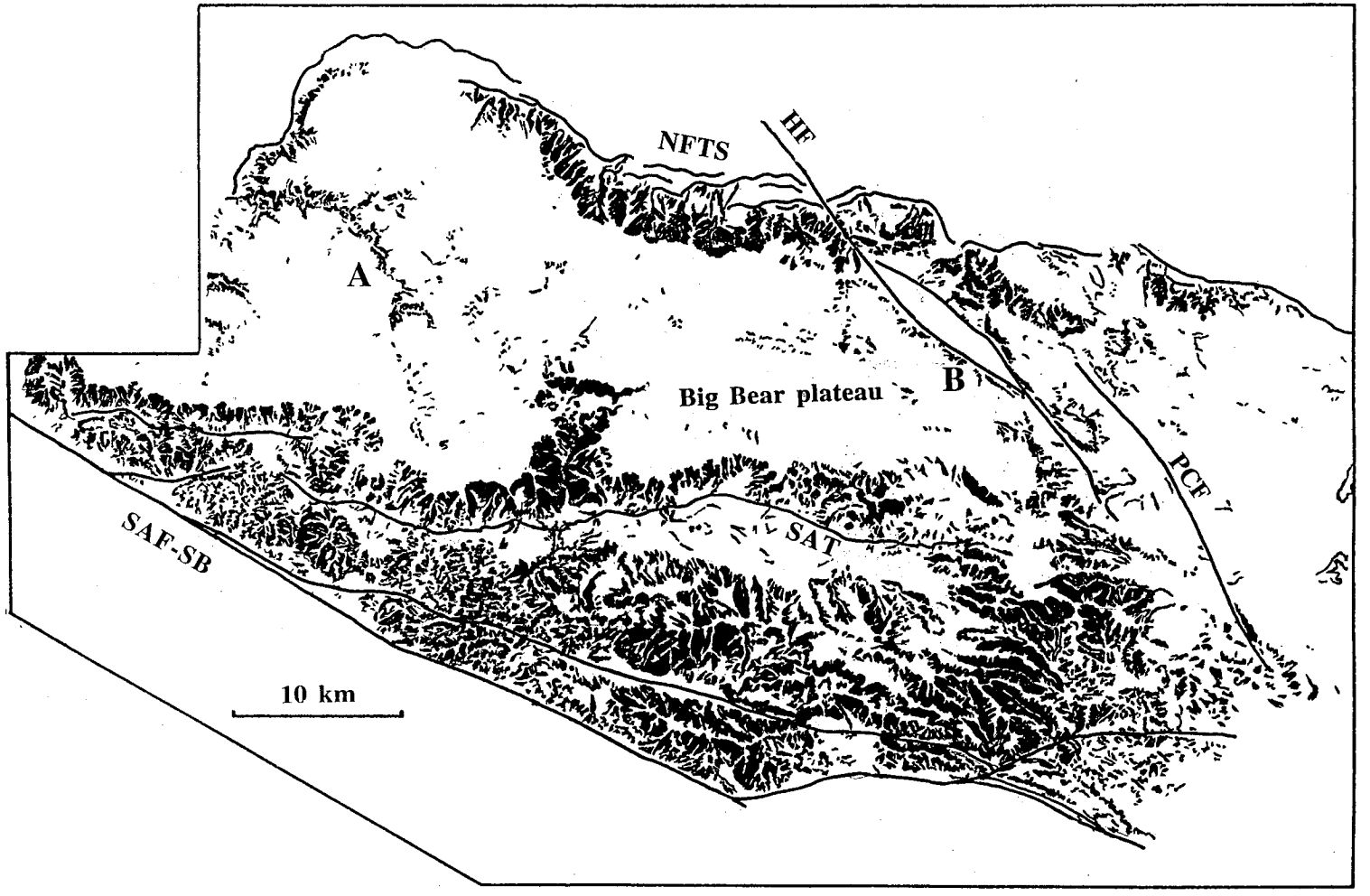

Figure 5: Distribution of talus landforms (active erosion) across the San Bernardino Mountains, based on airphoto mapping at 1:50,000 scale. Talus landforms are shown in black. Mapping is limited to regions south of the North Frontal thrust system (NFTS) and north of the San Andreas fault-San Bernardino strand (SAF-SB). Location A refers to cluster of active erosion around recent incision of Deep Creek. Location B refers to active erosion at the Helendale fault (HF) scarp. SAT = Santa Ana thrust, PCF = Pipes Creek fault.

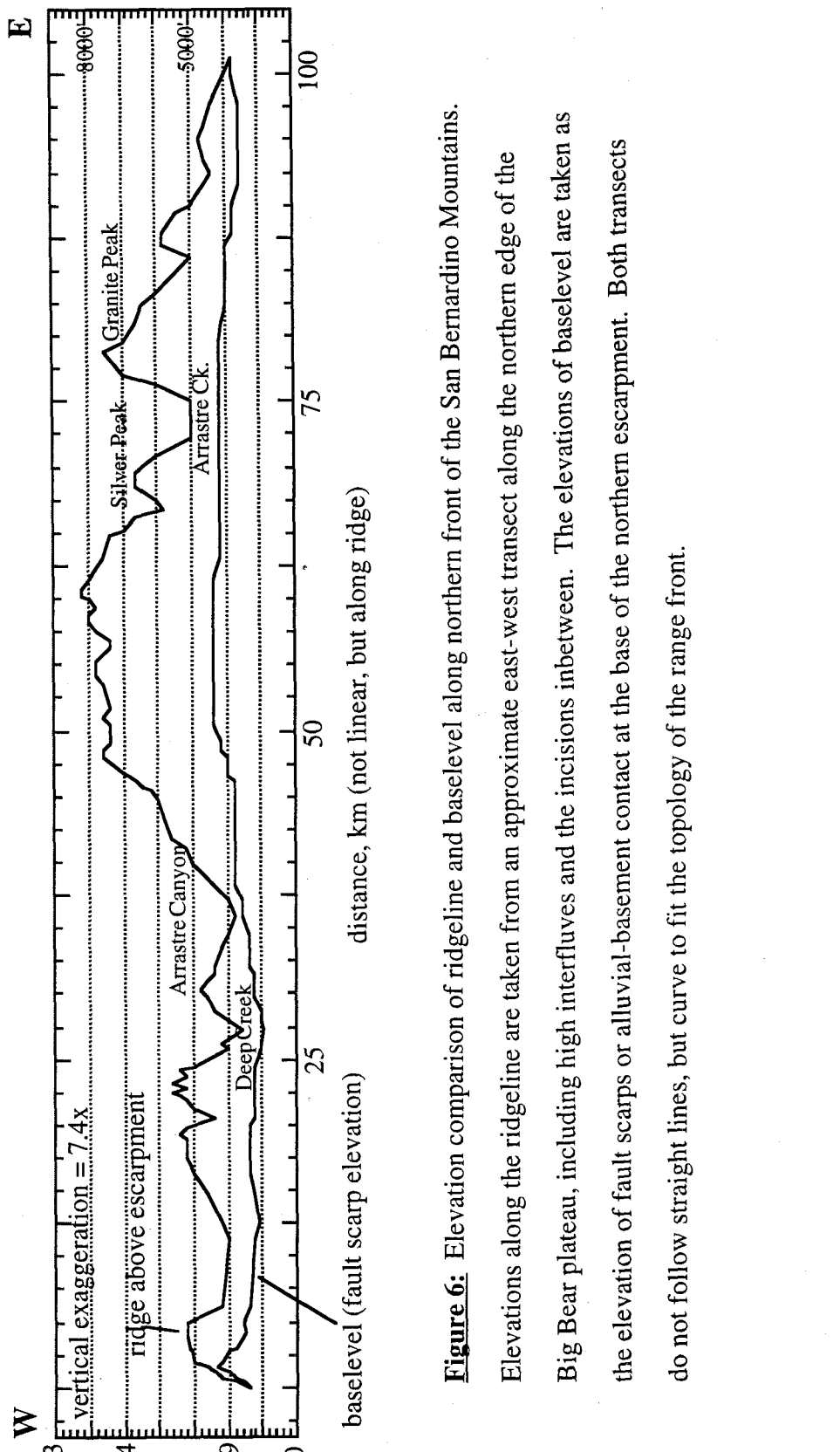

Figure 6: Elevation comparison of ridgeline and baselevel along northern front of the San Bernardino Mountains. Elevations along the ridgeline are taken from an approximate east-west transect along the northern edge of the Big Bear plateau, including high interfluves and the incisions inbetween. The elevations of baselevel are taken as the elevation of fault scarps or alluvial-basement contact at the base of the northern escarpment. Both transects do not follow straight lines, but curve to fit the topology of the range front.

motion, there are no hard constraints on either the magnitude of syntectonic erosion from atop the apparently slowly eroding plateau or the extent to which pre-deformational topography existed. Thus, using only topography to restore structural relief could over or underestimate the actual vertical displacement.

By adopting a theory for the generation of elevated, low-relief surfaces, it would be possible to guess what structural displacement the Big Bear plateau represents. Davis' (1899) theory of peneplanation, for example, would argue that the low relief surface had to have formed as a flat feature at low elevation prior to tectonic uplift and subsequent incision. In contrast, low relief surfaces have also been suggested to form atop mountainous plateaus due to climatic factors (Gregory and Chase, 1994), the mechanical limits of thickening crust (Molnar and Lyon-Caen, 1988), or rapid subterranean weathering along topographic steps above resistant rock exposures (Wahrhaftig, 1965). Low-relief surfaces have been used as tectonic constraints in many studies (e.g., Altiplano of Bolivian Andes; Gubbels et al., 1993), although there is debate as to what degree this is feasible (cf. Madole et al., 1987). There are cases in which low-relief surfaces have been used as datums based solely on presumptions of landscape evolution, such as Ringrose and Migon's (1995) restoration of fault offsets in Scotland using areal elevation distribution. All of these past studies caution that assuming the elevation of the Big Bear plateau represents the vertical displacement field of the thrust faults is not necessarily reasonable.

Atop the plateau is a deeply weathered horizon formed on granitic rocks, which is similar to weathered granite that occurs throughout the adjacent Mojave Desert (Oberlander, 1972; Dibblee, 1975). Although rock weathering is a destructive process that does not represent a single event, the product is a distinctive, *geologic* feature, which can be identified by changes in the mineralogy, grainsize, color, and other characteristics of the parent rock. A weathered rock surface is thus a better datum than low-relief topography alone. In addition, there are isolated locations in the SBMs and Mojave Desert where Miocene-Pliocene deposits overlie deeply weathered granite and paleosols. If the

weathered surface across the entire Big Bear plateau can be correlated with these buried saprolites, it can be demonstrated to be a relict horizon that formed prior to uplift. This surface may thus serve as a valuable structural index and yield information on the vertical displacement field of the thrust faults, if its geometry and evolution can be understood.

3.4. The potential of the weathered surface as a structural datum

In order to use a geologic feature as a datum to constrain structural displacement, several criteria must be met. First, the temporal relationship between the formation of the feature and the deformation being studied must be evident. Next, the pre-deformation geometry and distribution of the feature must be known. Other modifications of this geometry, such as by erosion, deposition, or other deformation, must also be defined. Lastly, the present geometry and distribution of the feature must be defined, so that the tectonic displacement can be extracted. An example of a geologic feature well suited as a datum is a deep marine sedimentary bed, which would predate uplift, have an originally flat geometry, and could be easily identified.

Unlike marine strata, a weathered surface is not an ideal marker horizon. Weathering is not easily datable unless buried under dated deposits, and produces a transitory horizon that moves downward as rock decays. A weathered surface also cannot be tied to an absolute reference elevation, such as sea level, and thus its pre-uplift geometry must be inferred by extrapolation from where buried or by comparison with similar modern environments. Third, defining the post-deformation distribution of the surface is not necessarily straightforward, because it does not represent an instantaneous event and may be time-transgressive. Continued weathering or intervals of repeated erosion and subsequent re-weathering during uplift are thus a problem.

Because of these limitations, it is necessary to first learn about the development of the weathered surface before using it to learn about the vertical displacement of the Big

Bear plateau. In particular, it is necessary to know whether the surface is relict or presently forming, the rate at which it may have been forming over the past few million years, the environmental conditions under which it developed, the magnitude of material removed by erosion since uplift initiated, and its pre-uplift and present-day distribution and geometry. Constraining these aspects of the surface's development will determine whether it is feasible to use as a structural datum and to what confidence limits it can be reconstructed to document vertical displacement associated with recent uplift of the plateau. These constraints would be easily determined if the entire weathered horizon were correlative (i.e., coeval) with saprolites buried by isolated Tertiary deposits surrounding the plateau. As explained in a review of previous work below (see Section 3.5.3), however, such a correlation has not been shown and no common marker within the weathered horizon has been found that uniquely demonstrates it is everywhere contemporaneous.

To learn about its evolution, it is thus necessary to conduct a detailed geomorphologic study of the surface. The topographic character and geomorphic relationships observed in the field and in airphotos can offer clues to the dynamics of how the surface evolved in concert with erosion. Documenting the vertical variations and thickness of the weathering profile, the degree to which the weathering has developed on different bedrock types, and the mineralogical and textural differences between parent rock and the products of weathering, are also critical to understanding how the weathered surface formed. These observations can also be used to develop an identification scheme, by which the distribution of the weathered surface atop and outside of the plateau can be mapped. If feasible, it may be possible to determine the vertical tectonic dislocation by subtracting the surface's pre-uplift geometry from its present-day distribution.

This geomorphologic approach provides a mainly qualitative documentation of the nature of weathering, which enables a comparison with analogous weathering in other locations. Previous studies have documented the rates of active granitic weathering in a variety of climatic and topographic regimes. From a comparison, it may be possible to

infer whether the upland surface is relict from a previous climatic stage atop the plateau, or to infer what rates of granitic weathering could be expected given the plateau's present climate and topography. Where Tertiary deposits overlie granitic saprolite around the plateau, there is also the potential to constrain paleogeographic aspects of the weathered surface and the magnitude of post-uplift erosion. These approaches will further the assessment of the weathered granitic surface as a structural datum.

3.5. Previous studies

3.5.1 Introduction

The weathered surface and distinct topographic form of the Big Bear plateau have been recognized in previous reports of SBMs geology (e.g., Mendenhall, 1907; Vaughan, 1922; Noble, 1932; Dibblee, 1975; Sadler, 1982a; Meisling and Weldon, 1989) (Figure 7a). Although these have also recognized the potential use of this surface as a structural datum, there have been no detailed studies of the nature of weathering. A similar surface in the surrounding Mojave Desert has been examined in greater detail (Oberlander, 1972), but the relationship between it and the surface atop the plateau has not been demonstrated. The strongest constraints on the evolution of these weathered horizons have come from local observations of overlying deposits, but these are not conclusive and the deposits themselves are too sparse to represent structural datums.

3.5.2 Previous descriptions of the weathered surface

The nature of the weathered surface atop the Big Bear plateau has been described only briefly in previous reports. The character of the surface in the Santa Ana Valley (Jacobs, 1982) and the far western tip of the range (Meisling, 1984) have been similarly described as a 10-30 m thick zone of disintegrated granitic grus. This "residual arkose" was described by Jacobs (1982) to be red-brown, to consist of 30% clay-silt and 70%

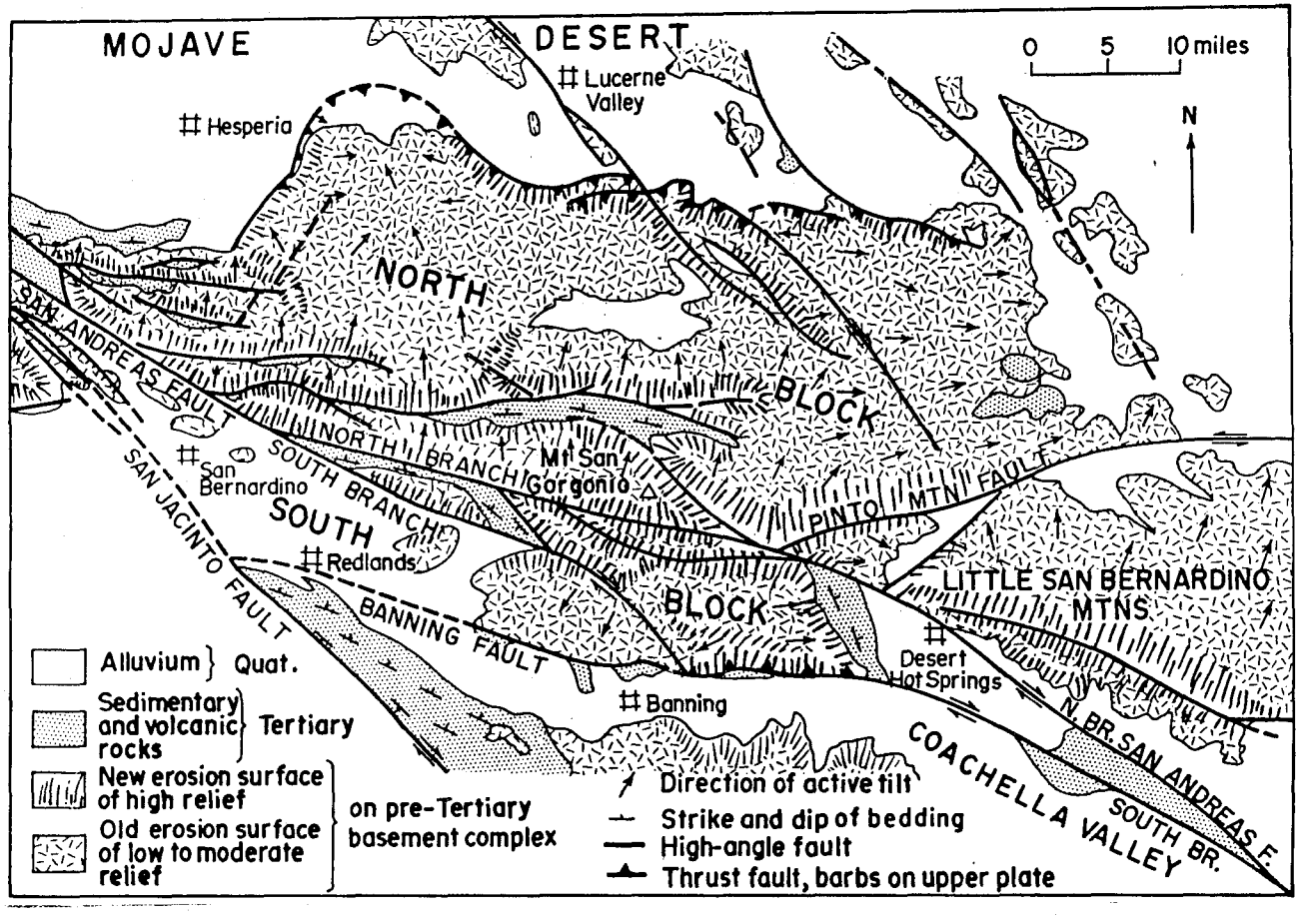

Figure 7a: Reproduction of Dibblee's (1975) interpretation of the geomorphology of the San Bernardino Mountains, including the distribution of the "old erosion surface".

unsorted mineral grains (quartz, feldspar, lithics), and to be capped by a banded paleosol. Meisling (1984) described the grus layer as a matrix derived from primarily biotite-quartz monzonite that surrounded round, residual granitic boulders (corestones), and argued the surface was continuous throughout the western part of the range (as far east as the Pinnacles and Ord Mountain). The observation that carbonate rocks were locally weathered down below granitic rocks and the presumed long period of time required to develop such deep granitic weathering suggested to Meisling (1984) that the weathering episode had occurred during a humid climate that preceded uplift. The upper meter or so of the soil present atop this weathered surface has also been described and classified in several localities (USDA, 1986). Beyond these general descriptions, however, there have been no detailed studies of the weathered surface atop the SBMs.

Across the Mojave Desert is a bouldery granitic rind that is similar to the surface atop the Big Bear plateau (Figure 7b) (Oberlander, 1972). The Mojave weathered profile is developed to more than 30 m thickness on primarily quartz monzonite and consists of large corestones (inselbergs if >100 m diameter) situated within a matrix of loose grus (regolith). Based on careful observation and comparison with similar weathering in Africa and Australia, Oberlander (1972) proposed that the Mojave weathered surface is not presently forming, but is relict from a previous, more humid environment. He argued that the present bouldery morphology of the surface was produced by recent erosion, which had stripped away much of the regolith and other fine grained products of the deep weathering. The corestones were explained by concentration of subsurface chemical weathering at joint intersections, which produced large volumes of regolith that, once eroded away, left behind large, unweathered boulders. According to Oberlander (1972), this solution weathering cannot occur subaerially, and thus the weathering that produced the present mantle of exposed corestones had to be relict. He also observed that the distribution and size of corestones varies randomly across the region, not showing a correlation with present topographic highs and lows that would be expected if weathering were active.

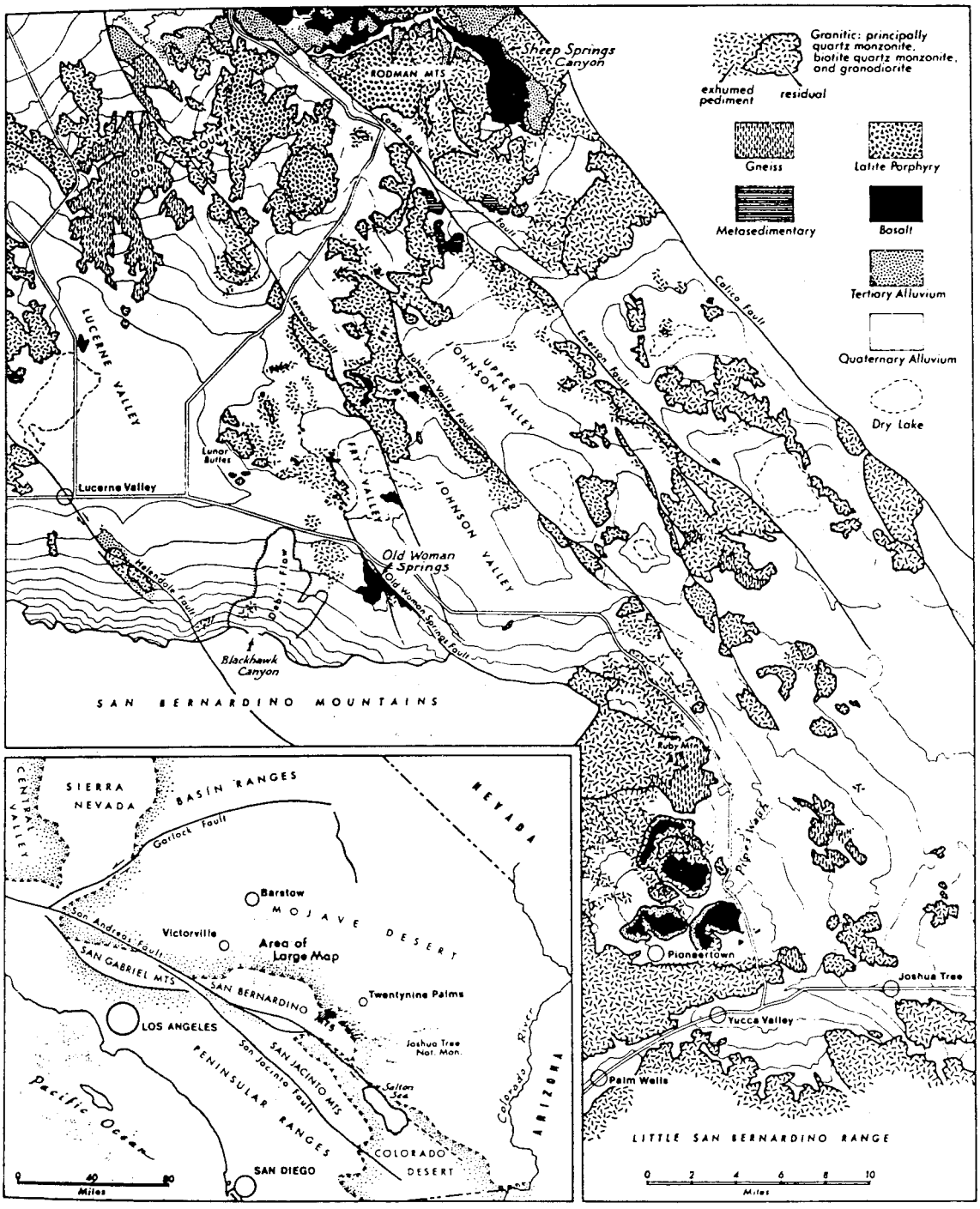

Figure 7b: Distribution of granitic pediment and residual granitic tors in the Mojave Desert to the northwest of the San Bernardino Mountains, including locations of basalts that overlie the weathered granite (from Oberlander, 1972).

Oberlander (1972) suspected that the Mojave was presently too arid for subsurface weathering to take place, and proposed that the weathering had developed during a previous, more humid period. The presence of carbonate crust (K-horizons, or caliche) of up to 1 m thickness atop alluvium in the Mojave indicates that meteoric water does not presently penetrate far below the surface, suggesting that the weathering of corestones at 30 m depth is not likely active. Similar, 2 m thick K-horizons in soils covered by the Bishop Ash elsewhere in the Mojave suggest that arid conditions (as opposed to leaching and deep weathering) have been present for at least ~0.7 Ma in some locations (Schlemon, 1980). Based on plant fossils, the Tertiary climate of the Mojave was more humid (up to 64 cm/yr precipitation, forest/grassland) than today (5 cm/yr now, barren desert), perhaps due to the development of a rainshadow by the Plio-Pleistocene rise of the Transverse Ranges (Axelrod, 1950). Oberlander (1972) thus proposed that the Mojave weathering occurred prior to the Quaternary rise of the SBMs. The bouldery mantle could have survived erosion for that long, because the exposed corestones become resistant (case-harden) due to the formation of an insoluble "patina" of iron and manganese oxides on their outer surface.

If Oberlander's (1972) hypothesis is valid for the weathering of the Mojave Desert, it need not be true for the weathered surface atop the SBMs. The two surfaces are similar in character, but the weathering atop the Big Bear plateau has not been studied in enough detail to show that a unique correlation between them exists. Even though the surface appears to taper downwards from the eastern flank of the plateau to connect with the adjacent Mojave surface, the existing data do not show that this surface is an isochronous, pre-uplift feature. The aridity that makes deep weathering unlikely in the present-day Mojave Desert is not present atop the SBMs. Much of the Big Bear plateau presently receives as much or more annual rainfall than the Mojave supposedly did during Tertiary weathering (Figure 8; Table 1) (Axelrod, 1950; Minnich, 1986; DOC, 1993; DOC, 1980-1993b; see also Minnich, 1986). The greater humidity of the SBMs is apparent in their lack of thick K-horizons in soils (USDA, 1986). Continued weathering and erosion of the

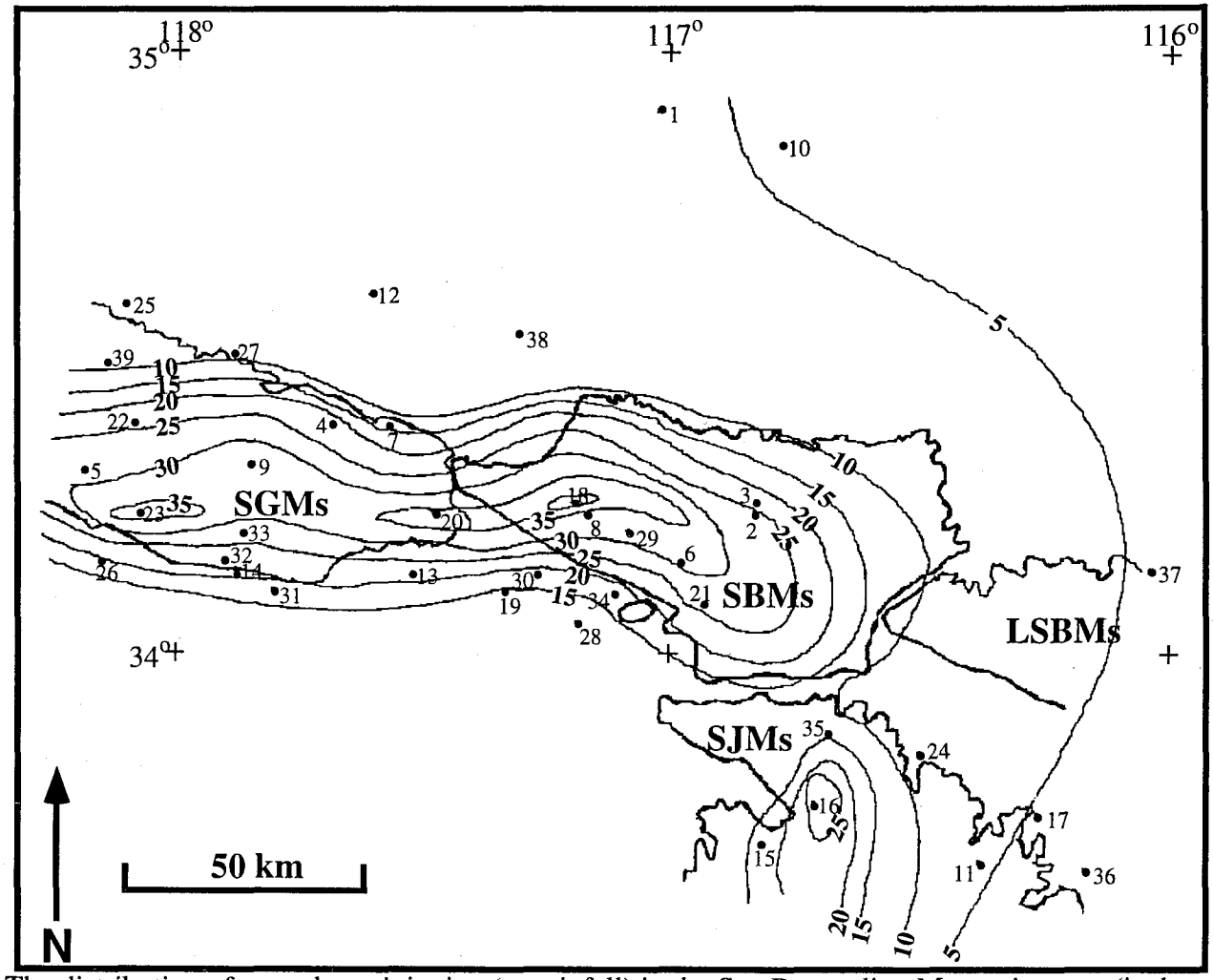

Figure 8: The distribution of annual precipitation (as rainfall) in the San Bernardino Mountains area (inches per year). The dots show the locations of climate stations with numbers (locations) corresponding to Table 1. The contours were drawn from the average annual rainfall at these locations, as listed in Table 1. A similar distribution is reported in Minnich (1986). Heavy lines show outlines of mountain ranges; SGMs = San Gabriel Mountains, SBMs = San Bernardino Mountains, LSBMs = Little San Bernardino Mountains, SJMs = San Jacinto Mtns.

Table 1: Climate data for locations in southern California. See Figure 8 for map of locations and contour diagram of average annual precipitation.

Station	Location (latxlong elev=ft)	Avg. ann. precip. (inches/yr)	Avg. ann. temp. (degrees F)
1. Barstow	34.90x117.017 2320'	6.76*	65.4*
2. Big Bear Dam	34.23x116.833 6815'	27.78***	
3. Big Bear Lake	34.25x116.883 6790'	22.65	46.6
4. Big Pines Park	34.38x117.683 6845'	24.30*	
5. Big Tujunga Dam	34.30x118.183 2317'	26.10	
6. Camp Angelus	34.15x116.983 5768'	32.22**	
7. Cajon West Summit	34.38x117.567 4779'	14.09***	
8. Crestline First Stn.	34.23x117.167 4900'	34.55***	
9. Crystal Lake	34.32x117.85 5370'	34.55	
10. Dagget Airport	34.85x116.783 1922'	3.93	67.6
11. Deep Canyon Lab	33.65x116.383 1200'	5.66	
12. El Mirage Field	34.60x117.60 2910'	8.93*	59.1*
13. Etiwanda	34.13x117.517 1390'	21.17**	
14. Glendora West	34.13x117.87 822'	20.62	
15. Hurkey Creek Park	33.68x116.683 4190'	19.30**	
16. Idyllwild	33.75x116.716 5380'	25.38*	52.4
17. Indio	33.73x116.267 -21'	3.64*	73.9
18. Lake Arrowhead	34.25x117.183 5205'	40.80	51.4
19. Lytle Creek Foothill	34.10x117.333 1160'	14.23***	
20. Lytle Creek Ranger	34.23x117.483 2730'	35.20*	
21. Mill Creek Intake	34.08x116.933 4945'	26.07***	
22. Mill Creek Summit	34.38x118.083 4990'	24.22**	
23. Mt. Wilson	34.23x118.067 5708'	37.50	55.9
24. Palm Springs	33.83x116.50 425'	5.31	73.2
25. Palmdale	34.58x118.10 2596'	6.92	61.6
26. Pasadena	34.15x118.15 864'	19.37	64.8
27. Pearblossom	34.50x117.883 3050'	9.89*	
28. Redlands	34.05x117.183 1318'	12.80	64.4
29. Running Springs	34.20x117.083 5965'	31.58**	
30. San Bernardino	34.13x117.267 1125'	15.61*	65.1
31. San Dimas	34.10x117.80 955'	18.02	
32. San Gabriel Canyon	34.15x117.90 744'	22.58	
33. San Gabriel Dam	34.20x117.867 1481'	28.46	
34. Santa Ana River	34.10x117.10 1970'	16.32***	
35. Snow Creek Upper	33.87x116.683 1940'	13.42	
36. Thermal Airport	33.633x116.167 -112'	3.16	72.5
37. Twentynine Palms	34.13x116.033 1975'	4.25	67.6
38. Victorville	34.53x117.30 2858'	4.95*	
39. Vincent	34.48x118.133 3135'	8.35	

-annual precipitation is based on summary of 1961-1990 (Department of Commerce, 1993a).
* indicates the annual precipitation is based on summary of 1961-1990 with partial data (all existing data used; Department of Commerce, 1993a).
** indicates the annual precipitation is a 6 year average (Department of Commerce, 1988-1993b).
*** indicates the annual precipitation is a 6 year average based on partial data (all existing data used; Department of Commerce, 1988-1993b).

plateau since the Tertiary thus cannot be ruled out based on existing geomorphic data.

In two other California locations, studies have argued that deep weathering profiles on granitic rock are the result of active weathering in present climate conditions. Nettleton et al. (1970) studied four soil profiles from a 30-m-thick weathered profile on tonalite (andesine, biotite, hornblende, quartz, orthoclase) in warm, semi-arid San Diego. Variations in soil chemistry, degree of mineral decomposition, clay mineralogy, and bulk density, correlated loosely with topographic position and moisture regimes at these locations, suggesting that the upper few meters of soil and saprolite are in equilibrium with their present environment and may be actively developing. However, Nettleton et al. (1970) do not present independent constraints on the age or rate of weathering and do not demonstrate that the entire weathered profile was produced under the present climate. Other studies of granitic weathering emphasize the character of the entire saprolite, rather than the upper few meters of soil (Power and Smith, 1994). It is also not clear that the four locations represent a temporally uniform toposequence (one location is located "several miles" away from the others; Nettleton et al., 1970). It is thus uncertain to what degree the present semi-arid climate of San Diego fosters deep weathering.

Wahrhaftig (1965) studied weathered granite along topographic steps in the Sierra Nevada. Backward-sloping benches along weathered granitic rock with up to 30 m of grus make up a portion of the western Sierra Nevada slope. Wahrhaftig (1965) proposed that these form under present conditions due to the difference in subsurface and subaerial weathering rates. According to this proposition, accidental, erosive exposures of bald granitic forms (i.e., corestones) create local base-levels, which weather slowly and cannot be removed by erosion. Active weathering and erosion of grus continues upslope, however, continuously lowering the surface and creating a step. Because it is related to present topography, weathering may be active, and thus the Mediterranean to dry-mountain climate of the Sierra Nevada may be favorable for granitic weathering (Wahrhaftig, 1965). However, the Sierran granites are not highly decomposed and have become grus only by

alteration and expansion of biotite (Wahrhaftig, 1965). In addition, it is unknown how long it took to develop the Sierran weathered profiles and benches, or what weathering rate occurs presently there. Subsurface weathering in glacial outwash on the eastern Sierras requires >140 Ka to disintegrate granitic stones (Birkeland, 1984; pp.196-197), implying grusification rates of <0.004 mm/yr (for 1-m diameter). Thus, even if Wahrhaftig's (1965) hypothesis is correct, the Sierran weathered profiles may have required a million or more years to form and developed in a variety of previous climates.

Based on these two examples, it is not reasonable to assume that weathering is inactive atop the SBMs. However, it is still possible that the degree of rock decay required a long time to develop. This would make the surface "relict," in the sense that it began forming prior to uplift and has been little-modified by weathering since.

3.5.3 Constraints on the origins of the weathered surface

Although Oberlander's (1972) geomorphic observations are consistent with his hypothesis for the antiquity of weathering in the Mojave Desert, they do not provide hard constraints that uniquely define the evolution of the weathered surface. Oberlander (1972) and other previous studies have provided further constraints on the age of the surface in the Mojave and atop the Big Bear plateau, by examination of dated deposits that locally overlie weathered granite. These scattered, Tertiary deposits are confined to the eastern and western flanks of the Big Bear plateau, the Santa Ana Valley to the south, and the Mojave Desert to the north (Figure 1a, 9 [Plate 1]). There are also thin, undated gravels scattered across the central plateau, which may have been deposited prior to uplift (Sadler and Reeder, 1983).

The strongest support for Oberlander's (1972) hypothesis was his observation of pre-Quaternary basalts that locally overlie weathered granite in the Mojave. These basalts are not contiguous and occur only in isolated locations, including several sites just north of the SBMs and several sites along the eastern flank of the Big Bear plateau (Figure 7b, 9).

Figure 9: See Plate 1, folded into backside cover of thesis.

On the eastern flank, the scattered basalt outcrops occur higher than 2 km elevation (Onyx Peak), and drop down eastward as the weathered surface tapers to the lower Mojave Desert. They typically consist of numerous individual flows of several meters thickness each, which are separated by paleosols and vesicular zones (Neville and Chambers, 1982; Neville, 1983). Although the northern and eastern basalts are probably related tectonically, they differ petrographically, do not share a single source vent, and are not considered to have been part of a single, regional flow system (Neville, 1983).

All of the basalts that have been dated in the area give late Miocene ages, including 6.9-9.3 Ma ages for basalts on the eastern flank of the Big Bear plateau and 6.0-8.2 Ma ages for basalts just north of the SBMs (Oberlander, 1972; Woodburne, 1975; Peterson, 1976; Morton, 1980) (Figure 9a). The basalts overlie red saprolites that grade downwards into the grus and corestone combination that is common across the Mojave. Because the basalts are discontinuous, however, the surfaces that they bury are demonstrably continuous with the surrounding bouldery surface of the plateau for only short distances (Oberlander, 1972). Discontinuous basalts can be connected to cover the greatest area of weathered surface (<10 km diameter) where the eastern flank of the plateau joins the adjacent Mojave (Figure 9a). Thus, although they locally demonstrate that the deep weathering occurred long before the construction of the Transverse Ranges, they do not show that the entire weathered surface is relict and represents a structural datum.

In several locations in what is now the western wing of the SBMs, the Miocene-aged Crowder Formation overlies deeply weathered granite, demonstrating locally that the weathered surface developed prior to uplift of the range (Figure 1a, 9). This deposit consists of fluvial, arkosic sand and gravel that is 17-9.5 Ma (locally dates weathered surface as pre-17 Ma), based on fossils and magnetostratigraphy and up to 980 m thick (Meisling and Weldon, 1989). Paleoflow indicators and clast provenance show that this unit was deposited by southward flow from the Victorville area (Meisling and Weldon, 1989). In places, the sediment was deposited into channels that were cut into fresh

bedrock beneath a weathered zone. Although the outcrop distribution of the Crowder Formation is discontinuous, its uniform nature across the area suggests it was deposited in a homogenous basin that was relatively smooth for considerable distance atop a deeply weathered surface (Meisling, 1984; Meisling and Weldon, 1989). Between the outcrops of this unit, the weathered surface is relatively flat or has a rolling topography, is somewhat contiguous, is mantled by soils, and dissected by streams (Meisling, 1984). This suggests the weathered granite surface atop the westernmost part of the Big Bear plateau may serve as a structural datum. It is not certain, however, how far east of the Crowder outcrops the weathered surface can be correlated as isochronous and pre-uplift (Figure 9a). If the Crowder Formation once covered a larger area to the east and has subsequently been eroded away, it also cannot be ruled out that significant syn-uplift erosion of the granite (and subsequent re-weathering) occurred.

In the vicinity of the Crowder Formation outcrops, an east-west trending series of reverse faults displaces the weathered surface and exposes fresh granite along hanging-wall scarps (Meisling and Weldon, 1989) (Figure 1a, 10). This fault system, known as the Cedar Springs reverse fault system, cuts the Crowder Formation (>9 Ma) and is buried by the Phelan Peak Deposits (<5 Ma), and was thus active in the late Miocene. This strongly supports the above argument, based on the overlying Crowder Formation, that the weathered surface developed along this western wing of the Big Bear plateau prior to uplift (Meisling, 1984; Meisling and Weldon, 1989). As a result, Meisling and Weldon (1989) were able to use the weathered surface locally as a datum to identify the tilting of the plateau associated with the western San Bernardino arch, where the weathered surface consistently dips ~30^{o} northwards.

Another Tertiary unit that overlies weathered granite in the SBMs is the Santa Ana Sandstone, present in the Santa Ana Valley south of the Big Bear plateau (Figure 1a, 9). This unit consists of multiple facies, with up to 1500 m total thickness of conglomerate, sandstone, and lacustrine sediments that are loosely constrained to a 15-4 Ma age, based on

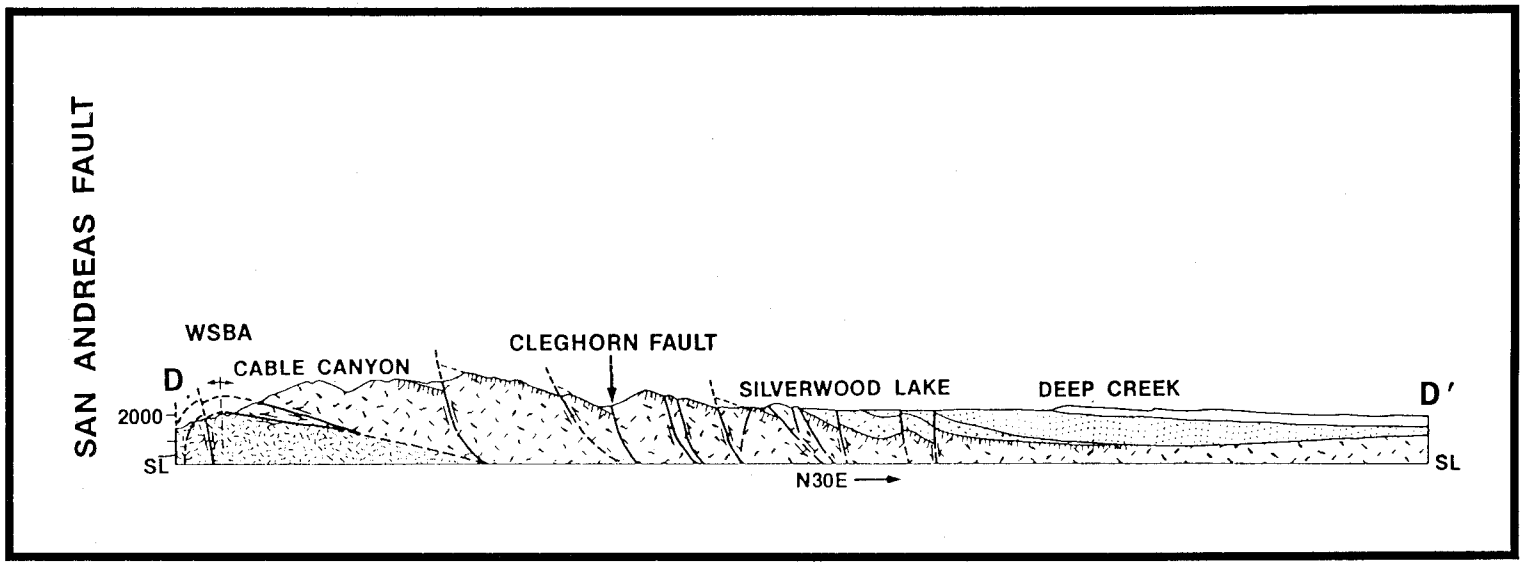

Figure 10: Southwest (D) to northeast (D') cross section across the western San Bernardino Mountains, showing the geometric relationship between fresh and weathered (hachred) granite surfaces along faults (from Meisling and Weldon, 1989). The faults include recent structures (Cleghorn fault) that have evolved from an earlier, pre-San Bernardino Mountains structural system (the Squaw Peak thrust system of the late Miocene). These thrusts offset the weathered surface, so the surface here is at least late Miocene in age. These faults also cut the Crowder Formation (mid to late Miocene age) that overlies the weathered surface (below the "wood" in Silverwood). The location of this cross section is near "p" on Figure 1.

fossils and interbedded basalt flows (Sadler, 1993). The age of the western facies of this unit, which overlies a thick red paleosol and deeply weathered granite, is closer to the 15 Ma extreme (Sadler, 1993). Correlating the weathered granite beneath the Santa Ana Sandstone with the weathered surface of the Big Bear plateau and Mojave Desert is not straightforward, because it is only exposed in limited outcrops. Despite similarities between the paleosol and soils atop the plateau (Jacobs, 1982; see Section 3.6.6), it is not possible to compare the gross geomorphic character of the different locations. In addition, the Santa Ana Sandstone has been translated relative to the Big Bear plateau along the Santa Ana thrust and smaller dextral faults (Sadler, 1993), making it more difficult to fix their relative positions during weathering and subsequent deposition. This problem is evident in the absence of similar Tertiary deposits atop the weathered granite of the plateau, directly above the Santa Ana Valley.

Quartzite-bearing gravels of possible pre-uplift origin have been identified in scattered locations atop the Big Bear plateau (Sadler and Reeder, 1983), but do not represent a single, mapable geologic unit (Bortugno and Spittler, 1986) (Figure 9a). Thin beds of gravel locally underlie select basalts along the eastern flank of the plateau (Chaparrosa Peak and Antelope Creek locations, Figure 9a), which must have been deposited during the Miocene (Sadler and Reeder, 1983). These buried gravels, as well as accumulations of unburied gravel near the basalts, also contain distinctive volcanic clasts derived from the Mojave to the north (Granite, Onyx, and Chaparrosa Peaks; Figure 9a). Because these now sit above their sources, they must have been transported prior to the uplift of the plateau (Sadler and Reeder, 1983). Thus, the gravel remnants argue that the weathered surface atop the eastern flank of the plateau formed prior to uplift and has remained partly intact and preserved from erosion since. Along the central part of the plateau, similar quartzite-bearing gravels contain no clasts derived from the Mojave and are not dated by overlying units (Sadler and Reeder, 1983). Here, the gravels are litters of loose, large, rounded quartzite clasts, which are not in situ, but have been eroded out of

their original beds and redeposited in local channels and colluvium (locations at Arrowbear, Holcomb Valley, Big Bear City, Moonridge, Manzanita Springs, Big Bear Lake, Rattlesnake Creek, and Deep Creek were field checked in this study and found to consist of unbedded clasts; Figure 9a). These gravels thus cannot be connected or correlated directly with pre-uplift gravels along the eastern flank of the plateau.

Based on clast composition and roundness, Sadler and Reeder (1983) proposed that all of these quartzite-bearing gravels were derived from central locations at either Gold or Sugarloaf Mountains (despite the presence of similar quartzite bedrock near some gravels, such as at Delamar Mtn., Shay Mtn., Onyx Peak, and Mineral Mtn.; Figure 9c). This does not provide a unique temporal correlation between buried gravels and those atop the central plateau, since quartzite clasts from Gold and Sugarloaf Mountains are present in sediments as old as the Crowder Formation and as young as Quaternary alluvium. However, it does suggest that gravels were transported prior to the development of the present drainage system of the range (Sadler and Reeder, 1983). Most gravel locations could not have received sediment from these central sources given the present distribution of trunk streams, while a few locations are topographically perched above depositional base and had to have been deposited before the modern incision of the SBMs regardless of their source (Granite Peak, Arrowbear, Deep Creek, and Manzanita Springs; Figure 9a) (Sadler and Reeder, 1983). These gravels may have been transported prior to or during the initiation of uplift, when the modern pattern of incision would have developed in response to lowered base-level.

The remnants of quartzite-bearing gravels atop the weathered granite of the central Big Bear plateau thus support the hypothesis that the weathered surface had developed before or nearly before uplift of the plateau initiated, and that it has been preserved from significant erosion since. However, there are limitations to this data that prevent this from being conclusive. Because the gravels consist of loose, recycled clasts atop the central plateau, they may represent lag deposits beneath which significant erosion has occurred.

Their limited geographic extent further limits the usefulness of the gravels, since they overlie the surface in only a few locations and do not provide constraint on its original geometry. The gravels themselves also do not serve as structural datums, since they are not conclusively isochronous and of unknown original geometry.

Finally, some constraints on the origin of the weathered surface come from radiogenic helium thermochronometry presented in Chapter 2 (Spotila et al., 1998). The low-temperature cooling history of the plateau defined by helium ages is consistent with exposure of the weathered surface in late Miocene and limited exhumation throughout the Cenozoic. Radiogenic helium isochrons, which represent structural datums in crystalline rock, are also subparallel to the weathered surface of the plateau and therefore suggest the surface is itself a structural horizon. Although these results are consistent with the hypothesis that the weathered surface is relict and represents structural deformation, they are not unique and therefore inconclusive.

3.5.4 The weathered surface as a structural datum

The overlying deposits show that at least locally, deep granitic weathering developed prior to uplift of the SBMs. The weathered surface has been well demonstrated as a structural datum only along the western tip and eastern flank of the Big Bear plateau (Figure 9a). In between these areas, the weathered surface is not well known and in need of further study prior to its use as a datum. Nevertheless, previous workers have speculated on its structural implications, based on the assumption that the entire surface correlates with the Tertiary weathering buried in isolated locations. This assumption requires that the entire surface developed prior to uplift, has been little eroded since uplift, and had an originally flat geometry.

Dibblee (1982) considered the entire weathered surface to be uneroded, and suggested that minor topographic features, such as Big Bear Valley, Holcomb Valley, and Cactus Flats, formed prior to uplift of the plateau. Both Dibblee (1982) and Sadler and

Reeder (1983) suggested that the greater elevation of the surface in the middle of the range (~2.5 km elevation) than on the eastern and western flanks (~1 km elevation) showed 1.5 km of structural relief or differential uplift accrued over the past few million years. This would be correct if the quartzite-bearing gravels were deposited prior to uplift and all overlying units were deposited on a near-horizontal surface, given their present, east-west elevation distribution (Figure 11). Based on the similarities with the weathered surface in the surrounding lowlands of the Mojave Desert, they also argued that the total surface uplift of the plateau equals the rock uplift along the thrust faults. On a smaller scale, Doyle (1982) attempted to restore a small vertical offset (~50 m) along the Helendale fault, by presuming that undated, discontinuous patches of weathered granite correlated over 8 km distance, formed prior to faulting, and were once horizontal. Structural and tectonic implications of the weathered surface, such as proposed by previous workers, will not be strongly supported until the nature of the surface is further explored.

3.6. Observations: characterization of the weathered surface

3.6.1 Introduction

A detailed study of the weathered surface was conducted to further understand its nature. Various geomorphologic observations were made to build a basic, complete characterization of the weathered surface, with several fundamental questions in mind;

- what is the origin of the low-relief surface?
- is the entire surface contiguous and temporally correlative with the weathered profiles beneath dated sediments and basalts?
- is the weathered surface relict from conditions prior to uplift?
- if not relict, how fast could the weathered profile have developed and how long has it been doing so?
- to what degree has the surface been lowered by weathering and removal of decayed

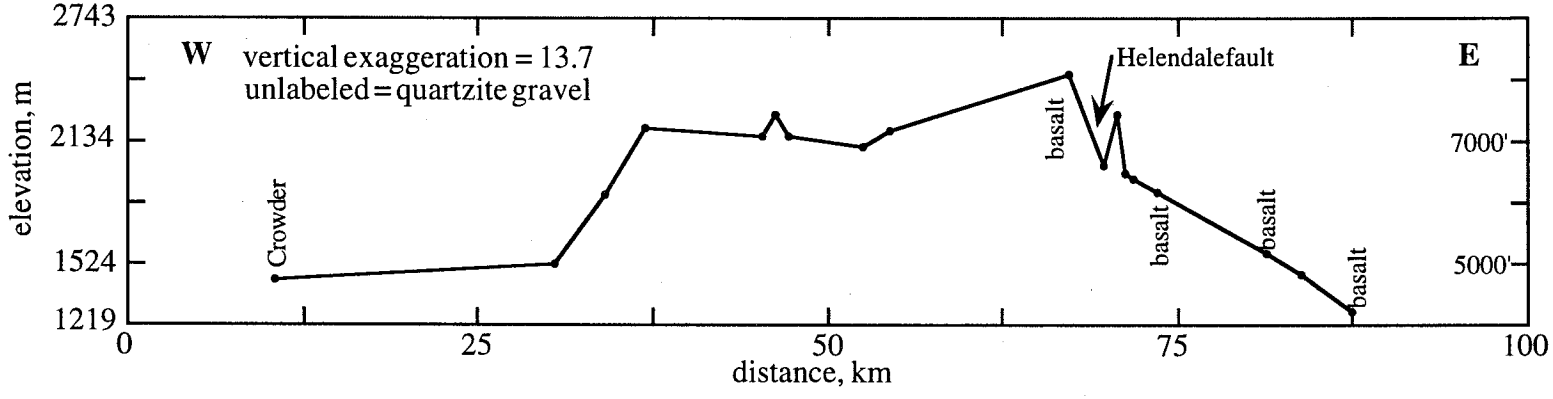

Figure 11: East-west elevation plot of deposits that overlie the weathered granite surface atop the Big Bear plateau from west (near Cajon Pass) to east (at basalts). All deposits atop the plateau are projected onto this broad eastward trend (parallel to the bounding thrust faults) and deposits outside of the plateau are excluded. The features include basalts, Tertiary sediments, and the quartzite bearing gravels of Sadler and Reeder (1983). One such gravel was excluded because it was likely uplifted along one of the secondary strike-slip faults (Granite Peak, #5 on Figure 9).

rock or simply erosion of fresh rock since uplift initiated?

- what was the original (pre-uplift) geometry of the weathered (or weathering) surface?

Analysis of the present topography and drainage network of the surface and geomorphic observations in outcrop and on stereo airphotographs contribute to determining how the surface formed, the degree to which it is actively forming, and the degree to which it is eroding or has experienced post-uplift erosion. This understanding is enhanced by deciphering a stratigraphy of the weathered profile from field relationships, which is necessary to follow marker horizons and structural levels across the range and to define where erosion cross-cuts the surface. In addition, all of these characteristics create an identification scheme to map the distribution of the surface across the range, which must be known for tectonic reconstruction. This map also defines which types of bedrock are the host for the weathered profile, which in turn bears on the boundary conditions and duration of weathering. Detailed observations of soil profiles and the products of weathering, including the grainsize, mineralogy, and color of the saprolite, also help determine how the surface formed and what conditions (e.g., climate) were required to produce it, and thus help to show whether the surface is relict or actively forming. These observations also enable tests of whether buried (i.e., Tertiary) and unburied weathered profiles are correlative. This characterization also enables comparisons with other locations of granitic weathering, where more may be known about the boundary conditions, rates, and other aspects of its origins.

3.6.2.1 Geomorphology of the weathered surface: Topography

Commensurate with occurring atop a plateau, the weathered surface has a relatively flat topography that contrasts with the steepness of its bounding escarpments (Figure 2b, see Section 3). Deeply weathered granite occurs along the gentle slopes of the upland surface, but not along steep slopes of the plateau margin or canyons where rapid erosion

occurs (as mapped; see Section 3.6.3; Figure 9a). The contrast between the mild topography of the weathered surface and the more rapidly eroding slopes is substantial and defines two distinct topographic domains (Figure 12a/b). The transition between these domains is sharp enough that a contact can be drawn between them, both along the edges of the plateau's escarpments and along the rims of young stream canyons that separate weathered granite preserved along interfluves (Figure 13a/b).

Although the upper plateau surface appears flat relative to the steep topography of the plateau's margins and canyons, it is not actually planar. The weathered surface consists of a hummocky, gently rolling topography, which is traced by gentle streams (Figure 14). On 1:50,000 scale airphotos, the surface appears mottled due to short wavelength (0.1-1 km), small amplitude (<100 m) elevation variations. This hummocky topography appears as irregular contour patterns of small, rounded hillocks and complicated, shallow drainage networks on topographic maps, which are distinct from the straighter contours of the plateau's margins and canyons (Figure 2c, 9). The roughness of the weathered surface is also apparent in unexaggerated elevation profiles across it (Figure 15a/b). The average slope of the entire upland surface (including shallow drainage networks and areas not capped by weathered granite) is ~10° (see Section 3.3).

The topographic character of the weathered surface, partly a function of the surficial nature of weathered granite (corestones and regolith, see Section 3.6.2.3), varies across the plateau. Four small areas (Figure 2c, 16) where weathered granite is mapped (see Section 3.6.3; Figure 9a) represent excellent examples of the range in possible topographic character. The surfaces above Big Bear Lake and at Burnt Flats (Figure 16a/b) are nearly flat and have only subtle, irregular hummocks. The Pinnacles (Figure 16c), in contrast, have more irregular topography that consists of many variously sized boulders that appear stacked atop each other. At the Morongo Canyon area (Figure 16d), hummocky weathered granite is present only along narrow interfluves and ridgelines, whereas fresh granite is present along canyon walls with regular, steep slopes. Although similar geomorphic

Figure 12a: Eastward view from Butler Peak (location b, Figure 1) of the weathered surface that slopes to the north towards Big Bear Lake (just out of picture to the left). Note how flat the weathered surface is in comparison to the steep margins of the post-uplift incision of Bear Creek Canyon. The high San Gorgonio block forms the background.

Figure 12b: Northward view from the San Gorgonio block (from just east of location j, Figure 1) of the Big Bear plateau north of Barton Flats. Note the contrast between the flat upper weathered surface and the steep, recently eroded margins of the plateau. The steep, south facing escarpment there is bounded by the Santa Ana thrust, located between the plateau and Barton Flats (foreground).

Figure 13a: Elevation profile across Deep Creek from 1:62500 topographic map with 40' contour interval. Location of transect located in Figure 2c.

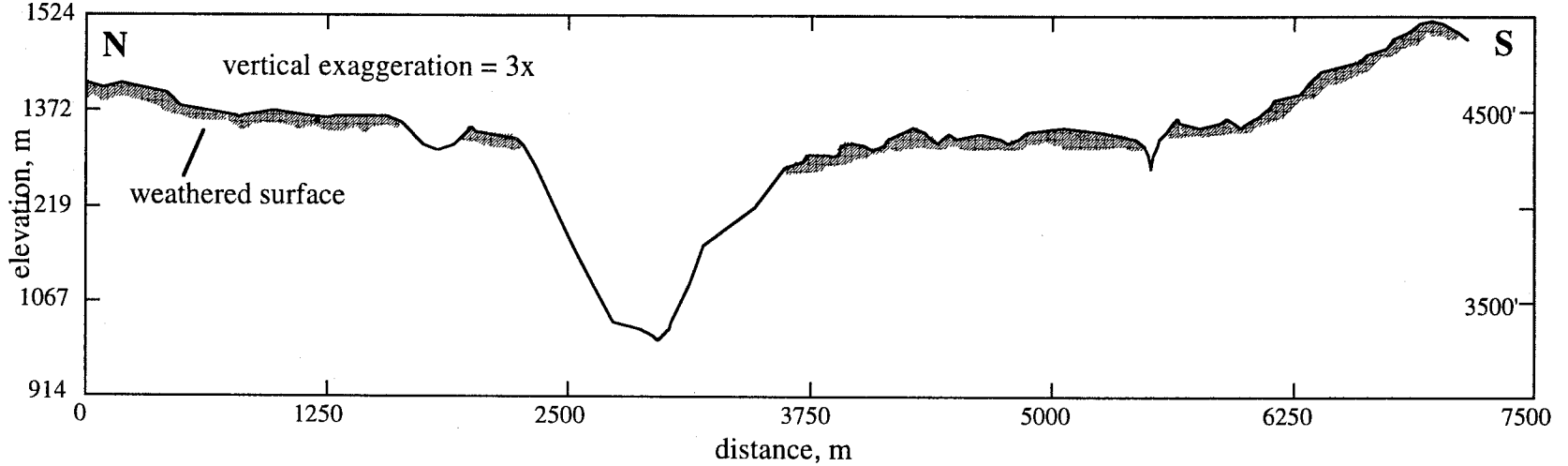

Figure 13b: Elevation profile up the southern escarpment of the Big Bear plateau near Clark's Grade. From 1:62500 topographic map with 40' contour interval. Location of transect located in Figure 2c.

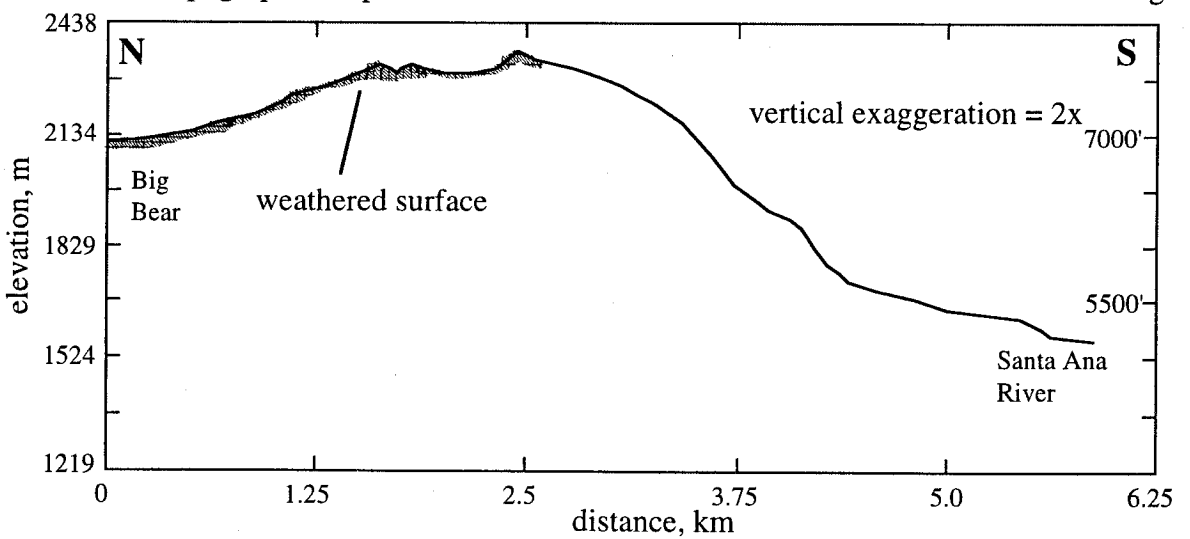

Figure 14: Photograph looking to the north from Butler Peak (location b, Figure 1) across the Big Bear plateau. Note the weathered granite surface has a distinct rolling, hummocky topography.

Figure 15a: Un-exaggerated elevation profile from Mojave River to Landers, with bend in section at Moonridge, based on 1:250,000 scale topographic map with 200' contour interval (location shown in Figure 1).

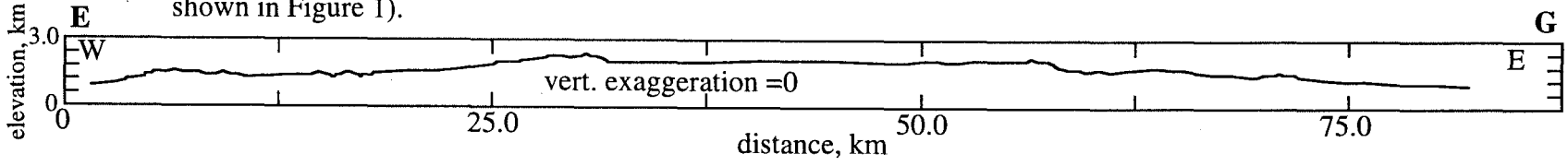

Figure 15b: Un-exaggerated elevation profile from Santa Ana River to Pitzer Buttes, with bend in section at Moonridge, based on 1:250,000 scale topographic map with 200' contour interval (location shown in Figure 1).

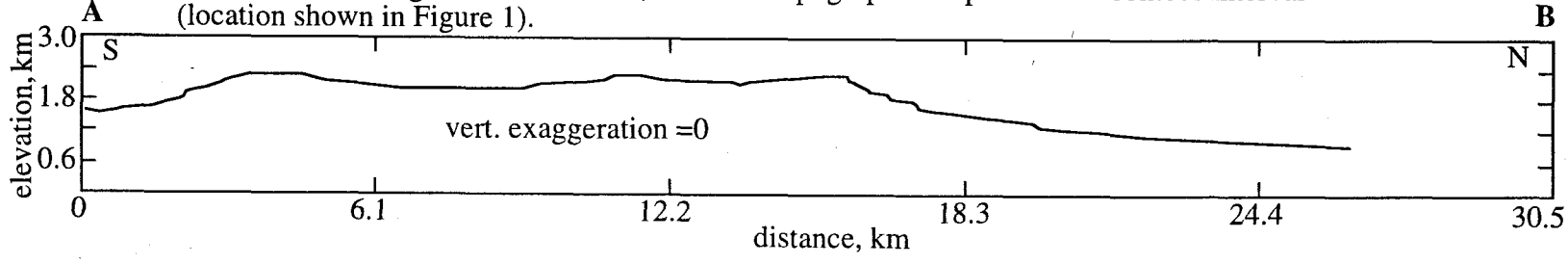

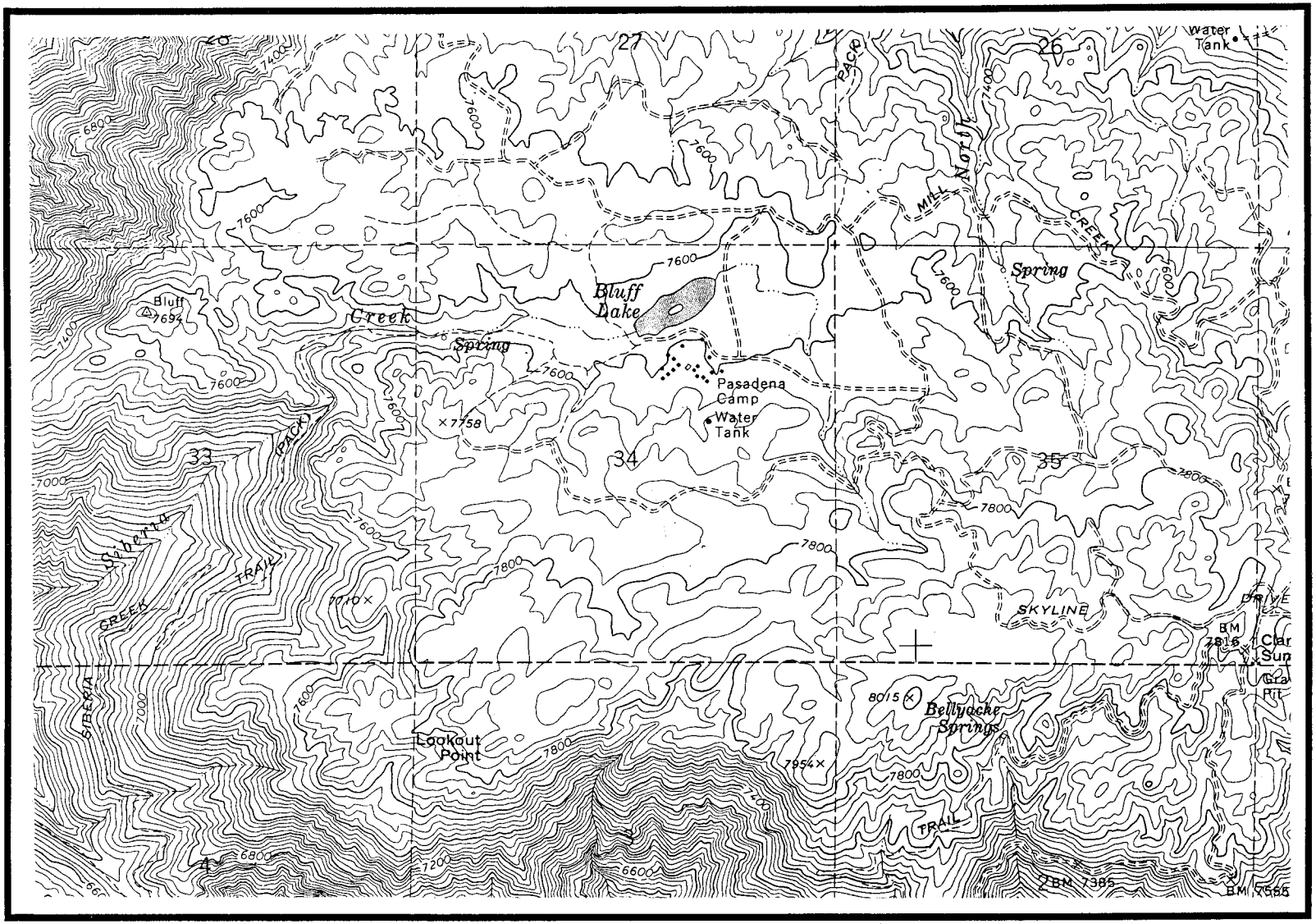

Figure 16a: Topographic map of the Big Bear Lake region, reproduced from the USGS 1:24,000 map with 40 foot contour interval (Big Bear Lake Quadrangle). See Figure 2c for location. Each square is a 1 mile x 1 mile section that can be located on the USGS map.

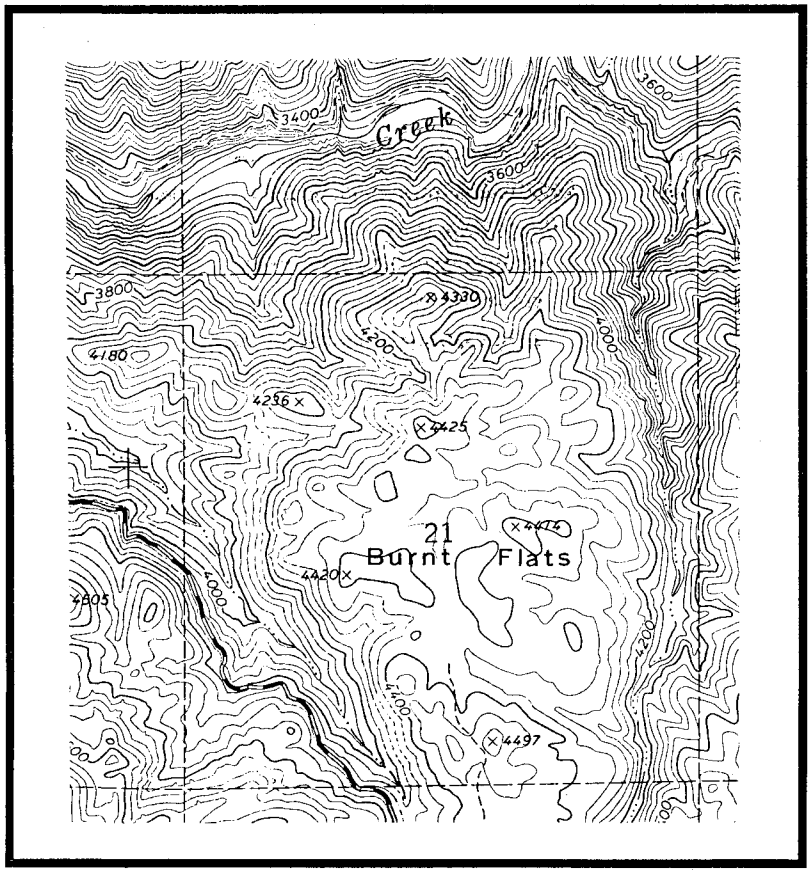

Figure 16b: Topographic map of the Burnt Flats region, reproduced from the USGS 1:24,000 map with 40 foot contour interval (Lake Arrowhead Quadrangle). See Figure 2c for location. Each square is a 1 mile x 1 mile section that can be located on the USGS map.

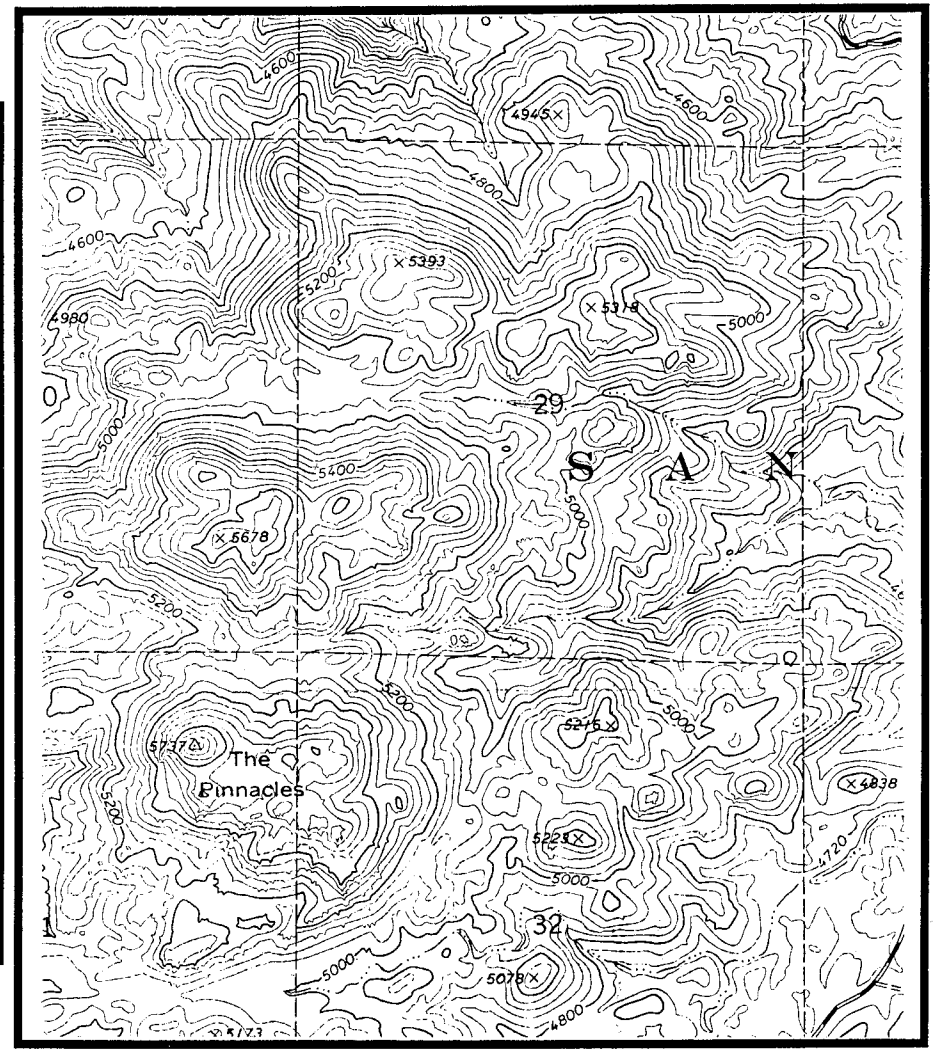

Figure 16c: Topographic map of the Pinnacles region, reproduced from the USGS 1:24,000 map with 40 foot contour interval (Lake Arrowhead Quadrangle). See Figure 2c for location. Each square is a 1 mile x 1 mile section that can be located on the USGS map.

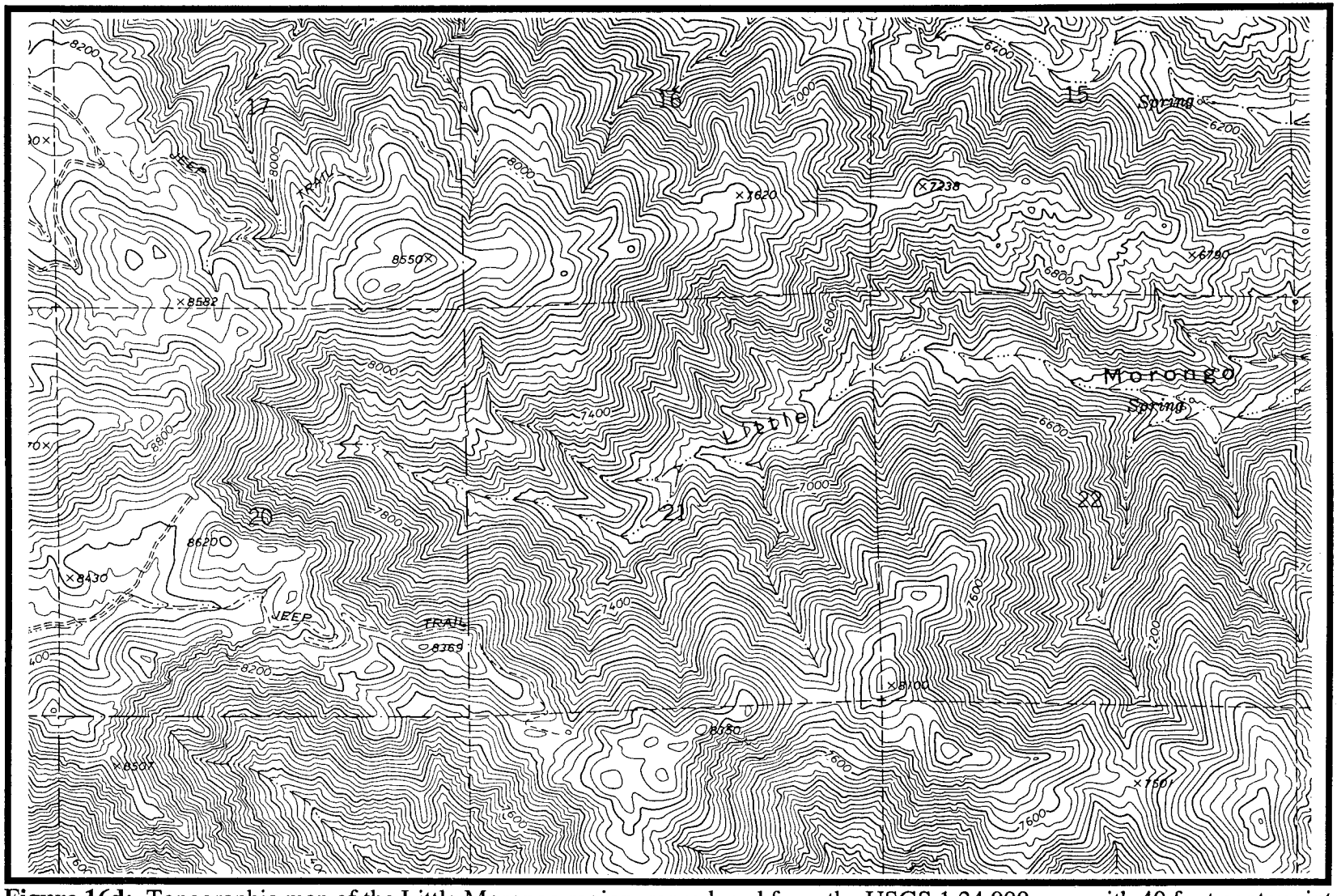

Figure 16d: Topographic map of the Little Morongo region, reproduced from the USGS 1:24,000 map with 40 foot contour interval (Onyx Peak quadrangle). See Figure 2c for location. Each square is a 1 mile x 1 mile section that can be located on the USGS map.

characteristics and weathered granite occur at each of these locations (Figure 9a), the topographic variation of the plateau is apparent (Figure 16).

The characteristic differences between these four locations can be represented by several easily-calculated topographic parameters. Average topographic gradient, which varies with wavelength, is very different for these four areas. At 100 m wavelength, the Big Bear and Burnt Flats regions have much lower average gradient (~6°) than the Pinnacles (~15°) and Morongo Canyon (~24°) (based on 1:24,000 scale topography, 40' contour interval; Table 2). The lower gradients are due to small hummocks (~10 m high) in the flat regions, whereas hummocks at the Pinnacles are ~27 m high. The steep gradients at Morongo are not due to hummocks, but the steep canyons that separate small strips of weathered surface. At longer wavelengths, average gradients at Big Bear and the Pinnacles decrease (Table 2), consistent with the observation that hummocks are typically <100 m in dimension. Gradients measured over more than a kilometer wavelength reflect the broad shape of the upland surface, rather than its local irregularity or hummockiness. At Big Bear, for example, long wavelength gradients reflect a regional tilt, averaging ~4° in the direction of tilt (N), 2.6° along random orientations, and 1.1° along tilt axis (E-W).

Total relief is a measure similar to the maximum long-wavelength gradient in an area. Where the upland surface is gently rolling and not incised, the total range in elevation per area is generally low and controlled by regional tilt (e.g., 154 m at Big Bear; Table 2). Total relief per area can be higher where large, irregular hillocks are present (e.g., 463 m at Pinnacles), or where deep canyons have incised into the upland surface (e.g., 586 m at Morongo). Another measure of gross topographic irregularity is contour density (total length of contours in an area), which is higher in areas of steep relief (Pinnacles, Morongo) and lower where topography is mild and hummocky (Big Bear, Burnt Flats) (Table 2). The degree to which hummocky topography is developed on surfaces is more specifically represented by the number of closed contours per area. The greatest average number of closed contours per area occurs at the Pinnacles (~29), consistent with the observation that

Table 2: Average gradient and topography of several locations on the Big Bear plateau (Figure 16a-d). These parameters are measured in the vicinity of the weathered surface. For some locations, such as Big Bear, the parameters are all measured on mapped weathered surface, whereas for others, like Morongo, the mapped weathered surface makes up only a very small area and thus the parameters include intervening canyons.

Average gradients, based on 10 randomly oriented measurements (each) on 1:24,000 scale, 40' contour interval maps:

wavelength (λ)	Big Bear	Pinnacles	Burnt Flats	Morongo
100 m	**6.8°**	**15.1°**	**5.4°**	**23.9°**
based on section#	#34	#29	#21	#22
500 m	**2.6°**	**7.6°**	nd	nd
1000 m	**2.6°**	**4.6°**	nd	nd
>1 km, in direction	**4.2°**N (2.5 km λ)	**6.7°**NE (3.1 km λ)	nd	nd
of tilting	**3.9°**N (3.2 km λ)	**10.8°**N (1.9 km λ)		

Other parameters:

parameter	Big Bear	Pinnacles	Burnt Flats	Morongo
total relief/mile^2	**154 m**	**463 m**	**251 m**	**586 m**
(based on average elevation range of several square miles each)				
length density of contours per mile^2	**30.1 km**	**86.3 km**	**42.5 km**	**128 km**
(based on section# XX; Figure 16)	#34	#29	1/4 of #21	#21
average #closed contour/mile^2	**~15**	**~29**	**~23**	**~4**
(based on average of several square miles each)				

it is the most hummocky. Big Bear and Burnt Flats have intermediate values, whereas Morongo Canyon has only a few closed contours per square mile (Table 2). This is because hummocky topography is present only in narrow bands along interfluves at Morongo, and the steep, smooth canyon walls are unweathered.

These four areas represent the topographic styles of the upland surface well. A cursory examination of the topography on Figure 9a reveals that, at least qualitatively, there is systematic variation of topographic style across the plateau. Flatter, gently rolling surfaces are most common in the central part of the plateau, around Big Bear Lake. More irregular, hummocky terrains are more common on the eastern and western portions of the plateau. Deep canyons are also incised into the plateau only near its margins, and the canyons on the eastern flank are particularly well-developed.

3.6.2.2 Geomorphology of the weathered surface: Present drainage network

Drainage networks are fundamental features of landscapes that directly reflect aspects of topography and indirectly reflect topographic evolution. Fluvial geomorphology offers insight to the "maturity" of a terrain, in the sense of how long a drainage system has been evolving and to what degree it is in equilibrium with its topographic setting. The drainage network (individual streams and basin divides) of the SBMs, as drawn from 1:62,500 scale topographic maps, is shown in Figure 17 (Plate 2). The outline of the Big Bear plateau is dotted on this map, facilitating a visual comparison of streams on the upland surface and those elsewhere in the range.

There are significant differences between upland basins and those along the margins of the plateau. Drainage basins around the southern and northern rims and eastern flank extend radially away from the center of the range, whereas those atop the central plateau (#1, 2, 5, 7, 8) are more complex (Figure 17). Streams in perimeter basins are typically orthogonal to the range-front and thus display a radial fabric. These streams are well-organized like tree-branches (i.e., fractal distribution), with small headwater streams

Figure 17: See Plate 2, folded into backside cover of thesis.

continuously combining and joining the trunk stream that runs along the center of each basin (e.g., basin #14). Individual streams in basins atop the upland surface, however, display a more irregular fabric and tend to be curvy and multi-directional (e.g., basin #1). Trunk-streams in these upland basins are not central or straight and are difficult to discern from secondary streams. This is reflected in the distribution and orientation of high-order (Strahler, 1952) streams in the SBMs, which are more irregular and curvy atop the plateau than in radial basins ($\geq$4th; Figure 18). The overall irregularity of drainage systems atop the plateau is associated with irregular, hummocky topography, whereas the straighter, more integrated streams along the margins of the range are consistent with steeper relief.

Variations in stream density (total stream length per area) and magnitude (number of stream unions; Shreve, 1966) across the SBMs (calculated for 6 small areas; Figure 17, 19) are also consistent with topographic differences between the plateau and margins. In areas of similar precipitation rates, stream density should be higher where more small-wavelength topographic irregularities (small hills, ridges) are present and stream gradients are lower. The stream density atop the central upland surface is the highest of six areas measured, consistent with its irregular, gentle topography (Figure 19). Stream magnitude should also be high where topography is irregular (more stream unions required to link many stream segments), which it is atop the upland surface (Figure 19). The stream density and magnitude along the eastern flank of the plateau (Figure 17, 19), however, are very low. Although the weathered surface is preserved along interfluves there, the deep canyons are more similar to canyons of the southern SBMs (e.g., Mill Creek, #4; Figure 17, 19). This is consistent with the observation that drainage basins along the eastern flank of the plateau are well-integrated and directed radially away from the center of the range.

The drainage basins atop the plateau are also generally larger than those along the margins of the range (Figure 20). The average ratio of basin area to range-front basin width is higher for drainages atop the plateau (68.4; for #1, 2, 5, 7, 8, 10, 11, 12; Figure 17) than for perimeter basins (32.1; for all other numbered basins; Figure 17). This

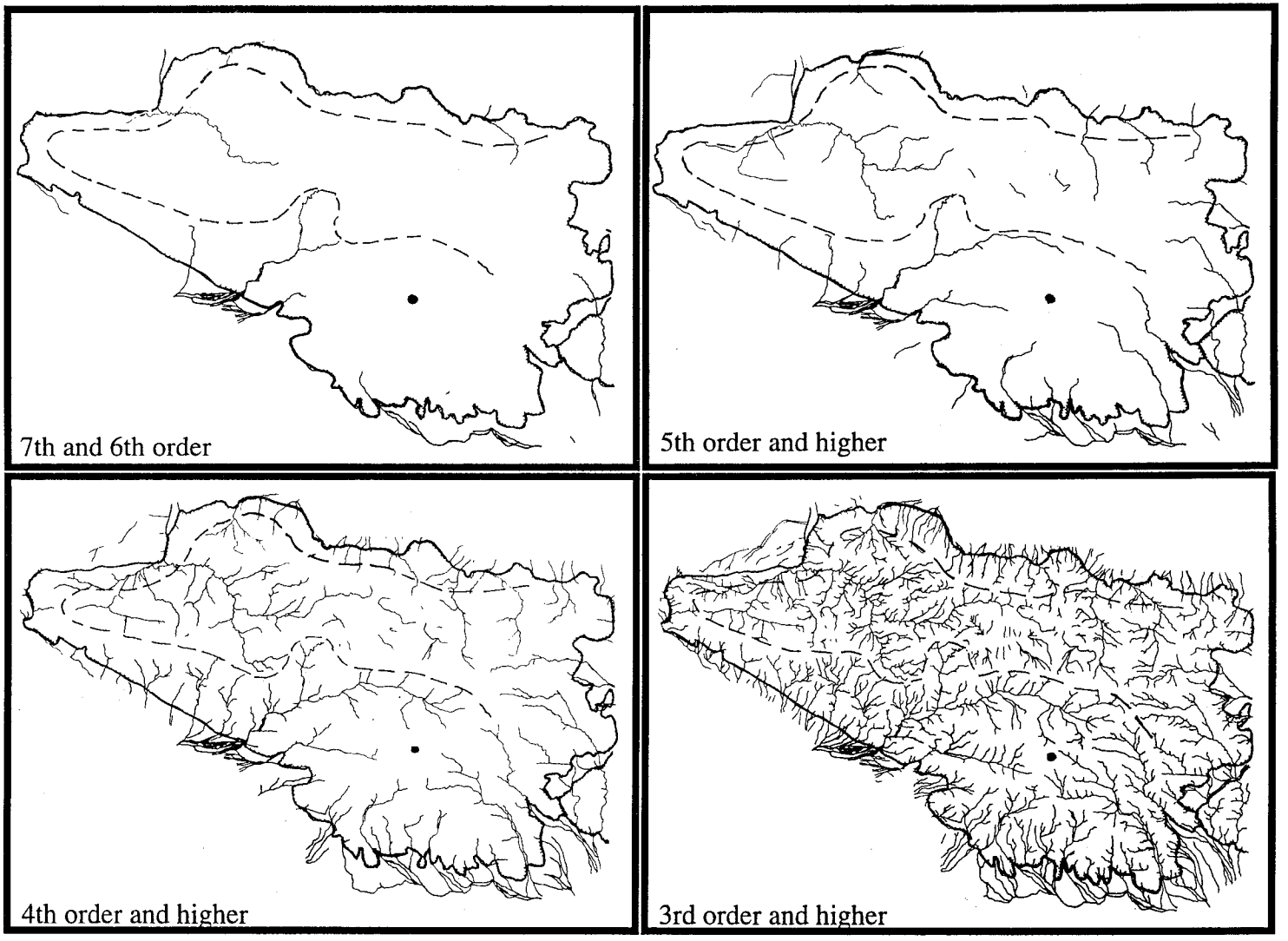

Figure 18: Distribution of stream order (Strahler, 1952) in the San Bernardino Mountains, based on the drainage data shown in Figure 17. The outline of the San Bernardino Mountains is a heavy hachured line and San Gorgonio Peak is shown as a black dot. The outline of the Big Bear plateau is shown as a dashed line.

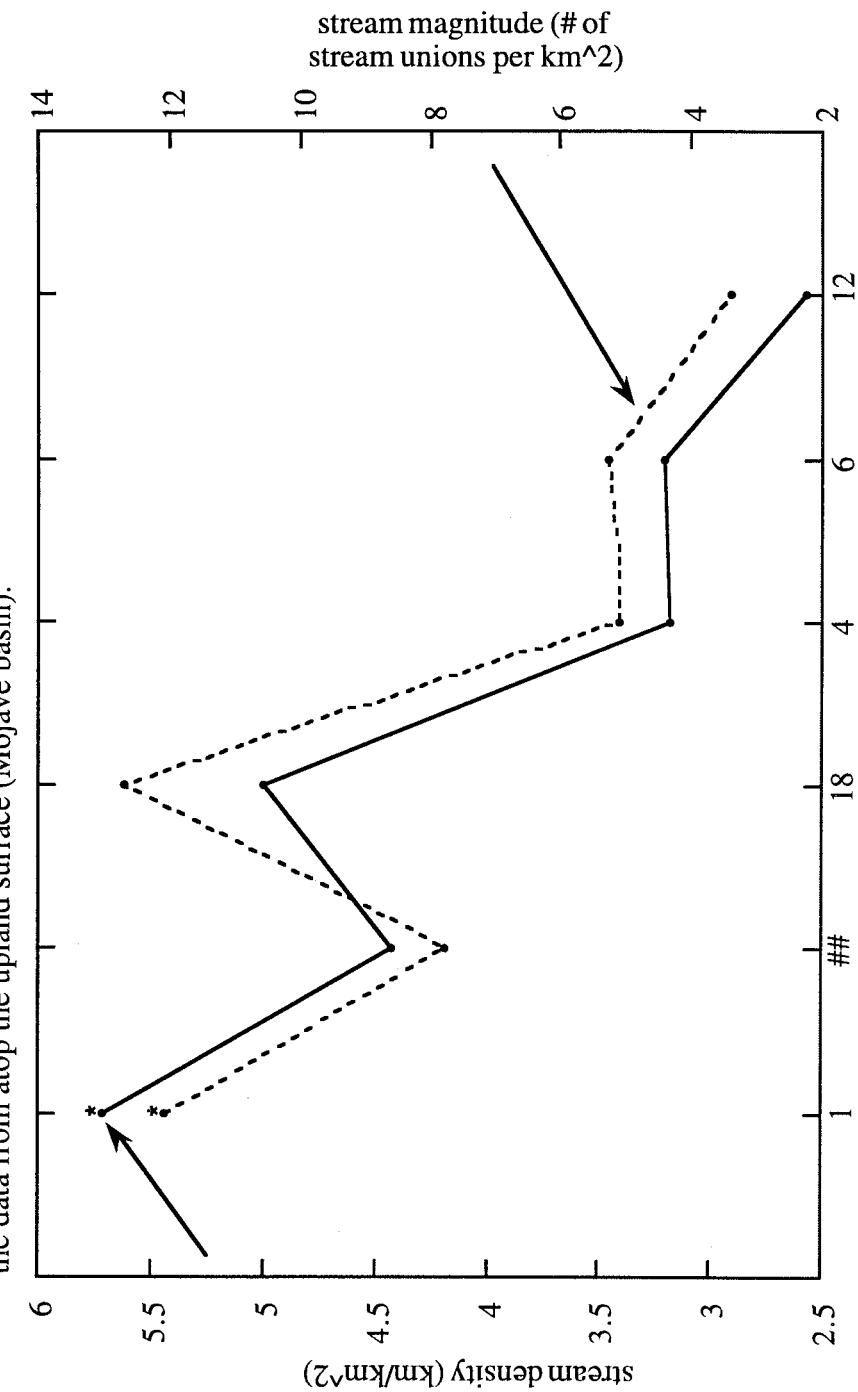

Figure 19: Stream density and total magnitude per area of small areas within 6 basins in the SBMs. The areas are shown on Figure 17 (Plate 2) and are 25.9 km^2 rectangles. Based on drainages drawn from 1:62500 scale topographic maps. Asterisk indicates the data from atop the upland surface (Mojave basin).

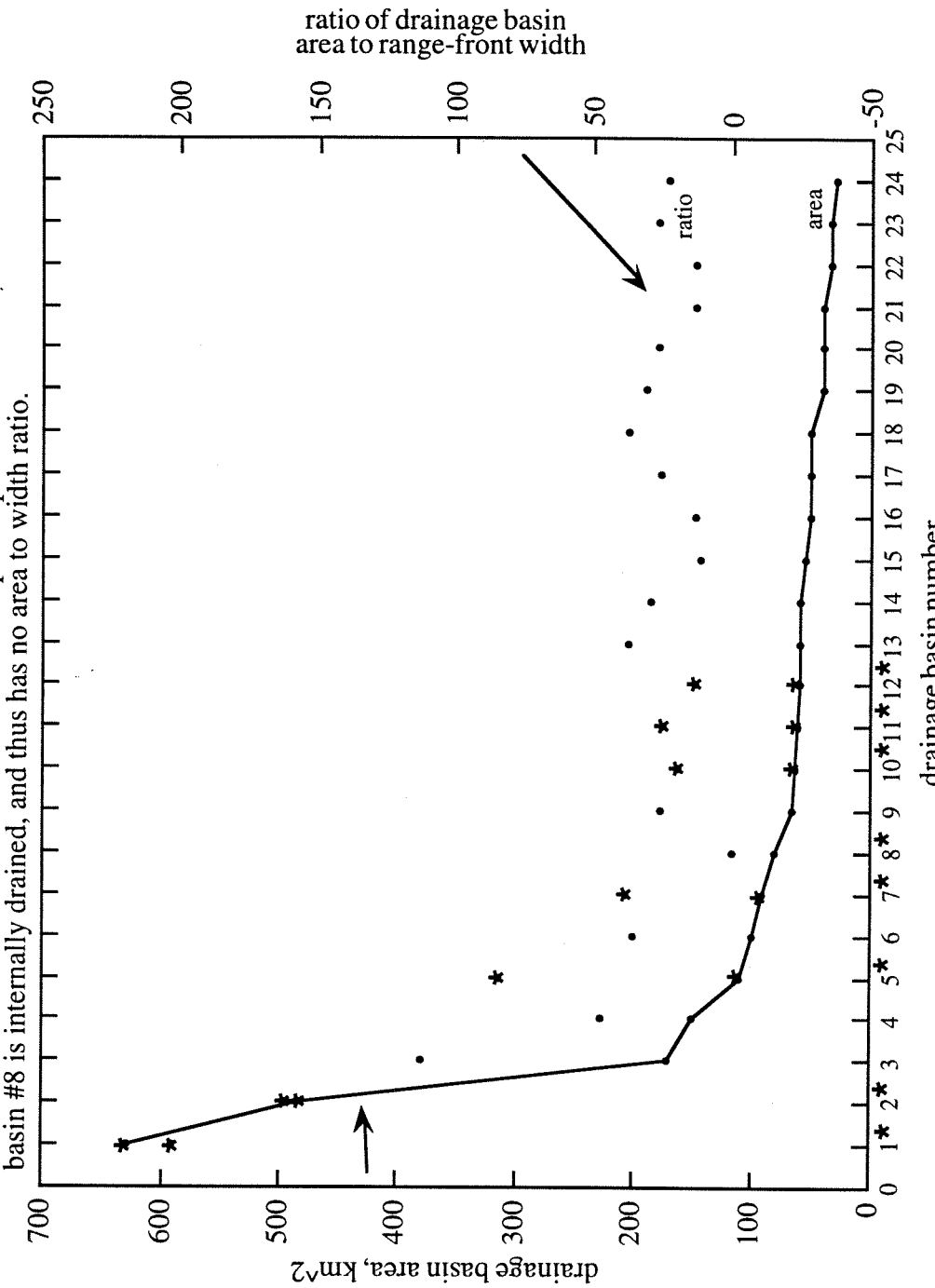

Figure 20: Plot of the drainage basin area and ratio of basin area to basin range-front width for the major drainages in the SBMs. Numbers correspond to those in Figure 17 (Plate 2). Asterisks indicate which basins are atop the upland surface. Note that basin #8 is internally drained, and thus has no area to width ratio.

reflects that the gentle, interior plateau is tapped by only a few rivers from the range-front and that the radial drainage system is not developed across the entire SBMs. The presence of a large, internally drained basin at ~2 km elevation on the plateau (#8, Baldwin Lake; Figure 17) similarly shows that radial drainages have not fully penetrated the range. In addition, substantial alluvial deposits are present atop the central plateau, indicating that much of its topography is depositional, not erosional (Figure 9b). Sadler and Reeder (1983) further noted that the large basins atop the central plateau are asymmetric (having greater area on one bank of the trunk stream), unlike symmetric perimeter basins (left and right banks equal).

A final difference between the upper plateau drainage basins and those along the margins of the range is stream gradient. As mentioned above (see Section 3.3), average stream gradients are much lower atop the plateau than along the margins. The profile of stream gradient along Deep Creek, the trunk stream of the largest drainage basin atop the plateau (Mojave basin, #1; Figure 17), is an excellent example of this. The gradient of the lower portion of Deep Creek is typical for mountainous topography (i.e., range perimeter), rising exponentially from low gradient at base-level to a steep upper segment (Figure 21). Near the upland surface of the plateau, however, the gradient flattens out at an abrupt inflection point as it reaches the more gentle plateau surface. This inflection is the transition between the perimeter-type and upland surface-type basins.

In several locations, this transition does not occur within a single basin but is represented by beheading of surface-type basins by perimeter-type basins. Coon Creek to the east of the San Gorgonio block (4 km SSE of Cienega Seca) provides the best example of this, in which a gentle, mature canyon has been penetrated by a steep, youthful canyon from the southeastern margin of the range. As a result, the headwaters of Coon Creek flow into the younger drainage system, and a pronounced inflection occurs between the upper Coon Creek and steeper stream gradient below. Other examples of channel beheading, or stream capture, may be found as well (Grout Creek pirated by Bear Creek [3 km WNW of

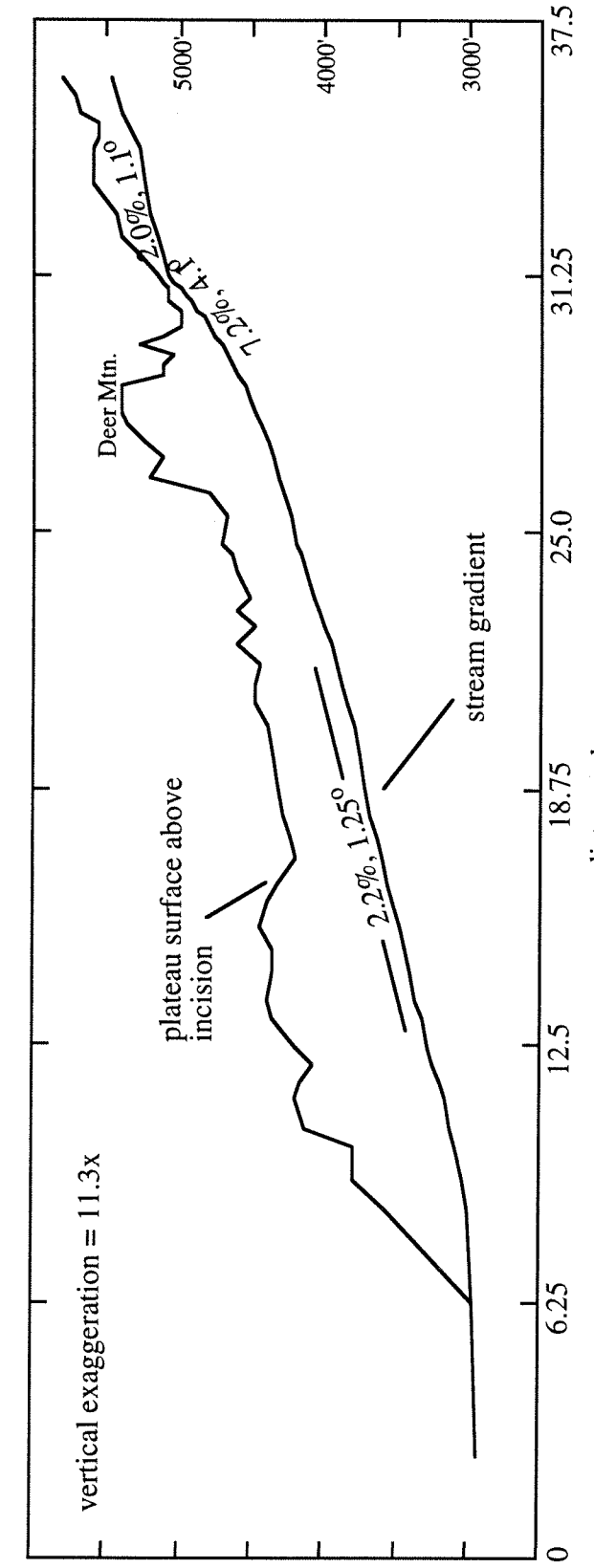

Figure 21: Comparison of the stream gradient along Deep Creek with the elevation of the Big Bear plateau above (or the ridge above), based on a 1:62500 scale topographic map with 40' contour interval. The line of section follows the creek, shown in Figure 2c. Note that the stream gradient increases monotonically to a knick point near Deer Mtn. Above this the gradient is lower. The change in gradient corresponds to the location where Deep Creek reaches the level of the plateau surface. The knick point would thus be the incision front that is working its way into the plateau. This suggests Deep Creek is not in equilibrium and is tapping into a more mature drainage system atop the plateau.

Big Bear Lake], small canyon pirated by Furnace Canyon [2 km NNW of Holcomb Valley], headwater-removal by northward migrating perimeter streams of Hooks Creek, Daley Canyon, and others [SE and SW of Lake Arrowhead]). Channel beheading indicates a cross-cutting geomorphic relationship, in which older drainage basins are modified by younger ones, consistent with the idea that the erosion is much slower atop the plateau than along its margins.

3.6.2.3 Geomorphology of the weathered surface: Field characterization

The weathered surface was observed at a number of field localities (Figure 1a) to check airphoto mapping (see Section 3.6.3) and to characterize its nature. As in the Mojave (Oberlander, 1972), the deep weathering atop the Big Bear plateau is manifest primarily on granitic rocks, because of both the prevalence of granitic bedrock atop the plateau and its high weatherability (see Section 3.6.4).

Across most of the plateau, deep granitic weathering is indicated by the accumulations of corestones that protrude from a surface floored by loose granitic regolith. The variously-size (typically 1-10 m diameter), rounded corestones are boulders of fresh, coherent granitic rock and often have weathering rinds. The regolith typically consists of coarse, mono-crystalline quartz, feldspar, and mica grains, which display no evidence for physical transport. This grus is crumbly and gives a dull thud when struck with a hammer, as opposed to the ring given by fresh granitic rock. In places, the grus has been reworked as colluvium, in which case it is even less coherent. The combination of corestones and regolith that is prevalent atop the Big Bear plateau is characteristic of deep granitic weathering (Ollier, 1975).

Exposures of the thick weathered profile are rare atop the plateau, and detailed field examinations are generally limited to fresh road-cuts. In many exposures, corestones occur embedded within a matrix of in situ regolith that retains rock fabric and structure (such as quartz veins) (Figure 22). The frequency of corestones increases downwards in the

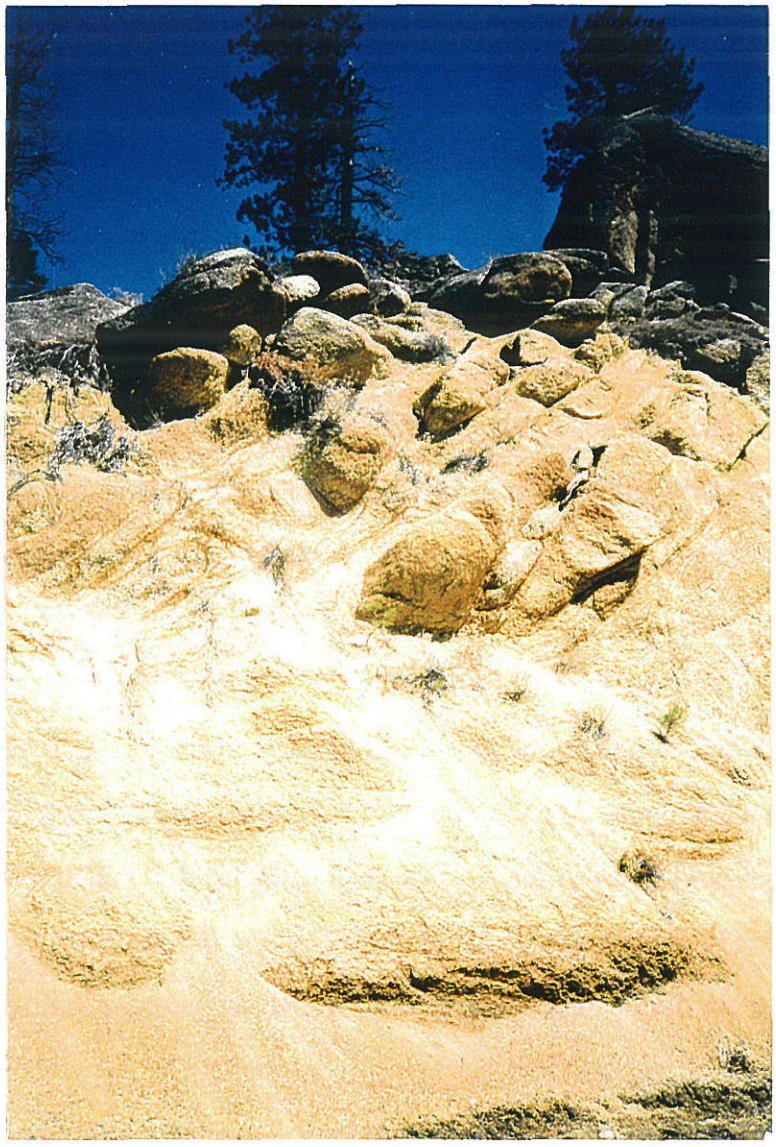

Figure 22: Photograph of an outcrop of granitic corestones set within a matrix of granitic grus or regolith (taken along road 3 km east of location b, Figure 1). Note that the grus formed by in situ weathering of granitic rock, and that each boulder was weathering inward at the time of active weathering. If weathering were to continue, the boulders would presumably decay to grus themselves. Height of outcrop is about 5 m.

profile. In exposures that span the greatest depth range, there is a gradual transition upwards from fresh granitic rock, to a prevalence of corestones and minor interstitial grus, to a prevalence of grus. The best example of this is the discontinuous road-cut along Deep Creek (Route 73; Figure 9a), which exposes most of the weathered profile. Fresh, hard quartz monzonite occurs at the base of the weathered zone, which gradually weakens upwards and becomes easier to shatter and fragment. This mechanical change is probably the result of minor weathering, although the rock is still somewhat fresh. The rock continues to weaken upwards, and gives way to a combination of resistant corestones and minor interstitial grus. Higher in the profile, the corestones become less frequent and the proportion of grus increases, although the regolith remains in situ and shows no evidence of having been reworked. A bouldery rind occurs at the top of the road-cut exposure, which contains more corestones than the section immediately below. This accumulation seems to be a lag deposit of large, hard-to-transport boulders, that are reworked and lowered as the weak, interstitial grus is removed by erosion.

Although not present at Deep Creek, well-developed soils mantle weathered profiles at several locations atop the plateau. As described in detail below (see Section 3.6.5.1), these soils are the products of further deep weathering of granitic regolith (i.e., saprolite). The soils observed in this study (Figure 1a) all fit a general field classification. Soils are capped by thin A-horizons, consisting of organic, loamy colluvium that has experienced little pedogenesis. Thicker (~1 m), reddish Bt-horizons occur below, consisting of decayed grus that retains no rock structure and includes significant clay and oxide accumulations. These grade downwards into thicker Crt-horizons, consisting of grus that retains rock structure and includes only minor clay and oxides. Evidence of pedogenesis decreases gradually with depth in the Crt-horizons, which eventually become C-R-horizons that consist of significant proportions of granitic corestones. The majority of the weathered profile at Deep Creek is C-R- and lower Crt-horizon, and at least ~5 m of upper soil (A, Bt, upper Crt) is missing that has been identified in other locations.

The total thickness of the weathered profile may be quite large. If the "stratigraphy" of weathered zones at Deep Creek is presently horizontal, the lower section of weakened, somewhat fresh rock is ~30 m thick and the upper, deeply weathered zone is ~55 m thick (Figure 9a). The upper section could be closer to 60 m, given that erosion is suggested by the lag deposit of corestones and the missing ~5 m of upper soil horizons. However, the Deep Creek thicknesses were measured over more than 1 km road-cut length and would be quite inaccurate if the weathered surface is tilted even a few degrees along the direction of the exposure. Given the irregular, hummocky topography of the surface, however, it is not possible to accurately measure its orientation in the vicinity of Deep Creek (Figure 9a, 16c). In other locations atop the central plateau, the thickness of the weathered profile has been found to be ~30 m, based on the depth to fresh granitic rock in wellholes (Brown, 1976) and other exposures (Meisling, 1984). The 60 m thickness of the deeply weathered zone at Deep Creek may thus be an overestimate.

To represent the characteristic profile of deeply weathered granite atop the plateau, the observations of many partial exposures were stacked together. Observed features were used to match weathering at other locations (Figure 1a) with the template of character-depth variations in weathering at Deep Creek (Figure 23). Although the resulting representation of the weathered profile is schematic and not preserved in any one location atop the plateau, it is consistent with observations of weathering at each location. The total thickness of the weathered profile was assumed to be 60 m for this schematic profile, despite the possible inaccuracy in the measurement at Deep Creek. Because the thicknesses of other exposures fit the Deep Creek template, the true total thickness of the weathered zone may actually be close to 60 m.

Because different locations across the plateau expose different levels of the weathered profile, there is regional variation in the character of the surface. Well-developed soils and thick piles of regolith, for example, are somewhat common in the Lake Arrowhead region (Figure 9a), whereas the prevalence of corestones in other areas

Figure 23: Schematic diagram of the characteristic profile of the weathered surface atop the San Bernardino Mountains. This representation is based on compilation of observations at specific locations atop the range, which expose different levels of the profile as shown on the right (refer to Figure 1 for locations). SP = soil profile.

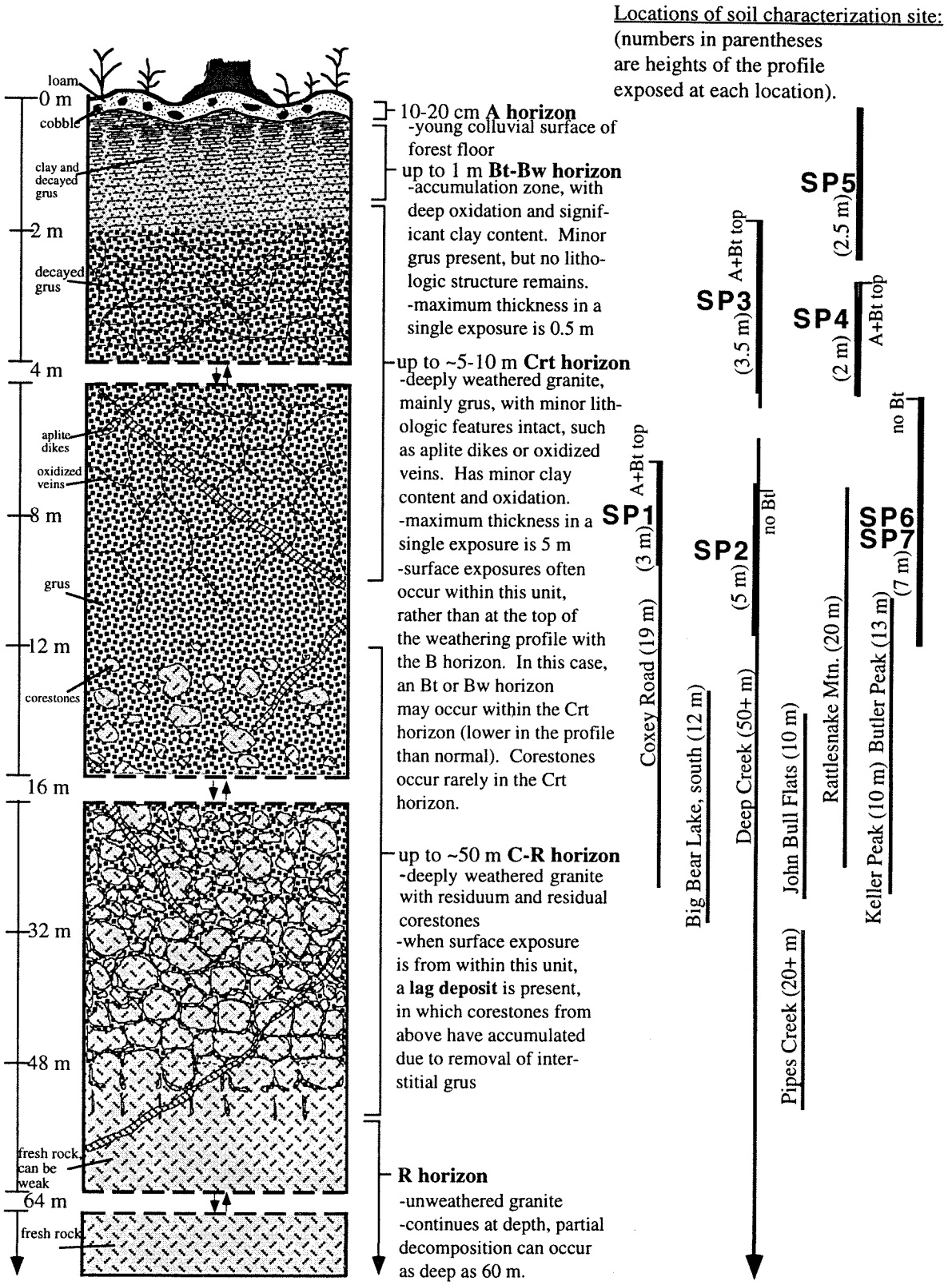

represent deeper levels of the weathered profile. Depending on how deeply the profile is exposed, the surficial expression of weathering may consist of primarily regolith or corestones. In some locations, for example, corestones are rare and most of the surface consists of grus (Figure 24a), whereas in others nearly 100% of the surface consists of a bouldery corestone rind (Figure 24b).

This variation partly controls the topographic expression of the weathered surface. Flatter regions and negative topographic forms, such as at Big Bear Lake or Burnt Flats (Figure 16a/b), consist of higher proportions of surficial regolith matrix than more hummocky areas, such as the Pinnacles (Figure 16c). Piles of corestones and larger masses of resistant granite (inselbergs) also make up the positive, protruding topographic forms of the hummocky terrain, which can be hundreds of meters in dimension (e.g., Butler Peak and the Pinnacles; Figure 9a, 17c). The correspondence between variations in the surficial form of weathering and topographic character is consistent across the plateau. The irregular, hummocky areas along the eastern and western flanks of the upland surface (Figure 9a) expose deeper levels of the weathered profile, whereas the upper level of the profile is more common atop the gentler regions of the central plateau.

Vegetative cover also varies systematically across the plateau. Steep, rapidly eroding slopes on unweathered granite are typically covered by chaparral (Figure 25a). Forests are generally developed on flatter areas atop the plateau, where thick regolith and soils are present (Figure 25b). Although the thick regolith and slow erosion along gentle slopes fosters the development of thicker vegetation, the thick vegetation also helps prevent the erosion of regolith and the development of more irregular topography. The distribution of vegetation is further controlled by the rainfall variation across the plateau (Figure 8), as only scrubby brush occurs in the arid northeast, but dense forests are present in the humid southwest.

Where granitic bedrock is not present across the plateau, the geomorphic character of the surface is somewhat different. Non-granitic lithologies tend to have greater relief

Figure 24a: Photograph of the weathered granite surface along the north side of Big Bear Lake (about 3 km east of location b, Figure 1a). Note that it consists fully of exposed bedrock. The large blocks are corestones that were exposed before they weathered into spherical forms. Joints separate these corestones and would have permitted movement of solutions capable of weathering the rock.

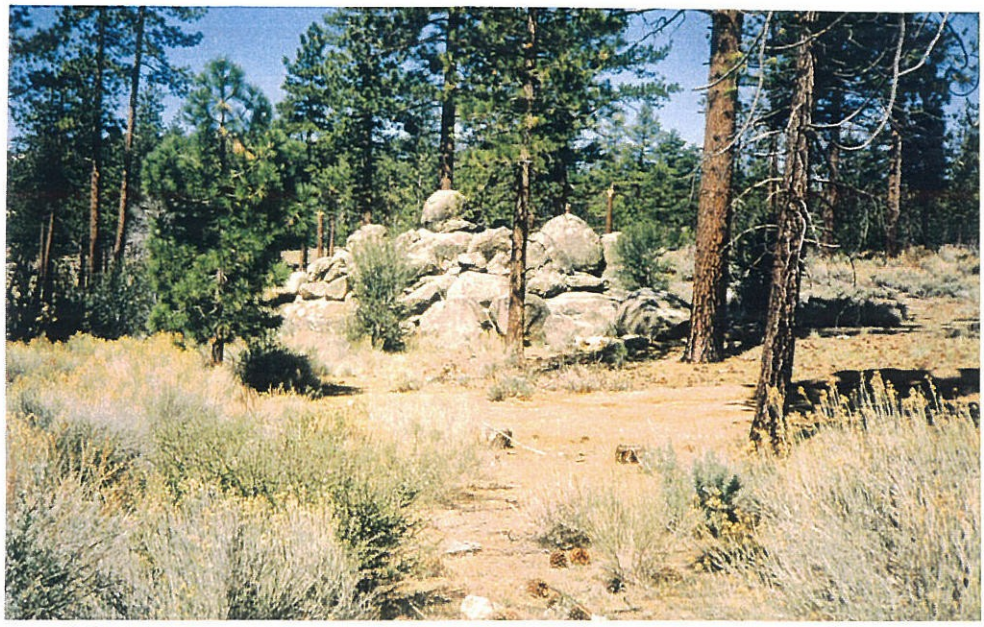

Figure 24b: Photograph of the weathered surface along the Coxey Road (location c, Figure 1a). Here the surface consists of limited exposure of corestones (~10% of area) surrounded by reworked granitic grus (regolith). Note the corestones here are much more rounded than those in Figure 24a. The greater rounding and lower percentage of corestones both argue that the Coxey Road location exposed a higher (more weathered) horizon of the weathered zone than does the location in Figure 24a.

Figure 25a: Photograph looking northwest from the Santa Ana River (location t, Figure 1a) of the typical vegetation covering steep slopes along the margins of the Big Bear plateau. Note that the steep landslide scar (from Slide Peak) has no vegetation and the other slopes have only chapparel. The thin soils along these slopes probably cannot hold water, and thus granite weathering would be slower here than along more gentle slopes.

Figure 25b: Photograph of the typical forest cover of much of the flat part of the Big Bear plateau (location #3, Figure 1a). Note that the deep roots of the trees allow accumulation of soil material that can retain water, creating conditions more favorable for bedrock weathering.

than granitic ones (see Section 3.6.4), although they generally occur as subtle, rounded hills or ridges whose gentle, hummocky topography is continuous with the weathered granitic surface (Figure 9a). These other rock types, particularly quartzites, do not outcrop as jagged, fresh rocks, but are typically expressed as accumulations of colluvium that contain blocks and fragments of unweathered rock. The colluvium is often mantled by well-developed, red soils (~10R4/6), such as above quartzite at Doble, Shay, and Delamar Mountains (Figure 9a). Thus, although the surface along other bedrock types has a different geomorphic expression, it does show some evidence of antiquity.

3.6.3 Distribution of the weathered surface

The distinctive topographic and geomorphic expressions of the weathered surface, as detailed above, make it possible to map it accurately as a geomorphic domain. The surface was mapped onto 1:62,500 scale topographic maps using 1:50,000 scale aerial photographs and was field checked in many locations (Figure 1a, 9). The diagnostic criteria for identifying the weathered surface included the distinct appearance of mottled, hummocky, gently rolling topography, as well as visible accumulations of corestones, inselbergs, regolith, or well-developed soils. The mapped surface thus represents the occurrence of certain geomorphic features, rather than a unique, contemporaneous marker horizon. Areas of steep slope that had characteristics of rapid erosion were easy to distinguish from the weathered surface. In some places, however, the geomorphic character observed on airphotos was inconclusive, and the weathered surface had to be mapped as questionable (Figure 9a).

Areas of low slope atop the plateau not mapped as weathered surface typically consist of alluvial surfaces (Figure 9b). The distribution of Quaternary alluvium atop the plateau illustrates that much of the surface is depositional, although perched high above regional base level. Other holes in the mapped weathered surface often consist of rounded, colluvial ridgelines or hillocks of non-granitic bedrock (Figure 9c). These typically consist

of quartzite or marble. In some locations, however, non-granitic bedrock surfaces have similar geomorphic character as the weathered granite (hummocky, mottled), and thus were mapped as the weathered surface. The geomorphic criteria of airphoto mapping did not require that the weathered surface be mapped solely on granites. Given that most of the plateau's surface area consists of granitic bedrock, however, the majority of the mapped weathered surface does correspond to deeply weathered granite (see Section 3.6.4).

The weathered surface is semicontinuous across the plateau, but often occurs in continuous stretches that exceed 10 km length (Figure 9a). Irregular, unconnected patches of weathered surface commonly occur at similar elevations near each other and are separated only by canyons and young streams (e.g., Deep Creek; Figure 12a) or non-granitic bedrock. This semi-continuous patchwork of weathering can be linked up across almost the entire plateau (Figure 9a). The weathered surface is most densely distributed on the west, where it ends abruptly at the fault-bounded northern and western margins. Across the central plateau, large holes in the surface are present due to lakes, alluvial basins, and changes in bedrock lithology (see Section 3.6.4). On the east, the surface is less-well connected as it descends gradually to the adjacent lowlands. On the southeast, where the southern plateau margin is obscured, weathered granite is nearly absent (Figure 1a).

Weathered granite that may correlate (see Section 3.6.6) with the upland surface of the plateau occurs in several other locations in and around the SBMs (Figure 9a). South of the plateau, weathered granite has been identified beneath the Santa Ana Sandstone (Santa Ana Valley; Jacobs, 1982) and along the northern slope of the San Gorgonio block (Sadler and Reeder, 1983; Figure 1a, 9). The patches along the San Gorgonio block, such as at Manzanita Springs (Figure 26), occur quite high (~2.5 km) and are very similar in character to the regolith-grus combination atop the central plateau (Figure 24b). Between these higher surfaces and the Santa Ana Valley, dipping (>10°) patches of weathered granite are visible in road-cut exposures along Route 38 (Figure 9a). Young canyons dissect these

Figure 26: Photograph of granitic corestones atop the San Gorgonio block at Manzanita Springs (location j, Figure 1a). These corestones indicate that weathered granite is present atop this part of the block. The geomorphology of the surface shown is identical to that atop the Big Bear plateau, although no exposures of well-developed soil or thick weathering profiles could be found.

patches and expose fresh rock, providing natural cross sections from weathered to unweathered granite.

As discussed previously (see Section 3.5.2), the weathered surface is present across the granitic rocks of the Mojave Desert (Oberlander, 1972). On the northeast, the plateau surface merges with granitic pediment of the surrounding lowlands, but this pediment does not continue very far westward along the rangefront (Figure 9a). North of the central plateau, exposures of weathered granitic basement are rare and only occur as isolated spurs that protrude from alluvium near northwest-trending strike-slip faults (e.g., Pitzer Buttes; Figure 9a). The remainder of the basement surface is buried by thick accumulations of alluvium (a foredeep) and Tertiary sediment (Sadler, 1982b). If weathered granite is present beneath these sediments, its position can only be approximated by the depth to basement (Figure 9a). Wells in the Lucerne Valley directly north of the plateau indicate basement is buried by as much as 500 m of sediment (Aksoy et al., 1986; Riley, 1956). A seismic line across the valley to the west resolved a similar sediment thickness of ~700 m (assuming seismic velocity = 2.75 km/s; Li et al., 1992). Meisling and Weldon (1989) also estimate a sediment thickness beneath the Antelope Valley of 450 m. The depth to basement north of the plateau thus seems to be deeper on the west than on the east, and may serve as a proxy for the buried weathered surface.

3.6.4 Parent rock of the weathered surface

Field observations (see Section 3.6.2.3) and the distribution of the weathered surface (see Section 3.6.3) indicate that it is primarily developed on granitic rock. A quick comparison between the plateau's geology (Bortugno and Spittler, 1986) and the mapped weathered surface (Figure 9a, c) shows that the geomorphic indicators of weathering occur predominantly on granitic bedrock, whereas the weathered surface is absent from many locations where non-granitic basement occurs.

Given that the weathered surface is more prevalent on granitic bedrock, other lithologies atop the plateau may have been more resistant to deep chemical weathering. About 70% of the plateau consists of granitic bedrock, so that a significant area of other lithologic types was exposed to the same environmental conditions responsible for granitic weathering (Table 3). Rocks that are resistant to weathering should occur as isolated highs in a deeply weathered terrain, due to differential relief that results from different rates of weathering on rocks of different chemistry and texture (etchplanation). Across the plateau, bodies of quartzite bedrock (very resistant to chemical weathering) and other non-granitic lithologies protrude above the weathered surface as isolated highs, such as at Onyx Peak, Shay, Gold, Ord, Blackhawk, Mineral, White, and Tip Top Mountains (Figure 9). The quartzite of Sugarloaf Mountain, for example, is 571 m higher than neighboring granitic rocks along the same ridge. Nearly all positive relief forms atop the plateau consist of non-granitic lithologies, and non-granitic bedrock does not outcrop with negative topogrpahic relief (e.g., Figure 27). Several inselbergs of plutonic rock are present, but these are rare and tend to be lithogies other than quartz monzonite (e.g., hornblende monzonite at Delamar Mt. and Redonda Ridge, diorite and gabrro on Rattlesnake Mt., granite and alaskite near Luna Mt.), except for tors at the Pinnacles, John Bull flat, and Round Mt. This indicates that local topographic relief is the result of variations in weathering rate.

To verify this, the average elevation of major rock types atop the plateau were calculated (Table 3; Figure 28). Granitic rock averages much lower than other bedrock types (e.g., 420 m lower than quartzites), consistent with observations of bedrock composition with positive relief and the weatherability of different lithologies. For example, easily weathered, feldspar- or mafic-rich rocks occur much lower than resistant quartzites. One exception to this is marble, which is somewhat weatherable but has high average elevation. This is attributed to the coincidence that marble only occurs in the high central plateau in association with other, more-resistant metasedimentary rocks (Figure 9). Locally, marble occurs lower than more resistant bedrock (Meisling, 1984).

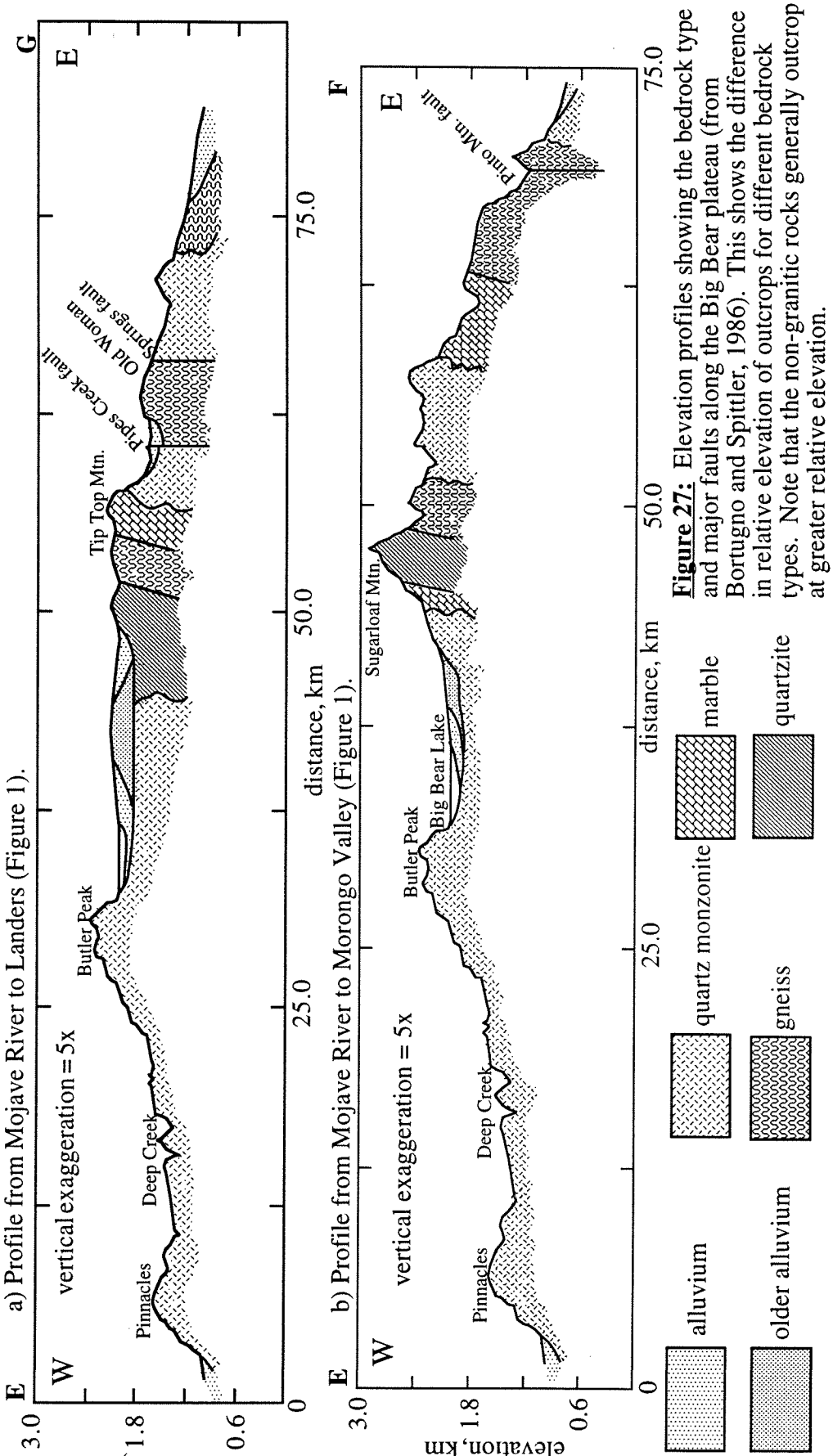

Figure 27: Elevation profiles showing the bedrock type and major faults along the Big Bear plateau (from Bortugno and Spittler, 1986). This shows the difference in relative elevation of outcrops for different bedrock types. Note that the non-granitic rocks generally outcrop at greater relative elevation.

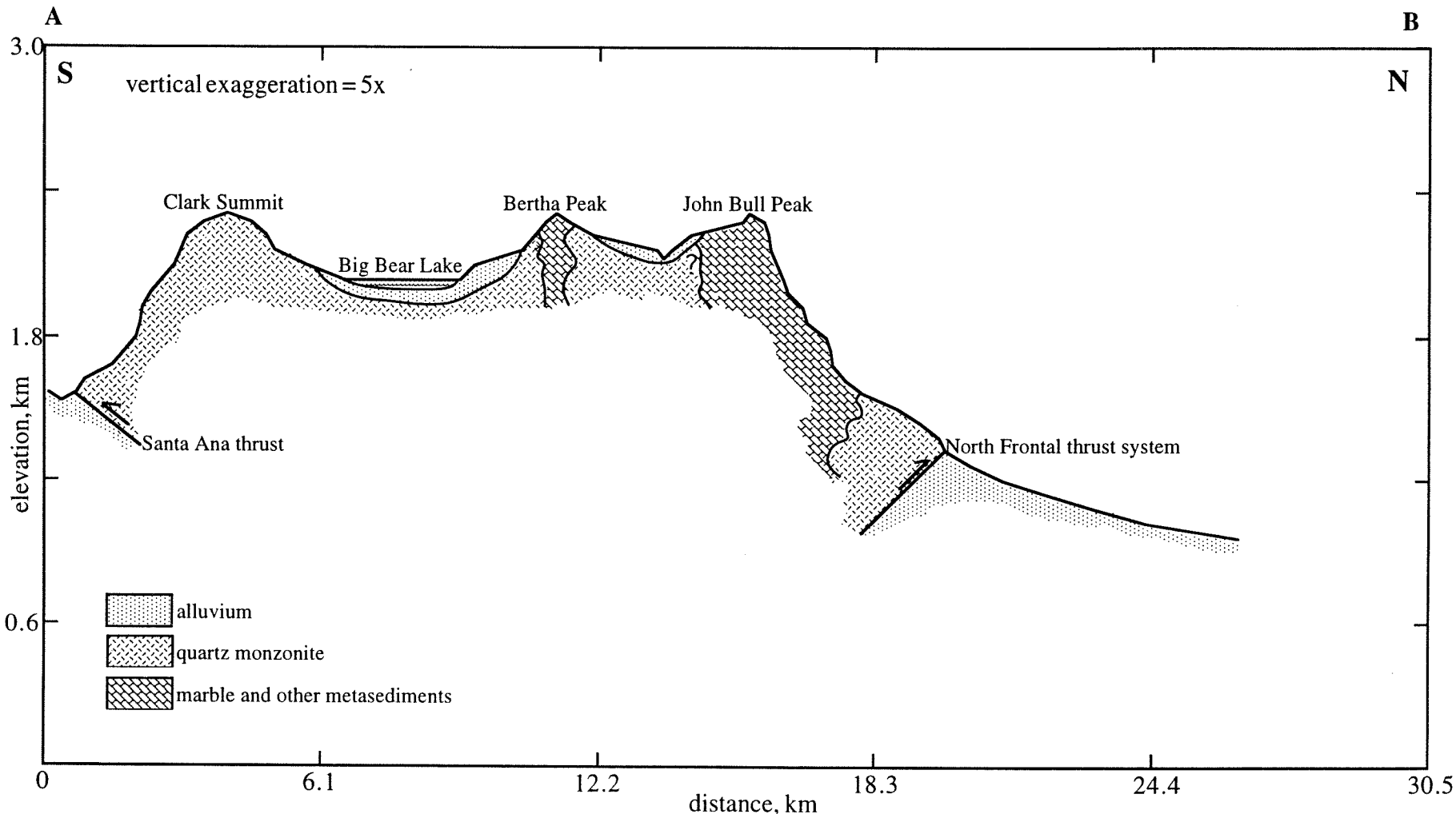

Figure 27b: Elevation profile from Santa Ana Valley to Lucerne Valley (Figure 1), showing the bedrock type and major faults (from Bortugno and Spittler, 1986). This shows the difference in relative elevation of outcrops for different bedrock types. Note that the non-granitic rocks generally outcrop at greater relative elevation.

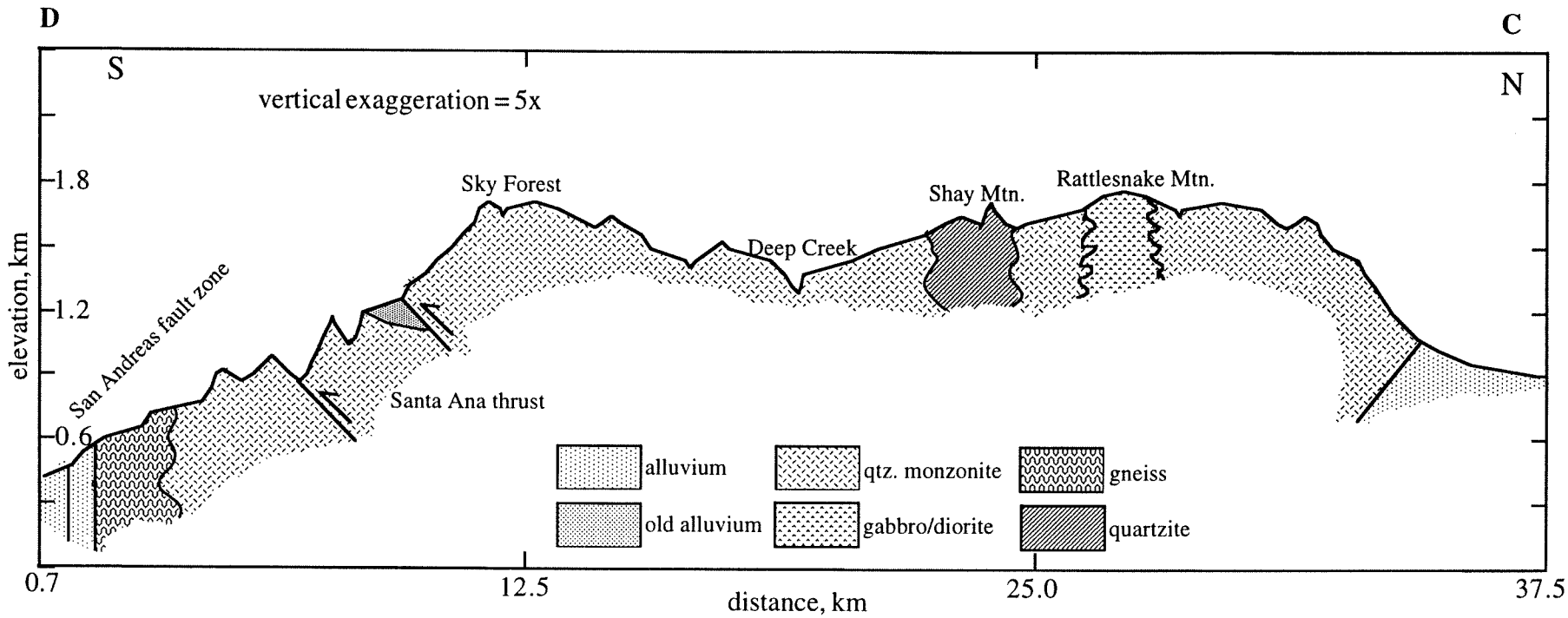

Figure 27c: Elevation profile from San Bernardino to Fifteenmile Valley (Figure 1), showing the bedrock type and major faults (from Bortugno and Spittler, 1986). This shows the difference in relative elevation of outcrops for different bedrock types. Note that the non-granitic rocks generally outcrop at greater relative elevation.

Table 3:

Surface area by lithology in the entire San Bernardino Mountains: based on a point count using the 1:62,500 geologic maps (Dibblee, 1964a, 1964b, 1967a, 1967b, 1968, 1971) and a 1 km grid, with a total of 2557 points counted.

	% area
hornblende quartz monzonite	1.4%
limestone	3.4%
gneiss, schist, pelite	20.2%
quartzite	5.2%
diorite	2.9%
monzonite, granite, granodiorite	46.3%
Tertiary/Quaternary units	20.6%

Surface area and average elevation by lithology on the Big Bear plateau: based on visual estimate of average elevation in 0.25 km^2 cubes of different rock type using 1:62,500 scale maps with 80' contour intervals. The total number of cubes for each rock type was tabulated and the average elevation for each rock type was found. The total number of cubes used = 2,243.3.

	% area	avg. elev.
hornblende quartz monzonite	4.53%	7084' (2159 m)
limestone	4.80%	7557' (2303 m)
gneiss, schist, pelite	4.65%	6956' (2120 m)
quartzite	11.91%	7194' (2193 m)
diorite	3.45%	6154' (1876 m)
monzonite, granite, granodiorite	70.66%	5816' (1773 m)

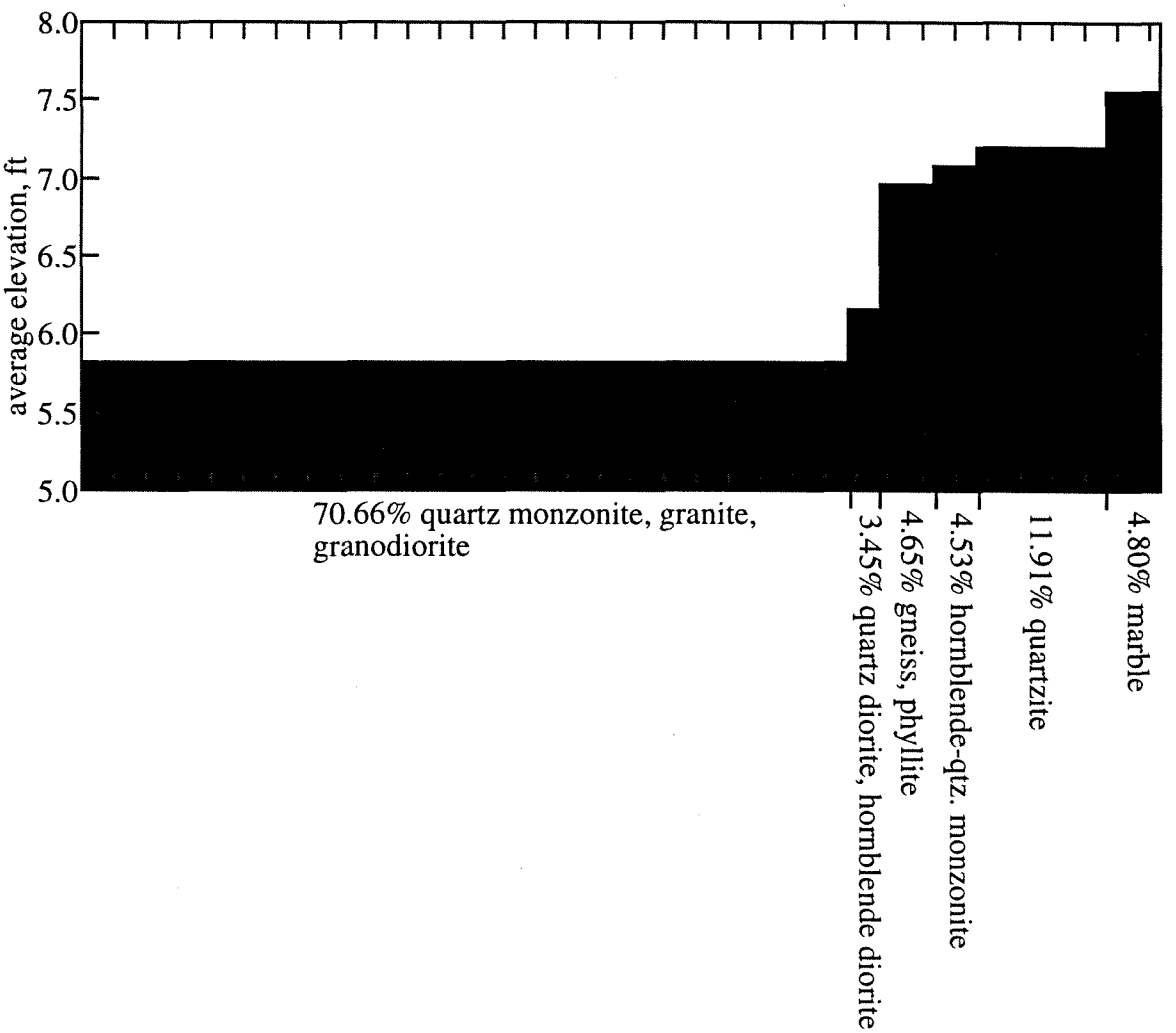

Figure 28: Plot of the average elevation and percentage of surface area of the main bedrock types atop the Big Bear plateau. This plot covers the entire area of that plateau that is relatively flat (approximately the area defined as the BB block in Figure 2c), and thus excludes the northern and southern escarpments and incised canyons. It also excludes regions that are overlain by lakes or unlithified sediments. Note that the non-granitic rocks have much higher average elevations than the quartz monzonite, granite, and granodiorite.

This plot was made using bedrock and elevation data from 1:62500 scale topographic (80 ft. contour) and geologic (Dibblee, 1964a, 1964b, 1967a, 1967b, 1971, 1968) maps. A grid with 0.25 km^2 cells was lain over these maps and the average elevations of small areas (<0.25 km^2) of a given bedrock type was estimated (probably accurate to within 1 contour). The average elevation was multiplied by the percentage of the cell covered by that rocktype. For each rocktype, these values were totalled for the whole plateau and divided by the total number of cells of that rocktype to get the average elevation of that rocktype. The total number of cells tabulated was 2243.3, corresponding to an area of 561 km^2.

Much of the relief of the surface was thus created by differential weathering (etching), the magnitude of which seems have required a prolonged duration of weathering. Note that non-granitic lithologies still have low relief, indicating that prolonged peneplanation (erosion) also took place during its formation.

The weathered surface is thus best developed on quartz monzonite and other granitic lithologies. Granitic rocks of the plateau consist of a large Mesozoic batholith made up of smaller plutons that vary locally in composition, such as the Rattlesnake Mt. Pluton (MacColl, 1964) or the hornblende quartz monzonite of Delamar Mountain (Dibblee, 1964a). Quartz monzonite is generally homogenous at the outcrop scale, however, and is typically coarse (2-5 mm diameter grains) and contains 15-25% quartz, 35-45% orthoclase, 30-40% plagioclase, and 0-10% biotite. Some common features to this granitic rock include aplite dikes, quartz veins, and lack of strong fabric.

3.6.5.1 Analysis of the products of deep weathering: Soil horizons

The soil horizons that mantle the thick weathered profile in rare locations across the Big Bear plateau represent the most decomposed products of the deeply weathered granite. The soils and underlying saprolite display no evidence of having experienced sedimentary transport (with the exception of A-horizons), and thus formed in situ as bedrock decayed. Because their nature holds significant clues as to how the weathered horizon has evolved, soil profiles were observed at 5 locations atop the plateau and 2 locations in the Santa Ana Valley (SP1-7; Figure 1a, 29). In addition to the basic field observations of these soils (see Section 3.6.2.3), soils were sampled and analyzed (see Section 3.6.5.2-6, Table 4).

Thin (~25 cm) A-horizons cap most soils, but are not present where sediments (such as Santa Ana Sandstone) overlie deeply weathered granite (e.g., SP6, SP7; Figure 1a). These consist of grayish-brown loam and are rich in organic matter derived from the forest floor above (e.g., SP1, SP3; Figure 27a/b). A-horizons are typically poorly sorted and often contain large (~15 cm), unrounded clasts of various composition. The contacts

Figure 29a: Photographs and descriptive diagrams of soil profiles in the San Bernardino Mountains. Figure 1 shows locations. Table 3 lists samples taken from each profile.

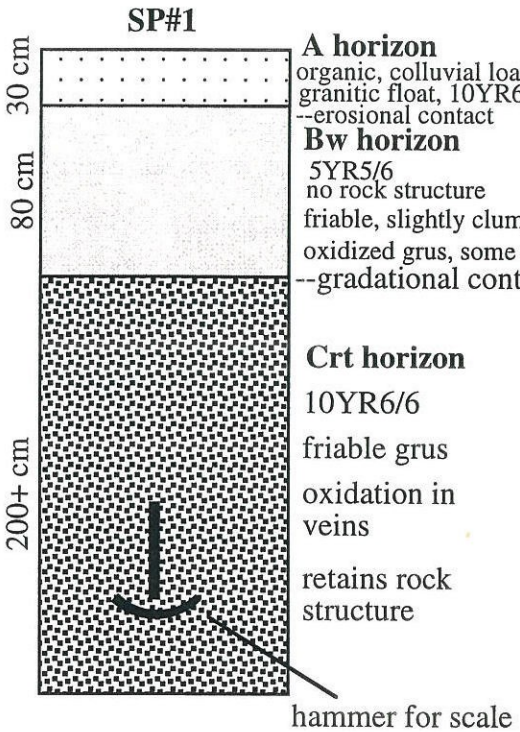

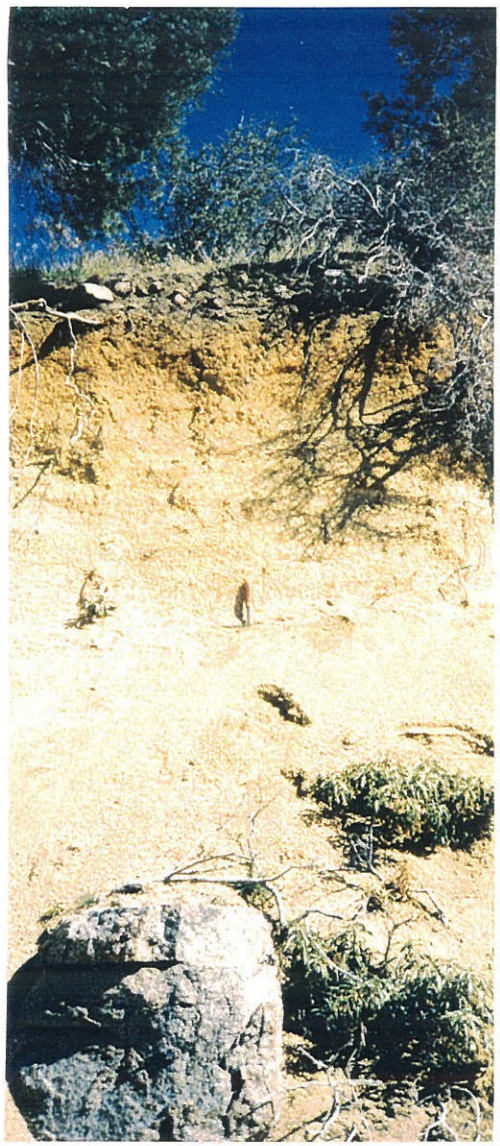

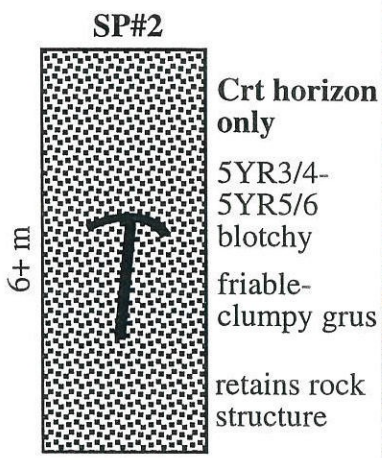

Figure 29b: cont.

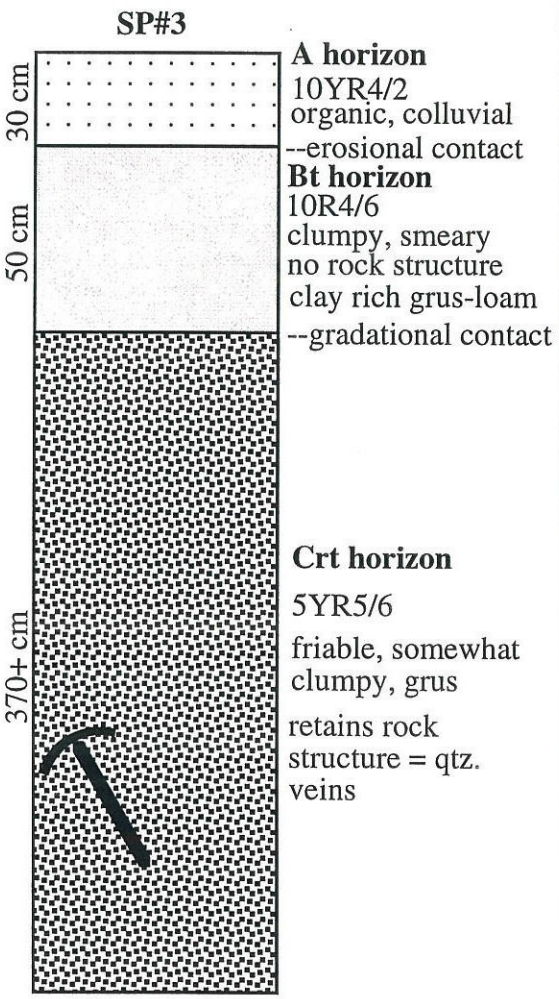

Figure 29c: cont.

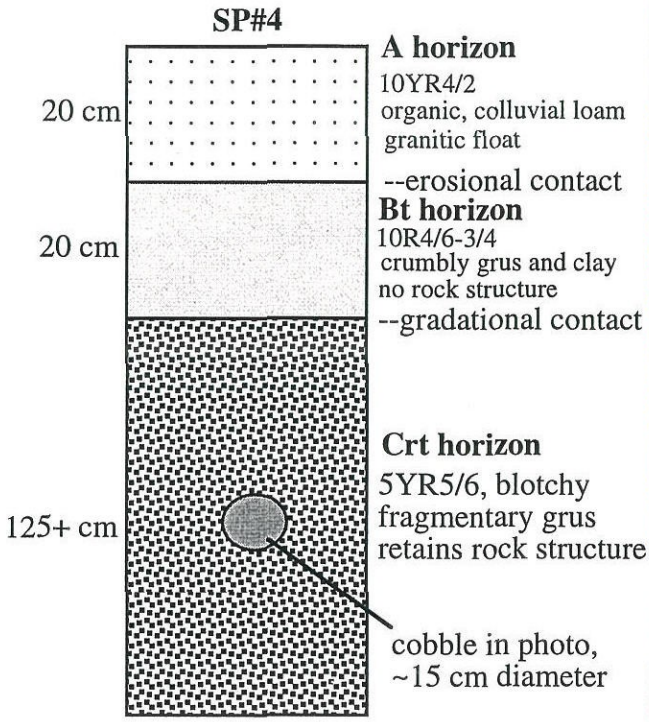

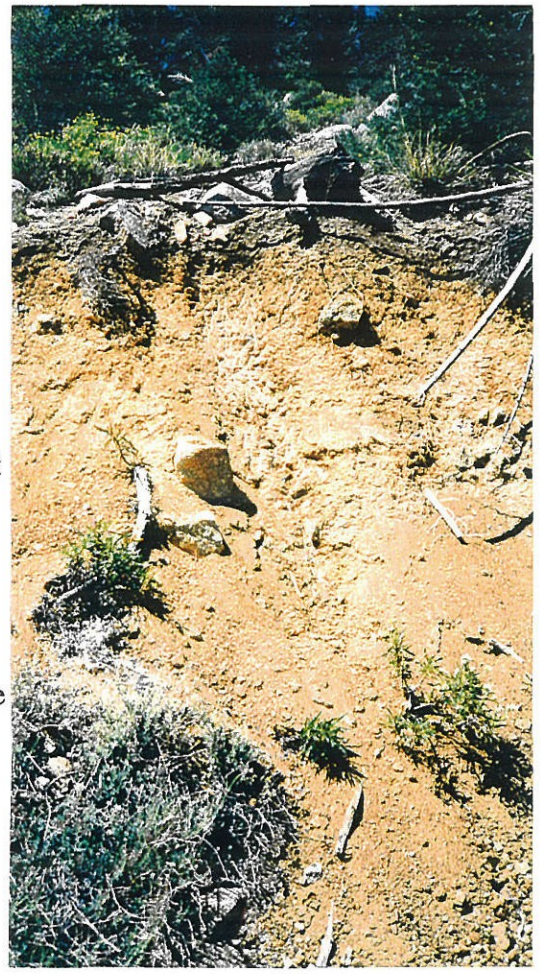

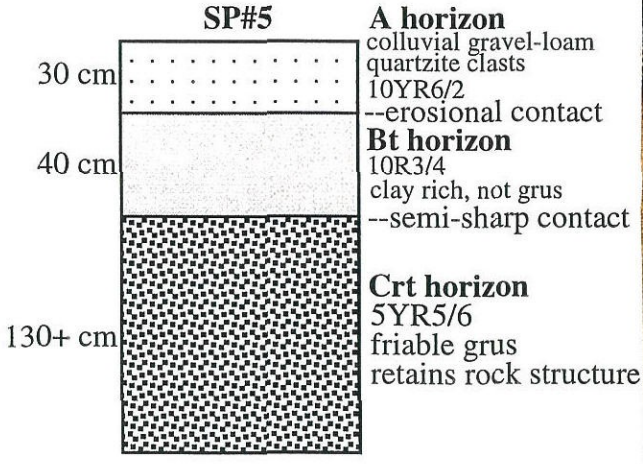

Figure 29d: cont.

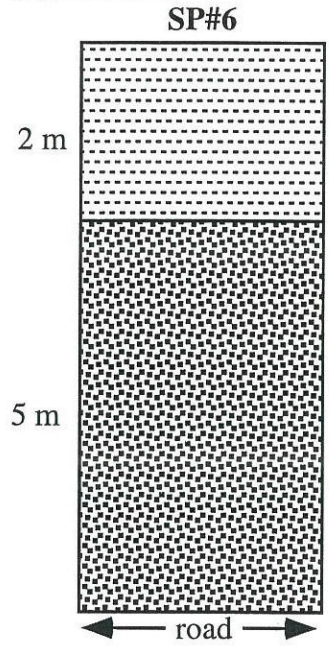

Qof
old fanglomerate (Jacobs, 1982) poorly sorted, large granite and gneiss clasts

--sharp erosional contact

Crt horizon
10R4/6-10R3/4
friable, loose grus, banded, blotchy
no bedrock structure

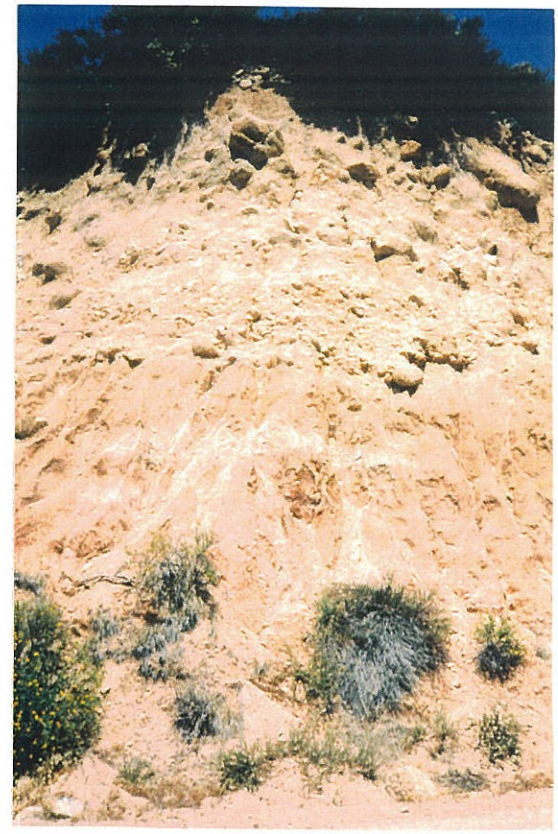

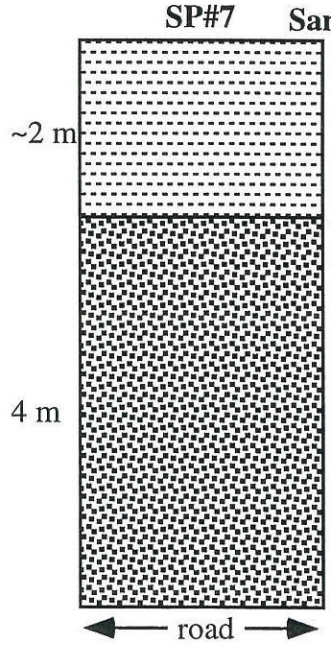

Santa Ana Sandstone
(Jacobs, 1982) white, friable consolidated sandstone, capped by poorly sorted fanglomerate.

--sharp erosional contact

Crt horizon
10YR5/4-5YR5/6
friable, loose grus, banded, blotchy
no bedrock structure

Table 4: Soil samples from locations on the weathered surface (Figure 1a). Samples were taken from the middle of the respective horizon. Although soil profiles are often made using multiple samples from every 10 or 20 cm of soil, this study was limited to one sample per thin horizon. Samples were typically more than several hundred grams in mass. Grainsize analyses (Table 5), color analyses (Table 6), and other characterizations (see text) were performed on these samples.

SP1 (116.986° x 34.295°, roadcut on 3N14 = Coxey Road):
SP1a = A horizon
SP1b = B horizon
SP1c = C horizon

SP2 (117.199° x 34.309°, roadcut on Rt. 173):
SP2c = C horizon

SP3 (117.186° x 34.279°, roadcut on Rt. 173):
SP3a = A horizon
SP3b = B horizon
SP3c = C horizon

SP4 (117.041° x 34.316°, roadcut on 3N14):
SP4a = A horizon
SP4b = B horizon
SP4c = C horizon

SP5 (117.065° x 34.345°, roadcut on 3N14, beneath a quartzite-bearing gravel):
SP5b = B horizon
SP5c = C horizon

SP6 (117.003° x 34.166°) and SP7 (116.969° x 34.170°) (roadcuts on 1N09, Santa Ana Valley beneath the Santa Ana sandstone; Jacobs, 1982):
SP6c = C horizon
SP6c1 = C horizon
SP6c2 = C horizon
SP7c = C horizon

between A- and B-horizons are sharp, and in one location (SP3), a clump of lower Bt-horizon was even entrained within an A-horizon. This suggests A-horizons form, at least in part, by reworking/erosion of local decayed rock and biogenic material. Bioturbation and soil creep may play significant roles in the formation of these colluvial horizons. A-horizons also retain roughly constant thickness over gentle rolling hills and troughs, suggesting they are actively forming on the present-day topography.

B-horizons are more variable by location than A-horizons. These vary in thickness from 20 to 80 cm and vary from loamy, to clay-rich, to grus-rich accumulations. They are typically orange-brown to red in color and are often sticky or clumpy, suggesting they are an accumulation horizon for clay (Bt-horizons) and sesquioxides (SP3; Figure 29b). In some locations, however, the B-horizon is reddish despite little accumulation of clay (Bw-horizons, SP1; Figure 29a). B-horizons often have the appearance and texture of granitic grus, indicating they formed directly from the decaying rock. However, they contain no actual rock structure, such as quartz veins or joint patterns, which are common in underlying C-horizons (Figure 23). This suggests that they are the most decomposed section of the weathered profile.

B-horizons pinch and swell in an irregular pattern that does not parallel topography in several locations (SP1, SP3). This suggests that erosive modification has outpaced or outdated their formation. The character of these horizons also varies from location, such as between the more developed (Bt) and less developed (Bw) (see Section 3.6.5.2-6). As shown schematically in Figure 23, the character of C-horizons (described below) also varies, such that different locations appear to match with different positions within the idealized weathered profile. However, some of the apparently lower exposures (SP1, SP4; Figure 23) possess weak B-horizons (Figure 29a/c). This suggests that they have experienced erosion of overlying, more weathered material, and subsequently resumed weathering so as to redevelop partial B-horizons. This further implies that the B-horizons do not represent a unique, contemporaneous marker horizon across the SBMs.

The most developed Bt-horizon occurs at SP5 (Figure 1a), which is buried by a distinctive, thin (30 cm), quartzite-bearing deposit (Figure 29c). This Bt-horizon, although thin, is far more weathered than any other soil found in the SBMs, based on clay content, color, bulk density, and mineralogy (see Sections 3.6.5.2-5). The gravelly deposit atop it consists of a loamy, tan matrix that is similar to A-horizons elsewhere, except for its prevalence of medium-sized (5-10 cm), pinkish quartzite clasts (Figure 29c). Because these clasts are semi-angular to semi-rounded, bedding is absent, and the matrix is not well sorted, this gravel does not appear to be an alluvial apron. However, the deposit is continuous over the area and had to have been transported from the nearest quartzite bedrock, some distance away (Figure 9a). Thus, this gravel may represent a debris-flow, which eroded away the A-horizon and some of the B-horizon prior to deposition. Although this deposit is not very similar to the ancient quartzite-bearing gravels elsewhere (Sadler and Reeder, 1983; P.M. Sadler, pers. comm.), it is of unknown age and may thus be of some antiquity. If so, its well-developed character may represent the deepest weathering attained atop the upland surface and indicate erosion of a once more extensive soil mantle.

C-horizons represent the thick accumulation of regolith that overlies the zone of corestones in the weathered profile (Figure 23). The boundary between B- and Crt-horizons is gradational. Crt-horizons consist of in situ, decayed grus that retain rock structures and contain only minor amounts of clay and oxides (Figure 29). Most of the clay and oxides in Crt-horizons is accumulated within fractures and between grains. Although they retain an interlocking grain texture like their parent granitic rock, Crt-horizons are extremely fragile and crumble at the slightest touch. This loose regolith is much thicker than overlying A- and B-horizons, and typically continues below their several-meter-thick road-cut exposures (Figure 29a). Evidence of pedogenesis in these decreases gradually downwards, as Crt-horizons grade into C-R-horizons, losing their redness and become more coherent with depth (Figure 23).

In several locations, C-horizons are not overlain by A- or B-horizons and show evidence of having been eroded. At SP2 (Figure 1a, 29a), for example, a mottled, deeply weathered saprolite (Crt-horizon) occurs as a 6-m thick outcrop without a proper soil cover. The saprolites buried by the Mio-Pliocene Santa Ana Sandstone and Pleistocene fanglomerates to the south of the plateau (SP6, SP7; Figure 1a) similarly consist only of Crt-horizons (Figure 29d). These are made up of deeply decayed grus and display erosional contacts with the overlying sediments. This suggests that upper soil horizons, which may have existed previously, were stripped off prior to deposition. In addition, these regolith accumulations in the Santa Ana Valley show sub-horizontal banding (~20 cm thickness) of pinkish and whitish colors and contain no real rock structures (such as veins). Although these features are reminiscent of sedimentary reworking and bedding, it is not certain whether this regolith has been transported.

3.6.5.2 Analysis of the products of deep weathering: Grainsize distribution of soils

The grainsize distribution of soils derived from the same parent rock qualitatively represents the degree to which rock has decomposed into saprolite. The average grainsize of fresh quartz monzonite in the SBMs is typically ~2-5 mm diameter grains (quartz and feldspar). As individual mineral species breakdown during weathering, however, the grainsize distribution of the rock fines. The grainsize distributions of ~100-g soil samples from the SBMs were measured to characterize their degree of weathering. These were measured to the nearest Ø, using dry sieving (62 μm - >4 mm fraction) and pipette analysis (<62 μm fraction) (Lewis and McConchie, 1994) (Table 5).

B- and C-horizons from different locations have consistently similar grainsize variations. The average distribution of B-horizons is 21.4% clay, 11.7% silt, 50.7% sand, and 16.3% granules, whereas for C-horizons the average distribution is 3.4% clay, 9.7% silt, 63.0% sand, 23.8% granules (Table 4, 5; Figure 30). B-horizons thus show considerably greater fines content. The silt-to-clay ratio of the average B-horizon is 0.55,

Table 5: Grainsize distribution (in 1-Ø divisions) of samples from soil profiles along the weathered surface of the San Bernardino Mountains.

SP5c (99.744g, mass %)
>4mm (> -2Ø) = 12.46
2-4 mm = 12.09
1-2 mm = 11.67
0.5-1 mm = 13.97
250-500 µm = 14.88
125-250 µm = 11.14
62.5-125 µm = 7.16
31.3-62.5 µm (5-4Ø) = 5.72
15.6-31.3 µm = 0.23
7.8-15.6 µm = 2.25
3.9-7.8 µm = 2.08
1.95-3.9 µm = 1.85
1-1.95 µm = 1.46
<1 µm (< 10Ø) = 3.03
clay (<3.9 µm) = **6.34%** (8.40)
silt (3.9-62.5 µm) = **10.28%** (13.63)
sand (0.0625-2 mm) = **58.82%** (77.97)
granules (>2 mm) = **24.55%**

SP4c (136.280g, mass %)
>4mm (> -2Ø) = 14.69
2-4 mm = 14.16
1-2 mm = 17.66
0.5-1 mm = 13.15
250-500 µm = 11.00
125-250 µm = 9.17
62.5-125 µm = 6.62
31.3-62.5 µm (5-4Ø) = 4.95
15.6-31.3 µm = 0.57
7.8-15.6 µm = 1.96
3.9-7.8 µm = 1.59
1.95-3.9 µm = 0.90
1-1.95 µm = 0.45
<1 µm (< 10Ø) = 3.14
clay (<3.9 µm) = **4.49%** (6.31)
silt (3.9-62.5 µm) = **9.07%** (12.75)
sand (0.0625-2 mm) = **57.60%** (80.94)
granules (>2 mm) = **28.85%**

SP5b (49.212g, mass %)
>4mm (> -2Ø) = 0.62
2-4 mm = 0.67
1-2 mm = 8.25
0.5-1 mm = 7.59
250-500 µm = 7.96
125-250 µm = 7.35
62.5-125 µm = 6.13
31.3-62.5 µm (5-4Ø) = 6.83
15.6-31.3 µm = 0.64
7.8-15.6 µm = 3.63
3.9-7.8 µm = 2.99
1.95-3.9 µm = 2.24
1-1.95 µm = 1.92
<1 µm (< 10Ø) = 43.19
clay (<3.9 µm) = **47.35%** (47.96)
silt (3.9-62.5 µm) = **14.09%** (14.27)
sand (0.0625-2 mm) = **37.28%** (37.76)
granules (>2 mm) = **1.29%**

SP3b (63.458g, mass %)
>4mm (> -2Ø) = 8.55
2-4 mm = 9.87
1-2 mm = 13.25
0.5-1 mm = 11.01

SP4b (116.808g, mass %)
>4mm (> -2Ø) = 11.13
2-4 mm = 10.15
1-2 mm = 15.14
0.5-1 mm = 13.48
250-500 µm = 11.84
125-250 µm = 9.28
62.5-125 µm = 6.13
31.3-62.5 µm (5-4Ø) = 4.25
15.6-31.3 µm = 0.75
7.8-15.6 µm = 1.90
3.9-7.8 µm = 1.37
1.95-3.9 µm = 1.94
1-1.95 µm = 1.59
<1 µm (< 10Ø) = 11.04
clay (<3.9 µm) = **14.57%** (18.51)
silt (3.9-62.5 µm) = **8.27%** (10.51)
sand (0.06-2mm) = **55.87%** (70.98)
granules (>2 mm) = **21.28%**

SP1b (71.682g, mass %)
>4mm (> -2Ø) = 4.27
2-4 mm = 19.88
1-2 mm = 19.25
0.5-1 mm = 11.28
250-500 µm = 11.16
125-250 µm = 11.21
62.5-125 µm = 6.48
31.3-62.5 µm (5-4Ø) = 3.96
15.6-31.3 µm = 1.20
7.8-15.6 µm = 2.10
3.9-7.8 µm = 1.42
1.95-3.9 µm = 1.20
1-1.95 µm = 1.05
<1 µm (< 10Ø) = 5.54
clay (<3.9 µm) = **7.79%** (10.27)
silt (3.9-62.5 µm) = **8.68%** (11.44)
sand (0.0625-2 mm) = **59.38%** (78.29)
granules (>2 mm) = **24.15%**

SP7c (99.985g, mass %)
>4mm (> -2Ø) = 1.62
2-4 mm = 11.71
1-2 mm = 24.35
0.5-1 mm = 22.74
250-500 µm = 16.84
125-250 µm = 10.30
62.5-125 µm = 5.77
31.3-62.5 µm (5-4Ø) = 3.17
15.6-31.3 µm = 0.94
7.8-15.6 µm = 1.13
3.9-7.8 µm = 0.53
1.95-3.9 µm = 0.06
1-1.95 µm = 0.71
<1 µm (< 10Ø) = 0.12
clay (<3.9 µm) = **0.89%** (1.03)
silt (3.9-62.5 µm) = **5.77%** (6.66)
sand (0.06-2mm) = **80.0%** (92.31)
granules (>2 mm) = **13.33%**

SP6c (130.655g, mass %)
>4mm (> -2Ø) = 12.78
2-4 mm = 25.08
1-2 mm = 17.88
0.5-1 mm = 10.44

SP6c1 (149.502g, mass %)
>4mm (> -2Ø) = 4.53
2-4 mm = 14.24
1-2 mm = 15.26
0.5-1 mm = 10.61
250-500 µm = 9.92
125-250 µm = 8.80
62.5-125 µm = 8.34
31.3-62.5 µm (5-4Ø) = 10.90
15.6-31.3 µm = 2.14
7.8-15.6 µm = 4.82
3.9-7.8 µm = 3.41
1.95-3.9 µm = 2.18
1-1.95 µm = 1.31
<1 µm (< 10Ø) = 3.55
clay (<3.9 µm) = **7.04%** (8.67)
silt (3.9-62 µm) = **21.27%** (26.18)
sand (0.06-2mm) = **52.93%** (65.15)
granules (>2 mm) = **18.77%**

SP3c (99.707g, mass %)
>4mm (> -2Ø) = 12.35
2-4 mm = 12.85
1-2 mm = 14.30
0.5-1 mm = 12.75
250-500 µm = 12.93
125-250 µm = 12.97
62.5-125 µm = 9.50
31.3-62.5 µm (5-4Ø) = 6.06
15.6-31.3 µm = 1.18
7.8-15.6 µm = 1.52
3.9-7.8 µm = 0.90
1.95-3.9 µm = 0.56\
1-1.95 µm = 0.22
<1 µm (< 10Ø) = 1.91
clay (<3.9 µm) = **2.69%** (3.60)
silt (3.9-62.5 µm) = **9.66%** (12.91)
sand (0.06-2mm) = **62.45%** (83.49)
granules (>2 mm) = **25.20%**

SP1c (98.858g, mass %)
>4mm (> -2Ø) = 12.07
2-4 mm = 27.76
1-2 mm = 20.50
0.5-1 mm = 13.65
250-500 µm = 10.91
125-250 µm = 6.50
62.5-125 µm = 3.29
31.3-62.5 µm (5-4Ø) = 1.72
15.6-31.3 µm = 0.80
7.8-15.6 µm = 0.64
3.9-7.8 µm = 0.38
1.95-3.9 µm = 0.0
1-1.95 µm = 0.38
<1 µm (< 10Ø) = 1.40
clay (<3.9 µm) = **1.78%** (2.96)
silt (3.9-62.5 µm) = **3.54%** (5.88)
sand (0.06-2mm) = **54.85%** (91.16)
granules (>2 mm) = **39.83%**

SP1a (66.740g, mass %)
>4mm (> -2Ø) = 8.24
2-4 mm = 10.27
1-2 mm = 14.19
0.5-1 mm = 11.56

250-500 µm = 9.18
125-250 µm = 8.59
62.5-125 µm = 8.13
31.3-62.5 µm (5-4Ø) = 6.53
15.6-31.3 µm = 3.39
7.8-15.6 µm = 3.56
3.9-7.8 µm = 2.23
1.95-3.9 µm = 1.57
1-1.95 µm = 1.08
<1 µm (< 10Ø) = 13.07
clay (<3.9 µm) = **15.72%** (19.27)
silt (3.9-62.5 µm) = **15.71%** (19.25)
sand (0.0625-2 mm) = **50.16%** (61.48)
granules (>2 mm) = **18.42%**

SP2c (47.464g, mass %)
>4mm (> -2Ø) = 0.53
2-4 mm = 5.88
1-2 mm = 31.01
0.5-1 mm = 30.40
250-500 µm = 17.79
125-250 µm = 8.47
62.5-125 µm = 3.50
31.3-62.5 µm (5-4Ø) = 1.37
15.6-31.3 µm = 0.38
7.8-15.6 µm = 0.50
3.9-7.8 µm = 0.13
1.95-3.9 µm = 0
1-1.95 µm = 0
<1 µm (< 10Ø) = 0
clay (<3.9 µm) = **0** (0)
silt (3.9-62.5 µm) = **2.38%** (2.54)
sand (0.0625-2 mm) = **91.17%** (97.46)
granules (>2 mm) = **6.41%**

250-500 µm = 9.02
125-250 µm = 7.51
62.5-125 µm = 5.58
31.3-62.5 µm (5-4Ø) = 4.30
15.6-31.3 µm = 1.18
7.8-15.6 µm = 1.88
3.9-7.8 µm = 1.71
1.95-3.9 µm = 0.39
1-1.95 µm = 0.53
<1 µm (< 10Ø) = 1.71
clay (<3.9 µm) = **2.63%** (4.23)
silt (3.9-62.5 µm) = **9.07%** (14.60)
sand (0.0625-2 mm) = **50.43%** (81.17)
granules (>2 mm) = **37.86%**

SP6c2 (127.267g, mass %)
>4mm (> -2Ø) = 4.93
2-4 mm = 14.61
1-2 mm = 16.85
0.5-1 mm = 12.11
250-500 µm = 12.12
125-250 µm = 10.01
62.5-125 µm = 7.92
31.3-62.5 µm (5-4Ø) = 11.24
15.6-31.3 µm = 0.35
7.8-15.6 µm = 2.52
3.9-7.8 µm = 2.30
1.95-3.9 µm = 1.82
1-1.95 µm = 1.04
<1 µm (< 10Ø) = 2.17
clay (<3.9 µm) = **5.03%** (6.25)
silt (3.9-62.5 µm) = **16.41%** (20.4)
sand (0.06-2mm) = **59.01%** (73.35)
granules (>2 mm) = **19.54%**

250-500 µm = 13.16
125-250 µm = 14.64
62.5-125 µm = 10.32
31.3-62.5 µm (5-4Ø) = 5.34
15.6-31.3 µm = 0.90
7.8-15.6 µm = 2.70
3.9-7.8 µm = 3.03
1.95-3.9 µm = 2.05
1-1.95 µm = 1.72
<1 µm (< 10Ø) = 1.88
clay (<3.9 µm) = **5.65%** (6.93)
silt (3.9-62.5µm) = **11.97%** (14.69)
sand (0.06-2mm) = **63.87%** (78.38)
granules (>2 mm) = **18.51%**

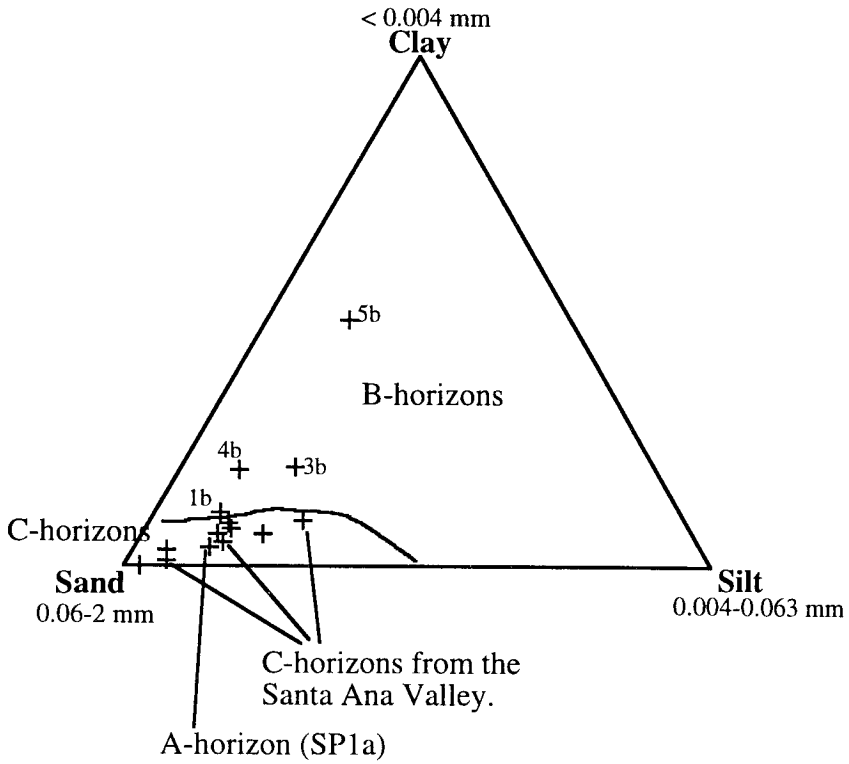

Figure 30: Ternary plot of grainsize distributions of soils of the SBMs. C horizons include both Big Bear plateau and Santa Ana Valley (from under the Santa Ana Sandstone) weathered surface samples. See Table 5 for data.

or about 5 times less than the 2.9 average ratio for C-horizons. This agrees with field observations that show B-horizons are deeply weathered accumulation zones and C-horizons are only partially decayed grus accumulations that retain rock structures.

Plots of the soils' cumulative grainsize distribution illustrate this same difference between B- and C-horizons. C-horizons show very similar distributions that rapidly decrease in weight-percent with decreasing grainsize (Figure 31a). The least-weathered, most rock-like C-horizon (SP2) has the steepest decrease in weight-percent with fining grainsize, whereas decrease in grainsize of C-horizons from under the Santa Ana Sandstone (SP6) are much more gradual. B-horizons vary more by location and have more gradual decreases in weight-percent with decreasing grainsize (Figure 31b). The most deeply weathered B-horizon (SP5), which is buried by a possible pre-uplift gravel (see Section 3.6.5.1), shows the most gradual, fine-grained distribution. Cumulative distributions of the average B- and C-horizon also show the magnitude of their textural differences (Figure 31c). The only measured grainsize distribution of an A-horizon is much more irregular than the smooth distributions of B- and C-horizons (Figure 31d), consistent with its poorly sorted, colluvial nature.

3.6.5.3 Analysis of the products of deep weathering: Bulk density of soils

Bulk density is another qualitative measure of the degree of rock weathering, which decreases as rocks decompose (cf. Birkeland, 1984, p.17). Bulk densities of soils from the SBMs were measured on samples sealed with Saran wrap using a $\pm$0.001 g scale and a $\pm$0.5 mL graduated cylinder. The results are correlated by soil horizon, with B-horizons averaging 1.24 g/cm^3 (most weathered), C-horizons averaging 1.57 g/cm^3 (intermediate), and semi-weathered San Gorgonio block samples averaging 2.03 g/cm^3 (least weathered) (Figure 32). In contrast, fresh granitic rock has a bulk density of about 2.7 g/cm^3. This is consistent with previous observations of degree of weathering.

Figure 31a: Cumulative grainsize plot of C-horizon soil samples from the San Bernardino Mountains. Includes 4 samples from the Santa Ana Valley. Refer to Table 3 for soil sample key and Figure 1 for location of soil samples.

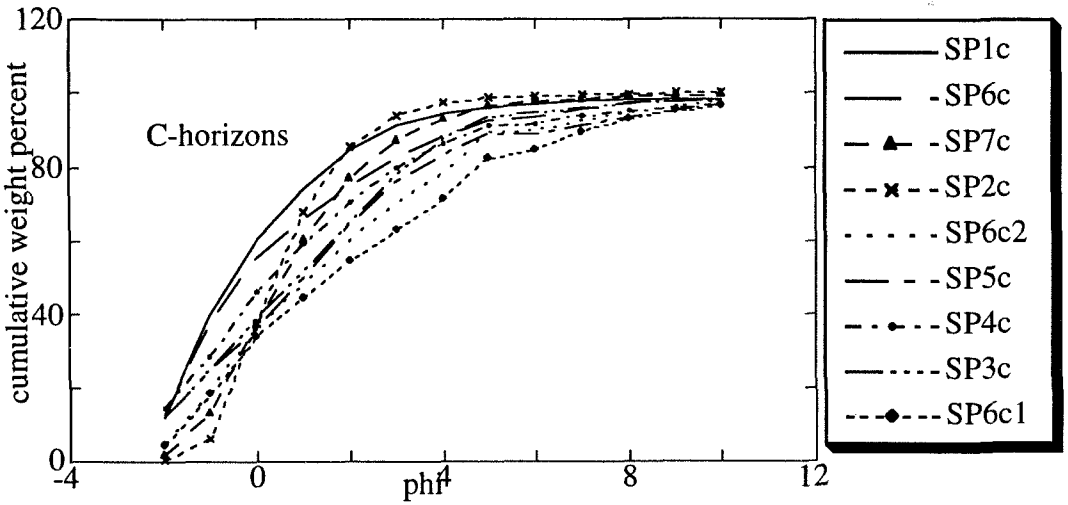

Figure 31b: Cumulative grainsize plot of B-horizon soil samples from the San Bernardino Mountains.

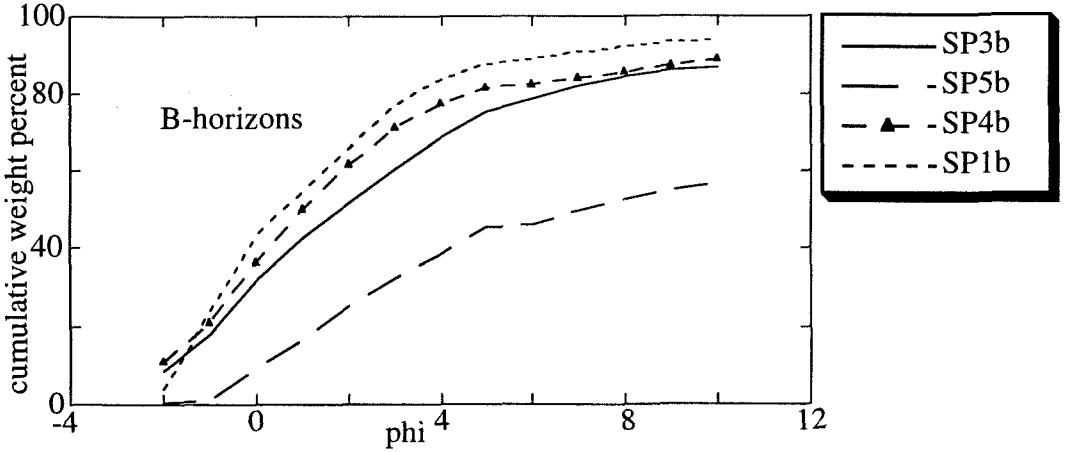

Figure 31c: Cumulative grainsize plot of the average B and C horizon soil samples from the San Bernardino Mountains.

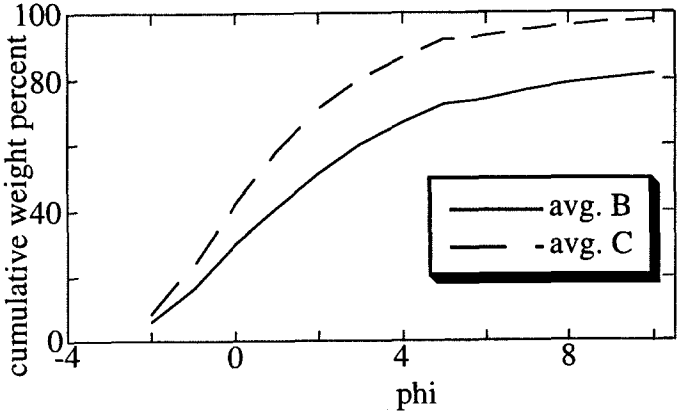

Figure 31d: Cumulative grainsize plot of one A-horizon soil sample from the San Bernardino Mountains (SP1a).

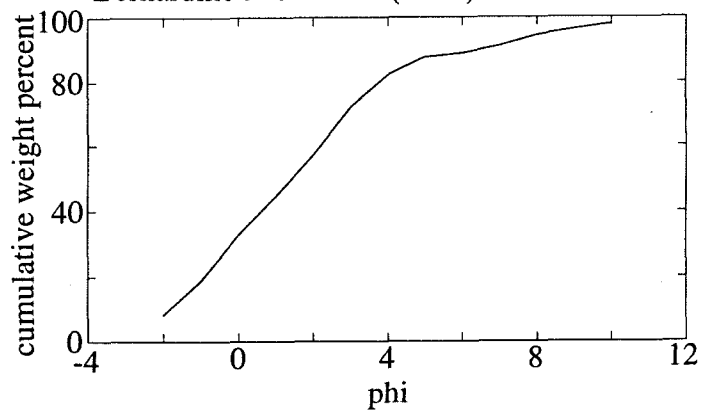

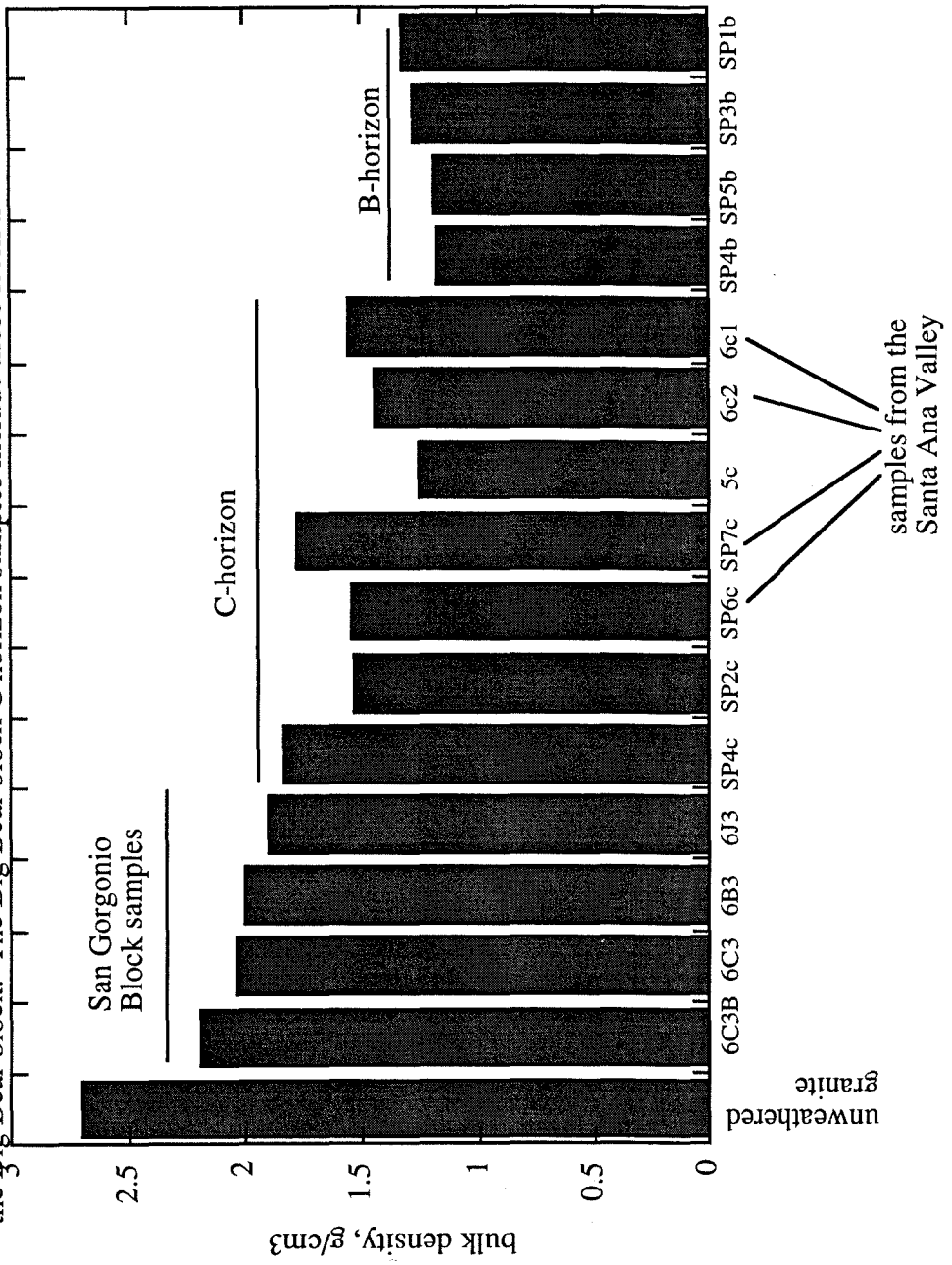

Figure 32: Plot of bulk density of soil samples from the San Bernardino Mountains. Note that the most dense samples are from unweathered rock and C horizons, whereas the lowest densities occur for B horizon samples. Note also that the San Gorgonio block samples (from Rt. 38, not Manzanita Springs) are high, suggesting they are significantly less weathered than samples from the Big Bear block. The Big Bear block C horizon samples include those from the Santa Ana Valley.

3.6.5.4 Analysis of the products of deep weathering: Mineralogy of soils

Because chemical weathering affects different minerals at different rates, it is useful to examine the mineralogic composition of soil particles to learn about the degree of weathering in a saprolite. The quartz monzonite parent rock of these soils consists of a simple collection of major minerals, including quartz, orthoclase, plagioclase, alternate biotite, and alternate hornblende (listed in increasing order of weatherability; Birkeland, 1984). The condition of these minerals in each loose soil samples sorted by grainsize (not thin section, so soil structures and ephemeral features were not examined) was documented with moderate-power microscopy. A schematic representation of the variability of weathering by soil horizon is shown in Figure 33.

Colluvial A-horizons show the least degree of weathering or pedogenesis. They typically contain unaltered, weatherable minerals (biotite and hornblende), as well as a high content of organic matter and charcoal. Although much less weathered, A-horizons are similar in composition to underlying B- and C-horizons at a given location. For example, these three horizons commonly share the presence of accessory minerals, such as magnetite, or the average size of primary quartz grains. This suggests A-horizons are derived locally from a similar parent rock, although they represent reworked colluvium.

Individual minerals of C-horizons are more weathered than A-horizons, yet their overall composition and texture still gives an appearance similar to little-decomposed, disaggregated monzonite. Coarse grains ($\geq$0.5 mm) in C-horizons are usually polymineralic and have original crystal shape or fractured surfaces, whereas finer grains ($\leq$0.5 mm) are monomineralic. The biotite in C-horizons is generally not coarser than ~0.5 mm and is typically flaky and fragile. Hornblende is similarly altered, but is also etched and present at coarser grainsizes. In several locations (SP4, SP3), however, pockets of less-weathered, hornblende-rich monzonite are present within decomposed C-horizons, suggesting that hornblende can also make rock more resistant (Section 3.6.4; Figure 28). Coarse ($\geq$0.5 mm) plagioclase is etched in C-horizons and disintegrates to white powder

Figure 33: Schematic diagram showing the relative stages of mineral weathering and decay in quartz monzonite from the weathered granitic surface of the San Bernardino Mountains, based on petrographic observations of soil samples. Stages of weathering proceed from left to right.

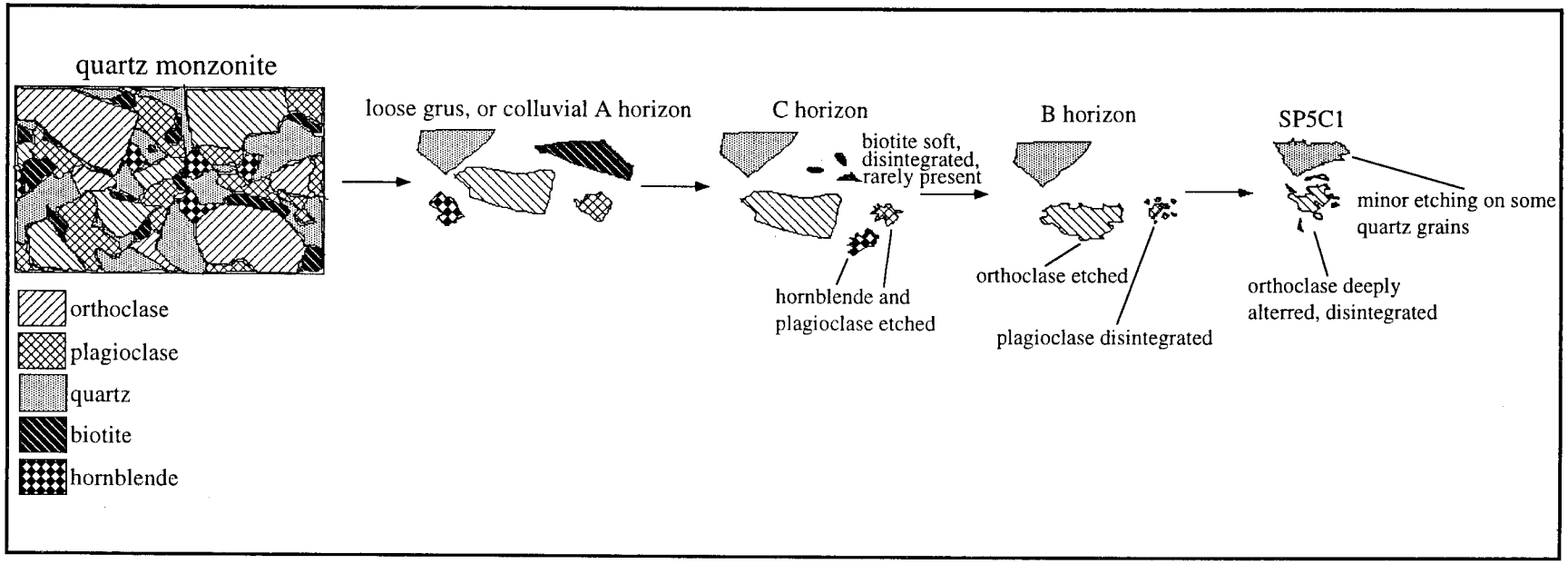

when touched, whereas orthoclase is only slightly decomposed and retains its mechanical integrity. At finer grainsizes (≤0.5 mm), there is enrichment of orthoclase relative to plagioclase and enrichment of quartz relative to both feldspars, which are more etched and rounded. Quartz of all grainsizes is unweathered and shows no etching, but quartz surfaces and fractures are often coated with red sesquioxides.

B-horizons show the greatest degree of mineralogic decay and alteration. Biotite and hornblende are generally absent from B-horizon samples, although fine (≤0.5 mm), soft, smeary biotite and slightly altered hornblende are occasionally present. The fine-grained hornblende probably survives, because it occurs embedded in polymineralic quartz grains, from which it fractures out only after quartz begins to decay. Quartz remains generally unweathered in B-horizons, however, although it is enriched relative to all other minerals and is more often stained red than in C-horizons. At locations SP5 and SP6, slight etching of quartz grains was apparent, although the cause of this is not known because grains were not examined under SEM. Plagioclase is highly etched, fragile, and somewhat rare relative to orthoclase, which is generally bleached, etched, and sometimes soft and crushable. The most deeply weathered B-horizon (SP5) shows an even greater degree of mineralogic decay. Quartz in this sample makes up most of the larger grains (≥0.5 mm) and is the only mineral present at fine grain sizes (≤0.5 mm), and orthoclase is the only other common mineral (although deeply etched, dissolved-looking, and with pink, flaky rinds).

Note that clay mineralogy analyses were not completed in this study, because Caltech's X-ray diffractometer was not functioning. Time did not permit another apparatus to be found, although clay analyses of soils may be completed in the future. Clays can be diagnostic clues for climate, topography, and other boundary conditions for weathering, and are thus very important to studies such as this.

3.6.5.5 Analysis of the products of deep weathering: Color of soils

Color, or more specifically redness (rubefaction, or the formation of iron oxides), is often used as a qualitative measure of the relative ages of soil horizons (cf. Birkeland, 1984; p. 25, 211). In order to determine which of the soils from the SBMs are the relative oldest, their colors were compared in detail.

Table 6 lists the dry color (measured in lab), naturally wet color (measured in situ in the field) of soil samples. Colors are based on best-fit matches with a Munsell soil color chart (Munsell, 1971). A-horizons are grayish-brown, whereas B- and C-horizons show brown to orangish-red colors. B-horizons were more red than C-horizons, and the most weathered B-horizon sample (SP5, from beneath quartzite-bearing gravel) showed the greatest color development (dark reddish-brown; 10R3/4).

To rate these soils by their degree of rubefaction, two classifications were determined for each sample (based on dry color). The index of Torrent et al. (1980) calculates redness as R=(weighted hue)x(chroma)/(value), whereas that of Harden (1982) calculates redness as +10 for each step in hue and chroma over the color of the parent rock (fresh quartz monzonite = 10YR8/3, very light tan). According to these classifications, B-horizons are redder than their respective C-horizons, consistent with field determination that B-horizons are more weathered. The reddest sample based on the Torrent et al. (1980) index is SP5 and the reddest based on the Harden index is SP3, consistent with other observations that these B-horizons are the most weathered.

3.6.6 Summary of observations and initial interpretations

The observations above clearly demonstrate that the low-relief surface of the SBMs corresponds to a deeply weathered granite horizon. The low-relief surface is characterized by a thick profile of extremely decomposed granite capped by well-developed soils. The nature of the saprolite and soil, with respect to bulk density, grainsize, mineralogy, and color, indicates that the original host rock has been thoroughly modified by chemical weathering. The distribution of the surface also shows that the weathered profile is almost

Table 6: Colors of horizons and samples from soil profiles along the weathered surface of the San Bernardino Mountains (Munsell, 1971). The best-fit color is listed, unless a range is given (when mottled or variable). Redness rating was calculated using the average dry color of each sample.

Sample	dry color	field color (natural wetness)	consistency	caking/clumping ?
SP1a	2.5Y4/2, dark grayish brown	10YR6/2-10YR4/2	organic loam	no
SP1b	10YR4/4, dark yellowish brown	10YR7/4-5YR5/6	granular, grus	no
SP1c	10YR6/8 (to 6/4), brownish yellow (best on grains)	10YR6/6	granular, grus	no
SP2c	10YR4/4, brown to grey-orange (7.5YR5/6) (mottled)	5YR3/4-5YR5/6	granular as rock	no
SP3a	-	10YR4/1	-	-
SP3b	7.5YR6/8, reddish yellow	10R4/6	few original minerals	yes
SP3c	7.5YR6/6, reddish brown	5YR3/4-5YR5/6	granular	some
SP4a	-	10YR4/2	-	-
SP4b	7.5YR4/4, dark brown (to 5YR4/4)	10R4/6-10R3/4	few original minerals	yes
SP4c	7.5YR5/6, yellowish red (mottled)	5YR5/6-10YR5/4	granular	some
SP5b	10R3/4, dark reddish brown (to 2.5YR3/4)	10R3/4	mostly clay	very much
SP5c	7.5YR6/6, strong brown	5YR5/6-10YR6/6	granular	some
SP6c	10YR5/6, red (mottled, 1/3 is white)	10R4/6-10R3/4	granular	no, rocklike
SP6c1	7.5YR6/6, reddish brown (mottled)	10R4/6-10R3/4	few original minerals	very much
SP6c2	5YR6/4, light reddish brown (mottled)	10R4/6-10R3/4	somewhat granular	very little
SP7c	5YR5/4, reddish brown (mottled)	10YR5/4-5YR5/6	somewhat granular	very little

Redness Rating:

Sample	Torrent index[†]	Harden index[††]
SP1a	0	0
SP1b	0	10
SP1c	0	0
SP2c	0-3	10-40 (mottled)
SP3b	3.33	60
SP3c	2.5	40
SP4b	2.5-5	20-30
SP4c	3	40
SP5b	10-13.33	40-50
SP5c	2.5-3	40
SP6c	12	30 (mottled)
SP6c1	2.5-4	40 (mottled)
SP6c2	3.33-4	30 (mottled)
SP7c	3-4	30 (mottled)

[†] (Torrent, 1980): redness = hue weight x chroma / value, (hue weights: 7.5R = 12.5, 10R = 10, 2.5YR = 7.5, 5YR = 5, 7.5YR = 2.5, 10YR = 0); e.g. 7.5YR7/8 = (2.5x8)/7 = 2.9.

[††] (Harden, 1982): redness = +10 for each step in hue and chroma above the parent (10YR8/3).

exclusively developed on granitic rocks (particularly monzonite). The weathered surface is present across much of the plateau and surrounding regions (Figure 9a) and displays similar profile characteristics wherever observed. This widespread, consistent distribution give it the potential to be a good structural datum.

The age of the upland surface would be constrained as pre-uplift if the granitic weathering across the Big Bear plateau was everywhere correlative (temporally) with the local weathered profiles buried by Tertiary sediment and basalt around the perimeter of the plateau. It is thus important to compare the characteristics of plateau surface with that in the Mojavè to the north and east and Santa Ana Valley to the south. In addition, it is also necessary to compare the plateau surface with that atop the San Gorgonio block, if they are to be used as correlative surfaces in later structural reconstructions.

The morphology and character of the weathered granite surface of the Mojave Desert is similar to that atop the plateau. Both consist of hummocky, irregular piles of corestones with interstitial grus, although the corestone piles and inselbergs of the Mojave tend to be more irregular, barren of grus, and are separated by accumulations of alluvium (Oberlander, 1972). Where the upland surface is more irregular atop the plateau, such as at the Pinnacles, its character is indistinguishable from that of the Mojave. Weathered granite beneath Miocene basalts at Old Woman Springs consists of a basal zone of corestones and regolith, overlain by 15 m of regolith, and capped by ~2 m thick, brick-red (2.5YR3/6-2.5YR4/6), clay-rich soils that consist of relatively unaltered quartz and orthoclase and decayed biotite and plagioclase (Oberlander, 1972). This is similar to soils atop the plateau (particularly SP5), but other Mojave characteristics, such as carbonate and ferruginous crusts and sedimentary reworking, are absent from upland soil profiles. Given these similarities and differences, it seems that the weathered surface atop the plateau likely shares its origins with the Mojave surface, but such a correlation is not required.

Although it is not possible to compare the morphology of the upland surface with the poorly exposed weathered profiles beneath the Mio-Pliocene Santa Ana Sandstone to

the south, the saprolites of these locations are somewhat similar. The Crt-horizons atop the plateau and in the valley are indistinguishable in terms of grainsize, bulk density, and general consistency. They are slightly different, however, in that the weathered granite beneath the Santa Ana Sandstone is slightly more reddish or pinkish than the Crt-horizons atop the plateau and is banded (Figure 29d). The buried saprolite also has no rock structure, has been eroded at the top, and may have experienced some sedimentary reworking. It thus seems possible, but not required, that the plateau surface and weathered granite beneath the Santa Ana Sandstone are correlative.

The patchy weathered surface high atop the north flank of the San Gorgonio block is similar in basic morphology and profile characteristics to the upland plateau surface. This is consistent with thermochronometric data that suggests they expose a similar structural level and represent the same horizon (Spotila et al., 1998). Saprolites and soils are not well exposed atop the higher patches of weathered granite on the San Gorgonio block, but lower patches exposed in road-cuts (Rt. 38; Figure 9a) are not as decayed as saprolites atop the plateau. These consist of grus, but contain almost no pedogenic material, have a fairly high bulk density (Figure 32), and consist of mostly unaltered minerals. This could suggest a lower degree of weathering than exhibited by the plateau surface. Given the stepped topography represented by the upper and lower patches of weathered granite atop the San Gorgonio block (Figure 9a), it is possible that these less-weathered surfaces have developed by weak, syn-uplift weathering, similar to that proposed for the Sierra Nevada (Wahrhaftig, 1965).

Given that the upland surface is not contiguous with and cannot be uniquely correlated with buried weathered profiles, it is not reasonable to conclude it is relict (i.e., pre-uplift) on this basis. Similarly, the characteristics of the weathered surface do not, by themselves, demonstrate that the weathered profile had to have developed prior to uplift. The weathered horizon certainly seems to have developed prior to the latest pulse of erosion, given the cross-cutting relationship evident in dissection and sculpting of poorly

preserved soil horizons. The weathered surface also appears overprinted by erosion where canyons have been incised into fresh granite. However, these observations may only indicate that erosion locally outpaces weathering. One way to determine whether the weathered surface is relict is to compare the above characterization with other locations of active granitic weathering. It is possible that the surface shares affinities to other locations, thus indicating that this style of weathering requires various conditions, such as climate or topography, that have not been present since uplift of the plateau.

The above observations also do not provide an estimate of what weathering rate was required to disintegrate such a thickness of granite or how long the weathering regime has persisted in the region. Given that the surface has not yet been shown to be relict, it is possible that granitic weathering is active in the present climatic conditions atop the SBMs. Without any constraint on the possible rates of active weathering, however, it is not possible to judge how long the thick weathered profile needed to accumulate. If weathering rates have been slow, the plateau may still be ancient (i.e., topography not significantly modified since uplift) even if granite is actively decaying. In addition, if the weathering rate has been slow and the difference in elevation of granitic and metasedimentary bedrock (~0.5 km) has been produced solely by differential weathering (i.e., etchplanation), the total duration of weathering in the region may have been quite prolonged. To explore this further, it is necessary to either acquire absolute constraints on the age of the weathered surface (e.g., cosmogenic dating) or to acquire constraints by analogy by investigating the range in weathering rates that occur in other locations and climates.

Given this uncertainty of likely weathering rates, it is not yet possible to estimate the thickness of bedrock that could have been removed by weathering and subsequent removal of disintegrated rock during the past several million years. Coarse-grained rocks rich in feldspars, micas, and mafic minerals (such as quartz monzonite) are very weatherable (Birkeland, 1984; pp. 70, 174), but deep weathering generally requires ample groundwater, heat, and time to permit slow, subsurface chemical reactions to proceed (cf.

Ollier, 1975; Chp. 10; Birkeland, 1984; Chp. 11). The thick accumulation of weathering products atop the SBMs has also required preservation from erosion. As mentioned above, erosion locally overprints the weathered surface, indicating it either postdates or outpaces weathering (such as in canyons). However, the fact that the weathered profile is locally preserved indicates that erosion has either been slower than active weathering on interfluves or that the magnitude of erosion has been too small to remove the relict products of an ancient, static weathered profile. Thus, preservation of the weathered profile indicates either very rapid rates of weathering or a very low magnitude or rate of erosion.

The degree to which the plateau is eroded (or eroding) is also reflected in the geomorphology of the weathered surface. Although the process of deep weathering should result in a fairly consistent profile "stratigraphy" (Ollier, 1975; p.123), the character of the surface varies by location (Figure 23). The differences between levels of the characteristic profile "stratigraphy" exposed across the plateau reflect variations in the magnitude of this erosion. Where the surface consists of resistant inselbergs or corestone piles, the granular, non-cohesive regolith has likely been stripped away by erosion. Systematic variation in the weathering features of the upland surface indicate the greatest magnitude of erosion on the eastern flank (bouldery rind is only partly preserved along interfluves between canyons cut into fresh rock), a lower magnitude of erosion on the west (well preserved bouldery rind), and the least magnitude of erosion in the central plateau (mantled by soils and regolith). The topographic character of the plateau also exhibits systematic variations consistent with these differences in the magnitude of erosion. Irregular, hummocky topography (e.g., Pinnacles; Figure 16c) occurs where corestones and inselbergs have been exposed by moderate erosion, as is prevalent on the west (Figure 9a). Flatter topography (e.g., Big Bear Lake; Figure 16a) occurs where more regolith has been preserved from erosion, as is common atop the central plateau. Where characteristic hummocky or low-relief surfaces are absent and steep canyons are present (e.g., Morongo Canyon and the eastern flank; Figure 9a, 16d), erosion has destroyed the surface to a greater degree. The fluvial

geomorphology (Figure 17) and distribution of late Quaternary alluvium (Figure 9b) similarly suggest that less erosion has occurred atop the central plateau than along the plateau's perimeter and eastern flank. Preserved alluvial surfaces indicate that much of the central plateau is depositional rather than erosional. The complicated, irregular network of gentle, curved streams atop the central plateau may represent a mature, low-energy, relict drainage network, in the sense that it reflects a rolling topography and has not developed a simple dendritic pattern equilibrated to the high relief (>1 km) at which it is perched (Bloom, 1991; p.287). The deeper, straighter, steeper canyons of the plateau perimeter and eastern flank, however, are indicative of more rapid incision.

Thus, although preservation of the weathered surface in parts of the SBMs indicates erosion has likely been limited or proceeded slowly over the last few million years, erosion atop the central plateau seems to have been of a significantly lower magnitude than that along the eastern flank. Given that the central plateau is perched higher than the eastern flank, it is perhaps strange that it does not erode more quickly. However, the central plateau is protected from erosion by a thicker vegetative cover and its north-to-south concave shape (Figure 4). Due to this concavity, east-west trending drainage divides separate the upper plateau from the steep escarpments and migrate inwards as the escarpments retreat, so that the gentle topography of the upland surface does not equilibrate to the relief it is perched at and rapid erosion is limited to the perimeter of the range.

The last information required to use the weathered surface as a datum is its geometry prior to deformation. The geomorphic observations above show that the upland surface presently has gentle topography and is somewhat smooth, save minor, short-wavelength undulations. The undulations and hummocks match those expected for deep granitic weathering, once slight variations in the geometry of the subsurface weathering front have been exposed by removal of overlying regolith (i.e., etchforms; Twidale, 1990). This suggests that the pre-uplift geometry of the surface was similar to today's, save the input of tectonics and minor subsequent erosion. A better understanding of the likely

topography of the weathered surface prior to uplift may result from examination of weathered granitic surfaces elsewhere and the paleogeographic constraints from pre-uplift deposits.

3.7. Comparison of the Big Bear plateau weathered surface to other deeply weathered granitic surfaces

3.7.1 Introduction

The above geomorphic observations and interpretations leave several major unanswered questions regarding the evolution of the upland surface. The major uncertainties include whether granitic weathering is active and (if so) at what rate, whether the nature of weathering indicates environmental conditions that are not present atop the plateau (such as a relict, tropical climate), the likely maximum rate of weathering given past conditions and the total time required to develop such a thick profile, and the range in topography upon which deep weathering may proceed (constraint on pre-uplift geometry). Insight on these issues may be gained by comparing the upland surface with weathered granite elsewhere. The formation of low-relief, weathered surfaces is a popular geomorphologic topic (cf. Ollier, 1975; Chp. 10), and there have been many extensive studies of active granitic weathering (e.g., Table 7). The evolution of the upland surface may be analogous to other places and may be understood better, by examining similarities and differences in their observed characters.

The locations listed in Table 7 indicate that active granitic weathering occurs in a range of climatic conditions, although there is uncertainty as to whether deep weathering has developed entirely under present conditions at some locations (see Section 3.5.2). According to Table 7, weathering is likely active in parts of the SBMs (e.g., Lake Arrowhead; avg. temp. ~11°C, avg. rain. ~104 cm/yr), but not in others (e.g., near the Mojave; 20°C, 10-15 cm/yr) (Table 1, Figure 8). For example, SBMs climate is nearly

Table 7: Summary of granitic weathering in other regions.

Location	T (avg.)	Rainfall (avg.)	Climate	Lithology	Age	Depth	Profile	Corest.	Rego.	Consistency
San Diego[1]	warm	25-50 cm/yr	semi-arid	tonalite	? (*A)	30 m	yes	yes	yes	weak/friable
Corsica[2]	16°C	69.8 cm/yr	semi arid	granitic	active?	?	?	?	yes	?
Sierra Nevada[3]	7-15°C	50-76 cm/yr	dry-mountain(*B)	granitic	?	30 m	yes	yes	yes	weak/friable
Ireland[2]	10°C	136-186 cm/yr	cool temperate	granite	active	~4 m	?	?	yes	?
Dartmoor, UK[4]	cool	190 cm/yr	cool temperate	granite	active	up to 35 m	yes	yes	yes	weak/friable
VA Piedmont[5]	10°C	104 cm/yr	cool temperate	granite	active	up to 30 m	yes	yes	yes	weak/friable
Australia[6]	various	75-150 cm/yr	warm temperate	granitic	active?	50-300 m	yes	yes	yes	weak/friable
Brazil[2]	24°C	97.5 cm/yr	subtropical	granite-gneiss	active	>30 m	?	?	yes	?
Hong Kong[7]	hot	213 cm/yr	tropical	granite	active	>60 m	yes	yes	yes	weak/friable
Sierra Leone[8]	hot	236 cm/yr	tropical	granite-gneiss	active	<5 m(*C)	yes	yes	yes	weak/friable
Guyana[9]	28°C	160 cm/yr	tropical	granite-meta.	active	6-46 m	?	yes	yes	weak/friable

T = annual temperature, Lithology = parent rock, Age = age of weathering (either relict or presently active), Depth = depth of weathered profile, Profile = presence of the basic profile defined in text, Corest. = presence of corestones, Rego. = presence of regolith, Consistency = mechanical strength of saprolite.
*A = see text for discussion
*B = dry mountain climate includes orographic rainfall and temperature variation, and receives most rainfall in less than half the year (Barry, 1981).
*C = common erosional stripping removes the weathered products, thus profile is normally only a few meters thick, even on interfluvs.

1. Nettleton et al., 1970
2. Power and Smith, 1994
3. Wahrhaftig, 1965
4. Williams et al., 1986; Eden and Green, 1971
5. Pavich, 1986; Pavich, 1989
6. Ollier, 1965; Mabbut, 1965
7. Ruxton and Bery, 1957
8. Teeuw et al., 1994; Teeuw, 1991
9. Eden, 1971

Table 7: continued.

Location	bρ-B	bρ-C	% clay, B-h	% clay, C-h	Grainsize Dist.	Orth.	Plag.	Bio.	Hnbd.	Qtz.	S-oxides
San Diego[1]	1.81	1.83	10-40%(*D)	5-21%(*D)	intermediate?	?	pw	w/a	pw	nw	no
Corsica[2]	?	?	<15%	<5%	arenaceous	nw/pw	pw	w	-	nw	minor
Sierra Nevada[3]	?	?	?	?	arenaceous?	nw	pw	w	nw	nw	?
Ireland[2]	?	?	<15%	<5%	arenaceous	nw	nw/pw	w	-	nw	no
Dartmoor, UK[4]	?	?	2-10.5%	<5%	arenaceous	pw	w	w/a	-	nw/pw	no
VA Piedmont[5]	2.0	1.7	15-40%	<5%	argillaceous?	?	a/w	w	-	nw	yes
Australia[6]	?	?	?	?	?	?	?	?	?	?	?
Brazil[2]	?	?	>45%(*E)	?	argillaceous	w	w/a	w/a	-	nw	yes
Hong Kong[7]	?	?	17-30%	<5%	argillaceous?	w/a	a	a	-	nw	yes
Sierra Leone[8]	?	?	5-50% (*F)	?	argillaceous	a ?	a ?	a ?	-	w	yes
Guyana[9]	?	?	15-35%	?	argillaceous	a(*G)	a	a	?	?	yes, but leached

bρ-B = bulk density of B horizon (g/cm^3), bρ-C = bulk density of C horizon, %clayB-h = clay content of B horizon (<4 μm), %clayC-h = clay content of C horizon, Orth.-Qtz. = degree of weathering of mineral phase (typically given as a continuum) where nw = not weathered, pw = partly weathered, w = weathered, a = absent (completely weathered away), dash (-) = mineral not present; S-oxide = presence of sesquioxide deposits.
*D = the high amount of clay is likely due to the parent composition, given that more than 50% of the rock is easily weathered plagioclase.
*E = includes fine silt as well as clay.
*F = clay defined as less than 2 μm size.
*G = a true laterite, with little original minerals

1. Nettleton et al., 1970
2. Power and Smith, 1994
3. Wahrhaftig, 1965
4. Williams et al., 1986; Eden and Green, 1971
5. Pavich, 1986; Pavich, 1989
6. Ollier, 1965; Mabbut, 1965
7. Ruxton and Bery, 1957
8. Teeuw et al., 1994; Teeuw, 1991
9. Eden, 1971

identical to that of the Sierra Nevada, where it has been argued that weathering is ongoing (Wahrhaftig, 1965). This suggests that the upland surface is not everywhere relict (sensu stricto). More detailed comparisons are useful in determining the extent to which the Big Bear plateau is analogous to weathered surfaces elsewhere.

As with any comparison, an appreciation of natural variability between examples is prudent. Minor differences in topography, water chemistry, parent composition, grainsize, or permeability may account for significant differences in weathered profiles, which should not be blamed on climate or time. Similarly, many weathered locations may not be representative of weathering in present environmental conditions, given variations in recent climate. For example, Corsica may have been more humid in the Pleistocene (Power and Smith, 1994) and the Virginia Piedmont may have been cooler and drier in recent glacial periods (Pavich, 1986). Conclusions based on this comparison are thus non-rigorous.

3.7.2 Comparison of observations

The macro-scale character of deeply weathered surfaces are generally very similar. Like atop the Big Bear plateau, deep granitic weathering in other locations is typically associated with low-relief, hummocky surfaces (e.g., central Australia; Mabbutt, 1965; see Section 3.7.4). These surfaces are generally floored by soils or regolith, but often contain large, resistant inselbergs (e.g., Mabbutt, 1965; Teeuw et al., 1994). Along several of these surfaces, resistant, non-granitic lithologies systematically outcrop at greater elevation than weathered granite. This phenomenon (etchplanation) is particularly evident in tropical locations, such as in Sierra Leone (metamorphic rocks form ridges, 400 m above weathered surface) or Hong Kong (felsite occurs as local peaks, 300 m above weathered surface) (Teeuw et al., 1994; Ruxton and Berry, 1957). The apparent etching atop the Big Bear plateau (Figure 27, 28) may indicate similar tropical weathering.

Deep granitic weathering is characterized by a consistent profile "stratigraphy," which consists of a basal zone of interlocking corestones and interstitial grus, a zone of

mixed grus and loose corestones, a zone of saprolite that retains rock structure, a layer of structureless regolith, and a mantle of thin (~1 m), well-developed soil (Ollier, 1975; pp. 122-123). Corestones and regolith make up all of the weathered profiles listed on Table 7, and all described locations, as well as the Big Bear plateau (Figure 23), exhibit the characteristic profile. One minor difference is that the transition from weathered to fresh granite (weathering front) in several locations is sharp (10's of cm; Ruxton and Berry, 1957; Ollier, 1975; p.121), whereas atop the plateau is more gradual. The consistent increase in weathering intensity upwards is due to the greater aggressivity of percolating waters, oxygen, and biogenic factors near the surface. Mantles of soil are thought to form from mineral decay at the expense of underlying saprolite. Soils form as clay and immobile oxides accumulate and cations are leached away, often consolidating ~400% by volume from saprolite (1 m soil = 4 m saprolite; Pavich, 1986).

Profile thickness (i.e., depth of weathering) is also fairly consistent and typically in the range of 30-50 m (Table 7). Although thicker profiles have been reported (cf. Ollier, 1975, p.121), the depth of granitic weathering atop the Big Bear plateau appears typical of deep weathering in both temperate and tropical locations, as well as semi-arid and Mediterranean ones (San Diego, Sierra Nevada). The thinner (~4 m) depth of weathering at cool, temperate Ireland (Power and Smith, 1994) is not necessarily indicative of climatic conditions, because a thick profile is present at Dartmoor (Table 7; Williams et al., 1986). Thinner profiles can result from routine episodes of erosive stripping. For example, the highly decayed profile at tropical Sierra Leone is thin due to high erosion rate (Teeuw et al., 1994), whereas thicker profiles may occur in temperate locations where erosion rates are slower (even if weathering rates are also lower). Profile thickness it thus not synonymous with degree of rock decay or indicative of climatic conditions.

The regolith of weathered profiles is universally loose, friable, and crumbly (Table 6, 7). Grusification in tropical regions results from creation of pore space by removal of the alteration products of easily-weathered minerals (biotite, hornblende, plagioclase),

which leaves behind a skeletal framework of resistant minerals that is easily disaggregated (Ruxton and Berry, 1957). However, grusification also occurs solely due to the alteration of biotite. Under humid, cool conditions, biotite undergoes hydration to form intermediate hydrobiotite and vermiculite (Power and Smith, 1994). This phase change corresponds to a 40% volume increase (1-2% of whole rock), which fractures granite from within (Nettleton et al., 1970; Wahrhaftig, 1965; Birkeland, 1984; p.85). A fundamental characteristic of deep granitic weathering (i.e., weak regolith) thus develops in temperate climates, due to only slight weathering of one constituent mineral. Perhaps a better proxy of deep weathering is saprolite bulk density, which reflects the opening of pores as weatherable material is removed from granite (cf. Birkeland, 1984; p.17). The bulk density of saprolites from the SBMs are somewhat lower than those of two non-tropical locations (Figure 32, Table 7), suggesting the upland surface may be more decomposed.

An even more sensitive indication of deep weathering is saprolite texture. As minerals decompose, the grainsize distribution of a saprolite becomes increasingly finer than the original, granule-sized granitic crystals. In temperate regions, soil and saprolite (B- and C-horizons) typically have arenaceous grainsize distributions (~5% clay, ~20% silt, ~75% sand), whereas tropical weathering profiles are argillaceous (>30% clay, ~10% silt, <60% sand) (Table 7; Power and Smith, 1994). An unusually high clay content occurs in semi-arid San Diego, however, which could be the result of a previous climate or the weatherability of the parent rock.

Arenaceous profiles develop by minor alteration of weatherable minerals and mechanical breakage of quartz and orthoclase during grusification, whereas argillaceous ones consist of resistant quartz sand and clay derived from complete alteration of weatherable minerals (bimodal). Grainsize distribution is thus an important distinction between temperate weathering and deeper, tropical weathering. Soil samples from the SBMs have arenaceous grainsize distributions (Table 5), consistent with temperate weathering conditions. The best-preserved B-horizon at SP5, however, is clearly

argillaceous (47% clay, 14% silt) and matches the soils typical of tropical locations (e.g., Sierra Leone and Brazil; Table 7). If this location is the most representative of deep weathering, it could indicate that more humid conditions were once present. The more arenaceous soils and saprolites of the SBMs need not refute this, by analogy to the variablility in grainsize of tropical soils in Sierra Leone (Figure 34; as compared to similar distribution of SBMs' soil in Figure 30). Given that SP5 is only one, un-dated soil, however, a robust conclusion is not warranted.

The mineral assemblages of saprolites at different locations indicate a progression of decomposition from biotite, to hornblende, to plagioclase, to orthoclase, to quartz (Table 7), similar to the sequence observed in the SBMs soils (Figure 33). This stability sequence is consistent with mineral weatherabilities based on calculated bonding energies and abrasion pH (rapidity at which a mineral's cations are released into solution), with the exception of hornblende and biotite (Birkeland, 1984; pp.70, 172; Nettleton et al., 1970). Hornblende (an inosilicate) has more cation-oxygen bonds (weak) and less silicon-oxygen bonds (strong) than biotite (a phyllosilicate) and should thus be more weatherable, but biotite may be more permeable and weather where fluids propagate along allow cleavage planes. Arenaceous saprolites in temperate climates exhibit weathering of biotite and plagioclase, but little or no alteration of orthoclase and quartz (Table 7). The high degree of decomposition in semi-arid San Diego may result from the high weatherability of the parent rock (tonalite, with >50% plagioclase content). In argillaceous profiles of warm, humid climates, plagioclase and biotite are completely weathered away and orthoclase is heavily altered. Under the wettest conditions, such as in swamps of tropical Sierra Leone, quartz may also undergo slow dissolution and become etched due to precipitation of iron oxides along microfractures (Teeuw et al., 1994).

The degree of mineral decomposition in B- and C-horizons of the SBMs do not clearly fit either of these two end-members. In many SBMs locations, biotite and plagioclase are heavily altered and orthoclase is only slightly weathered, similar to

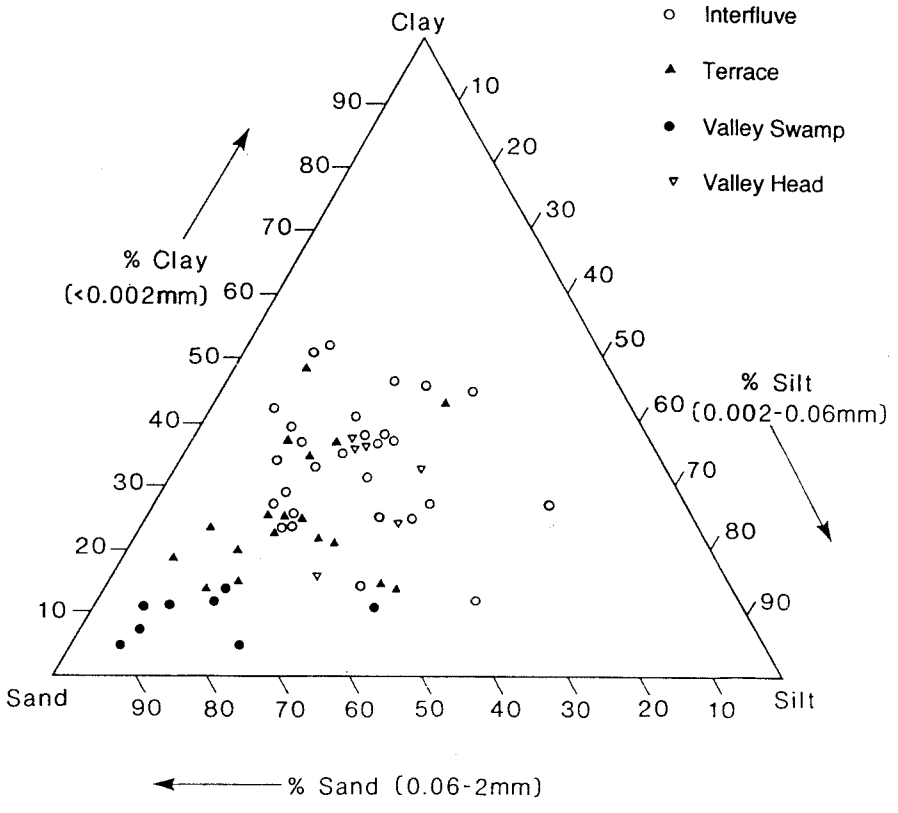

Figure 34: Ternary plot of grainsize distribution from soils in the Koidu Basin in Sierra Leone (from Teeuw et al., 1994). This illustrates how saprolite texture varies by topographic position and landform type within a single actively weathering granitic terrain.

arenaceous profiles (Table 7). In a few locations (e.g., SP5), biotite and plagioclase are absent and orthoclase is heavily altered, similar to some argillaceous profiles, but less decomposed than in others (e.g., Sierra Leone). An interesting similarity between SP5 and other tropical or humid-temperate weathering is the presence of a quartzite-bearing gravel cap. Very similar gravels are described for tropical Sierra Leone and Guyana (Teeuw et al., 1994; Eden, 1971), as well as in the Appalachians (Pavich, 1986), which are thought to be resistant lag deposits. This could suggest that SP5 experienced similar weathering conditions, in which only quartz survived. Given the looseness of this comparison, however, it can only be concluded that most weathering in the SBMs is at least as developed as in temperate locations, but generally less-well developed than in tropical ones.

Secondary phases (e.g., clay) in saprolites also offer valuable information on the weathering process. Large deposits of sesquioxides, for example, are typical of tropical soils, in which iron, aluminum, and magnesium are freed from primary minerals at a rapid rate (Birkeland, 1984; p. 249, Chp. 11). In Sierra Leone saprolite, significant accumulation of sesquioxides occur as mottles, nodules, and pisoliths (Teeuw et al., 1994). These were not identified in SBMs soils. Lateritic soils (oxic horizons) occur in tropical Guyana (Eden, 1971), which are rich in iron and aluminum oxides, contain little primary silicate minerals, and form a hard crust when dried. The only soil in the SBMs that could be likened to a laterite is SP5. Redness is also a good proxy for the degree of iron-oxide fixing in soils and is often used as a qualitative index of weathering (Birkeland, 1984; p.209). Redness (Torrent et al., 1980) values of tropical saprolites in Brazil (maximum = 12, average = 3.6; Power and Smith, 1994) and laterites of Guyana (typically ~8) are similar to redness of soils in the SBMs (max.~13, avg.~4; Table 6), suggesting they are comparably weathered. Redness (Harden, 1982) values of SBMs soils (max.= 60) also fall in the range of ~10^5 yrs old soils developed on sediments (Birkeland, 1984; p. 210), although the difference in parent make this a weak comparison. Despite the inherent

variability in soil color due to many factors other than age and climate, the redness of SBMs soils are similar to old soils in humid conditions.

3.7.3 Rates of granitic weathering

Although it is plausible that granitic weathering has been active atop the Big Bear plateau for some time, the rate of this weathering governs how much the surface may have been lowered during uplift and how long the entire weathered profile required to develop. Weathering rates were not determined in this study, but have been calculated for other locations using a variety of data. Likely weathering rates atop the plateau may be surmised, by analogy with other locations.

Weathering rates are often reported as isovolumetric rates of saprolite formation (i.e., lowering of weathering base, or the rate at which a volume of fresh rock becomes an equal volume of saprolite) (e.g., Velbel, 1985). Saprolitization is generally thought to be complete once all primary, weatherable minerals have been altered or removed (e.g., Velbel, 1985). Chemical denudation rates are also commonly reported, which represent the rate of ground loss due to solute removal and transfer (e.g., Saunders and Young, 1983). For isovolumetric weathering in the absence of erosion, the chemical denudation is related to rate of saprolite formation by the difference in density of the parent rock and saprolite, as $S[t] = A^*[t] = C[t]/(1-\rho_2/\rho_1)$; where S[t] = rate of subsurface saprolite formation (fresh rock equivalent, f.r.e.), A*[t] = rate of saprolite accumulation (weathered rock equivalent, w.r.e.), C[t] = chemical denudation (f.r.e.), ρ_2/ρ_1 = bulk density ratio of saprolite to parent (or $1-\rho_2/\rho_1$ = saprolite porosity) (e.g., Dethier, 1986). Because saprolite bulk densities are typically ~1.8 g/cm^3 (Table 7, Figure 32), compared to 2.7 g/cm^3 for fresh granite, saprolite formation can be approximated as $S[t] \sim 3C[t]$.

Previously determined weathering rates (C[t] and S[t]) in other locations are extremely variable (Table 8). These span about four orders of magnitude, illustrating the strong effect of climate, lithology, and other factors (e.g., parent texture, permeability,

Table 8: Rates of weathering and total denudation in various regions and on various lithologies.

Study	Location	Climate	Lithology	Weathering rate	M	Total Den.	M
Velbel,1985	so.Appl's Blue Ridge	humid, temperate	metamorphic	0.038 mm/yr RSF	1	0.04 mm/yr	2
Pavich, 1985	VA Piedmont	temperate	metapelite	-	-	0.02 mm/yr	4
Paces, 1986	central Europe	humid temperate	aluminosilicate	-	-	0.014 mm/yr	3
Thomas, 1994	Appalachians (summary)	humid temperate	siliceous	0.002-0.05 mm/yr RSF	2	-	-
Dethier, 1986	Pacific Northwest	cool, wet, maritime	various	0.03 mm/yr RSF	3	~0.06 mm/yr	?
Saunders and Young, 1983	summary	humid temperate	siliceous	0.002-0.05 mm/yr CD	3	-	-
Saunders and Young, 1983	summary	temperate	various	-	-	0.005-0.1 mm/yr	3
Saunders and Young, 1983	summary	semi-arid	various	-	-	0.1-1 mm/yr	3
Saunders and Young, 1983	summary	tropical	various	-	-	0.01-1 mm/yr	3
Saunders and Young, 1983	laboratory	various temperate	various	0.002-0.2 mm/yr CD	6	-	-
Edmond et al., 1995	Guayana	humid, tropical	igneous/meta.	~0.02 mm/yr RSF	3	~0.01 mm/yr	3
Williams et al., 1986	Dartmoor, UK	cool temperate	granitic	0.005 mm/yr CD	3	0.0065 mm/yr	?
Montgomery, 1994	Sierra Nevada	dry-wet mountain	granitic	-	-	0.01-0.02 mm/yr	3
Saunders and Young, 1983	Africa	tropical savanna	granitic	0.006-0.015 mm/yr CD	3	-	-
Pavich, 1986	VA Piedmont	temperate	granitic	0.004 mm/yr RSF	3	-	-
Birkeland, 1984; p. 196	Sierra Nevada	dry-wet mountain	granitic clasts	~0.004 mm/yr† RSF	5	-	-
Birkeland, 1984; p.175	Sierra Nevada	dry-wet mountain	granitic clasts	<0.00017 mm/yr* RSF	5	-	-
Birkeland, 1984; p.175	Colorado	wet-mountain/temperate	granitic clasts	0.0003-0.0045 mm/yr* RSF	5	-	-
Bierman and Turner, 1995	Australia	semi-arid	granite	-	-	0.0007 mm/yr£	4
Bierman et al., 1995	Llano, TX	semi-arid	granite	-	-	0.004 mm/yr£	4
Bierman et al., 1995	Atlanta, GA	humid, warm temperate	granite	-	-	0.006-0.01 mm/yr£	4
Bierman et al., 1995	Sierra Nevada	dry-wet mountain	granite	-	-	0.007 mm/yr£	4

RSF = rate of saprolite formation by isovolumetric weathering
CD = chemical denudation (mass lost by solute removal)
† = rate of saprolite formation on buried boulders (boulders completely disintegrate in 140,000 yrs, assume boulder size = 0.5 m radius)
* = subaerial weathering rate (rate of rind formation on exposed boulders)
£ = total denudation from tops of granitic inselbergs
M = method: 1 = geochemical mass balance, kinetic equations; 2 = various data, summarized; 3 = geochemical mass balance from solute flux, catchment size, biogenic production, etc.; 4 = cosmogenic radionuclides; ^{10}Be or ^{26}Al, ^{36}Cl; 5 = subaerial weathering rind thickness on Late Wisconsin tills (10 Ka), Birkeland (1984; p.196); 6 = loss of material from rock chips buried in soil, tombstones, etc. (experimental).

drainage, topography, biota) on weathering (cf. Thomas, 1994; Pavich, 1986; Ruxton and Berry, 1957). Rates of subsurface saprolite formation on granitic rock listed in Table 8 (including chemical denudation rates, where S[t] = 3C[t]) vary from 0.004-0.015 mm/yr. Rates of subaerial weathering rind formation (0.0045-0.003 mm/yr) and total denudation (including weathering and erosion) of exposed granitic inselbergs based on cosmogenic nuclides (0.0004-0.01 mm/yr) are lower, but still span a wide range. More rapid granitic weathering apparently occurs in humid-temperate and tropical climates, whereas the lower rates occur in semi-arid ones. The opposite is true of physical denudation rates, which are greater for arid regions than in temperate ones (Table 8).

Atop the central plateau, present rainfall and temperature are similar to humid temperate regions (Figure 8; Table 1, 7). By analogy, the rate of saprolite formation there may be close to the average rate of saprolite formation in humid temperate regions (<0.01 mm/yr, Table 8). It is not likely to be greater than this, given that the dry-mountain climate of the SBMs is such that most precipitation (and thus wet subsurface conditions favorable for weathering) occurs over only several months (Table 1), whereas humid temperate regions receive precipitation more regularly (Frakes, 1979). In the semi-arid parts of the plateau, such as the northwestern and eastern flanks, as well as in the Mojave Desert (Figure 8), weathering rates may be much lower. By analogy with total denudation rates of granitic inselbergs in other semi-arid regions (0.0007-0.007 mm/yr; Table 8), the large resistant corestones piles on the flanks of the plateau may have been preserved from significant erosion or weathering for some time.

Assuming a conservative saprolite formation rate of 0.01 mm/yr, 10 m of saprolite is produced per million years. Thus, in a state of equilibrium (i.e., saprolite formation = total denudation, saprolite thickness = constant), weathering and subsequent erosion of saprolite could not have shaped the upland surface topography (>100-m-scale relief) during the course of uplift. Assuming this rate, it is also possible to estimate the total time necessary to produce the saprolite atop the central plateau. The lower part of the ~30-m-

thick weathered profile contains corestones that have not yet turned to saprolite, so that the effective saprolite thickness atop the plateau is closer to ~20 m (Figure 23). Thus, the weathered profile may have required ~2 million years to form. In addition, if the difference in elevation of granitic and metasedimentary rocks (420 m average) developed due to weathering and removal of saprolite at this rate, the weathering may have been ongoing since the late Eocene.

Rate of saprolite formation is equivalent to rate of saprolite accumulation only in the absence of erosion (e.g., Williams et al., 1986; Dethier, 1982; Pavich, 1986). When both weathering and erosion are present, saprolite thickness will grow only if erosion is less than saprolite accumulation, as $A^*[t] = (S[t] - C[t] - E[t])/(\rho_2/\rho_1)$; where E[t] = rate of erosion (f.r.e.). Thus, if accumulation of the weathered profile atop the central plateau took several million years, the weathered surface must have been protected from significant (>thickness of weathered profile), syn-uplift erosion. If erosion was present or saprolite formation was slower over the past few million years, then accumulation would have been slower and the weathered profile would have required more time to develop (i.e., began prior to uplift). By comparison, the arid northwestern and eastern flanks of the plateau should have experienced lower syn-uplift weathering rates (i.e., Table 8) and higher syn-uplift erosion rates (based on lack of vegetative cover and other observations; see Section 3.6.6), since the onset of an orographic rainshadow (Figure 8). The preservation of deep weathering characteristics there limits syn-uplift erosion, however, supporting the idea that the central plateau has also been well-protected from erosion since uplift initiated.

3.7.4 Topography of granitic weathering

If the upland surface has escaped significant topographic modification by syn-uplift weathering and erosion, its present shape is a product of tectonic modification of preexisting topography. Thus, before it can be used as a structural datum, it is necessary to define its pre-uplift shape. It is possible that there is a standard topographic character

associated with prolonged deep weathering and erosion of granite, which was present in place of the SBMs prior to its perturbation by orogenesis. For example, it may be that low-relief, undulating surfaces are produced by long-term peneplanation at a relatively flat base-level (cf. Davis, 1899), as presumed in structural reconstructions of upland surfaces atop the front range of the Colorado Rockies (Madole et al., 1987). Examination of sites of prolonged weathering may reveal a common geomorphic template, applicable to the SBMs.

Actively weathering granitic terrains commonly share low-relief, hummocky topography as an attribute (Table 9), similar to the least-eroded patches of surface atop the Big Bear plateau (Figure 16). At short wavelengths (<100 m), gentle topography may result from flattening associated mass reduction (solute removal, elluviation of fines) as saprolite compacts into soil (Velbel, 1985). There is variability among the few locations examined, however, and there does not seem to be a rigid topographic template for deep weathering. Short wavelength irregularities, for example, occur due to variations in lithology (etching), joint pattern (i.e., inselbergs vs. corestones; Linton, 1955), or the subsurface topography of the weathering front (i.e., etchforms; Twidale, 1990). Erosional fabrics are present to differing extents and hummocky topography is often absent in the presence of integrated stream channels and ridgelines (Figure 35). Erosion often facilitates weathering by removing resistant, leftover saprolite and exposing more reactive, fresh rock (Pavich, 1986; Thomas, 1994). Saprolite may also form on irregular topography (cf. Thomas, 1994), such as on steep slopes in Hong Kong (30°; Ruxton and Berry, 1957; Table 9). The range exhibited by these few locations illustrates that deep weathering does not require or indicate a specific topography. Thus, the weathered surface of the SBMs does not evince preexisting topography or demonstrate that the broad plateau shape represents structural relief.

Although there is no set topographic template necessary for deep weathering, topography does systematically influence weathering. Ground slopes, for example, partly control erosion rate, and thus affect the rate at which saprolite may accumulate in a

Table 9: Topography of weathered surface locations.

Location	Total relief	Slope	Description
Sierra Leone (Teeuw et al., 1994)	~40 m (unknown area)	3.5° avg.	-convex interfluvs cover 50%, 30% area is swampy channeless drainage, 20% is floodplain and channels, substantial erosional stripping, colluvial deposition, sediment and solute transfer, elluviation -etchplanation well developed
Dartmoor (Williams et al., 1986)	232 m (4.75 km^2)	2-7°	-convex interfluvs, channel based drainage network, ridgelines developed, only slightly hummocky
Hong Kong (Ruxton and Berry, 1957)	low relief (s.l. to 400 m) (large area)	0-30°	-drowned, submaturely dissected landscape -typical profile occurs on slopes <15°, with partial profiles developing on steeper slopes due to erosional truncation. -etchplanation well developed
VA Piedmont (Pavich, 1986)	60 m (~3 km^2)	1-6°	-gentle erosional topography, less hummocky -streams and gentle canyons exist, channels cut the saprolite, saprolite thickness affected by topography so that the horizons are not flat
CO Front Range (Madole et al., 1987; Gregory and Chase, 1994)	700 m (broad area), 300 m (9 km^2)	as low as <1°	-remnants of relict low relief surface, buried by volcanics -various lithology, including granites

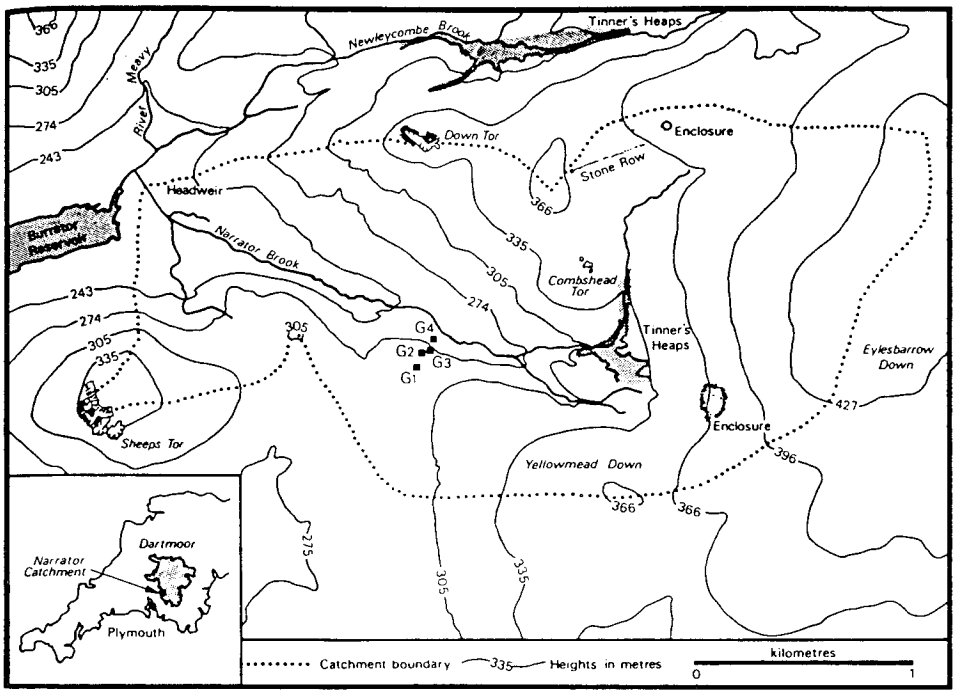

Figure 35a: Topographic map of the Dartmoor region (Narrator basin) of deep granitic weathering (from Williams et al., 1986). This shows the relief present in one actively weathering granitic terrain.

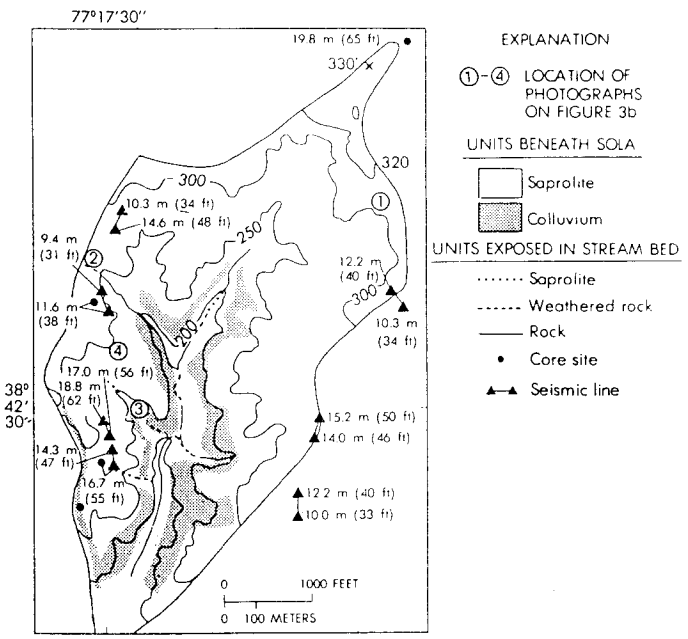

Figure 35b: Another example of the topography present in an actively weathering granitic terrain in the Virginia Piedmont (from Pavich, 1986). This also illustrates that significant relief may be present in actively weathering regions.

weathered profile. In Sierra Leone and the Virginia Piedmont, rapid elluviation of weathering products occurs along interfluves and gentle fluvial transport of fines occurs in lowlands, leaving behind resistant quartzite cobbles that are transported only during occasional storms (Teeuw et al., 1994; Pavich, 1986). Topography also partly controls hydraulic gradient and groundwater residence time. Long residence times in closed basins permit the slowest weathering reactions (i.e., quartz dissolution) to proceed, whereas medium residence times in well-drained soil facilitate rapid removal of solute (Williams et al., 1986). As a result, saprolite thickness (Figure 36), grainsize (Teeuw et al., 1994), clay mineralogy (Power and Smith, 1994), and soil chemistry (Nettleton et al., 1970) may vary with topographic position within a region. This illustrates the complex dynamics of the weathering-erosion-topography system.

3.7.5 Summary

Studies of other granitic terrains show that conditions favorable for weathering occur in most climates. Deep weathering may produce thick weathered profiles in all but polar or arid conditions (Table 7, 8). This demonstrates that the weathered surface of the Big Bear plateau is not necessarily relict and that weathering may be active. Only in the most arid regions of the SBMs and Mojave Desert may present rates of weathering be negligible. Weathering also probably occurred throughout uplift and well before, given that warm interglacial periods and more humid glacial ones extended back to the late Miocene (Frakes, 1979). Earlier climate was even warmer and more humid, consistent with the deep weathering observed beneath middle-Miocene deposits throughout the area (Frakes, 1979; Axelrod, 1950).

Most characteristics of deep weathering are not diagnostic of specific environmental conditions or age. However, a number of features observed in the weathered profile atop the plateau are generally associated with deep weathering in tropical locations. This includes the degree to which different lithologies are etched across the surface and the

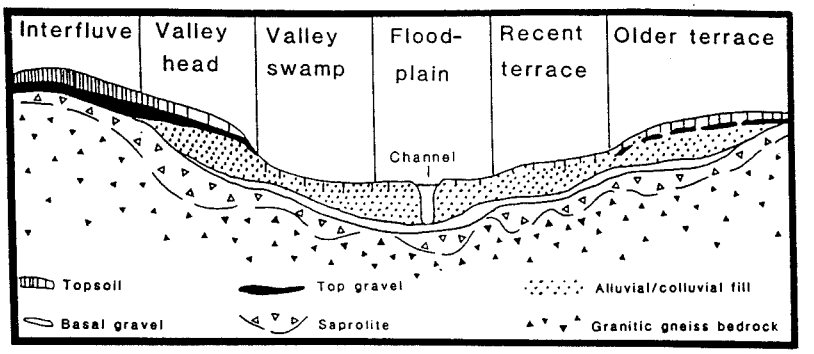

Figure 36a: A schematic representation of how saprolite character varies with topogrpahic position and landform type in an actively weathering granitic terrain in the Koidu Basin of Sierra Leone (from Teeuw et al., 1994).

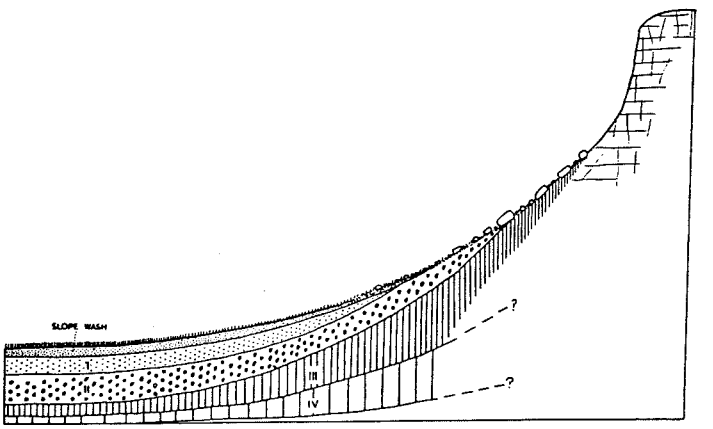

Figure 36b: A second example of how the profile of active deep granitic weathering may vary with topographic position in an actively weathering granitic terrain (Hong Kong, from Ruxton and Berry, 1957). The zones of weathering are typical of the basic profile: thin soil (I), regolith without rock structure (II), regolith with interstitial corestones (III), interlocking corestones with interstitial regolith (IV), and fresh rock.

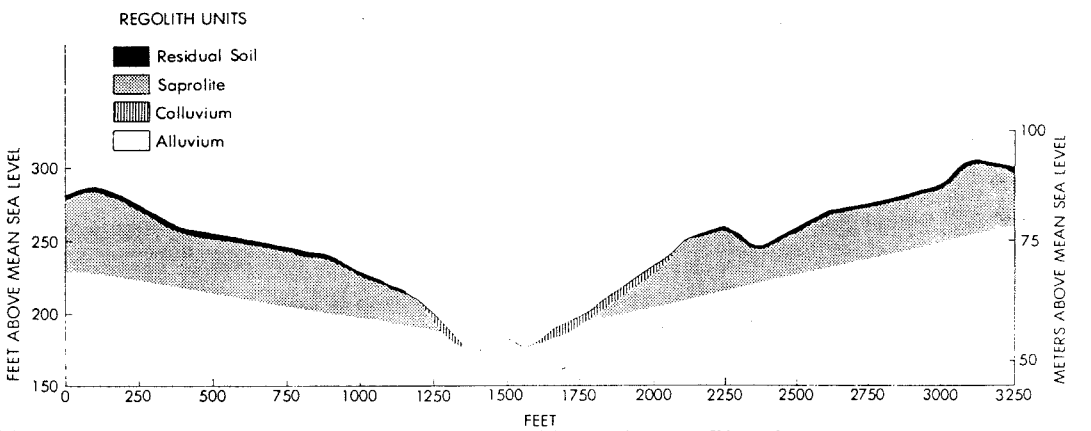

Figure 36c: A third schematic example of how the profile of active deep granitic weathering may vary with topographic position in an actively weathering granitic terrain (Virginia Piedmont, from Pavich, 1986).

grainsize distribution, mineral decomposition, and color of soils. The best-developed soils (e.g., SP5) could represent weathering under more humid conditions that are no longer present atop the plateau, implying that the weathered surface is locally relict from a previous (middle Miocene?) climate. However, these well-developed soils are extremely rare and may not be representative, and most saprolites of the SBMs are comparable to weathering in temperate locations (e.g., Virginia Piedmont). Other typical features of tropical weathering, such as quartz dissolution and major sesquioxide deposits, are also absent from all observed saprolites in the SBMs. It is thus inconclusive as to whether the upland surface possesses character attained under previous, more humid conditions, and a rigorous diagnosis about the climatic conditions responsible for weathering atop the plateau cannot be made. This is particularly true given the large effect of other variables on weathering, such as the nature of the parent rock, topography, biota, and other factors.

Although deep granitic weathering may proceed in a range of climates, the languid pace with which it proceeds in all but tropical conditions prevents accumulation of thick saprolites, except where physical denudation rates are nominal. Where thick weathering profiles occur in temperate basins, for example, outflowing streams typically have much greater solute yield than sediment yield (Williams et al., 1986). Given the likely rates of active weathering atop the central plateau and its degree of deep weathering, it seems likely that syn-uplift erosion has been restricted to canyon incision and recent regolith stripping. As an exception, significant erosion could have occurred in the early stages of uplift and then subsided, allowing the accumulation of saprolite atop the plateau. However, erosion rates would likely increase as SBMs' relief grew (Schumm, 1963; Ahnert, 1970) and geomorphic evidence suggests that rapid erosion has systematically encroached only to a limited extent atop the plateau (see Section 3.6.6), and thus it seems unlikely that a period of rapid erosion occurred early in the plateau's history and terminated once it had reached a certain height. The rates of weathering in other locations also imply that weathering and subsequent removal of weathered rock atop the plateau could not have accounted for the

magnitude of topographic variation in the upland surface (10^2-10^3 m). This implies that the broad topography of the upland surface is the product of either recent tectonic uplift or a paleotopographic high, rather than syn-uplift erosion or weathering.

Deep granitic weathering does not appear to be associated with a standard topographic form, based on weathering in other locations. Granitic weathering is often associated with low-relief, undulating terrain, but may take place on steep slopes and be associated with a dominantly erosional fabric. Examination of other locations thus fails to constrain the pre-uplift topography of the Big Bear plateau. Topography is a critical component in the dynamic interplay of weathering and erosion, and given the complexity it is not possible to predict the paleotopography of a weathered surface based on its character.

3.8. Implications of overlying deposits on the post-Miocene erosion rate and paleotopography of the weathered surface

3.8.1 Introduction

The above comparisons predict that the weathered surface atop the Big Bear plateau could have experienced significant erosion only before and/or during the initial stages of uplift, because of the slow rate at which granitic weathering typically proceeds. The comparisons also reveal that it is not safe to assume the surface was originally flat, because granitic weathering can occur on irregular topography. More can be learned about these aspects of the weathered surface by reinvestigating the deposits that overlie it.

As presented in Section 3.5.2, the age and distribution of these deposits demonstrate that the weathered surface locally approximates a pre-uplift horizon atop the eastern and westernmost parts of the plateau. By extrapolating from these buried surfaces, an approximate envelope (i.e., structure contour) map may be created locally that represents the pre-deposition, pre-erosion surface. The amount of erosion since deposition can then be determined by subtracting the present topography from this envelope. The shape of the

envelope may also reveal more information about the original geometry of the surface than is evident in single, buried exposures. Other aspects of the overlying deposits, such as clast provenance and paleoflow indicators, may also provide constraint on the pre-uplift geometry (i.e., paleogeography) of the weathered surface.

3.8.2 Estimates of post-Miocene erosion

The best location to assess the magnitude of erosion from the weathered surface is the eastern flank of the Big Bear plateau, the largest area covered by dated basalts. The discontinuous flows represent areas preserved from erosion, while the gaps between correlative flows represent post-Miocene erosion of both basalt and underlying granite. The largest group of basalts occurs atop the southeastern edge of the plateau, where flows have been correlated petrographically (Pioneertown and Chaparrosa Peak; Figure 1a, 37 [Plate 3]) (Neville, 1983). These alkali-olivine basalts are dated between 6.9 and 9.3 Ma, consist of 7-9 individual flows, vary in total thickness from 20 to 60 m, and are from an unknown source vent (Peterson, 1976; Morton, 1980; Neville, 1983). These remnant basalts appear to have an outcrop pattern that reflects a broad, eastward tilting plane, from which a remarkably smooth, gently tapering (maximum gradient = 5.5° east) envelope can be constructed (Figure 38). This envelope is much smoother than the present-day topography, and is consistent with the hypothesis that this topography has developed by erosion since the weathering and subsequent basalt eruption.

If the topographic surface these basalts were deposited on was relatively smooth, the volume of missing basalt and granite can be used to find an average erosion rate. The magnitude of post-eruption incision into this area of the Big Bear plateau varies from zero (where basalts and weathered surface are preserved along interfluves) to about 300 m (relief between interfluves and the deepest trunk streams cut into fresh granite, such as Morongo Creek), but is typically closer to 100 m (Figure 37). To estimate the average erosion rate since eruption, the missing volume per area between basalt outcrops must be

Figure 37: See Plate 3, folded into backside cover of thesis.

Figure 38: Reconstruction of the post-basalt (9-6 Ma) erosion on the east flank of the Big Bear plateau. The outcrops of basalt (from Dibblee, 1967b) are shown along with elevations atop them. From these elevations, an envelope map consisting of structure contours to the top of the basalt flows was constructed. This shows a smooth shape with moderate slope to the east. Residual elevation points are shown, representing the difference in elevation of the structure contours and the present day topographic (bedrock) surface. These can be considered the local depth of incision. 55 of these residual values were determined where topographic contours (80 foot interval) and structure contours intersected. The average of these was 479 ft (146 m). Note that basalts on the northwest are not dated or correlated with those on the southeast, and thus the basalt envelope is not connected across the Pipes Creek fault.

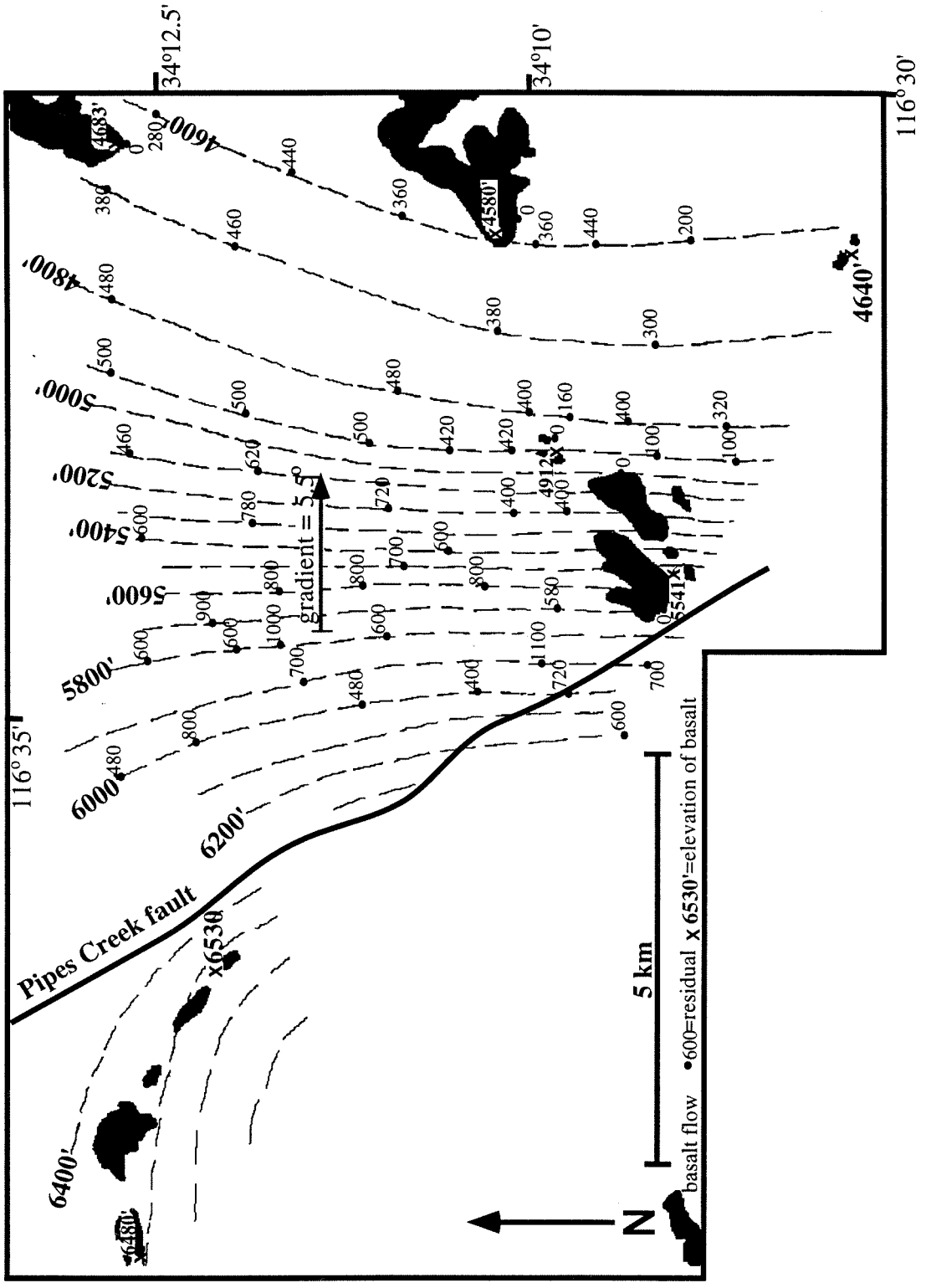
34°12.5'
34°10'
116°30'
116°35'
4600'
4800'
5000'
5200'
5400'
5600'
5800'
6000'
6200'
6400'
Pipes Creek fault
gradient = 5.5°
x6530'
x6480'
x4580'
x4640'
4683'
5 km
N
basalt flow
•600=residual x 6530'=elevation of basalt

calculated. This can be accomplished in cross section, by calculating the area between bedrock and an envelope of the basalt tops and dividing this by the width of cross section, to determine the average depth of incision. For a profile between Chaparrosa Peak and Black Hill (Figure 37; aa'), this result varies from 129 m (tight envelope) to 148 m (broad envelope) (Figure 39). When divided by the average age of these basalts (8.1 Ma), the estimated average erosion rate since the late Miocene is ~0.017 mm/yr. A tighter estimate can be made by averaging the relief between the present basement surface and a three-dimensional basalt envelope (Figure 38). Based on averaging 55 measurements of the difference between these, the average incision are about the same (146 m; Figure 38).

More basalts are present atop the plateau to the north and northwest (Ruby Mountain, Antelope Creek, Sleepy Creek, Onyx Peak; Figures 9a and 37), which consist of basanite, contain ultramafic xenoliths, and are thinner and more weathered than basalts at Pioneertown (Neville, 1983). Although these seem to have been deposited atop the same eastward tilting plane as the Pioneertown basalts, they are not petrographically correlative and thus cannot be connected to determine the volume eroded from the large area between them (Neville, 1983). The intervening Pipes Creek fault, of unknown vertical offset, also obscures the original topographic relationships between the Pioneertown basalts and those to the northwest. The northwestern basalts are also undated and, like the flows in the Mojave Desert to the north (Old Woman Springs and Fry Mountain, Figure 7b), of too limited outcrop distribution to be correlated amongst each other and used for determining post-eruption erosion rates.

The western wing of the Big Bear plateau is the second region where the weathered surface is well constrained as a pre-uplift feature. The preservation of the weathered surface and Crowder Formation that locally overlies it suggest that limited erosion has occurred since the late Miocene (Meisling, 1984). Some erosion is indicated, however, by the discontinuous distribution of Crowder beds and the weathered surface (Figure 9a), as well as the exposure of fresh granite on south-facing, fault-bounded ridges (Meisling and

Figure 39: Reconstruction of volume eroded since deposition of basalts on the eastern flank of the San Bernardino Mountains. Elevation profile runs southwest (A) to northeast (A') as shown on Figure 37. An envelope is drawn over the present basalt surface, which represents the topography of the upper basalt surface at the time of deposition. The area between this envelope and the present day topography below is the post-basalt eroded area. The average incision depth (D) can be determined by dividing this eroded area by the width of section. The erosion rate can be determined from D by dividing by the average basalt age (8.1 Ma; Morton, 1980; Peterson, 1976). The upper figure uses a broad evelope (i.e., smooths out minor irregularities in topography) to reconstruct the eroded volume and has no vertical exaggeration. The lower figure has high vertical exaggeration and has an envelope that mimics the details of the topography. The resulting values of D are comparable.

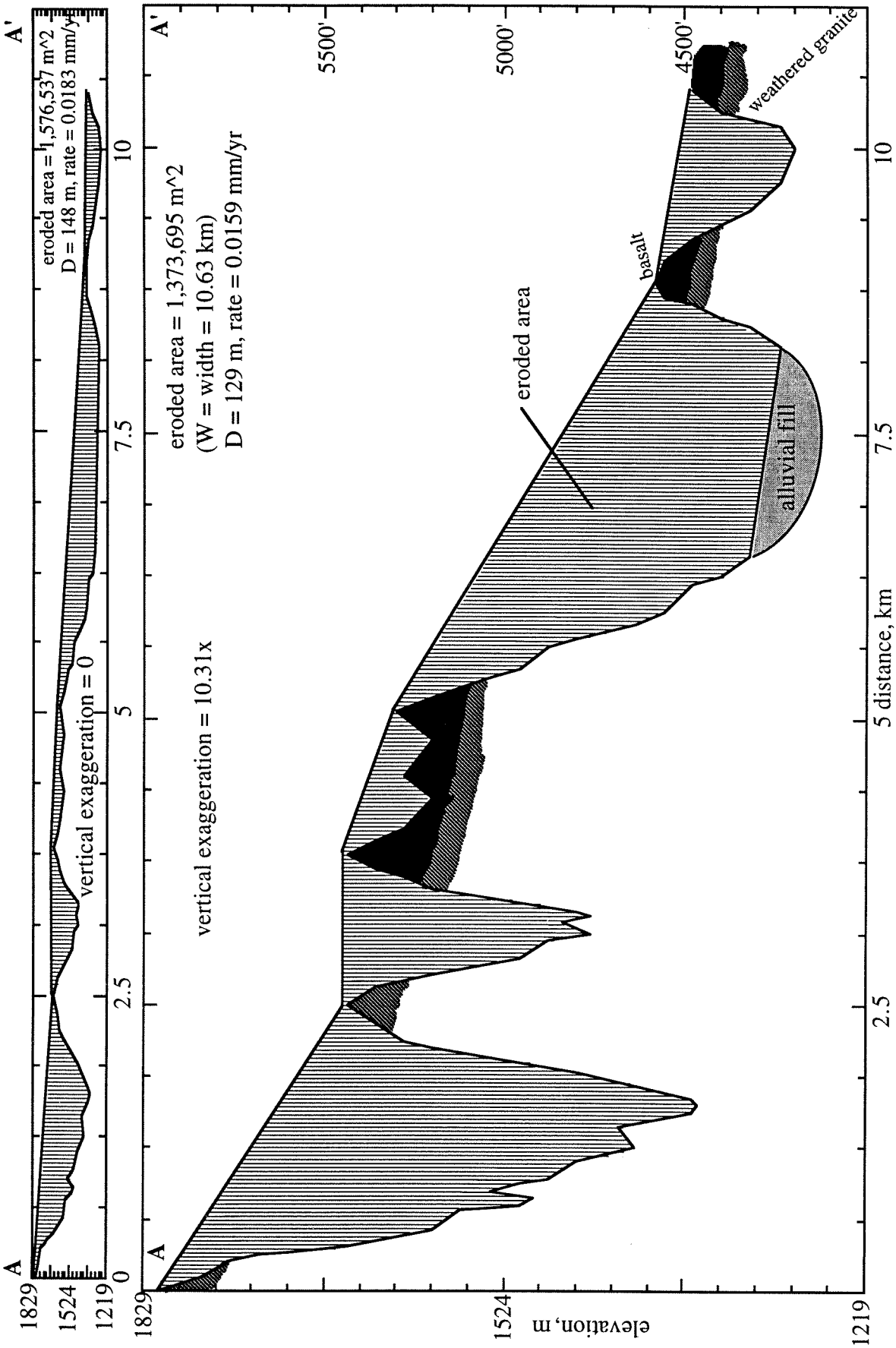
A
A'
1829
1524
1219
0
2.5
5
7.5
10
eroded area = 1,576,537 m^2
D = 148 m, rate = 0.0183 mm/yr
vertical exaggeration = 0
A
A'
eroded area = 1,373,695 m^2
(W = width = 10.63 km)
D = 129 m, rate = 0.0159 mm/yr
vertical exaggeration = 10.31x
5500'
5000'
4500'
eroded area
basalt
weathered granite
alluvial fill
elevation, m
5 distance, km

Weldon, 1989; Figure 10). It is not easy to assess the magnitude of this erosion, given the complexity of faulting. For example, a simple envelope cannot be drawn that represents the depositional surface beneath the Crowder beds.

In between these eastern and western locations, there are no dated deposits overlying the weathered surface of the central, high plateau. The scattered remnants of quartzite gravel, though not dated, were probably transported prior to the modern incision of the range, and thus their preservation suggests that erosion of the surface has been confined to the dissection of new channels inwards from the margins of the plateau (Sadler and Reeder, 1983). Given that the clasts have been recycled, however, it is possible that some granitic regolith has eroded away from beneath them, while they have been successively lowered as a lag deposit. This amount of erosion is likely to be small, given that the quartzite-bedrock-source of gravels, which were likely eroding in the Miocene, have survived and are still exposed atop the central plateau. Given these uncertainties, however, a precise estimate of how low the erosion rate has been atop the central plateau cannot be made.

The best estimate of average erosion since late Miocene deposition is thus <0.02 mm/yr (eastern basalts). Given that zero erosion has occurred where the basalt flows are preserved, the actual erosion rate within canyons would have been slightly higher. Because granite is weathered only along narrow interfluves and fresh granite is present in canyons of this part of the plateau, weathering could not have outpaced the rate of erosion since the late Miocene. This is consistent with the low typical rates of granitic weathering observed elsewhere (~0.01 mm/yr; Table 8).

3.8.3 Constraints on the pre-depositional geometry of the weathered surface

Overlying deposits constrain the geometry of the weathered surface on a local scale. The basalts on the eastern flank of the plateau, for example, were deposited atop an only slightly irregular surface, and filled only small paleochannels and depressions (Neville and

Chambers, 1982). The envelope constructed from correlative basalt flows at Pioneertown and Chaparrosa Peak is also remarkably smooth, suggesting that irregularities along the eastern weathered surface were small amplitude and wavelength (Figure 38). Similarly, the unconformity between the Crowder Formation and the weathered surface on the west indicates a low-relief, rolling topography at the time of deposition (Meisling, 1984). Although the quartzite-bearing gravels atop the plateau are not dated and consist of loose, recycled clasts, their present distributions also imply a rolling topography existed prior to their deposition. Over lengthscales of more than ~1 km, perched litters of quartzite clasts vary in elevation by more than 100 m (Figure 9a), suggesting gradients of ~6° may have been present atop the weathered surface prior to or during the initial stages of uplift (unless clasts have shifted substantially due to erosive recycling). These aspects indicate that, at least locally, the weathered surface had a somewhat irregular surface at short lengthscales prior to deposition, which was similar to its present rolling topography.

A number of previously recognized aspects of Tertiary deposits around the SBMs also indicate the presence of a pre-uplift topographic high where the central Big Bear plateau now sits. First, if little erosion has occurred atop the plateau since uplift (see above), the paucity of Mio-Pliocene sediments and basalts atop the central plateau (in contrast to their prevalence around the plateau's margins; Figure 1a) may indicate that the plateau was above depositional base-level prior to uplift (Sadler, 1982a). This is supported by the paleogeography of the Crowder Formation basin, as beds thicken westward, suggesting that Miocene topography rose to the east (Meisling and Weldon, 1989; see their figures 10-12). The older Cajon Formation supports this as well, given that Cajon beds are >2 km thick near Cajon Pass, but absent atop the SBMs (Meisling and Weldon, 1989).

More evidence for this paleotopography is the transport direction determined from the clast provenance of Miocene and Pliocene sediments. Clasts derived from the quartzite bedrock atop the central plateau are present in Tertiary sediments to the north (Old Woman Sandstone), west (Crowder Formation), south (Santa Ana Sandstone), and east (gravels

beneath basalts) (Sadler and Reeder, 1983). This suggests a radial pattern of clast dissemination prior to initiation of uplift (post- 2-3 Ma; May and Repenning, 1982; Sadler and Reeder, 1983). Clasts derived from distinctive volcanic rocks (Sidewinder Volcanics) of the Mojave Desert are present in sediments north (Old Woman Sandstone), west (Crowder Formation), and east (gravels beneath basalts) of the plateau, but not in sediments south of (Santa Ana Sandstone) or atop (undated quartzite-bearing gravels) the plateau (Meisling and Weldon, 1989; Sadler and Reeder, 1983). This suggests a southward flowing fluvial system that wrapped around and joined the radial drainage pattern of the plateau. Similarly, clasts derived from the San Gabriel Mountains terrane, which would have been southeast of the SBMs prior to offset along the San Andreas fault, are present in sediments south of the plateau (Santa Ana formation), but not in any other sediment atop or around the plateau (Sadler, 1993). Lastly, clasts derived from the eroding basalts on the eastern flank of the range are not present in gravels atop the central plateau (Sadler and Reeder, 1983). All of these transport directions are indicative of a paleotopographic high in the central plateau prior to uplift.

Although these points argue that the central plateau was higher than the surrounding area, including the eastern and western flanks, they do not constrain the size of such a paleotopographic high. The topography had to be sufficiently high to give the fluvial system the energy needed to transport cobble-sized quartzite clasts from the central plateau to the flanks (Sadler and Reeder, 1983). The direction eastern basalts flowed in the late Miocene may also help constrain the paleotopography. The correlated basalts thicken eastward from 20 m (Chaparrosa Peak) to 60 m (Pioneertown) (Neville, 1983), suggesting that the source vent for the basalts was situated closer to the Pioneertown flows. This would require that basalts flowed east to west, but presently these flows are resting on the down-to-the-east tilted weathered surface (Figure 37). This implies that present-day eastward tilt of the plateau's flank was produced tectonically following the late Miocene, and thus the paleotopographic high of the central plateau did not extend this far eastwards.

If the basalts higher up on the plateau, such as at Onyx Peak (~2.5 km, Figure 9a), also had sources to the east, the paleotopographic high may have been confined to only the very center of the plateau. This could be tested by finding paleoflow directions in basalts or identifying their sources, but it does suggest a limit to the magnitude of relief that existed between the central plateau and flanks.

3.8.4 Summary

The deposits atop the weathered surface offer several conclusions for its origin. On the east and west, Tertiary deposits demonstrate that parts of the weathered surface formed prior to uplift. Extrapolation of the buried surface from beneath basalts on the east shows that average incision since the late Miocene is <150 m (or <0.02 mm/yr), implying that erosion has outpaced weathering and consistent with slow weathering rates determined elsewhere. The weathered horizon east and west, as well as the deposits themselves, thus represent old, relict topography. Atop the central plateau, the magnitude of syn-uplift erosion is not known, but is limited by the preservation of pre-incision quartzite gravels. Other observations, such as the preservation of thick regolith, gentle character of topography and drainages, and thick vegetative cover, further suggest that erosion atop the central plateau is slower than along eastern and western flanks (see Sections 3.6.6). Average, syn-uplift erosion atop the central plateau is thus likely to be <<150 m.

Overlying units also show that the weathered surface locally had a gentle, slightly undulating topography during the late Miocene. Although overlying units do not constrain the broad, pre-uplift geometry of the weathered surface, paleogeographic indicators suggest a paleotopographic high existed in the late Miocene and Pliocene where the plateau now sits. Although the magnitude of this relict high is not known, it had to have been above depositional base-level and supplied quartzite clasts to the surrounding area. The resistant quartzite bedrock atop the central plateau may thus have been exposed prior to uplift, further emphasizing the antiquity of topography there. Such a paleotopographic high may

be partly related to displacement on the Squaw Peak thrust system in late Miocene and early Pliocene (Meisling and Weldon, 1989).

3.9. Conclusions: The development of the weathered surface and its use as a structural datum

This investigation offers insight as to whether or not the geomorphology of the Big Bear plateau constrains tectonic displacement. Observations confirm that the plateau is mantled by a low-relief surface, which consists of highly decomposed rock and fits the classic character of deep granitic weathering (cf. Ollier, 1975; Twidale, 1990). To serve as a structural datum, the surface's present distribution, age, pre-deformational geometry, and degree of modification by other factors since uplift (i.e., erosion) must be constrained. The distinctive character of the surface has enabled it to be mapped in detail. This character alone, however, is not indicative of its age or the conditions that formed it and does not show whether the surface is relict or time-transgressive. An evaluation of whether it represents a structural datum thus requires that an understanding of its development be synthesized from the above observations.

The weathered surface is a geologic feature, which is well represented by the idealized weathered profile (Figure 23). Its distribution atop the plateau is widespread, occurring on an irregular network of interfluves that is roughly contiguous and without major perturbations in elevation across the plateau (Figure 9a). Gaps in the surface are primarily the result of lithology, alluvial cover, or canyon incision from the plateau perimeter. Canyons cut fresh bedrock, and the weathered surface does not taper downwards at canyon margins. This is somewhat of a cross-cutting geomorphic relationship, which indicates that either dissection of the plateau post-dates development of the weathered profile or that erosion has vastly outpaced accumulation of weathered rock within canyons. The former possibility is supported by the observation of scattered

quartzite gravels overlying weathered granite, which probably traveled across the plateau prior to incision of modern canyons (unless recycled) (Sadler and Reeder, 1983). On the eastern and western plateau flanks and neighboring Mojave Desert and Santa Ana Valley, saprolite profiles buried by Tertiary deposits unequivocally indicate that, at least locally, deep weathering preceded uplift (Figure 9a). Unique correlations between these profiles and unburied patches of weathered granite elsewhere, however, have not been made. Also on the east and west, faults offset the surface and expose fresh bedrock (e.g., Squaw Peak thrust, Figure 10; Helendale fault, Figures 1a, 9a), showing that, at least locally, the weathering predates deformation of the plateau.

Granitic weathering is likely ongoing across humid parts of the plateau (Figure 8), given the similar climate of other actively weathering granitic terrains. Granite is unstable at the Earth's surface and weathers when exposed to water, so that, unlike the arid Mojave Desert (Oberlander, 1972), subsurface granitic decay is fostered where groundwater is trapped in the regolith mantle atop the plateau. Although granitic weathering may not be strictly relict, however, it is still possible that the weathered granitic landform represents a horizon that developed over a protracted duration. Stretches of the surface marked by inselbergs and corestones are fossil (i.e., weathered prior to regolith stripping; Twidale, 1990), yet roughly coplanar with stretches that may experience active decay. This suggests the entire surface is relatively ancient. In addition, by analogy with weathering rates in other granitic terrains, the thick weathered profile may have required several million years to accumulate.

If the surface did require a prolonged period of accumulation and development, the preservation of the saprolite profile may mark where the plateau has escaped major syn-uplift denudation. This is supported by the localized preservation of pre-incision quartzite gravels and Tertiary deposits atop the plateau (Sadler and Reeder, 1983). Quartzite bedrock presently exposed atop the central plateau has also been a source of clasts since the Miocene (Sadler and Reeder, 1983), indicating the antiquity of topography there. A

paucity of syn-uplift denudation is also supported by the character of streams that lace, rather than dissect, the weathered surface. These seem to represent a relict template of a gentle, mature system that has not yet equilibrated to a high relief perch, and suggest significant erosion of the plateau has been limited to rapid incision into fresh bedrock near the plateau perimeter. The cooling history of the plateau, based on radiogenic helium thermochronometry, is also consistent with low Cenozoic denudation (Spotila et al., 1998).

The eastern flank of the plateau has been denuded ~150 m (removed granite, saprolite, and basalt) since the late Miocene, but the central plateau has likely experienced even less erosion. The eastern flank should erode more rapidly due to lack of vegetation associated with arid conditions (cf. Douglas, 1967; Bloom, 1991; p.312) and steeper topographic gradients associated with the plateau's convexity (Figure 4). The degree of erosion is reflected in differences of the exposed levels of the idealized weathered profile across the plateau. The poorer preservation of the weathered surface on the east, limited to bouldery patches along narrow interfluves, is consistent with having experienced greater denudation than the more pristine surface (soils, thick regolith) of the central plateau. The topography and drainages of the eastern flank are similarly commensurate with a greater magnitude of erosion. The central plateau may thus have been eroded only slightly (10's of meters) during the past several million years of uplift. Variations in the exposed level of the weathered profile across the plateau, further indicate that erosion postdates or outpaces weathering. Thus, the upland surface has not likely been modified significantly by syn-uplift erosion or weathering.

If the gross topography (0.1-1 km relief) of the weathered surface has gone unmodified by weathering and erosion since uplift initiated, its shape may reflect tectonic dislocation. To determine the tectonic signal, however, the previous geometry of the surface must be constrained. It is not safe to assume that the surface was flat, simply because it is deeply weathered, given the range of topography of other actively weathering granitic terrains. Over short lengthscales (<1 km), the weathered surface is gentle and

undulating, both where exposed and where buried by Tertiary deposits. This is probably the result of slight variations in erosion of regolith (syn- or post-weathering) or the weatherability (i.e., joint spacing, texture, composition) of the bedrock (i.e., etchforms; Twidale, 1990). Over longer distances, the elevation of the weathered granite surface changes only gradually, except where abrupt steps occur at faults (e.g., the Helendale fault; Figure 1a, 9a). While this broad form may be the product of tectonic dislocation, it may also partly represent a pre-uplift, dome-like topography. Paleogeographic indicators (clast provenance, paleoflow, sediment thickness, etc.) imply that the location of today's central plateau has been above depositional base-level since the mid-Miocene. The magnitude of this paleo-high, however, is not constrained by available data. Given that significant relief is not indicated by these paleogeographic indicators, it is likely this paleo-high was minor.

Despite this uncertainty, the weathered surface provides greater constraint on the geomorphic history and uplift magnitude of the Big Bear plateau than topography alone. The present distribution of the surface, less its pre-uplift geometry, seems to define gross structural relief. To restore the vertical displacement, several assumptions regarding the initial shape of the surface must be made, and several measures must be taken to limit other inherent uncertainties. The following guidelines will be followed in creating structure contour diagrams in Chapter 4 for the reconstruction of vertical displacement from the weathered surface:

- Present elevations should be defined only by large, mapped patches of the surface (minimum dimension ~0.5 km), which unequivocally exhibit characteristics of deep weathering and are developed on granitic rock (preferably quartz or biotite monzonite). This will eliminate small, low-relief surfaces of dubious origins from the reconstruction (such as rounded ridgelines), and ensure that elevation differences are not due to lithologic contrasts (etching).
- Present elevations should be defined from an approximately uniform structural level within the idealized weathered profile (Figure 23), to avoid variations in exposure level due

to subsequent erosion and topogrpahic variations due to irregularities in the geometry of the subsurface weathering front. For example, elevations should not be taken from negative relief forms where gentle streams may have flowed, but from subtle, positive relief forms (i.e., crests of hummocks) that likely represent a uniform structural level. In addition, elevations should not be taken from the tops of the largest inselbergs (tors), which were likely exposed above the base of the low-relief surface throughout the course of weathering (cf. Twidale, 1990).

- Uncertainty limits should be assigned to the present elevation distribution of the surface that account for these variations in the profile level exposed. Where the weathered surface is preserved, the magnitude of erosion has likely been less than the thickness of the weathered profile (<50 m), based on typical rates of granite weathering and the maximum magnitude of incision on the east (where the surface is almost completely removed). Present elevations along the surface may thus have been lowered by erosion by as much as 50 m in the past few million years. Variations in the geometry of the subsurface weathering front are of a similar amplitude, as represented by the topographic undulations of the surface where overlying regolith has been stripped away. The typical short-wavelength undulations in the weathered surface and in the elevations of overlying quartzite gravels (~6°, Table 2) suggest that elevations along the positive relief forms may be as much as 50 m higher than the surrounding base-level. Uncertainty of $\pm$50 m ($\pm$100 m conservatively) should thus apply to elevations in reconstruction of weathered surface.
- The pre-uplift geometry of the surface should be approximated by the present elevations of the weathered profile outside of the range (i.e., where exposed or buried in the Mojave and Santa Ana Valley). This will partly avoid the paleotopographic high and is more reasonable than arbitrarily restoring the surface to a flat geometry. For example, subtracting the elevations of hanging wall and footwall weathered surfaces along the escarpments of thrust faults gives the vertical displacement without having to know the original geometry of the surface. Where adequate control on the geometry of the surface is

not available, however, all that can be done is to assume that it was nearly flat prior to uplift. Given the possibility that the plateau had paleotopography in its central portion, this assumption makes the displacement field that results an upper limit.

There are several possible tests of the above interpretations, which would enhance our understanding of the evolution of the weathered surface. If the weathered surface does mark a horizon of low syn-uplift erosion, many of its exposed granitic landforms should have gone undisturbed for a substantial period of time (cf. Twidale, 1990). This prediction could be tested with cosmogenic nuclide dating, which has been successfully applied to this problem elsewhere (e.g., Bierman et al., 1995). Another test of low erosion would be to determine if sediments derived from the plateau over the past few million years have exceeded the mass eroded during canyon incision. Although the predicted volume of eroded material could be easily determined, however, it would be difficult to assess what fraction of thick, buried alluvium in the surrounding valleys has been derived from the SBMs (as opposed to other ranges).

A final test would be to determined rates of weathering from atop the plateau. An obvious weakness in the above interpretations and the use of the surface as a datum are that actual rates of weathering were not determined in this study, but assumed by analogy with other locations. Although low values typify granitic weathering rates in the literature (Table 8), many previous workers have considered weathering rates to be strongly related to active tectonics. In stable continental interiors, weathering is very slow and bedrock is insulated from weathering action by laterite crusts that are already equilibrated to their environment (e.g., Edmond et al., 1995; Twidale, 1990). Weathering at active margins, however, may be more rapid, due to greater hydraulic gradients and greater surface area of exposed bedrock (Edmond et al., 1995; Thomas, 1994). In addition, the time necessary to create the observed profile is based on the assumption that the weathering front advances downward (i.e., assumed rate of saprolite formation), sub-parallel to the surface. This is an invalid assumption if the weathering front acts over a greater subsurface area due to

complex jointing and corestone distribution. The possibility that the weathered profile could have developed more quickly than assumed could be tested, by determining rates of weathering atop the plateau using either empirical, geochemical mass balance or theoretical kinetics of weathering reactions.

3.10. References

Ahnert, F., Functional relationships between denudation, relief, and uplift in large mid-latitude drainage basins, Amer. Journ. Science, 268, 243-263, 1970.

Aksoy, R., Sadler, P.M., and Biehler, S., Gravity anomalies over sedimentary basins on the Helendale fault trend, *in* Koose, M.A. and Reynolds, R.E., eds., Geology Around the Margins of the Eastern San Bernardino Mountains, Inland Geological Society, I, 121-128, 1986.

Allen, C.R., San Andreas fault zone in San Gorgonio Pass, southern California, Geol. Soc. Amer. Bull., 68, 315-350, 1957.

Axelrod, D.I., Evolution of desert vegetation in western North America, *in* Studies in late Tertiary Paleobotany, Carnegie Inst. Washington Pub., 590, 215-306, 1950.

Barry, R.G., Mountain Weather and Climate, Methuen, NY, 313 pp., 1981.

Bierman, P., and Turner, J., ^{10}Be and ^{26}Al evidence for exceptionally low rates of Australian bedrock erosion and the likely existence of pre-Pleistocene landscapes, Quat. Res., 44, 378-382, 1995.

Bierman, P., Gillespie, A., Caffee, M., and Elmore, D., Estimating erosion rates and exposure ages with ^{36}Cl produced by neutron activation, Geochimica et Cosmochimica Acta, 59, 3779-3798, 1995.

Birkeland, P.W., Soils and Geomorphology, Oxford University Press, New York, 372 pp., 1984.

Bloom, A.L., Geomorphology: A systematic analysis of late Cenozoic landforms, Prentice

Hall, New Jersey, 532 pp., 1991.

Bortugno, E.J., and Spittler, T.E., Geologic map of the San Bernardino Quadrangle, California, 1:250,000, California Division of Mines and Geology, Regional Geologic Map Series, Map No. 3A, 1986.

Brown, G., and Associates, Geology and ground water geology of Big Bear Valley, Assoc. of Engineering Geologists, So. CA Section, Annual Spring Field Trip Guidebook, 73-95, 1976.

Bryant, W.A., Eastern North Frontal Fault Zone and related faults, San Bernardino County, CA Div. Mines and Geo., Fault Evaluation Report, FER-182, 1986a.

Bryant, W.A., Western North Frontal Fault Zone and related faults, San Bernardino County, CA Div. Mines and Geo., Fault Evaluation Report, FER-186, 1986b.

Corbett, E.J., Seismicity and crustal structure of southern California: Tectonic implications from improved earthquake locations (Ph.D. thesis), Pasadena, CA, California Institute of Technology, 1984.

Davis, W.M., The geographical cycle, London Geogr. Journ., 14, 481-508, 1899.

D.O.C., Climatological Data Annual Summary, CA, 97: 13, NOAA, Dept. Comm., 1993a.

D.O.C., Hourly Precipitation Data, CA, v.38-43, NOAA, National Climatic Data Center, National Environmental Data and Information Service, Dept. Comm., 1988-1993b.

Dethier, D.P., Weathering rates and the chemical flux from catchments in the Pacific Northwest, U.S.A., *in* Colman, S.M., and Dethier, D.P., Rates of Chemical Weathering of Rocks and Minerals, Academic Press Inc., 503-530, 1986.

Dibblee, T.W., Geologic map of the Lucerne Valley 15' Quadrangle, scale = 1:62,500, U.S. Geological Survey, Misc. Geologic Investigations Map, I-426, 1964a.

Dibblee, T.W., Geologic map of the San Gorgonio Mountain 15' Quadrangle, scale = 1:62,500, U.S. Geological Survey, Miscellaneous Geologic Investigations Map, I-431, 1964b.

Dibblee, T.W., Geologic map of the Old Woman Springs 15' Quadrangle, scale = 1:62,500, U.S. Geological Survey, Misc. Geologic Investigations Map, I-518, 1967a.

Dibblee, T.W., Geologic map of the Morongo 15' Quadrangle, scale = 1:62,500, U.S. Geological Survey, Misc. Geologic Investigations Map, I-517, 1967b.

Dibblee, T.W., Geologic map of the Redlands 15' Quadrangle, scale = 1:62,500, U.S. Geological Survey, Open File Map, 74-1022, 1974a.

Dibblee, T.W., Geologic map of the Lake Arrowhead 15' Quadrangle, scale = 1:62,500, U.S. Geological Survey, Open File Map, 73-56, 1974b.

Dibblee, T.W., Late Quaternary uplift of the San Bernardino Mountains on the San Andreas and related faults, *in* Crowell, J.C., ed., San Andreas fault in southern California, CA Division of Mines and Geology Special Report, 118, 127-135, 1975.

Dibblee, T.W., Geology of the San Bernardino Mountains, southern California, *in* Fife, D.L. and Minch, J.A., eds., Geology and Mineral Wealth of the California Transverse Ranges, South Coast Geological Society, 149-169, 1982.

Douglas, I., Man, vegetation, and the sediment yield of rivers, Nature, 215, 925-928, 1967.

Eden, M.J., Some aspects of weathering and landform formation in Guyana (formerly British Guiana), Zeitschrift fur Geomorphologie, 15, 181-198, 1971.

Eden, M.J., and Green, C.P., Some aspects of granite weathering and tor formation on Dartmoor, England, Geografiska Annaler, 53A, 92-99, 1971.

Edmond, J.M., Palmer, M.R., Measures, C.I., Grant, B., and Stallard, R.F., The fluvial geochemistry and denudation rate of the Guayana Shield in Venezuela, Columbia, and Brazil, Geochim. et Cosmochim. Acta., 59, 3301-3325, 1995.

Frakes, L.A., Climates Throughout Geologic Time, Elsevier Scientific Publishing Company, NY, 310 pp., 1979.

Gregory, K.M., and Chase, C.G., Tectonic and climatic significance of a late Eocene low-relief, high-level geomorphic surface, Colorado, Journ. Geophys. Res., 99, 20141-

20160, 1994.

Gubbels, T.L., Isacks, B.L., and Farrar, E., High-level surfaces, plateau uplift, and foreland development, Bolivian central Andes, Geology, 21, 695-698, 1993.

Harden, J.W., A quantitative index of soil development from field descriptions: Examples from a chronosequence in central California, Geoderma, 28, 1-28, 1982.

Jacobs, S.E., Geology of a part of the upper Santa Ana River Valley, San Bernardino Mountains, San Bernardino County, California (M.S. Thesis), Los Angeles, California State University, 107 pp., 1982.

Lewis, D.W. and McConchie, D., Analytical Sedimentology, Chapman and Hall, NY, 197 pp., 1994.

Li, Y.-G., Henyey, T.L., and Leary, P.C., Seismic reflection constraints on the structure of the crust beneath the San Bernardino Mountains, Transverse Ranges, southern California, Journ. Geophys. Res., 97, 8817-8830, 1992.

Linton, D.L., The problem of tors, London Geog. Journ., 121, 470-487.

Mabbutt, J.A., The weathered land surface in Central Australia, Zeitschrift fur Geomorphologie, 9:1, 82-114, 1965.

MacColl, R.S., Geochemical and structural studies in batholithic rocks of southern California: Part 1, Structural geology of the Rattlesnake Mountain Pluton, Geol. Soc. Amer. Bull., 75, 805-822, 1964.

Madole, R.F., Bradley, W.C., Loewenherz, D.S., Ritter, D.F., Rutter, N.W., and Thorn, C.E., The Rocky Mountains, *in* Graf, W.L., ed., Geomorphic Systems of North America, Geol. Soc. Amer., Centennial Special Volume 2, 211-258, 1987.

Matti, J.C., and Morton, D.M., Paleogeographic evolution of the San Andreas fault in southern California: A reconstruction based on a new cross-fault correlation, *in* Powell, R.E., Weldon, R.J., and Matti, J.C., eds., The San Andreas fault system: Displacement, palinspastic reconstruction, and geologic evolution, Geol. Soc. Amer. Memoir, 178, 107-160, 1993.

May, S.R., and Repenning, C.A., New evidence for the age of the Old Woman sandstone, Mojave Desert, California, *in* Sadler, P.M., and Kooser, M.A., eds., Late Cenozoic stratigraphy and structure of the San Bernardino Mountains, Geol. Soc. Amer. Cordilleran Section Meeting Guidebook, 6, 93-96, 1982.

Meisling, K.E., Neotectonics of the north frontal fault system of the San Bernardino Mountains: Cajon Pass to Lucerne Valley, California (Ph.D. thesis), Pasadena, CA, California Institute of Technology, 394 pp., 1984.

Meisling, K.E., and Weldon, R.J., Late Cenozoic tectonics of the northwestern San Bernardino Mountains, southern California, Geol. Soc. Amer. Bull., 101, 106-128, 1989.

Mendenhall, W.C., Two mountain ranges of southern California (abstract), Geol. Soc. Amer. Bull., 18, 660-661, 1907.

Minnich, R.A., Snow levels and amounts in the mountains of southern California, Journ. of Hydrology, 89, 37-58, 1986.

Molnar, P., and Lyon-Caen, H., Some simple physical aspects of the support, structure, and evolution of mountain belts, *in* Clark, S.P. Jr., Burchfiel, B.C., and Suppe, J., eds., Processes in Continental Lithospheric Deformation, Geol. Soc. Amer. Special Paper, 218, 179-207, 1988.

Montgomery, D.R., Valley incision and the uplift of mountain peaks, Journ. Geophys. Res., 99, 13913-13921, 1994.

Morton, D.M., personal communication cited in Neville (1983), 1980.

Munsell, Soil Color Charts, Munsell Color Company, Baltimore, 1971.

Nettleton, W.D., Flach, K.W., and Nelson, R.E., Pedogenic weathering of tonalite in southern California, Geoderma, 4, 387-402, 1970.

Neville, S.L., and Chambers, J.M., Late Miocene alkaline volcanism, northeastern San Bernardino Mountains and adjacent Mojave Desert, *in* Cooper, J.D., ed., Geologic excursions in the Transverse Ranges, Geol. Soc. Amer. Annual Meeting Guidebook,

Fullerton, California, California State University, 103-106, 1982.

Neville, S.L., Late Miocene alkaline volcanism, south-central Mojave Desert and northeast San Bernardino Mountains, California, M.S. Thesis, University of California at Riverside, 143 pp., 1983.

Noble, L.F., The San Andreas rift in the desert region of southeastern California, Carnegie Institute of Washington Yearbook, 31, 355-363, 1932.

Oberlander, T.M., Morphogenesis of granitic boulder slopes in the Mojave Desert, California, Journal of Geology, 80, 1-20, 1972.

Ollier, C.D., Some features of granite weathering in Australia, Zeit. f. Geomorph., 9, 285-304, 1965.

Ollier, C.D., Weathering, Longman Group Limited, London, 304 pp., 1975.

Paces, T., Rates of weathering and erosion derived from mass balance in small drainage basins, *in* Colman, S.M., and Dethier, D.P., Rates of Chemical Weathering of Rocks and Minerals, Academic Press Inc., 531-550, 1986.

Pavich, M.J., Processes and rates of saprolite production and erosion on a foliated granitic rock of the Virginia Piedmont, *in* Colman, S.M., and Dethier, D.P., Rates of Chemical Weathering of Rocks and Minerals, Academic Press Inc., 552-590, 1986.

Pavich, M.J., Regolith residence time and the concept of surface age of the Piedmont "Peneplain," Geomorphology, 2, 181-196, 1989.

Pavich, M.J., Brown, L., Valette-Silver, J.N., Klein, J., and Middleton, R., ^{10}Be analysis of a Quaternary weathering profile in the Virginia Piedmont, Geology, 13, 39-41, 1985.

Peterson, D., Patterns of Quaternary denudation and deposition at Pipes Wash, Mojave Desert, California (Ph.D. thesis), Univ. Cal. Riverside, 279 pp., 1976.

Power, E.T., and Smith, B.J., A comparative study of deep weathering and weathering products: Case studies from Ireland, Corsica, and Southeast Brazil, *in* Robinson, D.A., and Williams, R.B.G., Rock Weathering and Landform Evolution, John Wiley and

Sons, 21-40, 1994.

Proctor, R.J., Geology of the upper Coachella Valley area, California, California Division of Mines and Geology Special Report, 94, 8-43, 1968.

Reynolds, R.E., and Reeder, W.A., Age and fossil assemblages of the San Timoteo Formation, Riverside County, California, *in* Kooser, M.A. and Reynolds, R.E., eds., Geology around the margins of the eastern San Bernardino Mountains, Inland Geological Society, 1, 51-56, 1986.

Riley, F.S., Data on water wells in Lucerne, Johnson, Fry, and Means Valley, San Bernardino County, CA, U.S.G.S., Open File Report, 1956.

Ringrose, P.S., and Migon, P., Analysis of digital elevation data for the Scottish Highlands and recognition of pre-Quaternary elevated surfaces, in Widdowson, M., ed., Palaeosurfaces; recognition, reconstruction, and palaeoenvironmental interpretation, Geol. Soc. Special Publ., 120, 25-35, Geol. Soc. of London, 1997.

Ruxton, B.P., and Berry, L., Weathering of granite and associated erosional features in Hong Kong, Bull. Geol. Soc. Amer., 68, 1263-1292, 1957.

Sadler, P.M., An introduction to the San Bernardino Mountains as the product of young orogenesis, *in* Cooper, J.D., ed., Geologic excursions in the Transverse Ranges, Geol. Soc. Amer. Annual Meeting Guidebook, Fullerton, California, California State University, 57-65, 1982a.

Sadler, P.M., Provenance and structure of late Cenozoic sediments in the northeast San Bernardino Mountains, *in* Cooper, J.D., ed., Geologic excursions in the Transverse Ranges, Geol. Soc. Amer. Annual Meeting Guidebook, Fullerton, California, California State University, 83-91, 1982b.

Sadler, P.M., The Santa Ana basin of the central San Bernardino Mountains: Evidence of the timing and uplift and strike-slip relative to the San Gabriel Mountains, *in* Powell, R.E., Weldon, R.J., and Matti, J.C., eds., The San Andreas fault system: Displacement, palinspastic reconstruction, and geologic evolution, Geol. Soc. Amer.

Memoir, 178, 307-322, 1993.

Sadler, P.M., Demirer, A., West, D., and Hillenbrand, J.M., The Mill Creek basin, the Potato Sandstone, and fault strands in the San Andreas fault zone south of the San Bernardino Mountains, *in* Powell, R.E., Weldon, R.J., and Matti, J.C., eds., The San Andreas fault system: Displacement, palinspastic reconstruction, and geologic evolution, Geol. Soc. Amer. Memoir, 178, 289-306, 1993.

Sadler, P.M., and Reeder, W.A., Upper Cenozoic, quartzite-bearing gravels of the San Bernardino Mountains, southern California; recycling and mixing as a result of transpressional uplift, *in* Anderson, D.W., and Rymer, M.J., eds., Tectonics and sedimentation along faults of the San Andreas system, Los Angeles, California, Society of Economic Paleontologists and Mineralogists, Pacific Section, 45-57, 1983.

Saunders, I., and Young, A., Rates of surface processes on slopes, slope retreat, and denudation, Earth Surface Processes and Landforms, 473-501, 1983.

Schlemon, R.J., Quaternary soil-geomorphic relationships, southeastern Mojave Desert, CA and AZ, in Fife, D.L. and Brown, A.R., eds., Geology and Mineral Wealth of the California Desert, South Coast Geological Society, 388-402, 1980.

Schumm, S.A., The disparity between present rates of denudation and orogeny, U.S. Geological Survey Professional Paper, 454-H, 13 pp., 1963.

Shreve, R.L., Statistical law of stream numbers, Journal of Geology, 74, 17-37, 1966.

Spotila, J.A., Farley, K.A., and Sieh, K., Uplift and erosion of the San Bernardino Mountains associated with transpression along the San Andreas fault, California, as constrained by radiogenic helium thermochronometry, Tectonics, in press, 1998.

Strahler, A.N., Dynamic basis of geomorphology, Geol. Soc. Amer. Bull., 63, 923-938, 1952.

Teeuw, R.M., Comparative studies of two adjacent drainage basins in Sierra Leone: some insights into tropical landscape evolution, Zeitschrift fur Geomorphologie, NF35(3), 257-267, 1991.

Teeuw, R.M., Thomas, M.F., and Thorp, M.B., Regolith and landscape development in the Koidu Basin of Sierra Leone, *in* Robinson, D.A., and Williams, R.B.G., Rock Weathering and Landform Evolution, John Wiley and Sons, 303-320, 1994.

Thomas, M.F., Ages and geomorphic relationships of saprolite mantles, *in* Robinson, D.A., and Williams, R.B.G., Rock Weathering and Landform Evolution, John Wiley and Sons, 287-301, 1994.

Torrent, J., Schwertmann, U., and Schulze, D.G., Iron oxide mineralogy of some soils of two river terrace sequences in Spain, Geoderma, 23, 191-208, 1980.

Twidale, C.R., The origin and implications of some erosional landforms, Journ. of Geology, 98, 343-364, 1990.

U.S.D.A., Soil Survey of San Bernardino County, CA: Mojave River area, U.S. Dept. Agriculture, Soil Conservation Service, 1986.

Vaughan, F.E., Geology of the San Bernardino Mountains north of San Gorgonio Pass, Univ. Cal., Dept. Geol. Sci. Bull., 13, 319-411, 1922.

Velbel, M.A., Geochemical mass balances and weathering rates in forested watersheds of the southern Blue Ridge, Amer. Journ. Science, 285, 904-930, 1985.

Wahrhaftig, C., Stepped topography of the southern Sierra Nevada, California, Geol. Soc. Amer. Bull., 76, 1165-1190, 1965.

Williams, A.G., Ternan, L., and Kent, M., Some observations on the chemical weathering of the Dartmoor granite, Earth Surface Processes and Landforms, 11, 557-574, 1986.

Woodburne, M.O., Cenozoic stratigraphy of the Transverse Ranges and adjacent areas, southern California, Geol. Soc. Amer. Special Paper, 162, 91p., 1975.

Chapter Four

Uplift kinematics of the San Bernardino Mountains, based on constraints from deformation of a deeply weathered surface

Spotila, James A.

California Institute of Technology

August, 1998

4.1. Abstract

The structural datum represented by the weathered surface atop the San Bernardino Mountains provides an excellent opportunity to learn about the kinematics of uplift. This horizon constrains the vertical displacement field of the Big Bear plateau in fine detail, and thus presents a chance to determine the degree of activity, subsurface architecture, and displacements along the major thrust faults (North Frontal thrust system, NFTS; Santa Ana thrust, SAT) of the range. The pattern of vertical deformation was determined by differencing the distributions of the weathered surface atop the hanging wall and footwall blocks. This deformation field shows that bounding thrusts have smooth, bell-shaped distributions of vertical displacement that reach a maximum of 1.8 km on the north and 1.1 km on the south. The corresponding net-slip along the NFTS is ~3.1 km, implying a slip rate of ~1.6 mm/yr over the past 2 Myr, but net-slip along the SAT is smaller (~2.2 km). Geomorphic analysis of these thrusts indicates the NFTS has been active at least up to the latest Pleistocene and may be decelerating, while the SAT displays little evidence for Quaternary motion and may have been dead for several Myr. A structural analysis of the pattern of vertical deformation suggests the northern thrust must steepen on the east but flattens on the west, thus implying a complex architecture that includes possible interaction with the southern thrust and upper-plate penetration by discontinuous strike-slip faults. The east-west variation in north-south horizontal shortening along these thrust faults is remarkably similar to that on high angle structures responsible for uplifting the San Gorgonio block and smaller crustal slices to the south. All combined, horizontal shortening in the range reaches a maximum of ~6.3 km and is tightly focused just northwest of the restraining bend in the San Andreas fault at San Gorgonio Pass. This suggests a local geometric complexity along the strike-slip fault zone is responsible for producing convergence that uplifted the range and that this fault bend has been fixed relative to the eastern side of the fault zone throughout the past few Myr due to transrotating domains in the Mojave Desert and eastern Transverse Ranges.

4.2. Introduction

The San Bernardino Mountains (SBMs) of southern California presently lie at a hub of major structural elements within the right-lateral boundary of the Pacific and North American plates, where several major strike-slip fault systems meet the San Andreas fault zone near its "Big Bend" and the smaller restraining bend of San Gorgonio Pass (Figure 1). This young mountain range has uplifted during the past few million years of evolution of the transpressive plate margin, and thus its kinematic history represents the long-term development of a complex strike-slip system. The basic development and the causal mechanisms of the complex pattern of deformation in southern California are not well understood (cf. Weldon et al., 1993). The SBMs thus offer a valuable opportunity to study how uplift and exhumation relate to convergence across strike-slip faults and the role of such transpression in the long-term (Myr) evolution of major transcurrent systems.

The Big Bear plateau, which makes up the bulk of the SBMs, has been uplifted along opposed, east-west trending thrust faults that bound it on the north (North Frontal thrust system [NFTS]) and south (Santa Ana thrust [SAT]) (Figure 2). Because of the lack of previously documented structural datums atop this crystalline block, its vertical deformation pattern and the kinematics of the low-angle structures are not well constrained. As a result, several basic problems regarding the relationship of orogeny and Pacific-North America transcurrent plate motion are outstanding.

One unsolved problem of the relationship between strike-slip fault development and orogeny in the SBMs is the means by which convergence across the San Andreas fault is translated into uplift. To understand how horizontal plate motions relate to the observed vertical displacements, the subsurface geometry of the structures that produce this uplift and link it to the San Andreas fault zone must be constrained. There are two basic conceptualized structural systems that can explain how strike-slip plate motion may be partitioned and accommodated by transpressive deformation. One idea is that horizontal shortening due to convergence across a strike-slip plate boundary may be accommodated in

fold and thrust belts, which may be decoupled from the strike-slip fault and internally deform one (or both) of the adjoining plates (e.g., the western Transverse Ranges; Namson and Davis, 1988) or occur as oblique "sawtooths" between segments of the strike-slip zone itself (e.g., Southern Alps thrusts along the Alpine fault, New Zealand; Norris and Cooper, 1997). A second concept is that near-vertical strike-slip faults themselves, as well as associated, subparallel, high-angle faults, accommodate convergence with oblique displacements. This concept predicts that the geometry of transpressive systems at depth is similar to palm-trees (cf. Sylvester, 1988), and has been interpreted to be the mode of deformation in the Loma Prieta earthquake and uplift of the Santa Cruz Mountains (Jones and Wesnousky, 1992; Schwartz et al., 1990).

The present hypotheses for the structural architecture of the SBMs also fit into these two basic concepts. Some previous studies have postulated that the northern thrust fault merges with a low-angle detachment at depth, citing as evidence the southward-deepening base of microseismicity (~10°S dip; Corbett, 1984), the seismic reflectivity of this apparent brittle-plastic transition (Li et al., 1992), several deep, small magnitude earthquakes with shallow nodal planes (Webb and Kanamori, 1985), and the lack of offset of an upper mantle seismic velocity anomaly (Hadley and Kanamori, 1977). This feature may decouple the brittle upper crust from ductile lower crust or could represent a lithologic boundary (perhaps between upper batholithic rocks and lower Pelona schist). In this hypothesis, the NFTS flattens at depth and is the main uplift structure for the Big Bear plateau, implying that the SAT is not necessary or significant. Other studies have alluded to the symmetry of thrusting on the north and south as evidence that a near-vertical, mushroom-shaped zone of distributed transpression occurs beneath the range (Sadler, 1982b). This hypothesis predicts that the NFTS and SAT are antithetic thrusts that steepen and merge at depth. The likelihood that oblique reverse motion along high-angle strands of the San Andreas fault zone itself is responsible for uplift and exhumation of crustal blocks in the southern SBMs similarly illustrates the importance of high angle structures (Spotila et al., 1998).

Direct evidence has yet to link near-surface faulting with proposed deeper crustal structures. The key to resolving the problematic structural kinematics of the SBMs is to constrain the crustal-scale geometry of the main thrusts and their relationship to the high-angle fault systems on the south. To do this, the relative contributions and displacement histories of the NFTS and SAT to the uplift of the Big Bear plateau must also be determined. This requires that an understanding of the major thrust faults be acquired, beyond existing knowledge, as described below.

The NFTS dips gently southward (~30°; based on field observations; Meisling, 1984; Miller, 1987) beneath the east-west trending, northern escarpment of the Big Bear block, and has juxtaposed crystalline basement rocks over Plio-Pleistocene sediments by pure thrust motion (Woodford and Harriss, 1928; Dibblee, 1975). It is considered a thrust system (Meisling and Weldon, 1989), because it does not consist of a single fault at the surface, but of a complex series of discontinuous fault strands and folds (such as the White Mountain thrust, Ord Mountain fault, and Ocotillo fold) across a zone about a kilometer wide (Sadler, 1982a, 1982b; Meisling, 1984; Bryant, 1986a, 1986b; Miller, 1987). This system may merge into a single fault plane at depth that is responsible (at least in part) for uplift of the Big Bear plateau, although its full crustal geometry is not constrained. Based on a seismic reflection profile across (Li et al., 1992), the NFTS retains is gentle dip in the upper kilometer or so of crust, but no data has constrained its orientation below this. The location of the thrust fault may be related in part to a broad stack of early-Tertiary, cataclastic detachments, which served as a pre-existing zone of weakness (Meisling, 1984; Silver, 1982). There is uncertainty as to whether the NFTS, which initiated sometime shortly after the 2-3 Ma deposition of the southward-flowing, low-energy facies of the Old Woman Sandstone and resulted in shedding of coarse debris to the north (May and Repenning, 1982), is presently active. Sadler (1982a, 1982b) proposed that the NFTS has gone extinct, based on observations of northwest-trending dextral faults that appear to have penetrated and modified its hanging-wall block (Figure 2). Meisling and Weldon (1989)

also propose that the NFTS was primarily active prior to ~1.5 Ma, based on the size and age of its scarps and the inference that deformation shifted to the San Andreas fault at about this time. Miller (1987) and Bryant (1986a, 1986b), however, argue that strike-slip faults do not have appreciable displacement in the upper plate of the NFTS and that there is ample evidence for latest Pleistocene (and perhaps even Holocene) offset along the thrust.

Opposite to the NFTS is the SAT, which dips gently northwards (~30°; based on field observations) along the southern escarpment of the Big Bear block and juxtaposes crystalline basement over the Mio-Pliocene Santa Ana Sandstone with major thrust (Jacobs, 1982; Sadler, 1993) and minor sinistral (Stout, 1976) motion. Motion along this thrust is loosely bracketed by 6.2 Ma basalt flows that it cuts on the east (Woodburne, 1975; McJunkin, 1976; Stout, 1976) and late Pleistocene alluvium that buries much of its trace (Dibblee, 1964a, 1974a). Although the opposing position of this thrust fault elicits the notion that it has played a role in uplift of the Big Bear block in conjunction with the NFTS, Meisling and Weldon (1989) have proposed that the SAT was a part of the south-vergent Squaw Peak thrust system, which was active prior to 4.1 Ma (age of Phelan Peak formation that locally overlies it). This proposal is based on the similarity between the relationship of the SAT and Santa Ana Sandstone with that of the Waterman Canyon fault and Crowder (9.5-17 Ma) formation to the west (Figure 2) (Weldon et al., 1993). Sadler and Reeder (1983), while not arguing the SAT is active, proposed the SAT consumed 10 km of Santa Ana Sandstone (based on clast roundness) and that it was of major importance to the uplift of the SBMs. The lack of more evidence for the timing of motion on the SAT, however, has obscured its role in creation of the modern topography. The relationship of the SAT and NFTS is thus poorly known, and in turn, the structural architecture and kinematics of uplift of the Big Bear plateau are unconstrained.

The second major unsolved problem of the relationship between strike-slip fault development and orogeny in the SBMs is the nature of the driving conditions responsible for the convergence that produced them. There are three major mechanisms that could

explain the convergence that built the SBMs. First, the SBMs may be analogous to the Transverse Ranges to the west of the San Andreas fault zone, which may owe their origins to convergence necessitated by the Big Bend in the San Andreas fault system in southern California (cf. Dickinson, 1996). The motion vector of the Pacific plate relative to the North American plate is directed N38°W (5 cm/yr) in the Transverse Ranges province (DeMets, 1995), but the San Andreas fault zone has a local trend of N65°W (in comparison a trend of N40°W north of the Garlock fault and N46°W through the Coachella Valley to the Salton Trough; Figure 1). This obliquity may require substantial plate motion to be accommodated by a broad zone of crustal thickening and block rotation in the Transverse Ranges, which the SBMs may be a part of. An alternative hypothesis is that a slab of cold, dense mantle lithosphere is sinking beneath the SBMs and Transverse Ranges and exerting tractions at the base of the crust that induce convergence and high topography above (cf. Humphreys et al., 1984; Sheffels and McNutt, 1986). This idea is based on the existence of a positive seismic velocity anomaly in the mantle under the Transverse Ranges that extends from 50 to 200 km depth. Finally, local convergence associated with geometric complexities along strike-slip faults in the San Andreas transform system may be sufficient to explain local crustal thickening in parts of the Transverse Ranges (cf. Humphreys and Weldon, 1994). Specifically, it has been proposed that the SBMs uplifted due to convergence in the restraining bend in the San Andreas fault at San Gorgonio Pass (Figure 1) (Dibblee, 1975; Weldon and Humphreys, 1986; Bennet et al., 1996). Spotila et al. (1998) also demonstrate that exhumation of small crustal blocks in the southern SBMs appears related to geometric complexities along the San Andreas fault zone.

To address these outstanding problems of SBMs neotectonics, the uplift kinematics of the Big Bear plateau must be constrained. A determination of the vertical displacement field of the range is a requisite, first order constraint, which could elucidate the roles and subsurface geometry of the bounding thrust faults and illustrate the spatial distribution of deformation with respect to potential causal mechanisms of SBMs' convergence. The

magnitude of recent rock uplift is locally demonstrated with thermochronometry (Spotila et al., 1998), but across the Big Bear plateau and the eastern San Gorgonio block the only control is the minimum constraint of topography. A new dataset that can provide a detailed estimate of rock uplift and exhumation is the low-relief, deeply weathered granitic surface, which was presented in Chapter 3 (Figure 2). This is a geologic feature that limits the magnitude of syn-uplift erosion and can be used (with some uncertainty) as a datum to reconstruct the vertical displacement field of the range. The weathered surface may not be an ideal structural datum and danger does exist in its use, but it represents the best opportunity to constrain the vertical displacement field of the range to the resolution necessary to make useful structural interpretations and to investigate how strike-slip plate motions translate to orogeny.

The initial goal of this study was to determine the vertical displacement field of the SBMs, by differencing structure contour diagrams of the weathered surface on upthrown (hanging wall; Big Bear and San Gorgonio blocks) and downthrown (footwalls; Mojave Desert, Santa Ana valley) sides of block-bounding structures (Figure 2). The weathered surface has permitted a determination of this displacement field with uncertainties that are small in comparison to the magnitude of vertical motion. As a result, the magnitude of motion along the near-surface NFTS and SAT are constrained. In addition, interpretations of their subsurface structure and relative role in uplift of the Big Bear plateau can be made from structural analyses of the pattern of vertical deformation, much as coseismic displacement fields reveal the source fault of individual earthquakes (e.g., Savage and Hastie, 1966). These interpretations are supplemented by geologic and geomorphic observations that bear on the relative degree of activity along the two thrust faults throughout the history of the SBMs. An assessment of dextral faults within the range also explores the degree to which thrusting has been replaced by strike-slip faulting, which bears on the kinematics of the SBMs. As a result, a new solution to the architecture of the

SBMs has been developed, which displays elements of previous concepts for the relationship of strike-slip faulting and orogeny.

The reconstruction of the weathered surface also provides a detailed constraint on the magnitude of rock uplift associated with the Big Bear plateau. When coupled with previous assessment of rock uplift in the southern SBMs (Spotila et al., 1998), a determination of horizontal shortening across the axis of the range can be made. The variation in convergence across the range provides new evidence that the SBMs were created locally in association with the restraining bend of San Gorgonio Pass, rather than by far-field transpression along the Big Bend or by downwelling in the mantle. Finally, both new kinematic understanding of the SBMs and direct fault observations themselves provide the basis for an assessment of likely future earthquake activity in the region.

4.3. Methodology

The first part of this study involves the use of the weathered surface to determine the vertical displacement field of the SBMs. A detailed reconstruction was possible atop the Big Bear plateau and San Gorgonio block, based on guidelines developed in Chapter 3 (Section 3.9). Determining the distribution of the surface in the surrounding lowlands, however, is less accurate and required different methods to determine the depth of burial beneath alluvium. These methodologies are described in detail below.

The next part of the study is an analysis of the geomorphic and geologic expressions of the NFTS and SAT, designed to elucidate the relative degree to which they have experienced activity during uplift of the Big Bear plateau. This is performed following the methods of Bull (1977) and using standard techniques of airphoto and topographic map interpretation, as well as by summarizing existing mapping and other published constraints. The assessment of dextral faulting within the SBMs that follows is based on similar techniques of establishing geomorphic and geologic evidence for fault

motion, and includes both original and previously published observations. Finally, structural analyses are presented, which include calculation of thrust displacements, construction of interpretive cross sections, and mass-balance determination of horizontal shortening across the range. The methods of these structural analyses are presented in tandem with their executions.

4.3.1 Structure contour diagram of the weathered surface atop the SBMs

To construct the structure-contour diagram of the weathered surface atop the Big Bear plateau and San Gorgonio block, guidelines were followed, based on the understanding of the nature of the surface developed in Chapter 3. Because of the variation in the exposure level of the surface relative to the schematic profile of deep weathering (see Figures 9 and 23 of Chapter 3), elevations for structure contours were selected only from points that most closely fall within the same structural level within the weathered profile. About three thousand sample points, shown on Figure 3 (Plate 4), were spaced every few-hundred meters (where possible) and taken from all large patches (>0.5 km^2) of the surface that displayed the characteristic, hummocky form on 1:50,000 scale airphotos. On the low-relief surface, points were sampled from subtle, positive relief forms (i.e., crests of hummocks), in order to minimize the lowering of the surface due to erosion. On stretches of the surface where large, positive-relief forms (i.e., inselbergs or tors) rise high above the surrounding low-relief base, sample points were taken only from around the base, in order to minimize topographic variations due to irregularities in the weathering front (only a few inselbergs were avoided; see Section 3.6.4, Chapter 3). In addition, most sample points (closed circles, Figure 3) were taken from where the weathered surface is developed on quartz monzonite or biotite monzonite, in order to eliminate elevation differences due to etchplanation (see Section 3.9, Chapter 3). In several locations where monzonite was absent, however, sample points were taken from other granitic lithologies, including

granite, granitic gneiss, and granodiorite (closed squares, Figure 3), on which the typical, low-relief surface was developed.

Elevations for each sample point were read from 1:62,500 scale topographic maps with 80 ft contour interval. Based on these elevation points, the structure-contour diagram was drawn manually at 200 ft contour interval (Figure 3). For simplicity and to maintain the original precision, the units of the contours were not changed to meters from the topographic maps. Structure contours were drawn continuously across the plateau and San Gorgonio block, except where the elevation of the weathered surface is obviously disrupted by faulting (Figure 3). The resulting structure contour diagram should be viewed as the present elevation distribution of a datum that best approximates a pre-uplift, nearly horizontal structural level, as represented by the monzonite surface of deep, protracted weathering.

There is some uncertainty in the elevation of these structure contours, due to possible erosion of the weathered profile and variations in the original geometry of the weathering front (see Section 3.9, Chapter 3). The magnitude of possible post-uplift erosion of the surface is likely less than the thickness of the weathered horizon, so that the structure contours could be as much as ~50 m too low in elevation. Note that this value represents erosion from where the weathered surface is preserved (i.e., interfluves), and is different from the incision that has removed both weathered and fresh rock from between the preserved surface (e.g., ~150 m of post-basalt dissection on the eastern flank; see Section 3.8.2, Chapter 3). Undulations in the weathering front may have resulted in residual highs (i.e., inselbergs) or lows, which add uncertainty to the elevation of structure contours. Local elevation variations on the hummocky surfaces that were sampled typically do not exceed ~50-100 m (164-328 ft) in amplitude over ~1 km distance (see Section 3.6.2.1, Chapter 3), suggesting that $\pm$100 m (328 ft, or ~1.5 contour on Figure 3) is a conservative estimate of uncertainty in the elevation of contours. There is also the possibility that a longer-wavelength variation existed in the weathering front as a pre-

existing high topography in the central part of what is now the Big Bear plateau (see Section 3.8.3, Chapter 3). If such a paleotopographic high existed, the elevations of structure contours in the central plateau would be too great and would not necessarily be accounted for by the ±100 m error limits. Given the uncertainty of the magnitude of such a residual high, however, the best approximation is to assume the surface was nearly flat and that the structure contours represent an upper limit of vertical displacement.

Several stretches of the structure contour diagram also have ambiguities that are not represented by these error limits. First, a large gap in sample points occurs in the area of Big Bear and Baldwin Lakes (Figure 3), where ~100-150 m of Pleistocene sediment is present (Brown, 1976). Existing borehole data does not resolve whether the weathered surface lies beneath these sediments, or if erosion removed the weathered horizon from valley prior to deposition (Brown, 1976). The structure contours across this valley were connected between sample points at the valley margins, thus making the simpler assumption that the weathered surface once connected across and has been removed by erosion. Second, in Santa Ana Valley to the south of the SAT, structure contours were drawn where the Mio-Pliocene Santa Ana Sandstone overlies weathered granite (based on field examination, not airphoto mapping; see also Jacobs, 1982). However, as noted in Chapter 3 (Section 3.6.6), the correlation between these surfaces and the weathered horizon atop the plateau is not unique. Radiogenic helium ages, however, demonstrate that the structural level of the weathered surface atop the San Gorgonio block is the same as the Big Bear plateau (Spotila et al., 1998). Finally, a large, positive-relief landform occurs atop the surface around Butler Peak (area of closed contours several km west of Big Bear Lake, Figure 3), which could have been interpreted as a residual high due to etchplanation (i.e., an inselberg). Because the weathered surface there is cut by faults, however, it was assumed that all positive relief is structural and thus structure contours were drawn to include this landform.

4.3.2 Structure contour diagram of the weathered surface of the Mojave Desert

Because granitic bedrock is not well exposed in the adjacent Mojave Desert, special methods were required to determine the geometry of the weathered surface there. These were necessary to enable measurement of net displacement along the NFTS, by comparing the position of the weathered surface atop the Big Bear plateau to the three-dimensional distribution of a correlative surface in the footwall block. Deeply weathered granitic rock occurs on most basement exposures across the Mojave Desert (Figure 4 [Plate 5]), which is roughly correlative in character and age to the weathering developed atop the plateau (see Section 3.9, Chapter 3; Oberlander, 1972). Ideally, a structure-contour diagram of this Mojave Desert weathered granite should be subtracted from the structural envelope of the weathered surface atop the SBMs (Figure 3) to determine the displacements along the NFTS.

Directly north of the NFTS, however, thick accumulations of alluvium in the foredeep of the SBMs bury basement and obscure the position of a correlative surface (Figure 4). To identify the weathered surface beneath this sediment, it was necessary to determine the depth to basement using existing borehole, seismic reflection, and Bouguer gravity data. Unfortunately, existing data do not permit determination of whether the basement of the sedimentary basins is capped by deeply weathered granitic horizons, fresh granitic rock, or non-granitic lithologies. Given the ubiquitous distribution of weathered granite in the basement exposures of the surrounding area (Figure 4), however, it is likely that buried basement also consists of weathered granite. This critical assumption enables construction of a structure-contour diagram of the weathered surface of the footwall block, although its accuracy is less certain where buried by alluvium.

Available borehole data (Aksoy et al., 1986; Riley, 1956; John S. Murk Engineers, 1985) are summarized on Figure 4. Wells in the valley to the north of the NFTS are for water resources, and are thus clustered in populated areas (Apple and Lucerne Valleys) and do not typically penetrate basement beneath water-bearing sediments. Wells that are

shallow and do not reach basement are shown on Figure 4 without corresponding data. The rare wells that do penetrate basement, or which are deep and thus useful for determining the minimum thickness of sediment, are labeled on Figure 4. These wells provide direct constraint on the depth to basement in select areas, and are valuable controls for the depths determined with geophysical methods.

A seismic reflection profile across the western segment of the NFTS and adjacent foredeep (Li et al., 1992) provides a very tight constraint on the two-dimensional geometry of the sedimentary basin and buried basement. This profile clearly imaged a reflection that corresponds to the sediment-basement interface, which dips southwards towards the NFTS and is offset (Figure 5). Using the two-way travel times of the common-depth-point seismic profile and an assumed 2.5 km/s p-wave velocity for unconsolidated sediments (Sheriff and Geldart, 1982; p. 75), depths to the sediment-basement interface along the north-south profile were determined for both the footwall and the hanging wall blocks (Figures 4 and 5).

Gravity anomalies can also provide constraint on the depth to basement in sedimentary basins, given the large density contrast between unconsolidated sediments and crystalline bedrock. The difference between a corrected gravity measurement and the theoretical value of gravity at the geoid for that location represents a local Bouguer anomaly, which can be explained by this density contrast. Using available complete Bouguer gravity anomaly data (corrected for tides, instrument drift, elevation, density, and terrain; Figure 6; Biehler et al., 1988) and a program that models gravity in two dimensions, the depth to basement was determined along three profiles north of the NFTS (Figure 4; aa', bb', cc'). Each of these profiles show negative gravity anomalies that are typically ~10 mGal in magnitude (Figure 6), associated with the low-density sediments within the basins they cross. The gravity model calculates the depth of these sediments by assuming a density contrast between sediment and basement of 0.4 g/cm^3 (a typical value for shallow alluvial basins; S. Biehler, pers. comm., 1998), assuming a regional gravity

gradient between the ends of the profile located on exposed basement, and using an algorithm that iteratively calculates the thickness of an infinitely-long slab of sediment needed to match all observed gravity anomalies at a spacing of ~1 km. The resulting depth profiles are non-unique, but depths are probably accurate to within several hundred meters.

The gravity data and resulting basement geometries determined for these three profiles are shown in Figure 7. Although the modeled basement geometries are simple, concave shapes, it is likely that the actual basins are complex, involving lower-plate sediments and overthrust basement and sediments (Figure 8). However, the models in Figure 7 can still be used to determine depth, given that the complex basins have the same gravity signature (i.e., total mass in a column is the same in either case; Figure 8). To avoid this complexity, the depths to basement from gravity models for the structure contour diagram in the Mojave were taken only from north of the surface trace of the NFTS. In addition to profiles in Figure 7, two previously determined profiles, calculated from gravity anomalies in the same manner (Aksoy et al., 1986), constrain the depth of basement further to the east (dd', ee'; Figure 4).

From these constraints on the elevation of basement beneath the alluvial valleys (equal to surface elevation minus basement depth) and the elevation distribution of exposed weathered granitic bedrock of the surrounding area (Figure 4), a structure-contour diagram of the presumed weathered surface of the Mojave Desert was constructed on a 1:62,500 scale topographic base (Figure 9 [Plate 6]). Because elevation data was given in units of feet, the resulting structure-contour map has a 200-foot contour interval. All available data were used in this structure-contour diagram, showing that a reasonable topography can be constructed by the different types of data and that the data are thus consistent. The uncertainty of the depth to basement is large (probably ~20-30%), given the non-uniqueness of the geophysical models and the paucity of borehole data in some areas (Figure 4), indicating that the uncertainty in contours is about $\pm$200 m (656 ft) on the west and $\pm$50 m on the east (164 ft). The uncertainty of the depth to the weathered surface on

the eastern half of the NFTS is particularly large because of limited data, although the utter lack of negative Bouguer anomalies (Figure 6) indicates that basement must be within several hundred feet of the surface (S. Biehler, pers. comm., 1998). In addition to the uncertainty in the elevation of structure contours, the ±100 m error limits that apply to the elevation of the datum represented by the weathered surface atop the hanging wall, due to erosion or variability in the weathering front geometry, also apply to the weathered surface of the footwall.

4.4. Observations

4.4.1 Geometry of the reconstructed weathered surface

The best-constrained region of the reconstructed weathered surface is along the Big Bear plateau, the hanging wall to the NFTS (Figure 3). The basic shape of the structure contours there is significantly smoother than the topography of the plateau. The elevation of structure contours are greater than topographic elevation where erosion has lowered or removed the weathered surface, and are lower than topography where resistant, non-granitic lithologies form residual highs. Having removed the effects of differential weathering and erosion, the resulting envelope map more closely represents vertical displacement on major structures that bound the plateau, as well as secondary faults that occur within it. The weathered surface rises from low elevation at the eastern and western ends of the NFTS to a crest along the center of the plateau, as shown by its bell-shaped, west-east elevation profile (AA'; Figure 10). In map view, this form is represented by two panels of north-trending contours on the northwest and northeast, which increase in elevation towards the center of the plateau and are perpendicular to the NFTS (Figure 3). The west-east symmetry of the smooth structural envelope and the exact spatial correlation between its extent and the position of the NFTS argue that the broad form of the structure contours represent vertical displacement along the thrust fault. In turn, the fact that the

structural envelope was constructed using objective, complex rules based on an understanding of the surface's development, but still has a geometry that fits the expected uplift pattern for a thrust fault (Savage and Hastie, 1966), is consistent with the idea that the weathered surface is a structural datum that was sub-horizontal prior to uplift.

Another salient feature of the structure contour map of the hanging-wall block is the increase in elevation of the surface towards the south, as represented by east-west contours that dip to the north (Figure 3). The increase in elevation of the surface away from the trace of the NFTS appears as the difference in elevation of profiles AA' and BB' (Figure 11). Points on BB' (south) are higher than their correlative points on AA' (north). Because vertical deformation due to displacement along thrust faults typically decreases away from the fault trace (Savage and Hastie, 1966), this upward tilt of the surface along the southern margin of the plateau in counter to what would be expected to result simply from slip along the NFTS and likely reflects an important structural feature at depth. If produced by the NFTS, this tilt may require that the thrust steepens at depth. However, the tilt may have been produced instead by north-side-up motion along the SAT on the south.

Although poorly constrained, motion along the SAT occurred prior to deposition of the Santa Ana Sandstone, which in turn occurred prior to the development of the weathered surface it buries in Santa Ana Valley. There is a clear offset of the weathered surface between the Big Bear plateau and the Santa Ana Valley (Figure 3), which had to have been caused by the SAT. This is certain, because the weathered surface is not folded downwards along the escarpment (based on radiogenic helium isochrons; Spotila et al., 1998). Unfortunately, the geometry of the weathered surface in Santa Ana Valley has not been determined to the degree the weathered surface has been in the Mojave Desert. However, the difference in elevation of the weathered surface atop the Big Bear plateau and the surface trace of the SAT illustrate the magnitude of vertical offset of the weathered surface on the south (Figure 12). Although the difference in elevation is substantial along the central portion of the SAT, the trace of the SAT increases in elevation to the east. The

SAT eventually terminates in high topography towards the east, and therefore cannot fully explain the upward tilt of the weathered surface in the southeastern part of the SBMs.

Towards the west, the trace of the SAT is complex and difficult to discern from high-angle structures of the Mentone and Barton Flats fault zones (see below). However, the juxtaposition of the weathered surface atop the Big Bear plateau and below Tertiary sediments on the south continues westward along the Waterman Canyon fault (Figure 3). This fault is considered a part of the late Miocene (9.5-4.1 Ma) Squaw Peak thrust system by Meisling and Weldon (1989), although direct control on its timing of motion is absent. The Waterman Canyon fault dips steeply northward (Meisling and Weldon, 1989), unlike the SAT, but shares a similar relationship between the prominent south escarpment of the Big Bear plateau and has a similar relationship to underthrust Tertiary sediment. The Tertiary sediments along the Waterman Canyon fault zone are likely correlative with the Crowder formation on the west (17-9.5 Ma), but display similarities with the Santa Ana Sandstone on the east (15-6.2 Ma) (Weldon et al., 1993; Sadler, 1993). For the purposes of plotting the vertical offset of the weathered surface along the southern escarpment of the Big Bear plateau, we have considered the Waterman Canyon fault to be an eastward continuation of the SAT (Figure 12), despite their different orientations. This speculation should be tested by further field evaluation of the Waterman Canyon fault and the Tertiary sediments along it.

Another outstanding feature of the geometry of the weathered surface atop the Big Bear plateau is the degree to which it is disrupted by secondary faults. Aside from the NFTS and SAT, a series of shorter faults exhibit vertical displacement in the structure contours and expose non-weathered granite along their traces. These include faults of the Squaw Peak thrust system on the west (such as the Waterman Canyon fault; Meisling and Weldon, 1989), un-named faults that occur near Green Valley (here termed the Green Valley fault zone), the Tunnel Ridge fault, un-named faults that separate the surface of Santa Ana Valley and the high San Gorgonio block to the south (here termed the Barton

Flats fault zone), the Pinto Mountain and Morongo Valley faults on the southeast, and northwest-trending faults of the Eastern California shear zone, which penetrate the plateau on the east (Helendale and Pipes Canyon faults) (Figure 3). This degree of deformation by minor faulting is not surprising, given that the weathered surface may be as old as late Miocene and record all vertical displacements over the past 10 Myr. Some of these faults, such as those of the Squaw Peak thrust system, are known to have been active only prior to onset of thrusting on the NFTS (Meisling and Weldon, 1989), although others, such as those of the Eastern California shear zone, are known to have been active within the last few Myr and as recently as the Holocene (cf. Dokka and Travis, 1990). Any structural interpretation of the SBMs using the structure contour diagram must reconcile the presence of active, secondary structures within the upper plate of the NFTS.

The structure contours of the weathered basement in the Mojave Desert show a non-trivial departure with topography, due to the thickness of sediments in the trough to the north of the NFTS (Figure 9). This indicates that uplift along the front of the NFTS is greater than the height of its scarp. The greatest depth to basement occurs on the west, where more than 1.2 km (>4000 ft) of sediment is present. A significant foredeep is present along most of the western section of the NFTS, with depths to basement typically ~200-500 m (~650-1650 ft). A deep graben is present along the Helendale fault, in which sediments reach ~0.7 km (~2300 ft) thickness (Aksoy et al., 1986). To the east of the Helendale fault, however, sediments are much thinner and the elevation of basement is not significantly different than surface elevations. This basic increase in basement elevation from west to east is illustrated in a profile across the mountain front (CC', Figure 13).

4.4.2 Comparison of the surficial expression of the NFTS and SAT

One means of elucidating the relative roles the two opposing thrust faults have played in the recent uplift of the Big Bear block is to compare the timing of activity on each. As presented above, the NFTS is known to have been uplifting the Big Bear block over the

last few Myr, whereas the activity along the SAT is broadly bracketed between 6.2 Ma and the late Pleistocene. To place a better constraint on the relative timing along these structures and to test whether the SAT has played a comparable role in recent uplift, the surficial expression of the SAT was compared to that along the NFTS, whose history is better known. Both the character of the thrust fault traces (Figure 14) and the geomorphology of their respective bedrock escarpments were characterized and compared (Table 1).

This comparison is limited by the different positions of these escarpments relative to local base-level and climatic gradient. The base of the northern escarpment is also local base-level for the north, whereas the base of the southern escarpment is perched high above local base level on the south (the piedmont-mountain boundary along San Bernardino Valley). In addition, the southern escarpment receives about five-times more annual precipitation than the rain-shadowed northern margin (Minnich, 1986). These differences make it difficult to assess whether differences in the geomorphology of the north and south are due to active tectonism. In the absence of direct constraints on the timing of motion on the SAT, however, this comparison is one means of learning more about its role in uplift of the Big Bear plateau.

The distribution of fault scarps in late Quaternary alluvium directly represents the degree of recent activity along a thrust fault. The surface traces of the NFTS and SAT were mapped using 1:50,000 scale airphotos, and the presence and nature of their fault scarps were compared (previous studies also taken into account; Table 1). The NFTS has large scarps in late Pleistocene alluvium along more than one-half of its east-west extent, the number and size of which are greater to the west of the Helendale fault (Figure 14). Their irregular and discontinuous distribution may be attributed to both complexity of the thrust system and along-strike variations in sedimentation and erosion. A wide range (0.05-0.3 mm/yr) in late Pleistocene vertical displacement rates may be calculated using the range in reported values of scarp height and estimates of scarp age (25 m and 0.5 Ma, Meisling and Weldon, 1989; 36-70 m and 0.4 Ma, Meisling, 1984; 40 m and 130 Ka, Bryant, 1986a,

1986b). In addition, there is evidence that active folding may accompany thrusting along the northern margin. Folded Pleistocene alluvium occurs in several locations, such as along the Ocotillo Ridge fold (Meisling, 1984; but may be a possible fault scarp [Bryant, 1986b]) or the folds exposing Old Woman Sandstone near the Helendale fault (Figure 14 [Dibblee, 1964b]). Folding is also suggested by the high gradient of alluvial fan surfaces along the range front (>7° at fan heads, as measured on 1:62,500 scale maps), with respect to typical alluvial gradients of <5° (e.g., Bull, 1964).

The SAT, however, has almost no scarps developed in preserved mid-late Pleistocene alluvium (Sadler, 1993; Table 1). The few scarps that are preserved are small, isolated, poorly defined, and occur near traces of strike-slip or high-angle reverse faults (Mentone fault zone, Deer Creek fault; Figure 14) and may be reactivated. In the Barton Flats area, for example, the east-west trending faults associated with uplift of the San Gorgonio block (Barton Flats fault zone) have a much greater impact on Quaternary sedimentary surfaces than does the SAT. In addition, folding and warping of sediments is only manifest in the late Miocene to Pliocene Santa Ana Sandstone (Sadler, 1993). The evidence for active tectonism along the SAT is thus apparently much less than for the NFTS.

The topography of the northern and southern escarpments may also reveal the degree of activity on the respective thrust faults. Because these escarpments are similar size and steepness (Table 1), they were characterized using other parameters that reflect the degree of tectonic activity (i.e., uplift, versus erosion and deposition) along mountain fronts (Bull, 1977). The sinuosity (S), defined as the length of a piedmont-mountain junction divided by the linear length of the front, was measured along the total length of both the SAT and NFTS using 1:62,500 scale maps. This parameter is generally greater for inactive mountain fronts that are embayed and retreating by erosion than for active fronts that uplift along range-bounding structures. The ratio (V) of valley width to valley depth along each front was also measured, as the average of 15 canyons along the central

portions of the NFTS and SAT. This parameter reflects the degree to which a mountain front has equilibrated to its base-level and is generally lower for active fronts, along which deep, v-shaped canyons incise rapidly to keep pace with the tectonic drop in base level. The northern margin of the range has both a higher value of S and a lower value of V (Table 1), suggesting it may be tectonically more active. These values are so close, however, that the two escarpments may be eroding at essentially the same rate.

The relative rates of uplift may also be represented by the balance of erosion and deposition, as reflected by the state of alluvial fans along a mountain front (Bull, 1977). The age of the oldest preserved alluvial fan surfaces is controlled by the rates of erosion and deposition, which are strongly affected by uplift rate. Inactive mountain fronts should erode more slowly and produce less sediment, and thus exhibit older fan surfaces preserved from burial. The indication that fans along the north are younger than fans along the south shows that deposition is more rapid on the north, although the age control on soils and surfaces is quite poor (Table 1). The degree to which fans are entrenched or incised also reflects the age of alluvial surfaces and the degree to which they are preserved from subsequent erosion due to decreasing sedimentation rates. The young fans along the north escarpment are moderately entrenched (possibly related to active tilting and warping of fans), particularly near the range front, but are much more intact than the fragmentary remains of fans and terraces along the southern escarpment (Table 1). As a result, alluvial fans along the north are also greater in size than on the south. These observations suggest that depositional rates are greater along the north than the south, although erosion rates appear high along both escarpments. This may partly reflect a greater uplift rate and sediment yield on the north, but the perched position of the base of the southern escarpment above local base-level is a also a likely explanation.

This comparison reveals ample evidence for recent compressive deformation along the northern margin of the Big Bear plateau, while evidence for late Quaternary thrusting along the southern escarpment is nearly absent. There are geomorphic indications that the

southern escarpment has been eroding as quickly as the north, but this may be attributed to its high position relative to local base level. Rapid erosion on the south may have been reinforced by the need to equilibrate to a drop in base level as the high San Gabriel Mountains pulled away from the western SBMs along the San Andreas fault over the past million years or so. Given that differences in climate and base level seemingly favor more rapid erosion on the south and that both the northern and southern escarpments appear to be experiencing similar degrees of erosion, the youthfulness of the northern margin seems to require significant tectonic uplift over the latter part of the Pleistocene.

4.4.3 Assessment of recent strike-slip faulting in the SBMs

One of the major arguments that uplift of the Big Bear plateau is not ongoing is the possibility that the block is presently being deformed by high-angle dextral faults that may offset the NFTS and SAT and render them inactive (cf. Sadler, 1982a, 1982b; Meisling and Weldon, 1989; versus Bryant, 1986a; Miller, 1987). If cross-cutting relationships between these two fault systems exist, constraints on the history of thrusting may be evident in the history of strike-slip faults within the range. To evaluate the possibility that thrusting has been replaced by dextral shear at the range front and within the SBMs, we summarized existing constraints on dextral fault displacements based on previous mapping and examined fault surface traces for geomorphic evidence of recent motion using 1:50,000 scale airphotos.

The fault map made using airphotos shows that many northwest-trending dextral faults occur to the north of the SBMs, within the blocks of the SBMs north of the San Andreas fault zone, and within the complex trace of the NFTS itself (Figure 14). Data that constrain total displacement (or a minimum estimate thereof) along these faults are listed in Table 2, along with descriptions of features along the faults that bear on degree of activity. Several other faults that occur in the Big Bear block were not included in this group, which show evidence for strike-slip motion but which do not exhibit strong geomorphic evidence

of recent motion in airphotos. These include the Tunnel Ridge fault, Bowen Ranch fault, Arrastre Canyon Narrows fault, and Lovelace Canyon fault, all of which are northeast trending, exhibit oblique-right lateral motion, occur in the northwestern part of the plateau, and have been previously studied (Meisling, 1984).

Although the traces of all of the faults listed in Table 2 have been previously recognized, four have not been previously named (Dollar Lake fault, Bighorn fault zone, Barton Flats fault zone, and Mentone fault zone; Table 2). The Dollar Lake fault has a well-developed geomorphic expression in airphotos and clearly cuts glacial sediments, and is continuous from just north of the Mill Creek fault to the Barton Flats fault zone. Although the northwestward projection of this fault aligns with the Deer Creek fault, a through-going connection is not geomorphically evident. The Bighorn fault zone (two traces) consists of a prominent geomorphic expression in bedrock on the northeast Big Bear plateau. The Barton Flats fault zone includes all high-angle faults that are present in the Santa Ana Valley and northern boundary of the San Gorgonio block, which display evidence for both dextral and reverse motion (Sadler, 1993). This fault system may have as much as 10 km dextral motion since the late Miocene (based on clast provenance in the Santa Ana Sandstone; Sadler, 1993) and is probably partly responsible for uplift of the San Gorgonio block relative to the Santa Ana Valley. The surface expression of this fault zone is very complex, probably because it has experienced very rapid erosion over the past million years or so. The Mentone fault zone consists of a series of high-angle fault segments with minor evidence for dextral offset. It occurs between the Mill Creek fault and Waterman Canyon fault and may represent a westward continuation of the Barton Flats fault zone. This zone displays the weakest evidence for Quaternary activity and could have a purely erosional topographic expression, although this could be due to rapid erosion rates along this portion of the southern SBMs. Nevertheless, it is included on Table 2 as a possible member of the diffuse system of northwest-trending dextral faults that occur between the NFTS and San Andreas fault in the SBMs.

Well-known strike-slip faults of the Eastern California shear zone (ECSZ) north of the NFTS (and west of the Johnson Valley fault) have a minimum of between 5 and 13 km of right-slip and were clearly active in the late Pleistocene (Table 2). These display well-developed expressions in latest Pleistocene alluvium and cut alluvial fans that locally bury the NFTS (Dibblee, 1964b). Although the history of motion on these faults is not well constrained, they disrupt bedrock, late Miocene basalts, Pliocene sediments, and Pleistocene alluvium similarly, and display no evidence to suggest they were not continuously active over the last few million years. Dokka and Travis (1990) claim that the ECSZ has migrated to the west over the last few million years, which suggests that these dextral faults were coactive with the NFTS in the Pleistocene.

A second set of northwest-trending, dextral faults occurs within the SBMs to the south (Figure 14). According to the data listed in Table 2, these faults may have accrued a similar magnitude of net slip as the ECSZ to the north (minimum of 3-9 km; Table 2). Although this estimate is slightly lower than the value for faults north of the NFTS, it is of the same order and shows that the ECSZ continues south of the north rim of the SBMs. Several of these southern dextral faults display strong evidence of recent displacement (e.g., Deer Creek, Dollar Lake, Pipes Canyon, and Barton Flats fault zones). This is consistent with the observation that seismicity in the SBMs following the 1992 Landers earthquake (and perhaps the last 100 yrs; Sadler, 1982a) was produced by mainly strike-slip ruptures, including the M=6.5 Big Bear earthquake (Figure 14; Hauksson et al., 1993; Jones and Hough, 1995). Other faults, however, do not have as pronounced geomorphic expressions and may not have experienced significant Quaternary motion (Helendale A, Helendale B, Bighorn, and Mentone fault zones). Nevertheless, it seems apparent that a system of dextral faults has experienced significant motion within the SBMs (and hanging-wall block of the NFTS and SAT) throughout the Quaternary.

Although the ECSZ is manifest north of and within the SBMs, there does not seem to be conclusive evidence that it offsets the trace of the NFTS. The Helendale, Silver Reef,

Old Woman Springs, and Lenwood fault display clear evidence for recent activity north of the range, but their surface traces do not directly intersect the NFTS. Several of the dextral faults within the Big Bear block occur along strike with the southward projection of faults to the north (Bighorn fault zone and Old Woman Springs fault, Pipes Canyon fault and Silver Reef fault), but no direct connection can be established through the NFTS. Both the Old Woman Springs and Helendale faults become more complex as they approach the rangefront, and appear to bend to the east to join the trace of the NFTS (Miller, 1987; Dibblee, 1964b). The character of the NFTS changes across the projection of the Helendale fault, from well-defined scarps on the west to a complex system of conjugate high-angle faults and folds on the east. This may indicate that the right-slip of the Helendale fault is transferred to the NFTS, as if the strike-slip fault terminated in a restraining bend. Directly south of the NFTS, two fault strands that align with the northern Helendale fault trace have been mapped in bedrock without dextral offset (Dibblee, 1964b) and displace the weathered surface in a large, graben-like structure (Sadler, 1982b). This implies that the Helendale fault does penetrate the NFTS, but changes character drastically from north to south.

The strike-slip faults situated along the trace of the NFTS itself (Sky High Ranch and Blackhawk faults), between the systems to the north and south, could indicate that thrusting along the northern margin of the NFTS has been replaced by right-slip. These structures have young traces and appear more youthful than thrust fault scarps nearby, and represent a significant component of the Pleistocene scarp distribution along the range front. However, these also occur along segments of the range front that locally trend northwest, and may instead represent tear faults connecting segments of the complex NFTS. In addition, the NFTS has certainly experienced late Pleistocene motion as well, and could not have been inactive during the half-million year history of these faults (0.5 km at ~1 mm/yr on Sky High Ranch Fault; Meisling, 1984).

These relationships imply that strike-slip faulting on northwest-trending faults and thrusting on the NFTS (not the SAT) have been coactive within the SBMs. Although strike-slip faults north of and at the range front may have been active more recently than the NFTS, they do not display a cross-cutting relationship to indicate the thrust fault has terminated. Instead, each fault system appears to have affected the other and interacted during the Quaternary. The presence of recent strike-slip faulting within the SBMs implies that the ECSZ penetrates the NFTS, albeit not as a throughgoing system. Because it may be mechanically difficult for thrusting and strike-slip to be coactive in the same volume of crust, the interpretation that the southern faults were a part of the ECSZ prior to uplift and have only recently been reactivated (i.e., post-NFTS) is attractive. However, the magnitude of net slip on the southern faults is comparable to that on the north, implying both fault systems may have experienced the same history of dextral shear. This suggests that all of the faults listed in Table 2 are a part of a single dextral system that has been contemporaneous with the NFTS. Thus, although strike-slip faulting occurs within the SBMs, it is not clear that it requires the NFTS to have terminated in recent times. A possible mechanical explanation for this could be that a throughgoing dextral system exists in the lower plate of the NFTS (and SAT), that shears the overlying plate diffusely. To better determine the relationship of the ECSZ and thrusting in the SBMs, detailed field studies of the strike-slip faults within the SBMs are required and recommended as a valuable direction of future research.

4.5. Structural analyses

4.5.1 Displacement along the near-surface NFTS and SAT

Vertical displacement along the thrust faults can be calculated as the difference in elevation of the structure contours atop the hanging-wall and footwall blocks. This can be determined in more detail for the NFTS than SAT, given the greater control on the

geometry of the weathered surface in the Mojave Desert than below the Santa Ana Sandstone.

Vertical displacement along the NFTS may be calculated most accurately along the surface trace of the fault, where the structure contour diagrams overlap. A rough estimate of this vertical displacement can be made by subtracting the west-east elevation profiles of the surface on the hanging-wall and footwall (AA' and CC'; Figure 15). The difference in these two profiles demonstrates that the structure contours of the weathered surface are separated by >1.5 km elevation at the center of the NFTS, but that this separation decreases along trend to the east and west. This estimate of vertical displacement is limited, however, by the horizontal separation between the elevation profile it was calculated from (e.g., the secondary offset of the Helendale fault, which cross the NFTS obliquely, occurs at different positions on AA' and CC').

A more accurate determination of vertical displacement along the near-surface of the NFTS is shown in Figure 16, which was created by subtracting the elevation of overlapping structure contours on the hanging wall and footwall from an irregular profile along the NFTS trace (DD', Figure 3). This plot is roughly similar to the previous estimate, showing a bell-shaped curve of vertical displacement that is lowest on the east and west (0 m east, 610 m west) increases to a maximum in the center of the NFTS (1798 m), and averages 983 m. Note that this plot does not extend to the western terminus of the NFTS, where it is replaced by older faults of the Squaw Peak thrust system (late Miocene) in Summit Valley, which displace the weathered surface by ~250 m (Meisling, 1984). The correspondence between the uniform variation in vertical displacement along the profile and the east-west extent of the surface trace of fault demonstrates that the uplift of the weathered surface of the northern Big Bear plateau can be easily explained by up-to-the-north thrusting on the NFTS. The displacement along DD' is also disrupted in several locations on the east by secondary faults, which seem to drop sections of the weathered surface

down rather than uplift them, given that the high regions between the faults match the envelope of displacement projected from the west (dashed line, Figure 16).

There is uncertainty in this vertical displacement due to the error limits on the elevations of the weathered surface in the hanging wall and footwall. The ±100 m uncertainty of the structure contours in the upper plate and the ±150 m error (±25% of ~200 m depth to basement) imply that the error limits on the maximum vertical displacement in the center of the NFTS are on the order of ±10% (r.m.s. error = ±180 m). Because the vertical displacement is calculated from contours that overlap, there is no added uncertainty due to a possible preexisting topographic high in the central portion of the weathered surface. There is, however, a lingering uncertainty as to whether the basement underneath the alluvium in the footwall is truly weathered and correlative to the weathered surface atop the hanging wall. To within this 10% uncertainty, the weathered surface enables quantification of the near-surface uplift along the NFTS and thus gives an important new constraint on the neotectonics of the SBMs.

Along the SAT, vertical displacement can only be estimated, because the depth of the weathered surface beneath the Santa Ana Sandstone has not been determined in detail. We have estimated this displacement by simple differencing the elevation of the weathered surface above the thrust and the elevation of the thrust surface trace itself (as read off 1:62500 scale topographic maps; difference between two curves in Figure 12). This provides a minimum estimate, to which the depth to the weathered surface in the footwall block would have to be added to fully represent the SAT's slip. However, the resulting plot is useful because it shows how slip varies along the trace of the thrust (Figure 17). This plot shows a simple, bell-shaped curve, on which vertical offset rises from zero on the east to a maximum of ~1.1 km in the center, and decreases symmetrically to the west.

Given these determinations of vertical displacement on the NFTS and SAT, several implications may be drawn for the neotectonics of the SBMs. Assuming a near-surface dip of ~35° (the median of published values 10-60°; Miller, 1987; Li et al., 1992; Meisling,

1984; Woodford and Hariss, 1928; Rzonca and Clark, 1982), the maximum net displacement (i.e. throw) on the NFTS is ~3.1 km (1.7 km average). This estimate is highly dependent on the assumed dip, with a possible range of 2.4-5.3 km (~40% uncertainty) for the likely dip range. Given this estimate, the slip to length ratio of the 70-km-long NFTS is 4.5×10^{-2} (2.4×10^{-2} average), a typical long-term value for faults (Cowie and Scholz, 1992; Dawers et al., 1993). This estimate of net slip also implies a range in average slip rate of 1.6-1.0 mm/yr, depending on whether the thrust initiated after 2 or after 3 Ma (May and Repenning, 1982). The horizontal component of this maximum net slip along the NFTS is about 2.6 km (average = 1.4 km), which resolves to 1.6 km of motion along the N37°W direction of Pacific-North American plate motion (about 1.6-1.1% of the total plate motion in 2-3 Myr; DeMets, 1995).

Similarly, the loose estimate of vertical motion along the SAT can be used to infer net displacement. Assuming an average dip of 30°N (Jacobs, 1982), the maximum vertical displacement corresponds to 2.2 km of net slip and 1.9 km of horizontal shortening. This value is significant, and more than half that along the NFTS. Given the ~50 km length of the fault, the implied slip to length ratio is approximately 4.4×10^{-2}, nearly identical to that of the NFTS. Given the unknown history of motion along the SAT (see below), a meaningful estimate of slip rate for when it was active cannot be made.

4.5.2 Degree of activity along the NFTS and SAT

Based on observations of the surface trace and bedrock escarpment of the NFTS and SAT, it is clear that the NFTS has been much more active in the late Quaternary. The paucity of scarps in late Pleistocene alluvium and the offset of its trace by the Deer Creek fault (Jacobs, 1982) indicate the SAT has probably been extinct since at least the mid-Pleistocene (absolute age control on sediments could test this interpretation). However, there does not seem to be direct evidence that the SAT has been dead since 4.1 Ma, as proposed by Meisling and Weldon (1989). On the contrary, the geomorphology of the

southern escarpment of the Big Bear plateau indicates very rapid erosion (see Chapter 3). Rapid incision of the western escarpment may have resulted from the lowering of base level associated with the northwestward motion of the San Gabriel Mountains along the San Andreas fault in the past ~1 Myr. However, the equally impressive eastern portion of the escarpment has probably experienced a rise in local base level due to uplift of the San Gorgonio block. The geomorphic expression of the escarpment thus implies that the SAT has not been extinct for too long. Whether it has been dead for 4, 2, or 0.5 Myr, the SAT does displace the weathered surface (Figure 12), however, and has thus played an important role in uplift of the Big Bear plateau and SBMs.

Although the NFTS does not generally displace Holocene alluvium, there does not appear to be strong evidence that it is an extinct structure. The distribution of scarps and the degree of activity based on the geomorphic expression of its bedrock escarpment argue that it has been active as recently as the late Pleistocene. The degrees of alluvial fan entrenchment (partly due to range-front warping) and embayment along the northern range front do exceed that of other active, thrust-faulted mountain fronts (e.g., Cucamonga thrust along the southern San Gabriel Mountains [Bull, 1978]), but this may simply indicate a lower uplift rate. Estimates of late Pleistocene uplift rate along the NFTS (0.05-0.3 mm/yr) are lower than the measurement of long-term uplift rate using the weathered surface (0.90-0.33 mm/yr; depending on whether maximum or average offset and 2 or 3 Myr are used), suggesting that the NFTS has decelerated (but not terminated) in the late Quaternary. In addition, cross-cutting relationships along the range front between the NFTS and dextral faults do not demonstrate that the ECSZ offsets the thrust, and the presence of dextral faults to the south does not require the NFTS to be inactive. Observations of recent seismicity along the NFTS (Feigl et al., 1995) also suggest it is still active.

4.5.3 Cross section analysis of subsurface fault geometries

To learn about the subsurface geologic structure responsible for uplift of the SBMs, three north-south cross sections have been constructed that incorporate available data. The goals of these constructions are to examine the relative degrees to which displacement on the NFTS and SAT are required to produce the observed shape of the weathered surface, to see if these structures can explain the uplift of the Big Bear plateau or if other structures must be invoked, and to explore the likely geometry of structures beneath the range. Note that other styles of investigation, such as elastic dislocation modeling of thrust planes using the constrained vertical displacement, would be helpful and are suggested as possible area of future research.

The interpretive cross sections in Figure 18 represent our best-guess of the structural geometry beneath the SBMs, but several caveats apply. First, these sections are not balanced, given the limited data provided by the weathered surface. There is simply not enough constraint from this datum (or the crystalline rocks of the SBMs) to construct the kinds of balanced sections typically drawn in fold and thrust belts laden with sediments. In addition, given the presence of major strike-slip structures within these sections, plane-strain cannot be assumed and thus balancing is not possible. Second, these sections incorporate surface geologic constraints as boundary conditions, which serve as a starting point for learning about the geometry below using the weathered surface. The resulting interpretations of structure throughout the brittle crust are thus partly dependent on observations made at outcrop scale. For example, to determine the net-slip along a thrust trace, a surface dip is projected upwards until it intersects the projection of the reconstructed weathered surface. Thus minor changes in assumed dip can greatly affect the result. In addition, the cross sections approximate the NFTS as a single plane, despite evidence that it consists of a complex array of structures. Lastly, no attempt is made to reconcile the observed uplift pattern with isostatic adjustment or fault geometry with stresses induced by high topography. As a result, these cross sections should be

considered non-unique solutions to the kinematics of the SBMs. Still, they are useful, because they illustrate the basic form the structures must have.

4.5.3.1 Geologic constraints on fault orientations used for cross sections

Near-surface fault attitudes and other geologic data used to construct the three cross sections are listed in Table 3. The cross sections were made without exaggeration using a 1:62,500 scale topographic base. In general, near-surface fault orientations were based on measurements in outcrop from previous studies. In addition to the data listed, geologic contacts (such as alluvium-bedrock) were taken from geologic maps of Dibblee (1964a, 1964b, 1967a, 1967b, 1974a, 1974b). All attitude data were projected onto the north-south trend of the cross sections. Attitude data are not available for a number of high-angle faults, so these were assumed to be vertical on cross sections. Several of these faults were drawn nearly vertical, with steep dips intended to show normal or reverse motion according to interpretations below (Green Valley fault zone, Barton Flats fault zone).

Beyond the near-surface constraints listed on Table 3, fault orientations throughout the entire upper crust were interpreted using the weathered surface atop the SBMs and in adjacent valleys. Elevations of the weathered surface in the Mojave Desert and atop the Big Bear block, Santa Ana valley, and San Gorgonio block are taken from the structure contour diagrams of Figures 3 and 9. The elevation of basement (presumed weathered surface) in the San Bernardino Valley (cross section CC') was taken from analysis of gravity data in Willingham (1981). In addition, elevations of bedrock following restoration of exhumation determined from radiogenic helium dating are shown on cross section BB' (Spotila et al., 1998).

Net displacements along the near-surface traces of the thrust faults were determined as the separation between the location of the surface on the footwall and the point of intersection between the projections of the fault plane and weathered surface atop the hanging wall (Figure 18). Variations in the elevation of the weathered surface atop the

hanging wall were then used to interpret the subsurface geometry of thrust faults. Because the net displacement along the thrusts are small in comparison to their down-dip widths (Figure 18), vertical undulations along the weathered surface were essentially produced by the fault segment directly below. Assuming that horizontal shortening is constant with depth (i.e., horizontal plate motions create homogeneous convergence), variations in fault dip are necessary to produce the vertical deformation of the weathered surface above. Starting at the surface and moving sequentially down, the vertical displacement (y) of the weathered surface (measured a distance equal to the horizontal shortening in the direction of vergence) can be combined with the constant horizontal motion (x) to determine the fault dip (δ) along segments of the thrust ($y/x = \tan\delta$). This was completed for thrust segments at a horizontal spacing of ~1.5 km.

4.5.3.2 Constraints on subsurface fault geometry from recent seismicity

Seismicity can help constrain the subsurface geometry of active faults. The spatial distribution of earthquakes was compared to fault locations (based on surficial data) along cross section lines in the SBMs, to look for clues as to their orientation. Figure 19 shows three profiles of recent (1981-1998) earthquakes along the cross section lines (see Figure 14 for profile locations), based on events of the Caltech seismic network that have been relocated by Hauksson (1998; in prep.) using a new three-dimensional velocity structure of the region. This seismicity is dominated by clusters of aftershocks of the 1992 Landers-Big Bear sequence (Hauksson et al., 1993; Jones and Hough, 1995) and the 1986 Palm Springs earthquake (San Gorgonio Pass fault zone; Jones et al., 1986). Apart from these aftershocks, the pattern of events is diffuse and fails to delineate major faults, such as the San Andreas. An elongate cluster of seismicity (mainly 1992 aftershocks) does occur to the north of the projection of the NFTS, which exhibits a similar dip to the south. This may represent diffuse footwall deformation or an active, blind thrust that has migrated northwards from the main strands of the NFTS (Miller, 1987). However, most of the

earthquakes in this cluster was produced by strike-slip following the Landers earthquake, indicating that the thrusts were not the primary modes of deformation (Hauksson et al., 1993). This cluster has thus not influenced our interpretations of the NFTS geometry at depth.

Several moderate earthquakes with thrust mechanisms did occur as aftershocks of the 1992 Landers-Big Bear sequence in the vicinity of the NFTS and SAT. Two such events (A=8/17/92; M4.8; B=8/18/92, M4.0) occurred below the Big Bear plateau at about the depth the surficial NFTS projects to, given the range in published foci depth (11-15 km; Hauksson et al., 1993; Jones and Hough, 1995). These had nodal planes that could correspond to the NFTS and their locations are plotted on cross section BB' (Figures 18b and 19). A similar event (C=7/9/92; M5.3) occurred above the projection of the NFTS, but may correspond to the projection of the SAT (Figures 18b and 19). This event has east-west trending nodal planes that dip north and south (Jones and Hough, 1995), and may have occurred along a reactivated section of the SAT. These three events are used as a check to the interpretations of thrust faults below.

Another thrust earthquake (D=12/4/92, M5.4) occurred in the northern cluster of aftershocks very close to the NFTS (Figures 18b and 19). This event has a tightly constrained focal plane solution and hypocenter, because surficial displacements associated with it were recorded in synthetic-aperture radar interferograms (Feigl et al., 1995). Based on an elastic dislocation model of the surface displacements, this event was produced by a 28 ± 4^{o}S dipping, 9 km^2 thrust fault 2.6 km below the surface (Feigl et al., 1995; consistent with seismologic observations of Hauksson et al., 1993; Jones and Hough, 1995). Although the location of this event (shown with error bars; Figure 18b) is north of the main strand of the NFTS, the rupture plane projects to small folds in alluvium at the surface (Dibblee, 1964b). This earthquake may have occurred on a northern, blind thrust fault within the NFTS, which may be young and propagating towards the surface. This is

consistent with the observation that the NFTS consists of a wide, complex zone, but does not support the interpreted geometry of the NFTS in cross section (Figures 18 and 19).

The seismicity is also useful for determining the geometry of the brittle-plastic transition in the crust beneath the SBMs. Above this rheological boundary, deformation occurs by brittle failure along fault planes and results in earthquakes, whereas below, deformation occurs ductily (aseismically). The brittle-plastic transition is thus an important feature and represents a discontinuity between two mechanical regimes within the crust, which is controlled compositionally and thermally. The brittle-plastic transition in the region has been considered by some workers to represent a detachment structure, along which an upper brittle plate rides over freely-flowing crust (cf. Yeats, 1981; Corbett, 1984; Li et al., 1992). If so, fault planes in the upper brittle crust should not penetrate the brittle-plastic transition without major changes in their mechanical behavior. The base of seismicity is thus used as the maximum depth to which cross sections are drawn.

The depth distribution of seismicity in the SBMs has been previously shown to consist of a complex and unusual geometry, including a region of deep earthquakes beneath San Gorgonio Pass that are among the deepest within southern California (e.g., Corbett, 1984). The plots of seismicity in Figure 19 show this general southward-deepening base of seismicity, from shallow depth (~14 km) in the Mojave Desert to the deep (~25 km) events of San Gorgonio Pass. Defining the precise geometry of the brittle-plastic transition is not, however, an objective task. In each profile on Figure 19, a light dashed line has been drawn as the literal base of seismicity. These lines exhibit complex and irregular geometries, which probably reflect holes in earthquake activity due to the short period of observation (17 yrs.), rather than mechanical heterogeneity of the upper crust. Smoother and straighter lines are also shown on each plot (heavy dashed lines, Figure 19), which represent an informal filtering of the shorter wavelength component of the lower limit of earthquake activity. These representations of the base of seismicity in the SBMs are similar to previously reported versions, including the striking, south-side-down step to the

seismicity in the vicinity of the San Andreas fault (Corbett, 1984; Magistrale and Sanders, 1995). We thus take these lines as the best approximation of the brittle-plastic transition below the SBMs, and plot them on each cross section (Figure 18). In each section, we do not extend the faults of the upper crust below this approximate brittle-ductile transition.

4.5.3.3 Cross section interpretation

Cross section AA' (Figure 18a) crosses the SBMs to the east of the SAT's termination, requiring that vertical deformation of the weathered surface be interpreted with the NFTS (or other structures) alone. The surface trace of the NFTS displays only a small vertical displacement of the weathered surface (~0.38 km), but has a much larger net displacement (~1.02 km) due to its shallow dip. To the south, the weathered surface rises substantially, requiring the NFTS to steepen according to the relationship of vertical displacement and fault dip assumed above. The NFTS must steepen to ~52°S to explain the bulge in the weathered surface south of Pipes Canyon, where it intersects the brittle-plastic transition at a depth of ~18 km. The uplift continues south of this intersection, however, requiring a separate mechanism of deformation. Given the northward dip of the Mission Creek fault and San Gorgonio Pass fault zone (projected from south), it is possible that this uplift can be explained by thrusting on the south. The vertical deformation of the weathered surface appears to terminate at the Mission Creek fault, however, suggesting it is more likely responsible. An alternative explanation is that the weathered surface is folded due to a kink in the NFTS. If the NFTS continues south as a detachment along the brittle-plastic transition, a fold could develop due to conservation of mass (i.e., kink-band migration) to the south of the restraining bend. Note that the strike-slip faults in this section were not drawn in the lower plate of the NFTS, given the uncertain kinematic relationship between these apparently coactive structural systems.

Cross sections BB' and CC' are more complex, given that both the NFTS and SAT display significant motion in the central and western SBMs. The assumed relationship

between vertical deformation and fault dip does not include a means to discern the components of motion accommodated by these opposing structures, given that both project beneath the uplifted region. However, the NFTS deforms the weathered surface in the absence of the SAT in section AA', has a larger displacement at its surface trace, and has been more active since the mid-Pleistocene (possible much longer), and thus appears to have played a larger role in uplift. We thus apply the relationship of vertical offset and fault dip to the NFTS, for two possible scenarios of motion along the SAT.

In the first case, the SAT is assumed to have been active prior to the NFTS, and vertical deformation in the hanging-wall block is backslipped prior to using the weathered surface to constrain the NFTS' dip. The magnitude of vertical displacement attributed to the SAT decreases northwards from the value measured along the SAT's escarpment (Figure 17) to zero along at the midpoint between the two thrusts, to loosely mimic the manner in which vertical dislocation decreases away from rupture planes (cf. Savage and Hastie, 1966). In the second case, the two thrusts are assumed to have been coactive for at least part of the NFTS's lifetime, and motion along the SAT is considered to be induced by a change in the NFTS's dip at their intersection. If the NFTS flattens south of this intersection, the resulting kink (or restraining bend) could induce thrusting, much as it may induce folding in section AA'. In this case, the geometry of the NFTS is still represented by vertical displacement of the weathered surface to the north of the kink. To the south, however, changes in the elevation of structure contours cannot be used to determine dip, due to the uncertain component of uplift along the SAT. Instead, the vertical offset used to estimate the dip of the southern NFTS is taken simply as the difference in elevation of the weathered horizon in Santa Ana Valley with that in the Mojave and San Bernardino Valleys (i.e. non-uplifted baselevel).

Cross section BB' shows that the NFTS must flatten at depth for both scenarios of motion along the SAT. The surface trace of the NFTS exhibits large vertical (1.84 km) and net (2.86 km) displacements, and remains nearly flat to the north of its intersection with the

SAT. The SAT has smaller vertical (0.68 km) and net (1.55 km) displacements, and is drawn to steepen at depth based on field observations (Jacobs, 1982) and in order to send it through the hypocenter that exhibited a 46°N thrust plane (Figure 18b). In the scenario in which the SAT was active prior to the NFTS, a significant component of the weathered surface's elevation is removed by back-slipping the SAT. This reduces the uplift that can be attributed to the NFTS, and thus the NFTS must flatten south of their intersection to as low as 20°S. The SAT is shown as being offset by the NFTS in this case. In the second scenario, the NFTS flattens to ~19°S south of its intersection with the SAT. Note that in both of these cases, the flattening of the NFTS does not result in such a different geometry than if the SAT is ignored ("NFTS only"; Figure 18b).

Unlike cross section AA', section BB' crosses the SBMs where a series of tectonic blocks are defined by high-angle structures. The interpretations of these structures follow those based on the geometry of radiogenic helium isochrons by Spotila et al. (1998). The San Gorgonio block tilts upwards to the north based on the weathered surface and isochrons, and must be separated from the low Santa Ana Valley by vertical displacement across the high-angle Barton Flats fault zone. Although the orientation of this fault system is unconstrained, it is shown with steep southward dip on the cross sections to indicate that is likely a reverse system with minor oblique right-slip (Sadler, 1993). The projection of elevations of the Yucaipa Ridge block rises above the blocks to the north, based on the magnitude of recent exhumation determined with helium ages. This block has probably risen by oblique-reverse motion along the Mill Creek and San Andreas faults (San Bernardino strand) that bound it (or the Mission Creek fault, projected from the southeast). The Mill Creek fault may join the San Andreas at depth, or may steepen and intersect the step in the brittle-plastic transition at 18 km depth (D. Yule, pers. comm., 1998).

In cross section CC', the NFTS must also flatten at depth for either case. Displacement along the surface trace of the NFTS (vertical = 1.15 km, net = 2.72 km) is slightly lower than to the east, whereas slip along the SAT (vertical = 1.03 km, net = 1.75

km) is slightly larger than in section BB'. The increase in slip along the SAT in this section may be related to slip transfer from right lateral faults of the Mentone fault zone (Figure 14). The SAT is drawn from its shallow dip at the surface to steepen to 45° at depth, so as to match section BB' and to be consistent with previous work (though its orientation is not known). If the SAT was active prior to the NFTS, the NFTS must flatten to the south given the magnitude of vertical offset attributed to the SAT (Figure 18c). In the second scenario, in which the SAT is coactive and formed due to the restraining bend in the NFTS, the NFTS flattens south of their intersection to ~14°. Thus, as with cross section BB', the NFTS must flatten with depth in either scenario. Note that although the NFTS flattens, it does not achieve adequate depth to merge with the brittle-plastic transition.

Section CC' occurs far enough west that the localized warp of the San Gorgonio block is not apparent. The low region between the SAT and Mill Creek fault is more likely the westward continuation of the structurally-low Santa Ana Valley, than a deeply eroded version of the San Gorgonio block. More helium dating in this area could resolve this discrepancy. Likewise, helium dating could resolve whether the subdued westward continuation of the Yucaipa Ridge block has experienced as great a magnitude of exhumation as to the east. Other structures shown in this cross section include the Green Valley fault zone (Figure 14), which are drawn as normal faults based on their topographic expression in airphotos. The poor geomorphic expression of these suggests they have been inactive for sometime, despite the vertical displacement on the weathered surface (as old as 10 Ma ?). Alternatively, they could be preexisting reverse faults associated with the late Miocene Squaw Peak thrust system (Meisling and Weldon, 1989) or active reverse faults associated with the kink in the NFTS directly below (analogous to the SAT). The effect of offset of the weathered surface by these structures is minimal, based on the similar NFTS orientation that resulted from an attempt to back-slip them and perform the dip analysis on the NFTS (Figure 18c). The Lovelace Canyon and Arrastre Canyon Narrows faults are shown cut by the NFTS, given their inactive appearance in airphotos.

4.5.4 Horizontal shortening in the San Bernardino Mountains

The pattern of vertical deformation across the entire SBMs is apparent in the geometry of the deformed weathered surface on the north and the magnitude of rock uplift and erosion inferred from radiogenic helium ages in the southern part of the range (Spotila et al., 1998). Figure 20 shows a simplified version of the structure contour map of the weathered surface along with estimated elevations of the southern blocks with denudation restored based on helium ages. If the pre-uplift topography of southern blocks was roughly continuous with the weathered surface of the Big Bear and San Gorgonio blocks to the north prior to denudation, then the restored elevation can be used a rough proxy (a minimum estimate) of the structural horizon of the weathered surface in the southern blocks. Given the likelihood that this relief did not exist prior to the last few million years (May and Repenning, 1982), the simplified contour diagram in Figure 20 should approximate the total vertical displacement of the modern SBMs. The most striking feature of the pattern of this displacement is the increase in rock uplift towards the south-central portion of the range.

This pattern of vertical displacement can be used to estimate the variation in horizontal plate motions accommodated by structures within different parts of the SBMs. The magnitude of north-south shortening accommodated in the Big Bear block can be calculated as the difference in length (dL) between the reconstructed weathered surface and a horizontal line, assuming the weathered surface was approximately horizontal prior to deformation (Figure 21). Where the weathered surface is eroded away at the escarpments of the range, it is projected upwards until it intersects the upward projections of the block bounding faults (using available constraints on fault dip). These estimates of horizontal shortening are simpler but essentially identical to the determination of slip along the surface traces of the thrusts in cross section (Figure 18). The horizontal shortening accommodated across the structures bounding the smaller, southern blocks, on which the weathered

surface is not preserved, can be estimated from the magnitude of denudation constrained by radiogenic helium ages. The projected horizontal length of these eroded blocks is the distance between the bounding faults at the elevations the blocks would have stood had they not been heavily denuded, as inferred from the helium ages (Spotila et al., 1998). The total shortening across five north-south profiles is thus represented as the difference between the length of the red line and horizontal profile width on Figure 21.

The total shortening across the SBMs is greatest in the middle (dL = 6.3 km, CC') and decreases to east and west (3.3 km, AA'; 0.8 km, EE'; Figure 22). This variation is similar to the pattern of displacement along the NFTS and SAT (Figures 16 and 17) and shows a remarkable correspondence to the present location of San Gorgonio Pass (i.e. it peaks just northwest of the fault bend). The uncertainty in these values is significant, but difficult to estimate given that it is most dependent on the dips used to project block-bounding faults upwards. Although the use of available dip data provides a best-guess, it is impossible to be certain that the faults retain their orientations over the several-kilometer distance of the projections. Given this best-guess, however, the maximum convergence of 6.3 km has a N38°W component of 5 km, which is 5% of the total Pacific-North American motion in 2 Myr (DeMets, 1995). The total volume of rock uplift in the SBMs can also be calculated from these profiles, as the sum of the area above base level (average elevation of buried basement to north and south) in each profile (AA' 33.9 km^2; BB', 76.1 km^2; CC', 98.0 km^2; DD', 66.4 km^2; EE', 15.3 km^2) multiplied by profile width (7.6 km for AA', 15.3 km for all others). Total volume of rock uplift in the SBMs is estimated at ~4200 km^3.

From the profiles shown in Figure 19, it is also possible to estimate the magnitude of erosion that has coincided with the uplift of the SBMs. By subtracting the existing topography from the projected envelope of rock uplift, based on the weathered surface and radiogenic helium ages, the eroded area along each profile can be calculated (i.e. two-dimensional mass balance). From the profiles it is apparent that most of the erosion in the

SBMs has occurred along the northern and southern escarpments of the Big Bear plateau and the southern blocks that have risen within the San Andreas fault zone, not from the top of the Big Bear plateau or San Gorgonio block (Figure 21). The magnitude of erosion in each profile can also be compared to the volume of sediments where the weathered surface is buried. Figure 21 shows that in all but the westernmost profile (AA'), the eroded area is far greater than the area of sediments deposited. This requires that sediments have been transported out of the reach of these profiles. For profile AA', it is consistent that the magnitude of deposition exceeds the magnitude of erosion, given westerly transport of sediments into Apple Valley from Deep Creek and easterly transport of sediments from Cajon Pass into San Bernardino Valley.

The average depth of incision in the SBMs, calculated by dividing the eroded area in each profile by the width of the range, varies from 0.16 to 0.71 km, with the greatest incision having occurred in the middle (CC', Figure 21). The average incision along profile EE' (0.16 km) is nearly identical to the value determined locally using the reconstructed envelope of basalts on the eastern part of the Big Bear plateau (see Section 3.8.2, Chapter 3), suggesting the loosely constrained profile envelopes are accurate. From these values of incision, erosion rates for the SBMs may be approximated by dividing by the ~2-3 Myr minimum age of the range (May and Repenning, 1982). These vary from 0.24-0.36 mm/yr in the middle to 0.05-0.08 mm/yr on the east, but average ~0.1-0.2 mm/yr. This is slightly lower than denudation rates calculated for other active California mountains (e.g., ~0.2-0.3 mm/yr, Santa Cruz Mountains; Anderson, 1990; ~0.5 mm/yr, Santa Monica Mountains; Meigs et al., 1998).

4.6. Discussions

4.6.1 The kinematics of strike-slip faults and uplift in the SBMs

The use of the weathered surface as a structural datum has given new insight into the three-dimensional geometry of structures responsible for the uplift of the SBMs.

Figure 23 shows a schematic summary of the major structural elements in the range, based on the structural analysis above. On the north, the Big Bear plateau has risen on opposing thrusts, although the NFTS is by far the dominant structure and the SAT is secondary. The orientation of the NFTS is not homogenous beneath the range, but varies from east to west and north to south. On the east, the fault must steepen at depth to have produced the observed vertical deformation, while on the west it must flatten given the apparent role played by the SAT. The shape of the NFTS thus varies from concave on one part of the range to convex or listric on the other. To the south, uplift structures display a different structural style. High-angle faults must accommodate large magnitudes of rock uplift of small crustal blocks south of the Big Bear plateau. These faults include oblique dextral-reverse faults of the San Andreas fault zone (Mill Creek fault, Mission Creek fault), as well as more diffuse, poorly known fault zone (Barton Flats fault zone). In addition, a possibly coactive, diffuse system of dextral shear appears to penetrate the entire package of convergent structures, implying a complex mechanical regime may be at work.

This kinematic picture shares similarities to previous hypotheses for the geometry of uplift structures beneath the SBMs and transpressive zones in general. The flattening of the NFTS at depth on the west mimics the decollement hypothesis that the thrust should merge with the gently-dipping brittle-plastic transition (cf. Corbett, 1984; Meisling and Weldon, 1989; Yeats, 1981), although the NFTS flattens above the base of seismicity and steepens elsewhere. On the east, the steepening of the NFTS mimics the "palm-tree" hypothesis that the thrust joins a high-angle zone of transpression (cf. Sadler, 1982b; Sylvester, 1988; Bartlett et al., 1981; Aydin and Du, 1995). This hypothesis does not match in detail, however, given that the NFTS is not symmetric and does not steepen into a central strike-slip zone at depth. A palm-tree geometry is dominated by high-angle strike-slip faults that flatten in the near-surface, such as in the Spitsbergen transpressive orogen (Lowell, 1981). In the SBMs, however, the NFTS is an independent structure that is decoupled from the strike-slip zone and strike-slip faults themselves remain high-angle near

the surface. The architecture of structures responsible for uplift of blocks in the southern SBMs is more similar to models of the Santa Cruz Mountains and rupture during the Loma Prieta earthquake, in which reverse motion occurs on interacting, high-angle strike-slip faults due to fault-normal convergence across the weak San Andreas fault (Mount and Suppe, 1987; Schwartz et al., 1990; Jones and Wesnousky, 1992; Shaw et al., 1994).

Thus, although the SBMs display features of several conceptualized models of transpressive areas, none seems to fully explain the apparent structure beneath the range. This may be a good example of a common phenomenon in structural studies, in which simplistic models of deformation fail when data adequate to describe a structural system become available. The SBMs have been produced by a complex structural architecture, in which major strike-slip faults have accommodated significant vertical motion, opposing thrust faults display complex geometries at depth, and secondary fault systems are common. Convergence has been accommodated by a series of distinct, decoupled structures of variable orientation and kinematic style, apparently in the absence of a single, organized structural stencil.

4.6.2 The cause of convergence in the SBMs

These new kinematic constraints and interpretations warrant a reevaluation of the major hypotheses for the nature of driving conditions responsible for convergence and uplift of the SBMs. Three ideas, that the SBMs are a result of the Big Bend in the San Andreas fault, that the SBMs are due to a density current created by downwelling of mantle lithosphere, and that the SBMs have a local cause due to geometric complexities along strike-slip faults, are explored below.

4.6.2.1 The SBMs as a product of the Big Bend

The coincidence of the convergent uplift of the Transverse Ranges and the obliquity between the trend of the San Andreas fault and the direction of plate motion have long been

considered causally related (e.g., Hill and Dibblee, 1953). Although some workers have suggested that the San Andreas fault has been bending steadily since its inception due to contraction in the Mojave Desert and left-lateral motions on the Garlock fault (e.g., Garfunkel, 1974; Bartley et al., 1990), others have considered the bend to have existed all along (cf. Dickinson, 1996). In either case, many models of southern California tectonics have sought to reconcile how plate motions must be accommodated by secondary, off-San Andreas structures. The western Transverse Ranges have been considered to accommodate the convergence necessitated by the Big Bend through thrusting and rotation (e.g., Dickinson, 1996). It is therefore possible that the SBMs are analogous to the western Transverse Ranges, and may have also been created in response to the oblique transform boundary (if in fact this is also the origin of the western Transverse Ranges). Bartley et al. (1990), for example, hypothesized that convergent structures of the Mojave block (including the SBMs) resulted from north-south contraction that resulted from the Big Bend in the San Andreas fault. However, there are several differences that indicate the SBMs are very different from the western Transverse Ranges.

One major difference between the SBMs and the western Transverse Ranges is the localization of horizontal shortening accommodated within them. The western Transverse Ranges are a fold and thrust belt that extends for nearly 200 km between the dextral San Andreas and Hosgri faults and has experienced a large magnitude of convergence across its entire length. The convergence across this belt may have exceeded 50 km in the past ~5 Myr (Namson and Davis, 1988; Namson and Davis, 1990; Dickinson, 1996) and presently may occur at ~1 cm/yr across its entire breadth (Donnellan et al., 1993; Molnar and Gipson, 1994). This contrasts with the SBMs, which have concentrated convergence in a narrow space that terminates abruptly on either side (Figure 22). In addition, Dickinson (1996) has shown that the entire western Transverse Ranges province can be divided into a series of internally-deforming, transrotating blocks, which accommodate all the convergence necessitated by the Big Bend that is not taken up by the major northwest-

trending strike-slip faults. This implies that there is no need to internally deform the plate to the east of the San Andreas fault (Dickinson, 1996) and thus the localized pulse of deformation in the SBMs may be the result of other causes.

A second point that suggests the SBMs are not the eastern analogy of the western Transverse Ranges is the difference in the rotation between these domains. The western Transverse Ranges can accommodate oblique dextral shear of the Pacific-North American transform margin only because they rotate clockwise about a vertical axis. Since the mid-Miocene, the western Transverse Ranges may have rotated as much as 90° clockwise (e.g., Kamerling and Luyendyk, 1979; Luyendyk et al., 1980; Hornafius, 1985; Terres and Luyendyk, 1985) and still appear to be rotating at a rate of ~6°/Myr (Luyendyk, 1991; Molnar and Gipson, 1994). The Mojave Desert and SBMs blocks, however, have apparently not rotated significantly ($\pm 5°$ or so paleomagnetic uncertainties) since the early Miocene (paleomagnetic data of Weldon, 1986; Valentine et al., 1993; Liu, 1990; Golombek and Brown, 1988; Ross et al., 1989; and the models of Dickinson, 1996; Schelle and Grunthal, 1996). It is this lack of rotation that has been used to argue that the Big Bend of the San Andreas fault has existed since its inception 5 Ma (cf. Dickinson, 1996). This also indicates a dissimilarity in the deformation of the SBMs and implies they may have formed due to other causes.

Finally, there is some doubt as to whether convergence must be accommodated near the San Andreas fault due to the Big Bend. Weldon and Humphreys (1986) questioned whether the upper crust of the western Transverse Ranges near the San Andreas fault could actually have accommodated the convergence necessitated by its obiqueness to plate motion. Instead, they postulated that the velocity field adjacent to the bent San Andreas fault had to parallel it, and that the convergence has to be accommodated in another manner. Geodetic data also shows that near the San Andreas fault, the crust moves parallel to the fault trend and rotates its direction around bends in the fault, as if it were a fluid (Lisowski et al., 1991). Further away from the fault trace (~10^2 km), however, the velocity field

straightens to parallel the Pacific-North American plate motion vector, implying that convergent mechanisms (i.e., Dickinson, 1996) are still required in the far-field (Lisowski et al., 1991). Given that the SBMs lie in such proximity to the San Andreas fault, it is therefore possible that they are not accommodating the convergence associated with the Big Bend (though they may still be the product of local fault complexities).

Thus there are significant differences between the western Transverse Ranges and the SBMs. If the convergence required by the Big Bend can be accommodated entirely by the plate west of the San Andreas fault (as shown by Dickinson, 1996), then the local deformation we have documented in the SBMs may have other driving conditions and may not be simply an eastern analog to the western Transverse Ranges.

4.6.2.2 The SBMs as a product of crustal buckling associated with a dense mantle root

A second postulated cause of convergence and uplift of the Transverse Ranges province is the sinking of a cold, dense slab of mantle lithosphere beneath them. The origin of this hypothesis is the presence of a positive seismic velocity anomaly between 50 and 200 km depth under the general location of the Transverse Ranges (based on inversion of teleseismic P waves; Hadley and Kanamori, 1977; Humphreys et al., 1984; Humphreys and Clayton, 1990) (Figure 24). This anomaly may represent a slab of detached mantle lithosphere that is being forced downwards due to convergence associated with the obliquity between the San Andreas fault system and the direction of plate motion (i.e., mantle subduction; Bird and Rosenstock, 1984; Namson and Davis, 1988) or a mantle downwelling associated with a local convective instability (Humphreys et al., 1984; Sonder, 1990). The alleged lithospheric slab is envisioned to sink under its own weight, causing crustal buckling (i.e., thrusting and high topography of the Transverse Ranges) through tractions exerted at the Moho along its axis (Humphreys and Hager, 1990). In this case, the uplift of the SBMs could be the result of a negative buoyancy force exerted across a wide area of the mantle, rather than convergence associated with crustal structures.

There are several models that explore how such a mantle anomaly could produce the Transverse Ranges. Humphreys and Hager (1990) present a geodynamic model of the velocity anomaly, in which the 2% velocity difference is attributed to a slab of mantle lithosphere that is ~500°C colder (and 1% more dense) than the surrounding mantle. They consider this slab as a small-scale convection cell that is related to the convergence between Pacific and North American lithosphere, which requires that mantle lithosphere be consumed at a rate comparable to plate motions over the last 10 Myr or so (several hundred kilometers of mantle lithosphere consumed), while the crust decouples from the sinking mantle and is translated laterally along the San Andreas fault without any convergence related to plate motion (Figure 25). The loss of mantle lithosphere may be balanced by upwelling of asthenosphere in the Salton Trough, as suggested by the presence of low crustal velocity there (Figure 24). Humphreys and Hager (1990) calculate a mantle flow regime based on a temperature field derived from the velocity anomaly, which shows that the slab should sink and induce tractions on the crust if a horizontal convergent force (i.e., plate motion) is present in the uppermost mantle. Although not tested directly by their model, Humphreys and Hager (1990) maintain that these tractions are responsible for the convergence in the upper crust and the creation of high topography in the Transverse Ranges (including the SBMs). In this model, plate convergence responsible for major mantle downwelling is not responsible for minor crustal thickening and convergence, but the downwelling itself produces the Transverse Ranges. Note that Humphreys and Weldon (1994) state instead that a combination of plate motion convergence and mantle downwelling may actually be responsible for the high topography of the Transverse Ranges.

Sonder (1990) presented another model, the negative buoyancy forces associated with a density anomaly of 1-2% exerted a low deviatoric stress that can locally change the orientation of the regional stress field. In the case of the Transverse Ranges, the predicted modification is a 23° counterclockwise rotation of the maximum horizontal compression

vector. This suggests that the alleged mantle downwelling is responsible for the both the Big Bend in the San Andreas fault and the convergence in the Transverse Ranges, rather than the mountains being a consequence of fault geometry (Sonder, 1990). In a different model, the velocity anomaly was considered to result from subduction of the Pacific lithosphere beneath the North American crust at the present position of the SBMs and San Gabriel Mountains (Sheffels and McNutt, 1988). This study, based on fitting topography and Bouguer gravity anomalies to models of isostatic compensation and crust and mantle structure, showed that the alleged high density anomaly could be mechanically coupled to the crust and cause a terminal bending moment that results in flexural uplift of the overlying elastic plate (i.e., Transverse Ranges).

Although these models of mantle downwelling and lithospheric subduction may be consistent with the generation of high topography in the Transverse Ranges and the seismic velocity anomaly below, they cannot demonstrate that convergence within the Transverse Ranges had to have been generated in this way. A similar velocity anomaly beneath the southern Sierra Nevada that has also been interpreted as mantle downwelling is not responsible for convergence at the surface (Jones et al., 1994), implying that such mantle convection does not require buckling and orogeny in the upper crust. Interpreting upper crustal convergence using small velocity anomalies at depth is also risky in the absence of other corroborating evidence for mantle downwelling or subduction, such as deep focus earthquakes or strain indicated by seismic anisotropy.

In addition, there are several possible discrepancies between tectonics in the upper crust and the proposed models. First, the seismic velocity anomaly is distributed across a wide region in southern California (particularly east of the San Andreas fault) that is much larger than the small regions of localized convergence (i.e. SBMs) in the upper crust (Figure 24). Convergence in the SBMs is focused on a narrow (tens of kilometers) region (Figure 20), that is a small fraction of the region along the eastern side of the San Andreas fault underlain by the velocity anomaly (Humphreys et al., 1984; Humphreys and Clayton,

1990). Although the distribution of the anomaly varies from study to study, no report shows a distribution that would result in such localized convergence above. For example, Hadley and Kanamori (1977) show a broad distribution of the anomaly that includes large areas outside of the Transverse Ranges (Los Angeles basin, Mojave Desert). Revenaugh (scattering of P-waves; 1995) shows the anomaly as centered to the south of the Transverse Ranges, with a distribution that is twice as large as the Transverse Ranges and extends ~100 km east of the SBMs. Hu et al. (P-wave polarization; 1994) show yet a different distribution, in which the anomaly is present primarily to the southwest of the San Andreas fault and is not present under the entire SBMs. Thus, it does not seem that a precise spatial association can be made between the alleged mantle root and the localized deformation of the SBMs.

A second discrepancy concerns the mobility of the crust with respect to the mantle lithosphere. If hundreds of kilometers of mantle lithosphere have been consumed, the presence of far less crustal convergence in the Transverse Ranges requires that crust has been laterally transported over the mantle anomaly (Humphreys and Hager, 1990). The lack of offset of the velocity anomaly by major crustal faults (Figure 24) also requires that the Moho be a zone of decoupling between the differential motions of the crust and mantle (Hadley and Kanamori, 1977). This implies that the spatial correlation between the Transverse Ranges topography and the velocity anomaly (Figures 1 and 24) is only true of the present day. When the western Transverse Ranges began uplifting at ~5 Ma, for example, they would have been situated far south of the present axis of the anomaly (if the anomaly is fixed to North America). Likewise, the SBMs would have sat far to the north of the anomaly, if fixed to Pacific. The only way around this problem is to allow the velocity anomaly to migrate in time and remain proximal to uplifting areas above (Humphreys and Hager, 1990). If the above models require ad hoc migration of the anomaly to have a spatial correlation with the Transverse Ranges back in time, the present-day spatial correlation does not by itself demonstrate the models.

Given these discrepancies, it seems worth exploring alternative origins of the seismic velocity anomaly that can explain its unique spatial coincidence with the Transverse Ranges. For instance, Hadley and Kanamori (1977) discuss the possibility that the anomaly represents a phase change in the upper mantle related to lithostatic load of high topography, rather than a thermal anomaly associated with sinking cold lithosphere. Another viable alternative is that the anomaly is associated with a decrease in lithospheric density (inversely proportional to seismic velocity), which could represent a Pratt-type mantle root that compensates the high topography of the Transverse Ranges (Jones et al., 1994). The magnesium oxide enrichment of ultramafic-xenolith-bearing basalts (as young as 6 Ma) derived from the mantle lithosphere beneath the SBMs, relative to basalts derived from normal upper mantle in the northern Mojave Desert (Neville et al., 1985), is independent evidence for low-density mantle beneath the Transverse Ranges. Such low-density mantle could result from depletion associated with partial melting and generation of Mesozoic arc batholith rocks along the plate margin.

In conclusion, it seems that the localized convergence within the SBMs cannot be clearly or uniquely explained by a density current in the mantle below the region. Downwelling of mantle lithosphere may occur below the Transverse Ranges and contribute broadly to convergence there, but can't seem to produce the localized SBMs specifically. If it does contribute to the forces that are responsible for the construction of high topography, these forces are likely filtered and translated into an ambient upper crustal force regime and pattern of existing weaknesses in the brittle crust.

4.6.2.3 The SBMs as a local product of geometric complexity of strike-slip fault systems

The localized nature of the SBMs is the primary argument against the above two explanations for the origin of the convergence that produced them. Convergence on the eastern side of the San Andreas fault zone is confined to only 70 km width in the SBMs and does not match the >100 km width of the Big Bend or mantle velocity anomaly.

Convergent deformation within the SBMs (excepting the western San Bernardino arch; Meisling and Weldon, 1989) also peaks across a narrow region (Figure 22) and does not exhibit a pattern that reflects the migration of other tectonic elements passed the SBMs over the past few million years. For example, the western Transverse Ranges and San Jacinto fault have each migrated >50 km to the northwest with respect to the SBMs, whereas a sinking mantle slab fixed to the Pacific plate would have migrated 84 km to the northwest with respect to the SBMs (Figure 1). It would thus be favorable to find a local set of driving conditions that have not moved or modified substantially with respect to the location of the SBMs during the time of their deformation.

It has been suggested previously that local perturbations in the geometry of strike-slip faults have produced most of the convergence observed throughout the entire Transverse Ranges province. For example, horizontal shortening and rotations in the westernmost western Transverse Ranges may be associated with a left step from the Newport Inglewood and Whittier Elsinore faults to the Hosgri fault (Weldon and Humphreys, 1986). In addition, Weldon and Humphreys (1986) and Humphreys and Weldon (1994) hypothesized that the deformation of the SBMs was due to fault-parallel convergence along the San Andreas fault in the little bend of San Gorgonio Pass (Figure 1). Bennet et al. (1996) also present GPS data that indicate as much as 12 mm/yr fault-normal convergence may occur along the San Andreas fault along the southern side of the SBMs due to this left-step, although this is poorly constrained. Dibblee (1975) suggested local convergence in the SBMs resulted from the conjugate relationship of the San Andreas fault zone and Pinto Mountain fault.

The simplest kinematic model of the left-step in the San Andreas fault zone at San Gorgonio Pass is represented by two dextral faults connected by a zone of pure convergence (Figure 26a). In this case, material converges in the stepover at the rate of motion along the strike-slip faults ($y[t] = d[t]$), but is not transported out of the step by lateral motion along the strike-slip fault, thus resulting in crustal thickening (i.e., uplift and

depression of brittle-plastic transition). Given the cross-sectional dimensions of the stepover (15 km depth x 15 km east-west width = 225 km^2), an excess crustal volume of 11,250 km^3 should have been produced by 2 Myr of motion (25 mm/yr; Weldon and Sieh, 1985) along the San Andreas fault according to this simple model. The total volume of rock uplift (~4200 km^3; Figure 21) and rock "depression" (~1300 km^3, calculated as the difference between the base in seismicity and nominal 15-km-depth of the brittle-ductile transition in southern California, using data of Magistrale and Sanders [1995]) in the SBMs, however, is only 5500 km^3. This suggests that the left-step has not accommodated the full rate of motion along the San Andreas fault since 2 Myr ago. However, these values predict ~25 km of convergence could have been accommodated by thickening of the brittle crust during the history of the SBMs, or about 50% of the motion along the San Andreas fault since 2 Ma.

This simple mass-balance check of the relationship between the horizontal shortening (i.e., increased volume) of the SBMs and the convergence in San Gorgonio Pass indicates that the local left-bend in the San Andreas fault could have been the condition driving their uplift. However, this requires that the SBMs have remained fixed with respect to San Gorgonio Pass throughout their history, given their tight focus of deformation. Because shortening in the SBMs cannot accommodate total convergence in the Pass, there must be some lateral transfer of crust through the left-bend along the San Andreas fault. For example, if no convergence occurs, crust moves parallel to the fault within the bend at a greater rate than outside of the bend, resulting in lateral translation of features with respect to the bend (Figure 26b). If only partial convergence occurs (Figure 26c), crustal thickening may take place at a high rate (y[t]) but must still be balanced by lateral translation (x[t]), which can move the thickened crust with respect to the fault bend. This can result in a steady-state pattern of topography (function of uplift, erosion, and isostatic adjustment) that is greatest at the edge of the fault bend and decreases monotonically away from the bend in the direction of fault motion (Anderson, 1990). The

rate of fault-parallel lateral translation (x[t]) in the bend can be calculated for the case of the SBMs and San Gorgonio Pass (30° oblique to San Andreas), assuming a rate of plate-motion parallel shortening as determined above (~half of San Andreas rate, or y[t] = 0.5d[t]; Figure 26d). In this case, the rate of lateral motion on faults in the bend should be 58% of the rate of the San Andreas fault outside of the bend. This is consistent with geologic estimates of the right-lateral rate on faults within the Pass of about half the San Andreas fault rate (D. Yule, pers. comm., 1998). Although this model fits observations, it still implies that thickened crust should advect at a high rate with respect to the fault bend (~15 mm/yr for SBMs, assuming the Peninsular Ranges are fixed).

To localize the SBMs uplift with respect to San Gorgonio Pass, it could be arbitrarily assumed that the fault-bend was fixed with respect to the eastern side of the San Andreas fault, in which case the Peninsular Ranges block would move at the full fault rate relative to the bend. However, it would be more agreeable to find some physical condition that fixed the Pass with respect to the SBMs, such as if structural systems to the east of the San Andreas fault pin the fault bend to that plate.

Several significant structural systems occur east of the San Andreas fault in the vicinity of San Gorgonio Pass, which could be directly related to its kinematics. Like the western Transverse Ranges, these active structural elements must play the role of accommodating southern California plate motion as crust negotiates the Big Bend in the San Andreas fault. To the northeast of the SBMs, ~8 mm/yr of dextral shear is distributed across north-northwest trending faults of the Eastern California shear zone (Dokka and Travis, 1990; Sauber et al., 1986; Savage et al., 1990) (Figure 1). This active fault system is the conduit for connection of the Basin and Range extensional province with the San Andreas fault zone and has accrued ~65 km (or 47 km, according to Dickinson, 1996) of right-slip since its inception between 6 and 10 Ma (Dokka and Travis, 1990). Although this fault system has been postulated to involve major block rotation (e.g., Nur et al., 1993; Garfunkel, 1974), paleomagnetic data implies that the shear zone is mainly irrotational

(Dickinson, 1996). However, the minor rotations (<5°) predicted by models of Carter et al. (1987) (counterclockwise), Dokka and Travis (1990) (counterclockwise), and Humphreys and Weldon (1994) (clockwise) are beyond resolution with existing paleomagnetic data. Given the proximity of the Eastern California shear zone and San Gorgonio Pass, the two may share a kinematic relationship (Figure 1). For example, Du and Aydin (1996) present a mechanical model based on fault strain energy that suggests the 1992 Landers earthquake rupture was produced by stresses imposed at San Gorgonio Pass.

To the southeast of the SBMs, the easternmost Transverse Ranges province consists of west-trending left-slip faults, which accommodate dextral shear via clockwise rotation of fault blocks (Carter et al., 1987) (Figure 1). This system of left-lateral faults has accrued ~50 km of displacement in the past 10 Myr (Powell, 1981), about 17 km of which has occurred along the Pinto Mountain fault that abuts the SBMs (Dibblee, 1992). This system has thus been active during at least part of the lifetime of the Eastern California shear zone, and may have played a role in connecting it with the San Andreas fault zone (Dickinson, 1996). Based on the observation of ~41° of clockwise rotation since the late Miocene within the easternmost Transverse Ranges, Carter et al. (1987) presented a model (after Freund, 1974), in which on the order of 100 km of dextral shear could be accommodated by the left-slip faults (52-63 km in the model of Dickinson, 1996). This implies that the two provinces of differing deformational style have both taken up similar magnitude of right-lateral motion between the Pacific and North American plates, and that they actually represent a semi-integrated mechanism of slip transfer between the San Andreas fault zone and the Basin and Range (Dokka and Travis, 1990). Observations of the oroclinal flexure of the Garlock and Pinto Mountain faults (Figure 1) and the high ratio of net slip to length on the left-lateral faults (~0.3 for the Pinto Mountain fault; Dibblee, 1992) are consistent with this hypothesis (Carter et al., 1987). Like the Eastern California

shear zone, the easternmost Transverse Ranges province may be kinematically related to San Gorgonio Pass, given their proximity.

Carter et al. (1987) present a model that could explain how the San Gorgonio bend may be produced by motions in both the Eastern California shear zone and easternmost Transverse Ranges, which in turn predicts that the Pass is fixed with respect to the eastern side of the San Andreas fault (and SBMs). In this model, right shear and slight counterclockwise rotations of the Eastern California shear zone and clockwise rotations and left-slip in the easternmost Transverse Range produce a deflection in the trace of the San Andreas fault that is localized between them (Figure 27a). The resulting counterclockwise and clockwise rotations on the trace of the San Andreas fault produce the restraining bend at San Gorgonio Pass, which in turn creates local convergence that produces the SBMs (fixed with respect to the Pass).

One potential difficulty with this model is that several studies have presented data showing the rotations and left-lateral faults of the easternmost Transverse Ranges are no longer a factor in accommodating plate motion (Richard, 1993; Dickinson, 1996; Bourne et al., 1997). In this case, rotation of this province could not influence the creation of the San Gorgonio bend. However, the geomorphic expression of the Pinto Mountain fault (Dibblee, 1992), some geodetic data (Johnson et al., 1994), and the effect of the Pinto Mountain fault on the Landers-Joshua Tree earthquake sequence (Sieh et al., 1993) show that at least some of the faults of the easternmost Transverse Ranges are still active. In addition, the slip rate along the southern San Andreas fault adjacent to the Salton Trough (25 mm/yr; Sieh, 1986) may not be the sum of the Eastern California shear zone (8 mm/yr) and the San Andreas fault north of the junction with it (25 mm/yr; Weldon and Sieh, 1985), suggesting the full motion of the shear zone is not simply transferred to the San Andreas where they meet at San Gorgonio Pass.

A second difficulty with the Carter et al. (1987) model is that data showing counterclockwise rotations of the Eastern California shear zone are controversial (cf.

Dickinson, 1996). Humphreys and Weldon (1994), however, present a model that localizes San Gorgonio Pass with respect to the eastern tectonic elements that functions with small clockwise rotations of the Eastern California shear zone (Figure 27b). In this model, clockwise rotation and left-slip in the easternmost Transverse Ranges accommodates only some of the dextral shear that is carried by the Eastern California shear zone, requiring the remainder to transfer to the San Andreas fault via the left slip on the Pinto Mountain fault and extension on the Morongo Valley fault (Johnson et al., 1994). This generally fixes the restraining bend to the intersection of the Pinto Mountain fault (and SBMs), the location of which is controlled by the boundary between the two clockwise-rotating domains to the north and south. Uplift of the SBMs could also be directly related to the Pinto Mountain fault itself, similar to the convergence produced by the confluence of the Garlock and San Andreas faults to the north (Bohannon and Howell, 1982). In any case, the model of Humphreys and Weldon (1994) provides a model based on alternative data that still presents a kinematic explanation that fixes the SBMs north of the San Gorgonio bend.

In either model, the rotating shear zones that help negotiate the Big Bend in the San Andreas fault (Figure 1, 27), in turn produce a smaller bend in San Gorgonio Pass that is fixed to their confluence (and the SBMs). In detail, the small bend may migrate slightly with respect to these domains of diffuse shear, given the instability of their junction. Johnson et al. (1994), for example, present a kinematic model that predicts migration of the triple junction (i.e., San Gorgonio Pass) to the northwest along the San Andreas fault at 1-8 mm/yr. This may be supported by possible westward-migration of the Eastern California shear zone since its inception (Dokka and Travis, 1990). For example, if the eastern half (~50 km) of the shear zone has been replaced by the western half, as suggested geodetically (Sauber et al., 1986), the rate of migration over 10 Myr is ~5 mm/yr. Similarly, the locus of activity along left-lateral faults of the easternmost Transverse Ranges seems to have migrated northwards since its inception (Powell, 1981). At the predicted rate, however,

the locus of shortening within the SBMs would have moved only ~10 km or so in 2 Myr, which does not negate the amazing correspondence between the observed shortening (Figure 22) and San Gorgonio Pass. Thus, it seems quite likely that the uplift of the SBMs has been produced by convergence created by the restraining bend of San Gorgonio Pass.

4.6.3 Implications for earthquake activity in the San Bernardino Mountains region

Based on our observations, we consider the NFTS to represent a potential seismic source in the SBMs. Although its slip rate may have decreased in last half million years or so, there are ample data suggesting that it has been active in the late Pleistocene and no conclusive evidence demonstrating it is extinct. If active, the NFTS may only manage to rupture in small segments, given the degree to which northwest-trending strike-slip faults appear to cut its upper plate. Dextral shear may control the present strain pattern in the SBMs, and allow the NFTS to rupture only where activated by strike-slip faults. If the entire NFTS can rupture in one event, however, it would likely have ~3 m of throw (based on scaling to its 70 km length; Wells and Coppersmith, 1994). If the thrust continues to slip at 1 mm/yr (lower estimate of long-term rate), this sized event would require a recurrence interval of ~3 Ka. This is not an uncommon number for off-San Andreas faults, including those associated with the Eastern California shear zone (Rubin and Sieh, 1997). The magnitude of such a rupture would be about Mw=7.5, as estimated from the likely seismic moment (calculated from its dimensions [30 km width x 70 km length], slip [3 m], and assuming rigidity [3.3×10^{11} dyne cm^{-2}]). This would be about twice as large as the Mw=7.3 1992 Landers earthquake (Sieh et al., 1993) and would be very damaging to local communities. However, this should be considered a worst-case scenario.

Observations also suggest that the SAT is not an active structure. Although this thrust has played a significant role in uplift of the Big Bear plateau, it does not appear to have sustained much motion since at least the mid-Pleistocene. However, there are many other structures that could produce damaging earthquakes within the SBMs. These include

the members of the diffuse, southward continuation of the Eastern California shear zone (Table 2), as well as structures responsible for localized uplift in the southern SBMs (such as the Mill Creek fault [although thought to be extinct] or the Barton Flats fault zone). The 6/28/92 Big Bear earthquake (M6.5; Figure 14) is an example of a moderate-sized event on secondary strike-slip faults within the range. An evaluation of the seismic hazard posed by these structures requires much more detailed analysis of secondary faulting than presented in this study, but it seems reasonable to conclude that the SBMs share a level of hazard equal to any other location within the Eastern California shear zone. These non-thrust faults may represent a hazard equal to or greater than the NFTS itself.

4.7. Conclusions

The use of the weathered surface as a structural datum has significantly improved our understanding of the architecture and kinematics of the SBMs' uplift. The vertical displacement field of the Big Bear plateau has been constrained in fine detail, thus enabling assessment of the displacement and geometry of the NFTS and SAT. These thrust faults have smooth, bell-shaped along-strike distributions of total vertical displacement and fully account for the uplift of the plateau. The NFTS has a maximum vertical displacement of 1.8 km, which corresponds to a net-slip of ~3.1 km and a long-term net-slip rate of ~1.6 mm/yr. Maximum vertical motion along the SAT has been 1.1 km (net-slip ~2.2), implying the SAT has played a less significant role in uplift of the plateau. Geomorphic analysis of the thrusts and corresponding escarpments also indicate the NFTS has been active up until at least the latest Pleistocene (but may be decelerating), whereas the SAT displays almost no evidence of Pleistocene and may be as old as early Pliocene. The pattern of vertical displacement also constrains the subsurface geometry of the thrusts. The NFTS likely steepens towards the south to accommodate a southward-increase in uplift along the eastern plateau. A similar southward rise in the weathered surface on the west can be accounted for by the SAT, so that the NFTS likely flattens towards the south.

Discontinuous strike-slip faults penetrate the upper plate of the thrusts and complicate the structural system, as do oblique-reverse faults that have uplifted smaller blocks in the southern part of the range. The structural architecture of the range is thus complex and involves interaction of both high and low angle contractile structures. The horizontal shortening accommodated by the NFTS and SAT combines with convergence along high-angle faults in the southern part of the range to a maximum of 6.3 km. This maximum occurs just northwest of the left-bend in the San Andreas fault at San Gorgonio Pass. The remarkable spatial association of maximum convergence on all structures and the location of this restraining bend implies a causal relationship. It is likely that a local geometric complexity along the San Andreas fault zone, itself the result of transrotation in the Mojave Desert and easternmost Transverse Ranges, is responsible for convergence in the SBMs.

4.8. References

Allen, C.R., San Andreas fault zone in San Gorgonio Pass, southern California, Geol. Soc. Amer. Bull., 68, 315-350, 1957.

Aksoy, R., Sadler, P., and Biehler, S., Gravity anomalies over sedimentary basins on the Helendale fault trend, *in* Kooser, M.A. and Reynolds, R.E., eds., Geology around the margins of the east San Bernardino Mountains, Inland Geol. Soc., 1, 121-128, 1986.

Anderson, R.S., Evolution of the northern Santa Cruz Mountains by advection of crust past a San Andreas fault bend, Science, 249, 397-401, 1990.

Aydin, A., and Du, Y., Surface rupture at a fault bend: the 28 June 1992 Landers, California, earthquake, Bull. Seism. Soc. Amer., 85, 111-128, 1995.

Bartlett, W.L., Friedman, M., and Logan, J.M., Experimental folding and faulting of rocks under confining pressure, Tectonophysics, 79, 255-277, 1981.

Bartley, J.M., Glazner, A.F., and Schermer, E.R., North-south contraction of the Mojave block and strike-slip tectonics in southern California, Science, 248, 1398-1401, 1990.

Bennet, R.A., Rodi, W., and Reilinger, R.E., Global positioning system constraints on

fault slip rates in southern California and northern Baja, Mexico, J. Geophys. Res., 101, 21943-21960, 1996.

Biehler, S., Tang, R.W., Ponce, D.A., and Oliver, H.W., Bouguer anomaly map of the San Bernardino Quadrangle, scale 1:250,000, Regional Geophys. Map Series, 3B, Calif. Div. of Mines and Geol., 1988.

Bilham, R., and Williams, P., Sawtooth segmentation and deformation processes on the southern San Andreas fault, California, Geophys. Res. Lett., 12, 557-560, 1985.

Bird, P., and Rosenstock, R.W., Kinematics of present crust and mantle flow in southern California, Geol. Soc. Amer. Bull., 95, 946-957, 1984.

Bohannon, R.G., and Howell, D.G., Kinematic evolution of the junction of the San Andreas, Garlock, and Big Pine faults, California, Geology, 10, 358-363, 1982.

Bourne, S.J., England, P.C., and Parsons, B., The motion of crustal blocks driven by flow of the lower lithosphere: Implications for slip rates of faults in the South Island of New Zealand and southern California, submitted to Nature, 1997.

Brown, G., and Associates, Geology and ground water geology of Big Bear Valley, Assoc. of Engineering Geologists, southern California Section, Annual Spring Field Trip Guidebook, 73-95, 1976.

Bryant, W.A., Eastern North Frontal fault zone, and related faults, southwestern San Bernardino County, Fault Evaluation Report, FER 182, CA. Div. Mines Geol., 1986a.

Bryant, W.A., Western North Frontal fault zone, and related faults, San Bernardino County, Fault Evaluation Report, FER 186, Calif. Div. Mines and Geol., 1986b.

Bull, W.B., Geomorphology of segmented alluvial fans in western Fresno County, California, U.S. Geol. Survey Prof. Paper, 352-E, 1964.

Bull, W.B., Tectonic geomorphology of the Mojave Desert, U.S. Geol. Survey Contract Report, 14-08-001-G-394, Office of Earthquakes, Volcanoes, and Engineering, Menlo Park, CA, 188 p., 1977.

Bull, W.B., Geomorphic tectonic activity classes of the south front of the San Gabriel

Mountains, California, U.S. Geol. Survey Contract Report, 14-08-001-G-394, Menlo Park, CA, 100 p., 1978.

Carter, J.N., Luyendyk, B.P., and Terres, R.R., Neogene clockwise rotation of the eastern Transverse Ranges, California, suggested by paleomagnetic vectors, Geol. Soc. Amer. Bull., 98, 199-206, 1987.

Corbett, E.J., Seismicity and crustal structure of southern California: Tectonic implications from improved earthquake locations (Ph.D. thesis), Pasadena, CA, California Institute of Technology, 1984.

Cowie, P.A., and Scholz, C.H., Displacement-length scaling relationships for faults: data synthesis and discussion, J. Struct. Geol., 14, 1149-1156, 1992.

Dawers, N.H., Anders, M.H., and Scholz, C.H., Growth of normal faults: Displacement length scaling, Geology, 21, 1107-1110, 1993.

DeMets, C., Reappraisal of seafloor spreading lineations in the Gulf of California: Implications for the transfer of Baja California to the Pacific Plate and estimates of Pacific-North America motion, Geophys. Res. Lett., *22*, 3545-3548, 1995.

Dibblee, T.W., Geologic map of the San Gorgonio Mountain 15' Quadrangle, 1:62,500 scale, U.S. Geol. Surv. Misc. Geologic Invest. Map, I-431, 1964a.

Dibblee, T.W., Geologic map of the Lucerne Valley 15' Quadrangle, 1:62,500 scale, U.S. Geol. Surv. Misc. Geologic Invest. Map, I-426, 1964b.

Dibblee, T.W., Geologic map of the Morongo Valley 15' Quadrangle, 1:62,500 scale, U.S. Geol. Surv. Misc. Geologic Invest. Map, I-517, 1967a.

Dibblee, T.W., Geologic map of the Old Woman Springs 15' Quadrangle, 1:62,500 scale, U.S. Geol. Surv. Misc. Geologic Invest. Map, I-518, 1967b.

Dibblee, T.W., Geologic map of the Redlands 15' Quadrangle, 1:62,500 scale, U.S. Geol. Surv. Open File Map, 74-1022, 1974a.

Dibblee, T.W., Geologic map of the Lake Arrowhead 15' Quadrangle, 1:62,500 scale, U.S. Geol. Surv. Open File Map, 73-56, 1974b.

Dibblee, T.W., Late Quaternary uplift of the San Bernardino Mountains on the San Andreas and related faults, *in* Crowell, J.C., ed., San Andreas fault in southern California, CA Division of Mines and Geology Special Report, 118, 127-135, 1975.

Dibblee, T.W., Geology and inferred tectonics of the Pinto Mountain fault, eastern Transverse Ranges, California, in Richard, S.M., ed., Deformation associated with the Neogene Eastern California Shear Zone, southwestern Arizona and southeastern California, Redlands, CA, San Bernardino County Museum Sp. Pub., 28-31, 1992.

Dickinson, W.R., Kinematics of transrotational tectonism in the California Transverse Ranges and its contribution to cumulative slip along the San Andreas transform fault system, Geol. Soc. Amer. Spec. Paper, 305, 46 p., 1996.

Dokka, R.K., and Travis, C.J., Late Cenozoic strike-slip faulting in the Mojave Desert, California, Tectonics, 9, 311-340, 1990.

Donnellan, A., Hager, B.H., King, R.W., and Herring, T.A., Geodetic measurement of deformation in the Ventura-Basin-region, southern California, J. Geophys. Res., 98, 21727-21739, 1993.

Du, Y., and Aydin, A., Is the San Andreas big bend responsible for the Landers earthquake and the eastern California shear zone, Geology, 24, 219-222, 1996.

Feigl, K.L., Sergent, A., and Jacq, D., Estimation of an earthquake focal mechanism from a satellite radar interferogram: Application to the December 4, 1992 Landers aftershock, Geophys. Res. Lett., 22, 1037-1040, 1995.

Freund, R., Kinematics of transform and transcurrent faults, Tectonophysics, 21, 93-134, 1974.

Garfunkel, Z., Model for the late Cenozoic tectonic history of the Mojave Desert, California, and for its relation to adjacent regions, Geol. Soc. Amer. Bull., 85, 1931-1944, 1974.

Golombek, M.P., and Brown, L.L., Clockwise rotation of the western Mojave Desert, Geology, 16, 126-130, 1988.

Hadley, D.M., and Kanamori, H., Seismic structure of the Transverse Ranges, California, Geol. Soc. Amer. Bull., 88, 1469-1478, 1977.

Hauksson, E.L., Jones, L.M., Hutton, K., and Eberhart-Phillips, D., The 1992 Landers earthquake sequence: Seismological observations, J. Geophys. Res., 98, 19835-19858, 1993.

Hauksson, E.L., Crustal structure and seismicity distribution across the Pacific and North America plate boundary in southern California, in prep., 1998.

Hill, M.L., and Dibblee, T.W., San Andreas, Garlock, and Big Pine faults, California: A study of the character, history, and tectonic significance of their displacement, Geol. Soc. Amer. Bull., 64, 443-458, 1953.

Hornafius, J.S., Neogene tectonic rotation of the Santa Ynez Range, western Transverse Ranges, California, suggested by paleomagnetic investigation of the Monterey Formation, J. Geophys. Res., 90, 12,503-12,522, 1985.

Hu, G., Menke, W., and Powell, C., Polarization tomography for P wave velocity structure in southern California, J. Geophys. Res., 99, 15245-15256, 1994.

Humphreys, E., Clayton, R., and Hager, B.H., A tomographic image of mantle structure beneath southern California, Geophys. Res. Lett., 11, 625-627, 1984.

Humphreys, E.D., and Clayton, R.W., Tomographic image of the southern California mantle, J. Geophys. Res., 95, 19725-19746, 1990.

Humphreys, E.D., and Hagar, B.H., A kinematic model for the late Cenozoic development of southern CA crust and upper mantle, J. Geophys. Res., 95, 19747-19762, 1990.

Humphreys, E.D., and Weldon, R.J., Deformation across the western United States: A local estimate of Pacific-North America transform deformation, J. Geophys. Res., 99, 19975-20010, 1994.

Jacobs, S.E., Geology of a part of the upper Santa Ana River Valley, San Bernardino Mountains, San Bernardino County, California (M.S. Thesis), Los Angeles, California State University, 107 pp., 1982.

John S. Murk Engineers, Inc., and LeRoy Crandall and Associates, Historic and present conditions, upper Mojave River basin, Mojave Water Agency, 1985.

Johnson, H.O., Agnew, D.C., and Wyatt, F.K., Present-day crustal deformation in southern California, J. Geophys. Res., 99, 23951-23974, 1994.

Jones, C.H., and S.G. Wesnousky, Variations in strength and slip rate along the San Andreas fault system, Science, 256, 83-86, 1992.

Jones, C.H., Kanamori, H., and Roecker, S.W., Missing roots and mantle "drips": Regional Pn and teleseismic arrival times in the southern Sierra Nevada and vicinity, California, J. Geophys. Res., 99, 4567-4601, 1994.

Jones, L.E., and Hough, S.E., Analysis of broadband records from the June 28, 1992 Big Bear earthquake: evidence of a multiple-event source, Bull. Seism. Soc. Amer., 85, 688-704, 1995.

Jones, L.M., Hutton, L.K., Given, D.D., and Allen, C.R., The North Palm Springs, California, earthquake sequence of July, 1986, Bull. Seism. Soc. Amer., 76, 1830-1837, 1986.

Kamerling, M.J., and Luyendyk, B.P., Tectonic rotations of the Santa Monica Mountains region, western Transverse Ranges, California, suggested by paleomagnetic vectors, Geol. Soc. Amer. Bull., 90, 331-337, 1979.

Li, Y.-G., Henyey, T.L., and Leary, P.C., Seismic reflection constraints on the structure of the crust beneath the San Bernardino Mountains, Transverse Ranges, southern California, J. Geophys. Res., 97, 8817-8830, 1992.

Lisowski, M., Savage, J.C., and Prescott, W.H., The velocity field along the San Andreas fault in central and southern California, J. Geophys. Res., 96, 8369-8389, 1991.

Liu, W., Paleomagnetism of Miocene sedimentary rocks in the Transverse Ranges: The implications for tectonic history, unpublished Ph.D. thesis, California Institute of Technology, Pasadena, California, 218 pp., 1990.

Lowell, J.D., Spitsbergen Tertiary orogenic belt and the Spitsbergen fracture zone, Geol.

Soc. Amer. Bull., 83, 3091, 3102, 1972.

Luyendyk, B.P., A model for Neogene crustal rotations, transtension, and transpression in southern California, Geol. Soc. Amer. Bull., 103, 1528-1536, 1991.

Luyendyk, B.P., Kamerling, M.J., and Terres, R.R., Geometric model for Neogene crustal rotations in southern California, Geol. Soc. Amer. Bull., 91, 211-217, 1980.

Magistrale, H., and C. Sanders, Evidence from precise earthquake hypocenters for segmentation of the San Andreas fault in San Gorgonio Pass, J. Geophys. Res., 101, 3031-3044. 1996.

May, S.R., and Repenning, C.A., New evidence for the age of the Old Woman sandstone, Mojave Desert, California, *in* Sadler, P.M., and Kooser, M.A., eds., Late Cenozoic stratigraphy and structure of the San Bernardino Mountains, Geol. Soc. Amer. Cordilleran Section Meeting Guidebook, 6, 93-96, 1982.

McJunkin, R., Geology of a portion of the central San Bernardino Mountains, San Bernardino Count, CA, unpublished M.S. thesis, CA. State Univ., Los Angeles, 1976.

Meigs, A., Brozovic, N., Johnson, M.L., Steady, balanced rates of uplift and erosion of the Santa Monica Mountains, California, submitted to Basin Research, 1998.

Meisling, K.E., Neotectonics of the north frontal fault system of the San Bernardino Mountains: Cajon Pass to Lucerne Valley, California (Ph.D. thesis), Pasadena, CA, California Institute of Technology, 394 pp., 1984.

Meisling, K.E., and Weldon, R.J., Late Cenozoic tectonics of the northwestern San Bernardino Mountains, southern California, Geol. Soc. Amer. Bull., 101, 106-128, 1989.

Miller, F.K., Reverse-fault system bounding the north side of the San Bernardino Mountains, in Recent reverse faulting in the Transverse Ranges, California, U.S. Geol. Surv. Prof. Paper, 1339, 83-95, 1987.

Miller, F.K., and D.M. Morton, Potassium-argon geochronology of the eastern Transverse Ranges and southern Mojave Desert, southern California, U.S. Geol.

Surv. Prof. Pap., *1152*, 30 pp., 1980.

Minnich, R.A., Snow levels and amounts in the mountains of southern California, Journ. of Hydrology, 89, 37-58, 1986.

Molnar, P., and Gipson, J.M., Very long baseline interferometry and active rotations of crustal blocks in the western Transverse Ranges, California, Geol. Soc. Amer. Bull., 106, 594-606, 1994.

Mount, V.S., and Suppe, J., State of stress near the San Andreas fault: Implications for wrench tectonics, Geology, 15, 1143-1146, 1987.

Namson, J., and Davis, T., Structural transect of the western Transverse Ranges, California: Implications for lithospheric kinematics and seismic risk evaluation, Geology, 16, 675-679, 1988.

Namson, J., and Davis, T., Late Cenozoic fold and thrust belt of the southern Coast Ranges and Santa Maria basin, CA, Amer. Assoc. Pet. Geol. Bull., 74, 457-492, 1990.

Neville, S.L., Schiffman, P., and Sadler, P., Ultramafic inclusions in late Miocene alkaline basalts from Fry and Ruby Mountains, San Bernardino County, California, American Mineralogist, 70, 668-677, 1985.

Norris, R.J., and Cooper, A.F., Erosional control on the structural evolution of a transpressional thrust complex on the Alpine fault, New Zealand, J. Struct. Geol., 19, 1323-1342, 1997.

Nur, A., Ron, H., and Beroza, G.C., The nature of the Landers-Mojave earthquake line, Science, 261, 201-203, 1993.

Oberlander, T.M., Morphogenesis of granitic boulder slopes in the Mojave Desert, California, Journal of Geology, 80, 1-20, 1972.

Powell, R.E., Geology of the crystalline basement complex, eastern Transverse Ranges, southern California [Ph.D. Thesis], Pasadena, California, California Institute of Technology, 1981.

Revenaugh, J., A scattered-wave image of subduction beneath the Transverse Ranges,

Science, 268, 1888-1892, 1995.

Richard, S.M., Palinspastic reconstruction of southeastern California and southwestern Arizona for the Middle Miocene, Tectonics, 12, 830-854, 1993.

Riley, F.S., Data on water wells in Lucerne, Johnson, Fry, and Means Valleys, San Bernardino County, California, U.S.G.S. Open File Report, 149 p., 1956.

Rockwell, T.K., Keller, E.A., and Johnson, D.L., Tectonic geomorphology of alluvial fans and mountain fronts near Ventura, California, in Morisawa, M., and Hack, J.T., eds., Tectonic Geomorphology, The Binghamton Symposia in Geomorphology: Intl. Series, 15, 183-208, 1984.

Ross, T.M., Luyendyk, B.P., and Haston, R.B., Paleomagnetic evidence for Neogene clockwise tectonic rotations in the central Mojave Desert, California, Geology, 17, 470-473, 1989.

Rubin, C.M., and Sieh, K., Loop dormancy, low slip rate, and similar slip-per-event for the Emerson fault, Eastern CA shear zone, J. Geophys. Res., 102, 15319-15333, 1997.

Rzonca, G.F., and Clark, D.W., Local Geology, Kaiser Cement Corporation, Cushenbury Facility, Lucerne Valley, California, in Fife, D.L., and Minch, J.A., eds., Geology and mineral wealth of the California Transverse Ranges, South Coast Geological Society, 676-679, 1982.

Sadler, P.M., An introduction to the San Bernardino Mountains as the product of young orogenesis, *in* Cooper, J.D., ed., Geologic excursions in the Transverse Ranges, Geol. Soc. Amer. Annual Meeting Guidebook, Fullerton, California, California State University, 57-65, 1982a.

Sadler, P.M., Provenance and structure of late Cenozoic sediments in the northeast San Bernardino Mountains, *in* Cooper, J.D., ed., Geologic excursions in the Transverse Ranges, Geol. Soc. Amer. Annual Meeting Guidebook, Fullerton, California, California State University, 83-91, 1982b.

Sadler, P.M., and Reeder, W.A., Upper Cenozoic, quartzite-bearing gravels of the San

Bernardino Mountains, southern California; recycling and mixing as a result of transpressional uplift, *in* Anderson, D.W., and Rymer, M.J., eds., Tectonics and sedimentation along faults of the San Andreas system, Los Angeles, California, Society of Economic Paleontologists and Mineralogists, Pacific Section, 45-57, 1983.

Sadler, P.M., The Santa Ana basin of the central San Bernardino Mountains: Evidence of the timing and uplift and strike-slip relative to the San Gabriel Mountains, *in* Powell, R.E., Weldon, R.J., and Matti, J.C., eds., The San Andreas fault system: Displacement, palinspastic reconstruction, and geologic evolution, Geol. Soc. Amer. Memoir, 178, 307-322, 1993.

Sauber, J., Thatcher, W., and Solomon, S.C., Geodetic measurement of deformation in the central Mojave Desert, California, J. Geophys. Res., 91, 12683-12693, 1986.

Savage, J.C., and Hastie, L.M., Surface deformation associated with dip-slip faulting, J. Geophys. Res., 71, 4897-4904, 1966.

Savage, J.C., Lisowski, M., and Prescott, W.H., An apparent shear zone trending north-northwest across the Mojave Desert into Owens Valley, eastern California, Geophys. Res. Lett., 17, 2113-2116, 1990.

Schelle, H., and Grunthal, G., Modeling of Neogene crustal block rotation: Case study of southeastern California, Tectonics, 15, 700-710, 1996.

Schwartz, S.Y., Orange, D.L., and Anderson, R.S., Complex fault interactions in a restraining bend on the San Andreas fault, southern Santa Cruz Mountains, California, Geophys. Res. Lett., 17, 1207-1210, 1990.

Shaw, J.H., Bischke, R.E., and Suppe, J., Relations between folding and faulting in the Loma Prieta epicentral zone: strike-slip fault-bend folding, in Simpson, R.W., ed., The Loma Prieta, California, earthquake of October 17, 1989: Tectonic processes and models, U.S. Geol. Surv. Prof. Paper, 1550-F, 3-21, 1994.

Sheffels, B., and McNutt, M., Role of subsurface loads and regional compensation in the isostatic balance of the Transverse Ranges, California: Evidence for intracontinental

subduction, J. Geophys. Res., 91, 6419-6431, 1986.

Sheriff, R.E., and Geldart, L.P., Exploration Seismology Volume 1: History, theory, and data acquisition, Cambridge University Press, New York, 253 pp., 1982.

Sieh, K.E., Slip rate across the San Andreas fault and prehistoric earthquakes at Indio, California (abstract), Eos Trans. AGU, 67, 1200, 1986.

Sieh, K.E., and 19 others, Near field investigations of the Landers earthquake sequence, April to July, 1992, Science, 260, 171-176, 1993.

Silver, L.T., Evidence and a model for west-directed early to mid-Cenozoic basement overthrusting in southern California, Geol. Soc. Am. Abst. with Prog., 14, 617, 1982.

Sonder, L.J., Effects of density contrasts on the orientation of stresses in the lithosphere: Relation to principal stress directions in the Transverse Ranges, California, Tectonics, 9, 761-771, 1990.

Spotila, J.A., Farley, K.A., and Sieh, K., Uplift and erosion of the San Bernardino Mountains associated with transpression along the San Andreas fault, California, as constrained by radiogenic helium thermochronometry, Tectonics, 17, 360-378, 1998.

Stout, M.L., Geologic guide to the San Bernardino Mountains, southern California, Assoc. Eng. Geol. So. Calif. Section, Annual Spring Field Trip, 4-28, 1976.

Sylvester, A.G., Strike-slip faults, Geol. Soc. Amer. Bull., 100, 1666-1703, 1988.

Terres, R.R., and Luyendyk, B.P., Neogene tectonic rotation of the San Gabriel region, California, suggested by paleomagnetic vectors, J. Geophys. Res., 90, 12,467-12,484, 1985.

Unruh, J.R., and Lettis, W.R., Kinematics of transpressional deformation in the eastern San Francisco Bay region, California, Geology, 26, 19-22, 1998.

Valentine, M.J., Brown, L.L., and Golombek, M.P., Cenozoic crustal rotations in the Mojave Desert from paleomagnitude studies around Barstow, California, Tectonics, 12, 666-677, 1993.

Webb, T.H., and Kanamori, H., Earthquake focal mechanisms in the eastern Transverse

Ranges and San Emigdio Mountains, southern California, and evidence for a regional decollement, Seismol. Soc. Amer. Bull., 75, 735-757, 1985.

Weldon, R.J., The late Cenozoic geology of Cajon Pass; Implications for tectonics and sedimentation along the San Andreas fault [Ph.D. thesis], Pasadena, California Institute of Technology, 400 p., 1986.

Weldon, R.J., and Humphreys, E., A kinematic model of southern California, Tectonics, 5, 33-48, 1986.

Weldon, R.J., Meisling, K.E., and Alexander, J., A speculative history of the San Andreas fault in the central Transverse Ranges, California, *in* Powell, R.E., Weldon, R.J., and Matti, J.C., eds., The San Andreas fault system: Displacement, palinspastic reconstruction, and geologic evolution, Geol. Soc. Am. Mem., 178, 161-198, 1993.

Weldon, R.J., and Sieh, K.E., Holocene rate of slip and tentative recurrence interval for large earthquakes on the San Andreas fault in Cajon Pass, southern California, Geol. Soc. Amer. Bull., 96, 793-812.

Wells, D.L., and Coppersmith, K.J., New empirical relationships among magnitude, rupture length, rupture width, rupture area, and surface displacement, Bull. Seism. Soc. Amer., 84, 1994.

Willingham, C.R., Gravity anomaly patterns and fault interpretations in the San Bernardino Valley and western San Gorgonio Pass area, southern California, in Geology of the San Jacinto Mountains, South Coast Geological Society, pp. 164-174, 1981.

Woodburne, M.O., Cenozoic stratigraphy of the Transverse Ranges and adjacent areas, southern California, Geol. Soc. Amer. Spec. Paper, 162, 1975.

Woodford, A.O., and Harriss, T.F., Geology of Blackhawk Canyon, San Bernardino Mountains, California, Univ. of Calif. Pub., Bull. of the Dept. of Geol. Sciences, 17, 265-304, 1928.

Yeats, R.S., Quaternary flake tectonics of the California Transverse Ranges, Geology, 9, 16-20, 1981.

Table 1: Observations that bear on the relative degree of activity along the northern (NFTS) and southern (SAT) thrust margins of the Big Bear plateau, based on previous work and airphoto mapping in this study.

Observation	North Frontal thrust system	Santa Ana thrust
	Fault scarps in alluvium	
1) distribution	discontinuous scarps occur along entire front; >2/3 of front contains scarps west of HF, <1/3 of front contains scarps east of HF	almost no scarps along trace; <5% of front contains scarps, despite large fan surfaces preserved across fault in Barton Flats
2) character and age	late Pleistocene (0.13-0.5 Ma[1,2]) alluvium contains most scarps, which reach 60 m[3,4] height. Holocene alluvium is generally not broken[1,3,4,5].	local scarps cut mid-late Pleistocene alluvium[6,7], possibly due to reactivation near strike-slip faults (MFZ, BFFZ); generally does not cut Quaternary sediments[8], scarps are small and unimpressive, except 30 m scarp in Hemlock Creek[7]
	Bedrock escarpments	
1) height†, length	1240 m, 80 km	960 m, 50 km
2) avg. ridgeline gradient	20°	21°
3) sinuosity[9]	S = 1.9*	S = 2.7
4) canyon geometry[9]	V = 1.2**	V = 1.3
	Alluvial fans	
1) oldest intact alluvial surface along front	Holocene-late Pleistocene[1,2,3,10]	mid-late Pleistocene[6,7]
2) fan entrenchment	older surfaces are somewhat entrenched, with degree of entrenchment increasing towards rangefront; may be due to tectonic tilting of fans	heavily entrenched fans, often with badlands-like topography and little preservation of original surfaces except in Barton Flats (east end)
3) fan size	very large apron of anastomising fans is build out from the range front, with little bedrock exposed, large fans built on 17 Ka Blackhawk landslide	only small fragments of fans remain, covering a small portion of the front

HF = Helendale fault; MFZ = Mentone fault zone; BFFZ = Barton Flats fault zone.
† Height = topographic relief, not vertical separation of weathered surface.
* Compared to S=2.6 measured by Bull (1977) along the same front. The discrepancy is attributed to the subjectivity involved in defining the piedmont-mountain interface, but should not affect the comparison of the NFTS and SAT here.
** Identical to that measured by Bull (1977).
1 = Bryant, 1986a; 2 = Meisling and Weldon, 1989; 3 = Miller, 1987; 4 = Meisling, 1984; 5 = Bryant, 1986b; 6 = Dibblee, 1964a; 7 = Jacobs, 1982; 8 = Sadler, 1993; 9 = Bull, 1977; 10 = Dibblee, 1964b.

Table 2: Dextral faults in SBMs, south of San Andreas fault (based on previous work and air-photo interpretation).

Fault	Total slip (or min. estimate)	Features	Latest activity
	A. North of the NFTS: faults that terminate or curve to join the NFTS		
Helendale	~1-6 km (dextral, multiple bedrock contacts[2])	tilting of Pleistocene and Tertiary sediments, scarps in latest Pleistocene (Holocene ?) alluvium[1], deflected drainage	latest Pleistocene ?
Silver Reef	~1 km dextral (dextral, bedrock contact[1])	cuts late Pleistocene alluvium, buried by 17 Ka Blackhawk landslide[1]	late Pleistocene
Old Woman Springs	amount unknown (km's?) (dextral)[3]	scarps in late Pleistocene (Holocene ?) alluvium and Miocene basalt[3,4]	latest Pleistocene ?
Lenwood	1.5-3.0 km (dextral, bedrock and structural features[3,5])	cuts late Pleistocene alluvium[3]	late Pleistocene ?
Total (east-west) = ~5-13 km (using 3 km as max. on Old Woman Springs f.)			
	B. South of the NFTS: faults within the SBMs block that cannot be joined with those north of the NFTS		
Deer Creek	0.3 km (dextral offset of SAT trace[8]) oblique-reverse motion too[8]	scarps in late Pleistocene alluvium[7], deflected drainages, shutter ridges	late Pleistocene ?
Dollar Lake	1-2.1 km (dextral, bedrock contacts[8])	scarps cut late Pleistocene glacial moraines[8]	latest Pleistocene - Holocene
Pipes Canyon	0.3-2.3 km (dextral, bedrock contacts[9]) 1.0-1.6 km (bedrock channel, Pipes Ck.)	juxtaposed bedrock and mid-late Pleistocene alluvium, folded alluivum in restraining bend, deflected drainges[9]	late Pleistocene ?
Helendale (A)	cuts bedrock with unknown offset[9] (dextral, shutter ridges)	sharp bedrock escarpment, possible bedrock shutter ridges, juxtaposed alluvium and bedrock but does not cut late Pleistocene alluvium[1] (?)	mid-Pleistocene ?
Helendale (B)	~0.8 km (dextral, bedrock contact[3], uncertain)	sharp bedrock scarp, juxtaposed alluvium and bedrock but does not cut late Pleistocene[1] (?)	mid-Pleistocene ?

Table 2: Continued.

Fault	Total slip (or min. estimate)	Features	Latest activity
B. South of the NFTS: faults within the SBMs block that cannot be joined with those north of the NFTS			
Bighorn (A+B)	~0.3 km (dextral, bedrock contact[3])	bedrock lineaments and escarpments, no sediments crossed, cuts weathered surface	?
Barton Flats	3-6 km (Tertiary facies) or up to 10 km (provenance)[10], 0.4 km ridge offset in old alluvium (dextral)	cuts Tertiary (<6 Ma) sediments[10], scarps in late Pleistocene alluvium[7], sharp topographic features possible shutter ridges, rift-like expression	latest Pleistocene ?
Mentone zone	unknown across entire shear zone (<1 km?) -individual strands offset ridgelines ~0.2 km (dextral), bedrock is also juxtaposed[11]	expression in bedrock appears eroded, bedrock shutter ridges occur, bedrock ridgelines are offset, does not cut mid-late Pleistocene alluvium	early Pleistocene ?
Total (east-west) = ~3-9 km (using 3 km for max. on Barton Flats zone)			
C. Within the NFTS zone: faults analagous to those to north or south (or tear faults within the thrust)			
Sky High Ranch	0.5 km (dextral, late Pleistocene fans)[6] ~1 mm/yr estimated[6]	back-facing scarps cut late Pleistocene but not Holocene[6], shutter ridges	latest Pleistocene
Blackhawk	0.5 km (dextral, Pleistocene fan)[4]	cuts late Pleistocene alluvium, cuts the 17 Ka Blackhawk landslide[3], back-facing scarps	latest Pleistocene - Holocene
Total (east-west) = ~1 km			

1) Dibblee, 1964b; 2) Miller and Morton, 1980; 3) Dibblee, 1967b; 4) Miller, 1987; 5) Dokka and Travis, 1990; 6) Meisling, 1984; 7) Dibblee, 1964a; 8) Jacobs, 1982; 9) Dibblee, 1967a; 10) Sadler, 1993; 11) Dibblee, 1974

Table 3: Attitudes of geologic features used on cross sections.

Geologic feature	Section	Attitude	Source
Arrastre Canyon Narrows f.	CC'	vertical	assumed*; Meisling (1984)
Barton Flats fault zone	BB'	subvertical	assumed*; and drawn so as to be reverse faults
Green Valley fault zone	CC'	subvertical	assumed*; and drawn so as to be normal faults
Helendale fault	BB'	vertical	assumed*
Lenwood fault	AA'	vertical	assumed*
Lovelace Canyon fault	CC'	vertical	assumed*; Meisling (1984)
Mill Creek fault	BB'	60°S	surface obs.; Allen (1957)
	CC'	75°S	surface obs.; Dibblee (1974a)
Mission Creek fault	AA'	65°N	surface obs.; Dibblee (1967a)
	BB'	45°N	surface obs.; Allen (1957), projected from south
North Frontal thrust system	AA'	21°S	average of nearby surface measurements; Miller (1987)
	BB'	40°S	surface obs.; Rzonca and Clark (1982)
	CC'	25°S	<1 km depth on seismic line; Li et al. (1992)
Old Woman Springs fault	AA'	70°S	surface obs.; Dibblee (1967b)
Pinto Mountain fault	AA'	vertical	assumed*
Pipes Canyon fault	AA'	vertical	assumed*
San Andreas fault, San Bernardino strand	BB', CC'	vertical	assumed*
San Gorgonio Pass fault zone	AA'	45°N††	1986 Palm Springs rupture; Jones et al. (1986)
Santa Ana Sandstone	BB'	27°N†††	below alluv., nearby surface obs.; Dibblee (1964a)
		15°S†††	beneath SAT, nearby surface obs.; Dibblee (1964a)
	CC'	12°N	projected from surface obs. to east, thin, buried under alluvium; Dibblee (1974a)
Santa Ana thrust	BB'	26°N§	surface obs.; Jacobs (1982)
	CC'	36°N†§	surface obs.; Jacobs (1982)

* Based on topographic expression as high angle, and lack of other data.

† Dibblee (1974a) shows the trace of the SAT to the west with a 75°S dip, but this occurs near where the Mentone Fault zone intersects the SAT, and thus the value of Jacobs (1982) from the east was used.

†† Surface dips on the San Gorgonio Pass fault zone are typically lower (25°N), but steepens at depth (D. Yule, pers. comm., 1998).

††† Santa Ana Sandstone forms a syncline beneath old fanglomerate to the east of the Deer Creek fault (Sadler, 1993).

§ Santa Ana thrust is thought to steepen at depth (Jacobs, 1982; Meisling and Weldon, 1989 -if part of Squaw Peak thrust system).

Figure 1: Major tectonic elements surrounding the San Bernardino Mountains (SBMs, shown as box delineating Figure 2). Inset shows location of southern California with respect to California and the San Andreas fault. The "Big Bend" of the San Andreas fault occurs south of the Garlock fault, and the circle indicates the location of the "little bend," or the restraining bend of San Gorgonio Pass. The relative motion of the Pacific plate relative to North America is shown as an arrow (N38°W trend; DeMets, 1995). BCF = Blue Cut fault, BWF = Blackwater fault, CF = Calico fault, CHF = Chiriaco fault, CRF = Camp Rock fault, DVFZ = Death Valley fault zone, ECsz = Eastern California shear zone (gray shade), eTR = eastern Transverse Ranges (ruled), GF = Garlock fault, GHF = Gravel Hills fault, HF = Helendale fault, LeF = Lenwood fault, LoF = Lockhart fault, LuF = Ludlow fault, N-IF = Newport-Inglewood fault, OV-SNFZ = Owens-Valley-Sierra-Nevada fault zone, PVF = Panamint Valley fault, Pen. Ranges = Peninsular Ranges, PiF = Pisgah fault, PMF = Pinto Mountain fault, PTF = Pleito thrust fault, SAF = San Andreas fault (m = Mojave segment, sb = San Bernardino segment, cv = Coachella Valley segment), SCF = Salton Creek fault, SGMs = San Gabriel Mountains, SJF = San Jacinto fault, SJMs = San Jacinto Mountains, SM-CF = Sierra Madre-Cucamonga fault, W-EF = Whittier-Elsinore fault, WWF = White Wolf fault, wTR = western Transverse Ranges (ruled).

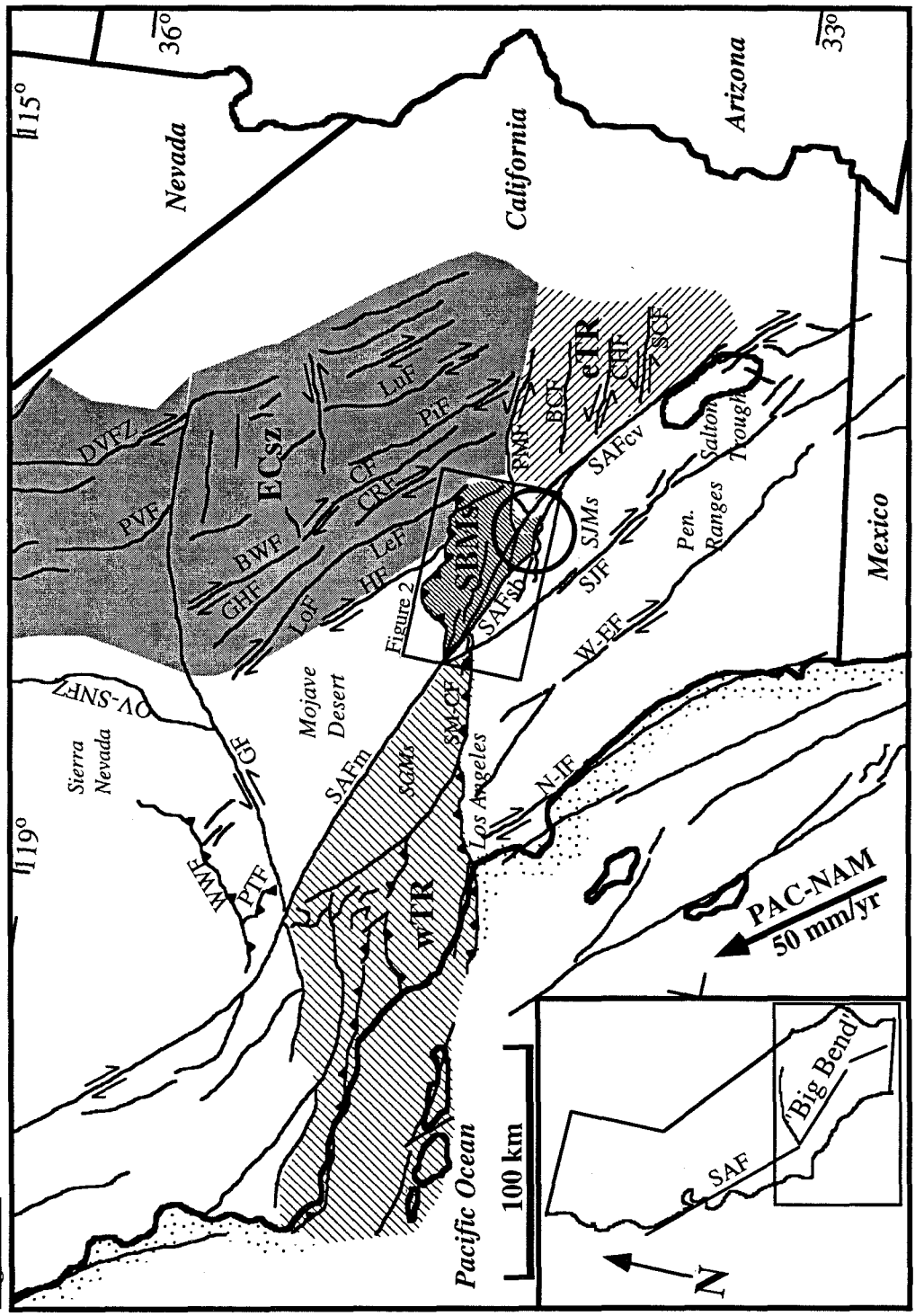
Nevada
California
Arizona
Mexico
Pacific Ocean
Sierra Nevada
Mojave Desert
Los Angeles
Pen. Ranges
Salton Trough
115°
119°
36°
33°
ECsz
eTR
wTR
SBMs
DVFZ
PVF
BWF
GHF
LoF
HF
LeF
CF
CRF
LuF
PtF
PMF
BCF
CHF
SCF
SAFcv
SJMs
SJF
SAFsb
W-EF
SAFm
SAMs
SM-OF
N-IF
WWF
PTF
GF
OV-SNFZ
Figure 2
PAC-NAM
50 mm/yr
100 km
N
SAF
Big Bend

Figure 1:

Figure 2: Simplified geologic and tectonic map of the San Bernardino Mountains (see Figure 1 for location). This shows the major blocks of the range and the fault systems that bound them (for more detailed fault map, refer to Figure 14). In addition, Tertiary sediments and the basic distribution of the weathered surface are shown. Letters refer to locations of Tertiary sediments as A = Old Woman Sandstone, B = eastern Santa Ana Sandstone overlying weathered surface and buried by basalt, C = central Santa Ana Sandstone, D = eastern Crowder Formation, E = Potato Sandstone, F = Mill Creek formation, G = Crowder Formation overlying weathered surface, H = general location of Cajon, Crowder, and Phelan Peak formations. BBB = Big Bear block, CHFZ = Crafton Hills fault zone, MB = Morongo block, Old WS = Old Woman Springs, SAV = Santa Ana Valley, SGB = San Gorgonio block, SGP-FZ = San Gorgonio Pass fault zone, YRB = Yucaipa Ridge block, WCB = Wilson Creek block, WCF = Wilson Creek fault.

Figure 2:

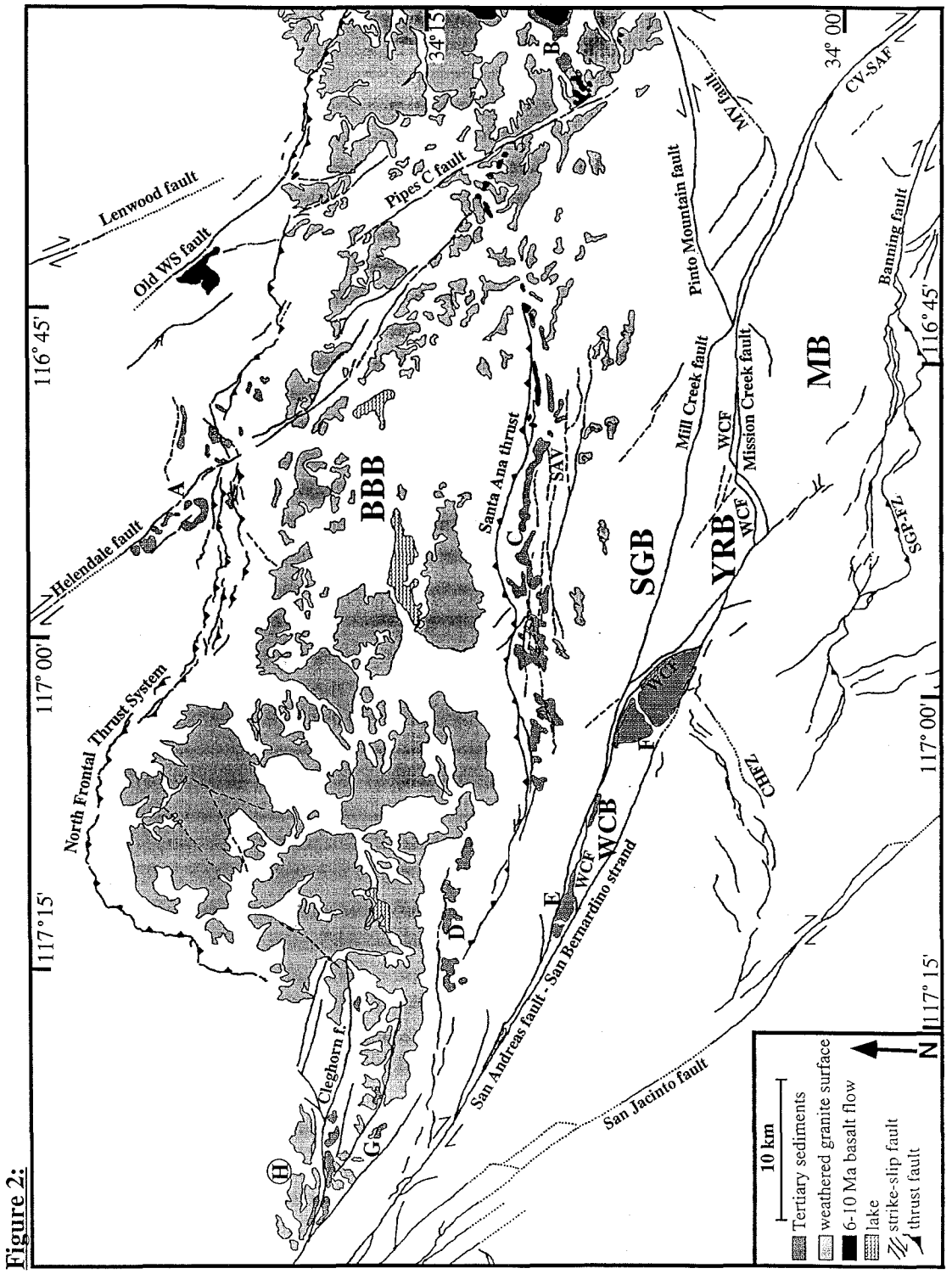
117° 15'
117° 00'
116° 45'
34° 15'
34° 00'
Lenwood fault
Old WS fault
Helendale fault
North Frontal Thrust System
Pipes C fault
MV fault
Pinto Mountain fault
Mill Creek fault
WCF
Mission Creek fault
Santa Ana thrust
SAV
Banning fault
CV-SAF
SGP-FZ
San Andreas fault - San Bernardino strand
San Jacinto fault
Cleghorn f.
CHF
BBB
SGB
YRB
MB
WCB
A
B
C
D
E
F
G
H
10 km
Tertiary sediments
weathered granite surface
6-10 Ma basalt flow
lake
strike-slip fault
thrust fault
N

Figure 3: See Plate 4, folded into the backside cover of thesis.

Figure 4: See Plate 5, folded into the backside cover of thesis.

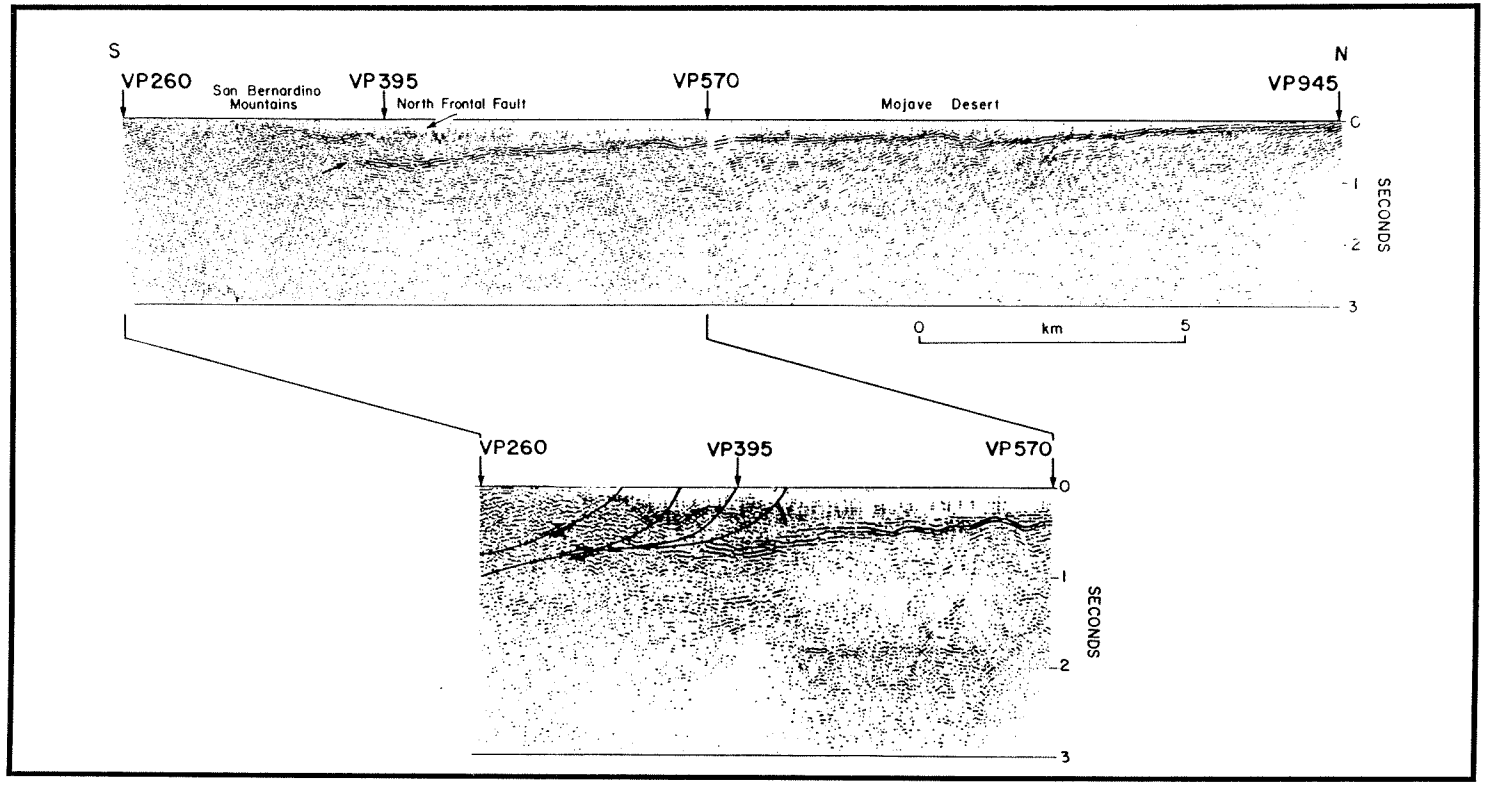

Figure 5: Seismic reflection profile along AA' (Figure 4), reproduced from Li et al. (1992). This shows the first 3 s (two-way travel time) of the common depth point time section from VP260 to VP945 of this CALCRUST seismic line. The depth to basement shown on Plate 6 for profile AA' is based on assuming a seismic velocity of 2.5 km/s. The strong reflection represents the basement surface beneath alluvium of the Mojave Desert. The expanded figure below shows this more clearly, as well as the disruption of this buried basement surface by the North Frontal Thrust System, which dips southwards. The thrust fault was not imaged below about 1 s (<1.5 km depth), and its apparent concave geometry shown here is likely the result of the velocity gradient near the Earth's surface (Li et al., 1992).

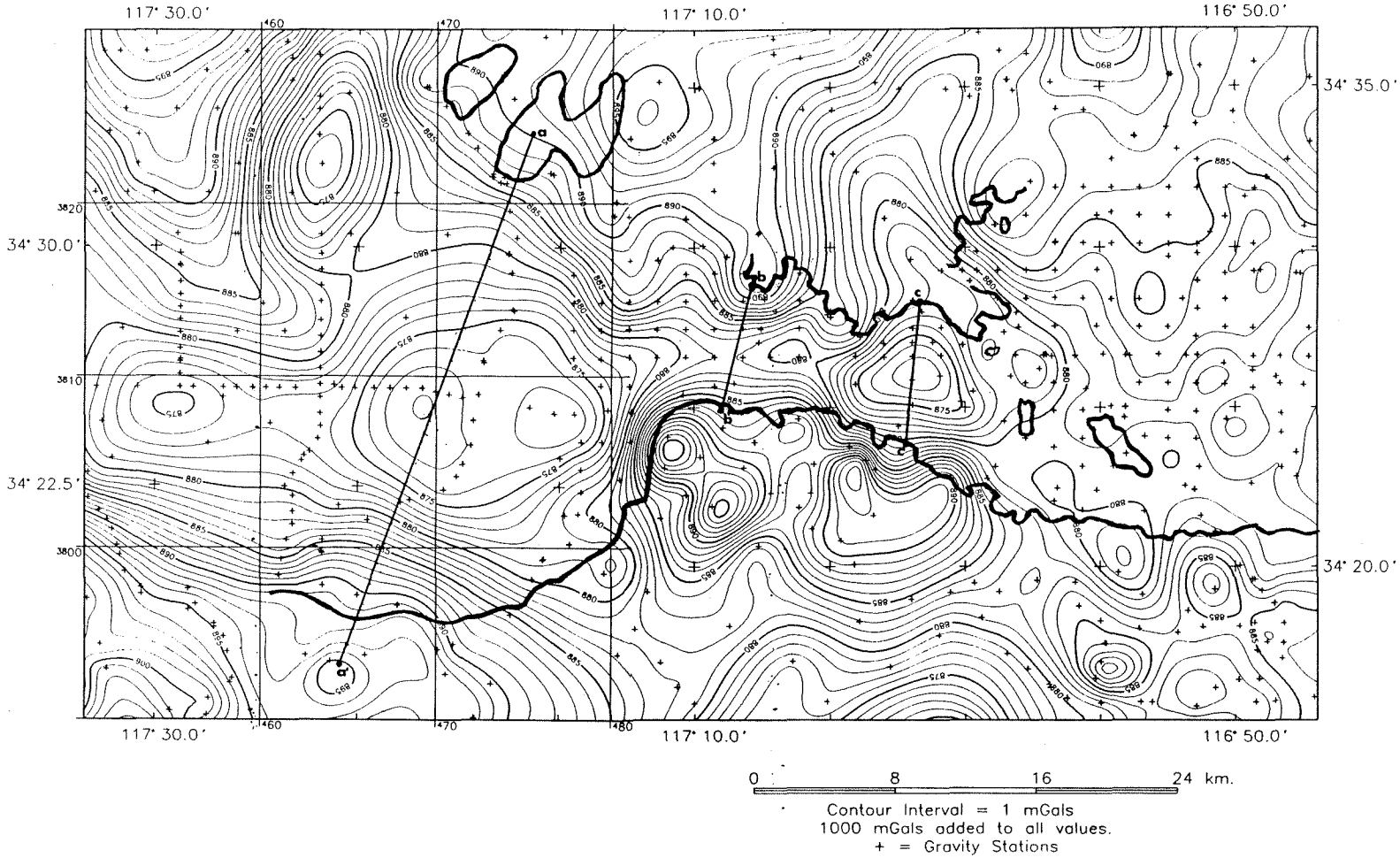

Figure 6: Map of complete Bouguer anomaly data for the area around the SBMs and neighboring Mojave Desert. The basic distribution of exposed basement (including a partial outline of the SBMs) are shown with a heavy line. Locations of three profiles, along which the depth of basement was calculated using this data, are also shown (aa', bb', cc'). Bouguer data is from Biehler et al. (1988) and was contoured using an automatic program.

Figure 7: Gravity anomalies and model sedimentary basins for the profiles shown in Figure 4 (data for profiles dd' and ee' are in Aksoy et al., 1986). Plots on the left show Bouguer anomalies (data from Shawn Biehler, pers. comm., 1998). Plots on the right show the modeled sedimentary basin necessary to produce the gravity anomaly, assuming a density contrast between basement and sediments of 0.40 g/cm^3 and using the end points (locations of exposed basement) as the regional gravity gradient. The modeled basin shows the depth to basement.

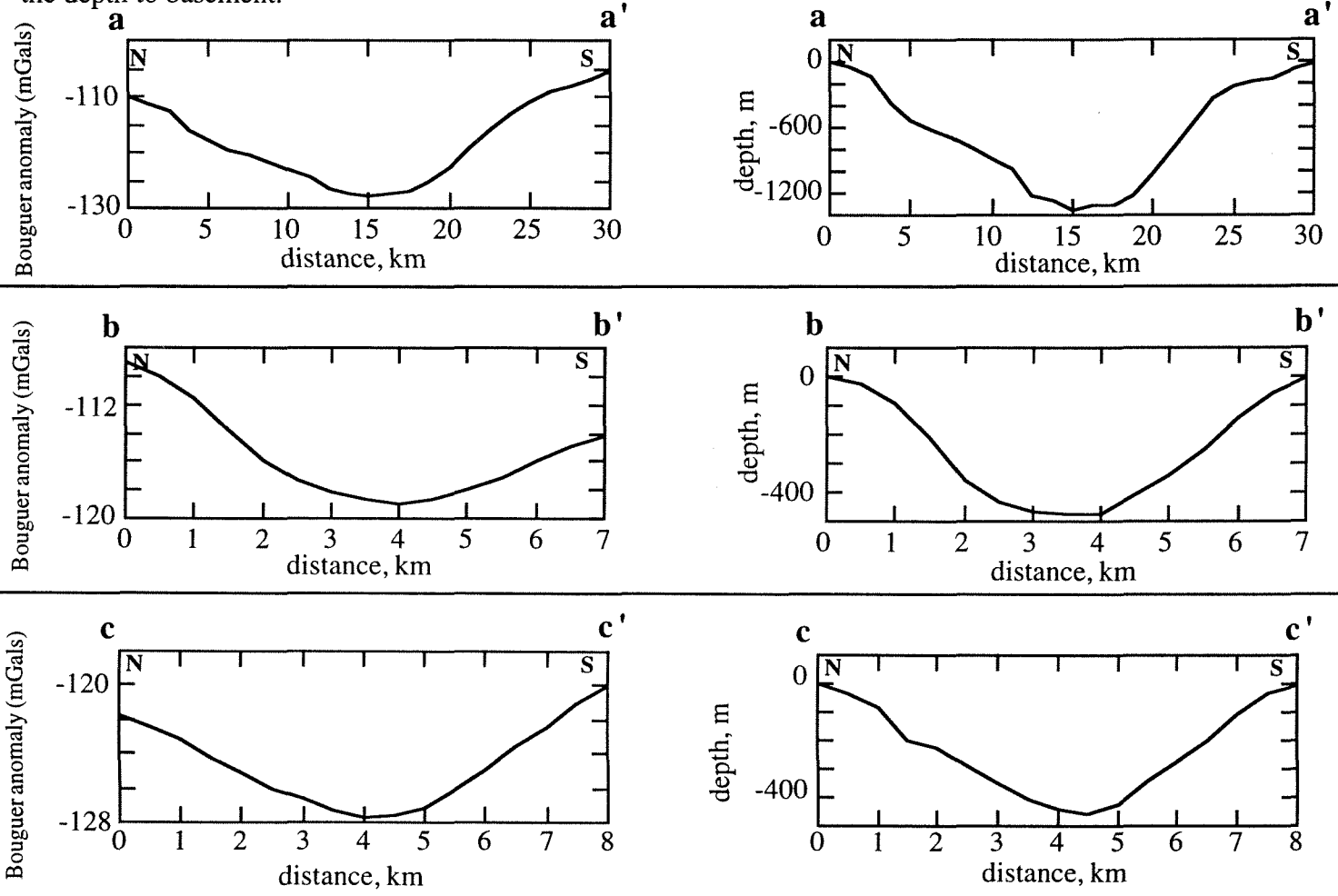

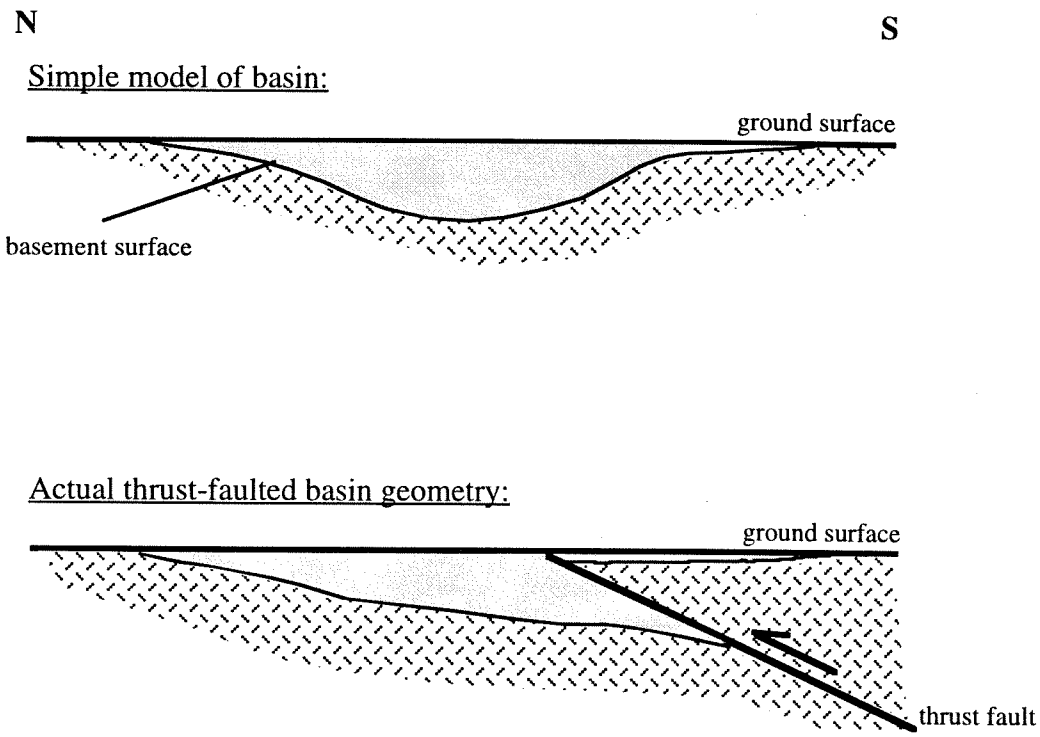

Figure 8: Conceptual diagram of how two different basin geometries may explain the same residual gravity anomaly. The upper case is similar to the basin models in Figure 7, in which the basin is assumed to have a simple, concave shape. In the lower diagram, a thrust fault brings basement over alluvium, but results in the same north to south variation in sediment thickness (lower + upper plates of thrust combine to have a sediment thickness equal to simple basin model). Residual gravity anomalies for these models would be similar, because the mass in any corresponding column of crust is identical.

Figure 9: See Plate 6, folded into the backside cover of thesis.

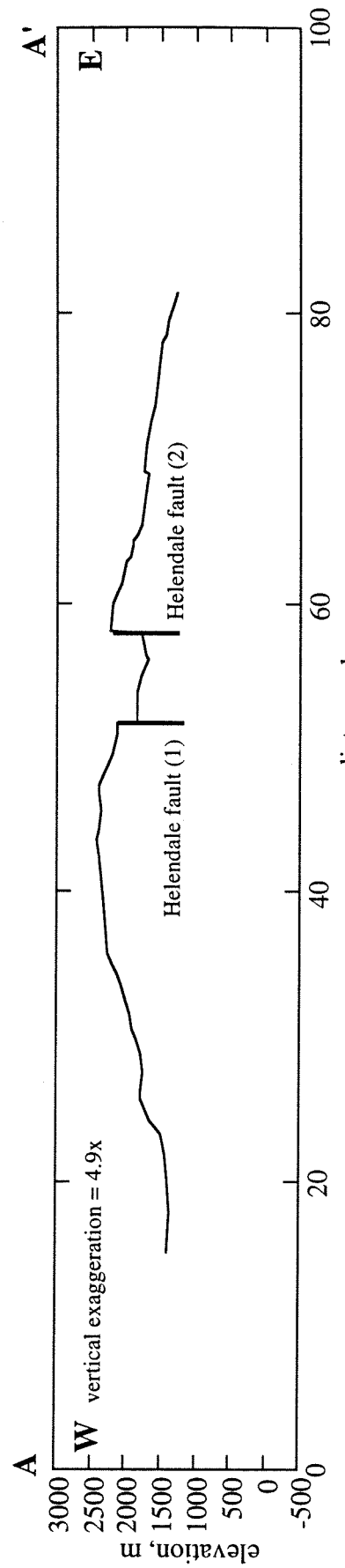

Figure 10: Elevation of structure contours to the weathered surface along profile AA' (Figure 3).

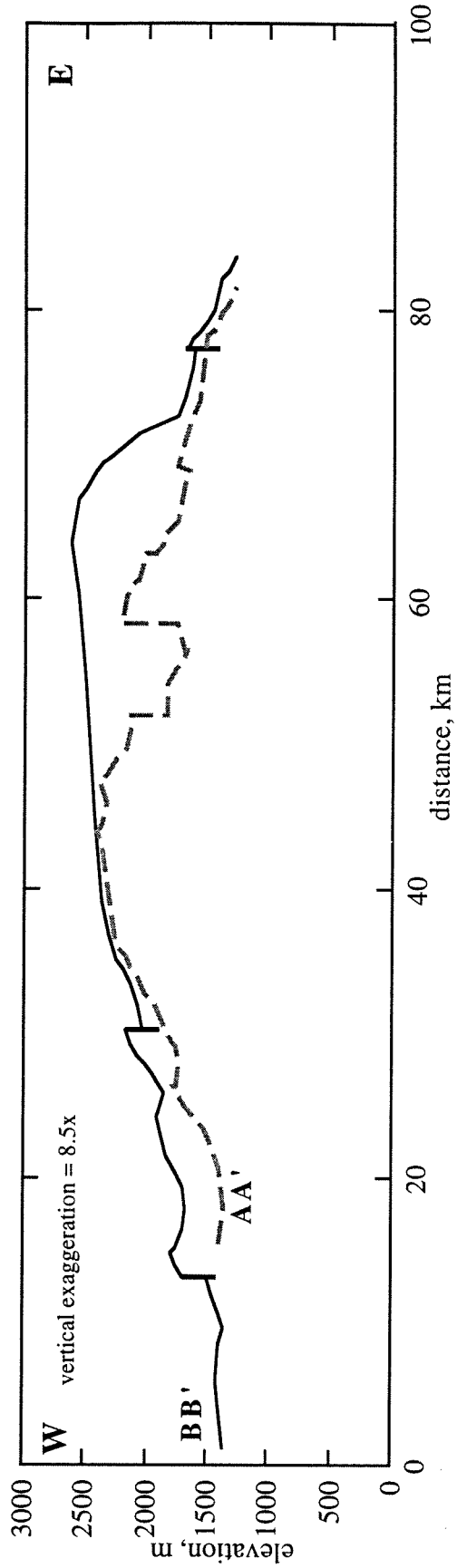

Figure 11: Comparison of elevation profiles along the weathered surface of the hanging-wall block from near the trace of the NFTS (gray, dashed; AA', Figures 3 and 10) and from further south (BB', Figure 3).

Figure 12: Plot of the elevation of the Santa Ana thrust surface trace versus the elevation of the weathered surface atop the Big Bear plateau above. The elevations were measured along a straight east-west line using 1:62500 scale topography. This shows how the Santa Ana thrust itself is uplifted along its eastern extent, and cannot be responsible for the vertical deformation of the weathered surface there. On the west, the elevation of the Waterman Canyon fault is plotted in place of the Santa Ana thrust. The Waterman Canyon fault holds a similar position relative to the Santa Ana Sandstone and the escarpment along the south side of the Big Bear plateau, and may be an eastward continuation of the Santa Ana thrust. The Santa Ana thrust, however, changes orientation and diverges from the escarpment to the west (Dibblee, 1974a).

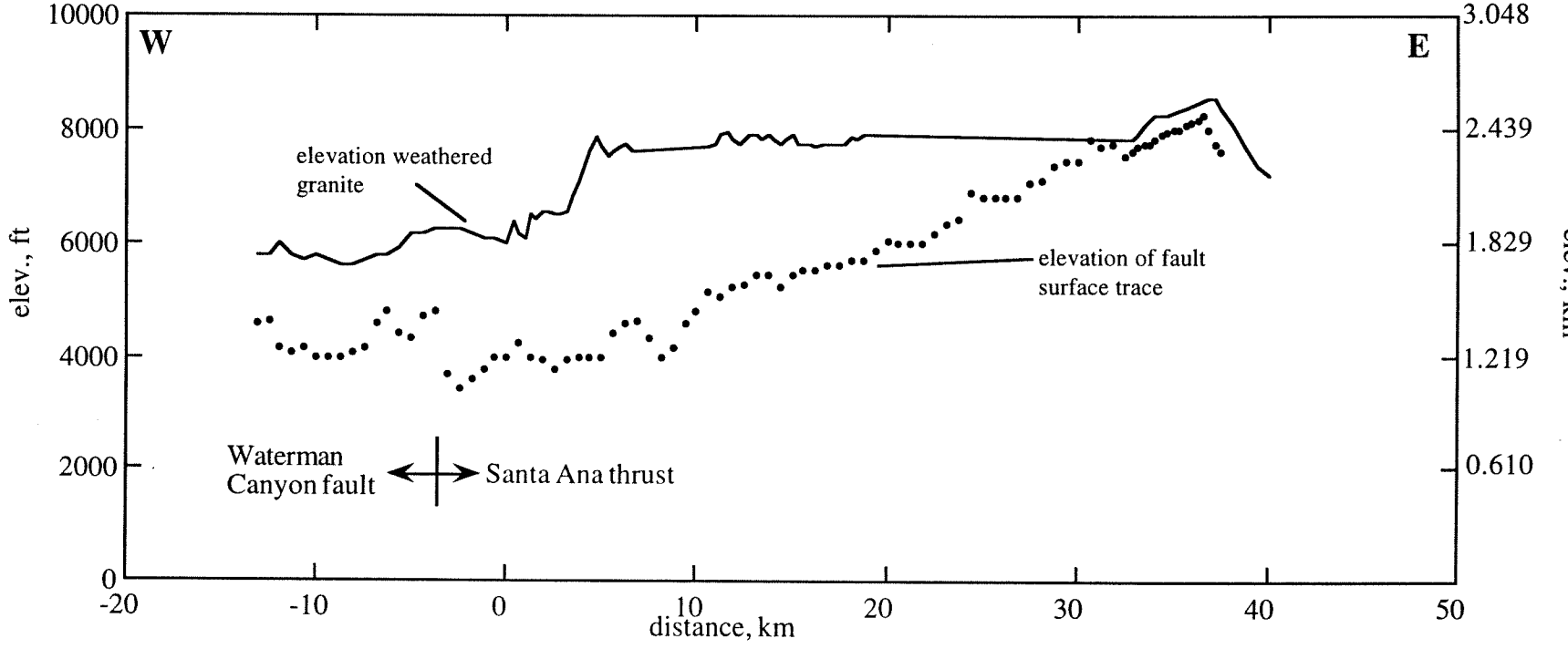

Figure 13: Plot of the elevation of structure contours to granitic basement (presumably weathered) in the footwall block (Mojave Desert) along profile CC' (Figure 9). Shown in gray is the elevation of structure contours to the weathered surface along AA' (Figure 3), the same as shown in Figure 10. The difference between these two plots is an estimate of vertical displacement along the trace of the NFTS.

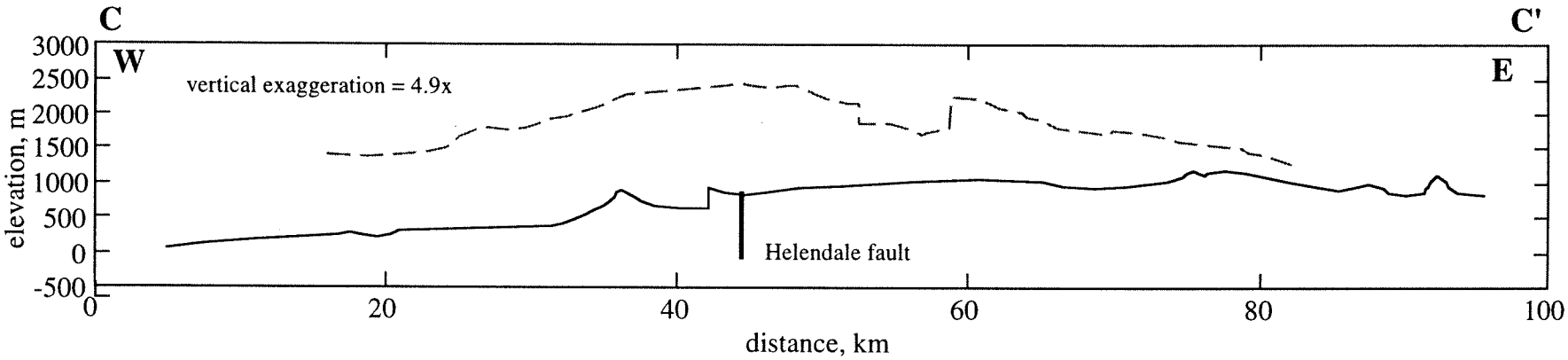

Figure 14: Fault map of the San Bernardino Mountains, showing the character of the North Frontal thrust system (NFTS), Santa Ana thrust (SAT), and northwest trending dextral faults within and to the north of the range. Other faults are also shown, including those of the Squaw Peak thrust system (CSRFS = Cedar Springs reverse fault system, Waterman Canyon fault), Green Valley fault zone, and various others. Arrows denote strike-slip motion, teeth denote thrust motion, and ball denotes normal motion (ball side down). Distribution of faults is based on airphoto mapping at 1:50,000 scale. Lakes of the SBMs are shown for location reference. Cross section lines AA', BB', and CC' (Figure 18) are shown as north-south solid gray lines. The dashed lines on either side represent the window used to plot seismicity on profiles AA', BB', and CC' (Figure 19). BFFZ = Barton Flats fault zone, CV = Coachella Valley strand of San Andreas fault, OWS = Old Woman Springs fault, SB = San Bernardino strand of San Andreas fault. Mainshock location and focal mechanism of the 1992 Big Bear earthquake sequence is also shown (Jones and Hough, 1995).

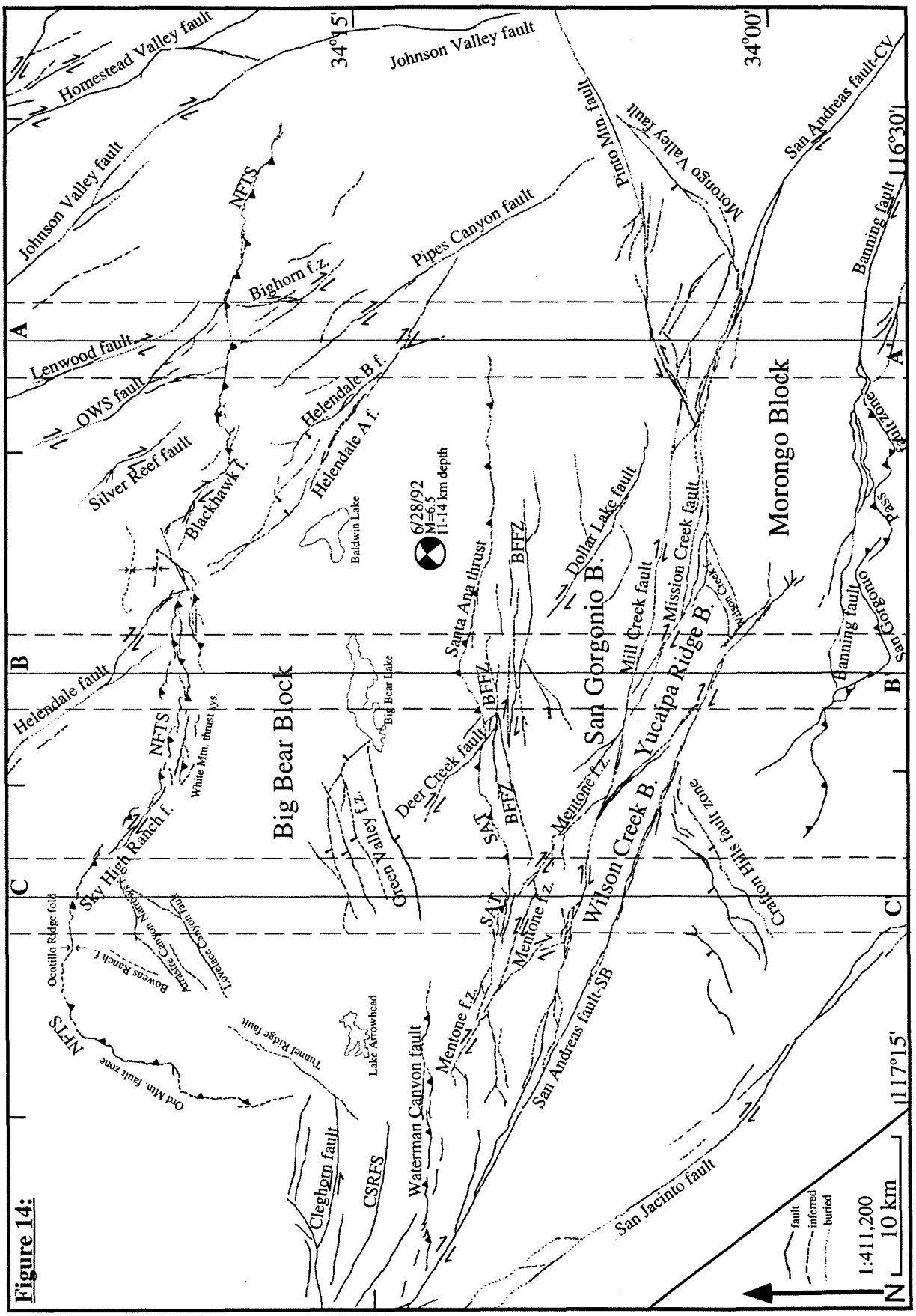
Homestead Valley fault
Johnson Valley fault
34°15'
Johnson Valley fault
NFTS
Bighorn f.z.
Pipes Canyon fault
Pinto Mtn. fault
Morongo Valley fault
San Andreas fault-CV
34°00'
Lenwood fault
OWS fault
Silver Reef fault
Blackhawk f.
Helendale B f.
Helendale A f.
Baldwin Lake
6/28/92
M=6.5
11-14 km depth
Banning fault
116°30'
Helendale fault
NFTS
White Mtn. thrust sys.
Big Bear Block
Big Bear Lake
Santa Ana thrust
BFFZ
Dollar Lake fault
Mill Creek fault
Mission Creek fault
Morongo Block
Green Valley f.z.
Deer Creek fault
SAT
BFFZ
Mentone f.z.
San Gorgonio B.
Wilson Creek B.
Yucaipa Ridge B.
Sky High Ranch f.
Occotillo Ridge fold
Dowens Ranch f.
Antelope Canyon Nanopoke
Tovaviace Canyon fault
NFTS
Ord Mtn. fault zone
Tunnel Ridge fault
Lake Arrowhead
Waterman Canyon fault
Mentone f.z.
San Andreas fault-SB
Cleghorn fault
CSRFS
Crafton Hills fault zone
Banning fault
San Gorgonio Pass
Eastzone
San Jacinto fault
A
A'
B
B'
C
C'
fault
inferred
buried
1:411,200
10 km
N
117°15'

Figure 14:

Figure 15: Vertical displacement along the near-surface NFTS, determined by differencing the elevation along the weathered surface of the hanging wall (AA') and footwall (CC'), where both are well constrained by data (Figures 3 and 9).

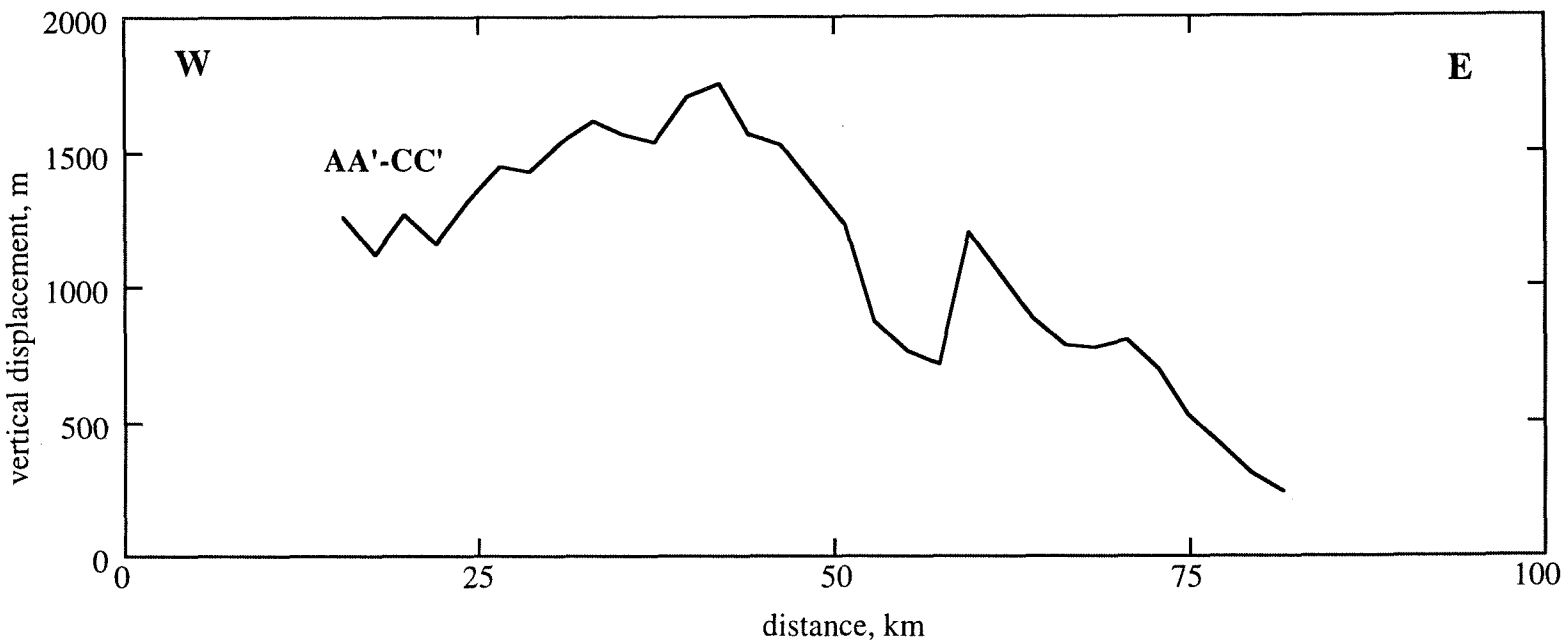

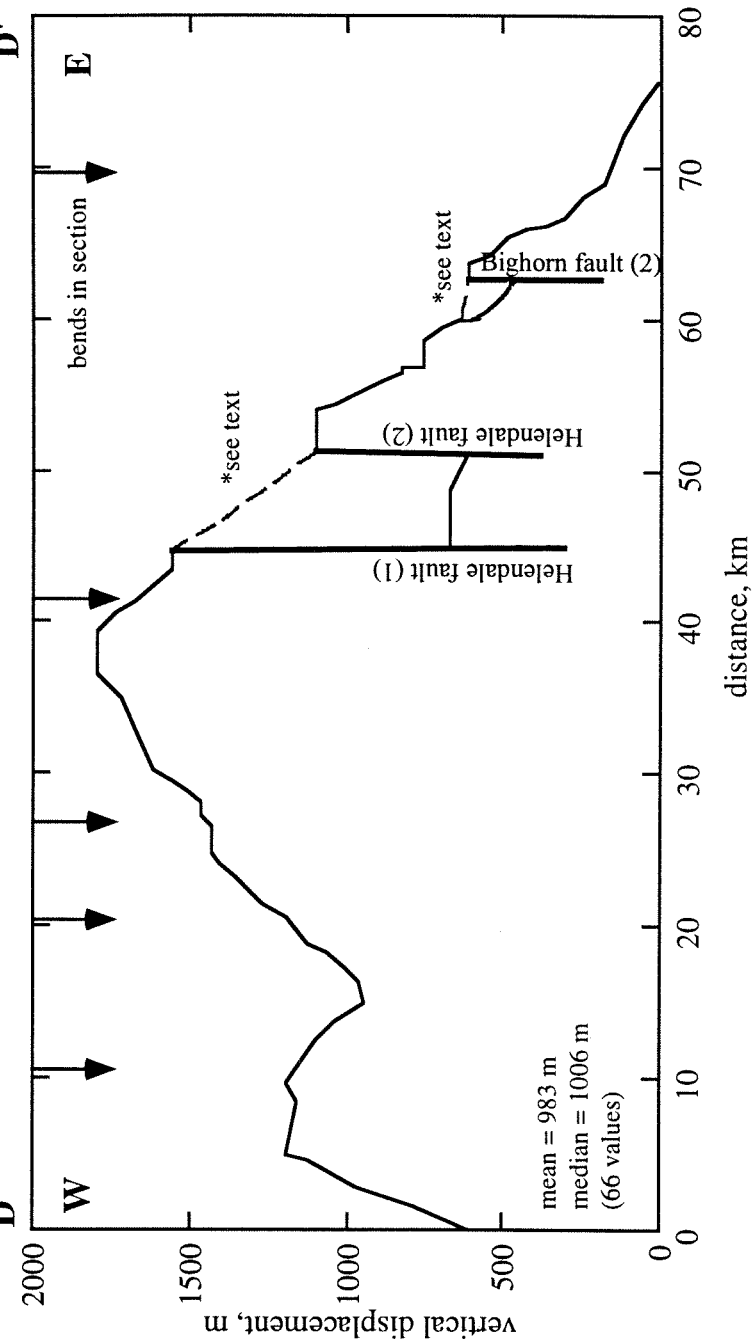

Figure 16: Displacement along the curved NFTS surface trace, along the line (DD') shown in Figure 3. Vertical displacement was determined by subtracting the interpolated elevation of basement in the footwall block from the elevation of structure contours to the weathered surface atop the hanging-wall block. The difference between this plot and Figure 15 is explained in text.

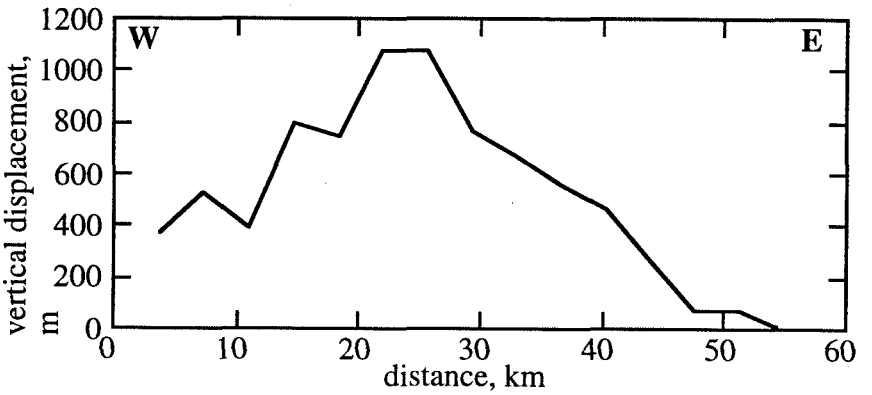

Figure 17: Plot of the difference in elevation of the Santa Ana thrust and weathered surface atop the Big Bear plateau (the difference between the two curves plotted in Figure 12). This represents the minimum vertical displacement the Santa Ana thrust may have. Given the symmetric, bell-shaped curve, it seems reasonable that the Santa Ana thrust has displaced the weathered surface.

Figure 18: North-south interpretive cross sections (AA', BB', CC') across the SBMs (locations shown in Figure 14). Cross sections were made from 1:62,500 scale topographic and geologic maps, and are shown with no vertical exaggeration. The brittle-plastic transition, based on the seismicity in Figure 19, is shown with a heavy, wide-dashed line. Faults are shown with medium lines, solid or dashed (where inferred). Circles denote lateral motion (cross = away, dot = towards), and arrows refer to reverse motion. The weathered surface from the structure contour diagrams on the SBMs and in the adjacent lowlands is drawn as a smooth solid line (dashed where inferred) that typically occurs just above topography (irregular, thinner line). This weathered surface envelope is labeled (w.s.). Sediments shown include Quaternary alluvium (alluv.), Old Woman Sandstone (OWss), and Santa Ana Sandstone (SAss). Delta symbols (δ) indicate fault segment dip according to dip analysis described in text. Measured values of slip (y = vertical component, x = horizontal component, z = net) are shown above the scarps on each thrust. Focal mechanisms are lower hemisphere plots with respect to cross-section plane.

Section AA' (Figure 18a): The shape of the NFTS is plotted based on dip analysis described in text. It steepens with depth and intersects the brittle-plastic transition north of the uplifted weathered surface. This requires that either the Mission Creek fault has reverse motion, or that the weathered surface is folded due to kink band migration (if the thrust continues along the brittle-plastic transition to the south, forming a restraining bend). The San Gorgonio Pass fault zone (shown as either 45° or 25° dip, projected from south) may also have reverse motion that uplifts the weathered surface.

Section BB' (Figure 18b): The NFTS is plotted based on dip analysis described in text for the upper crust. At the intersection with the SAT, the NFTS diverges into several possible orientations. That denoted "1" is for the first case, in which the SAT is considered extinct and backslipped as described in text. In this case, the NFTS flattens gradually below the intersection to a minimum dip of 21°. In case "2," the SAT is considered to have been active during motion on the NFTS and uplift of the Big Bear plateau. In this case, the

NFTS below intersection is given one dip, based on the elevation of the weathered surface in Santa Ana Valley as described in text. In this case, the NFTS dips only 19°S below the intersection. Another possible NFTS orientation is shown as a lighter line, based on assuming all uplift of the weathered surface is due to the NFTS. This scenario is not favored, but shows a similar orientation as the other cases. The NFTS is not plotted to the brittle-plastic transition because of the complexity of the uplift of the San Gorgonio and Yucaipa Ridge block. Earthquakes with thrust-fault mechanisms are also plotted. Events A and B, plotted simply as a depth range, have thrust mechanisms that could match the NFTS orientation and occur near the deepest portion of the NFTS. Event C has a 46°N nodal plane that matches the orientation and depth of the SAT. Event D has a southward dipping thrust plane that could lie on the NFTS, but occurs too deep to fit along its main strand and is likely due to rupture of a secondary, blind thrust to the north. Note the small anticline developed in alluvium that could represent such a blind thrust.

Section CC' (Figure 18c): The NFTS is plotted in upper crust (solid line) based on dip analysis described in text. At the intersection with the SAT (drawn assuming it steepens to 45° dip), the NFTS then diverges into several possible orientations. That denoted "1" is based on the first scenario, in which the SAT is considered extinct and is backslipped as described in text. For this case, the NFTS flattens gradually to a minimum 15° dip at the brittle plastic transition. In case "2," the SAT is considered to have been coactive in the uplift of the plateau at some stage, and the NFTS dip below the intersection is based on the lower elevation of the Santa Ana Valley (with respect to the plateau), as described in text. In this case, the NFTS dips 14° below the SAT, and the SAT is considered to form due to the resulting restraining bend in the NFTS. Two other NFTS orientations are drawn as well, in which the SAT is ignored and all uplift is attributed to the NFTS ("GVF modified" indicated the vertical offset along the Green Valley fault zone was backslipped prior to dip analysis, but this has little effect). Although these cases are not favored, the resulting dips are similar to those in which the SAT is considered.

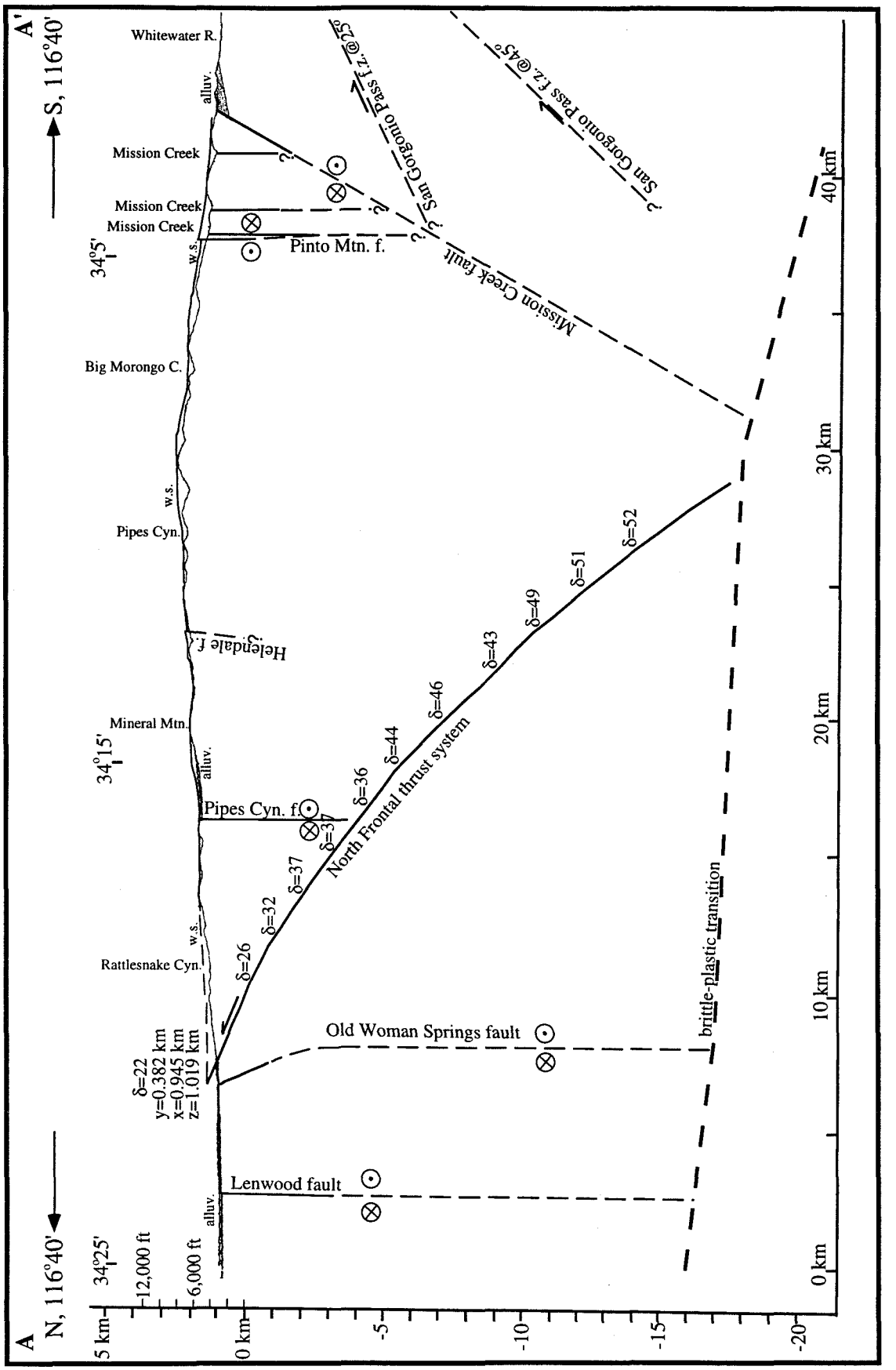
A
N, 116°40'
A'
S, 116°40'
34°25'
34°15'
34°5'
12,000 ft
6,000 ft
5 km
0 km
-5
-10
-15
-20
0 km
10 km
20 km
30 km
40 km
alluv.
Whitewater R.
Mission Creek
Mission Creek
Mission Creek
w.s.
Pinto Mtn. f.
Mission Creek fault
San Gorgonio Pass f.z. @25°
San Gorgonio Pass f.z. @45°
Big Morongo C.
w.s.
Pipes Cyn.
Helendale f.
Mineral Mtn.
alluv.
Pipes Cyn. f.
δ=37
δ=36
δ=44
δ=46
δ=43
δ=49
δ=51
δ=52
North Frontal thrust system
δ=26
δ=32
δ=37
w.s.
Rattlesnake Cyn.
δ=22
y=0.382 km
x=0.945 km
z=1.019 km
Old Woman Springs fault
brittle-plastic transition
Lenwood fault
alluv.

Figure 18a:

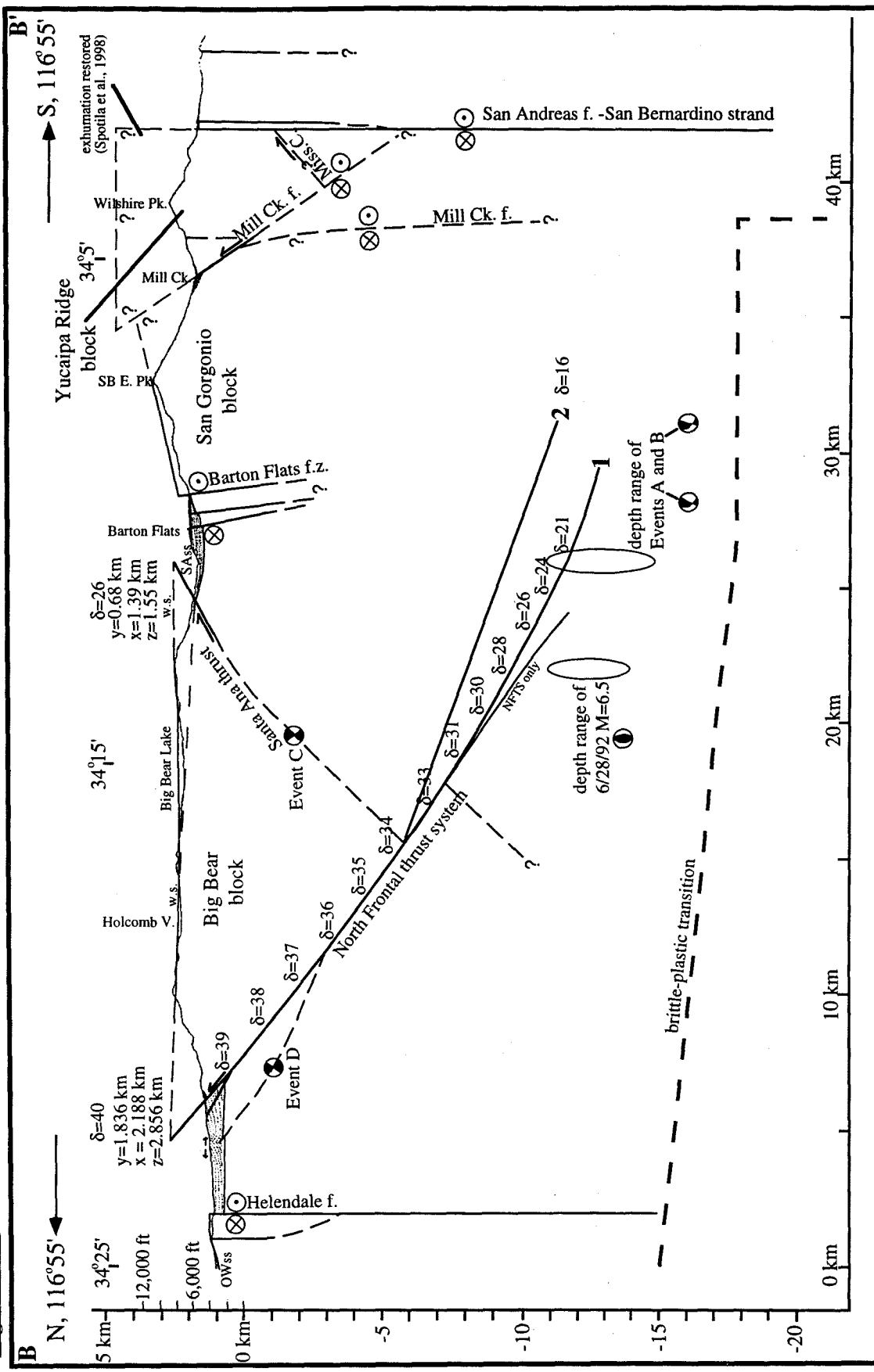
B
N, 116°55'
B'
S, 116°55'
exhumation restored
(Spotila et al., 1998)
San Andreas f. -San Bernardino strand
Mass. C
Wilshire Pk.
Mill Ck. f.
Mill Ck. f.
Mill Ck
34°5'
Yucaipa Ridge
block
SB E. Pk
San Gorgonio
block
Barton Flats f.z.
Barton Flats
SAss
δ=26
y=0.68 km
x=1.39 km
z=1.55 km
w.s.
Santa Ana thrust
Big Bear Lake
34°15'
Event C
Big Bear
block
Holcomb V.
w.s.
δ=40
y=1.836 km
x = 2.188 km
z=2.856 km
δ=39
δ=38
δ=37
δ=36
δ=35
δ=34
δ=33
δ=31
δ=30
δ=28
δ=26
δ=24
δ=21
δ=16
North Frontal thrust system
NF*S only
depth range of
Events A and B
depth range of
6/28/92 M=6.5
Event D
Helendale f.
owss
34°25'
12,000 ft
6,000 ft
5 km
0 km
-5
-10
-15
-20
0 km
10 km
20 km
30 km
40 km
brittle-plastic transition

Figure 18b:

Figure 18c:

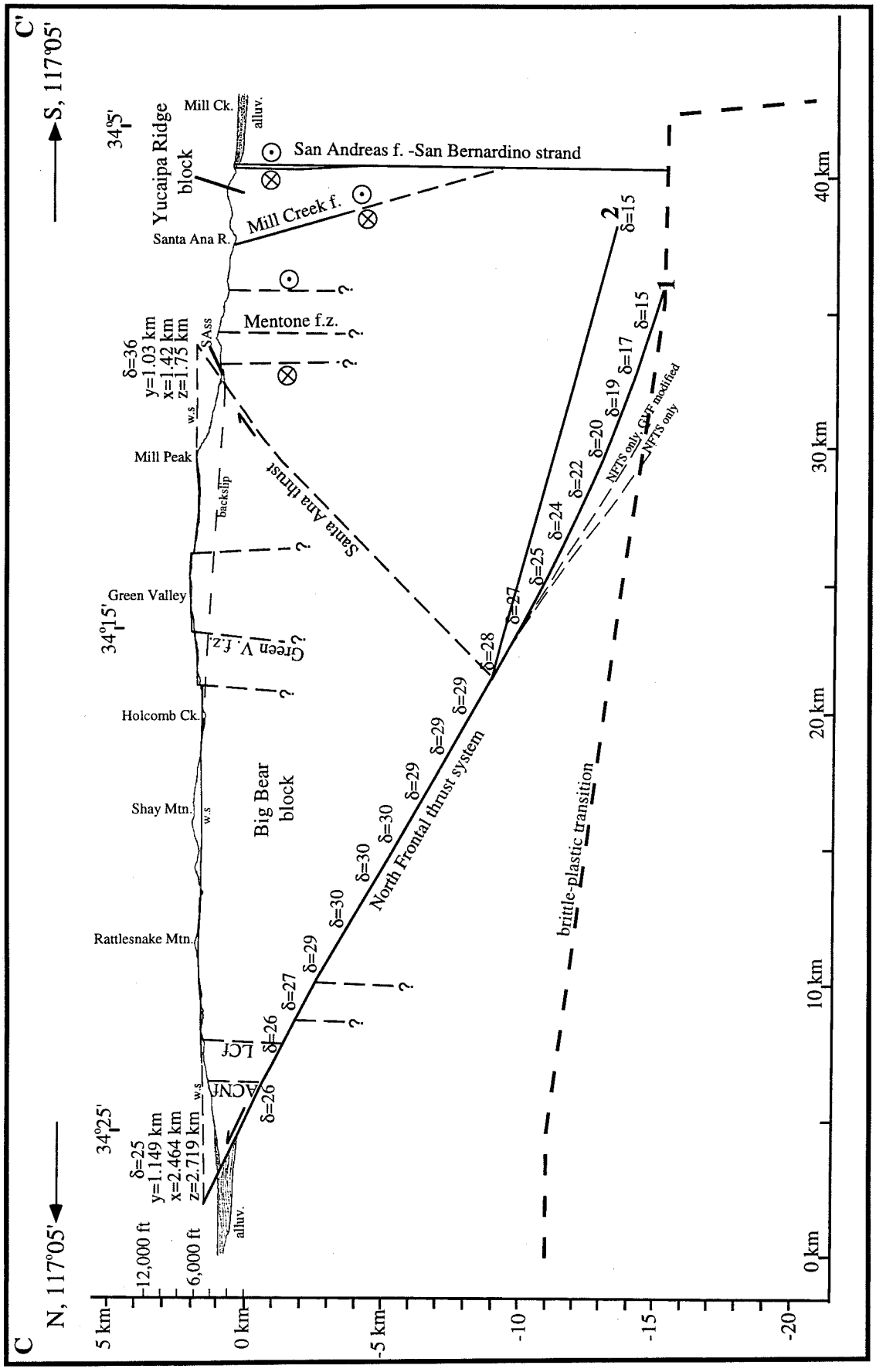
C
C'
N, 117°05'
S, 117°05'
34°25'
34°15'
34°25'
Yucaipa Ridge block
Mill Ck.
alluv.
San Andreas f. -San Bernardino strand
Mill Creek f.
Santa Ana R.
Mentone f.z.
δ=36
y=1.03 km
x=1.42 km
z=1.75 km
SAss
w.s
Mill Peak
Backslip
Santa Ana thrust
Green Valley
?Green V. f.z.
Holcomb Ck.
Shay Mtn.
Big Bear block
Rattlesnake Mtn.
LCF
ACNF
δ=25
y=1.149 km
x=2.464 km
z=2.719 km
12,000 ft
6,000 ft
δ=26
δ=27
δ=29
δ=30
δ=28
δ=37
δ=25
δ=24
δ=22
δ=20
δ=19
δ=17
δ=15
North Frontal thrust system
brittle-plastic transition
NFTS only
GVF modified
NFTS only
1
2
5 km
0 km
-5 km
-10
-15
-20
0 km
10 km
20 km
30 km
40 km

Figure 19: Seismicity plots along the north-south cross sections in the SBMs. Locations of plots AA', BB', and CC' are shown in Figure 14. This seismicity includes earthquakes recorded between 1981 and 1998 by the Caltech seismic network and relocated with a three-dimensional velocity model by Hauksson (1998, in prep.). The magnitude of events are scaled to circles in lower left. The velocity structure used for these events is represented by the light dashed lines and values given (km/s). Two heavy dashed lines represent the base of seismicity. The first (lighter) is the literal base of seismicity, whereas the second (darker) is flatter and more regular and meant to more closely reflect the homogeneous rheologic structure of the crust. This second line was used as the base of seismicity for the geological cross sections (Figure 18). Major faults are shown only in the upper crust as heavy solid lines (based on surface data). Note that the clusters of seismic activity do not correlate tightly with the fault geometry, and that the NFTS (as well as the San Andreas fault) is not defined by the seismicity. These clusters are dominated by the aftershocks of the 1992 Landers-Big Bear sequence (Hauksson et al., 1993) and the 1986 Palm Springs earthquake (Jones et al., 1986). Events A-D correspond to those plotted with focal mechanisms on Figure 18. Events A and C are projected onto profile BB' from the east (from Jones and Hough, 1995). MCF = Mill Creek fault, NFTS = North Frontal thrust system, SAF = San Andreas fault, SAT = Santa Ana thrust, SGPFZ = San Gorgonio Pass fault zone.

Figure 19:

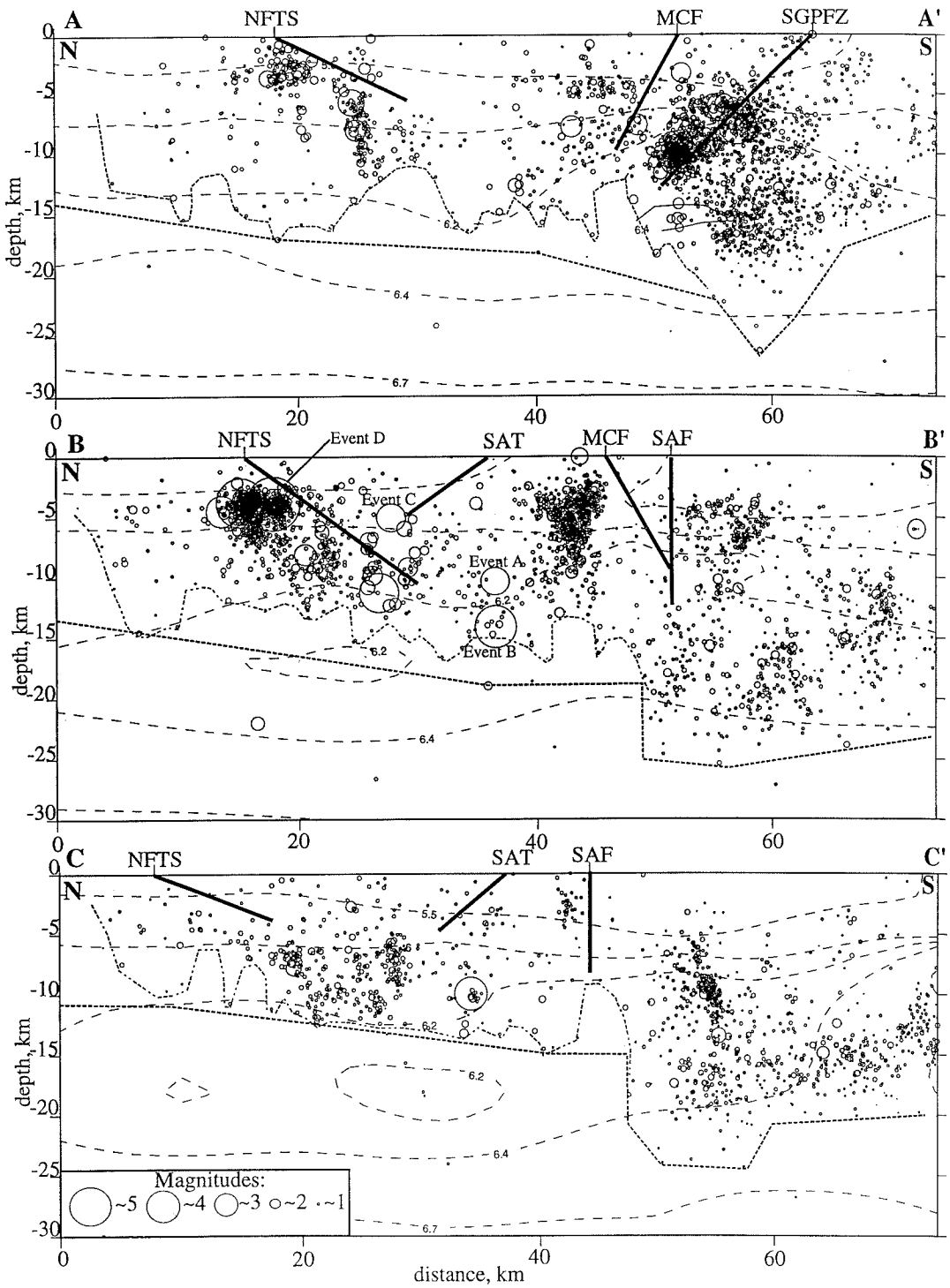
A
NFTS
MCF
SGPFZ
A'
N
S
depth, km
B
NFTS
Event D
SAT
MCF
SAF
B'
Event C
Event A
Event B
C
NFTS
SAT
SAF
C'
Magnitudes:
~5
~4
~3
~2
~1
distance, km

Figure 20: Summary diagram of the structure contours of weathered surface atop the San Bernardino Mountains and granitic basement in the adjacent Mojave Desert, Santa Ana Valley, and San Bernardino Valley. Contours are simplified versions of those in Figures 3 and 9. Contour interval is 200 m (labels are in hundreds of meters). The red triangles atop the Wilson Creek and Yucaipa Ridge blocks indicate the inferred elevation those blocks would have if erosion were restored (based on evidence for their exhumation from radiometric helium ages [Spotila et al., 1998]). Notice the dramatic increases in rock uplift toward the south towards San Gorgonio Pass. BBB = Big Bear block, MB = Morongo block, SGB = San Gorgonio Block, WCB = Wilson Creek block, YRB = Yucaipa Ridge block, SGP = San Gorgonio Pass, BFFZ = Barton Flats fault zone, NFTS = North Frontal thrust system, PMF = Pinto Mountain fault, SAF = San Andreas fault, SAT = Santa Ana thrust, SGPFZ = San Gorgonio Pass fault zone.

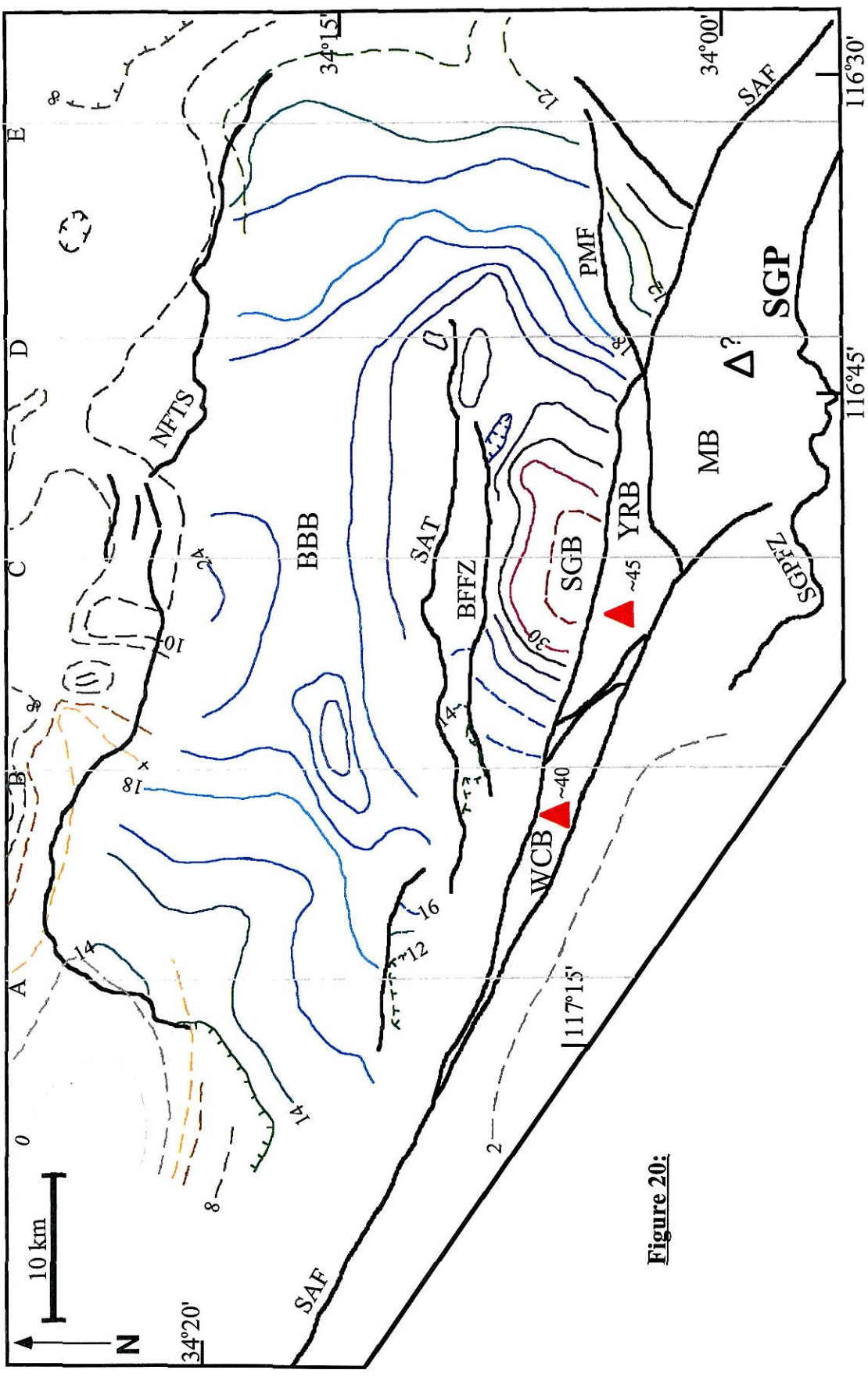
A
B
C
D
E
34°20'
34°15'
34°00'
116°45'
116°30'
117°15'
10 km
N
SAF
NFTS
BBB
SAT
BFFZ
SGB
YRB
WCB
MB
PMF
SGP
SGPFZ
~45
~40
Δ?

Figure 20:

Figure 21: North-south lines of horizontal shortening across the San Bernardino Mountains, based on the weathered surface and projected elevations from helium data (Spotila et al., 1998). The red line represents the envelope of the range, or what the topography of the mountain would be in the absence of erosion. Locations of the five profiles are shown on Figure 20. Small subscripts adjacent to fault dips refer to the following sources: 1 = Miller, 1987; 2 = Allen, 1957; 3 = Rzonca and Clark; 4 = Dibblee, 1974a; 5 = Jacobs, 1982; 6 = Li et al., 1992.

Figure 21:

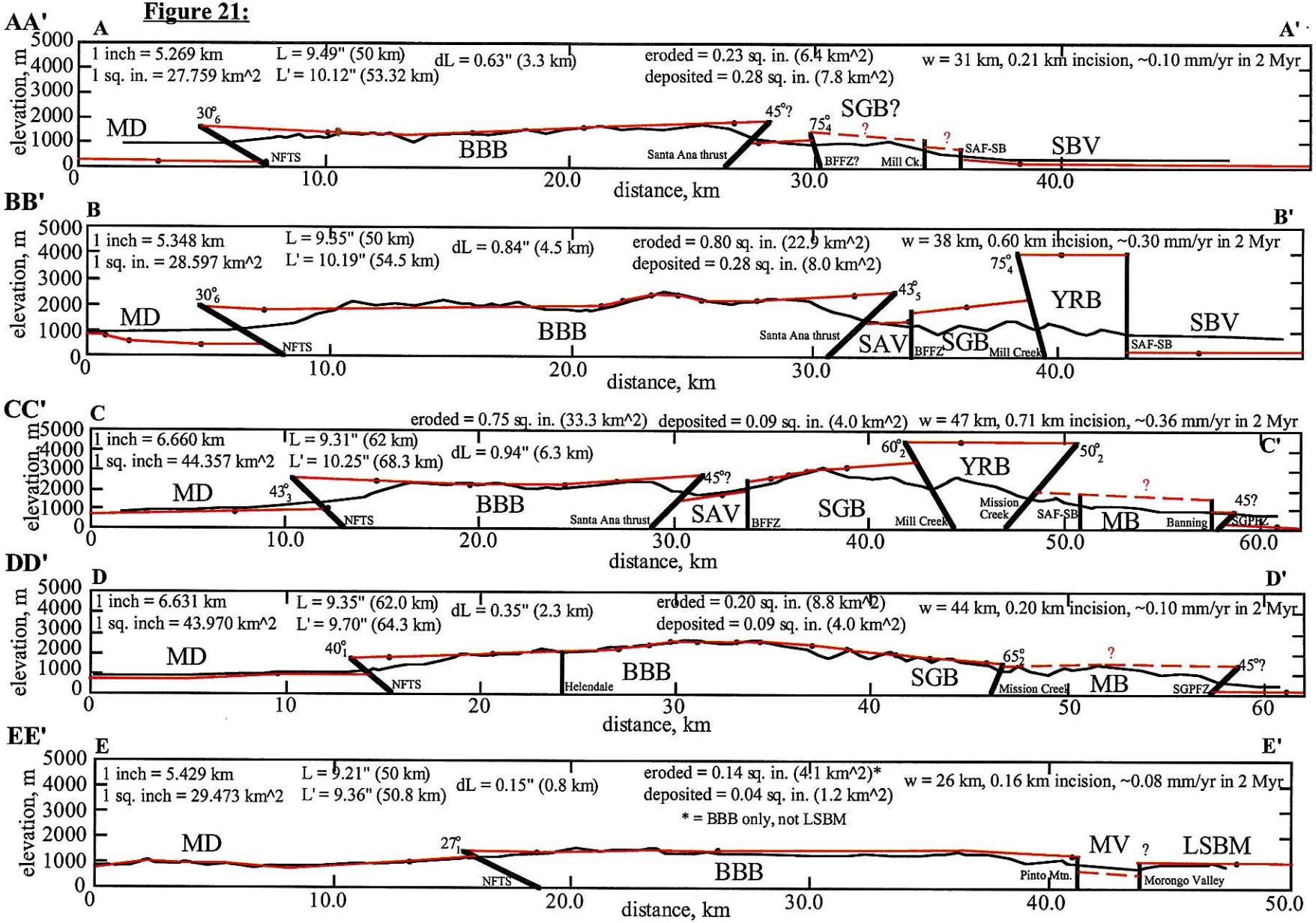
AA'
A
A'
1 inch = 5.269 km
1 sq. in. = 27.759 km^2
L = 9.49" (50 km)
L' = 10.12" (53.32 km)
dL = 0.63" (3.3 km)
eroded = 0.23 sq. in. (6.4 km^2)
deposited = 0.28 sq. in. (7.8 km^2)
w = 31 km, 0.21 km incision, ~0.10 mm/yr in 2 Myr
elevation, m
distance, km
MD
BBB
SGB?
SBV
NFTS
Santa Ana thrust
BFFZ?
Mill Ck.
SAF-SB
30°6
45°?
75°4
BB'
B
B'
1 inch = 5.348 km
1 sq. in. = 28.597 km^2
L = 9.55" (50 km)
L' = 10.19" (54.5 km)
dL = 0.84" (4.5 km)
eroded = 0.80 sq. in. (22.9 km^2)
deposited = 0.28 sq. in. (8.0 km^2)
w = 38 km, 0.60 km incision, ~0.30 mm/yr in 2 Myr
MD
BBB
SAV
SGB
YRB
SBV
NFTS
Santa Ana thrust
BFFZ
Mill Creek
SAF-SB
30°6
43°5
75°4
CC'
C
C'
eroded = 0.75 sq. in. (33.3 km^2)
deposited = 0.09 sq. in. (4.0 km^2)
w = 47 km, 0.71 km incision, ~0.36 mm/yr in 2 Myr
1 inch = 6.660 km
1 sq. inch = 44.357 km^2
L = 9.31" (62 km)
L' = 10.25" (68.3 km)
dL = 0.94" (6.3 km)
MD
BBB
SAV
SGB
YRB
MB
NFTS
Santa Ana thrust
BFFZ
Mill Creek
Mission Creek
SAF-SB
Banning
SGPFZ
43°3
45°?
60°2
50°2
45?
DD'
D
D'
1 inch = 6.631 km
1 sq. inch = 43.970 km^2
L = 9.35" (62.0 km)
L' = 9.70" (64.3 km)
dL = 0.35" (2.3 km)
eroded = 0.20 sq. in. (8.8 km^2)
deposited = 0.09 sq. in. (4.0 km^2)
w = 44 km, 0.20 km incision, ~0.10 mm/yr in 2 Myr
MD
BBB
SGB
MB
NFTS
Helendale
Mission Creek
SGPFZ
40°1
65°2
45°?
EE'
E
E'
1 inch = 5.429 km
1 sq. inch = 29.473 km^2
L = 9.21" (50 km)
L' = 9.36" (50.8 km)
dL = 0.15" (0.8 km)
eroded = 0.14 sq. in. (4.1 km^2)*
deposited = 0.04 sq. in. (1.2 km^2)
* = BBB only, not LSBM
w = 26 km, 0.16 km incision, ~0.08 mm/yr in 2 Myr
MD
BBB
MV
LSBM
NFTS
Pinto Mtn.
Morongo Valley
27°1

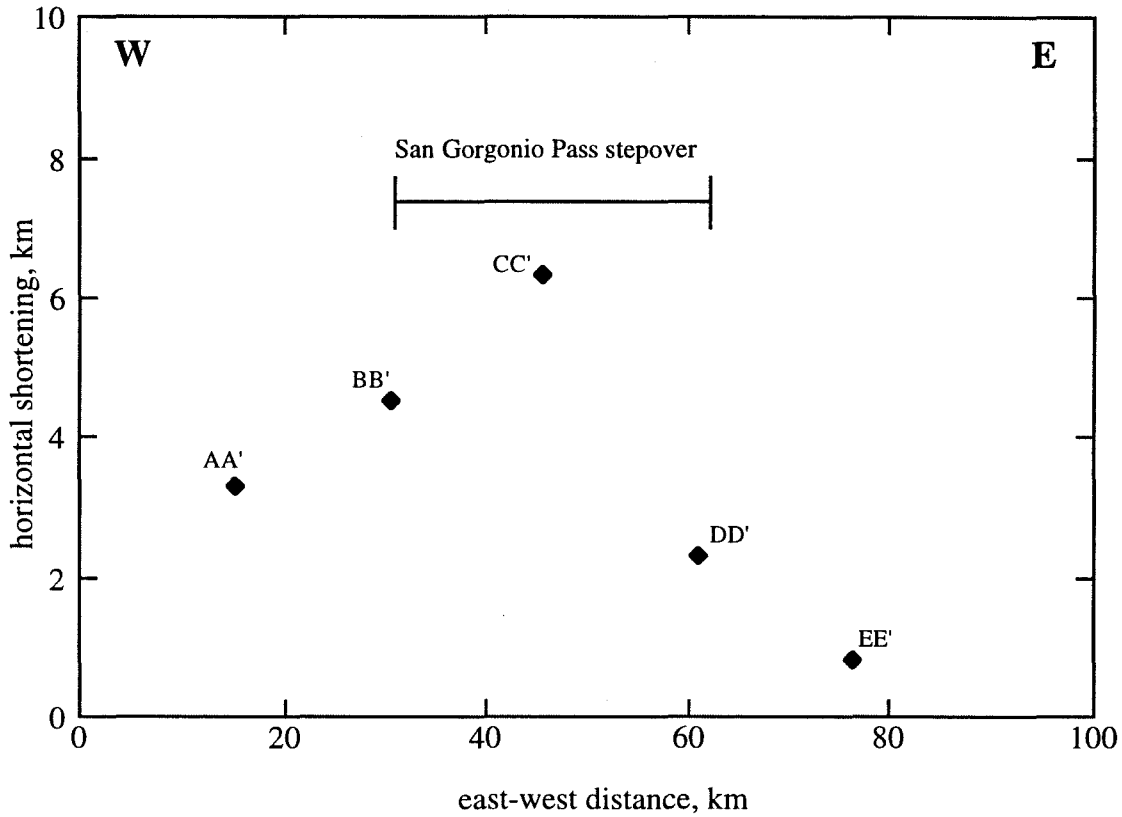

Figure 22: Plot of the variation in horizontal shortening along the strike of the San Bernardino Mountains, based on the analysis shown in Figure 21.

Figure 23: Schematic block-diagram of the architecture of structures beneath the SBMs. Faults correspond to colors listed in lower left. Fault motion is parallel to the direction of lines defining the fault plane.

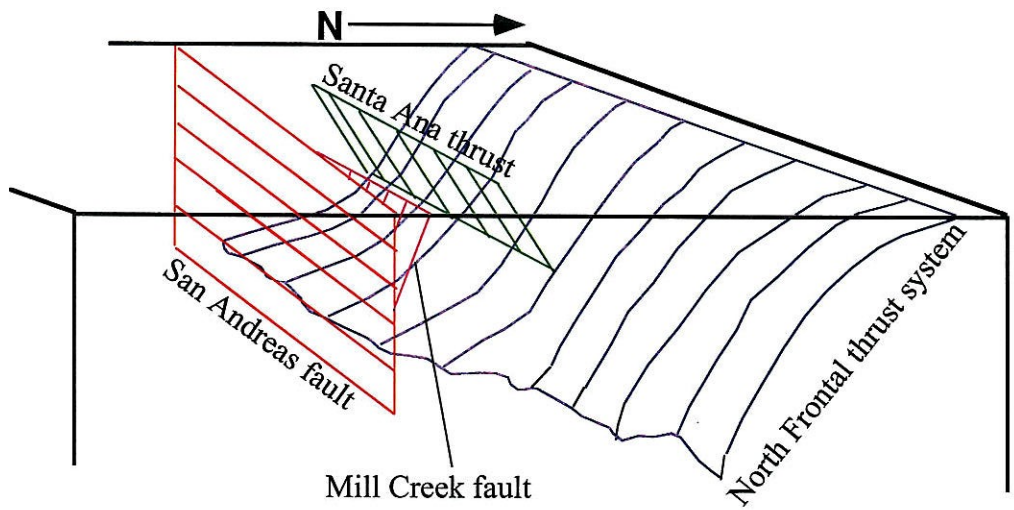

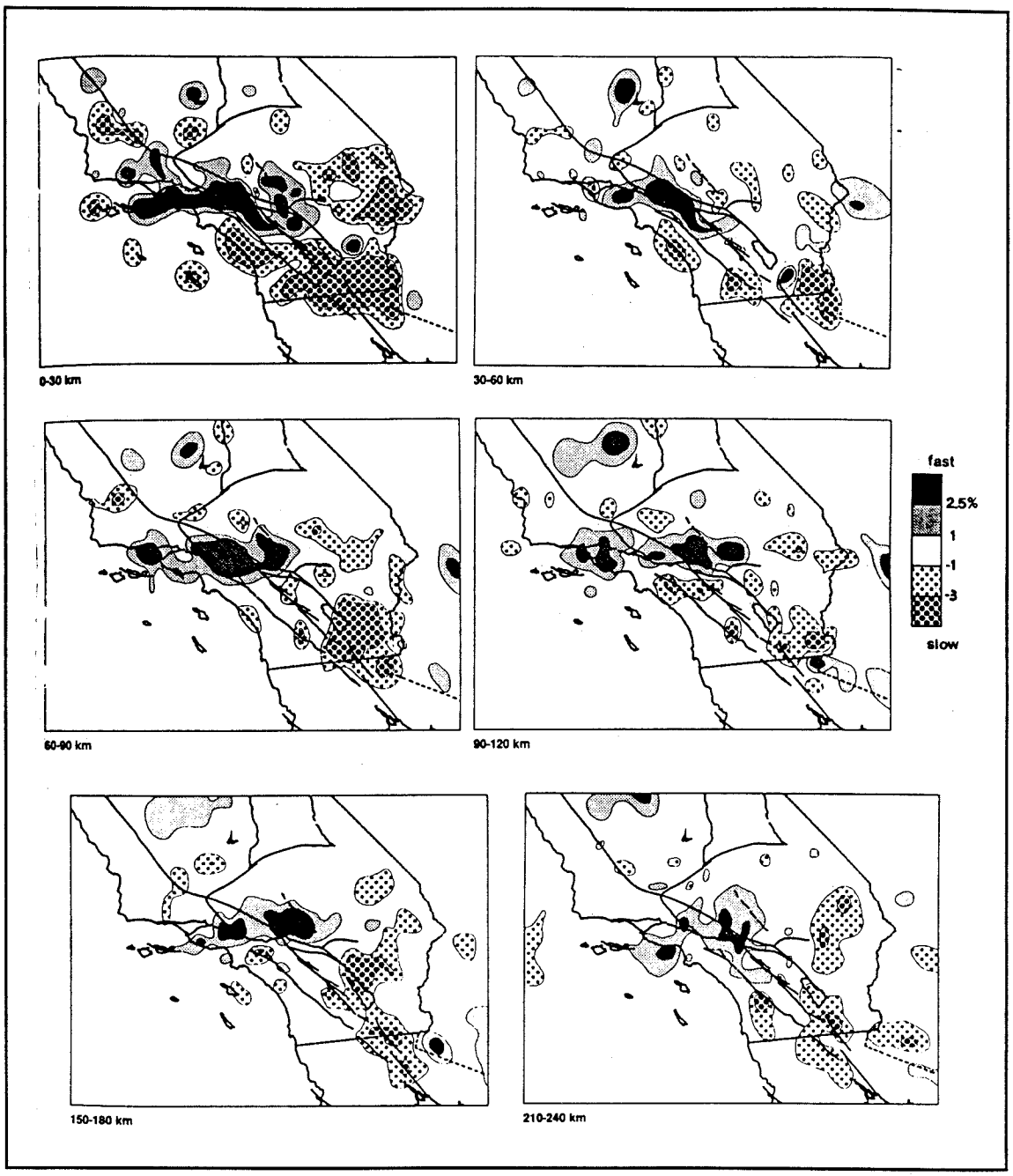

Figure 24: Maps of the seismic velocity anomalies in the mantle beneath the Transverse Ranges according to the P wave inversions of Humphreys and Clayton (1990). Each map represents the anomalies of a different depth range (0-240 km total). A scale bar on the right indicates the range in positive and negative seismic anomalies. Note the presence of high velocity anomalies beneath the general location of the Transverse Ranges and the presence of low velocity anomalies in the Salton Trough region (Figure 1).

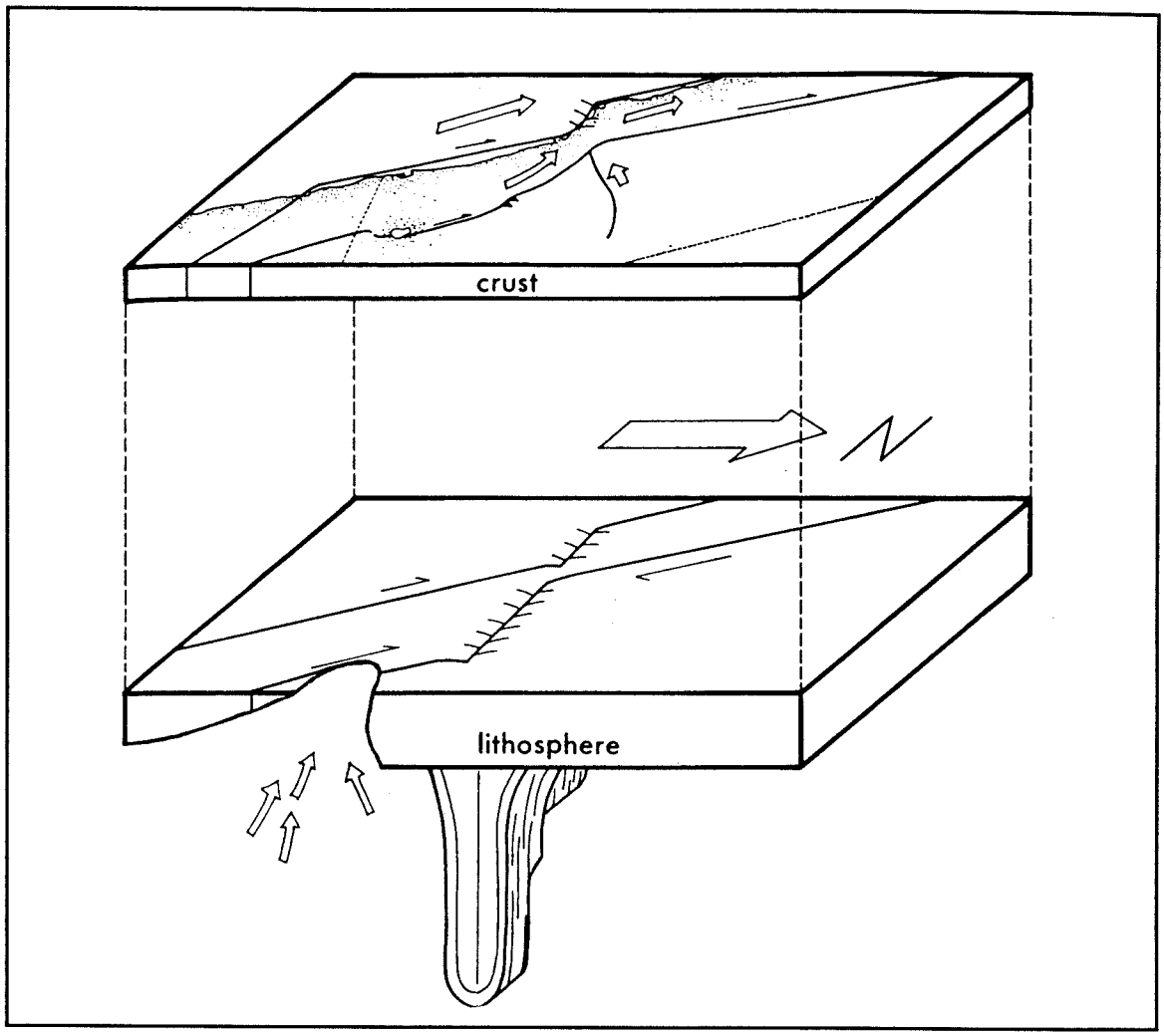

Figure 25: Schematic model of the lithospheric kinematics for southern (from Humphreys and Hager, 1990), which explains the seismic velocity anomaly below the Transverse Ranges as a cold, dense downwelling of mantle lithosphere. The downwelling part of this small scale mantle convection cell is balanced by passive upwelling of asthenosphere in the Salton Trough. According to this model, the negative buoyancy force associated with this sinking drip exerts tractions that cause convergence in the crust, in turn creating the topography of the Transverse Ranges (and SBMs).

Figure 26: Schematic illustrations of the dependence of transpressive orogen migration on the relative degree of strike-slip versus convergent deformation across a restraining bend. Shown are four different examples of a left-bend in a dextral strike-slip fault, analogous to the San Gorgonio Pass stepover. In each case, the left side of the fault (analogous to the Peninsular Ranges block west of the San Andreas fault) is held rigid, which means that it does not experience compressive deformation within the stepover.

A) Case for total convergence. In this example, the entire rate of motion along the strike-slip fault outside of the stepover (d[t]) is accommodated by convergence normal to the stepover (drawn perpendicular to the direction of motion in this case). The convergence effectively "consumes" material by crustal thickening (over thrust, underthrust, etc.), which can then be removed by erosion. In this case, the resulting thickened crust (the orogen) is held fixed with respect to the bend (as shown schematically in lower left, shading represents contours of uplift). If both sides deform, the resulting mountains on either side of the stepover still remain fixed relative to the position of the stepover (as shown in lower right).

B) Case for zero convergence. In this example, the deforming plate navigates the stepover without convergence by fluid-like advection and pure strike-slip motion along the bent segment of the fault. This requires that the net slip vector (d'[t]) be larger and oblique ($90-\alpha$) to the vector outside of the stepover (d[t]). Because lateral transport is effective, the deforming plate migrates with respect to the bend (as illustrated with the circle in lower left). If one plate is held fixed, topographic features on the adjacent plate (i.e., non-transpressive mountains) move at the entire fault rate relative to the stepover. If both plate move equally, then topographic features on either side move at half of the fault rate with respect to the stepover (as shown in lower right).

C) Case for partial convergence. This is a combination of the above two examples, in which the bent segment of the fault (45° oblique) has components of strike-slip ($x[t] = 0.96d[t]$) and convergent ($y[t] = 0.45d[t]$) motion. The resulting slip vector in the

stepover is still oblique (by 20°) and greater than that outside of the stepover. If the convergence is accommodated by crustal thickening on the deforming plate, the resulting orogen is translated away from the fault bend (at a rate = a[t], where a[t] = x[t] in the stepover and a'[t] = d[t] outside the stepover; as shown in lower left). This results in a transpressive orogen that trails off in the direction of plate motion that will remain high unless reduced by erosion or subsidence (Anderson, 1991).

D) Case for partial convergence along a secondary structure. In this example, the convergence occurs off the bent segment of the fault, while pure strike-slip motion occurs along the bent segment itself. The obliquity of the bent segment mimics that of San Gorgonio Pass (α = 60°) and the off-fault convergence (z[t]) is similar to that accommodated in the SBMs (~50% of the San Andreas fault rate in 2 Myr, parallel to the direction of San Andreas motion). The dark lines in the stepover represent a region where crustal thickening occurs along secondary structures, which takes up one-half of the rate along the fault zone. The other half is accommodated by strike-slip motion in the bend (x[t] = 0.58d[t]). This predicted strike-slip rate is similar to the maximum rate of dextral motion that can be attributed to pure strike-slip faults in the San Gorgonio Pass (D. Yule, pers. comm.), and thus all parameters in this example match those observed in the SBMs region. The resulting rate at which the thickened crust (i.e., orogen) is transported relative to the stepover will vary from zero (if the deforming plate is fixed with respect to the bend) to 0.58d(t) (if the right side is fixed, and a[t] = x[t] in the bend).

Figure 26:

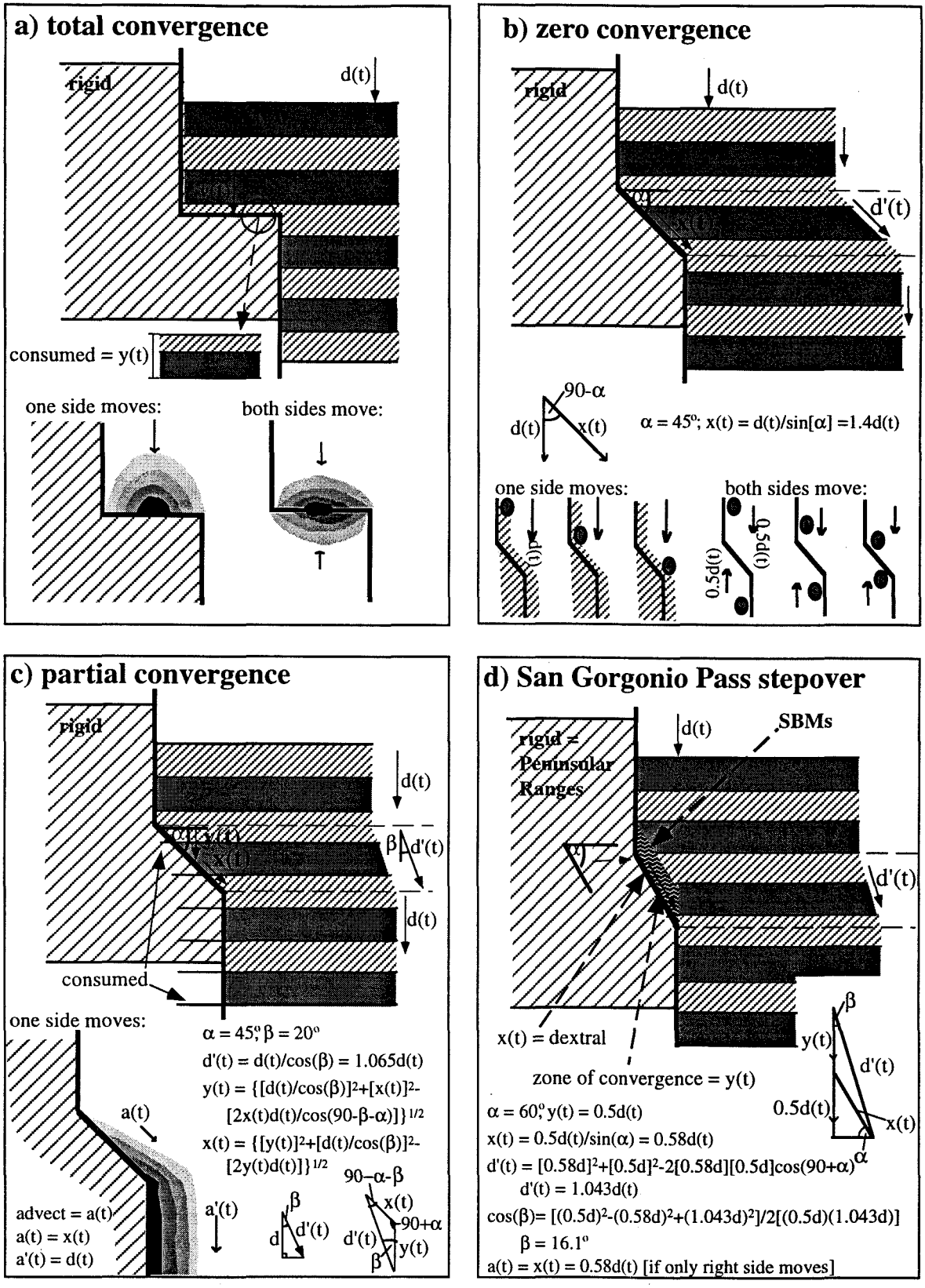
a) total convergence
rigid
d(t)
consumed = y(t)
one side moves:
both sides move:
b) zero convergence
rigid
d(t)
d'(t)
90-α
d(t)
x(t)
α = 45°; x(t) = d(t)/sin[α] =1.4d(t)
one side moves:
both sides move:
0.5d(t)
0.5d(t)
c) partial convergence
rigid
d(t)
β
d'(t)
x(t)
d(t)
consumed
one side moves:
α = 45°, β = 20°
d'(t) = d(t)/cos(β) = 1.065d(t)
y(t) = {[d(t)/cos(β)]²+[x(t)]²-
[2x(t)d(t)/cos(90-β-α)]}^1/2
x(t) = {[y(t)]²+[d(t)/cos(β)]²-
[2y(t)d(t)]}^1/2
a(t)
advect = a(t)
a(t) = x(t)
a'(t) = d(t)
a'(t)
β
d
d'(t)
90–α-β
x(t)
90+α
d'(t)
y(t)
β
d) San Gorgonio Pass stepover
rigid =
Peninsular
Ranges
d(t)
SBMs
d'(t)
x(t) = dextral
zone of convergence = y(t)
β
y(t)
d'(t)
0.5d(t)
x(t)
α
α = 60°, y(t) = 0.5d(t)
x(t) = 0.5d(t)/sin(α) = 0.58d(t)
d'(t) = [0.58d]²+[0.5d]²-2[0.58d][0.5d]cos(90+α)
d'(t) = 1.043d(t)
cos(β)= [(0.5d)²-(0.58d)²+(1.043d)²]/2[(0.5d)(1.043d)]
β = 16.1°
a(t) = x(t) = 0.58d(t) [if only right side moves]

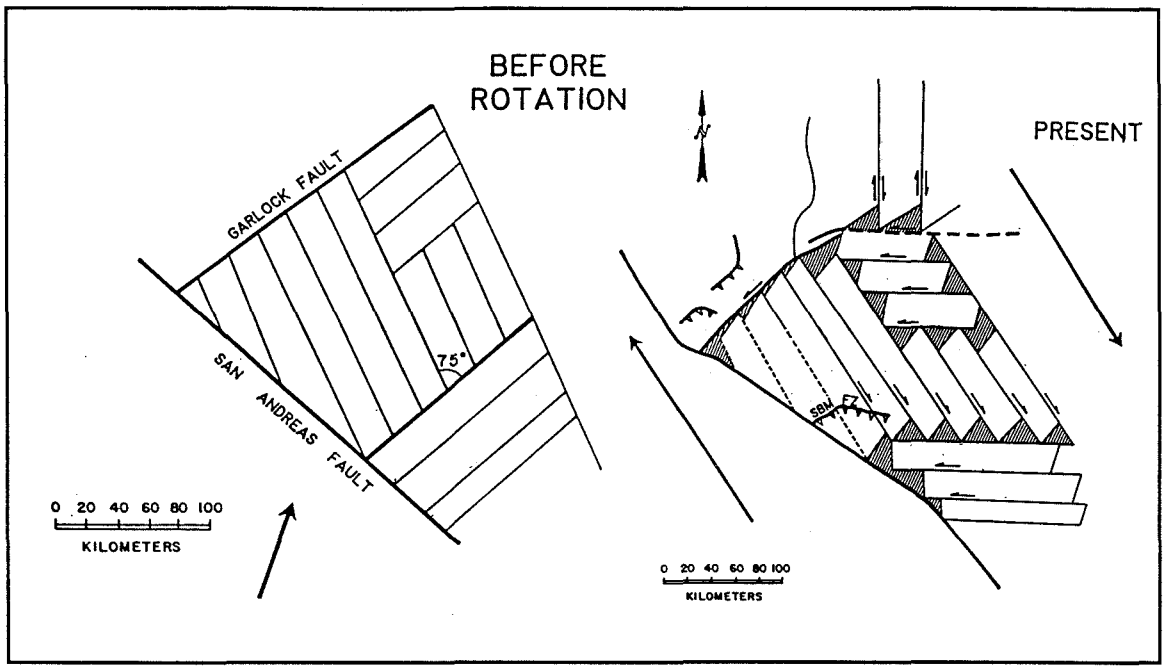

Figure 27a: Carter et al. (1987) rotational model for the eastern Transverse Ranges and Mojave Desert region. In this model, observed clockwise rotation of the left-lateral fault-blocks of the eastern Transverse Ranges is directly accommodating the right lateral shear induced by the counterclockwise rotating fault blocks of the northwest-trending dextral faults of the Eastern California shear zone. This model predicts a counterclockwise bend in the San Andreas fault north of San Gorgonio Pass and a clockwise rotation of the fault south of the pass, thereby creating the left-step geometry south of the SBMs. This model implies that the San Gorgonio Pass restraining bend is stationary with respect to the eastern side of the San Andreas fault. Refer to Figure 1 for names of faults.

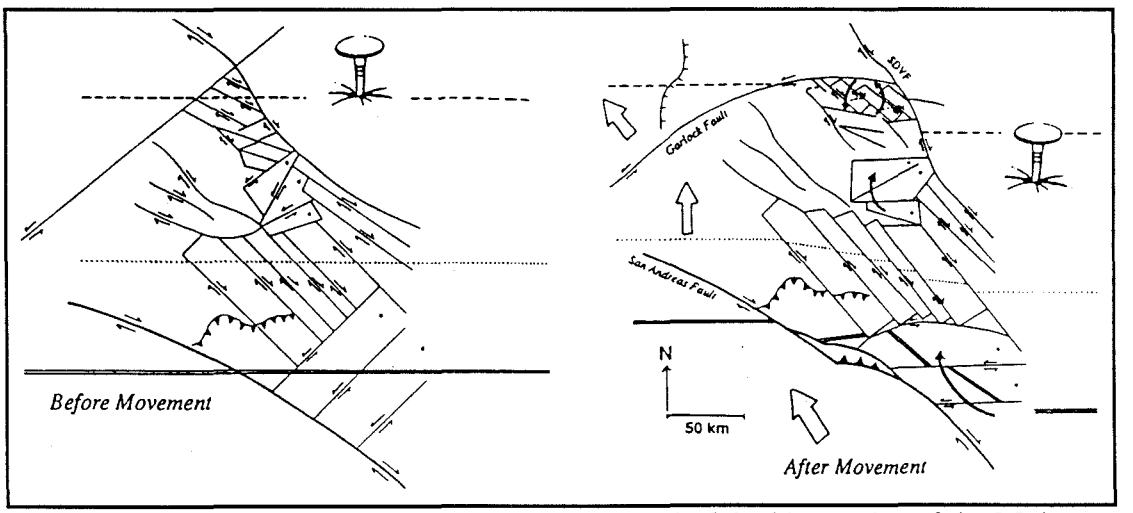

Figure 27b: Humphreys and Weldon (1994) model of the kinematics of the Mojave Desert region. In this model, observed clockwise rotations and left-lateral faulting in the eastern Transverse Ranges accommodate some of the dextral shear of the Eastern California shear zone, which rotates a small amount clockwise (as opposed to Figure 27a). This model also predicts that a left step will develop at San Gorgonio Pass where these two rotating systems meet. In the model, the left step develops without significant rotation of the San Andreas fault to the north or south. This implies that the San Gorgonio Pass restraining bend is stationary relative to the structural elements east of the San Andreas fault.

Chapter Five

Geologic investigations of a "slip gap" in the surficial ruptures of the 1992 Landers Earthquake, southern California

Spotila, James A.

Sieh, Kerry

California Institute of Technology

Reprinted from the *Journal of Geophysical Research*

Volume 100, No. B1, Pages 543-559, January 10, 1995

5.1. Abstract

A 3-km-long gap in the dextral surficial rupture of the 1992 M_W = 7.3 Landers earthquake occurs at the north end of a major fault stepover between the Johnson Valley and Homestead Valley faults. This gap is situated along a segment of the Landers rupture that has been modeled geophysically as having a deficit in average slip at depth. To better evaluate the nature of the slip gap, we document in detail the character and distribution of surficial rupture within it. Along the gap is a northwest-trending thrust-fault rupture with an average of less than 1 m of northeast-directed reverse-slip and nearly no oblique right-slip. We interpret this rupture to be limited to the shallow crust of the northern end of the stepover and to have been the secondary result of dextral shear, rather than a mechanism of rigid-block slip-transfer from the Landers-Kickapoo fault. A zone of en echelon extensional ruptures also occurs along the slip gap, which we interpret as the secondary result of diffuse dextral shear that accommodated less than 0.5 m of west-northwest extension. These secondary ruptures represent a discontinuity in the surficial dextral rupture of the Landers earthquake, which we propose resulted from the lack of a mature fault connection between the Johnson Valley and Homestead Valley faults. The rupture pattern of the slip gap implies a significant deficit in net-surficial slip, which compares favorably with some geophysical models. Aspects of this rupture pattern also suggest a temporal sequence of rupture that compares favorably with geophysical interpretations of the dynamic rupture propagation.

5.2. Introduction

Coseismic fault ruptures commonly consist of solitary principal fault segments, but in some cases rupture in a single earthquake propagates beyond one discrete fault segment to another. This was the case with the M_W = 7.3 Landers earthquake of June 28, 1992, during which dextral shear was distributed on six major fault segments separated

by complex 1-to 3-km-wide fault stepovers (Fig. 1) (Sieh et al., 1993). One of these complex stepovers is a dilational jog 17 km north of the mainshock epicenter, between the dextral Johnson Valley and Homestead Valley faults (JVF and HVF) (Fig. 2) (Sieh et al., 1993). The northern end of this stepover is a region of complex surficial faulting characterized by a lack of dextral slip; we term this region the Homestead Valley (HV) slip gap. The fresh surficial ruptures in this slip gap offered an unusual opportunity to investigate the interactions and evolution of active faults in a structural stepover.

The HV slip gap is located along a section of the Landers rupture that experienced an apparent deficit in average slip relative to two distinct high-slip sections of rupture to the north and south, which was identified by early seismologic investigations (Kanamori et al., 1992; Sieh et al., 1993; Campillo and Archuleta, 1993). Due to their limited resolution and non-uniqueness, these geophysical studies cannot resolve whether this deficit reflects a discontinuity in the rupture at depth. Such a discontinuity would indicate that the Landers earthquake was a double event, caused by two spatially and temporally distinct ruptures. More recent studies, however, present complex, non-unique dislocation models based on seismic and geodetic data, which suggest that the rupture in the HV slip gap was continuous at depth and characterized by reduced slip and a delay in dynamic propagation (Wald and Heaton, 1994; Cohee and Beroza, 1994). Resolving aspects of the rupture pattern that are ambiguous in these geophysical models, such as whether the rupture was discontinuous and, if so, what prevented continuous rupture and how slip was transferred across the discontinuity, is important to the study of interacting active faults.

This paper is a detailed geologic investigation of the surficial ruptures within the HV slip gap. Unlike remotely-sensed seismic and geodetic data, which must be inverted to model slip distribution and rupture dynamics and have limited resolution, surficial displacements and rupture geometries are directly-observable expressions of the kinematics and dynamics of the rupture. These geological data are, therefore, a unique

and critical source of information for interpreting the Landers rupture pattern. In combination with the detailed and abundant seismic and geodetic data, the well-exposed surficial ruptures provide an unprecedented opportunity to study coseismic rupture processes and the long-term tectonic evolution of an active fault stepover.

5.3. Field methods

In the week immediately following the Landers mainshock, we were part of a team of geologists that mapped the surficial ruptures and collected hundreds of measurements of vertical and lateral fault offsets along the entire rupture zone (Sieh et al., 1993). In July and August of 1992, one of us (J.A.S.) mapped the surficial faulting in the HV slip gap in greater detail and measured many more offsets. In order to determine whether any through-going surficial faulting was present along the HV slip gap, we made numerous transects perpendicular to the trend of the fault zone. Fractures with more than 1 cm of lateral or vertical offset were mapped at a scale of 1:6,000 on topographic maps or aerial photographs. We traced all fractures with vertical or strike-slip offset along their entire length or to their connections with the through-going dextral ruptures at the ends of the slip gap. Less prominent fractures were mapped only along transects, but, due to their ubiquity, not necessarily to their full extent.

We determined the along-strike component of horizontal displacement on fractures by matching crack edges or linear features such as tire tracks, channels, and road edges across the fractures. The total lateral offset across a zone of fractures was determined by summing the offsets of single fractures across the zone. This differed from measurements in the more urban regions of the Landers rupture zone to the south, where far-field determinations of lateral offset were possible due to the presence of straight dirt roads and lines of utility poles. We also measured vertical offsets across all fractures. We interpreted the sense of vertical motion on non-strike-slip fractures to be

normal where open fissures were present or a dipping normal-fault surface could be identified. We also identified thrust-fault ruptures by their characteristic scarps (see Observations, Fig. 3a, 3b). Dips of these faults were obtained using the "rule of v's" on the surficial trace and topography, and by direct measurement where the fault surface was exposed in channels or hand-dug trenches. We estimated net dip-slip for the thrust faults from fracture dip, vertical displacement, ground slope, and dimensions of the collapsed hanging wall (Fig. 3c).

The degree and style of fracture exposure and preservation depended on the surficial material. Fractures on hard, flat alluvial surfaces were typically well-exposed and well-preserved, whereas fractures in sand or talus or on steep bedrock or colluvial slopes were commonly difficult to recognize and were less pervasive. Because our field work was completed in the summer months and soon after the rupture, there was no degradation of fractures due to precipitation. However, fractures in loose sand were degraded by wind erosion, and after two months many fractures in sand had disappeared.

5.4. Observations

The JVF-HVF stepover and the HV slip gap are among the more geometrically complex portions of the 1992 Landers surficial rupture (Fig. 1, 2). Our field mapping confirmed that no through-going dextral surficial rupture occurred in 1992 along a 3-km section of the HVF (as mapped by Dibblee, 1967) between the northern and southern segments of HVF rupture (NHVF and SHVF respectively). This dextral slip gap is directly north of the termination of the Landers-Kickapoo fault (LKF) (Landers fault of Sieh et al., 1993 and Kickapoo fault of Hart et al., 1993) and SHVF ruptures, and is occupied by a hill of quartz monzonite (Fig. 2). The NHVF and SHVF become diffuse zones of en echelon fractures in loose sandy alluvium and colluvium as they near the hill and then terminate. The LKF and SHVF come within about 100 m of merging with each

other 1 km south of the slip gap, and the SHVF assumes the same northerly trend as the LKF to the north of the LKF's termination (Fig. 2). Dextral surficial displacements greater than 2 m on the LKF, SHVF, and NHVF decrease rapidly to zero as they approach the slip gap (Fig. 4). Representative lateral and vertical offsets for the major ruptures in the JVF-HVF stepover are shown in Figure 2.

5.4.1 The thrust fault

Although there are no major strike-slip ruptures within the HV slip gap, there is a 3.1-km-long thrust-fault rupture along the northeast flank of the hill between the NHVF and SHVF (Fig. 5, Table 1). Movement on this N52°W, southwest-dipping thrust fault formed a distinctive scarp in both loose-sandy and hard-gravely alluvium (Fig. 3a). This scarp is characterized by a disaggregated wedge of the hanging-wall block covering a part of the footwall ground surface, which is separated from the intact, undeformed hanging-wall block by tensile fractures (Fig. 3b, 3c). The thrust fault has interesting geometric relations with the neighboring strike-slip ruptures. Although the thrust is present on both sides of the NHVF and appears to cross it in map view (Fig. 5), no thrust scarp is actually present within 25 m of the dextral rupture zone and, therefore, neither surficial fault trace offsets the other. At the southern end of the thrust trace, a 100-m-long, northeast-trending tear-fault that consists of a wide zone of en echelon fractures terminates about 150 m away from the SHVF.

The arcuate trace of the thrust fault wraps around a northeast-sloping hillside, primarily at the boundary between the higher, steeply-sloping bedrock or colluvium and the gentler-sloping alluvial surfaces below (Fig. 5). Along most of its trace, the thrust cuts thin alluvium or colluvium that is typically less than 10 m thick (based on projection of the hill's bedrock slope under the alluvium). The sinuous, irregular surficial trace is typical of shallow to moderately dipping dip-slip fault ruptures and consists of numerous splays of parallel thrust segments that are commonly discontinuous or connected by tear faults, and which have geometries that are dependent on local topography. The general

conformity of the surficial trace to local topography indicates that the fault dips shallowly to the southwest. Along its northern segment, the thrust trace diverges from the hillside and continues across a gently sloping, sandy alluvial surface. At several localities west of the NHVF, the northeast-facing scarp crops out on southwest-sloping channel walls and, therefore, is opposed to the local topographic gradient.

Displacement on most of the thrust-fault trace is pure dip-slip, with the southwest side up and a northeast-directed horizontal component of shortening. It was commonly difficult to determine whether there was a strike-slip component to the thrust motion, because linear features that crossed the thrust fault obliquely were shortened across it and, therefore, had apparent lateral displacements. Fortunately, there were many features that were parallel to the gradient of the hill (channel beds, bike tracks) and crossed the thrust fault orthogonally, which we used to determine strike-slip offsets. Of 27 linear features that cross the thrust, 23 showed no strike-slip offsets, 18 of which were more or less orthogonal to the thrust scarp (Fig. 5, Table 1b). For the five oblique features, we estimated the amount of apparent lateral offset that should have been present given the obliquity of the feature and the horizontal shortening on the thrust fault (estimated from the estimates of net dip-slip on the thrust fault, which are discussed below), and found that in each case it matched the observed lateral displacement to within about 10 cm. Of the 4 strike-slip offsets we identified (3 dextral and 1 sinistral), two (locs. 4 and 5; Fig. 5, Table 1a) occur on segments of the thrust fault that are oblique to the average thrust trend (similar to tear-faults) and the other two are much smaller than the net-dip slip or vertical offsets at the same location. All of these strike-slip offsets, as well as the 10-cm uncertainty in our estimates of lateral offsets of oblique features, are significantly smaller than the respective vertical or net dip-slip offsets of the same location. This indicates that the ratio of reverse-slip to strike-slip is very large along the entire thrust trace. We conclude that the motion on the thrust fault was very close to pure reverse, and that the

minor lateral offsets are localized and probably due to slight changes in the strike of the rupture.

We dug several small trenches across the thrust scarp to investigate its geometry and to determine net dip-slip offsets. In each of these, we identified a southwest-dipping fault surface by pulverized bits of rock and centimeter-wide zones of weak disaggregated material within more intact alluvium. This fault surface separates the buried footwall ground surface from the intact hanging wall (Fig. 3b, 3c). Direct measurements of the dip of the fault surface agree with the shallow southwest dips determined by the rule of v's. Dip estimates from both methods range from 4^{o} to 29^{o} and average about 20^{o} (Fig. 5, Table 1a). This variation of dips indicates that the thrust fault forms an irregular plane, rather than a smooth curvilinear one. Our hand-dug trenches were not deep enough to resolve whether the thrust plane becomes more uniform or changes orientation in the shallow subsurface.

The vertical offset on the thrust reaches a maximum of 119 ± 15 cm in the southeast, and averages about 32 cm along its entire length (Appendix 1). Large offsets near the southeast and northwest ends of the rupture result in a slip function with a rough saddle shape (Fig. 6). Net dip-slip on the thrust was determined from the values of dip, the vertical offsets, and the dimensions and orientations of the scarp measured in trenches (Fig. 3c, Table 1a). We estimate the maximum net slip to be 222 ± 40 cm southwest over northeast and estimate the average net dip-slip (Appendix 1) to be about 74 cm. A component of horizontal shortening accompanies this net dip-slip. At one location, a cemented sand channel is compressed and shortened normal to the thrust trend with less than 20 cm of vertical offset and no strike-slip offset, leaving a 10 m wide zone of overlapping sand crusts. At two locations, we were able to measure the horizontal shortening on linear features that were each intersected and shortened at two separate places along a curved segment of the thrust fault, and combine this shortening with vertical offsets and fault dips to estimate the net dip-slip (Table 1a).

5.4.2 Zone of en echelon extension

In addition to the thrust fault, there are smaller, non-strike-slip ruptures in the HV slip gap. We mapped numerous normal-fault ruptures along the hill west of the thrust fault. These discontinuous ruptures are typically hundreds of meters long and roughly form a broad, left-stepping, weak en echelon pattern along the southward projection of the NHVF (Fig. 5). These ruptures consist of either normal-fault scarps, open fissures, or grabens with predominantly west-side-up vertical offsets as large as 64 cm (representative offset values are shown in Fig. 5). At one location (5 m northwest of loc. p; Fig. 5), a large open fracture cuts obliquely through both the hanging wall and footwall of the thrust fault without being offset across the scarp, which demonstrates that at least one tensile fracture formed after rupture of the thrust fault. We identified small measurable lateral offsets on only four of these ruptures (dextral offsets of 3, 5, 15, and 6 cm) (Fig. 5), in marked contrast to the individual en echelon splays along the northern LKF that have over 1 m of right-slip (Fig. 2). We therefore consider this en echelon fracture zone to be mainly extensional. The average trend of the 33 fractures with > 1 cm vertical offset is N09°E (Appendix 2), which corresponds to a direction of horizontal extension of N81°W.

Although about half of these fractures have open fissures, the horizontal extension on any particular fracture is not equal to the width of the fissure. This is because the apertures of the fissures appeared to have been widened by collapse of the fissure walls and are discontinuous and occur only along small fractions of the total length of the ruptures. The extension on each fracture must be reflected solely in the vertical offsets along segments of the rupture that have no fissure. These vertical offsets would have a component of horizontal extension if the faults have non-vertical dips. We were not able to measure the dips of these fractures because their exposed surfaces were normally small and poorly preserved, but they generally appeared near-vertical. However, it is possible

that the dips of these fractures could have been as low as about 75° without appearing non-vertical to the naked eye. To estimate the maximum horizontal extension on each fracture (not including the localized fissures), we used a hypothetical 75° dip, the maximum vertical offsets, and the ground slopes at each fracture. We then summed the net extension distributed across the hill (along the N81°W average extension direction) given the spatial distribution and lengths of these fractures (Appendix 3). Our best estimate of the maximum N81°W extension across the hill accommodated by the normal fractures is much less than 0.5 m (Appendix 3).

We also identified hundreds of smaller fractures in the HV slip gap that were typically less than 25 m long, had millimeter-sized apertures, and had less than 1 cm of vertical or lateral slip. Some of these fractures occurred in steeply sloping sand or colluvium and appeared to be the result of slumping due to ground shaking, but most others probably resulted from tectonic strain. In most cases, these fractures occurred in discontinuous, narrow bands that were not mapable at 1:6,000. Rather than attempting to map all of these in full detail, we noted their orientations and dimensions where we encountered them (Fig. 5). These fractures seemed to be distributed roughly evenly across the hill. The density of this distribution was very low, however, and the hill was not nearly as pervasively fractured as the shear zones along the main Landers rupture (such as along the SHVF; Johnson et al., 1994) (Fig. 5). In addition, these fractures were not organized into discrete shear zones that are present elsewhere along the Landers rupture, which are 50 - 200 m wide, have pervasive extensional and left-lateral fractures, are bounded by narrow fault zones which accommodate most of the zone's dextral displacement, and which commonly have mole-tracks or other compressional features (Johnson et al., 1994). We therefore consider these fractures to be minor responses to tensile stress exerted on the hill, rather than a pervasive dextral shear zone. The distribution of these cracks suggests that they did not contribute much extension to that accommodated by the larger normal fractures.

We noted enough of these small tensile fractures to analyze their trends, and define a dominant north-northeast tendency (Fig. 7). The correlation coefficient (Appendix 4) for fractures within the N05°E to N30°E trend range was 2.4. This implies that the average orientation of these fractures is similar to the N09°E average trend of the larger normal fractures, and that both were produced by west-northwest extension.

5.4.3 Slip distribution within the HV slip gap

The surficial ruptures of the HV slip gap did not accommodate as much slip as the neighboring strike-slip ruptures. The maximum dip-slip on the thrust fault resolves to less than 1 m of right-slip along the strike of the HVF and the average dip-slip resolves to only about 30 cm of right-slip, indicating that the thrust fault did not accommodate as much right-slip as the LKF/SHVF or NHVF ruptures. Although we could not precisely determine the amount of right-slip in the zone of extensional fractures, it does not seem realistic that it could have been more than the 0.5 m maximum extension (but could be less). Thus, the average displacements on the thrust fault and the extensional fractures probably accommodate less than a meter of combined right-slip across the slip gap, in contrast to the combined 6 m of right-slip to the south (JVF, LKF, and SHVF) and the 3 m of right-slip to the north (NHVF) (Fig. 2).

Even when net dip-slip is added to the strike-slip, there appears to be a slip deficit in the gap. Figure 8 shows both the net dip-slip along the thrust fault and the extensional fractures in the slip gap (km 19 to 22), as well as the displacement along the adjacent strike-slip ruptures. This figure clearly shows a marked deficiency in net surficial displacement along the 5-km-long reach from km 17 to km 22, even though slip on the secondary ruptures is included. This demonstrates the existence of a surficial slip gap along the Landers rupture.

5.5. Interpretations

Our detailed observations of the surficial rupture within the HV slip gap aid in understanding the processes of the 1992 rupture and the tectonic development of the JVF-HVF stepover. In our interpretation of these data, we first consider the likely kinematic relations between various coseismic ruptures and develop a model of the overall rupture pattern in the stepover. This model is developed by showing that a simpler, more intuitive model is inconsistent with our observations. We then discuss geophysical evidence of the slip distribution and the likely dynamic sequence of the 1992 rupture in the HV slip gap. Finally, we discuss the tectonic development of the JVF-HVF stepover and HV slip gap and relate it to the 1992 rupture pattern.

5.5.1 Kinematic interpretation of the thrust fault

Based on their geometric relation, movement on the thrust fault seems to be closely linked to dextral slip on the LKF and on the north-trending segment of the SHVF that lies north of the LKF's termination (Fig. 2). The north-directed motion of the block west of the LKF can easily be envisioned to generate contraction across the thrust fault as a result of rigid-block translation, as depicted schematically in Figure 9.

Significant difficulties exist with this simple, rigid-block interpretation, however. First, dextral slip on the LKF and SHVF decrease to zero northward, and surficial dextral rupture terminates south of the southeastern end of the thrust fault (Fig. 2, 5). Even though the maximum right-slip on the LKF of about 2.5 m is roughly equal to the maximum net dip-slip of more than 2 m on the thrust, these offsets are separated by a distance of more than 4 km, along which dextral slip on the LKF decreases to zero and the rupture terminates. This precludes a transform-like junction of the two faults, such as is shown in Figure 9, because such a model predicts that the dextral LKF rupture (or northern SHVF rupture) would directly connect with the thrust.

A second difficulty with the rigid-block model is the lack of oblique right-slip on the thrust fault. The azimuth of the LKF slip vector (N05°E) is not consistent with N38°E-directed, pure reverse-slip on the thrust fault. In the case of rigid translation between the thrust fault and the LKF (ignoring the SHVF), the average horizontal slip vector (Appendix 1) of 144 cm along the LKF would resolve to 78 cm right-slip along the thrust (in addition to a dip-slip component), far greater than we observed (Fig. 5, Table 1). Furthermore, when the SHVF slip is taken into consideration, the problem becomes one of three rigid blocks; the block west of the LKF, the block between the LKF and SHVF, and the block east of the SHVF. When a "displacement-space" diagram (similar to the velocity-space diagrams of plate tectonics) is drawn for these three blocks using the maximum dextral offsets along the LKF and SHVF, the resultant slip vector across the thrust fault is over 4 m in magnitude (Fig. 10). This slip vector resolves to a horizontal shortening component of 3 m and a dextral component of 3.3 m on the thrust fault, which are much larger than we observed (Fig. 5, Table 1). Furthermore, the ratio of horizontal shortening (or net dip-slip) to right-slip predicted by this diagram is close to unity and, therefore, much smaller than we document (Table 1). The lack of right-slip on the thrust fault marks a discrepancy in horizontal slip vectors that suggests that the right-slip on the LKF/SHVF was not directly transferred onto the thrust fault through rigid-block translation.

A third problem with the rigid-block interpretation regards the relative vertical offsets along the faults in the JVF-HVF stepover. If the entire western side of the LKF had been uplifted on the thrust fault as a rigid block, as the west-side-up motion on the LKF suggests, then the sense of vertical motion along the northern JVF should have been east-side-up, rather than the west-side-up offsets that we document (Fig. 2). The west-side-up offset on the northern JVF implies that the thrust fault does not extend southward to the JVF and, therefore, only underlies a northern fraction of the block west of the LKF. Furthermore, the opposite sense of vertical motion of the northeastern (uplifted on the

thrust fault) and southwestern (down-dropped on the JVF) edges of the block west of the LKF resembles the vertical component of the elastic displacement field typical of thrust-fault ruptures, in which near-field uplift is accompanied by far-field subsidence of the hanging-wall block. Although it is beyond the scope of this paper, it may actually be possible to estimate the dimensions, orientation, and slip of the thrust fault at depth from an elastic dislocation model of this deformation pattern.

A fourth problem with the rigid-block interpretation concerns the subsurface geometric relations of the LKF and thrust. A rigid-block model predicts that the LKF terminates down-dip at its intersection with the thrust fault, thereby defining a northeastward-tapering wedge of crust (Fig. 9). If the thrust fault continues to the southwest with a 20^{o} dip, the down-dip width of the LKF should increase from zero on its northern end to only 3.5 km at its intersection with the JVF. Even if the thrust steepens to a 45^{o} dip in the shallow subsurface, the LKF would only be 8 km deep at its intersection with the JVF. The aftershocks around the LKF, however, extend more or less uniformly to a depth of about 14 km (Fig. 11) (Hauksson et al., 1993). This distribution implies that the LKF ruptured to about 14 km depth along most of its length, for if it had ruptured only the upper part of the seismogenic crust, variations in stress with depth would have probably been manifest in the aftershock distribution (Hauksson et al., 1993). This implies that, in the subsurface, the thrust fault is limited to the northern end of the JVF-HVF stepover or that the thrust fault and LKF do not bound a rigid block.

The short, 3-km-length of the thrust fault may be another indication that its down-dip width is only a few kilometers. The down-dip widths of many historical reverse-fault ruptures are smaller than their rupture lengths. For example, the 1945 Mikawa, Japan, earthquake was caused by a thrust rupture 12 km long and 11 km wide (Ando, 1974). Of 67 historical, non-subduction-zone earthquakes of $M > 4.5$ with a reverse component of motion and known rupture widths, only 12 do not have length greater than width (Wells and Coppersmith, 1994). The aspect ratio (ratio of length to width) of these ruptures

averages 1.9 (1.8 for pure reverse ruptures and 2.1 for oblique reverse/strike-slip ruptures). This suggests that the down-dip widths of reverse-fault ruptures are typically half the rupture length and almost always smaller than the rupture length. The common excess of length relative to width suggests that it is unlikely that the 3-km-long thrust fault extends with a 9 km down-dip width from its surficial trace to an intersection with the JVF.

Given these significant problems, it does not seem that the thrust fault and LKF/SHVF intersect and transfer slip in a rigid-block fashion. We propose that the secondary thrust rupture is limited in the shallow subsurface to the northern end of the JVF-HVF stepover, and we hypothesize that failure of the thrust was induced by static or dynamic stresses that resulted from dextral shear along the LKF/SHVF and the rapid termination of LKF/SHVF right-slip at the southern end of the HV slip gap. This abrupt termination is indicated by the rate of decrease in slip per rupture length (Appendix 5), which is, on average, more than 4 times higher along ruptures that terminate at the HV slip gap than along ruptures which terminate elsewhere in the JVF-HVF stepover (Table 2). This value of about 2×10^{-3} m/m for the northern end of the LKF may have concentrated shear stresses that induced failure of the thrust. Furthermore, Hauksson's (1994) analysis of aftershocks showed that the post-mainshock maximum principal stresses along the LKF and HVF were N40°E and N46°E, respectively. These are the most easterly-trending stress values for the entire Landers rupture zone and are nearly perpendicular to the thrust fault, further supporting the idea that the thrust fault rupture was induced by stresses resulting from dextral shear along the Landers rupture. Static and dynamic models of the ruptures would be necessary to determine whether or not this "induced-slip" model could explain the nearly pure dip-slip we observe on the thrust fault, but these are beyond the scope of this paper.

It is worth noting that our interpretation of the relation between the LKF/SHVF and thrust fault is comparable to the interpretation of Peltzer et al. (1994) of the JVF-HVF

stepover based on Synthetic Aperture Radar interferometry. They suggest the block between the LKF and northern JVF behaved rigidly and was tilted 0.01° to the southwest about a N20°W axis, and argue that the vertical displacements on the LKF and thrust fault were responsible for this tilt (Peltzer et al., 1994). This interpretation implies that the block west of the LKF behaved rigidly, similar to the rigid-block model discussed above. However, we propose that the thrust fault was not necessary to produce this tilt, since it can be explained solely by the vertical displacements along the JVF and LKF. If the western side of the JVF and the eastern side of the LKF are held fixed, these vertical offsets yield southwest-directed tilts with N20°W axes of from 0.01° to 0.05° (Fig. 2). In addition, the interferogram that implies this tilt is only clear in the southwestern part of the block west of the LKF, due to a loss of coherence in the northeastern part near the thrust fault (Fig. 5 of Peltzer et al., 1994). This suggests that the rigid tilt was confined to the southern part of the block between the LKF and JVF, and is consistent with our interpretation that the thrust fault is limited to the northern end of the JVF-HVF stepover and does not bound a rigid block with the LKF.

5.5.2 Kinematic interpretation of the zone of en echelon extension

Several observations support the hypothesis that the en echelon zone of normal faults and tensile fractures that traverses the hill in the HV slip gap is related to the southern termination of the NHVF. First, the northern end of the en echelon zone is within a few hundred meters of the southern surficial termination of the NHVF. Second, the trend of the zone is parallel to the NHVF (Fig. 5). Third, the average north-northeast trend of the individual fractures of the zone is oblique to the trend of the NHVF by about 35° to 50°. This, along with the weak left-stepping pattern of the fractures, is consistent with dextral shear along the azimuth of the NHVF. Finally, the slip on the fractures of the en echelon zone generally diminishes southwestward, away from the NHVF. We propose that the en echelon extensional fractures mark a zone of diffuse dextral shear that

corresponds to southward propagation of the surficial NHVF rupture. The abrupt termination of the NHVF at the surface, indicated by the rate of decrease in dextral slip per rupture length of about 4 x 10^{-3} m/m (Table 2, Appendix 5), may have resulted in enough stress to cause the secondary rupture of this zone of en echelon fractures. The lack of strike-slip offset on these fractures, their spatial arrangement, and the minimal extension they accommodate, however, suggest they do not make up a pervasive strike-slip shear zone like those elsewhere along the Landers rupture. As with the thrust fault, static and dynamic models of the ruptures would be necessary to test this "induced-slip" model.

5.5.3 Model of the JVF-HVF stepover rupture pattern

Our kinematic interpretations of the ruptures in the HV slip gap imply that dextral shear in the shallow crust resulted in secondary, non-strike-slip deformation, instead of a through-going right-lateral rupture. The stresses created by right-slip along the LKF/SHVF and by the NHVF and the rapid termination of this right-slip (Table 2) may have induced the failure of the thrust fault and the zone of en echelon extension, but did not produce a continuous connection between the northern and southern strike-slip faults or transfer slip via the rigid translation of blocks. This discontinuity in the 1992 dextral rupture indicates that there must have been a barrier to the dynamic rupture propagation.

The three-dimensional rupture pattern implied by our proposed lack of a continuous rupture through the slip gap is shown schematically in Figure 12. In this speculative model, we consider the thrust fault to be limited to the shallow crust and do not connect it with either the LKF or the SHVF. We represent the zone of en echelon extension as a continuation of the NHVF, and show it to be contiguous with the NHVF at depth. Our observations do not require this, however, and this zone could be physically separated from the major fault that induced its movement. We also postulate that the northern JVF and SHVF ruptures were limited to the shallow crust, because of the near-

absence of aftershocks along them (Fig. 11, 12). We do not know the rupture pattern below the thrust fault and zone of en echelon extension in the slip gap (Fig. 12). It is simplest to assume that the lack of a through-going dextral rupture at the surface reflects a similar discontinuity at depth (as shown in Fig. 12), but our geological observations do not preclude other possibilities. There are, however, other sources of evidence that suggest the rupture may have been discontinuous at depth in the slip gap.

There is a cluster of aftershocks in the HV slip gap that is more dense than elsewhere along the Landers rupture zone (Fig. 11 and Hauksson et al., 1993), which may indicate that post-mainshock stresses in the slip gap were higher than elsewhere. This aftershock cluster could have resulted from a lack of continuous rupture at depth bounded by high-slip ruptures. The terminations of these ruptures could have induced high stresses, an idea that is consistent with the hypothesis of Mendoza and Hartzell (1988) that aftershocks commonly occur in the volume of crust that surrounds the ends of high-slip ruptures. A similarly dense aftershock cluster occurred between the southern end of the JVF and the northern end of the Eureka Peak fault, where no through-going rupture occurred (Sieh et al., 1993; Hauksson et al., 1993). The dense cluster of aftershocks, however, does not require a gap in continuous faulting. It could also have resulted from stresses produced by a slip deficit along a continuous dextral rupture or by a stress heterogeneity due to the bend in strike from the LKF/SHVF to the NHVF along a continuous rupture.

Another source of evidence that suggests there may not have been a through-going rupture in the HV slip gap is the lack of a seismic waveguide there after the earthquake. North and south of the slip gap there are narrow, low-velocity zones along the Landers ruptures that trap short-wave-length shear waves of aftershocks that occur along the fault zone (Li et al., 1994). Li et al. (1994) interpret these to reflect the existence of a continuous, low-velocity plane at depth, but are not certain whether this plane is the 1992 rupture zone or a pre-1992 "geological wear zone." In the area of the

fault bend from the LKF to the HVF, there is no waveguide from the surface to a depth of 6 km (Li et al., 1994). Although this may correlate with the surficial-rupture discontinuity in the slip gap, this absence of a waveguide continues north of the slip gap along the entire NHVF, in contrast to the surficial rupture. We, therefore, hesitate to use this intriguing approach to identify the pattern of rupture at depth, but recognize the possibility that the lack of a waveguide in the slip gap could indicate a fault discontinuity.

Thus, the aftershocks and the lack of a seismic waveguide in the HV slip gap are consistent with a discontinuous rupture at depth, but do not require one. The rupture discontinuity we propose exists in the near-surface of the slip gap may, therefore, continue at depth.

5.5.4 Geophysical evidence of the slip distribution in the HV slip gap

The deficiency in both right-slip and net slip on the surficial ruptures of the HV slip gap relative to the dextral ruptures to the north and south may reflect a similar deficit in slip at depth. Although our observations do not constrain the rupture pattern at depth, models of seismic and geodetic data offer insight into the amount of slip that occurred beneath the surficial slip gap.

Some analyses of seismic (Kanamori et al., 1992; Sieh et al., 1993; Campillo and Archuleta, 1993; Dreger, 1994) and geodetic (Hudnut et al., 1994) data resolve a deficit in the average slip at depth on the ruptures of the slip gap, which suggest that the surficial deficit continues to the base of the seismogenic crust. However, other analyses of seismic (Velasco et al., 1994), geodetic (Freymueller et al., 1994), and Synthetic-Aperture-Radar-interferometry (Massonnet et al., 1993) data vaguely show two high-slip sections of rupture north and south of the slip gap, but do not indicate that the slip throughout the slip gap is below 2 m. The detailed inversions of geophysical data by Cohee and Beroza (1994) and Wald and Heaton (1994) also suggest that the slip gap was a patch of lesser

right-slip between two high-slip sections of rupture, but indicate that 3 m of slip occurred in the shallow crust of the slip gap, which is much more than we document.

All of these geophysical models of the displacement in the slip gap are non-unique due to the assumptions they incorporate, and have limited spatial and temporal resolution due to the smoothing of data they employ. These models are, therefore, ambiguous and inconsistent. Although some show a slip deficit at depth that is consistent with the discontinuity in rupture that we propose, others suggest that the rupture was through-going. We, therefore, cannot conclude whether the surficial slip deficit or rupture discontinuity continues at depth on the basis of geophysical models.

5.5.5 Sequence of events during the 1992 Landers earthquake

The sequence of ruptures propagating into and through the HV slip gap can be inferred from the geometrical relations of the faults. The orientation and transport direction of the thrust fault suggests that it ruptured in response to dextral slip on the LKF, which requires that rupture of the LKF preceded the rupture of the thrust fault. The NHVF seems to have ruptured after the thrust fault, because the thrust fault continues without diminution of offset for 500 m northwestward of its intersection with the NHVF (Fig. 5). If the NHVF ruptured first, the abrupt southern termination of its rupture would have produced substantial extension along the westernmost segment of the thrust fault that would have inhibited a contractional rupture. The zone of en echelon extension also seems to have ruptured after the thrust fault, because at least one fracture within it cut the thrust scarp without being offset (loc. p; Fig. 5). The zone of extension may have also ruptured after the NHVF, because it seems to have been a secondary continuation of the NHVF south of its abrupt termination.

This geologically determined sequence implies a general northward propagation of rupture, and is therefore consistent with the unilateral northward propagation determined seismologically (e.g., Kanamori et al., 1992). The rupture of the zone of en

echelon extension after the NHVF is an exception to this general northward propagation. However, this fine detail of the rupture dynamics, which can be inferred from geological data, probably cannot be resolved from the geophysical data.

Other aspects of the rupture propagation in the detailed model of Wald and Heaton (1994) can be compared with our interpretations. In Figure 13, we reproduce their spatio-temporal development of the Landers rupture (Fig. 16 of Wald and Heaton, 1994), which shows the time progression of the Landers rupture for their combined dislocation model. In this figure, the rupture propagates from the hypocenter to the slip gap in 6 sec, but lingers for 4 sec while 4 m of slip occurs on the faults within the JVF-HVF stepover. In the 10-11 sec interval after the initiation of rupture, a 1-m burst of slip occurs in the upper 5 km of the HV slip gap. We suggest that this burst reflects the rupture of the thrust fault. Simultaneously, 0.5 m of isolated slip occurs at a depth of 10 to 15 km in the slip gap. We suggest that this reflects initiation of rupture on the NHVF that may have been discontinuous with the ruptures south of the slip gap. The continuation of shallow slip in the slip gap during the next 2 sec and its connection with the slip to the north on the NHVF are consistent with the southeastward rupture of the en echelon fractures after the initial rupture of the NHVF.

Although the correlations of our interpretations with the model of Wald and Heaton (1994) are highly speculative and can be no more accurate than the models themselves, the correlation of geologic and seismologic models is intriguing. If the details of the rupture propagation inferred in their model do, in fact, relate to localized characteristics of the rupture that we have documented at the surface, then a major gap between geological and geophysical interpretations of coseismic processes may have been bridged for the first time.

5.5.6 Tectonic development of the slip gap

Although our study did not focus on the geologic evidence of previous faulting in the JVF-HVF stepover, we made several observations that have implications for its long-term tectonic development. Based on these observations, we propose that the LKF and the secondary faults in the HV slip gap are less mature than the JVF and NHVF/SHVF, and that they are in the process of connecting the JVF and HVF strike-slip systems.

The NHVF has a total dextral offset of about 300 m, based on an offset lens of marble (Dibblee, 1967), offset drainages and shutter ridges, and bedrock and geomorphic offsets of a small hill (Zachariasen and Sieh, 1994). The SHVF may have a similar amount of previous right-slip, given its similar topographic expression and an offset shutter ridge on the southeast side of the hill in the slip gap (Fig. 2, 5). This 300 m of cumulative slip would have been produced in about 100 1992-sized ruptures and appears adequate to form integrated, continuous fault zones. The JVF also has a through-going trace and displays truncations and offsets of geologic units along it (Dibblee, 1967), which suggests that it has also has substantial previous right-slip. Both the JVF and the HVF strike-slip systems have been active in the Holocene (Hecker et al., 1993; Lindvall and Rockwell, 1993; Herzberg and Rockwell, 1993).

The LKF and smaller faults in the HV slip gap seem to have much less cumulative offset than the JVF and HVF systems. Although the LKF is a pre-existing structure (Sowers et al., 1994; Lindvall and Rockwell, 1993), both its lack of conspicuous tectonic landforms and the complex en echelon character of its trace (Fig. 2) suggest that it has significantly less cumulative offset than the more integrated traces of the NHVF, SHVF, and JVF. This interpretation is supported by the correlation between smoothness of fault traces and cumulative offset (Wesnousky, 1988; Tchalenko, 1970). The lack of deflection of the JVF trace at its confluence with the LKF also argues that the total offset on the LKF is small. Furthermore, there is no gravity anomaly associated with the LKF, whereas the JVF has a gravity anomaly that suggests it is associated with a bedrock scarp buried by alluvium (Sowers et al., 1994). If both faults typically rupture with similar-

sized vertical offsets as they did in 1992, the lack of a geophysically apparent bedrock scarp along the LKF suggests that it has ruptured fewer times than the JVF.

The thrust fault may have ruptured in as few events as the LKF, if it is mechanically related to the LKF. Although we observed old scarps along the trace of the thrust fault, these were only several times the size of the 1992 scarps. The 200-m-high hill in the hanging-wall of the thrust fault, however, would imply much more uplift. More than 500 thrust ruptures of average 1992 vertical offset are required to have fully uplifted this hill, which is more rupture events than the LKF or even the JVF, SHVF, or NHVF have probably sustained. However, there is no evidence that precludes uplift of this hill by mechanisms other than the thrust fault and there is evidence that the hill may have existed before the thrust fault was active. The 300 m bedrock and geomorphic offsets of a smaller hill across the NHVF show that the HVF strike-slip system was active after creation of the present topography of the region (Zachariasen and Sieh, 1994). The hill in the slip gap could have also existed before the HVF system was active, and would have therefore existed before the JVF-HVF stepover, LKF, and thrust fault were active (assuming they are all mechanically related). We therefore consider it possible that the thrust fault has ruptured as few times as the LKF and the hill in the slip gap may not have been uplifted entirely in concert with slip on the thrust fault.

The fractures in the en echelon zone of extension in the slip gap also appear to have little cumulative slip. We compared the size and sense of the 1992 vertical offsets with the steepness and sense of topographic relief around each fracture and found that virtually none of the fractures could have sustained more than ten previous 1992-sized ruptures. Although these estimates do not take into account heavy erosion, they do suggest that the normal fractures have ruptured far fewer times than the JVF or NHVF/SHVF. This, along with the kinematic relationship between the extension and the NHVF in 1992, implies that the zone of extension is an immature southern continuation of the NHVF. The individual extensional fractures may be similar to splays of a strike-

slip fault that have not yet integrated into a continuous fault zone due to a lack of sufficient cumulative slip. Similar discontinuous en echelon surficial shears are produced by strike-slip on a subsurface fault in shear box and Reidel experiments with granular material, which eventually integrate into an irregular but continuous fault zone as cumulative displacement increases (Tchalenko, 1970). Fault zones in the Earth's crust are thought to evolve from initial en echelon geometries in a similar fashion (Wesnousky, 1988; Bjarnasson et al., 1993).

Thus, it seems that the JVF and the HVF systems have more cumulative offset than the LKF, the en echelon zone of extension, and possibly the thrust fault. This precludes the possibility that rupture of the LKF-thrust-en echelon system could have been a characteristic feature of all the previous ruptures of the JVF and HVF. Therefore, we propose that the connection between the JVF and HVF strike-slip systems is in the process of developing. The 1992 rupture pattern suggests this even more strongly, because no through-going dextral rupture broke through the slip gap and the only right-slip between the LKF/SHVF and NHVF was accommodated by secondary faulting. This inability to break through in 1992 indicates that the connection between the JVF and HVF is not yet fully functional. If the JVF-HVF stepover was complete, the LKF would have transferred its several meters of right-slip to the NHVF via a continuous rupture, rather than terminating and resulting in non-strike-slip deformation, and would exhibit more maturity. There was probably a physical barrier that prevented the LKF from transferring slip with a through-going rupture, such as the 30^{o} bend in strike between it and the NHVF or perhaps an absence of a continuous, pre-existing fault zone. Such a barrier would be both the result and indication of the immaturity and incompleteness of the connection between the JVF-HVF stepover.

The juvenile LKF-thrust-en echelon system, therefore, seems to represent a nascent connection, which in 1992 and in a limited number of previous ruptures has begun to connect the JVF and HVF systems. The 1992 rupture pattern may therefore

mark the early stages of the transition to a single, contiguous strike-slip system. This interpretation is consistent with the observation of Nur et al. (1993) that recent earthquake ruptures in the Eastern California shear zone have been on northerly-trending faults that have less cumulative slip than the northwest-trending faults in the zone.

5.6. Summary and conclusions

We document a gap in dextral surficial rupture along a 3-km-long segment of the Landers earthquake rupture. Along this gap is a northwest-trending, southwest-dipping thrust-fault rupture, which has an average of less than 1 m net dip-slip and virtually no oblique right-slip. Our observations suggest that this thrust fault does not bound a rigid block that moved to the north along the Landers-Kickapoo fault, but seems to be a secondary effect of dextral shear that is confined to the shallow crust of the northern end of the Johnson Valley fault-Homestead Valley fault stepover. A zone of en echelon extensional ruptures also accommodates less than 0.5 m of N81°W extension in the gap, which seems to have been produced as a secondary effect of dextral shear that can be considered an immature southward continuation of the Northern Homestead Valley fault. These induced-slip interpretations of the rupture kinematics could be tested by elastic dislocation models, which are beyond the scope of this paper. The combined right-slip of less than 1 m accommodated by these secondary ruptures and their combined net slip are significantly smaller than the right-slip on the dextral ruptures to the north and south, which implies that there is a deficit in surficial slip along this segment of the Landers rupture.

The lack of through-going dextral rupture that seems to have resulted in the secondary thrust and extensional ruptures suggests that there was a discontinuity in the Landers rupture at the north end of the Johnson Valley fault-Homestead Valley fault stepover. This discontinuity implies that the dynamic propagating rupture was prevented

from breaking through the crust, and we propose that this is because the connection between the Johnson Valley and Homestead Valley strike-slip systems is incomplete. This hypothesis is supported by the apparent immaturity of the faults that compose the connection between the strike-slip systems. Despite this absence of a complete connection, the Landers rupture managed to continue along the Northern Homestead Valley fault and other major faults north of the slip gap. This suggests that coseismic ruptures can jump across fault segments that are not fully connected and, therefore, that fault segment length is not, by itself, a reliable indicator of future rupture dimensions.

Our observations do not resolve whether an absence in continuous dextral rupture or a deficit in net slip occurred at greater depth along this segment of the rupture. Aftershocks and the lack of a seismic waveguide along this segment suggest that there could have been a gap in continuous faulting, but this is not conclusive. Geophysical analyses of seismic and geodetic data show this segment as both a lack of right-slip that extends throughout the seismogenic crust and a patch of lessor slip between two high-slip sections of a continuous dextral rupture. The ambiguities of these analyses prevent us from using them to determine whether there is a slip deficit or rupture discontinuity throughout the seismogenic crust in the slip gap. Our interpretation of the sequence of ruptures in the surficial gap, however, seems to correlate with the geophysical models of the dynamic rupture propagation.

5.7. Appendix

1) The average displacement for a fault rupture segment is calculated as follows: the rupture is divided into segments defined by the locations of offset measurements (there is one segment for each measurement, and the ends of each segment are defined by the midpoints between locations of measurements), each offset is then multiplied by its segment length, these products are then added together for the entire fault, and finally the

sum is divided by the total fault length to get the length-weighted average fault displacement.

2) The average trend of the extensional fractures is calculated as follows: for a length-weighted average, the trend of each fracture is multiplied by its length and the values are summed and divided by the total length (result = N09°E). An offset-weighted average can also be calculated as follows: the trend of each fracture is multiplied by its vertical offset and the values are summed and divided by the total vertical offset (result = N10°E). The similarity of these two averages shows that extensional fractures are dominantly north-northeast trending.

3) To estimate the maximum N81°W horizontal extension across the en echelon normal faults, we summed the extension on fracture splays that are arranged in a parallel series. We added the extension on fractures that could be intersected by semi-straight lines across the hill along the average extension direction, and found that the greatest extension was always much less than 0.5 m. Admittedly, this estimate of the extension has limited accuracy given the assumed 75° dip, the exclusion of open fissure widths, the use of maximum vertical offsets instead of average offsets, and the difficulty of arranging the fractures into a parallel series. However, our goal was to define an upper limit for the amount of extension and we feel that the 0.5 m maximum limit is accurate for this purpose.

4) The correlation coefficient for the trends of the tensile fractures is calculated as follows: the ratio of the number of fractures with trends of a certain range to the total number of fractures is divided by the ratio of that given range in trend to the overall range in trend (180°).

5) The ratio of the decrease in slip to the rupture length over which the decrease occurs is calculated as follows: for the end of a given rupture, all of the dextral slip values that are decreasing in the direction of the rupture termination (usually within several km of the termination) are divided individually by the distance of the

measurement site from the end of the rupture, and these values are then averaged for each fracture terminus (Table 2). These values can be considered to be twice the longitudinal strain exerted on either side of the fault by the termination of the rupture.

5.8. Acknowledgments

We thank Anne Lilje for major help on figures and data tabulation, Egill Hauksson for Figure 11, and Dave Wald and Tom Heaton for Figure 13. We also thank Gilles Peltzer, Dave Wald, Egill Hauksson, Mark Abolins, Rob Brady, and Judy Zachariasen for helpful discussions, and Anthony Crone, Wayne Thatcher, and an anonymous reviewer for helpful reviews. This study was funded by the Jet Propulsion Laboratory-Director's Discretionary Fund 7300064703235 and the Southern California Earthquake Center/National Science Foundation grant EAR-8920136. Contribution 5439, Division of Geological and Planetary Sciences, California Institute of Technology.

5.9. References

Ando, M., Faulting in the Mikawa Earthquake of 1945, Tectonophysics, 22, 173-186, 1974.

Bjarnasson, I.T., P. Cowie, M. Anders, L. Seeber, and C. Scholz, The 1912 Iceland earthquake rupture; growth and development of a nascent transform system, Bull. Seismol. Soc. Am., 83, 416-435, 1993.

Bryant, W.A., Fault evaluation report FER-234: Surface fault rupture along the Johnson Valley, Homestead Valley, and related faults associated with the Ms=7.5 28 June 1992 Landers earthquake, Calif. Div. Mines and Geol. Special Publication, 42, 1992.

Campillo, M., and R. J. Archuleta, A rupture model for the 28 June 1992 Landers, California, earthquake, Geophys. Res. Lett., 20, 647-650, 1993.

Cohee, B.P., and G.C. Beroza, Slip distribution of the 1992 Landers earthquake and its implications for earthquake source mechanics, Bull. Seismol. Soc. Am., 84, 692-712, 1994.

Dibblee, T.W., Geologic map of the Emerson Lake Quadrangle, San Bernardino County, California, U.S.G.S. Misc. Geol. Investigations Map, I-490, 1967.

Dreger, D.S., Investigation of the rupture process of the 28 June 1992 Landers earthquake utilizing TERRAscope, Bull. Seismol. Soc. Am., 84, 713-724, 1994.

Freymueller, J., N.E. King, and P. Segall, The coseismic slip distribution of the Landers earthquake, Bull. Seismol. Soc. Am., 84, 646-659, 1994.

Hart, E.W., W.A. Bryant, and J.A. Treiman, Surface faulting associated with the June 1992 Landers earthquake, California, Calif. Geol., 46, 10-16, 1993.

Hauksson, E., State of stress from focal mechanisms before and after the 1992 Landers earthquake sequence, Bull. Seismol. Soc. Am., 84, 917-934, 1994.

Hauksson, E., L.M. Jones, K. Hutton, and D. Eberhart-Phillips, The 1992 Landers earthquake sequence: seismological observations, J. Geophys. Res., 98, 19,835-19,858, 1993.

Hecker, S., T.E. Fumal, T.J. Powers, J.C. Hamilton, C.D. Garvin, D.P. Schwartz, and F.R. Cinti, Late Pleistocene-Holocene behavior of the Homestead Valley fault segment--1992 Landers, California surface rupture, Eos Trans. AGU, 74, 43, 612, 1993.

Herzberg, M., and T. Rockwell, Timing of past earthquakes on the northern Johnson Valley fault and their relationship to the 1992 rupture, Eos Trans. AGU, 74, 43, 612, 1993.

Hudnut, K.W., Y. Bock, M. Cline, P. Fang, Y. Feng, J. Freymueller, X. Ge, W.K. Gross, D. Jackson, M. Kim, N.E. King, S.C. Larsen, M. Lisowski, Z-K. Shen, J. Svarc, and J. Zhang, Coseismic displacements of the 1992 Landers earthquake sequence, Bull. Seismol. Soc. Am., 84, 625-645, 1994.

Johnson, A.M., R.W. Fleming, and K.M. Cruikshank, Shear zones formed along long, straight traces of fault zones during the 28 June 1992 Landers, California, earthquake, Bull. Seismol. Soc. Am., 84, 499-510, 1994.

Kanamori, H., H-K. Thio, D. Dreger, E. Hauksson, and T. Heaton, Initial investigations of the Landers, California, earthquake of 28 June 1992 using TERRAscope, Geophys. Res. Lett., 19, 2267-2270, 1992.

Li, Y.-G., J.E. Vidale, K. Aki, C.J. Marone, and W.H.K. Lee, Fine structure of the Landers fault zone: segmentation and the rupture process, Science, 265, 367-370, 1994.

Lindvall, S., and T.K. Rockwell, Recurrent Holocene faulting along the Johnson Valley portion of the 1992 Landers earthquake surface rupture, Geol. Soc. Am. Abstracts with Programs, 25, 70, 1993.

Massonnet, D., M. Rossi, C. Carmona, F. Adragna, G. Peltzer, K. Feigl, and T. Rabaute, The displacement of the Landers earthquake mapped by radar interferometry, Nature, 364, 138-142, 1993.

Mendoza, C., and S.H. Hartzell, Aftershock patterns and main shock faulting, Bull. Seismol. Soc. Am., 78, 1438-1449, 1988.

Nur, A., R. Hagai, and G.C. Beroza, The nature of the Landers-Mojave earthquake line, Science, 261, 201-203, 1993.

Peltzer, G., K.W. Hudnut, and K.L. Feigl, Analysis of coseismic surface displacement gradient using radar interferometry: new insights into the Landers earthquake, revised for J. Geophys. Res., June, 1994.

Rockwell, T.K., D.P. Schwartz, K. Sieh, C. Rubin, S. Lindvall, M. Herzberg, D. Padgett, and T. Fumal, Initial paleoseismic studies following the Landers earthquake: implications for fault segmentation and earthquake clustering, Eos Trans. AGU, 74, 43, 67, 1993.

Rubin, C., and K. Sieh, Long recurrence interval for the Emerson fault: implications for

slip rates and probabilistic seismic hazard calculations, Eos Trans. AGU, 74, 43, 612, 1993.

Sieh, K., L. Jones, E. Hauksson, K. Hudnut, D. Eberhart-Phillips, T. Heaton, S. Hough, K. Hutton, H. Kanamori, A. Lilje, S. Lindvall, S. F. McGill, J. Mori, C. Rubin, J. A. Spotila, J. Stock, H-K. Thio, J. Treiman, B. Wernicke, and J. Zachariasen, Near-field investigations of the Landers earthquake sequence, April to July 1992, Science, 260, 171-176, 1993.

Sowers, J.M., J.R. Unruh, W.R. Lettis, and T.D. Rubin, Relationship of the Kickapoo fault to the Johnson Valley and Homestead Valley faults, San Bernardino County, California, Bull. Seismol. Soc. Am., 84, 528-536, 1994.

Tchalenko, J., Similarities between shear zones of different magnitudes, Geol. Soc. Am. Bull., 81, 1625-1640, 1970.

Velasco, A.A., C.J. Ammon, and T. Lay, Empirical Green function deconvolution of broadband surface waves: rupture directivity of the 1992 Landers, California (Mw = 7.3), earthquake, Bull. Seismol. Soc. Am., 84, 735-750, 1994.

Wald, D.J., and T.H. Heaton, Spatial and temporal distribution of slip for the 1992 Landers, California earthquake, Bull. Seismol. Soc. Am., 84, 668-691, 1994.

Wells, D.L., and K.J. Coppersmith, New empirical relationships among magnitude, rupture length, rupture width, rupture area, and surface displacement, Bull. Seismol. Soc. Am., 84, 1994.

Wesnousky, S., Seismological and structural evolution of strike-slip faults, Nature, 335, 340-343, 1988.

Zachariasen, J., and K. Sieh, The kinematics of slip transfer between two *en echelon* strike-slip faults: a case study from the 1992 Landers earthquake, southern California, submitted to J. Geophys. Res., June, 1994.

Table 1a: Offset and dip data for the thrust fault at locations shown in Figure 5 (locations 1 - 13). All dip and net-slip data that was collected on the thrust fault is given here, although we measured many more vertical offsets (Fig. 6) and strike-slip offsets (or lack of strike-slip) (Table 1b) on the thrust fault. Dashes indicate no data, a zero (0) indicates that value was measured to be zero, and a query (?) indicates the value could not be determined. Net dip-slip offsets were calculated as shown in Figure 3c and by extrapolating from the amount of horizontal shortening on the thrust. R.L. = right-lateral, L.L. = left-lateral.

Table 1b: List of linear features that cross the thrust fault rupture with zero strike-slip offset at locations shown in Figure 5 (locations a - w). Eighteen of these features were orthogonal or nearly orthogonal to the thrust scarp, so that apparent lateral offset due to horizontal shortening did not have to be determined. The five oblique features (as indicated) were found to have less than 10 cm of strike-slip offset by estimating the amount of apparent lateral displacement that should have been present given the horizontal shortening (estimated from net dip-slip) at that location.

Table 1a. Measurements of thrust fault offset and dip.

LOCATION	DATA SOURCE	VERTICAL OFF-SET (cm-WSU)	STRIKE-SLIP OFFSET (cm)	FAULT DIP (degrees-SW)	DIP-SLIP OFFSET (cm)
1	trench	74 ± 15	0 (a, Table 1b)	21 ± 5	190 ± 20
2	rule of v's	25 ± 5	?	22 ± 5	-
3	rule of v's	25 ± 5	?	23 ± 5	-
4	shortened bike track	15 ± 5	23 ± 15 r.l.	22 ± 10	33 ± 10
5	offset track	3 ± 1	10 ± 5 l.l.	-	-
6	rule of v's	20 ± 5	?	4 ± 3	-
7	channel cut across thrust	-	0 (p, Table 1b)	17 ± 3	-
8	trench	25 ± 8	0 (q, Table 1b)	5 ± 3	89 ± 20
9	rule of v's	-	0 (t, Table 1b)	25 ± 5	-
10	trench	103 ± 10	?	20 ± 5	222 ± 40
11	shortened dirt road	34 ± 3	0 (u, Table 1b)	17 ± 5	114 ± 15
12	trench	50 ± 5	20 ± 20 r.l.	21 ± 5	120 ± 30
13	offset road	34 ± 5	15 ± 10 r.l.	24 ± 5	85 ± 30

Table 1b. Features crossing the thrust with zero strike-slip offset.

a. dirt road (oblique)	m. channel bed
b. tire tracks	n. dirt road
c. dirt road	o. channel incision
d. dirt road	p. channel incision
e. dirt road (oblique)	q. channel incision
f. dirt road (oblique)	r. channel bed
g. dirt road	s. channel bed
h. tire tracks	t. cemented channel
i. tire tracks	u. dirt road (oblique)
j. tire tracks	v. dirt road
k. tire tracks	w. dirt road (oblique)
l. tire tracks	

Table 2: The ratio of the decrease in slip to the rupture length over which the decrease occurs for each rupture termination in the JVF-HVF stepover (Appendix 5). Note that ratios are significantly greater for ruptures that terminate at the HV slip gap than for those which terminate elsewhere.

Fault	ratio	Fault	ratio
northern end of JVF	3×10^{-4}	southern end of NHVF	4×10^{-3}
southern end of SHVF	7×10^{-4}	northern end of SHVF	1×10^{-3}
southern end of LKF	6×10^{-4}	northern end of LKF	2×10^{-3}
average	5.3×10^{-4}	average	2.3×10^{-3}

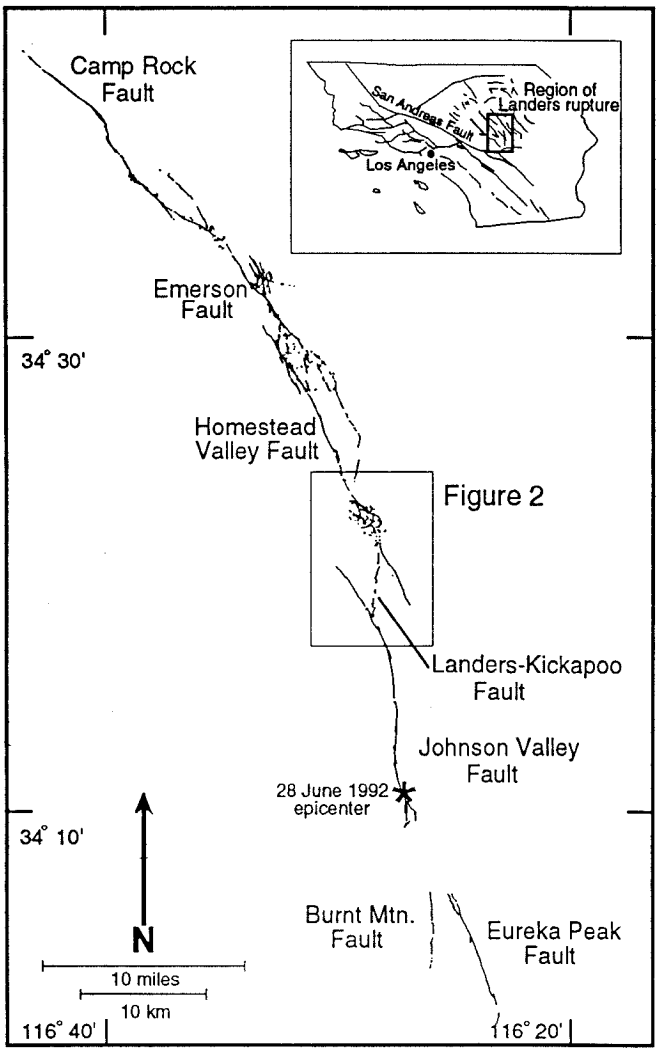

Figure 1: Map of the Landers earthquake surficial rupture in southern California (from Sieh et al., 1993). In this paper, we discuss the ruptures in the stepover between the Johnson Valley and Homestead Valley faults. The 28 June 1992 mainshock epicenter is shown along the Johnson Valley Fault with a star.

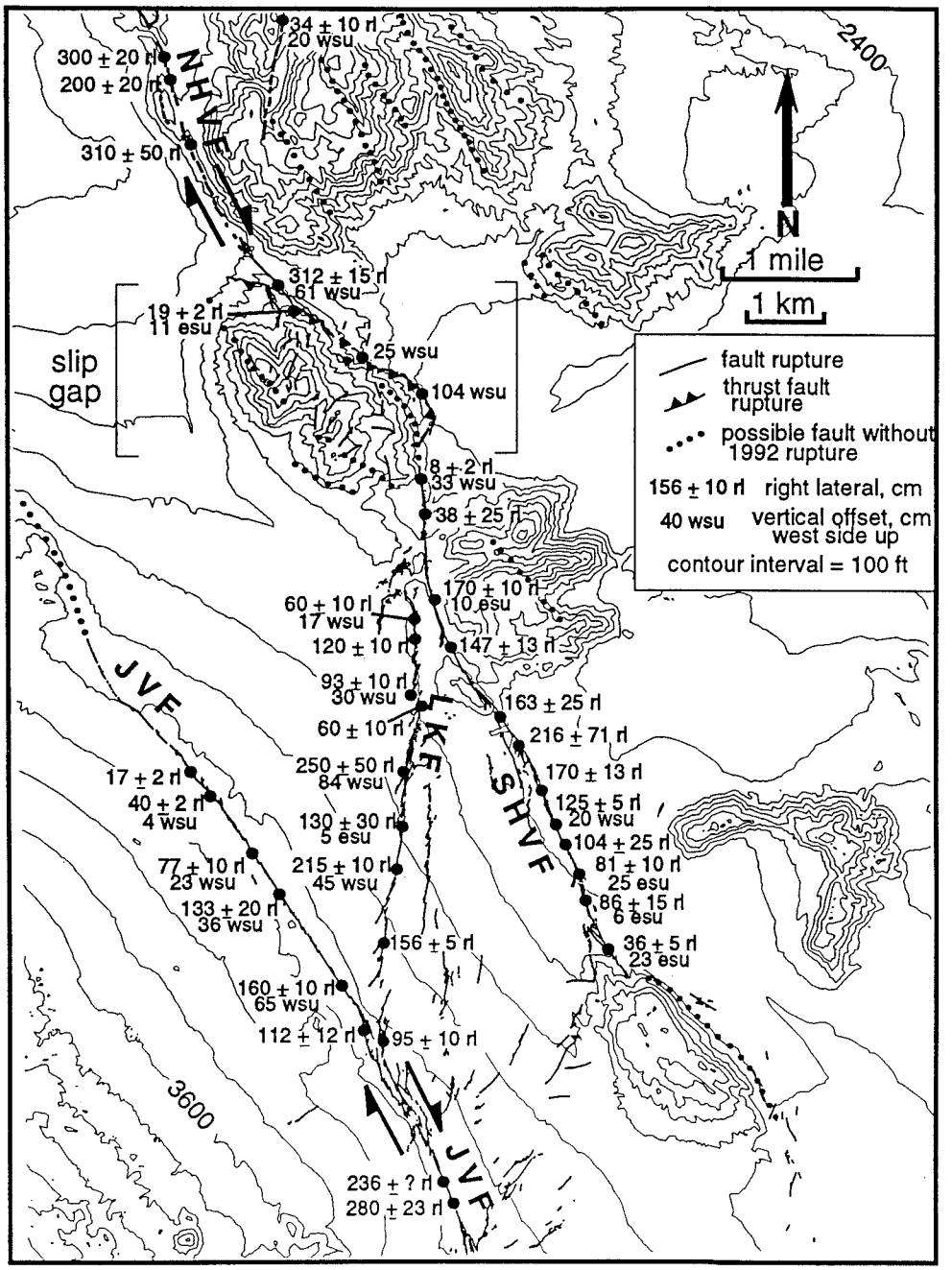

Figure 2: Map of the JVF-HVF stepover and HV slip gap. Surficial ruptures are solid dark lines, topographic contours are thin lines, and possible pre-existing faults without 1992 rupture are dotted lines. Representative offset measurements are included for the major ruptures. Some minor 1992 fractures south of the LKF between the JVF and SHV are from Bryant (1992). NHVF = Northern Homestead Valley fault, LKF = Landers-Kickapoo fault, SHVF = Southern Homestead Valley fault, JVF = Johnson Valley fault.

Figure 3: Determination of dip-slip on the thrust fault in the HV slip gap requires understanding of the geometry of the fault and scarp. A: Photograph and simplified interpretive drawing of a scarp along the thrust fault at location 10 (shown in Fig. 5). View is to the northwest, and vertical offset here is southwest-side-up about 1 meter. The stippled surface is the collapsed hanging-wall block. B: Photograph and simplified interpretive drawing of a hand-dug exposure of the thrust fault at location 8 (shown in Fig. 5). View is to the southeast, and vertical offset here is southwest-side-up about 25 cm (scale bar and 6-cm-wide tape measure for scale). The stippled surface, which is the collapsed hanging-wall block, is separated from bedded alluvium by tensile fractures and overlies a pre-rupture ground surface. The thrust fault surface is defined by crushed pebbles and a zone of relative weakness in the alluvium. C: Schematic diagram that illustrates our interpretation of the thrust fault scarp. This cross section, drawn perpendicular to the thrust trend, represents the general case in which the thrust fault plane could be defined, its dip (d) measured, and tensile fractures (t) separated the collapsed hanging-wall block from the intact hanging-wall block. The ground slope (g) and slope of the collapsed hanging wall (s) were measured in the plane of the trench. A standard range in values for these parameters is given. The lower drawing shows how we assume the collapsed hanging-wall block should be restored. From this assumption, the net dip-slip (X) was calculated using the given equation with the fault dip (d), ground slope (g), and vertical offset (V).

Figure 3:

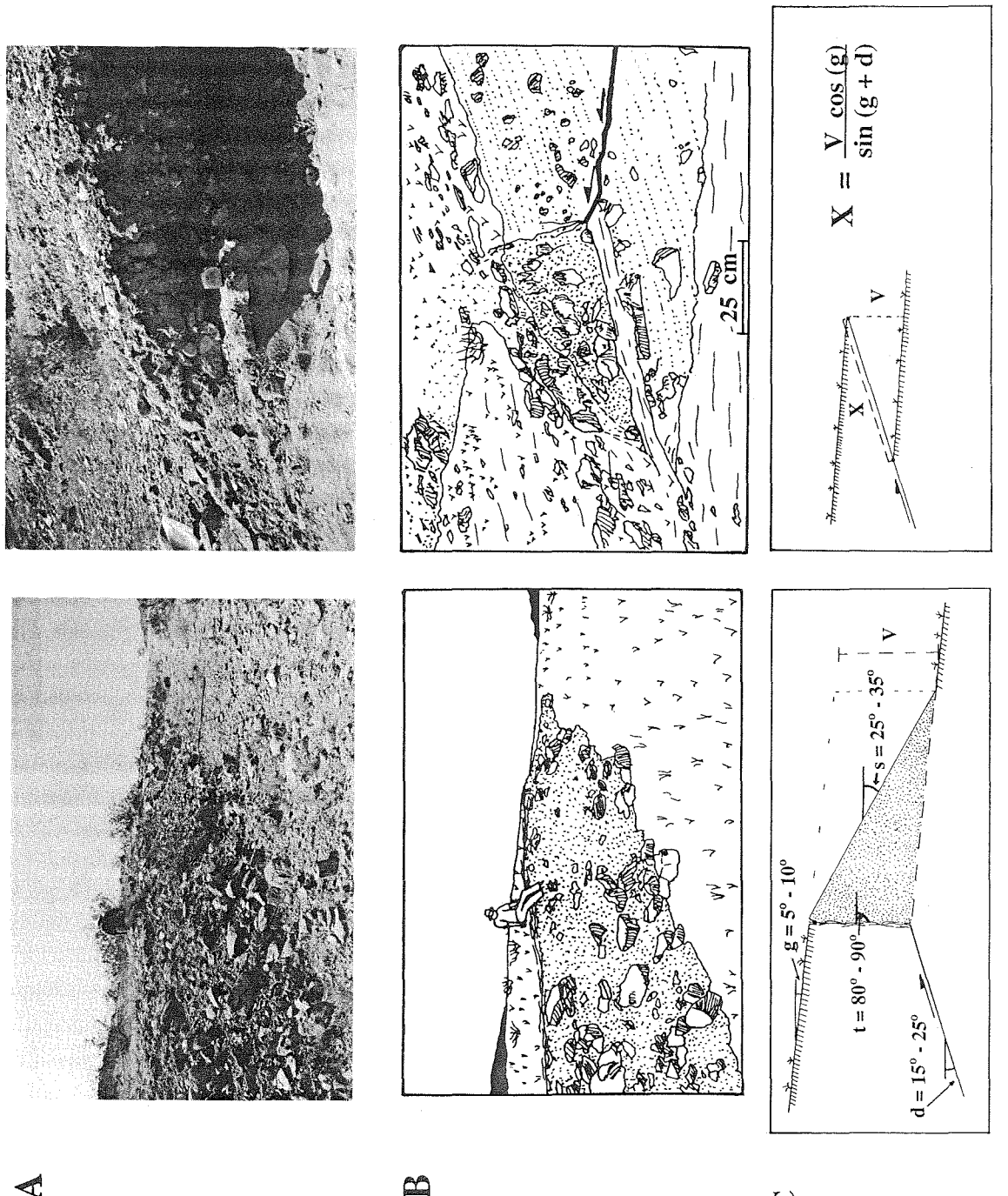

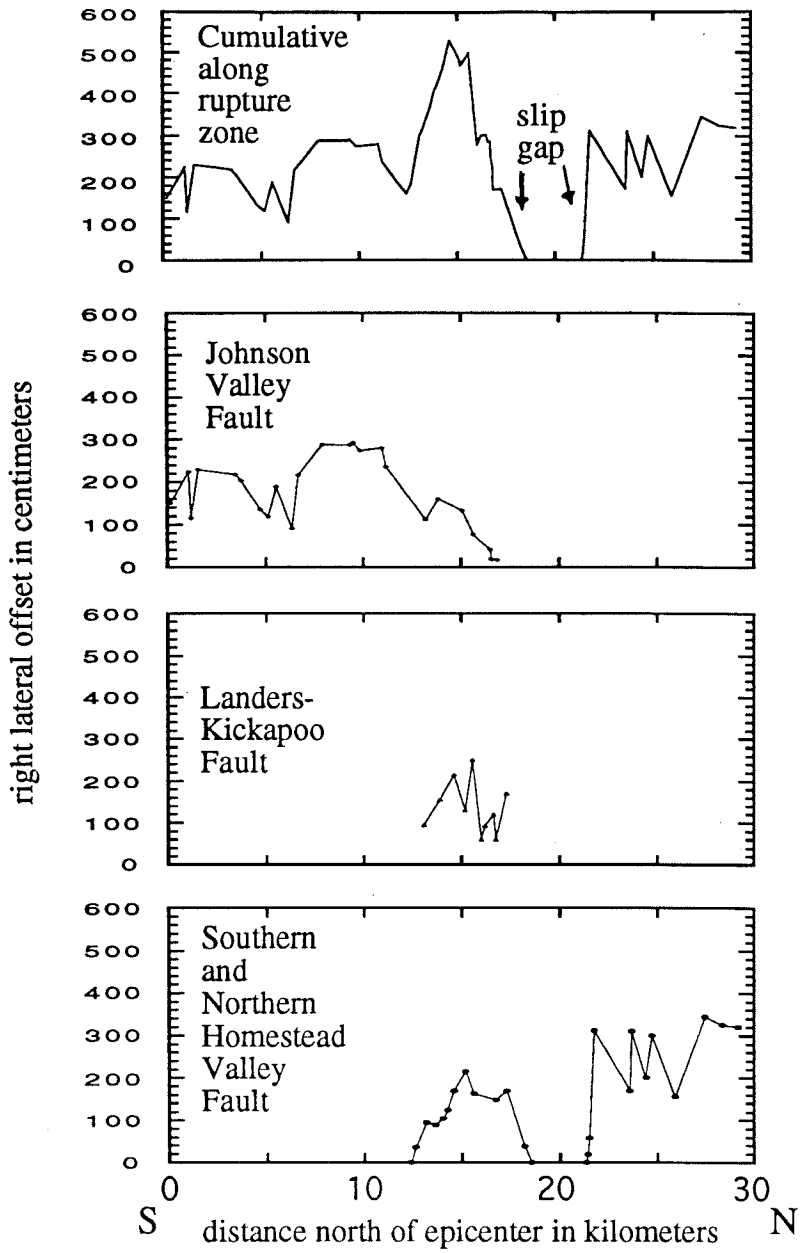

Figure 4: Graph of the distribution of right-slip along the JVF, LKF, SHVF, and NHVF, which demonstrates the gap in dextral slip. The top profile shows the cumulative right-slip, tabulated by linear interpolation. The location of the HV slip gap is indicated. The displacement along the LKF does not decrease to zero because it joins other ruptures at both ends.

Figure 5: Detailed map of the HV slip gap showing adjacent strike-slip ruptures, the thrust fault rupture, and secondary extensional ruptures. Representative offset measurements are shown, except along the thrust fault. Numbers along the thrust fault refer to 13 sites of detailed measurements shown in Table 1a, and letters along the thrust fault refer to 23 sites of zero strike-slip offset shown in Table 1b.

Figure 5:

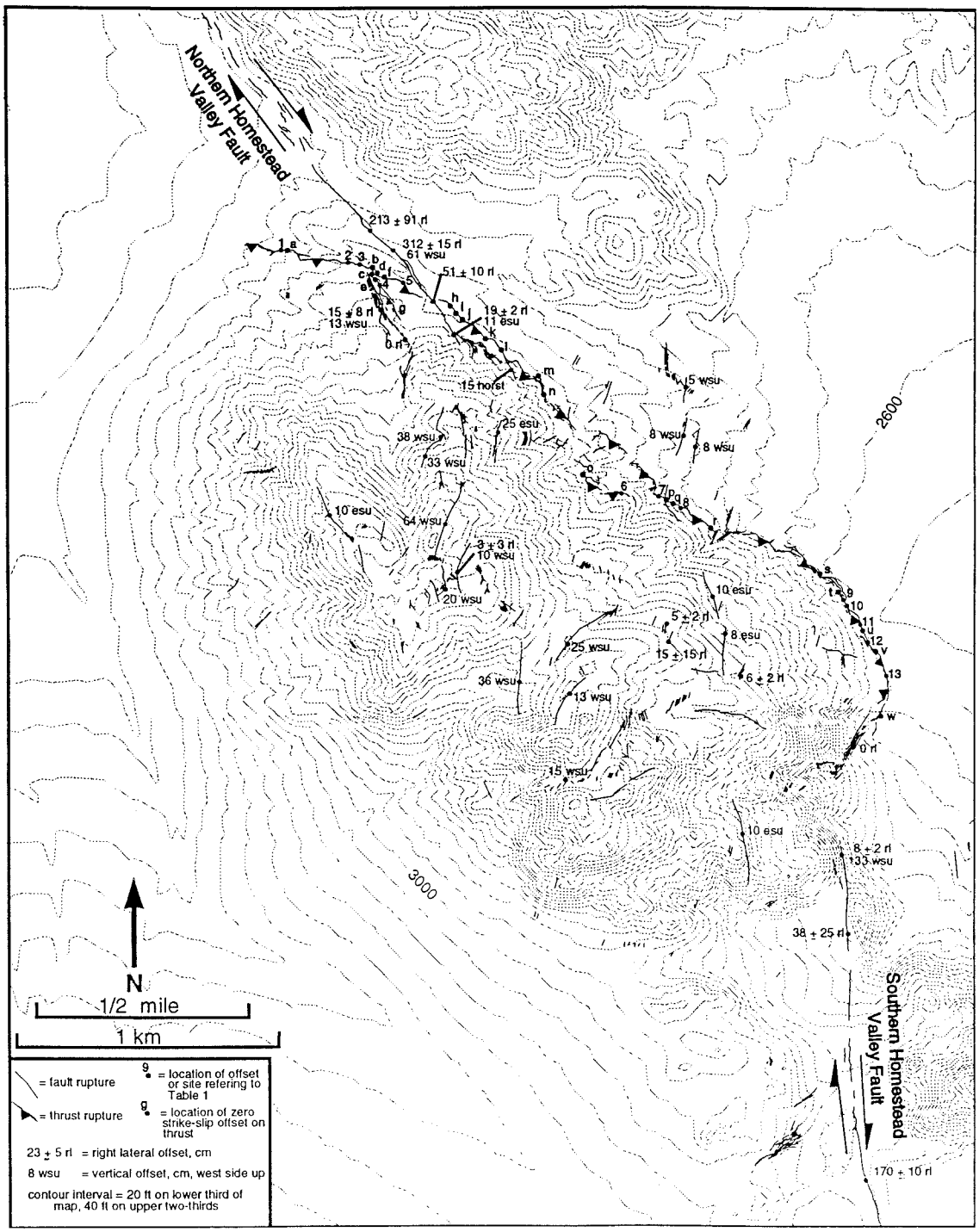
Northern Homestead Valley Fault
213 ± 91 rl
312 ± 15 rl
61 wsu
51 ± 10 rl
15 ± 8 rl
13 wsu
19 ± 2 rl
11 esu
0 rl
15 horiz
5 wsu
25 esu
38 wsu
33 wsu
8 wsu
8 wsu
10 esu
64 wsu
3 ± 3 rl
10 wsu
20 wsu
10 esu
5 ± 2 rl
8 esu
25 wsu
15 ± 15 rl
6 ± 2 rl
36 wsu
13 wsu
0 rl
15 wsu
10 esu
8 ± 2 rl
133 wsu
38 ± 25 rl
170 ± 10 rl
2600
3000
N
1/2 mile
1 km
= fault rupture
= thrust rupture
= location of offset or site refering to Table 1
= location of zero strike-slip offset on thrust
23 ± 5 rl = right lateral offset, cm
8 wsu = vertical offset, cm, west side up
contour interval = 20 ft on lower third of map, 40 ft on upper two-thirds
Southern Homestead Valley Fault

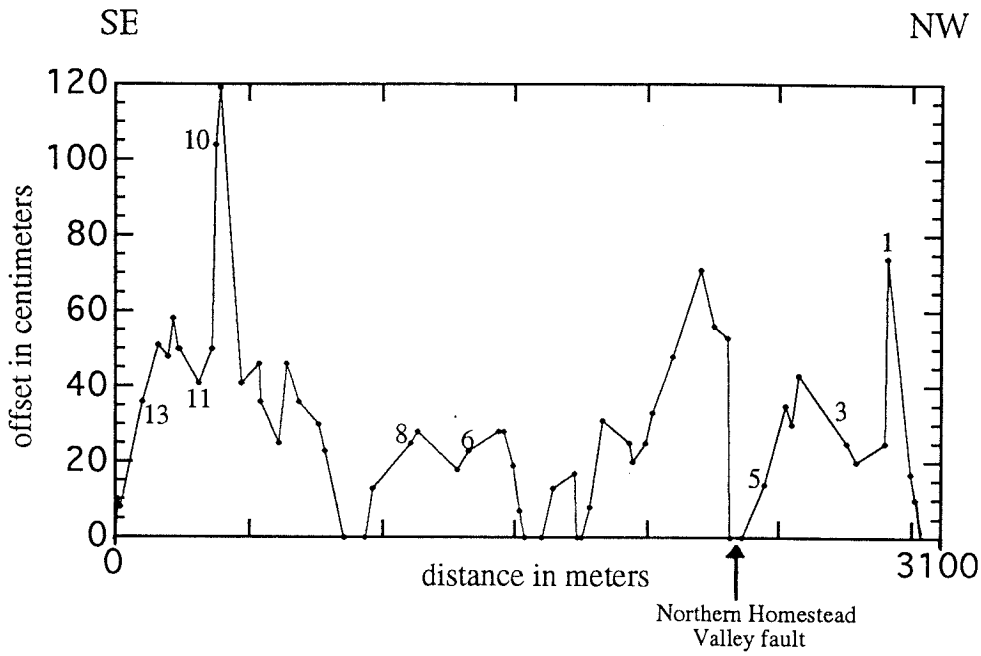

Figure 6: The distribution of southwest-side-up vertical offset along the thrust fault. Numbers refer to locations in Figure 5 and in Table 1a, and the arrow points to the location where the thrust surficial trace is intersected by the NHVF.

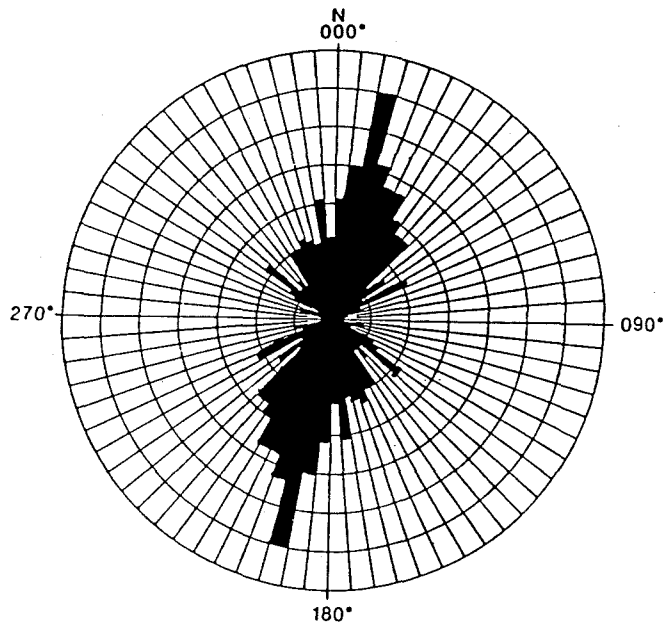

Figure 7: Rose diagram of trends of 322 small extensional fractures in the HV slip gap. Each segment between concentric circles corresponds to 5 fractures of a given trend. The dominant north-northeast trend of the fractures suggests they may be associated with extension produced by dextral shear along the northwest trend of the NHVF.

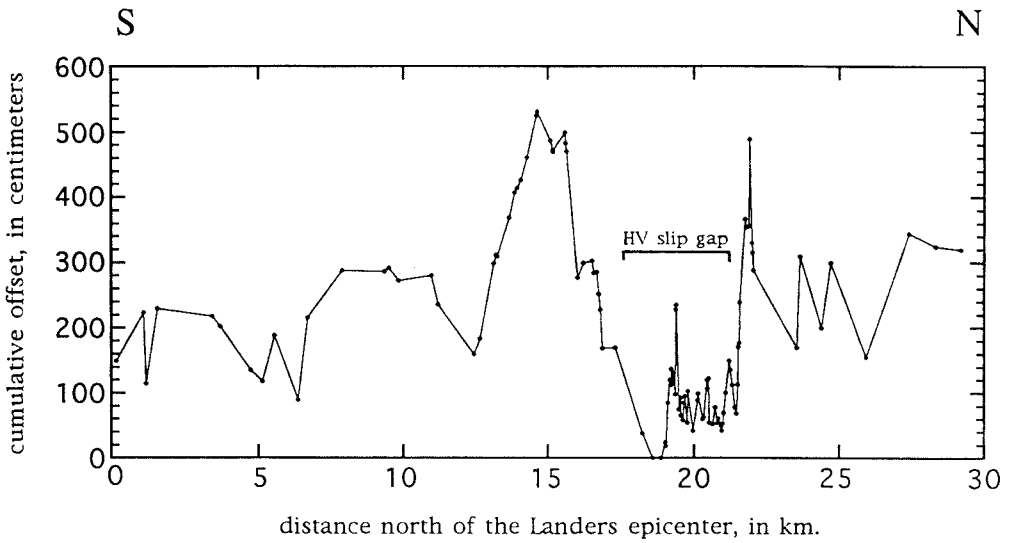

Figure 8: Distribution of cumulative net slip in the JVF-HVF stepover. The right-slip distribution on the major strike-slip faults is taken from Figure 4, and the net dip-slip along the thrust and the vertical offset along the en echelon fractures are included. The locations of all offsets were projected onto the N15°W trend of the Landers zone, and the location of the HV slip gap (as shown) was defined by the limits of major surficial strike-slip ruptures (the terminations of the NHVF and SHVF surficial ruptures). Even with the dip-slip included, the slip gap remains a 5-km-long trough in the slip distribution.

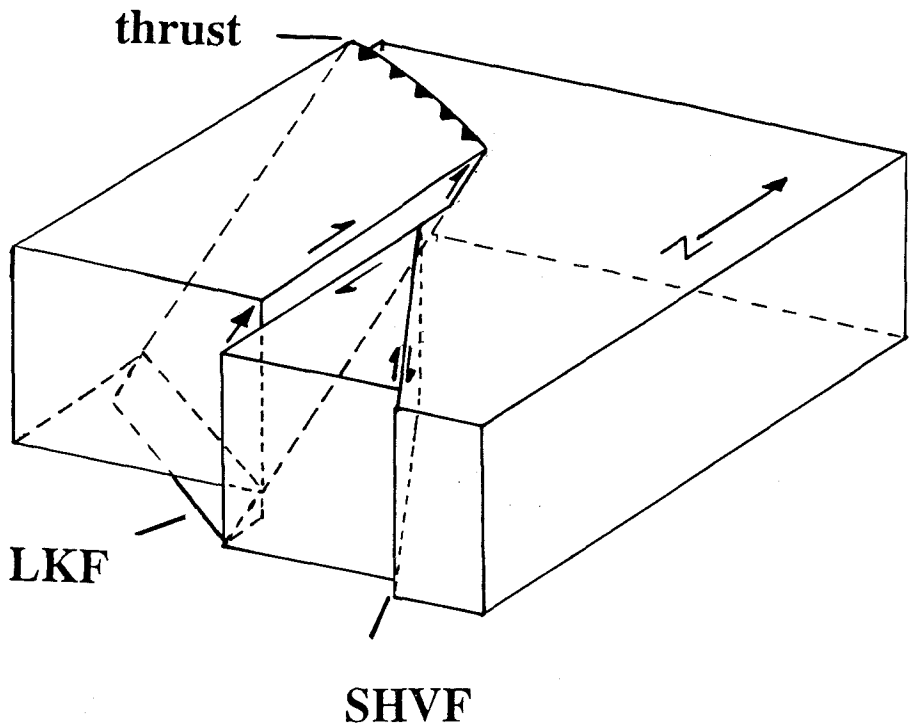

Figure 9: Schematic block diagram of the rigid-block model for the kinematics of the thrust fault and LKF. In this model, the block west of the LKF moved to the north above the thrust, which detaches it from underlying crust. This model is not consistent with several observations. LKF = Landers-Kickapoo fault, SHVF = Southern Homestead Valley fault.

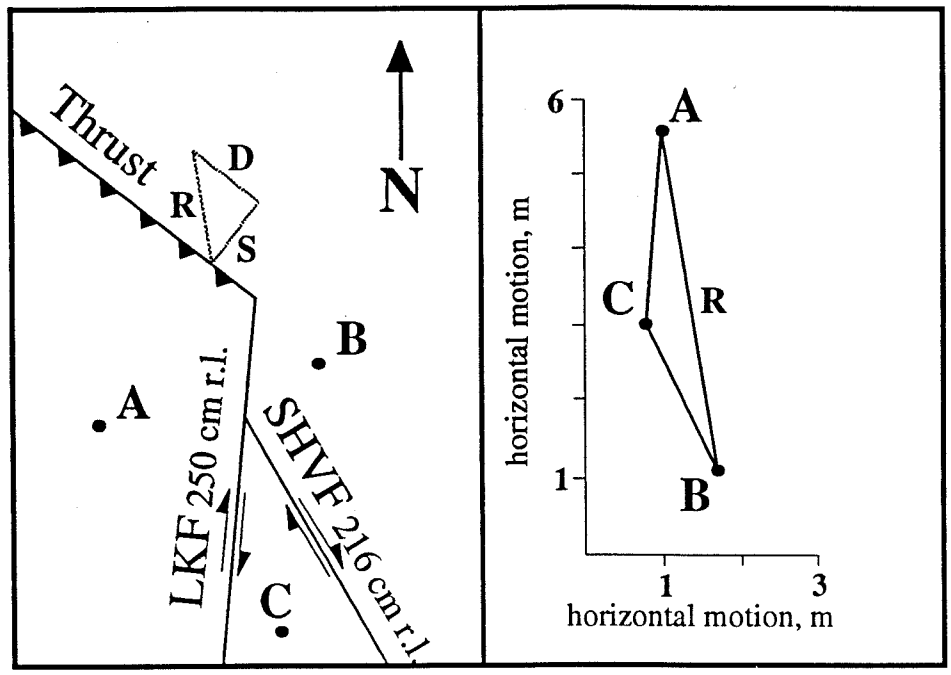

Figure 10: Schematic "displacement-space" vector diagram for the JVF-HVF stepover. On the left, the N05°E LKF, the N27°W SHVF, and the N52°W thrust fault separate three blocks, on which three points (A, B, C) are displaced by the maximum dextral displacements measured on the LKF and SHVF (250 cm and 216 cm respectively). On the right, the displacement vectors between points A and C (across the LKF) and points C and B (across the SHVF) are added to get the resultant vector of displacement between points A and B across the thrust fault (R). This resultant vector is 448 cm directed N10°W, which can be separated into a component of horizontal shortening (S) of 300 cm directed N38°E and a dextral component (D) of 333 cm on the N52°W thrust fault. LKF = Landers-Kickapoo fault, SHVF = Southern Homestead Valley fault.

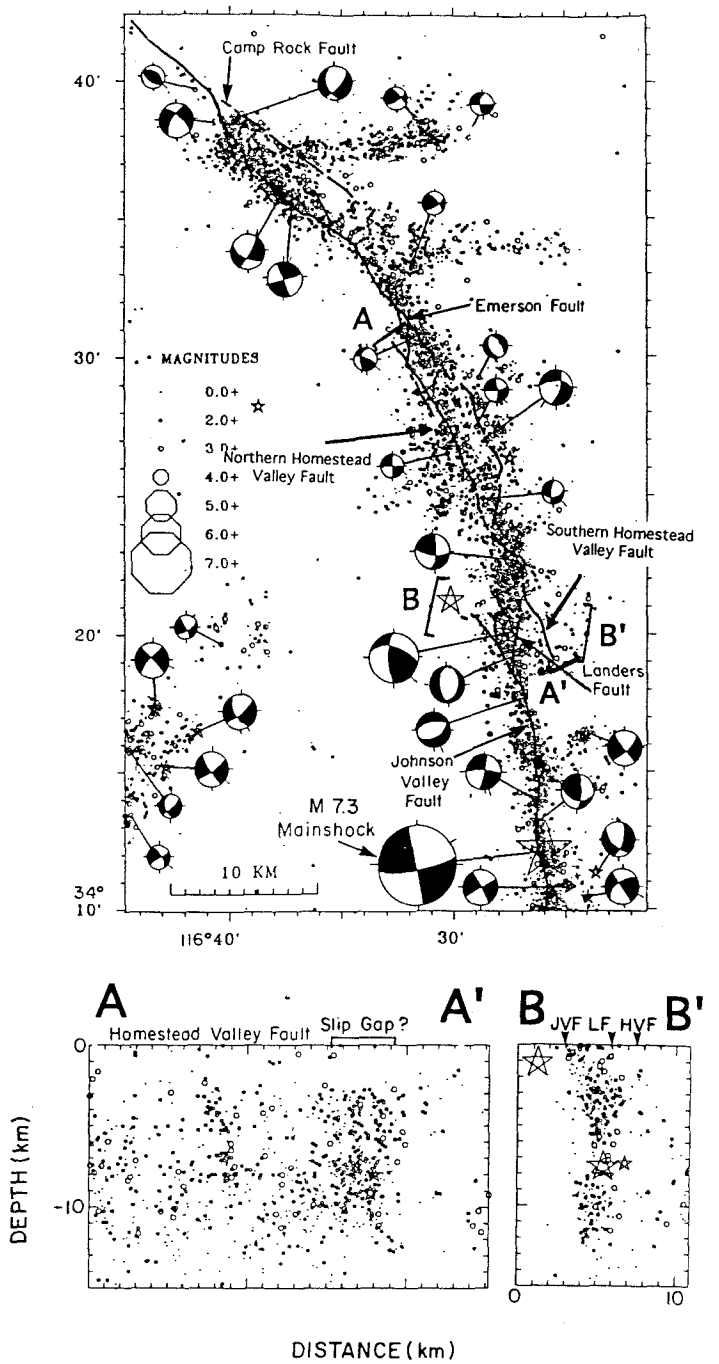

Figure 11: Map and two cross-sections through aftershocks of the Landers earthquake (adapted from Hauksson et al., 1993). Focal mechanisms for the larger aftershocks and the mainshock are shown (focal mechanisms for smaller aftershocks are given in Hauksson, 1994). Note the dense cluster of aftershocks in the HV slip gap, which extends to 14 km depth.

Figure 12: Schematic block diagram of our favored model for fault interaction in the JVF-HVF stepover. The lined planes represent our interpretations of the three-dimensional 1992 rupture surfaces. The thrust fault rupture is limited to the shallow crust, and was induced by stress from a right-lateral couple that resulted, in part, by the slip on the LKF, although these two faults do not intersect or bound a rigid block. The NHVF propagated southwards into the slip gap as the en echelon zone of extension, which appears to have been induced by a right-lateral couple as well. The query (?) represents the uncertainty regarding the geometry of ruptures below the near-surface, although we tentatively show an absence of a through-going rupture that is similar to the discontinuity we interpret at the surface. NHVF = Northern Homestead Valley fault, LF = Landers-Kickapoo fault, SHVF = Southern Homestead Valley fault, JVF = Johnson Valley fault.

Figure 12:

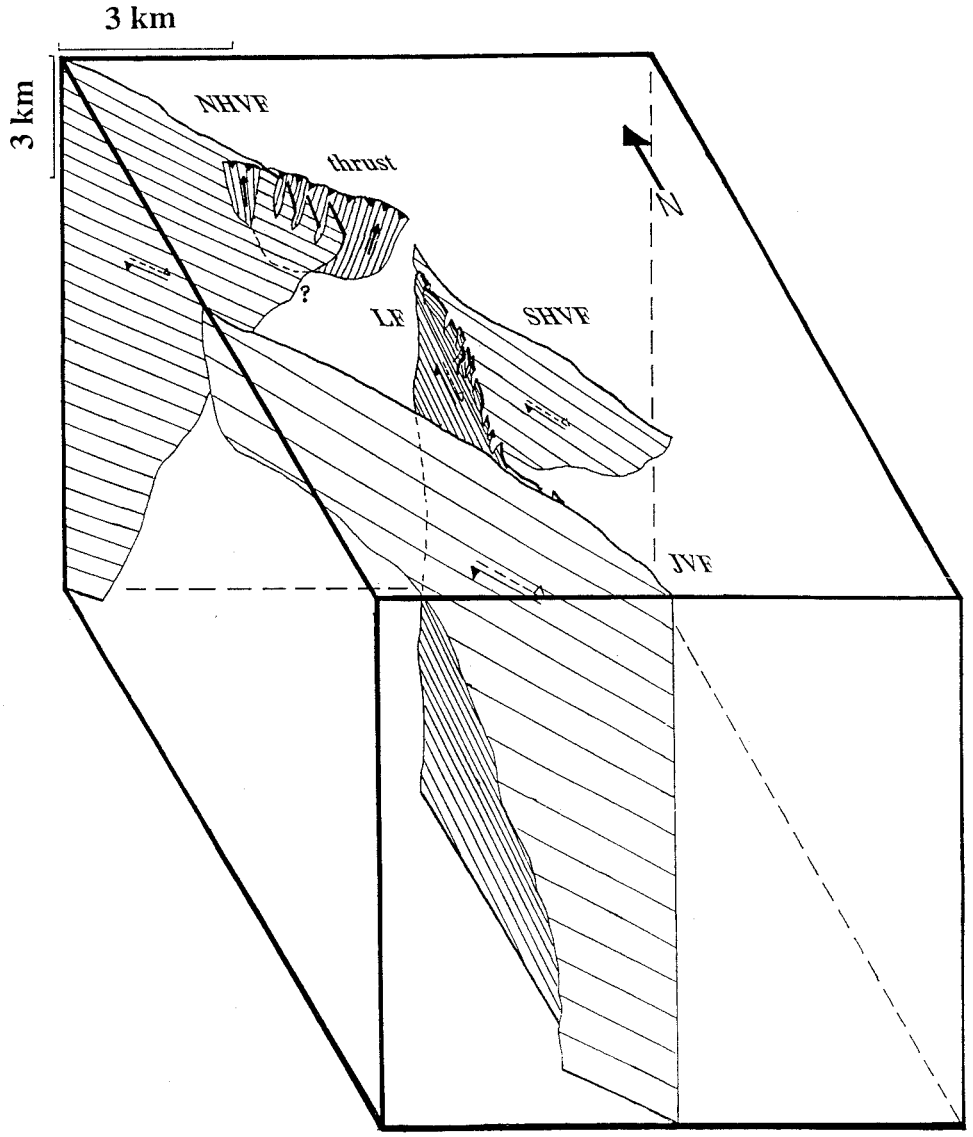

Figure 13: Spacio-temporal progression of the Landers rupture for a combined dislocation model from Wald and Heaton (1994) (adapted from their Figure 16). Each rectangle is the cross section of the rupture plane and shows dextral slip for a different 1-sec interval. The model incorporates strong-ground-motion, teleseismic body-waves, and geodetic data. We propose that the shallow burst of slip in the slip gap 10 to 11 sec into the earthquake is the thrust fault rupture, and that the deep slip during this same interval is the initiation of rupture on the NHVF. Depth is from 0 to 15 km, and rupture is divided into three segments; CR/E (Camp Rock/Emerson faults), HV (Homestead Valley fault), and L/JV (Landers-Kickapoo/Johnson Valley faults). Contour interval is 0.5 m of slip. Lines traversing several rectangles indicate periods of nearly constant rupture velocity.

Figure 13:

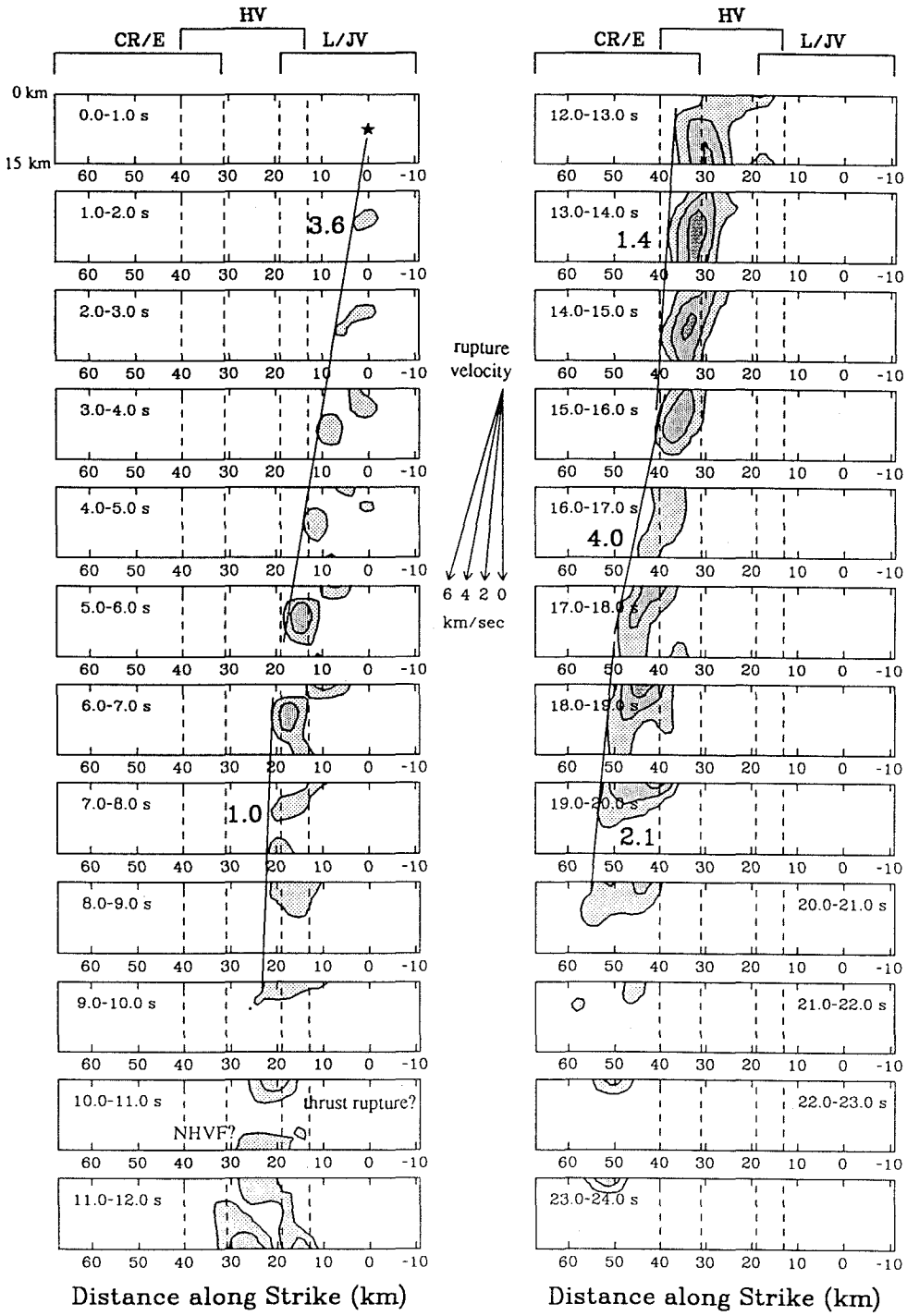
HV
CR/E
L/JV
0 km
15 km
0.0-1.0 s
1.0-2.0 s
3.6
2.0-3.0 s
3.0-4.0 s
4.0-5.0 s
5.0-6.0 s
6.0-7.0 s
7.0-8.0 s
1.0
8.0-9.0 s
9.0-10.0 s
10.0-11.0 s
thrust rupture?
NHVF?
11.0-12.0 s
60 50 40 30 20 10 0 -10
rupture velocity
6 4 2 0
km/sec
12.0-13.0 s
13.0-14.0 s
1.4
14.0-15.0 s
15.0-16.0 s
16.0-17.0 s
4.0
17.0-18.0 s
18.0-19.0 s
19.0-20.0 s
2.1
20.0-21.0 s
21.0-22.0 s
22.0-23.0 s
23.0-24.0 s
Distance along Strike (km)
Distance along Strike (km)